IMPACT FACTOR
11.082
#1 NUCLEAR MEDICINE, MOLECULAR IMAGING AND MOLECULAR RADIOTHERAPY JOURNAL

Vol. 63 ▪ No. 10 ▪ October 2022

JNM
The Journal of Nuclear Medicine

FEATURED ARTICLE

mCRPC Patients Receiving ^{225}Ac-PSMA-617 Therapy in the Post–Androgen Deprivation Therapy Setting: Response to Treatment and Survival Analysis. Mike Sathekge et al. See page 1496.

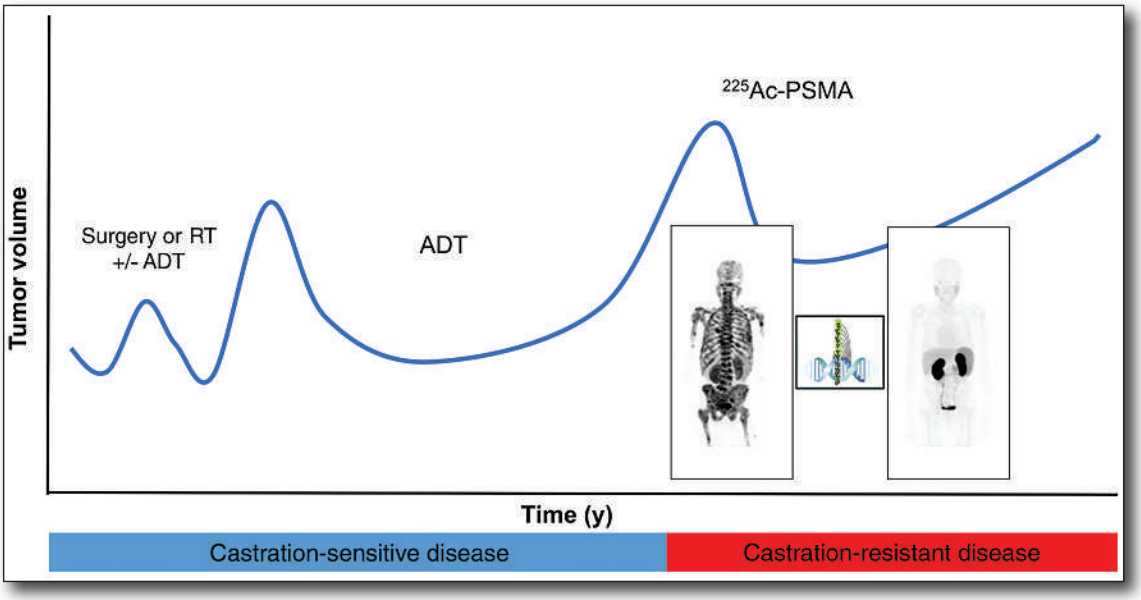

PET and IBD: assessing immune responses with targeted imaging of disease activity in inflammatory bowel disease. Minjung Seo et al. See page 1586.

SNMMI Value Initiative
SOCIETY OF NUCLEAR MEDICINE & MOLECULAR IMAGING

illuccix®
(kit for the preparation of gallium Ga 68 gozetotide Injection)

Illuccix is now separately reimbursed in the hospital outpatient setting!

Consider Illuccix® when evaluating patients with suspected prostate cancer metastasis, who are candidates for initial definitive therapy, or suspected recurrence based on elevated serum prostate-specific antigen (PSA) level.[1]

GUIDED BY ILLUMINATION

^{68}Ga-PSMA-11 (also known as gallium Ga 68 gozetotide) is a widely accessible radioisotope for PSMA PET imaging with:

- Nationwide distribution network of generators and cyclotrons, including those within major academic centers and community health systems[2]
- Capability for either high-volume production or on-site, on-demand production[2,3]
- Flexibility to image patients throughout the day, even on short notice[3]

Illuccix® for the preparation of ^{68}Ga-PSMA-11 is poised to expand the potential of PSMA PET imaging and help guide more informed management decisions in prostate cancer.[1-4]

References: 1. Illuccix (kit for the preparation of gallium Ga 68 gozetotide injection) prescribing information. **2.** Massat MB. Nuclear medicine prepares for greater 68Ga demand. *Appl Radiol.* 2021;50(2):30-31. https://appliedradiology.com/articles/nuclear-medicine-prepares-for-greater-ga-68-demand. Accessed July 13, 2021. 3. Velikyan I. 68Ga-based radiopharmaceuticals: production and application relationship. *Molecules.* 2015;20(7):12913-12943. 4. ARTMS and Telix Pharmaceuticals announce successful production of PSMA-11 with cyclotron produced 68Ga from a solid target [news release]. Telix Pharmaceuticals; January 12, 2021. https://telixpharma.com/news-media/artms-and-telix-pharmaceuticals-announce-successful-production-of-68ga-psma-11-with-cyclotron-produced-68ga-from-a-solid-target/.

TELIX PHARMACEUTICALS

US-ILL-2200073 09/2022

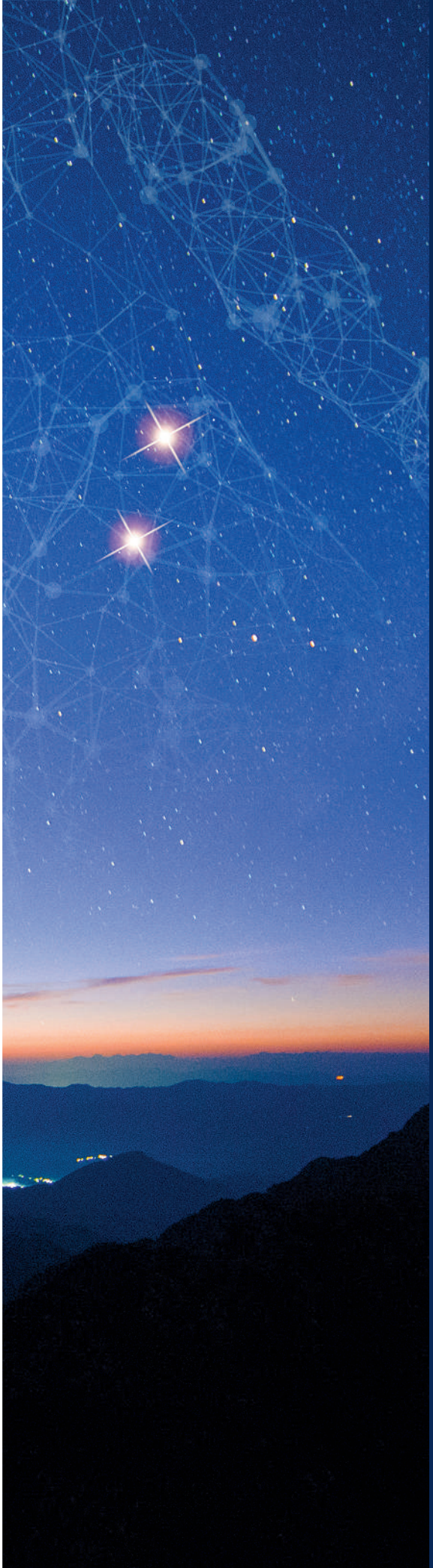

Introducing Illuccix® in your practice

Speak with a live representative to get all your questions answered and prep work completed ahead of time so you receive reimbursement upon delivery of your first dose of Illuccix®. Schedule your one-on-one onboarding appointment by:

- Calling 1-(844) 45-TELIX (1-844-455-8638)
- Going to https://illuccixhcp.com/booking

This service is available Monday through Friday 8:00 AM to 8:00 PM ET.

INDICATIONS AND USAGE

Illuccix®, after radiolabeling with Ga 68, is a radioactive diagnostic agent indicated for positron emission tomography (PET) of prostate-specific membrane antigen (PSMA) positive lesions in men with prostate cancer:

- with suspected metastasis who are candidates for initial definitive therapy
- with suspected recurrence based on elevated serum prostate-specific antigen (PSA) level

Important Safety Information

WARNINGS AND PRECAUTIONS

Risk for Misdiagnosis

Image interpretation errors can occur with gallium Ga 68 gozetotide PET. A negative image does not rule out the presence of prostate cancer and a positive image does not confirm the presence of prostate cancer. The performance of gallium Ga 68 gozetotide for imaging of biochemically recurrent prostate cancer seems to be affected by serum PSA levels and by site of disease. The performance of gallium Ga 68 gozetotide for imaging of metastatic pelvic lymph nodes prior to initial definitive therapy seems to be affected by Gleason score. Gallium Ga 68 gozetotide uptake is not specific for prostate cancer and may occur with other types of cancer as well as non-malignant processes such as Paget's disease, fibrous dysplasia, and osteophytosis. Clinical correlation, which may include histopathological evaluation of the suspected prostate cancer site, is recommended.

Radiation Risks

Gallium Ga 68 gozetotide contributes to a patient's overall long-term cumulative radiation exposure. Long-term cumulative radiation exposure is associated with an increased risk for cancer. Ensure safe handling to minimize radiation exposure to the patient and health care workers. Advise patients to hydrate before and after administration and to void frequently after administration.

ADVERSE REACTIONS

The safety of gallium Ga 68 gozetotide was evaluated in 960 patients, each receiving one dose of gallium Ga 68 gozetotide. The average injected activity was 188.7 ± 40.7 MBq (5.1 ± 1.1 mCi). No serious adverse reactions were attributed to gallium Ga 68 gozetotide. The most commonly reported adverse reactions were nausea, diarrhea, and dizziness, occurring at a rate of < 1%.

DRUG INTERACTIONS

Androgen deprivation therapy and other therapies targeting the androgen pathway Androgen deprivation therapy (ADT) and other therapies targeting the androgen pathway, such as androgen receptor antagonists, can result in changes in uptake of gallium Ga 68 gozetotide in prostate cancer. The effect of these therapies on performance of gallium Ga 68 gozetotide PET has not been established.

You are encouraged to report suspected adverse reactions of prescription drugs to the FDA.

Please note this information is not comprehensive. Please see brief summary of the full prescribing information on the next page, or visit illuccixhcp.com for full prescribing information.

Illuccix (kit for the preparation of gallium Ga 68 gozetotide Injection)
BRIEF SUMMARY: Consult the full prescribing information for complete product information

WARNINGS AND PRECAUTIONS

Risk for Misdiagnosis
Image interpretation errors can occur with gallium Ga 68 gozetotide PET. A negative image does not rule out the presence of prostate cancer and a positive image does not confirm the presence of prostate cancer. The performance of gallium Ga 68 gozetotide for imaging of biochemically recurrent prostate cancer seems to be affected by serum PSA levels and by site of disease [see Clinical Studies (14)]. The performance of gallium Ga 68 gozetotide for imaging of metastatic pelvic lymph nodes prior to initial definitive therapy seems to be affected by Gleason score [see Clinical Studies (14)]. Gallium Ga 68 gozetotide uptake is not specific for prostate cancer and may occur with other types of cancer as well as non-malignant processes such as Paget's disease, fibrous dysplasia, and osteophytosis. Clinical correlation, which may include histopathological evaluation of the suspected prostate cancer site, is recommended.

Radiation Risks
Gallium Ga 68 gozetotide contributes to a patient's overall long-term cumulative radiation exposure. Long-term cumulative radiation exposure is associated with an increased risk for cancer. Ensure safe handling to minimize radiation exposure to the patient and health care workers. Advise patients to hydrate before and after administration and to void frequently after administration [see Dosage and Administration (2.1, 2.3)].

ADVERSE REACTIONS

Clinical Trials Experience
Because clinical trials are conducted under widely varying conditions, adverse reaction rates observed in the clinical trials of a drug cannot be directly compared to rates in the clinical trials of another drug and may not reflect the rates observed in practice. The safety of ILLUCCIX has been established based on studies of another formulation of gallium Ga 68 gozetotide in patients with prostate cancer [see Clinical Studies (14)]. Below is a display of the adverse reactions in these studies. The safety of gallium Ga 68 gozetotide was evaluated in 960 patients, each receiving one dose of gallium Ga 68 gozetotide. The average injected activity was 188.7 ± 40.7 MBq (5.1 ± 1.1 mCi). No serious adverse reactions were attributed to gallium Ga 68 gozetotide. The most commonly reported adverse reactions were nausea, diarrhea, and dizziness, occurring at a rate of < 1%.

DRUG INTERACTIONS

Androgen deprivation therapy and other therapies targeting the androgen pathway Androgen deprivation therapy (ADT) and other therapies targeting the androgen pathway, such as androgen receptor antagonists, can result in changes in uptake of gallium Ga 68 gozetotide in prostate cancer. The effect of these therapies on performance of gallium Ga 68 gozetotide PET has not been established.

USE IN SPECIFIC POPULATIONS

Pregnancy

Risk Summary
ILLUCCIX is not indicated for use in females. There are no available data with gallium Ga 68 gozetotide injection use in pregnant women to evaluate for a drug-associated risk of major birth defects, miscarriage, or adverse maternal or fetal outcomes. All radiopharmaceuticals, including ILLUCCIX, have the potential to cause fetal harm depending on the fetal stage of development and the magnitude of the radiation dose. Animal reproduction studies have not been conducted with gallium Ga 68 gozetotide.

Lactation

Risk Summary
ILLUCCIX is not indicated for use in females. There are no data on the presence of gallium Ga 68 gozetotide in human milk, the effect on the breastfed infant, or the effect on milk production.

Pediatric Use

The safety and effectiveness of gallium Ga 68 gozetotide in pediatric patients have not been established.

Geriatric Use

The efficacy of gallium Ga 68 gozetotide PET in geriatric patients with prostate cancer is based on data from two prospective studies [see Clinical Studies (14)]. Most patients in these trials were 65 years of age or older (72%). The efficacy and safety profiles of gallium Ga 68 gozetotide appear similar in younger adult and geriatric patients with prostate cancer, although the number of younger adult patients in the trials was not large enough to allow definitive comparison.

TELIX PHARMACEUTICALS

US-ILL-2200073 09/2022

JNM

Volume 63 • Number 10 • October 2022

JNM The Journal of NUCLEAR MEDICINE

The Official Publication of **SNMMI**

MISSION STATEMENT: *The Journal of Nuclear Medicine* advances the knowledge and practice of molecular imaging and therapy and nuclear medicine to improve patient care through publication of original basic science and clinical research.

JNM (ISSN 0161-5505 [print]; ISSN 2159-662X [online]) is published monthly by SNMMI, 1850 Samuel Morse Drive, Reston, VA 20190-5316. Periodicals postage is paid at Herndon, VA, and additional mailing offices. Postmaster, send address changes to *The Journal of Nuclear Medicine,* 1850 Samuel Morse Drive, Reston, VA 20190-5316. The costs of publication of all nonsolicited articles in *JNM* were defrayed in part by the payment of page charges. Therefore, and solely to indicate this fact, these articles are hereby designated "advertisements" in accordance with 18 USC section 1734.

DISCLOSURE OF COMMERCIAL INTEREST: Johannes Czernin, MD, editor-in-chief of *The Journal of Nuclear Medicine,* has indicated that he is a founder of Sofie Biosciences and holds equity in the company and in intellectual property invented by him, patented by the University of California, and licensed to Sofie Biosciences. He is also a founder and board member of Trethera Therapeutics and holds equity in the company and in intellectual property invented by him, patented by the University of California, and licensed to Triangle. He also serves on the medical advisory board of Actinium Pharmaceuticals and on the scientific advisory boards of POINT Biopharma, RayzeBio, and Jubilant Pharma and is a consultant for Amgen. No other potential conflicts of interest were reported. Manuscripts submitted to *JNM* with potential conflicts are handled by a guest editor.

EDITORIAL COMMUNICATIONS should be sent to: Editor-in-Chief, Johannes Czernin, MD, *JNM* Office, SNMMI, 1850 Samuel Morse Drive, Reston, VA 20190-5316. Phone: (703) 326-1185; Fax: (703) 708-9018. To submit a manuscript, go to https://submit-jnm.snmjournals.org.

BUSINESS COMMUNICATIONS concerning permission requests should be sent to the publisher, SNMMI, 1850 Samuel Morse Drive, Reston, VA 20190-5316; (703) 708-9000; home page address: jnm.snmjournals.org. Subscription requests and address changes should be sent to Membership Department, SNMMI at the address above. Notify the Society of change of address and telephone number at least 30 days before date of issue by sending both the old and new addresses. Claims for copies lost in the mail are allowed within 90 days of the date of issue. Claims are not allowed for issues lost as a result of insufficient notice of change of address. For information on advertising, contact Team SNMMI (Kevin Dunn, Rich Devanna, and Charlie Meitner; (201) 767-4170; fax: (201) 767-8065; TeamSNMMI@cunnasso.com). Advertisements are subject to editorial approval and are restricted to products or services pertinent to nuclear medicine. Closing date is the first of the month preceding the date of issue.

INDIVIDUAL SUBSCRIPTION RATES for the 2022 calendar year are $603 within the United States and Canada; $648 elsewhere. Make checks payable to the SNMMI. CPC IPM Sales Agreement No. 1415158. Sales of individual back copies from 1999 through the current issue are available for $60 at http://www.snmmi.org/subscribe (subscriptions@snmmi.org; fax: (703) 667-5134). Individual articles are available for sale online at http://jnm.snmjournals.org.

JNM The Journal of NUCLEAR MEDICINE

Lantheus Xenon Xe-133 Gas

PROVEN | RELIABLE | TRUSTED

- Optimized vial size and delivery system[1]
- Calidose® Dispenser System is specifically designed and FDA approved for use with Lantheus Medical Imaging Xenon-133[1]
- Lantheus Medical Imaging is a leading U.S. manufacturer of Xenon-133[2]
- We are the longest continuous supplier of Xenon-133 since its launch in 1971[3]

Calidose® Dispenser

Specify *Lantheus Xenon Xe-133*
when ordering from your local Radiopharmacy

To order from Lantheus, contact your Lantheus Sales Representative or call Customer Service: 1-800-299-3431
www.lantheus.com

Lantheus

FIND > FIGHT > FOLLOW™

Please see full Prescribing Information on following page.

INDICATIONS AND USAGE:
Inhalation of Xenon Xe 133 Gas has proved valuable for the evaluation of pulmonary function and for imaging the lungs. It may also be applied to assessment of cerebral flow.

CONTRAINDICATIONS:
None known.

Important Safety Information:
Adverse reactions related to the use of this agent have not been reported to date.

WARNINGS:
Xenon Xe 133 Gas delivery systems, i.e., respirators or spirometers, and associated tubing assemblies must be leakproof to avoid loss of radioactivity into environs not specifically protected by exhaust systems.

Xenon Xe 133 adheres to some plastics and rubber and should not be allowed in tubing or respirator containers.

The unrecognized loss of radioactivity from the dose for administration may render the study non-diagnostic.

The vial stopper contains dry natural rubber latex and may cause allergic reactions in providers or patients who are sensitive to latex.

PRECAUTIONS:
General:
Xenon Xe 133, as well as other radioactive drugs, must be handled with care and appropriate safety measures should be used to minimize radiation exposure to patients and to clinical personnel.

Radiopharmaceuticals should be used only by physicians who are qualified by training and experience in the safe use and handling of radionuclides and whose experience and training have been approved by the appropriate government agency authorized to license the use of radionuclides.

References: 1. Xenon Xe-133 Gas [package insert], N. Billerica, MA: Lantheus Medical Imaging, Inc. 2. ©2022 Millennium Research Group, Inc. All rights reserved. Reproduction, distribution, transmission or publication is prohibited. Reprinted with permission. 3. Quality data on file, Lantheus Medical Imaging, Inc.

XENON Xe 133 GAS

FOR DIAGNOSTIC USE

DESCRIPTION: Xenon Xe 133 Gas is supplied in a mixture of xenon gas (5%) in carbon dioxide (95%). It is contained within septum sealed glass vials and is suitable for inhalation in the diagnostic evaluation of pulmonary function and imaging, as well as assessment of cerebral blood flow. Xenon Xe 133 Gas is reactor-produced as a by-product of Uranium U235 fission. Each vial contains the labeled amount of Xenon Xe 133 radioactivity at the time of calibration. The contents of the vial are in gaseous form, contain no preservatives, and are ready for use.

Xenon Xe 133 is chemically and physiologically related to elemental Xenon, a non-radioactive monoatomic gas which is physiologically inert except for anesthetic properties at high doses.

PHYSICAL CHARACTERISTICS

Xenon Xe 133 decays by beta and gamma emissions with a half-life of 5.245 days.[1] Significant radiations which are emitted by the nuclide are listed in Table 1.

Table 1. Principal Radiation Emission Data from Xenon-133

Radiation	Mean Energy (KeV)	Mean % per Disintegration
Beta-2	100.6	99.3
Ce-K-2	45.0	53.3
Ce-L-2	75.3	8.1
Ce-M-2	79.8	1.7
Gamma-2	81.0	36.5
$K_{\alpha 2}$X-ray	30.6	13.6
$K_{\alpha 1}$X-ray	31.0	25.3
K_{β}X-ray	35.0	9.1

[1]Kocher, David C., "Radioactive Decay Data Tables," DOE/TIC-11026, p. 138,1981.

EXTERNAL RADIATION

The specific gamma ray constant for Xenon Xe 133 is 3.6 microcoulombs/Kg-MBq-hr (0.51R/hr-mCi) at 1 cm. The first half value thickness of lead is 0.0035 cm. A range of values for the relative attenuation of the radiation emitted by this radionuclide that results from the interposition of various thicknesses of Pb is shown in Table 2. For example, the use of 0.20 cm of Pb will decrease the external radiation exposure by a factor of 1,000.

Table 2. Radiation Attenuation by Lead Shielding

cm of Pb	Radiation Attenuation Factor
0.0035	0.5
0.037	10^{-1}
0.12	10^{-2}
0.20	10^{-3}
0.29	10^{-4}

To correct for physical decay of this radionuclide, the fractions that remain at selected time intervals after the time of calibration are shown in Table 3.

Table 3. Xenon Xe 133 Physical Decay Chart (Half Life 5.245 days)

Day	Fraction Remaining	Day	Fraction Remaining
0*	1.000	8	.349
1	.877	9	.302
2	.768	10	.268
3	.674	11	.235
4	.591	12	.206
5	.518	13	.181
6	.452	14	.157
7	.398		

* Calibration day

CLINICAL PHARMACOLOGY: Xenon Xe 133 is a readily diffusible gas which is neither utilized nor produced by the body. It passes through cell membranes and freely exchanges between blood and tissue. It tends to concentrate more in body fat than in blood, plasma, water or protein solutions. In the concentrations used for diagnostic purposes it is physiologically inactive. Inhaled Xenon Xe 133 Gas will enter the alveolar wall and enter the pulmonary venous circulation via the capillaries. Most of the Xenon Xe 133 that enters the circulation from a single breath is returned to the lungs and exhaled after a single pass through the peripheral circulation.

INDICATIONS AND USAGE: Inhalation of Xenon Xe 133 Gas has proved valuable for the evaluation of pulmonary function and for imaging the lungs. It may also be applied to assessment of cerebral flow.

CONTRAINDICATIONS: None known.

WARNINGS:

Xenon Xe 133 Gas delivery systems, i.e., respirators or spirometers, and associated tubing assemblies must be leakproof to avoid loss of radioactivity into the environs not specifically protected by exhaust systems.

Xenon Xe 133 adheres to some plastics and rubber and should not be allowed to stand in tubing or respirator containers. The unrecognized loss of radioactivity from the dose for administration may render the study non-diagnostic.

The vial stopper contains dry natural rubber latex and may cause allergic reactions in providers or patients who are sensitive to latex.

PRECAUTIONS:

General

Xenon Xe 133, as well as other radioactive drugs, must be handled with care and appropriate safety measures should be used to minimize radiation exposure to clinical personnel. Also, care should be taken to minimize radiation exposure to patients consistent with proper patient management.

Exhaled Xenon Xe 133 Gas should be controlled in a manner that is in compliance with the appropriate regulations of the government agency authorized to license the use of radionuclides.

Radiopharmaceuticals should be used only by physicians who are qualified by training and experience in the safe use and handling of radionuclides and whose experience and training have been approved by the appropriate government agency authorized to license the use of radionuclides.

Carcinogenesis, Mutagenesis, Impairment of Fertility

No long term animal studies have been performed to evaluate carcinogenic potential or whether Xenon Xe 133 affects fertility in males or females.

Pregnancy

Animal reproductive studies have not been conducted with Xenon Xe 133 Gas. It is also not known whether Xenon Xe 133 Gas can cause fetal harm when administered to a pregnant woman or can affect reproduction capacity. Xenon Xe 133 Gas should be given to a pregnant woman only if clearly needed.

Ideally, examination using radiopharmaceuticals, especially those elective in nature in a woman of childbearing capability, should be performed during the first few (approximately 10) days following the onset of menses.

Nursing Mothers

It is not known whether Xenon Xe 133 is excreted in human milk. Many drugs are excreted in human milk, therefore formula feedings should be substituted for breast feeding, because of the potential for adverse reactions in nursing infants.

Pediatric Use

Safety and effectiveness in the pediatric population has not been established.

Geriatric Use

Clinical studies of Xenon Xe 133 Gas did not include sufficient numbers of subjects aged 65 and over to determine whether they respond differently from younger subjects. Other reported clinical experience has not identified differences in responses between the elderly and younger patients. In general, dose selection for an elderly patient should be cautious, usually starting at the low end of the dosage range, reflecting the greater frequency of decreased hepatic, renal, or cardiac function, and of concomitant disease or other drug therapy.

ADVERSE REACTIONS: Adverse reactions related to the use of this agent have not been reported to date.

DOSAGE AND ADMINISTRATION: Xenon Xe 133 Gas is administered by inhalation from closed respirator systems or spirometers.

The suggested activity range employed for inhalation by the average adult patient (70 kg) is:

Pulmonary function including imaging: 74-1110 MBq (2-30 mCi) in 3 liters of air.

Cerebral blood flow: 370-1110 MBq (10-30 mCi) in 3 liters of air.

The patient dose should be measured by a suitable radioactivity calibration system immediately prior to administration.

RADIATION DOSIMETRY

The estimated absorbed radiation doses[2] to an average patient (70 kg) for pulmonary perfusion and cerebral blood flow studies from a maximum dose of 1110 MBq (30 mCi) of Xenon Xe 133 in 3 liters of air are shown in Table 4.

Table 4. Radiation Doses

	Effective Half-Time	Lungs*	Brain	Whole Body
			mGy/1110 MBq	(rads/30 mCi)
Pulmonary Perfusion	2 min.	2.5 (0.25)	0.014 (0.0014)	0.027 (0.0027)
Cerebral Blood Flow	5 min.	6.3 (0.63)	0.035 (0.0035)	0.068 (0.0068)

* 99% of activity is in lungs.

[2]Method of Calculation: A Schema for Absorbed-Dose Calculation for Biologically Distributed Radionuclides, Supplement No. 1, MIRD pamphlet No. 1, *J. Nucl. Med.*, p.7 (1968).

HOW SUPPLIED: The Xenon Xe 133 Gas is supplied as part of the Calidose™ system, consisting of 3 mL unit dose vials and the Calidose™ dispenser for shielded dispensing.

Normally vials containing either 370 or 740 MBq (10 or 20 mCi)/vial, packed 1 vial or 5 vials per shield tube, are supplied.

The NDC number for: 10 mCi vial is 11994-127; 20 mCi vial is 11994-128.

Store at room temperature.

This radiopharmaceutical is approved for distribution to persons licensed pursuant to the Code of Massachusetts Regulations 105 CMR 120.100 for the uses listed in 105 CMR 120.547 or 120.552 or under equivalent regulations of the U.S. Nuclear Regulatory Commission, an Agreement State, or a Licensing State.

The contents of the vial are radioactive. Adequate shielding and handling precautions must be maintained.

Lantheus Medical Imaging, Inc.

331 Treble Cove Rd., N. Billerica, MA 01862 USA
For Ordering Tel. Toll Free 800-299-3431
(For Massachusetts & International, Call 978-667-9531)
All Other Business 800-362-2668

Patent: http://www.lantheus.com/patents/index.html

Printed in U.S.A.
515083-0719

Discussions with leaders: Frank Bengel talks with Jeroen Bax, an internationally recognized leader in integrating nuclear imaging and cardiology in clinical practice. . . . . ***Page 1455***

Single-cell radiotracing: Bartos and colleagues from Germany and Korea describe the process for single-cell radiotracer allocation via immunomagnetic cell sorting and provide examples of promising applications in neuroscience, oncology, and radiochemistry. . . . . ***Page 1459***

α-Synuclein PET and PD: Seibyl looks at the rationale for development of an α-synuclein–targeting PET agent in Parkinson disease and at the promise of such an agent for imaging and as part of therapeutic regimens. . . . . ***Page 1463***

Dosimetry in radiopharmaceutical therapy: O'Donoghue and colleagues provide an educational overview of current radiopharmaceutical therapy in the context of dosimetry, including internal dosimetry methods, incorporating dosimetry calculations into therapy, patient-specific dosimetry workflow, and future prospects. . . . . ***Page 1467***

Single-domain antibody theranostics: Wei and colleagues offer a focused summary of the latest developments in single-domain antibody–derived agents and propose strategies that can be used to improve the theranostic value of these agents. . . . . ***Page 1475***

Addressing PSMA controversy: Pomykala and colleagues respond to recent commentary in the literature questioning both the utility of prostate-specific membrane antigen PET imaging in patient selection for PSMA-targeted therapy and its use in staging and disease prediction. . . . . ***Page 1480***

PSMA PET/CT screening and VISION: Sartor provides perspective on the use of prostate-specific membrane antigen PET/CT in selection of patients for PSMA-targeted therapy through the lens of the VISION trial protocol, criteria, and results. . . . . ***Page 1482***

VISION-ineligible patient outcomes: Hotta and colleagues assess the outcomes of patients with metastatic castration-resistant prostate cancer treated with ^{177}Lu-prostate-specific membrane antigen who would have been screen failures based on PSMA PET/CT criteria in the VISION trial. . . . . ***Page 1484***

rhPSMA for therapy in prostate cancer: Wurzer and colleagues identify the prostate-specific membrane antigen–targeted radiohybrid ligand with the most favorable pharmacokinetics for ^{177}Lu-radioligand therapy. . . . . ***Page 1489***

^{225}Ac-PSMA in the post-ADT setting: Sathekge and colleagues report on treatment outcomes and survival using this novel agent immediately after androgen deprivation therapy in a series of patients with metastatic castration-resistant prostate carcinoma. . . . . ***Page 1496***

^{177}Lu-DOTATATE in chronic kidney disease: Alsadik and colleagues investigate the efficacy and safety of ^{177}Lu-DOTATATE in neuroendocrine tumor patients with reduced renal function. . . . . ***Page 1503***

SSTR2 heterogeneity assessed by CoV: Fonti and colleagues test the utility of the coefficient of variation from ^{68}Ga-peptide PET/CT in evaluation and quantification of somatostatin receptor subtype 2 expression heterogeneity in patients with neuroendocrine tumors and metastatic lesions. . . . . ***Page 1509***

DNA damage after ^{131}I therapy: Signore and colleagues explore whether thyroid remnant ablation with low activities of ^{131}I is associated with DNA damage by evaluating the CometAssay, micronuclei, and chromosome aberrations with multicolor fluorescent in situ hybridization. . . . . ***Page 1515***

PD-L1 PET imaging in SCCHN: Verhoeff and colleagues report on ^{89}Zr-DFO-durvalumab (anti–programmed death ligand 1) PET/CT imaging in patients with recurrent or metastatic squamous cell carcinoma of the head and neck before monotherapy with durvalumab. . . . . ***Page 1523***

Interobserver variability in PSMA PET/CT: Hagens and colleagues document the interobserver variability of 3 frequently used clinical radiotracers targeting the prostate-specific membrane antigen (^{18}F-DCFPyL, ^{18}F-PSMA-1007, and ^{68}Ga-PSMA-11) in primary prostate cancer staging. . . . . ***Page 1531***

^{18}F-PFPN PET and malignant melanoma: Zhang and colleagues detail the biodistribution and radiation dosimetry of ^{18}F-PFPN in healthy volunteers and examine its diagnostic utility in patients with malignant melanoma. . . . . ***Page 1537***

^{223}Ra-induced transient myelotoxicity: Parlani and colleagues explore the consequences of ^{223}Ra treatment on bone marrow biology in a preclinical model. . . . . ***Page 1544***

In vivo imaging of reactive astrogliosis: Villemagne and colleagues characterize the clinical performance of ^{18}F-SMBT-1, a novel MAO-B PET tracer, as a potential surrogate marker of reactive astrogliosis in neurodegeneration. ***Page 1551***

Reactive astrogliosis in aging and AD: Villemagne and colleagues assess the clinical performance of ^{18}F-SMBT-1 PET across the Alzheimer disease continuum as a potential surrogate marker of reactive astrogliosis and early neurodegeneration. . . . . ***Page 1560***

Tracking innate immune activation: Lucot and colleagues investigate translocator protein 18 kDa PET plus PET imaging of the triggering receptor expressed on myeloid cells for detection of innate immune responses in a mouse model of dopaminergic neuron degeneration. . . . . ***Page 1570***

Total-body PET/CT in arthritis: Abdelhafez and colleagues detail the performance of an ultra-low-dose, ^{18}F-FDG total-body PET/CT protocol for evaluating systemic joint involvement in autoimmune inflammatory arthritides and correlate results with joint-by-joint rheumatologic examination and standardized rheumatologic outcome measures. . . . . ***Page 1579***

PET and IBD: Seo and colleagues describe studies conducted to elucidate whether ^{18}F-FSPG PET imaging of antiporter system x_C^- of immune cells can accurately assess inflammatory bowel disease activity in murine models and patients. . . . . ***Page 1586***

^{18}F-FDG fetal dosimetry and PET/MRI: Zanotti-Fregonara and colleagues analyze data from 11 women injected with ^{18}F-FDG for cancer staging and scanned with PET/MRI during the first 2 trimesters of pregnancy. . . . . ***Page 1592***

Toward broader ^{68}Ga-citrate use: Suilamo and colleagues study the kinetics and dosimetry for PET applications in inflammatory and infectious diseases and cancer. . . . . ***Page 1598***

Data-driven motion correction in brain PET: Spangler-Bickell and colleagues present a reader-based evaluation and atlas-based quantitative analysis of a fully data-driven motion correction approach for brain PET in a clinical cohort. . . . . ***Page 1604***

PET/MRI and PET/CT radiomics harmonization: Leithner and colleagues determine whether ComBat harmonization improves ^{18}F-FDG PET radiomics-based tissue classification in pooled PET/MRI and PET/CT datasets. . . . . ***Page 1611***

Achieve IAC Accreditation for Your Facility

The trusted leader in accreditation for over 30 years, offering the mark of quality your patients are searching for.

Customer Service

Facilities are busy caring for their patients and accreditation should not interfere with that. IAC clinical staff are available to guide applicant facilities through the accreditation process via phone, live chat or e-mail quickly and efficiently.

Quality & Safety Focused

Offering a meaningful clinical peer review of case studies (with pathology) to evaluate diagnostic quality, report accuracy and report completeness, IAC is a partner in quality. IAC provides quality improvement-focused solutions, such as the IAC QI Self-Assessment Tool, to help facilities optimize processes and improve patient safety and outcomes.

Continuous Improvement

Accreditation must be thorough to truly affect the quality of care provided, however, IAC continues to explore ways to enhance the application process to make it simpler, more efficient and cost-effective to applicants.

Join the more than 14,000 IAC-accredited facilities who consistently express the highest levels of satisfaction with IAC's customer service and resources. IAC offers accreditation for diagnostic imaging and for vascular and cardiac interventional procedures:

Vascular Testing · **Echocardiography** · **Nuclear/PET** · **MRI** · **CT / Dental CT**
Vein Center · **Deep Venous** *(New!)* · **Hemodialysis Access** *(New!)* · **Peripheral Arterial** *(New!)*
Carotid Stenting · **Cardiac Electrophysiology** · **Cardiovascular Catheterization**

Learn more about IAC or **get started today**.

IAC

Improving health care through accreditation®

intersocietal.org | 800.838.2110

SNMMI Therapeutics Conference

November 17-19, 2022 • Washington, DC

Attend the SNMMI Fall Therapeutics Conference

Registration is now available for the **SNMMI Fall Therapeutics Conference, November 17-19, 2022**, at the **Gaylord National Resort and Convention Center**, located on the Potomac River in the Washington, DC metropolitan area. The resort is a short distance from both downtown DC and historic Old Town Alexandria, and is accessible to all three DC area airports. This two-and-a-half-day event will explore the latest innovations and clinical applications in radiopharmaceutical therapy, including:

- Setting up a Theranostics Clinic
- Thyroid Therapies
- Prostate Therapies
- Neuroendocrine Therapies
- Pediatric Therapies
- Radiopharmaceutical Supply Chain
- Dosimetry for Therapies
- Therapy Clinical Trials Primer

Register today:
www.snmmi.org/TC2022

PLANNING COMMITTEE

Co-Chairs

Phillip Koo, MD
Banner MD Anderson Cancer Center

Neeta Pandit-Taskar, MD, FSNMMI
Memorial Sloan Kettering Cancer Center

Members

Dmitry D. Beyder, MPA, CNMT
Barnes-Jewish Hospital

Yuni K. Dewaraja, PhD, FSNMMI
University of Michigan

Stephen A. Graves, PhD, DABR
University of Iowa

Thomas A. Hope, MD
University of California San Francisco

Andrei H. Iagaru, MD, FACNM
Stanford University

Daniel Lee, MD
Ochsner Medical Center

Helen R. Nadel, MD, FRCPC, FSNMMI
Lucile Packard Children's Hospital - Stanford

Joseph R. Osborne, MD, PhD, FACNM
New York Presbyterian Hospital (Cornell Campus)

Alan B. Packard, PhD, FSNMMI
Boston Children's Hospital/Harvard Medical School

ABNM CertLink: Update and "By the Numbers"

Kirk A. Frey, MD, PhD, Associate Executive Director, American Board of Nuclear Medicine

The American Board of Nuclear Medicine (ABNM) CertLink program is the mechanism offered to permit diplomates to satisfy American Board of Medical Specialties (ABMS) Maintenance of Certification (MOC) Part 3 requirements on a continuous, quarterly basis as opposed to a periodic (10-year cycle) half-day, high-stakes examination. CertLink offers several distinctive advantages over the previous periodic approach. Although CertLink provides the ABMS-required summative evaluation of diplomate cognitive ability, it is implemented in a formative context, providing participants with questions intended to emphasize common or new clinical aspects of nuclear medicine and molecular imaging. Each question item is accompanied by a critique describing the key concept, together with citation(s) to the literature for diplomates who want deeper understanding, particularly of new innovations in the field.

Approximately 1,250 active ABNM diplomates currently participate in the CertLink program, which launched in April 2018. Earlier this year, ABNM conducted a review and assessment of the program to determine direction(s) for potential future improvement. An important communication pathway leading to feedback from participating diplomates is the opportunity to provide comments to ABNM at the item response/review step in the examination. Review of the initial 3 years was based on the first 108 distinct exam items distributed, with the opportunity for up to 135,000 potential diplomate comments. ABNM received and reviewed 1,136 comments over this period. Each comment was reviewed and investigated by ABNM, but individual responses to commenting diplomates were beyond the scope of board resources. A majority of CertLink question items received diplomate comments. Twenty-six received $\geq$10 comments; of these, 8 items were excluded from final scoring on the basis of unanticipated problems. Several overall comment themes were identified.

Image Quality and Display. Frequent comments addressed difficulty in review of diagnostic images. In the current CertLink 2.0 release, images are an integral component within the question page, and the zoom feature of the workstation browser program must be employed. When finished zooming in on an image, the browser display must be reset to lower resolution to complete the question and see the next question. The ABNM CertLink FAQ and instruction page on the Web will be updated to document this approach. In addition, ABNM will further emphasize image quality and clarity in future published items, recognizing the critical image-rich aspect of nuclear medicine and molecular imaging practice.

Review of Questions and Images with Item Critique. Another frequent comment was the desire to re-review a question and images at the level of item feedback and critique stage of the examination. Current feedback is limited to identification of the correct vs. incorrect scoring of the diplomate response, together with a brief discussion of the key concept in the question and citation(s) to supporting literature. ABNM is investigating the possibility of redisplay of questions and images as a part of the feedback phase, and, if feasible, this will be added as an update to the examination procedure.

Key Point/Focus of Question(s). Diplomates also commented on the relationship of the key concept of an exam item to the current practice scope of the diplomate. In this context, it must be appreciated that ABNM certification covers the entire spectrum of practice in the field. ABNM does not offer subspecialty certifications for focused practice areas such as cardiovascular or pediatric nuclear medicine and molecular imaging or for diplomates who may not have ongoing experience with related therapy and theranostics. Continued ABNM certification applies to the entire breadth of nuclear medicine and molecular imaging content. An advantage of the CertLink approach is that it permits diplomates to remain current in aspects of practice that are potentially outside the constraints of their present practice—the formative aspect of CertLink, directing diplomates to literature resources for further learning and clarification.

Additional comments identified item-specific aspects. These included the possibility of incorrect scoring: incorrect key distractor, multiple correct distractors, or no correct distractor presented. Each comment was investigated by ABNM, and, in some instances, unanticipated problems with items were confirmed. In most such instances, such items were deleted from final scoring of the overall exam. In addition, ABNM conducts a retrospective psychometric statistical analysis of each item to identify items that did not perform as intended. In most instances, these were also deleted from final diplomate assessments, supporting the overall validity of the summative CertLink results for satisfaction of MOC Part 3 requirements.

ABNM CertLink is fully operational and functioning as intended. However, it is not a "final product" and will continue to undergo prospective changes and improvements, many at the suggestion of participating diplomates. Diplomates are encouraged to continue offering comments during item review. These constitute important input for potential program modifications. ABNM will further strengthen item delivery and feedback aspects of the program, with continued emphasis on supporting participant awareness of important clinical innovations and changes throughout all aspects of nuclear medicine and molecular imaging. Diplomates who have not yet activated participation in CertLink should consider enrolling to obtain the benefits of both ABMS Part 3 evaluation as well as formative resources and assistance with the evolving landscape of clinical practice.

Making Nuclear Medicine a Household Phrase

Munir Ghesani, MD, SNMMI President

Although certain medical terms are known to the general public—dialysis, biopsy, and chemotherapy, for example—nuclear medicine does not usually fall into that category. Nuclear medicine remains relatively unknown, misunderstood, and underutilized, to the detriment of patients. As nuclear medicine and molecular imaging professionals, we know the vital role that it plays in patient care. On behalf of the entire field, SNMMI is working to make sure that others outside of our community know it as well.

As part of SNMMI's Value Initiative, the society launched a robust consumer awareness campaign to educate the public about what nuclear medicine is and what it can accomplish. By translating the latest research and telling compelling stories, the society has successfully reached patients, caregivers, referring physicians, legislators, regulators, and payers about the benefits of nuclear medicine. In fact, in the campaign's first 6 months, stories about nuclear medicine and molecular imaging were featured in media reaching more than 1 billion consumers.

The consumer awareness campaign began with the creation of core messages focused on the fact that nuclear medicine can diagnose and treat disease effectively and safely, with minimal side effects and exceptional results for patients. With the latest advances in nuclear medicine therapies, messages were also developed about radiopharmaceutical treatments.

Once the key messages were drafted, a plan was made to garner media attention throughout the country and specifically in the Washington, DC, market, where a heavy concentration of regulators and legislators reside. The society developed relationships with reporters who cover science and health for major newspapers and magazines, radio, television, and online news publications. SNMMI promoted stories about recently published research in nuclear medicine and molecular imaging, connecting these stories to current events or occasions to provide relevance. Stories highlighting patients who have benefited from nuclear medicine imaging and therapy were also made available to the media.

Since the campaign's inception, the society has garnered many high-profile media placements. Nuclear medicine was spotlighted on the popular New York radio channel Q104.3 in a 3-part series with award-winning radio host Shelli Sonstein. The first interview in September 2021 focused on nuclear medicine as an innovative cancer treatment, and the second in February 2022 covered nuclear medicine in nononcologic disease. Sonstein saw so much value in these interviews that she had SNMMI back a third time this past July to discuss nuclear medicine as a tool to both diagnose and treat prostate cancer, as well as research from the Annual Meeting.

Munir Ghesani, MD

On the television front, SNMMI has secured interviews on many news shows. Placements include the Fox 5 DC Morning Show (unusual imaging patterns on ^{18}F-FDG PET/CT scans possibly due to COVID Omicron variant infections), Fox Good Day LA (PET/CT artificial intelligence model for predicting risk of future heart attack), ABC 7 DC News (cardiac nuclear medicine), NBC 4 DC News (nuclear medicine to diagnose and treat cancer), Fox 5 DC Good Day DC (nuclear medicine as a game-changer), Fox DC Weekend Show (nuclear medicine to diagnose colon cancer), Fox Good Day LA (nuclear medicine to treat Parkinson's disease), and DCTV District Life Show (nuclear medicine to diagnose and treat prostate cancer).

Nuclear medicine was also covered in several print and online publications. *CURE Magazine* published an article about the U.S. Food and Drug Administration approval of Pluvicto, interviewing Richard Wahl, MD, about the treatment. SNMMI patient advocates also represented the society in interviews with *Health Central Online*, *Authority Magazine,* and *Thrive Global*. *Authority Magazine* also interviewed Helen Nadel, MD, SNMMI vice president, about inspiring women in STEM fields.

Complementing our consumer awareness campaign, the society has also continued its outreach to patient and referring physician associations with the goal of educating patients and the medical community about the value of nuclear medicine, molecular imaging, and radionuclide therapy. SNMMI's Patient Advocacy Advisory Board (PAAB) advises the society on development of patient education materials and public policy. This year, the PAAB welcomed 2 new members: Cancer ABCs and the Pheo-Para Alliance. The society also educates referring physicians by presenting at events hosted by organizations such as the Pediatric Endocrine Society, Large Urology Group Practice Association, American Urological Association, and San Antonio Breast Cancer Symposium.

The consumer awareness campaign has seen much success, and this is only the beginning. As advances in nuclear medicine and molecular imaging continue—especially with the effectiveness and increased availability of radiopharmaceutical therapies—we expect that media interest in our field will continue to grow. And with more awareness from consumers, referring physicians, legislators, and other key audiences, nuclear medicine will be well on its way to becoming a common household phrase.

Bertagnolli to Serve as NCI Director

President Joe Biden announced on August 10 his intention to appoint Monica Bertagnolli, MD, as the 16th (and first woman) director of the National Cancer Institute (NCI). She currently serves as the Richard E. Wilson Professor of Surgery in surgical oncology at the Harvard Medical School, as well as a surgeon at the Brigham and Women's Hospital and a member of the Gastrointestinal Cancer and Sarcoma Disease Centers at the Dana–Farber Cancer Institute (all in Boston, MA). She has championed collaborative initiatives to transform the data infrastructure for clinical research and is the founding chair of the Minimal Common Oncology Data Elements (mCODE) Executive Committee. She is a past president and chair of the board of directors of the American Society of Clinical Oncology and has served on the board of directors of the American Cancer Society and the Prevent Cancer Foundation.

"I look forward to working with Dr. Bertagnolli to advance the President's call to end cancer as we know it," said Secretary Xavier Becerra, U.S. Health and Human Services, referring to the President's renewed Cancer Moonshot initiative. "Her decades of cancer research expertise around patient-centered care and her work to create more inclusive clinical trials will be instrumental as we accelerate the rate of research and innovation to fight cancer."

The White House

TerraPower Announces Funding Raised for Nuclear Technologies

Terrapower (Bellevue, WA) announced on August 15 the close of an equity raising effort that yielded >$750 million. The effort was led by TerraPower founder Bill Gates and by SK Inc./SK Innovation (Seoul, South Korea). Additional funding will come from other investors. According to a press release from TerraPower, this effort will enhance the company's "groundbreaking work in advanced nuclear energy technologies and nuclear medicine."

"TerraPower is committed to solving some of the toughest challenges that face this generation through innovation," said TerraPower President and CEO Chris Levesque. "Whether it's addressing climate change with carbon-free advanced nuclear energy or fighting cancer with nuclear isotopes, our team is deploying technology solutions, and investors across the world are taking note." TerraPower's recent growth has been driven in part by a U.S. Department of Energy (DOE) Advanced Reactor Demonstration Program (ARDP) award and the construction of the Natrium demonstration plant at a retiring coal facility in Wyoming. Part of the ARDP award requires a match of 50% of project costs, up to $2 billion.

The TerraPower Isotopes (TPI) program is "supporting the transformation of the fight against cancer by advancing the next generation of isotopes." Across a range of partnerships, the program is focusing on isotopic materials harvested from DOE storage to be used in targeted α therapy. The press release noted that TPI has "unique access to ^{225}Ac and is working to provide this isotope to the pharmaceutical community for the development of drugs that target and treat cancer." TerraPower's radiochemistry laboratory also supports other radioisotope development initiatives within the company as part of its nuclear innovation mission. For more information on the TPI, visit: https://www.terrapower.com/wp-content/uploads/2022/03/2022-TPI-Isotopes.pdf.

New European Data Law and FDA

In a perspective article published on August 9 by the U.S. Food and Drug Administration (FDA), Heather Messick, JD, an international policy analyst, looked at the current and likely future effects of the General Data Protection Regulation (GDPR), a law enacted by the European Union (EU) in 2018 requiring that organizations put in place certain measures to collect, use, or store personal data originating from persons in the European Economic Area (the 27 EU member states plus Iceland, Norway, and Lichtenstein) to ensure that the data are protected, even if transferred out of the area. The GDPR defines personal data as: "any information relating to an identified or identifiable natural person ("data subject"); an identifiable person is one who can be identified, directly or indirectly, in particular by reference to an identifier such as a name, an identification number, location data, online identifier, or to one or more factors specific to the physical, physiological, genetic, mental, economic, cultural, or social identity of that person." Of note, coded data, referred to in the law as "pseudonymised data," are considered to be personal data and subject to the protections of the law. Messick outlined a number of concerns for the FDA in its current interactions with the EU, particularly in clinical and other scientific trials, New Drug Applications/Biologic License Applications, and adverse event reporting. The FDA is assessing implications for collaborative medical research involving sites in EU member states and the United States. In March, the EU and the United States agreed "in principle" on a new data agreement for cross-border transfers of personal privacy data for commercial purposes. The FDA will continue to monitor both requirements and interpretations of the GDPR in the coming year. The complete perspective article is available at: https://www.fda.gov/international-programs/global-perspective/how-european-data-law-impacting-fda.

U.S. Food and Drug Administration

NIH Centers of Excellence for Telehealth in Cancer Care

The National Cancer Institute (NCI) announced on August 18 that it will award $23 million to 4 academic institutions to establish centers of excellence to conduct research on the role of

telehealth in delivering cancer-related health care. The 5-y awards will establish the NCI Telehealth Research Centers of Excellence (TRACE) initiative, which is being supported by the Cancer Moonshot program to accelerate the rate of progress against cancer.

"One of the Cancer Moonshot goals is to make the cancer experience less burdensome for patients and their families and caregivers," said Katrina Goddard, PhD, director of the NCI Division of Cancer Control and Population Sciences. "We are awarding these centers of excellence to better understand how telehealth can contribute to improved health outcomes across the cancer care continuum."

The research being undertaken by the 4 centers will study the role of telehealth in fields from prevention to screening, diagnosis to treatment, and survivorship. Each center will be led by an academic institution that has assembled diverse teams of researchers to conduct large trials in real-world clinical settings such as hospitals, cancer centers, oncology practices, and primary care offices. The centers will be led by the New York University Grossman School of Medicine (NY), Northwestern University (Evanston, IL), the University of Pennsylvania (Philadelphia), and Memorial Sloan Kettering Cancer Center (New York, NY)

In addition to developing innovative ways to use telehealth in cancer care, the centers will focus on identifying and addressing telehealth-related disparities among vulnerable populations, including racial and ethnic groups, rural residents, older adults, people who are uninsured or have low incomes, people who are socially isolated, and people who have limited digital literacy. All participating centers are also committed to training the next generation of telehealth-focused researchers.

National Cancer Institute

DOE Medical User Group Meetings

The Department of Energy (DOE) Isotope Program held its Annual Medical Isotope User Group Meetings in a virtual format in September and October. The meetings, which focused on emerging α and β emitters, are organized to facilitate free discussion and collaboration among users of specific isotopes and to encourage information exchange about their applications in medicine. The webinar-style sessions featured brief presentations by leading researchers showcasing progress in these emerging fields, followed by interactive panel discussions. The ^{225}Ac User Group Meeting was held on September 1 and was moderated by Cathy Cutler, PhD, from the Brookhaven National Laboratory (Upton, NY). The ^{211}At User Group Meeting was held on September 6 and moderated by Yawen Li, PhD, from the University of Washington School of Medicine (Seattle). On September 19, the ^{134}Ce User Group Meeting was moderated by Stosh Kozimor, PhD, from the Los Alamos National Laboratory (NM). The final event, the ^{212}Pb User Group Meeting was moderated by Matt O'Hara from the Pacific Northwest National Laboratory (Richland, WA).

U.S. Department of Energy

FROM THE LITERATURE

Each month the editor of Newsline selects articles on diagnostic, therapeutic, research, and practice issues from a range of international publications. Most selections come from outside the standard canon of nuclear medicine and radiology journals. These briefs are offered as a window on the broad arena of medical and scientific endeavor in which nuclear medicine now plays an essential role. The lines between diagnosis and therapy are increasingly blurred, as radiolabels are used as adjuncts to treatment and/or as active agents in therapeutic regimens, and these shifting lines are reflected in the briefs presented here. We have also added a small section on noteworthy reviews of the literature.

^{18}F-Fluorocholine PET/CT and Parathyroid Imaging

Jacquet-Francillon et al. from the Saint-Étienne University Hospital/University of Saint-Étienne, Hospices Civils de Lyon, Université Jean Monnet (Saint-Étienne), and the Université de Lyon (Saint-Étienne; all in France) reported in the August 2 issue of *Frontiers in Medicine (Lausanne)* (2022;9: 956580) on a study evaluating the performance of quantitative criteria in ^{18}F-fluorocholine PET/CT for localization of hyperfunctioning parathyroid glands, as well as correlations between detection rates of ^{18}F-fluorocholine PET/CT and serum parathyroid hormone levels. The retrospective study included 120 patients (135 lesions) with biologic hyperparathyroidism who had undergone imaging with ^{18}F-fluorocholine PET/CT. Images were assessed first with visual analysis and then with a blinded reading of standardized measurements of SUV_{max} and liver, thyroid, and size ratios. Results were compared with histology, with a special emphasis on differentiation between adenomas and hyperplasias. The researchers found that areas under the receiver operating characteristic curve representing SUV_{max} and liver ratio were significantly increased in the study group; optimal cutoff values for these variables were >4.12 and >27.4, respectively. Beyond threshold values of SUV_{max} >4.12 and/or liver ratio >38.1, all lesions were confirmed to be adenomas on histology. ^{18}F-fluorocholine PET/CT was correlated with serum parathyroid hormone levels. The authors concluded that semiquantitative measurements (specifically, SUV_{max} and liver ratio) should be considered as additional tools in interpretation of ^{18}F-fluorocholine PET/CT. Although these quantitative parameters have lower overall performance than visual analysis, they have higher specificity in identifying adenomas, so that above certain PET/CT threshold values, all lesions are adenomas. PET/CT in this setting is also useful for detection of hyperfunctional parathyroids.

Frontiers in Medicine (Lausanne)

Discordant Understanding of the Freeform PET/CT Report in Head and Neck SCC

In an article published on August 18 ahead of print in *JAMA Otolaryngology: Head and Neck Surgery*, Patel et al. from the Wake Forest School of Medicine (Winston-Salem, NC) reported on a study focusing on clinicians' perceptions of PET/CT freeform reports and the incidence of discordance between clinician understanding and the intention of the nuclear medicine physicians generating the reports. The retrospective study included 171 patients (45 women, 126 men; median age, 61 y, range, 54–65 y) with head and neck squamous cell carcinoma (HNSCC; 149 with stage III–IV disease) in routine oncologic management who underwent ^{18}F-FDG PET/CT for assessment of response to radiation treatment with or without concurrent chemotherapy. Four clinicians independently reviewed the freeform PET/CT reports and assigned perceived modified Deauville scores (MDS). These results were then compared with the criterion standard nuclear medicine MDSs derived from image review. Clinical outcomes assessed included locoregional control, progression-free survival, and overall survival. The researchers found that although reliability/agreement between oncology clinicians was moderate ($\kappa = 0.68$), consensus was minimal ($\kappa = 0.36$) between clinicians and nuclear medicine physicians. Exact agreement between clinician consensus and nuclear medicine physicians was 64%. The authors concluded that "the results of this cohort study suggest that considerable variation in perceived meaning exists among oncology clinicians reading free-form HNSCC postradiation therapy PET/CT reports, with only minimal agreement between MDS derived from clinician perception and nuclear medicine image interpretation." These data suggest that nuclear medicine use of "a standardized reporting system, such as MDS, may improve clinician–nuclear medicine communication and increase the value of HNSCC postradiation treatment PET/CT reports."

JAMA Otolaryngology: Head and Neck Surgery

Improving Transthoracic Lung Mass Biopsy with Intraprocedural CT and Prior PET/CT Fusion

Lin et al. from the China-Japan Friendship Hospital (Beijing, China) and the Hospital Seberang Jaya (Penang, Malaysia) reported on August 13 in *BMC Pulmonary Medicine* (2022;22[1]: 311) on a study evaluating the utility of intraprocedural CT and prior PET/CT fusion imaging in improving the diagnostic yield of CT-guided transthoracic core-needle biopsy in lung masses. The study included 145 individuals with lung masses suspicious for malignancy scheduled to undergo image-guided transthoracic core-needle biopsy. Seventy-six patients had undergone PET/CT imaging ≤14 d before biopsy, and their imaging data were integrated with intraprocedural CT images. The resulting fused images were used to plan puncture sites. The remaining 69 patients underwent routine CT-guided biopsy procedures. Clinical characteristics, diagnostic yield of the biopsies, diagnostic accuracy, procedure-related complications, and procedure duration were compared between the 2 patient groups. Final clinical diagnosis

was determined by histopathology and/or at ≥6-mo follow-up. The overall diagnostic yield and accuracy rate were 80.3% and 82.9%, respectively, for the fusion imaging group, with corresponding percentages of 70.7% and 75.4% for the group under routine procedures. The diagnostic yield for malignancy in the fusion imaging group was higher than that in the routine group (98.1% and 81.3%, respectively). No serious procedure-related adverse events were noted in either of the groups. The authors concluded that "core-needle biopsy with prior PET/CT fusion imaging is particularly helpful in improving diagnostic yield and accurate rate of biopsy in lung masses, especially in heterogeneous ones, thus providing greater potential benefit for patients."

BMC Pulmonary Medicine

Fibroblast-Activation Protein Expression in Interstitial Lung Disease

In an article published on August 19 ahead of print in the *American Journal of Respiratory and Critical Care Medicine,* Yang et al. from the State Key Laboratory of Respiratory Disease (Guangzhou), the First Affiliated Hospital of Guangzhou Medical University, Southern Medical University (Guangzhou), Wuxi People's Hospital of Nanjing Medical University, General Hospital of Southern Theatre Command of PLA (Guangzhou), and the Shenzhen International Institute for Biomedical Research (all in China) reported on a study investigating whether the expression intensity of fibroblast-activation protein (FAP), a recognized surface biomarker of activated fibroblasts, can be used to estimate/measure the amounts of activated fibroblasts in interstitial lung disease (ILD). The researchers detailed multiple in vitro studies characterizing FAP expression in human primary lung fibroblasts and clinical lung specimens, including qPCR, Western blot, immunofluorescence staining, deep-learning measurement of whole-slide immunohistochemistry, and single-cell sequencing. They also analyzed FAP-targeted PET/CT imaging in patients with various ILDs to determine correlations between FAP tracer uptake and pulmonary function parameters. They found that FAP expression was significantly upregulated in the early phase of lung fibroblast activation in response to a low dose of profibrotic cytokine. Single-cell sequencing data indicated that almost all FAP-positive cells in ILD lungs were collagen-producing fibroblasts. Immunohistochemistry confirmed that FAP expression levels were closely correlated with fibroblastic foci on human lung biopsy sections from patients with ILDs. The total SUV for the FAP-inhibitor PET tracer was significantly related to lung function decline in these patients. The authors concluded that these results "strongly support that in vitro and in vivo detection of FAP can assess the profibrotic activity of ILDs, which may aid in early diagnosis and selection of an appropriate therapeutic window."

American Journal of Respiratory and Critical Care Medicine

Preoperative PET/CT in Advanced Serous Ovarian Cancer

Wang et al. from the First Affiliated Hospital of Chongqing Medical University, the People's Hospital of Yubei District of Chongqing City, and Chongqing General Hospital/University of Chinese Academy of Sciences (all in China) reported on August 18 ahead of print in *Acta Obstetricia et Gynecologica Scandinavica* on a study analyzing and comparing the predictive values of preoperative PET/CT score, CT score, metabolic parameters, tumor markers, and hematologic markers for incomplete resection after debulking surgery for advanced serous ovarian cancer. The retrospective study included data from 62 such patients who had undergone ^{18}F-FDG PET/CT imaging before primary or secondary debulking surgery. Variables assessed included PET/CT and CT predictive scores (based on the Suidan model), SUV_{max}, metabolic tumor volume, human epididymis protein 4, cancer antigen 125, lymphocyte-to-monocyte ratio, platelet-to-lymphocyte ratio, and neutrophil-to-lymphocyte ratio. Preoperative PET/CT was found to have the highest predictive value for incomplete resection in the primary debulking surgery group (sensitivity, 65.0%; specificity, 88.9%). In the secondary debulking surgery group, preoperative PET/CT and CT scores were the same but remained higher than the other tumor and hematologic variables (sensitivity, 80.0%; specificity, 94.7%). A preoperative PET/CT score ≥3 predicted a high risk of incomplete resection after primary debulking, and a preoperative PET/CT score ≥2 was highly predictive of incomplete resection after secondary debulking. The authors concluded that "the preoperative PET/CT score may be a feasible and quantitative model for predicting incomplete resection after debulking surgery for advanced serous ovarian cancer."

Acta Obstetricia et Gynecologica Scandinavica

Multiparametric Model for PET in Thymic Lesion Diagnosis

In an article published on August 16 in *BMC Cancer* (2022;22[1]:895), Wang et al. from the Beijing Friendship Hospital/Capital Medical University and the First Medical Center/Chinese PLA General Hospital (both in Beijing, China) reported on a study investigating the diagnostic performance of multiparametric ^{18}F-FDG PET combined with clinical characteristics in differentiating thymic epithelial tumors from thymic lymphomas. The study included 173 patients (80 with thymic epithelial tumors and 93 with thymic lymphomas) who underwent ^{18}F-FDG PET/CT before treatment. PET/CT parameters included in the evaluation were lesion size, SUV_{max}, SUV_{mean}, total lesion glycolysis, metabolic tumor volume, and tumor-to-normal liver SUV ratio. Clinical data were also included in assessing differential diagnostic and comparative efficacy. Age, clinical symptoms, and PET metabolic parameters were found to differ significantly between patients with thymic epithelial tumors and those with thymic lymphomas. The calculated SUV ratio showed the highest individual differentiating diagnostic value (sensitivity, 76.3%; specificity, 88.8%). A combined model of age, clinical symptoms,

and SUV ratio resulted in the highest differentiating diagnostic value (sensitivity, 88.2%; specificity, 96.3%). The clinical efficacy of the model was confirmed by further analysis. The authors concluded that this "multiparameter diagnosis model based on ^{18}F-FDG PET and clinical characteristics had excellent value in the differential diagnosis of thymic epithelial tumors and thymic lymphomas." They added that use of this model has the potential to avoid unnecessary treatment and surgery.

BMC Cancer

Tau Distribution in Early-Onset AD

Frontzkowksi et al. from University Hospital/LMU Munich (Germany), the German Center for Neurodegenerative Diseases (DZNE) (Munich, Germany), the Munich Cluster for Systems Neurology (SyNergy) (Germany), Lund University (Sweden), the Vrije Universiteit Amsterdam/Amsterdam UMC (The Netherlands), and Skåne University (Lund, Sweden) reported on August 20 in *Nature Communications* (2022;13[1]: 4899) on a study combining resting-state functional MR and longitudinal ^{18}F-flortaucipir PET imaging to investigate tau distribution and accumulation in individuals with early-onset AD. The study drew data from almost 300 participants in 2 independent clinical trials, each cohort including patients with biomarker-confirmed and symptomatic Alzheimer disease (AD), cognitively normal but amyloid-positive individuals, and cognitively normal controls with no AD-associated pathologies. High-resolution resting-state functional MR imaging data from 1,000 healthy participants was used to map the topology of globally connected "hubs" across the brain. ^{18}F-flortaucipir PET patterns in AD patients and others in the study were mapped to the topology of these globally connected hubs to determine the degree to which individual tau patterns are expressed in globally connected hub regions in the frontoparietal association cortex compared to weakly connected nonhub regions. Detailed imaging analyses indicated: (1) that individual tau deposition patterns on PET are stronger in globally connected hub regions in younger patients with symptomatic AD and that these patterns are associated with earlier symptom onset; (2) that this hub-like pattern of tau deposition at baseline PET is associated with subsequent accelerated tau accumulation on annual assessment; and (3) that this hub-like pattern contributes to the acceleration of cognitive decline. The authors concluded that "this suggests that earlier symptom manifestation is not driven by specific pathophysiological characteristics but rather by a tau distribution pattern that preferentially targets brain hubs important for cognitive function." They added that "knowledge about drivers of tau onset, heterogeneous tau spreading patterns, and clinical trajectories may become important to facilitate precision medicine prediction of cognitive and pathological progression, as well as for patient stratification in clinical trials."

Nature Communications

Articular ^{18}F-FDG Uptake in RA

In an article published online ahead of print in the *Journal of Rheumatology*, Ferraz-Amaro et al. from the Hospital Universitario de Canarias (Tenerife. Spain), Kettering Health (Dayton, OH), and Columbia University College of Physicians and Surgeons (New York, NY) reported on a study using ^{18}F-FDG PET/CT to quantify joint inflammation in rheumatoid arthritis (RA) and explore correlations between PET-derived uptake parameters and RA disease activity measures. The authors studied 34 patients with RA who were part of the Rheumatoid Arthritis Study of the Myocardium. Associations between disease activity scores and articular ^{18}F-FDG SUVs were calculated. Weighted joint volume SUVs representing 25%, 50%, 75% and maximal (100%) uptake were calculated as global parameters of the total volume of joint inflammation in each patient. The 25%, 50%, and 75% weight joint volume SUVs were found to be significantly correlated with the number of swollen joints. No associations were found between articular FDG uptake and nonarticular RA-related variables, such as disease duration, seropositivity, or RA treatments. The authors concluded that although articular FDG uptake was significantly correlated with the number of swollen joints in RA, it was not associated with biochemical measures of inflammation and disease activity.

Journal of Rheumatology

Reviews

Review articles provide an important way to stay up to date on the latest topics and approaches through valuable summaries of pertinent literature. The Newsline editor recommends several general reviews accessioned into the PubMed database in August. Sparano et al. from the University of Florence (Italy) and the Institut Gustave Roussy/Université Paris-Saclay (Villejuif, France) provided an overview of "Strategies for radioiodine treatment: What's new?" in the August 4 issue of *Cancers (Basel)* (2022;14[15]: 3800). In the August 3 issue of the *Journal of Clinical Medicine* (2022:11[15]: 4514), Dondi et al. from the ASST Spedali Civili di Brescia (Italy), the Università degli Studi di Brescia (Italy), Ente Ospedaliero Cantonale (Bellinzona, Switzerland), Lausanne University Hospital/University of Lausanne (Switzerland), and the Università della Svizzera Italiana (Lugano, Switzerland) surveyed the "Emerging role of FAPI PET imaging for the assessment of benign bone and joint disease." Albano and experts from the same universities reported in the August 5 issue of *Cancers (Basel)* (2022; 14[15]:3814) on "The role of [^{68}Ga]Ga-pentixafor PET/CT or PET/MRI in lymphoma: A systematic review." In the same issue of *Cancers (Basel)* (2022;14[15]: 3768), Rasul and Haug from the Medical University of Vienna (Austria) summarized "Clinical applications of PSMA PET examination in patients with prostate cancer."

Integrating Nuclear Imaging and Cardiology in Clinical Practice

A Conversation Between Jeroen J. Bax and Frank M. Bengel

Jeroen J. Bax[1] and Frank M. Bengel[2]

[1]*Leiden University Medical Center, Leiden, The Netherlands; and* [2]*Hannover Medical School, Hannover, Germany*

Frank M. Bengel, director of the Department of Nuclear Medicine and Dean of Research at Hannover Medical School (Germany), talked with Jeroen J. Bax, a professor of medicine and cardiology, director of noninvasive imaging, and director of the Echo Lab at the Leiden University Medical Center (The Netherlands), about contributions at the intersection of advanced cardiology and nuclear medicine/molecular imaging. Dr. Bax studied medicine from 1984 to 1990 before launching his research career at the University of Miami (FL), where his primary foci were in the fields of immunology and associated basic science. In 1996, he received his doctorate from the Vrije Universiteit Amsterdam (The Netherlands) with a focus on SPECT metabolic imaging. He completed his training as a cardiologist in 2002 at the Leiden University Medical Center. His main interests include clinical cardiology, heart failure, cardiac resynchronization therapy, and the application of a wide range of imaging modalities to these clinical fields. He has served on the editorial boards of various journals, including as associate editor for the *Journal of the American College of Cardiology* (*JACC*) and *Heart*. From 2016 to 2020, he served as president of the European Society of Cardiology (ESC). Dr. Bax has authored more than 700 papers in international peer-reviewed journals. He received the ESC Silver Medal in 2008, the American Society of Nuclear Cardiology Distinguished Service Award for contributions to cardiovascular imaging and cardiology in 2019, and the American College of Cardiology Distinguished Scientist Award (Clinical Domain) in 2020.

Dr. Bengel: *Jeroen, not many people started their careers in nuclear cardiology and moved on to become worldwide leaders in general cardiology. Your perspective on nuclear medicine today and your view on the role of diagnostic imaging in clinical medicine should be of interest to readers of* The Journal of Nuclear Medicine *(*JNM*). Let's start from the beginning: Early in your career, you chose a PhD thesis in nuclear cardiology in Amsterdam and worked on myocardial viability imaging with* ^{18}*F-FDG. What attracted you to this technique and to nuclear imaging in general?*

Dr. Bax: After 3.5 years of learning the fundamentals of medicine in Leiden in The Netherlands, I wanted to do something else. I went to the University of Miami, where I did my first research in immunology, leading to my first scientific publication. During the rest of my medical school training, I did research in neurology, and this confirmed my interest in doing scientific projects. When I finished medical school, cardiology excited me most, and I completed my PhD thesis in Amsterdam at the Free (or Vrije) University Medical Center. I spent 4 years on developing ^{18}F-FDG imaging with SPECT, using special collimators. There was high hope that ^{18}F-FDG SPECT would support a broader availability of the technology. We performed perfusion and ^{18}F-FDG studies to determine viability and echocardiography before and after revascularization to determine functional outcome. Also, we compared ^{18}F-FDG imaging to stress echocardiography, thallium imaging, and MRI. During my PhD studies, then, I learned about many cardiac imaging techniques before I even started training in cardiology.

Jeroen J. Bax, MD, PhD

Dr. Bengel: *So you always appreciated the range of different imaging techniques and the ways in which they complement one another. Were you able to continue along that path during your cardiology training?*

Dr. Bax: I used my specialty training to learn more about cardiac imaging modalities, but I also started to approach problems from a clinical perspective. Imaging has to have clinical and therapeutic relevance, just like viability imaging is used to predict whether impaired cardiac function will improve after revascularization. I trained in cardiology in Leiden and for 1 year in Brussels (Belgium). I learned everything about echocardiography there. But I also learned how to build up a laboratory, because they had a fantastic organization, with perfect scheduling and standardized reporting. This helped me to build a well-structured echocardiography laboratory after my return to Leiden. From structured imaging and reporting, we created a large database. That turned out to be critically important for my future research, which has built significantly on database analyses. Today, we have very big databases of all imaging procedures and for different diseases, therapies, etc., and we use these to identify ways in which imaging can improve clinical outcomes for cardiac patients.

Dr. Bengel: *You are emphasizing the importance of a clinical perspective for the best use of imaging techniques.*

Dr. Bax: Yes, I used my training to also learn more about specific therapeutic aspects of cardiovascular medicine. I worked closely with cardiac surgeons, helping them with their procedures by providing standardized echocardiography. I also spent time in invasive angiography and in fundamental electrophysiology, implanting devices such as pacemakers, cardiac defibrillators, and others. And I tried to learn how multimodality imaging can be used to optimize these powerful therapeutic procedures.

DOI: 10.2967/jnumed.122.264806

Dr. Bengel: *At the end of your cardiology specialty training, the question came: What's next?*

Dr. Bax: Leiden offered me a position to build a noninvasive imaging department with a very strong focus on echocardiography. I built the echo lab using my experience from Belgium. Then we started to collaborate with the other imaging modalities, including nuclear medicine. We also did CT coronary angiography, then with 320 slices. Eventually we began to work more and more with MRI, specifically for assessing myocardial viability and later in nonischemic cardiomyopathies. We gradually built this imaging hub in cardiology where we had all the modalities, and noninvasive imaging had a fixed role in standard care algorithms of patients admitted to our hospital. This approach of having standardized imaging in almost all patients of a given disease entity was fundamental for big database generation. From those databases, we generated all of our observational research and publications.

Dr. Bengel: *Your approach toward noninvasive cardiac imaging is that you want to use the modality or the combination of modalities that is best for answering specific clinical questions. Are multimodality skills generally recommended to cardiac imagers?*

Dr. Bax: Every disease is characterized by an anatomic, a functional, and a molecular or inflammatory component. Take a heart valve as an example: the anatomic point is that you have, let's say, an aortic valve with 3 cusps and other features, and you can measure size and geometry. The functional component is the extent of the gradient over that valve; that is, what are the functional consequences of the anatomic substrate? Then comes the component of inflammation. We are learning now more and more that the earlier phases of valve stenosis formation involve inflammation. You cannot address all these different aspects with a single technique. You need very high anatomic resolution, provided by CT or MRI. You need good measures of functional consequences of anatomic abnormalities, provided by MRI or echocardiography. And you also want to know about inflammation, where nuclear imaging can help. Integration of different modalities is important to understand, diagnose, and risk-stratify and ultimately to decide on the best treatment for each specific disease.

Dr. Bengel: *What would be your advice for a nuclear physician who is trained in using radioisotopes for diagnosis but not necessarily trained in echocardiography or clinical cardiovascular disease? How can nuclear physicians acquire the depth of knowledge needed to provide clinically relevant services in a multimodality environment?*

Dr. Bax: We need to strive for clinical collaboration and integration. Some modalities may be run by radiology, some by cardiology, and some by nuclear medicine, but the final common pathway is the patient with a specific disease. And that specific disease needs a specific treatment. For that treatment, you need to have diagnostic information, which may include anatomic, functional, or inflammatory abnormalities. What is unique for nuclear medicine is the ability to reliably assess inflammation and other molecular components of a disease. And, of course, nuclear imaging can also assess functional components of a disease. So, what is needed is an integrated and patient-oriented approach: Which test to start with? What information is needed so that the clinician can treat the patient? Nuclear physicians have an important role in such an environment. You can never be an expert in all modalities. Your goal, instead, is to have a multimodal platform. Knowing what the other modalities can provide is already a big step toward a multimodal approach.

Dr. Bengel: *You mention inflammation as a key component of cardiovascular disease. This also plays a role in other organ diseases, where it can often be identified using the same nuclear medicine approaches. What do you think of systems-based medicine, which looks less at specific organs and more at biologic mechanisms and their effects on the body as a whole?*

Dr. Bax: I like the concept of systems-based expertise. Nuclear medicine typically is a cross-sectional specialty that reaches into many other, often organ-centered, specialties. There, nuclear medicine can bring in its functional- and molecular-focused information, and this may be increasingly relevant as therapies start to target molecular mechanisms. A good example in cardiology is the increasing attention toward what we call "myocardial diseases" (although many of them are systemic diseases that affect the heart but have effects on the rest of the body). This includes amyloidosis, sarcoidosis, infectious diseases, and others. Those diseases are very good targets and areas in which nuclear medicine is increasingly relevant for decision making.

Dr. Bengel: *Let's get away from the specifics of nuclear imaging, toward more general aspects of academic medicine and research. You built an extremely prolific program, producing a large number of publications and educating many young trainees. How did you build your research program in Leiden?*

Dr. Bax: It started with just 1 fellow in the early 2000s, and the program grew from there. The key is to have the right projects and to attract motivated young people. Having imaging databases and expanding them in a structured way was another very important point, because this provided the data for our projects. Today, we have on average about 15 to 20 researchers in the lab. As the program grew, we collaborated with other labs, so that many other centers wanted to send individuals to train in multimodality imaging and to do research.

Dr. Bengel: *You also mentioned that clinical databases were an important component for your research program.*

Dr. Bax: In the early 2000s, cardiology moved toward following clear guidelines, provided by the American College of Cardiology, the American Heart Association, and later the ESC. We decided in Leiden to set up clinical care tracks for different diseases. All patients undergo the same diagnostic tests and therapeutic procedures for specific diseases, based on our care track algorithms. Results are protocolized and put into databases. We adjusted these time after time as the field changed and when new medications, diagnostics, or therapies were introduced. Through these care track–driven clinical databases, large and well-structured cohorts of patients were generated. These clinical care pathways directly feed into our research. Our data resource is not prospective trials or experimental science but analysis and reporting of true practical clinical care.

`Integration of different [imaging] modalities is important to understand, diagnose, and risk-stratify and ultimately to decide on the best treatment for each specific disease.´

Dr. Bengel: *This feedback algorithm, where the research can directly lead to adjusting clinical care, would be a very useful approach in nuclear medicine, where theranostics are rapidly growing and where we have both diagnostic as well as therapeutic options in our own hands.*

Dr. Bax: Randomized controlled trials are, of course, fundamental for introduction of new therapies, but they do not fully answer the question of how a new therapy is best implemented in daily practice. There is often a significant difference between a randomized controlled trial in a completely optimized and well-defined environment and its implementation in daily clinical practice. That is what makes the creation and analysis of our own clinical databases interesting and a way in which care can be further refined.

It is very important for clinicians to think academically and ask questions. We do this every day, but why do we do this? Does a technique or innovation really work, or can it be improved? If so, then how? Those sorts of questions help to advance the field. It is our current experience using research from our big clinical databases that this sort of resource can be used to design evidence-creating randomized trials.

Dr. Bengel: *Very good point. Let's get to your "second career" as a leader in the ESC and international cardiology. How did this happen?*

Dr. Bax: Through our research, I visited many cardiology clinics, which resulted in a broad international network, building bridges and relationships. This also included interactions and involvement in scientific committees of various societies, including the ESC, the American Society of Nuclear Cardiology, and our international meeting, the International Conference of Nuclear Cardiology. I was asked by the ESC president to become the program chair of the large ESC congress. This showed me the importance of coming together and being engaged and learning from each other. Later on, I became chair of the ESC Guideline Committee. Finally, I was asked whether I wanted to run for vice president of the ESC and then president. During that presidency, I realized the importance of relationships with industry. On the one hand, frequent criticism suggests that medical societies should not be working too closely with industry and that boundaries should be clearly defined. But when it comes to education, congresses, guidelines, etc., all these activities constantly bring the two together. Modern drug development, for example, is so advanced today that industry and medical doctors really need to work together.

Dr. Bengel: *That is quite relevant to nuclear medicine, where major pharmaceutical companies are now increasingly involved as a result of the success of theranostics in oncology. How do you make sure that you can still shape the future of the field with sufficient independence from—but at the same time sufficient integration with—industry?*

Dr. Bax: For many organizational activities in the ESC, we worked closely together. In education, for example, a committee was asked to build programs based on clinical needs and created by physicians. These were then communicated to industry for support. Industry needs clinical advice and vice versa. When it comes to daily practice, however, you want to be independent and not biased by specific industry relations. Hence, we need to be transparent and self-reflective.

The same is true for the creation of guidelines, a key process within the ESC. Randomized controlled trials are the best evidence, and nonrandomized trials form only a middle layer of evidence. Guidelines are being constructed purely based on evidence and expert opinions, and this is done by medical specialists. Industry is not taking part here. They do not even see anything of the process until it is finalized and published. Achieving a bias-free perception of our work is ultimately beneficial to everybody.

Dr. Bengel: *The successful creation of clinical guidelines that define the specialty is a key achievement of the ESC. Publication of guidelines also makes up a large part of the success of the* European Heart Journal, *where the guidelines contribute greatly to the numbers of citations. Has this been an active political development in the ESC?*

Dr. Bax: At the time when I led the congress program, the then president of ESC taught me that 3 things are important within the society: the congress, guidelines, and journals. There was always a strong focus on these issues. ESC now holds several other meetings in addition to their main annual congress. All of these create revenue and educate specialists. Scientific societies should make use of their broad membership resources to create valuable content such as meetings, which move the field forward.

You also asked about journals. In the 1990s to early 2000, there were 2 top journals in the field, *Circulation* and *JACC,* where I served as an associate editor for a few years. Then came the *European Heart Journal,* benefiting indeed from the success of ESC guidelines and emerging as the third major cardiology journal. I also served as an associate editor there. This experience helped me recognize that, in the end, it is important how a journal is run. If you work diligently on interpreting the submitted science and keep in touch with what is clinically relevant, this will lead to success.

Dr. Bengel: JACC, Circulation, *and the* European Heart Journal *all have their cardiovascular imaging spin-off journals today, where good science that cannot be accommodated in the main journal can be published in the spin-offs.* JNM *also wants high-quality cardiovascular contributions so that cardiovascular imaging remains well represented within the nuclear medicine community. What is your advice for* JNM *to sustain a leading position in cardiovascular imaging publications and continue to receive good submissions?*

Dr. Bax: As a leading journal in nuclear medicine, *JNM* should have outstanding review articles contributed by leading physicians in cardiovascular disease. Such reviews may highlight the clinical needs of cardiologists that can be addressed by nuclear medicine. Then for the research itself, you can also actively recruit submissions by leaders in the field. Abstracts from congresses may be screened for this purpose. You could think about topics that are of more specific relevance for the nuclear medicine community so that these may be preferentially submitted to *JNM*.

Dr. Bengel: *In your leadership role at the ESC congress in Rome in 2016, you were able to meet Pope Francis. How much does the pope know about medical science and maybe even nuclear medicine?*

Dr. Bax: It was a huge honor for the ESC that Pope Francis really came. He was very interested in treatment of patients, patient care, and was really engaged, discussing openly about medicine, the congress, and our specialty. We felt that he really cared. Caring for people remains important in today's medicine, where technology tends to dominate and where there is so much time pressure and need for documentation. Let's not forget to look each other in the eyes and just listen and find out what is important for patients, so that they are comfortable. That's something that the meeting with Pope Francis helped to reinforce.

Dr. Bengel: *Final question: Your son is studying medicine—what is your advice for young people? How can they find their way in the field of medicine, and what will be important for their careers?*

Dr. Bax: It is difficult, because just as we were different from the generation before us, the younger generation is different from our generation. The world is changing very rapidly. When it comes to medicine, patient care is central, and the next generation of doctors will understand that. I think that the work/life balance needs to be discussed more with this younger generation. Members of the next generation definitely think more about these things than we did, and we should accept this. My specific advice to the next generation of medical doctors is that becoming a good clinician is very important. If possible, combine this with research. The way we are practicing medicine is becoming more difficult, with expanding rules, regulations, protocols, and administrative and computer tasks that keep us away from the patient. To become a good physician, you can also become a good researcher and must always be a good human being.

Single-Cell Radiotracer Allocation via Immunomagnetic Sorting to Disentangle PET Signals at Cellular Resolution

Laura M. Bartos[1], Sebastian T. Kunte[1], Philipp Beumers[1], Xianyuan Xiang[2,3], Karin Wind[1], Sibylle Ziegler[1,4], Peter Bartenstein[1,4], Hongyoon Choi[5,6], Dong Soo Lee[5–7], Christian Haass[2,3,8], Louisa von Baumgarten[9,10], Sabina Tahirovic[8], Nathalie L. Albert[1], Simon Lindner*[1], and Matthias Brendel*[1,4,8]

[1]*Department of Nuclear Medicine, University Hospital of Munich, LMU Munich, Munich, Germany;* [2]*Biomedical Center, Division of Metabolic Biochemistry, Faculty of Medicine, Ludwig-Maximilians-Universität München, Munich, Germany;* [3]*CAS Key Laboratory of Brain Connectome and Manipulation, the Brain Cognition and Brain Disease Institute, Shenzhen Institutes of Advanced Technology, Chinese Academy of Sciences, and Shenzhen-Hong Kong Institute of Brain Science–Shenzhen Fundamental Research Institutions, Shenzhen, China;* [4]*Munich Cluster for Systems Neurology, Munich, Germany;* [5]*Department of Nuclear Medicine, Seoul National University Hospital, Seoul, Republic of Korea;* [6]*Department of Nuclear Medicine, Seoul National University College of Medicine, Seoul, Republic of Korea;* [7]*Department of Molecular Medicine and Biopharmaceutical Sciences, Graduate School of Convergence Science and Technology, Seoul National University, Seoul, Republic of Korea;* [8]*German Center for Neurodegenerative Diseases, Munich, Germany;* [9]*Department of Neurosurgery, University Hospital of Munich, LMU Munich, Munich, Germany; and* [10]*German Cancer Consortium, Munich, Germany*

With great interest, our independent groups of scientists located in Korea and Germany recognized the use of a very similar methodologic approach to quantify the uptake of radioactive glucose (^{18}F-FDG) at the cellular level. The focus of our investigations was to disentangle microglial ^{18}F-FDG uptake. To do so, CD11b immunomagnetic cell sorting was applied to isolate microglia cells after in vivo ^{18}F-FDG injection, to allow simple quantification via a γ-counter. Importantly, this technique reveals a snapshot of cellular glucose uptake in living mice at the time of injection since ^{18}F-FDG is trapped by hexokinase phosphorylation without a further opportunity to be metabolized. Both studies indicated high ^{18}F-FDG uptake of single CD11b-positive microglia cells and a significant increase in microglial ^{18}F-FDG uptake when this cell type is activated in the presence of amyloid pathology. Furthermore, another study noticed that immunomagnetic cell sorting after tracer injection facilitated determination of high ^{18}F-FDG uptake in myeloid cells in a range of tumor models. Here, we aim to discuss the rationale for single-cell radiotracer allocation via immunomagnetic cell sorting (scRadiotracing) by providing examples of promising applications of this innovative technology in neuroscience, oncology, and radiochemistry.

Key Words: scRadiotracing; cell sorting; ^{18}F-FDG; PET; cellular resolution; tracer uptake

J Nucl Med 2022; 63:1459–1462
DOI: 10.2967/jnumed.122.264171

The following sections discuss knowledge gaps of cellular tracer uptake and potential applications of scRadiotracing in different fields of molecular imaging.

Received Mar. 22, 2022; revision accepted May 16, 2022
For correspondence or reprints, contact Matthias Brendel (matthias.brendel@med.uni-muenchen.de).
*Contributed equally to this work.
Published online May 19, 2022.

POTENTIAL APPLICATIONS OF scRADIOTRACING IN NEUROSCIENCE

Spatiotemporal alterations in the ^{18}F-FDG PET signal comprise a well-established readout in the diagnostic workup of patients with neurologic disorders (*1–3*). However, the method lacks the cellular resolution to distinguish respective contributions of different cell types to the ^{18}F-FDG uptake. Most earlier studies claimed that neuronal activity and neuronal ^{18}F-FDG uptake dominate glucose uptake and consumption in the mammalian brain (*4*). However, several recent studies highlighted a significant contribution of glial cells to the energy metabolism of the brain (*5–7*), questioning ^{18}F-FDG PET as a pure biomarker of neuronal activation (*8*). We applied immunomagnetic cell sorting after in vivo radiotracer injection and brain extraction, followed by subsequent measurement of γ-emission and cell count in enriched cell fractions to calculate radiotracer uptake per specific single cell (scRadiotracing; Fig. 1 shows the workflow). Subsequently, our 2 recent studies exploring scRadiotracing technology identified high microglial ^{18}F-FDG uptake in mouse models with amyloid pathology (*7,9*). Furthermore, microglial ^{18}F-FDG uptake was the most likely reason for elevated ^{18}F-FDG PET signals in these mice (*7,9*). However, many remaining questions about altered ^{18}F-FDG PET signals may also be addressed by an analysis of glucose uptake at cellular resolution. Recently, we discovered a reduction in the ^{18}F-FDG PET signal in a progranulin knockout mouse model with hyperactivated microglia and in a mouse model with homeostatic microglia (Trem2 knockout) (*10*). Although this finding speaks for reduced brain function in both genotypes, it still remains unclear whether progranulin knockout microglia have lower ^{18}F-FDG uptake or whether the net signal is driven by reduced neuronal activity despite higher ^{18}F-FDG uptake by activated microglia (*7,9*). This example illustrates the need to study glucose uptake at cellular resolution. Given the growing evidence for an astrocyte–neuron lactate shuttle (*11,12*), it will be of interest to reveal whether increasing neuronal activity (*13*) can stimulate glial ^{18}F-FDG uptake, which could be addressed using scRadiotracing. The presence of such shuttle systems questions the cellular glucose uptake regardless of

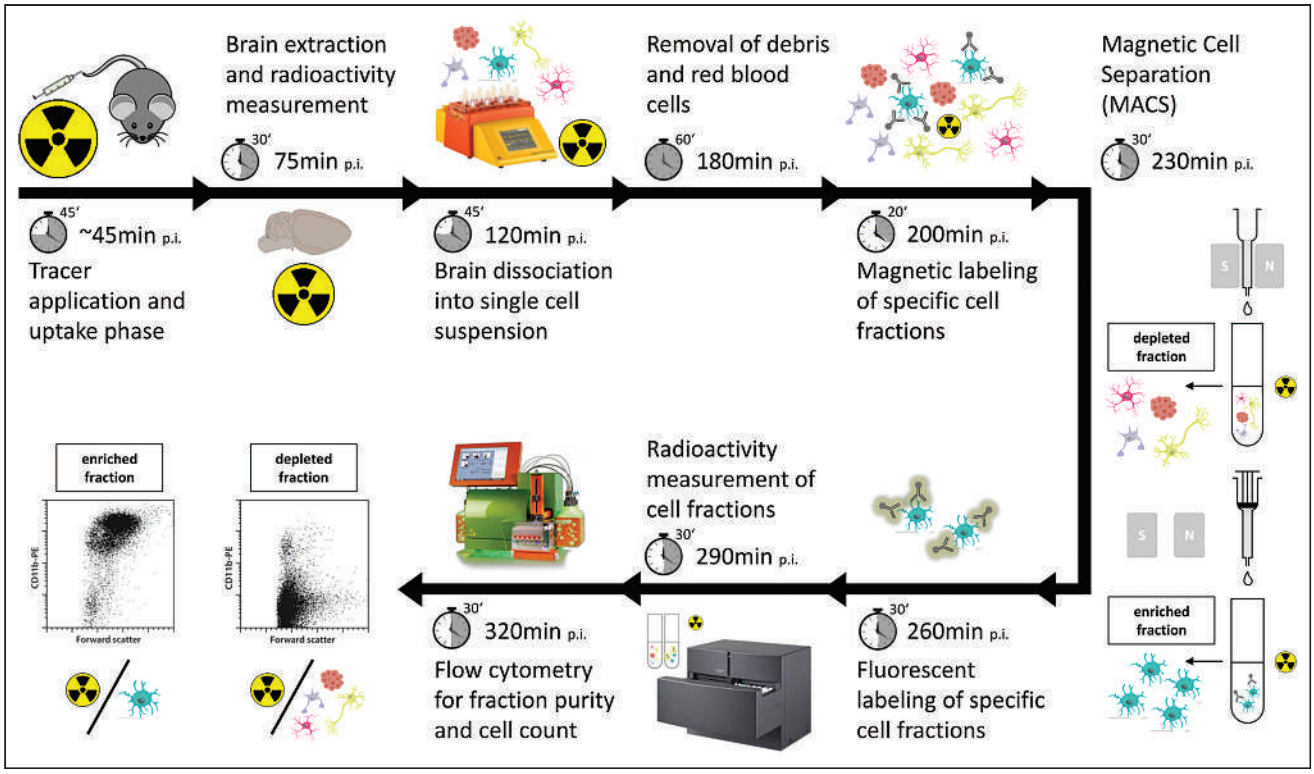

FIGURE 1. Workflow of scRadiotracing to determine microglial ^{18}F-FDG uptake in brain at cellular resolution. After tracer injection into tail vein, brain is removed during tracer-specific uptake period. After generation of single-cell suspension, immunomagnetic cell separation is used to separate fractions of enriched cells from their depleted counterparts, which contain bound radioactivity. Fluorescent labeling, γ-counting, and flow cytometry are used to calculate radioactivity per cell as primary readout. Time to complete each step is indicated, together with summed time during workflow. CD11b is used to detect microglia. p.i. = after injection; S/N = south and north pole of the magnet. (Courtesy of Miltenyi Biotec B.V. & Co. KG. All rights reserved. Copyright © 2022.)

the individual glucose consumption of different cell types, which is undeniably high in active neurons (*14*). In this regard, there could be an imbalance between the cellular localizations of glucose uptake and energy consumption. Importantly, scRadiotracing after ^{18}F-FDG injection could be specifically used to allocate glucose uptake, whereas other tracers could be used to track metabolites of aerobic and anaerobic glycolysis at the cellular level. Furthermore, uptake mechanisms during acute stimulation of glucose consumption by physiologic (*15*) or pharmacologic interventions could be deciphered by scRadiotracing. To this end, task-related stimuli could be applied together with resurgent functional PET methodology (*16*) and scRadiotracing in experimental models. scRadiotracing could be applied after brain extraction at the time of maximal stimulation, determined by the functional PET readout, to track the changes in cellular ^{18}F-FDG uptake in contrast to unstimulated conditions.

NOTEWORTHY

- Cellular sources of ^{18}F-FDG and other PET imaging radiotracers are poorly understood.
- scRadiotracing facilitates determination of in vivo radiotracer uptake per specific single cell.
- scRadiotracing is of high interest when radiotracer targets are expressed and pathologically altered on different cell types, such as is applicable for TSPO.

As another example in the field of neuroimaging, tau PET tracers emerged as valuable biomarkers for the differentiation of tauopathies from controls (*17*). However, the translation of in vitro tau PET tracer binding to an in vivo signal is still under debate, and the detailed cellular sources of autoradiography and tau PET signal elevations remain unclear. Hence, our novel scRadiotracing approach could be used to calculate tau PET tracer uptake at cellular resolution of single neurons and astrocytes in models of tauopathies in order to close this knowledge gap. Brain subregion analyses by scRadiotracing are also feasible as long as the product of the cellular yield and the tracer abundance exceed the detection limit of the γ-counter. In this regard, we successfully dissected the hippocampus to study region-specific ^{18}F-FDG uptake in mice with amyloid pathology (*9*). In tauopathies, this feature could be used to compare single-cell radiotracer uptake of regions with high and low tau abundance.

POTENTIAL APPLICATIONS OF scRADIOTRACING IN NEUROONCOLOGY AND ONCOLOGY

The novel combination of tracer injection and immunomagnetic cell sorting could also facilitate dedicated analysis of tumor cells in experimental models of brain tumors together with analysis of specific immune cell fractions and tumor surrounding cells such as neurons and ependymal cells. This ability could be highly valuable since the target of several tracers for glioblastoma imaging, including the 18-kDa translocator protein (TSPO), is not restricted to a single cell type. Determining the radiotracer uptake of TSPO

ligands at cellular resolution in the brain is of general interest since the target is expressed not only by microglia cells but also by tumor cells, astrocytes, endothelial cells, and neurons (*18*). Since blood–brain barrier disruption is often questioned as a strong influencer of PET tracer signals in brain tumor imaging, scRadiotracing could also act as a proof of cellular radiotracer allocation. Here, the magnitude of radiotracer uptake per cell could be multiplied by respective absolute cell numbers to investigate whether the entire PET signal is explained by cellular sources.

Apart from brain tumors, the aforementioned oncologic investigation (*19*) already applied scRadiotracing in a wide range of tumor models, including renal cell carcinoma, colorectal carcinoma (CT26, MC38), and breast cancer. Importantly, the authors used not only ^{18}F-FDG but also ^{18}F-labeled glutamine to disentangle its metabolism in tumor cells and the tumor microenvironment (*19*). This use shows that scRadiotracing is not limited to ^{18}F-FDG and highlights the broad range of potential scRadiotracing applications in experimental oncology. For example, prostate-specific membrane antigen radiotracers are preferred for targeting of prostate cancer cells because they exhibit very low glucose consumption and therefore cannot be detected by ^{18}F-FDG PET. However, prostate-specific membrane antigen is expressed not only in prostate cells but also in several other tissues, such as nonprostatic epithelial cells, other neoplastic cells, and tumor-associated neovasculature. Prostate-specific membrane antigen uptake was also associated with inflammatory and infectious processes (*20*). Thus, scRadiotracing could be used to differentiate prostate-specific membrane antigen uptake in prostatic cancer cells from others and to avoid pitfalls in prostate cancer diagnostics. The same applies to the diagnostics of well-differentiated neuroendocrine tumors such as gastroenteropancreatic neuroendocrine tumors and meningiomas using radiolabeled somatostatin receptor (SSTR) ligands. The importance of neuroendocrine tumor diagnostics and therapy is underpinned by an interventional multicenter phase III clinical trial (NETTER) to compare peptide receptor radionuclide therapy using ^{177}Lu-DOTA^{0}-Tyr^{3}-octreotate with high-dose octreotide LAR therapy in patients with metastasized or locally advanced, inoperable, SSTR-positive, midgut carcinoid tumors. However, SSTR expression is not exclusive to neuroendocrine tumor or meningioma cells. Tracer uptake was also observed by inflammatory pathologies such as cardiovascular disease and ischemia and by various other benign and malignant tumors (*21*). scRadiotracing has the potential to resolve such inconclusive results by use of back translation in experimental models. This may help to determine off-target sources and prevents false-positive findings. In cases with borderline SSTR expression, dual scRadiotracing may also be suitable to elucidate whether SSTR radioligands or ^{18}F-FDG is better suited for follow-up PET imaging of the individual patient.

POTENTIAL APPLICATIONS OF scRADIOTRACING IN RADIOCHEMISTRY AND RADIOTRACER DEVELOPMENT

scRadiotracing might also be a versatile tool in tracer development to investigate cell-specific uptake of acutely isolated cells when compared with cell cultures, in which the metabolic activity of cells may be altered. In general, ex vivo radiopharmaceutical research methods rely mostly on macroscopic samples for quantification in a γ-counter or on autoradiography blocking experiments, including correlation studies with immunohistochemistry staining. However, such techniques do not investigate tracer enrichment on the cellular level. Nevertheless, cellular-level investigations are of particular interest when the specificity of a novel tracer has to be explored or when the radioactivity distribution is to be assigned to specific cell types. In neuroinflammatory tissue, the discrimination of tracer accumulation in different microglia phenotypes could be of eminent importance. Such approaches could support the development of specific ligands for homeostatic and disease-associated microglia, which would facilitate monitoring of therapeutic agents that modulate distinct microglia phenotypes. In principle, scRadiotracing could be applied to any radiotracer binding to an intracellular target. However, it is questionable whether ligands of membrane-bound targets on the surface of cells also qualify for scRadiotracing analysis. Upstream cell processing promises a gentle mechanical and enzymatic dissociation preserving cell integrity and surface epitopes, but it has to be proven whether high-affinity binders withstand hydrolytic treatment. This also applies to subsequent downstream applications beyond quantification in a γ-counter. In this respect, ligands showing a high internalization rate may most likely be applicable to scRadiotracing analysis.

METHODOLOGIC LIMITATIONS AND CONSIDERATIONS

First, we note the difficulty in quantifying the uptake of a whole cell population via scRadiotracing. The procedure of cell dissection and harvesting may over- or underestimate the proportion of viable cells in the brain or in specific regions (*22*), hampering extrapolation to absolute cell numbers. Cell proportions can also be influenced by proliferation and cell loss, which lead to subsequent alterations in cell density. Thus, scRadiotracing facilitates robust calculation of radiotracer uptake per cell, but extrapolation to the whole fraction is erroneous. A full allocation model of radiotracer uptake per cell type and fraction could be established by simultaneous light sheet microscopy (*23*). Light sheet microscopy offers the possibility to quantify the absolute number of cells per cell type in a 3-dimensional and analysis of a subsample allows combination of cellular tracer uptake with absolute cell numbers.

Unlike well-established nearly irreversibly bound ^{18}F-FDG, all non–^{18}F-FDG radioligands may suffer from higher instability during the scRadiotracing procedure. For instance, the binding stability of a TSPO ligand to the TSPO complex at the mitochondrial membrane could decrease during the scRadiotracing procedure. This decreased binding stability also accounts for current tau ligands such as ^{18}F-PI-2620, which is characterized by a decrease in target-bound radiotracer over time in 4-repeat tauopathies (*24*).

Loss of processes and synapses potentially impacts quantitative results in scRadiotracing. ^{18}F-FDG in neuronal synapses comprises one important example of missed radiotracer in the scRadiotracing workflow (*7,9*). Optimization of the dissociation procedure has the potential to further enhance the accuracy of scRadiotracing. In a similar regard, consideration of live and dead cells may stabilize scRadiotracing results since cells with leaky membranes can be excluded.

Cell separation after TSPO tracer injection was also proposed by a recent study using a similar technique of fluorescence-activated cell sorting (FACS) to determine the cellular source of a ^{125}I-labeled SPECT TSPO ligand (^{125}I-CLINDE) (*25*). Here, the long half-life of ^{125}I offered the opportunity to conduct the experiments with less of a time constraint. In a comparison of the two approaches, immunomagnetic cell sorting systems can be installed relatively simply within a radiation protection controlled area, and the higher cell yield is another advantage of immunomagnetic cell sorting over FACS, which allows even proteomic analyses (*26*). On the other

hand, FACS offers the advantage of direct separation of genetically determined fluorescent cells (i.e., green fluorescent protein), which cannot be achieved via immunomagnetic cell sorting. Furthermore, specific cell populations, such as homeostatic or disease-associated microglia, can be selected via FACS gating, when discriminative antibodies are used. Considering the stability of radiotracer binding once more, there is a need to investigate the impact of emitted energy during cell sorting via FACS, which could be of high relevance for tracers bound at voltage channels. Head-to-head comparisons of both approaches will be required to allow recommendations on whether immunomagnetic cell sorting or FACS systems are to be preferred for scRadiotracing.

scRadiotracing in human tissue after in vivo or in vitro tracer application comprises another promising methodologic variant (*25*). In vitro application of radiotracer to tissue allows investigation of small amounts of tissue that do not yield a sufficient signal-to-noise ratio when the tracer is applied in vivo (i.e., before surgery on tumors). However, scRadiotracing after tracer application in vivo could be used to validate in vitro scRadiotracing in the same tissue when amounts are large enough. Furthermore, blocking with cold ligands could be performed to test for the specificity of cellular radiotracer binding using in vitro scRadiotracing. As a limitation, we note that the extensive workflow (Fig. 1) likely restricts scRadiotracing to an experimental setting and prevents it from use in clinical routine at the current stage.

CONCLUSION

We highlighted some of the broad range of highly demanded applications for the novel scRadiotracing workflow to elucidate tracer uptake mechanisms and their underlying cell biology.

DISCLOSURE

Matthias Brendel was funded by the Deutsche Forschungsgemeinschaft (DFG) under Germany's Excellence Strategy within the framework of the Munich Cluster for Systems Neurology (EXC 2145 SyNergy – ID 390857198), and Philipp Beumers and Nathalie L. Albert were funded by the Deutsche Forschungsgemeinschaft (DFG, German Research Foundation), project number 421887978. No other potential conflict of interest relevant to this article was reported.

REFERENCES

1. Baumgartner A, Rauer S, Mader I, Meyer PT. Cerebral FDG-PET and MRI findings in autoimmune limbic encephalitis: correlation with autoantibody types. *J Neurol.* 2013;260:2744–2753.
2. Jack CR Jr, Bennett DA, Blennow K, et al. NIA-AA Research Framework: toward a biological definition of Alzheimer's disease. *Alzheimers Dement.* 2018;14:535–562.
3. Guedj E, Varrone A, Boellaard R, et al. EANM procedure guidelines for brain PET imaging using [^{18}F]FDG, version 3. *Eur J Nucl Med Mol Imaging.* 2022;49:632–651.
4. Sokoloff L. Energetics of functional activation in neural tissues. *Neurochem Res.* 1999;24:321–329.
5. Zimmer ER, Parent MJ, Souza DG, et al. [^{18}F]FDG PET signal is driven by astroglial glutamate transport. *Nat Neurosci.* 2017;20:393–395.
6. Ulland TK, Song WM, Huang SC-C, et al. TREM2 maintains microglial metabolic fitness in Alzheimer's disease. *Cell.* 2017;170:649–663.e13.
7. Xiang X, Wind K, Wiedemann T, et al. Microglial activation states drive glucose uptake and FDG-PET alterations in neurodegenerative diseases. *Sci Transl Med.* 2021;13:eabe5640.
8. Sokoloff L, Reivich M, Kennedy C, et al. The [^{14}C]deoxyglucose method for the measurement of local cerebral glucose utilization: theory, procedure, and normal values in the conscious and anesthetized albino rat. *J Neurochem.* 1977; 28:897–916.
9. Choi H, Choi Y, Lee EJ, et al. Hippocampal glucose uptake as a surrogate of metabolic change of microglia in Alzheimer's disease. *J Neuroinflammation.* 2021; 18:190.
10. Götzl JK, Brendel M, Werner G, et al. Opposite microglial activation stages upon loss of PGRN or TREM2 result in reduced cerebral glucose metabolism. *EMBO Mol Med.* 2019;11:e9711.
11. Lee Y, Morrison BM, Li Y, et al. Oligodendroglia metabolically support axons and contribute to neurodegeneration. *Nature.* 2012;487:443–448.
12. Patel AB, Lai JC, Chowdhury GM, et al. Direct evidence for activity-dependent glucose phosphorylation in neurons with implications for the astrocyte-to-neuron lactate shuttle. *Proc Natl Acad Sci USA.* 2014;111:5385–5390.
13. Adachi K, Cruz NF, Sokoloff L, Dienel GA. Labeling of metabolic pools by [6-^{14}C]glucose during K(+)-induced stimulation of glucose utilization in rat brain. *J Cereb Blood Flow Metab.* 1995;15:97–110.
14. Vergara RC, Jaramillo-Riveri S, Luarte A, et al. The energy homeostasis principle: neuronal energy regulation drives local network dynamics generating behavior. *Front Comput Neurosci.* 2019;13:49.
15. Rischka L, Gryglewski G, Pfaff S, et al. Reduced task durations in functional PET imaging with [^{18}F]FDG approaching that of functional MRI. *Neuroimage.* 2018; 181:323–330.
16. Verger A, Guedj E. The renaissance of functional ^{18}F-FDG PET brain activation imaging. *Eur J Nucl Med Mol Imaging.* 2018;45:2338–2341.
17. Beyer L, Brendel M. Imaging of tau pathology in neurodegenerative diseases: an update. *Semin Nucl Med.* 2021;51:253–263.
18. Nutma E, Ceyzeriat K, Amor S, et al. Cellular sources of TSPO expression in healthy and diseased brain. *Eur J Nucl Med Mol Imaging.* 2021;49:146–163.
19. Reinfeld BI, Madden MZ, Wolf MM, et al. Cell-programmed nutrient partitioning in the tumour microenvironment. *Nature.* 2021;593:282–288.
20. de Galiza Barbosa F, Queiroz MA, Nunes RF, et al. Nonprostatic diseases on PSMA PET imaging: a spectrum of benign and malignant findings. *Cancer Imaging.* 2020;20:23.
21. Helgebostad R, Revheim ME, Johnsrud K, Amlie K, Alavi A, Connelly JP. Clinical applications of somatostatin receptor (agonist) PET tracers beyond neuroendocrine tumors. *Diagnostics (Basel).* 2022;12:528.
22. Keller D, Ero C, Markram H. Cell densities in the mouse brain: a systematic review. *Front Neuroanat.* 2018;12:83.
23. Stelzer EHK, Strobl F, Chang B-J, et al. Light sheet fluorescence microscopy. *Nature Reviews Methods Primers.* 2021;1:73.
24. Song M, Beyer L, Kaiser L, et al. Binding characteristics of [^{18}F]PI-2620 distinguish the clinically predicted tau isoform in different tauopathies by PET. *J Cereb Blood Flow Metab.* 2021;41:2957–2972.
25. Tournier BB, Tsartsalis S, Ceyzeriat K, et al. Fluorescence-activated cell sorting to reveal the cell origin of radioligand binding. *J Cereb Blood Flow Metab.* 2020;40: 1242–1255.
26. Sebastian Monasor L, Muller SA, Colombo AV, et al. Fibrillar Aβ triggers microglial proteome alterations and dysfunction in Alzheimer mouse models. *eLife.* 2020;:9:e54083.

α-Synuclein PET and Parkinson Disease Therapeutic Trials: Ever the Twain Shall Meet?

John P. Seibyl

Institute for Neurodegenerative Disorders, New Haven, Connecticut

Neurodegenerative disorders are common brain afflictions with increasing prevalence in countries with aging populations. This is true for the two most common neurodegenerative disorders, Alzheimer disease (AD) and Parkinson disease (PD), both demonstrating increases in prevalence over the last decade, with more than 6 million diagnosed with AD and 1 million with PD in the United States (*1,2*). The impact on the individual patient, the burden on families, and the societal and financial costs are becoming more urgent as these epidemiologic trends play out (*3*).

Recently, progress has been made in understanding the etiology of neurodegenerative disorders at the molecular level. We know that these diseases represent a series of pathologic brain conditions characterized by protein misfolding and the progressive accumulation of cytotoxic fibrils and oligomers that are believed to result in selective neurologic and functional impairment (*4*). The unrelenting progression of symptoms and disability represents ongoing neuronal degeneration resulting from dissemination of these cytotoxic proteins in the brain. In AD, there are PET biomarkers targeting the 2 aberrant proteins, β-amyloid contained in neuritic plaques and tau found in neurofibrillary tangles, the pathology described originally by Alois Alzheimer.

These imaging biomarkers have already been deployed to support the development of therapeutics that target amyloid (*5*). The equivalent protein in PD is α-synuclein (a-syn), found in Lewy bodies. Currently, there is no available PET agent for interrogating a-syn deposition and no easy way to track in vivo brain changes mechanistically relevant to clinical progression (*6*).

WHY A-SYN PET IN PD?

Dopamine transporter (DaT) imaging using SPECT and ^{123}I-tropane imaging agents such as ^{123}I-ioflupane demonstrate significant reductions in striatal binding ratios in PD patients enrolled in longitudinal studies of 1–2 y or more. DaT SPECT is also an important tool for identifying DaT deficits in premotor and at-risk individuals (*7,8*). Yet DaT imaging interrogates one piece of the pathology of PD, presumably the consequence of a-syn deposition in the substantia nigra. DaT SPECT does not directly assess a-syn, which represents an upstream process against which disease-modifying treatments are targeted. Hence, the 2 imaging biomarker targets, DaT and a-syn, are theoretically complementary.

Received Feb. 19, 2022; revision accepted Apr. 7, 2022.
For correspondence or reprints, contact John P. Seibyl (jseibyl@indd.org).
Published online Jul. 19, 2022.

DOI: 10.2967/jnumed.122.263918

A-syn is a 140-amino-acid protein highly prevalent in the brain, representing 1% of the cytosolic protein and thought to be localized to the presynaptic terminal, where it facilitates the release of neurotransmitter into the synapse. The protein undergoes extensive posttranslational modification and is natively unstructured, rather taking its conformation from its local milieu. Within cells, fibrils form oligomers, thought to be the cytotoxic form of a-syn. Different conformational states characterize the different synucleinopathies (*9,10*).

A-syn has now emerged as a key target for development of a PET biomarker in the evaluation of the pathophysiology and putative treatments for modifying the course of PD. Why? First, the primary brain pathologies in PD are Lewy neurites and Lewy bodies, which are composed of aggregated a-syn resulting from misfolding of protein and seeding and whose pattern of brain spread is suggested by postmortem brain examination of Lewy body distribution (*11,12*). These studies indicate a discrete pattern of Lewy body formation that describes a pathway of spread going from the brain stem systematically to the midbrain (including nigrostriatal projections) and finally to higher cortical regions. A-syn is found in many body tissues outside the brain, including the skin, salivary glands, and gut. Biopsy of tissue in PD can demonstrate this and has been proposed as another biomarker in clinical therapeutic trials. Interestingly, recent work suggests that the gastrointestinal tract may have a role in the etiology of PD. Alterations in the microenvironment of the gut biota can lead to inflammatory changes and conditions that favor the formation of a-syn fibrils (*13*). These may then travel into the central nervous system via the vagus nerve or through vascular pathways. Once seeded in the lower brain stem, fibrils are believed to cross the synapse to affect adjacent connected neurons (Fig. 1). The presence of these alien fibrils creates conditions that enhance the formation of additional fibrils and aggregates. As a-syn spreads superiorly, involvement in midbrain structures may result in some premotor symptoms associated with PD, including rapid-eye-movement sleep behavior disorder and hyposmia. Both of these have been used for cohort enrichment for enrollment of at-risk or premotor individuals (*14*).

Another reason for interest in a-syn in PD comes from genetic studies. Genomewide association studies have shown a strong association of variations in the a-syn gene with PD (*15,16*). In addition, mutations in the a-syn gene promote formation of a-syn aggregates and fibrils. These findings support a-syn as an important target of disease-modifying treatments and potentially a path to better understanding of the onset and longitudinal course of disease across the synucleinopathies: PD, dementia with Lewy bodies, and multiple-system atrophy. Further, knowing how differences in a-syn conformational structure

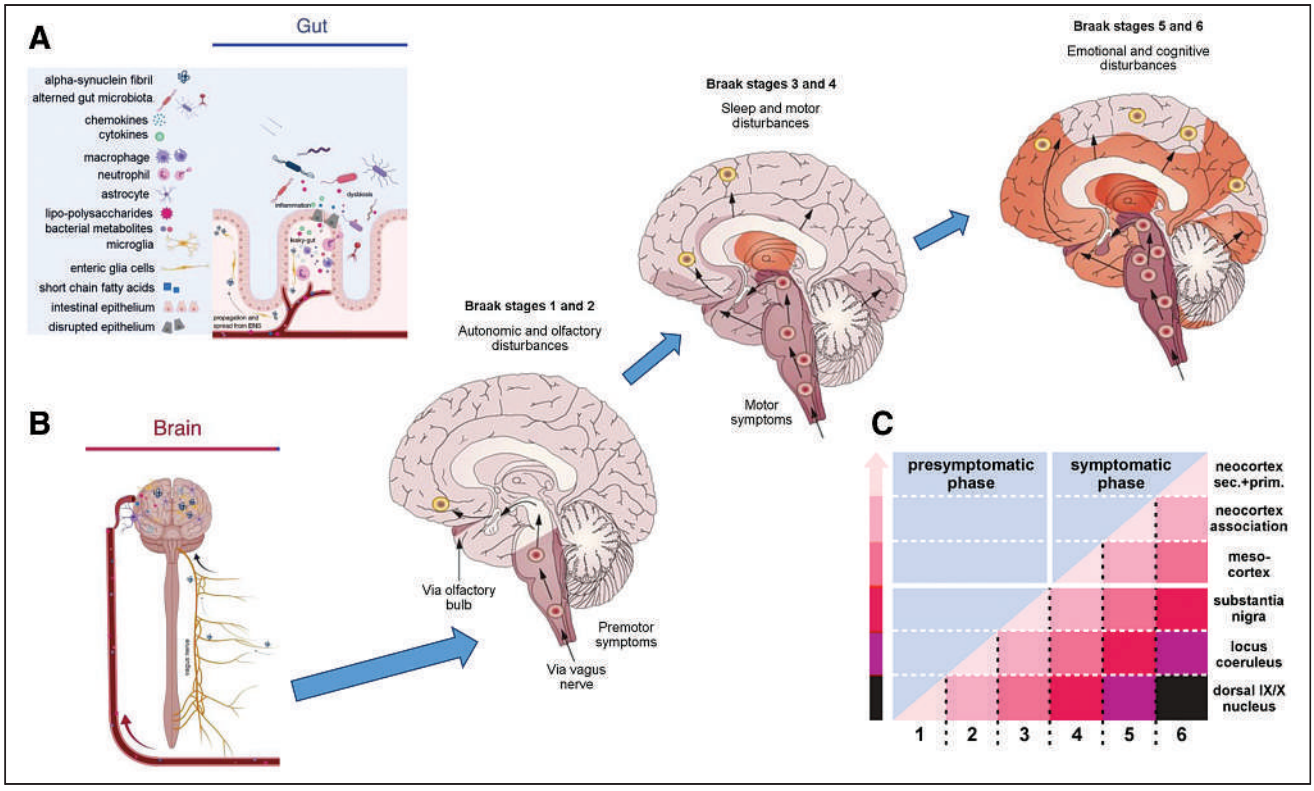

FIGURE 1. Etiologic model of PD and other synucleinopathies. (A) Proposed model for development of Lewy body diseases such as PD suggests gut may be locus of initial production of a-syn fibrils. This takes place in context of inflammatory changes associated with disruption of integrity of intestinal epithelium, as occurs in different microbiota environments. (B) These fibrils are taken up by vagus nerve and transported to lower brain stem. (C) Through process of cell-to-cell spread following along network lines, additional cells become affected, systematically moving up through brain stem to midbrain and cortex and resulting in progressive symptoms reflective of involved region. Motor symptoms begin at stage 3, when substantia nigra becomes involved. ENS = enteric nervous system. (Adapted from (*11,13*).)

affect pathophysiologic manifestations of disease may offer additional clues to treatment, clarify phenotype with regard to differential diagnosis and prognosis, and offer needed tools—such as at-risk screening, proof of target engagement, and assessment of drug efficacy—needed to conduct therapeutic trials.

The enthusiasm for a PET biomarker of a-syn is underscored by the sponsorship of the Michael J. Fox Foundation, which has offered a $2 million prize to the first team that develops a viable selective a-syn PET tracer and agrees to make that tracer available broadly. The ability to image a-syn deposition in the brain was described in the program announcement as "a game-changing achievement for the Parkinson's disease field." Efforts by both industry and academic groups are under way in this and other a-syn biomarker initiatives.

NEW ROLES FOR PET IMAGING IN PD

Up to now, treatment for PD has been symptomatic, rather than disease-modifying. Designing a clinical trial for a drug that actually slows, stops, or reverses clinical symptoms and improves function is exceedingly difficult. Questions arise as to which participants to enroll, what metric to use for measuring treatment efficacy, and how many subjects are needed to power a potentially small reduction in a process that changes relatively slowly as PD progresses.

Medications taken for managing symptoms, such as L-DOPA, can be another confounder in determining off-medication clinical status. To get true off-medication assessments, several weeks of withdrawal from the symptomatic medications may be necessary. This is not easily done or ethical given the amount of increased morbidity experienced by patients off medications for that period (*17*). Another issue regarding medications is whether the putative disease-modifying agent has any direct symptomatic effect, making it harder to tease out symptom relief from true efficacy in altering the mechanisms of disease (*18*).

Questions about when in the course of illness to recruit the test cohort are extremely important since clinical manifestations occur only after years of silent, abnormal pathologic processes. How does one diagnose and treat a disease that is not clinically manifest? This presymptomatic phase of illness is when a disease-modifying intervention might be most effective, rather than later when there is less salvageable tissue. Recruiting from this cohort also gets around the medication issues mentioned above. The length of this window between initiation of pathology and subsequent clinical manifestation is on the order of years. As an example, use of the DaT agent ^{123}I-ioflupane and SPECT imaging in the Parkinson Progression Marker Initiative de novo PD cohort (*19*), which was serially scanned over 4 y (baseline and years 1, 2, and 4), allows back-extrapolation of striatal specific binding ratio curves to the point of normalcy, permitting a rough estimate of the duration of the clinically silent course of progressive change in the brain. This duration turns out to be about 13 y in the most affected brain regions, thus suggesting the important roles that a-syn PET might play in the arena of clinical trials. For example, a-syn might provide early confirmation of disease pathology in at-risk individuals, serve as a screening tool to ensure the diagnostic integrity of the cohort, offer a

biomarker directly related to the mechanisms of disease progression, provide evidence of target engagement, and assess the efficacy of an intervention designed to slow this progression.

AD DRUG DEVELOPMENT AND TAU PET: A MODEL FOR A-SYN PET?

The recent development and application of imaging biomarkers in AD are a model and reminder of the ways that PET imaging supports therapeutic trials by providing a window on primary pathophysiology. The recent, albeit controversial, FDA approval of the amyloid-targeting antibody aducanumab for AD serves as an example of the integration of PET biomarkers into clinical drug trials and hints to future clinical roles (*20*). Perhaps most relevant to the development of a radiotracer for the α-synucleinopathies is the recent history of the development of radiotracers for the tauopathies. The parallels between tau and a-syn are significant and could provide a road map of expectations for some potential paths toward the successful development of an a-syn PET agent.

Tau PET developed as follows. Briefly, phase 1 was the period of concept formation, articulation of need, and scientific and medical community buy-in as to the need or desire for targeted tau imaging biomarkers. Next was phase 2, a period of radiochemistry development called the wandering lost-in-the-desert-of-failed-compounds stage. Even so, while wandering, research teams were getting more sophisticated about binding affinities and selectivity of candidate structures. The move out of the desert was phase 3, when one or more promising structures were discovered and in vitro and nonclinical evaluation occurred. This led to phase 4, or the human proof-of-concept trials in AD, where there was characterization of the pharmacokinetics and validation of an outcome measure (*21*). Phase 5 was sharing of the pioneering compound among investigators and incorporation into clinical trials as an exploratory outcome. While this was happening, further development of second-generation tau tracers was initiated. Finally, phase 6 was the extensive incorporation of tau tracers as biomarkers in clinical trials and more nuanced understanding of differences in affinity to tau isoforms relative to the use of the radiotracer (*22*).

A-SYN PET: WHY HAS IT BEEN SO DIFFICULT?

Considering the tau PET experience just outlined, why has it been so difficult to develop an a-syn radiotracer for PD? Why not simply label the therapeutic? Although compelling, this strategy generally does not work out because the properties of a good therapeutic, such as high lipophilicity for brain penetrance, causes a higher background level and a lower PET signal-to-noise ratio. Further, radiotracers require nanomolar to subnanomolar affinity and high selectivity for a-syn, as well a preference for kinetics that offer fast washout of background signal and no confounding labeled metabolites. Fayyad et al. proposed several additional obstacles to developing an a-syn imaging biomarker: no good compound leads (e.g., dyes or tissue stains), lack of a library of compounds for selectivity screening against tau and β-amyloid, low target density, and poor PET resolution (*23*). Other issues include the potential confounders of isoform heterogeneity and cost. Recent work suggests that the field is addressing these concerns. For example, Ferrie et al. described an ultrahigh-throughput in silico screening strategy using idealized pseudo ligands (exemplars) to identify compounds, including confirmation of the binding site and evaluation of the structure–activity relationship of analogs for development of multiple molecules with nanomolar affinity for a-syn fibrils (*24*). More sophisticated understanding of the conformation-dependent binding sites on a-syn (*25*) can be used to inform radiotracer (and drug) development (*26*). Finally, there have been initial a-syn PET human studies with promising structures but mixed results to date (*27,28*).

CONCLUSION

Will we ever develop an a-syn PET tracer for clinical trials? Optimistically, there are several factors that suggest we will. There are increasingly pressing needs from the numbers of therapeutic trials with new a-syn–targeting treatments. The body of knowledge about a-syn function (binding sites, conformational states, and structure–activity relationship) and dysfunction (misfolding, aggregate formation, seeding, and spread) inform the medicinal and radiochemistry development as well as the in vivo validation of a-syn PET ligands. In addition, prior experience in AD suggests that imaging of proteinopathy in PD may be a useful clinical research tool and offers a road map for development of a-syn PET. Perhaps most encouraging is the recent presentation (March 2022) of the first apparently successful human a-syn PET agent, AC-12589, from AC-Immune and Oskar Hansson and colleagues at Lund University, Sweden. These very preliminary studies in multiple-system atrophy, PD, and controls demonstrated the expected increased uptake in cerebellar white matter in multiple-system atrophy, but not PD or healthy volunteers. The lack of specific uptake in PD could be related to a-syn conformational differences with multiple-system atrophy, relative target affinity, small sample size, or other factors.

In summary, we already know a great deal about pathologic a-syn formation and spread, as well as how to develop and validate imaging tools for clinical and research needs, and even a promising compound in initial human trials. We just need to keep going and make our way through the desert.

DISCLOSURE

No potential conflict of interest relevant to this article was reported.

REFERENCES

1. Bloem BR, Okun MS, Klein C. Parkinson's disease. *Lancet.* 2021;397:2284–2303.
2. Rajan KB, Weuve J, Barnes LL, et al. Population estimate of people with clinical Alzheimer's disease and mild cognitive impairment in the United States (2020-2060). *Alzheimers Dement.* 2021;17:1966–1975.
3. Feigin VL, Vos T, Alahdab F, et al.; GBD 2017 US Neurological Disorders Collaborators. Burden of neurological disorders across the US from 1990-2017: a global burden of disease study. *JAMA Neurol.* 2021;78:165–176.
4. Stefanis L. Alpha-synuclein in Parkinson's disease. *Cold Spring Harb Perspect Med.* 2012;2:a009399.
5. Musiek ES, Gomez-Isla T, Holtzman DM. Aducanumab for Alzheimer disease: the amyloid hypothesis moves from bench to bedside. *J Clin Invest.* 2021;131: e154889.
6. Eberling JL, Dave KD, Frasier MA. Alpha-synuclein imaging: a critical need for Parkinson's disease research. *J Parkinsons Dis.* 2013;3:565–567.
7. Simuni T, Siderowf A, Lasch S, et al. Longitudinal change of clinical and biological measures in early Parkinson's disease: Parkinson's Progression Markers Initiative Cohort. *Mov Disord.* 2018;33:771–782.
8. Simuni T, Uribe L, Cho HR, et al. Clinical and dopamine transporter imaging characteristics of non-manifest LRRK2 and GBA mutation carriers in the Parkinson's Progression Markers Initiative (PPMI): a cross-sectional study. *Lancet Neurol.* 2020;19:71–80.
9. Schweighauser M, Shi Y, Tarutani A, et al. Structures of alpha-synuclein filaments from multiple system atrophy. *Nature.* 2020;585:464–469.
10. Ayers JI, Lee J, Monteiro O, et al. Different alpha-synuclein prion strains cause dementia with Lewy bodies and multiple system atrophy. *Proc Natl Acad Sci USA.* 2022;119:e2113489119.

11. Braak H, Del Tredici K, Rüb U, et al. Staging of brain pathology related to sporadic Parkinson's disease. *Neurobiol Aging.* 2003;24:197–211.
12. Braak H, Sastre M, Bohl JR, de Vos RA, Del Tredici K. Parkinson's disease: lesions in dorsal horn layer I, involvement of parasympathetic and sympathetic pre- and postganglionic neurons. *Acta Neuropathol (Berl).* 2007;113:421–429.
13. Fitzgerald E, Murphy S, Martinson HA. Alpha-synuclein pathology and the role of the microbiota in Parkinson's disease. *Front Neurosci.* 2019;13:369.
14. Siderowf A, Jennings D, Stern M, et al.; PARS Investigators. Clinical and imaging progression in the PARS cohort: long-term follow-up. *Mov Disord.* 2020;35:1550–1557.
15. Grenn FP, Kim JJ, Makarious MB, et al. The Parkinson's disease genome-wide association study locus browser. *Mov Disord.* 2020;35:2056–2067.
16. Tan MMX, Lawton MA, Jabbari E, et al. Genome-wide association studies of cognitive and motor progression in Parkinson's disease. *Mov Disord.* 2021;36:424–433.
17. Fahn S. A new look at levodopa based on the ELLDOPA study. *J Neural Transm Suppl.* 2006;(70):419–426.
18. Holloway RG, Shoulson I, Fahn S, et al. Pramipexole vs levodopa as initial treatment for Parkinson disease: a 4-year randomized controlled trial. *Arch Neurol.* 2004;61:1044–1053.
19. Marek K, Chowdhury S, Siderowf A, et al. The Parkinson's progression markers initiative (PPMI): establishing a PD biomarker cohort. *Ann Clin Transl Neurol.* 2018;5:1460–1477.
20. Salloway S, Cummings J. Aducanumab, amyloid lowering, and slowing of Alzheimer disease. *Neurology.* 2021;97:543–544.
21. Barret O, Alagille D, Sanabria S, et al. Kinetic modeling of the tau PET tracer ^{18}F-AV-1451 in human healthy volunteers and Alzheimer disease subjects. *J Nucl Med.* 2017;58:1124–1131.
22. Barthel H, Seibyl J, Lammertsma AA, Villemagne VL, Sabri O. Exploiting the full potential of beta-amyloid and tau PET imaging for drug efficacy testing. *J Nucl Med.* 2020;61:1105–1106.
23. Fayyad M, Salim S, Majbour N, et al. Parkinson's disease biomarkers based on alpha-synuclein. *J Neurochem.* 2019;150:626–636.
24. Ferrie JJ, Lengyel-Zhand Z, Janssen B, et al. Identification of a nanomolar affinity alpha-synuclein fibril imaging probe by ultra-high throughput in silico screening. *Chem Sci.* 2020;11:12746–12754.
25. Hsieh CJ, Ferrie JJ, Xu K, et al. Alpha synuclein fibrils contain multiple binding sites for small molecules. *ACS Chem Neurosci.* 2018;9:2521–2527.
26. Lengyel-Zhand Z, Ferrie JJ, Janssen B, et al. Synthesis and characterization of high affinity fluorogenic alpha-synuclein probes. *Chem Commun (Camb).* 2020;56:3567–3570.
27. Kuebler L, Buss S, Leonov A, et al. [^{11}C]MODAG-001-towards a PET tracer targeting alpha-synuclein aggregates. *Eur J Nucl Med Mol Imaging.* 2021;48:1759–1772.
28. Maurer A, Leonov A, Ryazanov S, et al. ^{11}C radiolabeling of anle253b: a putative PET tracer for Parkinson's disease that binds to alpha-synuclein fibrils in vitro and crosses the blood-brain barrier. *ChemMedChem.* 2020;15:411–415.

Dosimetry in Radiopharmaceutical Therapy

Joe O'Donoghue, Pat Zanzonico, John Humm, and Adam Kesner

Department of Medical Physics, Memorial Sloan Kettering Cancer Center, New York, New York

Learning Objectives: On successful completion of this activity, participants should be able to (1) identify the dose (i.e., activity) prescription algorithms for radiopharmaceutical therapy and the advantages and disadvantages of each such algorithm; (2) describe the workflow for patient-specific dosimetry for radiopharmaceutical therapy; and (3) identify the advantages and disadvantages of α-particle emitters for radiopharmaceutical therapy.

Financial Disclosure: Intellectual property of Dr. Zanzonico and collaborators has been licensed to Y-mAbs through an agreement between Memorial Sloan Kettering and Y-mAbs. The authors of this article have indicated no other relevant relationships that could be perceived as a real or apparent conflict of interest.

CME Credit: SNMMI is accredited by the Accreditation Council for Continuing Medical Education (ACCME) to sponsor continuing education for physicians. SNMMI designates each *JNM* continuing education article for a maximum of 2.0 AMA PRA Category 1 Credits. Physicians should claim only credit commensurate with the extent of their participation in the activity. For CE credit, SAM, and other credit types, participants can access this activity through the SNMMI website (http://www.snmmilearningcenter.org) through October 2025.

The application of radiopharmaceutical therapy for the treatment of certain diseases is well established, and the field is expanding. New therapeutic radiopharmaceuticals have been developed in recent years, and more are in the research pipeline. Concurrently, there is growing interest in the use of internal dosimetry as a means of personalizing, and potentially optimizing, such therapy for patients. Internal dosimetry is multifaceted, and the current state of the art is discussed in this continuing education article. Topics include the context of dosimetry, internal dosimetry methods, the advantages and disadvantages of incorporating dosimetry calculations in radiopharmaceutical therapy, a description of the workflow for implementing patient-specific dosimetry, and future prospects in the field.

Key Words: radionuclide therapy; alpha particles; Auger electrons; dosimetry; radiobiology; radiopharmaceutical

J Nucl Med 2022; 63:1467–1474
DOI: 10.2967/jnumed.121.262305

Currently, there is intense interest in radiopharmaceutical therapy (RPT), particularly in terms of a theranostic paradigm that incorporates both diagnostic and therapeutic elements. Ideally, this consists of matched pairs of radiopharmaceuticals: a diagnostic partner (labeled with a positron-emitting or single-photon–emitting radionuclide) that provides information about disease extent and phenotype and serves to predict the utility of a therapeutic partner (usually labeled with a β- or α-particle–emitting radionuclide) that delivers targeted radiation. A key issue in protocol design is the choice of therapeutic activity and the time schedule for its administration. These may be based on patient-specific information or a simpler one-size-fits-all (i.e., population-averaged) approach.

The RPT strategy should align with the therapeutic objective: curative or palliative. A treatment designed to maximize the likelihood of cure would aim to deliver a high therapeutic dose over a relatively short time. The scope for future retreatment would be limited, similar to the case of external-beam radiotherapy (XRT). In contrast, a treatment designed to maximize the duration of disease control would entail a less aggressive delivery of therapy over an extended period, ideally retaining the option for future retreatment. Most current RPT designs for systemic treatment conform with the latter approach. Examples of clinical applications of RPT are provided in the supplemental material (available at http://jnm.snmjournals.org) (*1–23*).

Traditionally, in medicine, *dose* refers to the mass amount (e.g., mg) of drug administered. For radiopharmaceuticals, the analogous quantity is activity (e.g., MBq). Prescribing treatment in terms of mass dose is rational for nonradioactive drugs because there is little way of knowing how much localizes in target and nontarget tissues and how this localization varies among patients. In contrast, most radiopharmaceuticals permit quantification of their biodistribution and enable the administered activity to be modified on the basis of patient-specific factors via the metric of absorbed dose, the radiation energy deposited per unit mass (expressed as grays).

The aim of dosimetry is to estimate the absorbed dose to normal tissues and tumors and thereby anticipate the biologic effects of radiation. Calculation of absorbed dose takes into account (patient-dependent) anatomy and radiopharmaceutical biodistribution and (patient-independent) radionuclide properties. For RPT, the absorbed dose is calculated as the area under the dose rate–versus–time curve for a given target volume and generally requires multiple point estimates of dose rate. The dose rate in a tissue is proportional to the activity concentration in that tissue (self-dose) and in other tissues within range of the radionuclide's emissions (cross-dose). For radionuclides typically used for therapy, most of the energy is emitted as short-range particles, and for those tissues that receive the highest absorbed doses, self-dose is the dominant contribution (Fig. 1; Table 1).

The key physical determinants of biologic response are the radiation quantity (absorbed dose) and quality (linear energy transfer [LET]). XRT and brachytherapy treatments are prescribed, and normal-tissue tolerances defined, in terms of absorbed dose. However, for RPT, patient-specific dosimetry remains controversial. Important, recently introduced therapies featuring $^{223}RaCl_2$, ^{177}Lu-DOTATATE, and ^{177}Lu-PSMA-617 are prescribed on the basis of activity, not absorbed dose. Several factors contribute to this current practice. First, protocol design and pivotal clinical studies are increasingly dictated by industrial sponsors, for whom it is advantageous to minimize logistical complexity and maximize throughput. As more RPTs are

Received Dec. 14, 2021; revision accepted Jul. 14, 2022.
For correspondence or reprints, contact Adam Kesner (kesnera@mskcc.org).

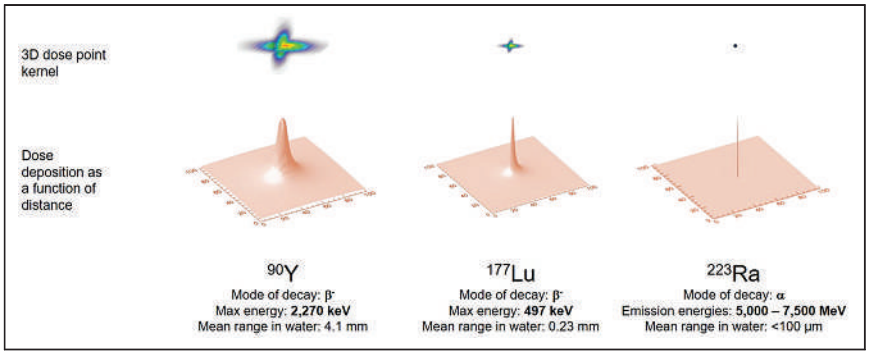

FIGURE 1. Graphical representation of dose deposition ranges delivered by different radionuclides having varying modes of decay. Top row shows relative geometric dose deposition delivered by point source of activity. Bottom row shows same data represented with 2-dimensional curve, illustrated as point spread function. Figure illustrates variable dose deposition properties and is not to scale.

approved, simplified treatment delivery will become even more desirable. Second, a dosimetry-based protocol requires reliable tumor and normal-tissue dose–response information. However, RPT dose–response data remain largely anecdotal. There is a chicken-and-egg element to this: dosimetry is not performed because dose–response data are lacking, and dose–response data are lacking because dosimetry is not performed. Each radiopharmaceutical has a range of administered activity that results in at least some clinical responses without excessive adverse effects, generally identified in chemotherapy-like dose-escalation (i.e., phase 1 and 2) trials. Third, dosimetric and clinical factors in RPT make direct comparisons with XRT problematic. Absorbed dose distributions are driven by biology in RPT but by the geometry of intersecting radiation beams in XRT. XRT dose distributions are uniform at the microscopic level, but in RPT they are nonuniform. Clinically, RPT is a systemic treatment in which targets may differ in size, location, and phenotype. Tumors too small to be imaged cannot be treated with XRT but are valid targets for RPT. Further, RPT patients have typically received prior therapies, complicating normal-organ radiation response.

Prescribing RPT on the basis of a one-size-fits-all activity ignores patient-specific differences and sets limits on treatment that are defined by the most susceptible patients (*24,25*). A dosimetry-based approach is predicated on the assumption that better clinical results can be achieved using individualized absorbed dose estimates rather than fixed activities. However, this hypothesis must be tested clinically. Recent approvals of new therapeutic radiopharmaceuticals were based on the results of randomized controlled clinical trials (*3,12,26*). For dosimetry, too, clinical trials will be required to determine whether it can improve RPT outcomes.

TABLE 1
Summary Characteristics of Commonly Used Radionuclides in RPT

Isotope	Primary emission	Half-life	LET	Maximum range in tissue (therapeutic radiation)
^{211}At	α	7.21 h	High	80 μm
^{212}Pb	α	10.6 h	High	100 μm
^{213}Bi	α	45.6 min	High	100 μm
^{223}Ra	α	11.4 d	High	70 μm
^{225}Ac	α	10.0 d	High	85 μm
^{227}Th	α	18.7 d	High	70 μm
^{67}Cu	β	61.8 h	Low	2.1 mm
^{90}Y	β	64.1 h	Low	11 mm
^{131}I	β	8.02 d	Low	3.3 mm
^{153}Sm	β	46.5 h	Low	3.3 mm
^{177}Lu	β	6.65 d	Low	1.8 mm

DOSE PRESCRIPTION ALGORITHMS

There are 3 prescription algorithms for RPT: fixed administered activity (e.g., MBq, MBq/kg of body mass, and MBq/m^2 of body surface area), maximum tolerated absorbed dose (MTAD), and prescribed tumor-absorbed dose (PTAD).

The approach using a fixed administered activity is patient-independent and does not require any patient measurements, apart from possibly mass and height. Treatment activities are based on chemotherapylike dose-escalation phase 1 and 2 clinical trials. For example, ^{177}Lu-DOTATATE (Lutathera; Advanced Accelerator Applications) treatment of somatostatin receptor–expressing neuroendocrine tumors is generally delivered in 4 cycles of 7.4 GBq at 8-wk intervals (*27*). For $^{223}RaCl_2$ (Xofigo; Bayer), 6 administrations of 55 kBq/kg are given at 4-wk intervals (*28*). A fixed administered activity is the simplest, most convenient, and least expensive approach. Inevitably, however, some patients could safely have received higher (and presumably more therapeutically effective) activities and were thus underdosed. Conversely, other patients receiving the same fixed activity may have experienced excessive normal-tissue side effects and were therefore overdosed (*24*).

The MTAD and PTAD approaches are both patient-specific and involve absorbed-dose projections. These approaches typically require a series of measurements, either performed in advance of the therapy or during the first administration of a multiadministration treatment. The objective is to predict the activity to administer to achieve a specified absorbed dose either to the dose-limiting normal tissue or to the tumor.

In the MTAD approach, it is likely that only a small number of normal tissues will receive absorbed doses approaching tolerance limits. For ^{131}I-iodide treatment of metastatic thyroid cancer, one approach is to prescribe a therapeutic activity that is calculated to deliver 2 Gy to blood (*29*). For renal toxicity, an MTAD of 23 Gy is often used as a guideline, based on XRT data, and is reasonably consistent with RPT experience with ^{90}Y-DOTA-octreotide after appropriate radiobiologic corrections for dose rate (*30*). However, it may be an inappropriately low threshold for ^{177}Lu-DOTATATE (*31*). Organ MTAD likely depends on the type of emissions, uniformity of the activity/dose distribution, dose rate, prior treatment, and life expectancy (*32*).

Treating patients according to PTAD is a concept extended from XRT practice. However, there are few dose–response data available for RPT on which to base treatment prescription. In a small series of postthyroidectomy thyroid cancer patients, Maxon et al. (*33*) successfully treated lymph node metastases in 74% of patients with thyroid remnants and in 86% of athyrotic patients with a single administration of ^{131}I calculated to deliver lesion-absorbed

doses of 85 and 140 Gy, respectively. Dewaraja et al. (*34*) found that for ^{90}Y-microsphere radioembolic therapy of liver tumors, the mean absorbed dose and biologically effective dose (an absorbed dose-based metric that takes account of radiobiologic features) that yielded a 50% tumor control probability were 292 and 441 Gy, respectively (*34*). The current state of knowledge of tumor dose response was recently summarized (*35*). However, only macroscopic, imageable tumors are amenable to the PTAD approach.

PARADIGM FOR PATIENT-SPECIFIC DOSIMETRY

The paradigm for patient-specific dosimetry for RPT (Fig. 2) is as follows: administration of a test activity of either the therapeutic or a surrogate radiopharmaceutical; measurement—by serial imaging and possibly blood and whole-body counting—of its time-dependent biodistribution; definition of the pertinent anatomy by high-resolution structural imaging (CT, MRI); derivation of time-dependent activity concentration or absorbed dose rate, with appropriate adjustment for differences in half-life between the therapeutic and surrogate radionuclides; integration of time–activity data to yield region- or voxel-specific time-integrated activity coefficients (alternatively, time–dose-rate data can be integrated directly to yield absorbed dose); calculation of absorbed dose coefficients for organ at risk or tumor for the therapeutic radiopharmaceutical (optional modifications for radiobiologic modeling can be incorporated at this step); and prescription of the activity to deliver the intended absorbed dose to the organ at risk or tumor.

Implicit in this paradigm is that the absorbed dose coefficients for the full RPT will be the same as those projected on the basis of the test study, and this is more likely to be true when the test and therapeutic radiopharmaceutical are chemically identical. If the test and therapeutic radiopharmaceuticals are different or if target tissue uptake depends nonlinearly on administered mass or activity (*36*), this approach may be less reliable. Changes in the patient's condition between test and therapy administrations, such as thyroid stunning (*37*), may also undermine this approach.

The time and effort required for the dosimetry paradigm may be considerable. Preparation and assay of the radiopharmaceutical may take 10–20 min; its administration may take less than a minute for a bolus injection to as long as 1–2 h for a slow infusion. The imaging time per point ranges from 2–5 min for a single static image to 20–40 min for a whole-body scan or single-bed-position SPECT/CT study to 1–2 h for a multiple-bed-position SPECT/CT study. A single imaging time point may be sufficient for reasonably accurate dosimetry, greatly reducing the time commitment. Segmentation (i.e., contouring) of normal organs and tumors can be particularly time-consuming—several hours—if done manually. Automated and semiautomated segmentation procedures can accelerate this process, and ultimately, artificial intelligence (AI)–based routines may make segmentation fully automated and rapid. Subsequent steps in the workflow—fitting or integrating mathematic functions to measured data and calculating absorbed doses or dose distributions—are computer-intensive but largely automated. Individuals performing clinical dosimetry calculations must have appropriate training and a full understanding of the process. Recent international guidance suggests allotting 1.1 d of a medical physicist's time to perform calculations per case (*38*).

MEASUREMENT OF ACTIVITY AND TIME–ACTIVITY DATA

Radiopharmaceutical activity is routinely measured with a dose calibrator with uncertainties of ±5% or less. However, for isotopes with complex decay schemes—with nonequilibrium progeny such as some α-particle emitters, pure β-particle emitters (e.g., ^{90}Y), and nonstandard source geometries—dose calibrator uncertainties can be significant (*39*). For such isotopes, reference standard sources traceable to a national agency should be used to verify accuracy. Any uncertainties associated with activity measurements will be propagated through the entire dosimetry analysis (*40*).

Therapeutic radiopharmaceuticals are often single-photon emitters, and their time-dependent activities or activity concentrations may be measured by serial planar γ-camera imaging (i.e., the

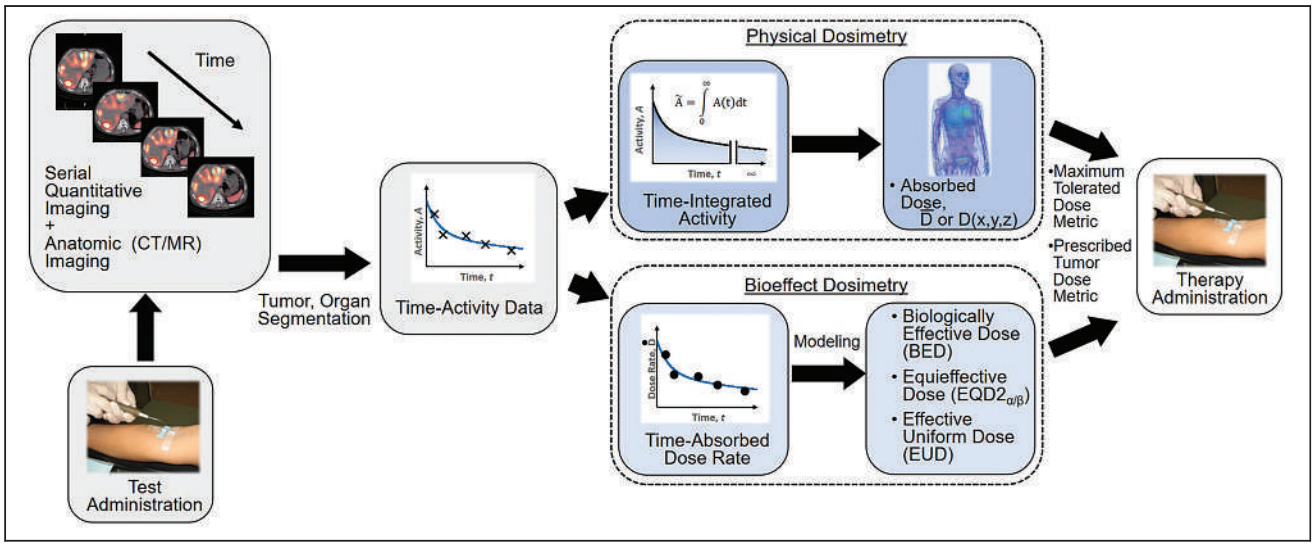

FIGURE 2. General workflow for RPT dosimetry. Process begins with test administration (may be either pretherapy administration or first cycle of multidose therapy regimen). Serial quantitation measurements can then support calculation of absorbed doses, either in terms of tumor and organ mean doses (D) or dose distributions (D[*x*,*y*,*z*]). Dose estimation per unit of administered activity can then be used to tailor treatment. The term *dose metric* may refer to absorbed dose (for physical dosimetry) or biologically effective dose (BED), equieffective dose ($EQD2_{\alpha/\beta}$), or effective uniform dose (EUD) (for bioeffect dosimetry).

conjugate-view method (*41*)), SPECT/CT (*42*), or a combination of planar and SPECT/CT imaging (the hybrid method (*42*)). Subject to corrections for collimator–detector response, scatter, attenuation, and partial-volume effects, the count rate per voxel in reconstructed tomographic images is proportional to the local activity concentration. The corrected count rate (cps) per voxel is divided by a measured system calibration factor [(cps/voxel)/(kBq/mL)] to yield activity concentrations:

$$\text{SPECT activity concentration (kBq/mL)} = \frac{\text{cps/voxel}}{\text{calibration factor}}. \quad \text{Eq. 1}$$

SPECT/CT imaging is relatively time-consuming (15–30 min per bed position). A practical alternative is hybrid SPECT/planar imaging, in which both SPECT/CT and planar scans are acquired at a single time point and only the more rapid planar scans are acquired at the remaining time points (Fig. 3) (*42*). The multiple planar scans provide the shapes of the source-region time–activity curves (i.e., the kinetics), and the single SPECT/CT study provides a (more accurate) point estimate of activity. Comparison of the contemporaneous planar and SPECT/CT scans provides a SPECT/CT-to-planar scaling factor.

Quantitative PET remains more mature than quantitative SPECT, but with rare exceptions (*10*), positron-emitting radionuclides are not used for RPT. Positron emitter–labeled surrogates may, however, be used to provide time–activity data for therapeutic radiopharmaceuticals (*43*), such as the ^{124}I/^{131}I PET/therapeutic radionuclide pair in metastatic thyroid cancer. The PET and therapeutic radionuclides must be well matched in terms of physical half-life for serial PET scans to be performed over a sufficiently long total time frame to yield reliable estimates of the time–activity data for the therapeutic radionuclide. ^{124}I (physical half-life, 4.18 d) and ^{131}I (physical half-life, 8.04 d) satisfy this criterion. In contrast, ^{68}Ga-DOTATATE (physical half-life, 67.7 min) is too short-lived to estimate later tissue activities of ^{177}Lu-DOTATATE (physical half-life, 6.65 d).

For radiopharmaceuticals with well-characterized kinetics that exhibit little variability among patients, population-averaged normal-organ time–activity curves may be scaled by image-derived, patient-specific organ activities measured at a judiciously selected single time point (*44,45*). The utility of this method has been demonstrated for ^{90}Y-DOTATOC (*46*) and ^{177}Lu-DOTATATE/DOTATOC (*47*) for kidney dosimetry. The reliability of single-time-point imaging for planning RPT requires further validation and may be less applicable to tumors.

The hematopoietic bone marrow is radiosensitive and is often dose-limiting for RPT (*48*). However, quantifying activity in red marrow for dosimetry is especially challenging as it is a widely distributed source region with regional variations in activity concentration. One practical approach is based on counting weighed samples of peripheral blood in a scintillation well counter. For radiopharmaceuticals that do not localize to blood or marrow cells, the activity concentration in plasma has been estimated as equal to that in the red marrow extracellular fluid (~20% of the marrow by volume) at equilibrium (*49,50*). Alternatively, red-marrow activity concentration may be estimated by scintigraphic imaging of vertebrae (*51,52*).

Whole-body clearance kinetics may be measured by serial conjugate-view whole-body scans or probe-based counts beginning shortly after radiopharmaceutical administration but before the patient's first postadministration void or bowel movement. The initial net (background-subtracted) geometric-mean whole-body or probe count rate corresponds to 100% of the administered activity. The values at each subsequent time point, normalized to the 100% count-rate value, yield whole-body activity (as a percentage of the administered activity).

CALCULATION OF ABSORBED DOSE

Calculation of absorbed doses requires estimating the source region time-integrated activity coefficients, calculated as areas under curves of activity/activity concentration or dose rate. These data may be fitted by mathematic functions (typically sums of exponentials) and integrated analytically to infinity. Alternatively, numeric methods (e.g., trapezoidal integration) may be used to integrate to the last measured point with an additional contribution to account for terminal behavior. Operationally, the terminal contribution may be taken to correspond to physical decay or apparent clearance derived from the last 2 measurements. Although it has been recommended that the last measurement be performed no earlier after administration than twice the radionuclide's physical half-life (*53*), this is rarely done for radionuclides with relatively long half-lives (e.g., ^{131}I [8.0 d] and ^{177}Lu [6.7 d]). Areas under curves can also be deduced by compartmental modeling (*54*).

There are 3 approaches to calculating absorbed dose from internal radionuclides: dose factor–based calculation (such as the MIRD formalism), dose point kernel convolution, and Monte Carlo (MC) radiation transport simulation (*55*).

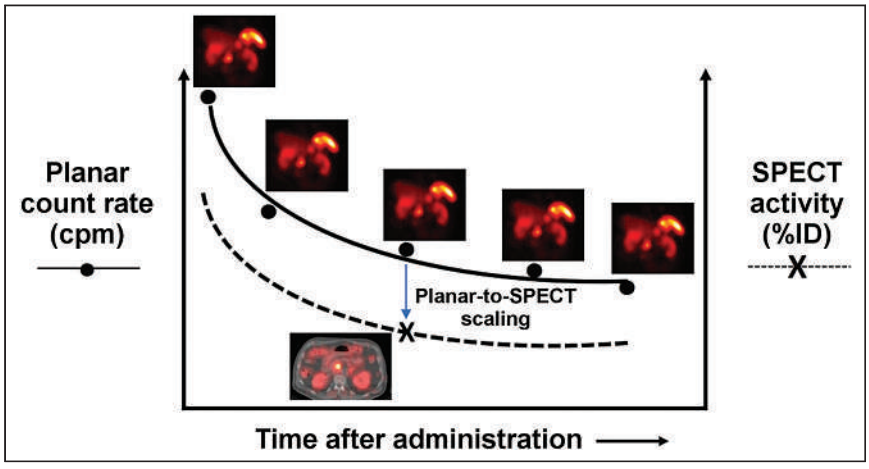

FIGURE 3. Hybrid SPECT/planar imaging approach to imaging-based measurement of time–activity data (*55*).

In the organ-level time-independent formulation of the MIRD schema(*56*), the absorbed dose coefficient $d(r_T, T_D)$ (mGy/MBq) is defined, for a target region r_T irradiated over a time period T_D, as the absorbed dose (mGy) normalized to the administered activity (MBq):

$$d(r_T, T_D) = \sum_{r_S} \tilde{a}(r_S, T_D) S(r_T \leftarrow r_S). \quad \text{Eq. 2}$$

Here, $\tilde{a}(r_S, T_D)$ is the time-integrated activity coefficient, and $S(r_T \leftarrow r_S)$ is known as the S value (or S coefficient), the absorbed dose to r_T per unit time-integrated activity in source region r_S. S values have been tabulated

for a large number of radionuclides and source-region–target-region pairs in several reference anatomic models from newborns to adult men and women (*57*). Self-irradiation dose factors for tumors, modeled as unit-density spheres, are also available (*58,59*). Several computer programs for organ-level dosimetry have been developed; these include OLINDA (approved by the U.S. Food and Drug Administration) (*58*), MIRDOSE (its predecessor) (*60*), IDAC-Dose 2.1 (*61*), and MIRDcalc (*59*); the latter two are freely available.

Suborgan and subtumor dosimetry, or voxel-level dosimetry, is addressable by MC radiation transport simulation (*62,63*), dose point kernel convolution (*64,65*), or voxel S values (*66*). MC simulation has the advantages of applicability to inhomogeneous media, complex 3-dimensional geometries, and conditions in which charged-particle equilibrium is not achieved (e.g., tissue interfaces). A historical drawback of MC was its large computational burden, but technologic advances have made it increasingly practical. Dose point kernel has also been adapted to heterogenous media by applying relatively simple multiplicative scaling factors to those in water-equivalent media, yielding results that closely approximate those of MC with reduced computational overhead.

A software tool that has been developed, MIRDcell, adapts the MIRD formalism to cellular and subcellular dosimetry (*67*). This freely downloadable applet models the radiation dose to the cellular and subcellular compartments (i.e., the cell membrane, cytoplasm, and nucleus modeled as concentric unit-density spheres) for both isolated cells and collections of cells using cellular S values (*68*). It also models the responses of the labeled and unlabeled cell populations as a function of the fraction of cells radiolabeled.

UNCERTAINTIES IN DOSE ESTIMATION

Sources of uncertainty in radiopharmaceutical dosimetry include assay of administered activity, determination of organ and tumor volumes or masses, measurement of time-dependent activity distributions, estimation of time-integrated activities, and translation of activity/time-integrated activity and anatomic data to dose-rate/absorbed dose. The European Association of Nuclear Medicine has published guidelines on uncertainty analysis for RPT absorbed-dose calculations (*69*). Error propagation in RPT results in net uncertainties of 10%–15% for absorbed dose estimates to the major organs and much higher values for small lesions. Efforts to determine and minimize the quantitative uncertainties in SPECT/CT activity quantification have been reviewed (*70*). Harmonization of calibration procedures, acquisition protocols, and reconstruction techniques will be required to achieve, in multicenter trials, the precision needed to build robust dose–response data.

BIOEFFECTS MODELING

Factors other than absorbed dose can impact the outcome of RPT. Historically, the linear-quadratic model has been used to describe normal-tissue and tumor responses to radiation (*71,72*):

$$SF = e^{-\left(\alpha D + G(T)\beta D^2\right)}, \qquad \text{Eq. 3}$$

where SF is the surviving fraction (i.e., the fraction of irradiated cells that has not undergone reproductive failure), D is the absorbed dose (in Gy), α is the linear sensitivity coefficient (in Gy^{-1}), β is the quadratic sensitivity coefficient (in Gy^{-2}), and $G(T)$ is a modifier that, for RPT, depends on the dose-rate curve and the time constant for repair (*73*).

The modulation of biologic response due to differences in dose rate or fraction size has led to the concept of biologically effective dose (*71,74*). This is the absorbed dose (Gy) projected to cause some biologic effect if it were delivered at the mathematic limit of infinitely low dose rate. The equieffective dose (EQDX, in Gy), like biologically effective dose, is dependent on the α/β ratio and is usually written as $EQDX_{\alpha/\beta}$ (*75*). Typically, X = 2 Gy is taken as the reference dose because of its common use in conventionally fractionated XRT, yielding $EQD2_{\alpha/\beta}$. Using this notation, the biologically effective dose could be expressed as $EQD0_{\alpha/\beta}$ (i.e., a reference dose per fraction of 0 Gy, corresponding to radiation treatment delivered by an infinite number of infinitesimally small fractions or at an infinitesimally low dose rate).

Tumor therapeutic response and normal-tissue toxicity may not correlate with mean absorbed doses because of spatial nonuniformity in the dose distribution. The equivalent uniform dose is the single value of absorbed dose that, if distributed uniformly, would achieve the same overall survival fraction as a nonuniform dose distribution (*76,77*). The equivalent uniform dose has been formulated as the "equivalent uniform biological effective dose" (*77*). Several studies have shown a better response correlation with equivalent uniform dose than with tumor mean absorbed dose (*78–80*).

RPT WITH α-EMITTERS

The radiobiologic advantages of high-LET radiation include intense ionization density along particle tracks that produce difficult-to-repair DNA damage and a reduced dependency on dose rate and local oxygen tension (*81*). In addition to high-LET radiobiologic advantages, the short range of α-particles (40–90 μm) can produce highly localized dose delivery (*82*) with the possibility of beneficial normal-tissue sparing if parts of critical organs lie beyond their emission range (e.g., marrow stem cells from radium deposition on bone surface). Other high-LET radiations include Auger electrons, emitted from some radionuclides. However, high-LET effects from Auger electron emission have only nanometer ranges and are not currently of clinical significance (*83*).

Alpha-particle–emitting radionuclides that have been used in clinical trials include ^{213}Bi (*84,85*), ^{211}At (*86,87*), ^{212}Pb (*88*), ^{223}Ra (*89*), ^{225}Ac (*90,91*), and ^{227}Th (*92*), listed in Table 1. These radionuclides may be separated into those that emit a single α-particle (^{213}Bi, ^{211}At, and ^{212}Pb) and those that undergo multiple decays with up to 4 (^{223}Ra and ^{225}Ac) or 5 (^{227}Th) α-particle emissions.

For ^{213}Bi, the combination of a short 46-min half-life and absence of α-particle–emitting progeny allows for the administration of relatively high, imageable (440-keV γ-ray) activities (~37 MBq) (*84*). ^{211}At has a longer 7.2-h half-life and emits characteristic x-rays (77–92 keV) suitable for quantitative imaging (*93*). ^{212}Pb (10.6-h half-life) decays via β-particle emission, but its progeny emit, on average, one α-particle either via ^{212}Bi (36%) or ^{212}Po (64%). It has 2 disadvantages: the first is that one of its progeny, ^{208}Tl, emits a very-high-energy γ-ray (2.6 MeV; 36%) that complicates radiation protection; the second is that about 40% of ^{212}Pb β-transitions are accompanied by nuclear deexcitation by internal conversion, producing an Auger-electron cascade and charge-neutralization effect that can lead to molecular fragmentation and release of ^{212}Bi (*94,95*). However, ^{212}Pb has the advantage that it forms a theranostic pair with ^{203}Pb for imaging (52-h half-life; 279-keV γ-ray) and for patient selection and dosimetry (*96,97*).

Imaging ^{223}Ra, ^{225}Ac, or ^{227}Th poses challenges for accurate activity quantification. Because of their long half-lives and multiple α-particle–emitting progeny, trials with these radionuclides use only kBq/kg activities, compared with MBq/kg activities for

^{213}Bi and GBq activities for ^{177}Lu. The resulting low-count images are noisy. Another challenge is determining the fate of the radioactive progeny dissociated from the radiopharmaceutical, as α-particle decay results in a high (100 keV) nuclear recoil energy that disrupts chemical bonds. Radioactive progeny can thus potentially translocate from the site of the parent decay, as with bismuth translocation to the kidney after ^{225}Ac decay in blood (*98*). Although current γ-cameras are ill-equipped for imaging many α-particle–emitting radionuclides, scanners with improved energy resolution may distinguish the imaging signals from multiple progeny (*99*).

Xofigo is the first, and thus far only, α-particle–emitting radiopharmaceutical approved by the Food and Drug Administration, for the treatment of patients with castration-resistant prostate cancer metastatic to bone with no visceral component. Initial studies in Europe and the United States included imaging and dosimetry, but this is not required for current protocols. The low administered activities of ^{223}Ra (55 kBq/kg per treatment) produce noisy images (*100*) in which bone lesions are often inconspicuous, and a ^{99m}Tc-diphosphonate or ^{18}F-fluoride bone scan is required for definitive identification. The partial-volume effect reduces lesion contrast further, and even though uptake in bony lesions is stable, the lack of lesion mass information makes accurate dose estimation problematic.

Dosimetry of α-particle emitters is additionally challenging with respect to imaging because of their short emission range, 2 orders of magnitude smaller than γ-camera pixel dimensions. Even if γ-camera images of α-particle–emitting radionuclides can provide biodistribution data (*100*), subvoxel microscopic nonuniformities in dose distributions may produce different biologic effects depending on the association of the agent to tumor cells or normal tissue structures. Obtaining source microdistribution within patients is currently not possible except in limited cases from biopsy or surgical samples (*101*). One possibility may be to infer this information from preclinical studies in tumor-bearing animals by autoradiographic methods. Using α-particle MC codes, digitized histologic images, and radiobiologic modeling, cell survival fractions may thus be deduced (*67,102,103*).

Currently, there is considerable interest in RPT with α-particle–emitting radionuclides, at least partly because of reports of remarkable clinical responses in some patients with macroscopic disease, often after a limited clinical response to RPT with β-particle–emitting radionuclides (*104–106*). From a purely dosimetric perspective, α-particles have a limited range (several cell diameters), and optimal target sizes would be expected to be of submillimeter dimensions. In addition, the adverse effects of nonuniform radiopharmaceutical uptake in macroscopic disease would be expected to be severe. Taken together, this suggests that α-RPT would be optimally used in the adjuvant or neoadjuvant setting, specifically addressing subclinical microscopic disease. The unanticipated clinical effectiveness of α-RPT for macroscopic disease may be related to immunologic or abscopal factors or to absorbed dose contributions from diffusible α-particle–emitting progeny. Despite our lack of understanding of the biologic mechanisms involved, clinical implementation of α-RPT is accelerating. However, its full potential may not be realized unless rigorous dosimetric analyses are performed (*107*). It is a field that warrants proceeding cautiously since many unknowns remain.

FUTURE PERSPECTIVES

RPT has emerged as a major new treatment modality spurred by the recent approval of Lutathera, ^{177}Lu-vipivotide tetraxetan (Pluvicto; Novartis), and Xofigo and the anticipation of new agents to follow. At present, the ability to perform accurate 3-dimensional dosimetry for RPT is clinically achievable, though requiring specialized software and technical capabilities and a significant commitment of time by the treating facility and patient. The available dose–response data, though still sparse, suggest that patient-specific dosimetry may help to improve RPT by minimizing toxicity or maximizing efficacy. However, additional dose–response data are still required and should remain a priority of future studies. Constructing a tumor dose–based prescription will be challenging, as at least some of the targets will be either phenotypically diverse or too small to be imaged. The use of RPT for the treatment of bulky macroscopic disease is likely transitional, and in the future, this type of disease conformation may be better treated by the addition of a supplementary XRT component, as part of a combined-modality therapy. RTP can selectively target and treat subclinical microscopic disease, even if imaging is not possible.

Practical dosimetry is rapidly advancing, progressing beyond historical obstacles. New imaging hardware has recently been introduced as well: γ-cameras and SPECT scanners with solid-state detector technologies that allow better energy resolution, SPECT scanners with full-ring detector geometries (making whole-body SPECT faster and more feasible), and whole-body PET scanners allowing whole-body dynamic imaging and reliable imaging of much lower administered activities than those currently used. Advancements in commercial software and regulatory approval of tools that facilitate clinical implementation will provide new opportunities for standardization of methods across centers. Artificial intelligence–assisted workflows that may reduce dosimetry time and effort and improve standardization are also being developed.

RPT dosimetry remains a work in progress. Specialized centers will continue to refine dosimetric methodology, introduce novel radiopharmaceuticals, investigate combined-modality therapies, and elucidate issues such as patient-specific susceptibility to radiation injury, interactions with the immune system, and abscopal effects of radiation. Work to standardize and validate dosimetry calculations and simplify the dosimetry process must continue, bearing in mind Einstein's dictum of "… as simple as possible but no simpler." In particular, scenarios in which single-time point imaging provides adequate dosimetric accuracy will need to be identified. The opposing considerations of minimizing complexity and maximizing throughput on the one hand and optimizing treatment for individual patients on the other need to be recognized and reconciled. This will be especially important as the field expands—the recent approval of ^{177}Lu-PSMA-617 therapy will have a major impact on patient load, and it is likely that an increasing number of RPT agents will become available. If dosimetry is to become more than an academic exercise, we need to show that it makes a significant difference to clinical outcomes with RPT. Ultimately, the only acceptable way of achieving this is through multicenter randomized controlled clinical trials comparing dosimetry-based prescriptions with one-size-fits-all activity-based prescriptions.

ACKNOWLEDGMENT

We thank Dr. Lukas Carter for his contribution to Figure 2.

REFERENCES

1. Benua RS, Leeper RD. A method and rationale for treating metastatic thyroid carcinoma with the largest safe dose of I-131. In: Medeiros-Neto G, Gaitan E, eds. *Frontiers in Thyroidology.* Vol 2. Plenum Medical Book Co.; 1986:1317–1321.

2. Hammes J, van Heek L, Hohberg M, et al. Impact of different approaches to calculation of treatment activities on achieved doses in radioiodine therapy of benign thyroid diseases. *EJNMMI Phys.* 2018;5:32.
3. Strosberg J, El-Haddad G, Wolin E, et al. Phase 3 trial of ^{177}Lu-dotatate for midgut neuroendocrine tumors. *N Engl J Med.* 2017;376:125–135.
4. Sandström M, Garske-Roman U, Granberg D, et al. Individualized dosimetry of kidney and bone marrow in patients undergoing ^{177}Lu-DOTA-octreotate treatment. *J Nucl Med.* 2013;54:33–41.
5. Chicheportiche A, Ben-Haim S, Grozinsky-Glasberg S, et al. Dosimetry after peptide receptor radionuclide therapy: impact of reduced number of post-treatment studies on absorbed dose calculation and on patient management. *EJNMMI Phys.* 2020;7:5.
6. Kayano D, Kinuya S. Current consensus on ^{131}I MIBG therapy. *Nucl Med Mol Imaging.* 2018;52:254–265.
7. Pandit-Taskar N, Zanzonico P, Hilden P, Ostrovnaya I, Carrasquillo JA, Modak S. Assessment of organ dosimetry for planning repeat treatments of high-dose ^{131}I-MIBG therapy: ^{123}I-MIBG versus posttherapy ^{131}I-MIBG imaging. *Clin Nucl Med.* 2017;42:741–748.
8. Kramer K, Pandit-Taskar N, Zanzonico P, et al. Low incidence of radionecrosis in children treated with conventional radiation therapy and intrathecal radioimmunotherapy. *J Neurooncol.* 2015;123:245–249.
9. Pandit-Taskar N, Zanzonico PB, Kramer K, et al. Biodistribution and dosimetry of intraventricularly administered ^{124}I-omburtamab in patients with metastatic leptomeningeal tumors. *J Nucl Med.* 2019;60:1794–1801.
10. Souweidane MM, Kramer K, Pandit-Taskar N, et al. Convection-enhanced delivery for diffuse intrinsic pontine glioma: a single-centre, dose-escalation, phase 1 trial. *Lancet Oncol.* 2018;19:1040–1050.
11. Hofman MS, Emmett L, Sandhu S, et al. ^{177}Lutetium-PSMA-617 versus cabazitaxel in patients with metastatic castration-resistant prostate cancer (TheraP): a randomised, open-label, phase 2 trial. *Lancet.* 2021;397:797–804.
12. Sartor O, de Bono J, Chi KN, et al. ^{177}Lutetium-PSMA-617 for metastatic castration-resistant prostate cancer. *N Engl J Med.* 2021;385:1091–1103.
13. Violet J, Jackson P, Ferdinandus J, et al. Dosimetry of ^{177}Lu-PSMA-617 in metastatic castration-resistant prostate cancer: correlations between pretherapeutic imaging and whole-body tumor dosimetry with treatment outcomes. *J Nucl Med.* 2019;60:517–523.
14. Pandit-Taskar N, O'Donoghue JA, Beylergil V, et al. ^{89}Zr-huJ591 immuno-PET imaging in patients with advanced metastatic prostate cancer. *Eur J Nucl Med Mol Imaging.* 2014;41:2093–2105.
15. Benešová M, Umbricht CA, Schibli R, Müller C. Albumin-binding PSMA ligands: optimization of the tissue distribution profile. *Mol Pharm.* 2018;15:934–946.
16. Charlton DE. The range of high LET effects from ^{125}I decays. *Radiat Res.* 1986; 107:163–171.
17. Warters RL, Hofer KG. Radionuclide toxicity in cultured mammalian cells: elucidation of the primary site for radiation-induced division delay. *Radiat Res.* 1977; 69:348–358.
18. Adant S, Shah GM, Beauregard J-M. Combination treatments to enhance peptide receptor radionuclide therapy of neuroendocrine tumours. *Eur J Nucl Med Mol Imaging.* 2020;47:907–921.
19. de Jong M, Breeman WAP, Valkema R, Bernard BF, Krenning EP. Combination radionuclide therapy using ^{177}Lu- and ^{90}Y-labeled somatostatin analogs. *J Nucl Med.* 2005;46(suppl 1):13S–17S.
20. Kunikowska J, Zemczak A, Kołodziej M, et al. Tandem peptide receptor radionuclide therapy using ^{90}Y/^{177}Lu-DOTATATE for neuroendocrine tumors efficacy and side-effects: Polish multicenter experience. *Eur J Nucl Med Mol Imaging.* 2020;47:922–933.
21. Ballal S, Yadav MP, Bal C, Sahoo RK, Tripathi M. Broadening horizons with ^{225}Ac-DOTATATE targeted alpha therapy for gastroenteropancreatic neuroendocrine tumour patients stable or refractory to ^{177}Lu-DOTATATE PRRT: first clinical experience on the efficacy and safety. *Eur J Nucl Med Mol Imaging.* 2020;47:934–946.
22. Kratochwil C, Bruchertseifer F, Giesel FL, et al. ^{225}Ac-PSMA-617 for PSMA-targeted α-radiation therapy of metastatic castration-resistant prostate cancer. *J Nucl Med.* 2016;57:1941–1944.
23. A study of stereotactic body radiotherapy and ^{177}Lu-PSMA-617 for the treatment of prostate cancer. ClinicalTrials.gov. website. https://clinicaltrials.gov/ct2/show/NCT05079698. Published October 15, 2021. Updated July 13, 2022. Accessed August 22, 2022.
24. Wehrmann C, Senftleben S, Zachert C, Müller D, Baum RP. Results of individual patient dosimetry in peptide receptor radionuclide therapy with ^{177}Lu DOTATATE and ^{177}Lu DOTA-NOC. *Cancer Biother Radiopharm.* 2007;22:406–416.
25. Eberlein U, Cremonesi M, Lassmann M. Individualized dosimetry for theranostics: necessary, nice to have, or counterproductive? *J Nucl Med.* 2017;58(suppl 2): 97S–103S.
26. Parker C, Nilsson S, Heinrich D, et al. Alpha emitter radium-223 and survival in metastatic prostate cancer. *N Engl J Med.* 2013;369:213–223.
27. Bodei L, Mueller-Brand J, Baum RP, et al. The joint IAEA, EANM, and SNMMI practical guidance on peptide receptor radionuclide therapy (PRRNT) in neuroendocrine tumours. *Eur J Nucl Med Mol Imaging.* 2013;40:800–816.
28. XOFIGO (^{223}Radium dichloride) injection for intravenous use. Package insert. Bayer Healthcare Pharmaceuticals; 2013.
29. Benua RS, Cicale N, Sonenberg M. The relation of radiation dosimetry to results and complications in the treatment of metastatic thyroid cancer. *AJR.* 1962;87:171–182.
30. Wessels BW, Konijnenberg MW, Dale RG, et al. MIRD pamphlet No. 20: the effect of model assumptions on kidney dosimetry and response—implications for radionuclide therapy. *J Nucl Med.* 2008;49:1884–1899.
31. Sandström M, Freedman N, Fröss-Baron K, Kahn T, Sundin A. Kidney dosimetry in 777 patients during ^{177}Lu-DOTATATE therapy: aspects on extrapolations and measurement time points. *EJNMMI Phys.* 2020;7:73.
32. Wahl RL, Sgouros G, Iravani A, et al. Normal-tissue tolerance to radiopharmaceutical therapies, the knowns and the unknowns. *J Nucl Med.* 2021;62(suppl 3):23S–35S.
33. Maxon HR, Thomas SR, Hertzberg VS, et al. Relation between effective radiation dose and outcome of radioiodine therapy for thyroid cancer. *N Engl J Med.* 1983; 309:937–941.
34. Dewaraja YK, Devasia T, Kaza RK, et al. Prediction of tumor control in ^{90}Y radioembolization by logit models with PET/CT-based dose metrics. *J Nucl Med.* 2020;61:104–111.
35. Sgouros G, Dewaraja YK, Escorcia F, et al. Tumor response to radiopharmaceutical therapies: the knowns and the unknowns. *J Nucl Med.* 2021;62(suppl 3):12S–22S.
36. Glatting G, Bardiès M, Lassmann M. Treatment planning in molecular radiotherapy. *Z Med Phys.* 2013;23:262–269.
37. Woolfenden JM. Thyroid stunning revisited. *J Nucl Med.* 2006;47:1403–1405.
38. *Medical Physics Staffing Needs in Diagnostic Imaging and Radionuclide Therapy: An Activity Based Approach.* IAEA; 2018. IAEA Human Health Reports No. 15.
39. *Nuclear Medicine Physics.* IAEA; 2015.
40. Bailey DL, Hofman MS, Forwood NJ, et al. Accuracy of dose calibrators for ^{68}Ga PET imaging: unexpected findings in a multicenter clinical pretrial assessment. *J Nucl Med.* 2018;59:636–638.
41. Thomas SR, Maxon HR, Kereiakes JG. In vivo quantitation of lesion radioactivity using external counting methods. *Med Phys.* 1976;03:253–255.
42. Dewaraja YK, Frey EC, Sgouros G, et al. MIRD pamphlet no. 23: quantitative SPECT for patient-specific 3-dimensional dosimetry in internal radionuclide therapy. *J Nucl Med.* 2012;53:1310–1325.
43. Bockisch A. Matched pairs for radionuclide-based imaging and therapy. *Eur J Nucl Med Mol Imaging.* 2011;38(suppl 1):S1–S3.
44. Gustafsson J, Taprogge J. Theoretical aspects on the use of single-time-point dosimetry for radionuclide therapy. *Phys Med Biol.* 2022;67.
45. Devasia TP, Dewaraja YK, Frey KA, Wong KK, Schipper MJ. A novel time-activity information-sharing approach using nonlinear mixed models for patient-specific dosimetry with reduced imaging time points: application in SPECT/CT after 177Lu-DOTATATE. *J Nucl Med.* 2021;62:1118–1125.
46. Madsen MT, Menda Y, O'Dorisio TM, O'Dorisio MS. Technical note: single time point dose estimate for exponential clearance. *Med Phys.* 2018;45:2318–2324.
47. Hänscheid H, Lapa C, Buck AK, Lassmann M, Werner RA. Dose mapping after endoradiotherapy with ^{177}Lu-DOTATATE/DOTATOC by a single measurement after 4 days. *J Nucl Med.* 2018;59:75–81.
48. Hindorf C, Glatting G, Chiesa C, Lindén O, Flux G. EANM Dosimetry Committee guidelines for bone marrow and whole-body dosimetry. *Eur J Nucl Med Mol Imaging.* 2010;37:1238–1250.
49. Sgouros G. Bone marrow dosimetry for radioimmunotherapy: theoretical considerations. *J Nucl Med.* 1993;34:689–694.
50. Siegel JA, Pawlyk DA, Lee RE, et al. Tumor, red marrow, and organ dosimetry for ^{131}I-labeled anti-carcinoembryonic antigen monoclonal antibody. *Cancer Res.* 1990;50(suppl):1039s–1042s.
51. Ferrer L, Kraeber-Bodere F, Bodet-Milin C, et al. Three methods assessing red marrow dosimetry in lymphoma patients treated with radioimmunotherapy. *Cancer.* 2010;116:1093–1100.
52. Siegel JA, Lee RE, Pawlyk DA, Horowitz JA, Sharkey RM, Goldenberg DM. Sacral scintigraphy for bone marrow dosimetry in radioimmunotherapy. *Int J Rad Appl Instrum B.* 1989;16:553–559.
53. Siegel JA, Thomas SR, Stubbs JB, et al. MIRD pamphlet no. 16: techniques for quantitative radiopharmaceutical biodistribution data acquisition and analysis for use in human radiation dose estimates. *J Nucl Med.* 1999;40:37S–61S.
54. MIRD Committee. *MIRD Primer 2022*. Society of Nuclear Medicine and Molecular Imaging. In press.
55. Capala J, Graves SA, Scott A, et al. Dosimetry for radiopharmaceutical therapy: current practices and commercial resources. *J Nucl Med.* 2021;62(suppl 3):3S–11S.
56. Bolch WE, Eckerman KF, Sgouros G, Thomas SR. MIRD pamphlet no. 21: a generalized schema for radiopharmaceutical dosimetry—standardization of nomenclature. *J Nucl Med.* 2009;50:477–484.

57. Snyder WS, Ford MR, Warner GG, Watson SB. *MIRD Pamphlet No. 11: "S," Absorbed Dose Per Unit Cumulated Activity for Selected Radionuclides and Organs.* Society of Nuclear Medicine and Molecular Imaging; 1975.
58. Stabin MG, Sparks RB, Crowe E. OLINDA/EXM: the second-generation personal computer software for internal dose assessment in nuclear medicine. *J Nucl Med.* 2005;46:1023–1027.
59. Kesner A, Olguin E, Zanzonico P, Bolch W. MIRDCalc V 1.0: a community spreadsheet tool for organ-level radiopharmaceutical absorbed dose calculations [abstract]. *J Nucl Med.* 2018;59(suppl 1):473.
60. Stabin MG. MIRDOSE: personal computer software for internal dose assessment in nuclear medicine. *J Nucl Med.* 1996;37:538–546.
61. Andersson M, Johansson L, Eckerman K, Mattsson S. IDAC-Dose 2.1, an internal dosimetry program for diagnostic nuclear medicine based on the ICRP adult reference voxel phantoms. *EJNMMI Res.* 2017;7:88.
62. Furhang EE, Chui CS, Kolbert KS, Larson SM, Sgouros G. Implementation of a Monte Carlo dosimetry method for patient-specific internal emitter therapy. *Med Phys.* 1997;24:1163–1172.
63. Johnson TK, Vessella RL. On the possibility of 'real-time' Monte Carlo calculations for the estimation of absorbed dose in radioimmunotherapy. *Comput Methods Programs Biomed.* 1989;29:205–210.
64. Liu A, Williams L, Wong J, Raubitschek A. A voxel source kernel (VSK) method for rapid, patient-specific dose estimates in radioimmunotherapy (RIT) [abstract]. *J Nucl Med.* 1997;38(suppl):106P.
65. Prestwich WV, Nunes J, Kwok CS. Beta dose point kernels for radionuclides of potential use in radioimmunotherapy. *J Nucl Med.* 1989;30:1036–1046.
66. Bolch WE, Bouchet LG, Robertson JS, et al. MIRD pamphlet no. 17: the dosimetry of nonuniform activity distributions—radionuclide S values at the voxel level. Medical Internal Radiation Dose Committee. *J Nucl Med.* 1999;40:11S–36S.
67. Vaziri B, Wu H, Dhawan AP, Du P, Howell RW. MIRD pamphlet no. 25: MIRDcell V2.0 software tool for dosimetric analysis of biologic response of multicellular populations. *J Nucl Med.* 2014;55:1557–1564.
68. Goddu SM, Howell RW, Bouchet LG, Bolch WE, Rao DV. *MIRD Cellular S Values.* Society of Nuclear Medicine and Molecular Imaging; 1997.
69. Gear JI, Cox MG, Gustafsson J, et al. EANM practical guidance on uncertainty analysis for molecular radiotherapy absorbed dose calculations. *Eur J Nucl Med Mol Imaging.* 2018;45:2456–2474.
70. Lassmann M, Eberlein U, Tran-Gia J. Multicentre trials on standardised quantitative imaging and dosimetry for radionuclide therapies. *Clin Oncol (R Coll Radiol).* 2021;33:125–130.
71. Barendsen GW. Dose fractionation, dose rate and iso-effect relationships for normal tissue responses. *Int J Radiat Oncol Biol Phys.* 1982;8:1981–1997.
72. Withers HR, Thames HD Jr, Peters LJ. A new isoeffect curve for change in dose per fraction. *Radiother Oncol.* 1983;1:187–191.
73. Baechler S, Hobbs RF, Prideaux AR, Wahl RL, Sgouros G. Extension of the biological effective dose to the MIRD schema and possible implications in radionuclide therapy dosimetry. *Med Phys.* 2008;35:1123–1134.
74. Dale RG. Dose-rate effects in targeted radiotherapy. *Phys Med Biol.* 1996;41:1871–1884.
75. Bentzen SM, Dorr W, Gahbauer R, et al. Bioeffect modeling and equieffective dose concepts in radiation oncology: terminology, quantities and units. *Radiother Oncol.* 2012;105:266–268.
76. Niemierko A. Reporting and analyzing dose distributions: a concept of equivalent uniform dose. *Med Phys.* 1997;24:103–110.
77. O'Donoghue JA. Implications of nonuniform tumor doses for radioimmunotherapy. *J Nucl Med.* 1999;40:1337–1341.
78. Amro H, Wilderman SJ, Dewaraja YK, Roberson PL. Methodology to incorporate biologically effective dose and equivalent uniform dose in patient-specific 3-dimensional dosimetry for non-Hodgkin lymphoma patients targeted with ^{131}I-tositumomab therapy. *J Nucl Med.* 2010;51:654–659.
79. Dewaraja YK, Schipper MJ, Roberson PL, et al. ^{131}I-tositumomab radioimmunotherapy: initial tumor dose-response results using 3-dimensional dosimetry including radiobiologic modeling. *J Nucl Med.* 2010;51:1155–1162.
80. Hobbs RF, Wahl RL, Frey EC, et al. Radiobiologic optimization of combination radiopharmaceutical therapy applied to myeloablative treatment of non-Hodgkin lymphoma. *J Nucl Med.* 2013;54:1535–1542.
81. Sgouros G. Dosimetry, radiobiology and synthetic lethality: radiopharmaceutical therapy (RPT) with alpha-particle-emitters. *Semin Nucl Med.* 2020;50:124–132.
82. Humm JL, Cobb LM. Nonuniformity of tumor dose in radioimmunotherapy. *J Nucl Med.* 1990;31:75–83.
83. Idrissou MB, Pichard A, Tee B, Kibedi T, Poty S, Pouget JP. Targeted radionuclide therapy using auger electron emitters: the quest for the right vector and the right radionuclide. *Pharmaceutics.* 2021;13:980.
84. Sgouros G, Ballangrud AM, Jurcic JG, et al. Pharmacokinetics and dosimetry of an alpha-particle emitter labeled antibody: ^{213}Bi-HuM195 (anti-CD33) in patients with leukemia. *J Nucl Med.* 1999;40:1935–1946.
85. Ahenkorah S, Cassells I, Deroose CM, et al. ^{213}Bismuth for targeted radionuclide therapy: from atom to bedside. *Pharmaceutics.* 2021;13:599.
86. Zalutsky MR, Reardon DA, Akabani G, et al. Clinical experience with alpha-particle emitting ^{211}At: treatment of recurrent brain tumor patients with ^{211}At-labeled chimeric antitenascin monoclonal antibody 81C6. *J Nucl Med.* 2008;49:30–38.
87. Hallqvist A, Bergmark K, Bäck T, et al. Intraperitoneal α-emitting radioimmunotherapy with ^{211}At in relapsed ovarian cancer: long-term follow-up with individual absorbed dose estimations. *J Nucl Med.* 2019;60:1073–1079.
88. Delpassand E, Tworowska I, Esfandiari R, Torgue J, Hurt JD, Nunez R. Phase I dose-escalation study of AlphaMedix for targeted-alpha-emitter therapy of PRRT-naive neuroendocrine patients [abstract]. *J Clin Oncol.* 2021;39(suppl):4117.
89. Wale DJ, Viglianti BL, Gross MD, Ferretti A, Rubello D, Wong KK. Nuclear medicine therapy with ^{223}Radium-dichloride for osseous metastases in prostate carcinoma. *Am J Clin Oncol.* 2019;42:99–106.
90. Rosar F, Krause J, Bartholomä M, et al. Efficacy and safety of ^{225}Ac-PSMA-617 augmented ^{177}Lu-PSMA-617 radioligand therapy in patients with highly advanced mCRPC with poor prognosis. *Pharmaceutics.* 2021;13:722.
91. Zacherl MJ, Gildehaus FJ, Mittlmeier L, et al. First clinical results for PSMA-targeted α-therapy using ^{225}Ac-PSMA-I&T in advanced-mCRPC patients. *J Nucl Med.* 2021;62:669–674.
92. Hagemann UB, Wickstroem K, Hammer S, et al. Advances in precision oncology: targeted ^{227}thorium conjugates as a new modality in targeted alpha therapy. *Cancer Biother Radiopharm.* 2020;35:497–510.
93. Turkington TG, Zalutsky MR, Jaszczak RJ, Garg PK, Vaidyanathan G, Coleman RE. Measuring ^{211}astatine distributions with SPECT. *Phys Med Biol.* 1993;38:1121–1130.
94. Mirzadeh S, Kumar K, Gansow OA. The chemical fate of Bi-212-dota formed by beta-decay of ^{212}Pb $(DOTA)^{2-}$ complex. *Radiochim Acta.* 1993;60:1–10.
95. Bartoś B, Lyczko K, Kasperek A, Krajewski S, Bilewicz A. Search of ligands suitable for Pb-212/Bi-212 in vivo generators. *J Radioanal Nucl Chem.* 2013;295:205–209.
96. Banerjee SR, Minn I, Kumar V, et al. Preclinical evaluation of $^{203/212}$Pb-labeled low-molecular-weight compounds for targeted radiopharmaceutical therapy of prostate cancer. *J Nucl Med.* 2020;61:80–88.
97. Dos Santos JC, Schäfer M, Bauder-Wüst U, et al. Development and dosimetry of ^{203}Pb/^{212}Pb-labelled PSMA ligands: bringing "the lead" into PSMA-targeted alpha therapy? *Eur J Nucl Med Mol Imaging.* 2019;46:1081–1091.
98. Schwartz J, Jaggi JS, O'Donoghue JA, et al. Renal uptake of ^{213}bismuth and its contribution to kidney radiation dose following administration of ^{225}actinium-labeled antibody. *Phys Med Biol.* 2011;56:721–733.
99. Takeda Si, Odaka H, Ishikawa S-n, et al. Demonstration of in-vivo multi-probe tracker based on a Si/CdTe semiconductor Compton camera. *IEEE Trans Nucl Sci.* 2012;59:70–76.
100. Carrasquillo JA, O'Donoghue JA, Pandit-Taskar N, et al. Phase I pharmacokinetic and biodistribution study with escalating doses of ^{223}Ra-dichloride in men with castration-resistant metastatic prostate cancer. *Eur J Nucl Med Mol Imaging.* 2013;40:1384–1393.
101. Fanchon LM, Dogan S, Moreira AL, et al. Feasibility of in situ, high-resolution correlation of tracer uptake with histopathology by quantitative autoradiography of biopsy specimens obtained under ^{18}F-FDG PET/CT guidance. *J Nucl Med.* 2015;56:538–544.
102. Minguez Gabiña P, Roeske JC, Mínguez R, Rodeño E, Gomez de Iturriaga A. Microdosimetry-based determination of tumour control probability curves for treatments with ^{225}Ac-PSMA of metastatic castration resistant prostate cancer. *Phys Med Biol.* 2020;65:235012.
103. Goddu SM, Rao DV, Howell RW. Multicellular dosimetry for micrometastases: dependence of self-dose versus cross-dose to cell nuclei on type and energy of radiation and subcellular distribution of radionuclides. *J Nucl Med.* 1994;35:521–530.
104. Ballal S, Yadav MP, Bal C, Sahoo RK, Tripathi M. Broadening horizons with ^{225}Ac-DOTATATE targeted alpha therapy for gastroenteropancreatic neuroendocrine tumour patients stable or refractory to ^{177}Lu-DOTATATE PRRT: first clinical experience on the efficacy and safety. *Eur J Nucl Med Mol Imaging.* 2020;47:934–946.
105. Kratochwil C, Bruchertseifer F, Giesel FL, et al. ^{225}Ac-PSMA-617 for PSMA-targeted α-radiation therapy of metastatic castration-resistant prostate cancer. *J Nucl Med.* 2016;57:1941–1944.
106. Kratochwil C, Bruchertseifer F, Rathke H, et al. Targeted alpha-therapy of metastatic castration-resistant prostate cancer with ^{225}Ac-PSMA-617: swimmer-plot analysis suggests efficacy regarding duration of tumor control. *J Nucl Med.* 2018;59:795–802.
107. Sgouros G. The case for dosimetry in alpha-emitter therapy. *J Med Imaging Radiat Sci.* 2019;50(suppl 1):S45–S46.

Single-Domain Antibody Theranostics on the Horizon

Weijun Wei[1], Muhsin H. Younis[2], Xiaoli Lan[3,4], Jianjun Liu[1], and Weibo Cai[2]

[1]*Department of Nuclear Medicine, Institute of Clinical Nuclear Medicine, Renji Hospital, Shanghai Jiao Tong University School of Medicine, Shanghai, China;* [2]*Departments of Radiology and Medical Physics, University of Wisconsin−Madison, Madison, Wisconsin;* [3]*Department of Nuclear Medicine, Union Hospital, Tongji Medical College, Huazhong University of Science and Technology Wuhan, China; and* [4]*Hubei Key Laboratory of Molecular Imaging Wuhan, China*

Single-domain antibody (sdAb) is among the most promising vectors for developing molecular imaging tracers. Several sdAb tracers targeting human epidermal growth factor receptor 2 or programmed death ligand 1 have entered clinical practice. However, radiolabeled single-valent sdAbs generally have high kidney retention, limiting their therapeutic applications. Therefore, engineering strategies such as PEGylation or incorporation of renal cleavable linkers can be adapted to improve pharmacokinetics and reduce kidney retention. In this Focus on Molecular Imaging review, we try to summarize the latest developments in sdAb-derived agents and propose potential strategies that can be used to improve the theranostic value of radiolabeled sdAbs.

Key Words: nanobody; immuno-PET; radiopharmaceuticals; theranostics; cancer

J Nucl Med 2022; 63:1475–1479
DOI: 10.2967/jnumed.122.263907

The term *molecular imaging* has been well defined as the "visualization, characterization, and measurement of biological processes at the molecular and cellular levels in humans and other living systems" (*1*). With the increasingly approved therapeutic antibodies and commercial supply of long-lived radionuclides such as ^{89}Zr and ^{64}Cu, immuno-PET imaging with radiolabeled monoclonal antibodies has fulfilled some of the tasks by visualizing target expression and guiding antibody development (*2*). Safety profiles, easy access, availability in large amounts, and robust labeling protocols are natural advantages of developing monoclonal antibody–based tracers, but slow clearance, less optimal tumor-to-background ratios, poor penetration in tumor interstitium, and noticeable radiation dose are practical considerations hindering their routine clinical use. Additionally, imaging at several time points in a week is inconvenient for patients.

Immuno-PET imaging with radiolabeled single-domain antibodies (sdAbs) has rapidly evolved (*3,4*). There are 2 major types of sdAbs, one isolated from human antibody repertoires and another from camelid heavy-chain–only antibodies. But sdAbs can also be engineered from sharks. As the smallest antibody fragment, with a molecular size of 15 kDa, variable domain of the heavy chain of heavy-chain–only antibodies (VHH, or Nanobody; Ablynx) is characterized by high affinity, high stability, efficient extravasation, and, most importantly, ease of engineering. Herein, we present the latest progress in sdAb theranostics and lay out future innovation and translation perspectives.

AGENTS TARGETING BIOMARKERS ON TUMOR CELLS

Human Epidermal Growth Factor Receptor 2 (HER2)

HER2 is among the most thoroughly explored receptor tyrosine kinases for molecular imaging. Currently, 2 HER2-specific sdAb tracers have been translated for clinical use. ^{68}Ga-NOTA-2Rs15d was preclinically investigated in 2013 (*5*), followed by successful clinical translation in 2016 (*6*). More recently, the same group developed ^{131}I-4-guanidinomethyl-3-iodobenzoate (GMIB)-anti-HER2-VHH1 (*7*), in which ^{131}I was attached to the VHH1 (2Rs15d) via the linker *N*-succinimidyl-GMIB (SGMIB). Accumulation of ^{131}I-GMIB-anti-HER2-VHH1 was observed in patients with metastatic breast cancers (*8*). A low dose (46 ± 28 MBq for healthy subjects and 64 ± 46 MBq for patients) was administered in the study. A phase I/II dose-expansion study to evaluate the safety, tolerability, dosimetry, and efficacy of ^{131}I-GMIB-anti-HER2-VHH1 is currently ongoing (NCT04467515). Increased tumor uptake and faster clearance of radioiodinated sdAbs are favored for radioimmunotherapy. Feng et al. recently reported that iso-^{131}I-SGMIB-VHH_1028 exhibited significantly higher tumor uptake and lower kidney accumulation than ^{131}I-SGMIB-2Rs15d (^{131}I-GMIB-anti-HER2-VHH1). More importantly, the theranostic agent significantly suppressed tumor growth and prolonged survival (*9*).

Meanwhile, Zhao et al. developed another sdAb tracer, ^{99m}Tc-NM-02, and conducted an early phase I study (NCT04040686) enrolling 10 patients with breast cancer (*10*). After bolus injection of 458 ± 37 MBq of ^{99m}Tc-NM-02 (100 μg of NM-02), no adverse effects were reported and tumor uptake of ^{99m}Tc-NM-02 correlated well with HER2 expression (Fig. 1). Traditionally, *N*-succinimidyl-4-^{18}F-fluorobenzoate, a nonresidualizing prosthetic agent, was used to develop the HER2-specific probe ^{18}F-RL-I-5F7, which imaged HER2 status, but the diagnostic efficacy was compromised by a problematic renal background (*11,12*). Residualizing prosthetic agents for ^{18}F labeling are favored for improving the tumor trap of the tracers. By migrating high temperature and organic solvents, which may denature the sdAbs, click chemistry reactions are increasingly used to facilitate ^{18}F labeling. Zhou et al. harnessed a tetrazine/*trans*-cyclooctene inverse electron-demand Diels-Alder cycloaddition reaction and incorporated a renal brush border enzyme-cleavable linker and a polyethylene glycol (PEG) 4 chain between ^{18}F and 5F7 in developing ^{18}F-5F7GGC (*13*), which yielded high retention in the tumor with very little background activity. Several clinical trials are investigating either the diagnostic (NCT04591652, NCT03331601, and NCT03924466) or the

Received Apr. 17, 2022; revision accepted Jul. 7, 2022.
For correspondence or reprints, contact Jianjun Liu (nuclearj@163.com) or Weibo Cai (wcai@uwhealth.org).
Published online Jul. 14, 2022.

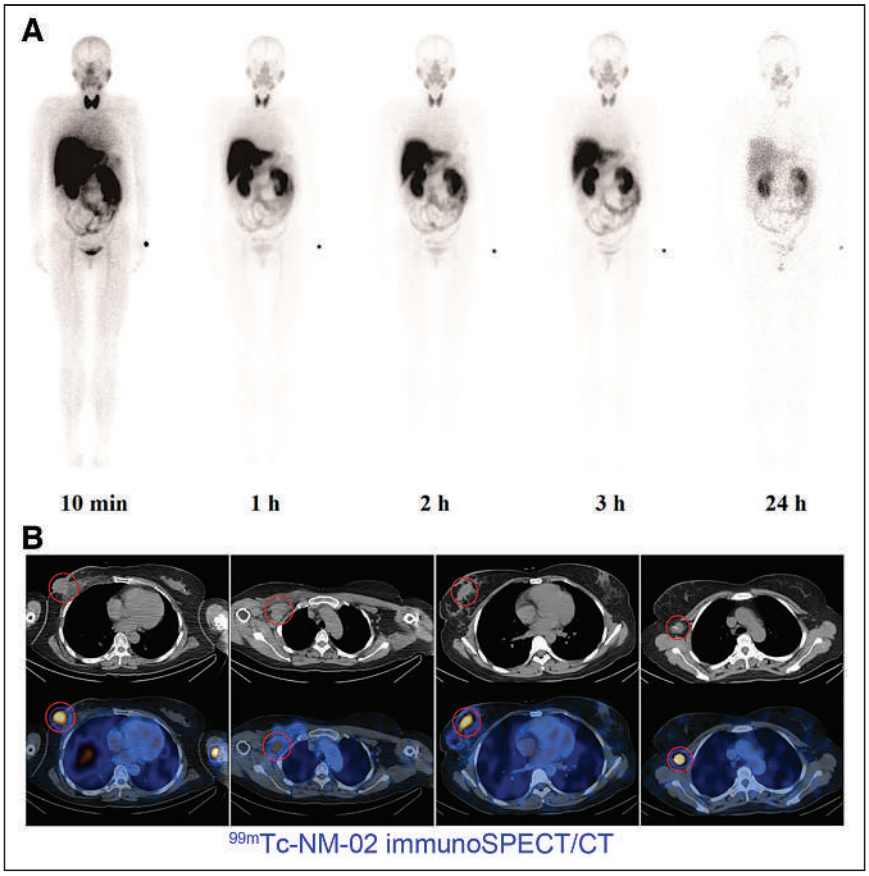

FIGURE 1. ^{99m}Tc-NM-02 immuno-SPECT/CT imaging of breast cancers. (A) Whole-body SPECT images at different time points (10 min, 1 h, 2 h, 3 h, and 24 h) after injection of radiotracer. (B) Varying uptake patterns in patients with breast cancer. From left to right: heterogeneous uptake in primary tumor and in metastatic lymph node in patient with HER2 3+ breast cancer, and homogeneous uptake in primary tumor and in metastatic lymph node in another patient with HER2 3+ breast cancer. Primary and metastatic tumors are indicated by red circles. (Reprinted from (*10*).)

theranostic (NCT04467515) value of radiolabeled HER2-targeting sdAbs in HER2-overexpressing solid tumors.

Epidermal Growth Factor Receptor (EGFR)

EGFR is another receptor tyrosine kinase involved in cancer development and progression. Although monoclonal antibody and small-molecule–based tracers have entered clinical translation, no sdAb-based tracers have achieved clinical translation so far. 7C12 and 7D12 are the most widely used EGFR-targeting sdAbs in molecular imaging. Vosjan et al. synthesized ^{89}Zr-Df-Bz-NCS-7D12 and reported the diagnostic value in A431 tumor–bearing mice (*14*). The generally introduced His_6 tag could be used for site-specific labeling using $[^{99m}Tc(CO)_3]^+$. ^{99m}Tc-7C12 and ^{99m}Tc-7D12 were labeled with ^{99m}Tc at their His_6 tag tails. ^{99m}Tc-7C12 showed a higher tumor uptake, higher kidney uptake, and lower liver uptake than ^{99m}Tc-7D12 (*15*). D10, another anti-EGFR sdAb, was also site-specifically labeled with $[^{99m}Tc(CO)_3]^+$, and ^{99m}Tc-D10 detected small tumors more efficiently than ^{99m}Tc-cetuximab (*16*).

Programmed Death Ligand 1 (PD-L1)

PD-L1 is an immune checkpoint that interacts with the receptor programmed death 1 on T cells, inhibiting T-cell activation and suppressing antitumor immunity. Immune checkpoint blockade with antibodies targeting the programmed death 1/PD-L1 axis has prolonged survival in cancer patients. However, reliable biomarkers that can predict the responses are lacking. PD-L1 status revealed by immunohistochemistry is not always associated with treatment efficacy (*17*), possibly because of inherent artifacts of immunohistochemistry such as tissue sampling errors and inequivalent interpretation of the staining results (*18*).

Xing et al. developed the sdAb-derived ^{99m}Tc-NM-01 and reported the physiologic uptake of the tracer in the liver, spleen, and, to a lesser extent, bone marrow and lungs. The translational study showed intratumoral and intertumoral heterogeneity of PD-L1 expression and a good correlation between the SPECT signal and immunohistochemistry results (*19*). Although ^{99m}Tc-labeled tracers have long half-lives and good availabilities, the low spatial resolution and lack of quantitation with SPECT are potential challenges in quantifying PD-L1. To this end, ^{68}Ga-labeled sdAb tracers targeting PD-L1 have been developed (*20–22*). Although site-specific labeling yields well-defined and homogeneous conjugates, there were no differences in binding affinities and diagnostic efficacies between the site-specifically and randomly labeled sdAb tracers (*22*). KN035 is an engineered sdAb derivative with a molecular weight of 79.6 kDa. Li et al. developed ^{89}Zr-Df-KN035 and reported the diagnostic efficacy in glioma xenografts and the circulation profiles in nonhuman primates (Supplemental Fig. 1; supplemental materials are available at http://jnm.snmjournals.org) (*23*). An ongoing clinical trial is evaluating the safety and biodistribution of ^{89}Zr-Df-KN035 in patients with PD-L1−positive solid tumors (NCT04977128). Notably, KN035, with a commercial name of envafolimab (Alphamab Oncology), has been approved for treating late-stage solid tumors in China and late-stage biliary tract carcinoma and soft-tissue sarcoma in the United States.

Biomarkers for Multiple Myelomas

CD38 (*12,24,25*), B-cell maturation antigen (*26*), CS1 (*27,28*), and paraprotein (*29*) are promising targets exploited for molecular imaging of multiple myeloma. ^{68}Ga-NOTA-Nb1053 is the first-generation CD38-specific sdAb tracer that realized precise delineation of disseminated multiple myeloma in preclinical settings (Fig. 2A). And the tracer had advantages over ^{18}F-FDG in terms of diagnostic contrast and specificity (Fig. 2B) (*12*). By taking advantage of biorthogonal click chemistry (*24*), ^{18}F-Nb1053 was further innovated and the diagnostic value was also confirmed in multiple myeloma models (Figs. 2C and 2D). The justification for developing ^{18}F-labeled cousins is that such tracers allow distribution to multiple centers on clinical translation. 2F8 is an sdAb binding to human CD38 independently of daratumumab. A recent work developed ^{99m}Tc-H_6-2F8 and ^{177}Lu-diethylenetriaminepentaacetic acid (DTPA)-2F8 using untagged and tagged 2F8, respectively. Although the former showed a specific uptake facilitating diagnosis of subcutaneous multiple myeloma, the latter at either a

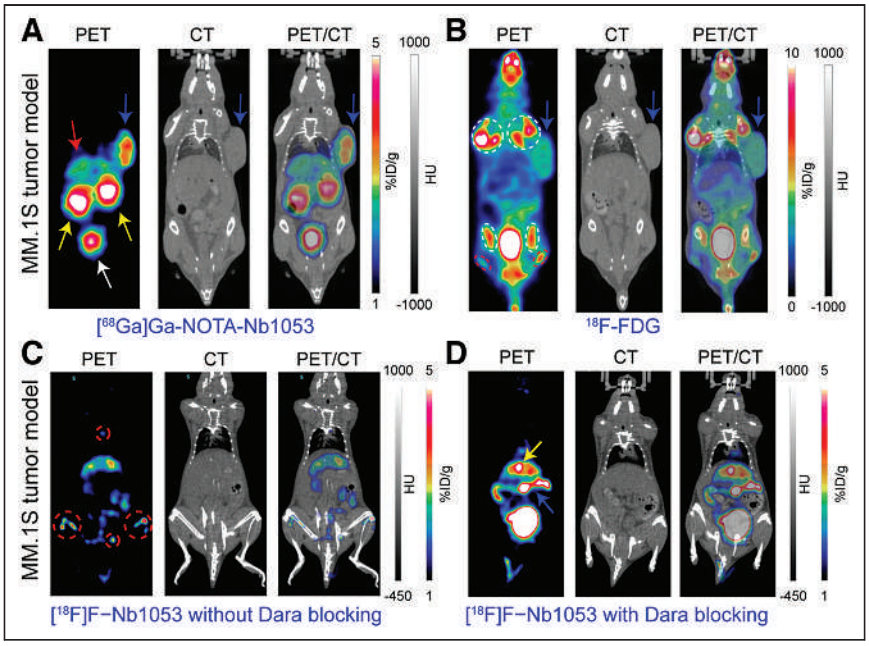

FIGURE 2. Preclinical immuno-PET imaging of multiple myelomas. (A) Immuno-PET imaging with ^{68}Ga-NOTA-Nb1053 delineated subcutaneous MM.1S tumor (blue arrows) with excellent contrast. Unbound tracer was largely excreted from urinary system (kidneys indicated by yellow arrows and bladder by white arrow), and small proportion was catabolized in liver (red arrow). (B) In comparison, PET imaging with ^{18}F-FDG visualized subcutaneous MM.1S tumor (blue arrows) with substantial uptake in normal tissues, such as bone joints (white circles) and muscles (red circles). (C) Immuno-PET imaging with ^{18}F-Nb1053 also clearly outlined involved bones (red circles). (D) In contrast, no obvious ^{18}F-Nb1053 uptake was observed in disseminated MM.1S models that were premedicated with CD38-targeting monoclonal antibody daratumumab. The gallbladder is indicated by the yellow arrow. %ID = percentage injected dose; Dara = daratumumab; HU = Hounsfield units. (Reprinted from (*12,24*).)

high dose (18.5 ± 0.5 MBq) or a low dose (9.3 ± 0.3 MBq) significantly prolonged the median survival of the tumor-bearing mice (*30*). Notably, His_6 tag-free 2F8 was used in constructing ^{177}Lu-DTPA-2F8, and the agent was intravenously given at 3 consecutive times with coinjection of a 150 mg/kg dose of Gelofusine (B. Braun). The formulation matters because a single injection of radiolabeled His_6-tagged sdAb may lead to unacceptable nephrotoxicity. In our experience, bolus injection of 3.7 − 7.4 MBq of ^{177}Lu-labeled His_6-tagged sdAb is still too toxic in preclinical models.

Carbonic Anhydrase IX

Carbonic anhydrase IX catalyzes the conversion of carbon dioxide and water to carbonic acid ($CO_2 + H_2O \rightleftarrows HCO_3^- + H^+$) and is regulated by the von Hippel–Lindau hypoxia-inducible factor axis. Carbonic anhydrase IX is highly expressed in over 95% of clear cell renal cell carcinomas. Radiolabeled sdAb is excreted through the kidneys, detracting from imaging of the primary foci of renal cell carcinoma. Therefore, research on renal cell carcinoma–targeted tracers should focus on solving the impact of renal physiologic excretion and reabsorption. Modifications such as the incorporation of the albumin-binding domain (ABD) may alter the physiologic distribution and improve the diagnostic performance of the tracers (*31*). Recent exquisite work by van Lith et al. adopted the strategy and developed 3 sdAb-derived tracers, that is, ^{111}In-DTPA-B9, low-affinity ^{111}In-DTPA-B9-ABD, and high-affinity ^{111}In-DTPA-B9-ABD (*32*). Their results showed the high affinity and specificity of [^{111}In]In-DTPA-B9 in CAIX-expressing head and neck cancer xenografts. Although low-affinity ^{111}In-DTPA-B9-ABD and high-affinity ^{111}In-DTPA-B9-ABD had increased tumor uptake, the uptake was partially CAIX-independent because the preinjected girentuximab failed to thoroughly reduce the uptake. The authors concluded that the low absolute uptake of ^{111}In-DTPA-B9 and the CAIX-independent uptake of low-affinity ^{111}In-DTPA-B9-ABD and high-affinity ^{111}In-DTPA-B9-ABD preclude these tracers from being used to image hypoxia-induced CAIX expression.

Other Theranostics-Relevant Biomarkers

"One marker fits all" is not realistic from a diagnostic perspective; sdAb tracers targeting other emerging biomarkers are warranted. Epithelial cell adhesion molecule (*33*), glypican 3 (*31*), and dipeptidyl peptidase 6 (*34,35*) are also promising biomarkers exploited for sdAb molecular imaging.

IMAGING TUMOR MICROENVIRONMENT

The tumor microenvironment comprises multiple types of cells, including immune cells, vascular cells, and stromal cells. Given this complexity, it is still challenging to gain a full understanding of the tumor microenvironment and to image it. Although PD-L1−targeted tracers have been discussed in the above section, other representative sdAb tracers targeting tumor microenvironment markers are illustrated in the section.

Intratumoral CD8-positive ($CD8^+$) T cells can selectively detect and eradicate cancer cells. With the progression of the tumors, $CD8^+$ T cells differentiated to a hyporesponsive state with impaired cytotoxic capacity. Although lymphocyte activation gene 3 and programmed death 1 are expressed by both early and late dysfunctional T cells, CD38, CD39, CD101, and TIM3 are expressed predominantly by late dysfunctional T cells. These exhaustion markers are spatiotemporally regulated in the tumor microenvironment. Imaging $CD8^+$ T cells may provide a certain clinical value (*36*). Since the clinical translation of ^{89}Zr-IAB22M2C, a minibody tracer targeting $CD8^+$ T cells (*37,38*), several sdAb-derived tracers have been reported. ^{89}Zr-VHH-X118-PEG_{20}, an sdAb tracer that recognizes mouse CD8a, monitored the antitumor immune responses (*39*). The tracer also tracked immune cell distribution and infiltration in the graft-versus-host disease model (*40*) and in models of influenza A virus (*41*). In the context of immunotherapy, the tracer could depict the infiltration of $CD8^+$ T cells into the tumors and predict the therapeutic responses (*42*). We reported that ^{68}Ga-NOTA-SNA006a, an antihuman CD8α sdAb tracer, could visualize $CD8^+$ tumors and track human $CD8^+$ T cells in humanized models (Supplemental Fig. 2) (*43*). The tracer is currently undergoing clinical translation (NCT05126927).

Secondary to CD8, CD4 is another lineage marker exploited for molecular imaging of T cells. Traenkle et al. generated a series of sdAbs specifically recognizing human CD4 and further labeled the most promising candidate (Nb1) with ^{64}Cu (*44*). Imaging studies showed that ^{64}Cu-CD4-Nb1 $CD4^+$ specifically accumulated in T-cell–rich tissues, including lymph nodes, thymus, liver, and spleen. Lecocq et al. developed an antimouse lymphocyte activation gene

3sdAb tracer and reported the efficacy of the tracer in imaging dynamic lymphocyte activation gene 3 expression on tumor-infiltrating lymphocytes (*45*).

Macrophage mannose receptor (CD206) is an endocytic C-type lectin receptor (175 kDa) highly expressed on macrophages. Nb3.49 is an sdAb cross-reactive for both mouse (dissociation constant, 12 nM) and human (dissociation constant, 1.8 nM) macrophage mannose receptor, and the ^{68}Ga-labeled version is ready for clinical translation (*46,47*). Varasteh et al. further reported the specific uptake of the tracer in atherosclerotic lesions of *APOE*$^{-/-}$ mice on the high-fat diet (*48*). Along with this progress, Devoogdt and coauthors characterized a series of sdAb tracers targeting 3 atherosclerosis-related markers, that is, vascular cell adhesion molecule-1 (*49*), lectinlike oxidized low-density lipoprotein receptor-1 (*50*), and macrophage mannose receptor (*51*), in *APOE*$^{-/-}$mice and atherosclerotic rabbits. The authors reported that a multiparametric study of atherosclerosis using different sdAb tracers was feasible (*52*). Two ongoing clinical trials are exploring the use of ^{68}Ga-NOTA-antimacrophage mannose receptor-VHH2 in patients with cancers, cardiovascular atherosclerosis, or abnormal immune activation (NCT04758650 and NCT04168528). Meanwhile, imaging immune-related cells by targeting other markers is actively explored in preclinical studies (*53*). The most promising sdAb-derived molecular imaging or theranostic agents are listed in Supplemental Table 1.

CHALLENGES AND POTENTIAL SOLUTIONS IN NANOBODY THERANOSTICS

Most of the sdAb agents explored in preclinical models are immunoreactive with human antigens but not with murine antigens, indicating that the preclinical evidence may not reliably mirror clinical imaging outcomes, especially for those targeting immune checkpoints. Therefore, the use of humanized models and nonhuman primates is suggested before moving to clinical trials. Better safety profiles, higher affinity, better tissue penetration, and less immunogenicity are the merits of sdAbs for molecular imaging and endoradiotherapy (*54*). Since sdAbs, monoclonal antibodies, and antibody fragments are biomacromolecules, the production and quality control procedures should follow similar protocols. In other words, sdAbs for translational studies should be produced in current good-manufacturing-practice grade, either in bacteria, yeast, or Chinese hamster ovary systems. The His_6 tag is generally introduced to facilitate purification, but it may potentially cause immunogenicity. Removal of the His_6 tag is preferred at the initial plasma design stage or after purification of the sdAbs.

Notably, the kidney accumulation of radiometal-labeled sdAbs is exceptionally high because of excretion and reabsorption, leading to limited detection efficiency near the kidneys and undesired nephrotoxicity at therapeutic doses. Engineering strategies for migrating such drawbacks should be explored (*55*). Receptors such as megalin and cubilin are involved in the reabsorption of proteins (e.g., albumin and sdAb) in the proximal tubule (*56*). The introduction of cleavable linkers between chelator and sdAb (*57*), PEGylation (*39*), and the development of sdAb fusion proteins (*31,32*) are potential strategies to improve the pharmacokinetics and pharmacodynamics of sdAbs. For instance, the Belgium team has elucidated that the removal of the His_6 tag dramatically reduced kidney retention of radiometal-labeled sdAbs (*5,58*). Moreover, replacement of the His_6 tag with the HEHEHE tag reduced kidney retention of radiometal-labeled Affibody molecules (*59*), but the efficacy needs to be investigated in sdAb-derived agents. Along with the engineering strategies, small molecules (e.g., fructose and maleate), positively charged amino acids (e.g., lysine), and Gelofusine are reported to reduce kidney retention of radiolabeled sdAbs, but these are not general approaches because the efficiencies vary greatly between different tracers (*12,60*).

From a diagnostic perspective, only probes solving unmet clinical demands and having easy accessibility and high reproducibility will carve a niche in the companion diagnostics field. For multiinstitutional studies and commercial development, standardized and kit-based radiolabeling protocols can be innovated and adapted (*61*). In addition to solely imaging the patients for staging and restaging, new tracers may be introduced as companion diagnostics with the same or similar scaffold harnessed for therapeutic applications. Preliminary evidence has shown the promise of sdAb-derived theranostic pairs (*6,8*). In the HER2-targeted theranostic pair, the therapeutic agent ^{131}I-GMIB-anti-HER2-VHH1 was developed using ^{131}I-SGMIB as the prosthetic group, leading to increased stability and lower kidney accumulation of the radiopharmaceutical. The future of nuclear medicine will be continuously shaped by theranostics (*62*); α-particle−labeled sdAbs are also promising therapeutic components in the sdAb theranostic toolbox (*63*).

CONCLUSION

Molecular imaging has substantially improved the diagnosis and treatment of cancers. With further optimization and translation, sdAb theranostics may play important roles in the management of human diseases, especially cancers.

DISCLOSURE

This work was supported in part by the National Key Research and Development Program of China (grant 2020YFA0909000), the National Natural Science Foundation of China (grants 82171972 and 82001878), the Shanghai Rising-Star Program (grant 20QA1406100), the University of Wisconsin–Madison, and the National Institutes of Health (grant P30CA014520). Weibo Cai is a scientific advisor, stockholder, and grantee of Focus-X Therapeutics, Inc. No other potential conflict of interest relevant to this article was reported.

REFERENCES

1. Mankoff DA. A definition of molecular imaging. *J Nucl Med.* 2007;48(6):18N, 21N.
2. Wei W, Rosenkrans ZT, Liu J, Huang G, Luo QY, Cai W. ImmunoPET: concept, design, and applications. *Chem Rev.* 2020;120:3787–3851.
3. Chakravarty R, Goel S, Cai W. Nanobody: the "magic bullet" for molecular imaging? *Theranostics.* 2014;4:386–398.
4. Rashidian M, Ploegh H. Nanobodies as non-invasive imaging tools. *Immunooncology Technol.* 2020;7:2–14.
5. Xavier C, Vaneycken I, D'Huyvetter M, et al. Synthesis, preclinical validation, dosimetry, and toxicity of ^{68}Ga-NOTA-anti-HER2 Nanobodies for iPET imaging of HER2 receptor expression in cancer. *J Nucl Med.* 2013;54:776–784.
6. Keyaerts M, Xavier C, Heemskerk J, et al. Phase I study of ^{68}Ga-HER2-Nanobody for PET/CT assessment of HER2 expression in breast carcinoma. *J Nucl Med.* 2016;57:27–33.
7. D'Huyvetter M, De Vos J, Xavier C, et al. ^{131}I-labeled anti-HER2 camelid sdAb as a theranostic tool in cancer treatment. *Clin Cancer Res.* 2017;23:6616–6628.
8. D'Huyvetter M, Vos J, Caveliers V, et al. Phase I trial of ^{131}I-GMIB-Anti-HER2-VHH1, a new promising candidate for HER2-targeted radionuclide therapy in breast cancer patients. *J Nucl Med.* 2021;62:1097–1105.
9. Feng Y, Meshaw R, McDougald D, et al. Evaluation of an ^{131}I-labeled HER2-specific single domain antibody fragment for the radiopharmaceutical therapy of HER2-expressing cancers. *Sci Rep.* 2022;12:3020.
10. Zhao L, Liu C, Xing Y, et al. Development of a ^{99m}Tc-labeled single-domain antibody for SPECT/CT assessment of HER2 expression in breast cancer. *Mol Pharm.* 2021;18:3616–3622.

11. Vaidyanathan G, McDougald D, Choi J, et al. Preclinical evaluation of ^{18}F-labeled anti-HER2 Nanobody conjugates for imaging HER2 receptor expression by immuno-PET. *J Nucl Med.* 2016;57:967–973.
12. Wang C, Chen Y, Hou YN, et al. ImmunoPET imaging of multiple myeloma with [^{68}Ga]Ga-NOTA-Nb1053. *Eur J Nucl Med Mol Imaging.* 2021;48:2749–2760.
13. Zhou Z, Meshaw R, Zalutsky MR, Vaidyanathan G. Site-specific and residualizing linker for ^{18}F labeling with enhanced renal clearance: application to an anti-HER2 single-domain antibody fragment. *J Nucl Med.* 2021;62:1624–1630.
14. Vosjan MJ, Perk LR, Roovers RC, et al. Facile labelling of an anti-epidermal growth factor receptor Nanobody with ^{68}Ga via a novel bifunctional desferal chelate for immuno-PET. *Eur J Nucl Med Mol Imaging.* 2011;38:753–763.
15. Gainkam LO, Huang L, Caveliers V, et al. Comparison of the biodistribution and tumor targeting of two ^{99m}Tc-labeled anti-EGFR nanobodies in mice, using pinhole SPECT/micro-CT. *J Nucl Med.* 2008;49:788–795.
16. Krüwel T, Nevoltris D, Bode J, et al. In vivo detection of small tumour lesions by multi-pinhole SPECT applying a ^{99m}Tc-labelled nanobody targeting the epidermal growth factor receptor. *Sci Rep.* 2016;6:21834.
17. Bensch F, van der Veen EL, Lub-de Hooge MN, et al. ^{89}Zr-atezolizumab imaging as a non-invasive approach to assess clinical response to PD-L1 blockade in cancer. *Nat Med.* 2018;24:1852–1858.
18. Hirsch FR, McElhinny A, Stanforth D, et al. PD-L1 immunohistochemistry assays for lung cancer: results from phase 1 of the blueprint PD-L1 IHC assay comparison project. *J Thorac Oncol.* 2017;12:208–222.
19. Xing Y, Chand G, Liu C, et al. Early phase I study of a ^{99m}Tc-labeled anti-programmed death ligand-1 (PD-L1) single-domain antibody in SPECT/CT assessment of PD-L1 expression in non-small cell lung cancer. *J Nucl Med.* 2019;60:1213–1220.
20. Lv G, Sun X, Qiu L, et al. PET imaging of tumor PD-L1 expression with a highly specific nonblocking single-domain antibody. *J Nucl Med.* 2020;61:117–122.
21. Yang Y, Wang C, Wang Y, et al. Dose escalation biodistribution, positron emission tomography/computed tomography imaging and dosimetry of a highly specific radionuclide-labeled non-blocking nanobody. *EJNMMI Res.* 2021;11:113.
22. Bridoux J, Broos K, Lecocq Q, et al. Anti-human PD-L1 Nanobody for immuno-PET imaging: validation of a conjugation strategy for clinical translation. *Biomolecules.* 2020;10:1388.
23. Li D, Cheng S, Zou S, et al. Immuno-PET Imaging of ^{89}Zr labeled anti-PD-L1 domain antibody. *Mol Pharm.* 2018;15:1674–1681.
24. Wei W, Zhang D, Wang C, et al. Annotating CD38 expression in multiple myeloma with [^{18}F]F-Nb1053. *Mol Pharm.* November 30, 2021 [Epub ahead of print].
25. Shi L, Chen B, Liu T, et al. ^{99m}Tc-CD3813: a Nanobody-based single photon emission computed tomography radiotracer with clinical potential for myeloma imaging and evaluation of CD38 expression. *Mol Pharm.* 2022; Epub ahead of print.
26. Wei W, Zhang Y, Zhang D, et al. Annotating BCMA expression in multiple myelomas. *Mol Pharm.* November 29, 2021 [Epub ahead of print].
27. De Veirman K, Puttemans J, Krasniqi A, et al. CS1-specific single-domain antibodies labeled with actinium-225 prolong survival and increase CD8+ T cells and PD-L1 expression in multiple myeloma. *OncoImmunology.* 2021;10:2000699.
28. Ghai A, Zheleznyak A, Mixdorf M, et al. Development of [^{89}Zr]DFO-elotuzumab for immunoPET imaging of CS1 in multiple myeloma. *Eur J Nucl Med Mol Imaging.* 2021;48:1302–1311.
29. Puttemans J, Stijlemans B, Keyaerts M, et al. The road to personalized myeloma medicine: patient-specific single-domain antibodies for anti-idiotypic radionuclide therapy. *Mol Cancer Ther.* 2022;21:159–169.
30. Duray E, Lejeune M, Baron F, et al. A non-internalised CD38-binding radiolabelled single-domain antibody fragment to monitor and treat multiple myeloma. *J Hematol Oncol.* 2021;14:183.
31. An S, Zhang D, Zhang Y, et al. GPC3-targeted immunoPET imaging of hepatocellular carcinomas. *Eur J Nucl Med Mol Imaging.* 2022;49:2682–2692.
32. van Lith SAM, Huizing FJ, Franssen GM, et al. Novel VHH-based tracers with variable plasma half-lives for imaging of CAIX-expressing hypoxic tumor cells. *Mol Pharm.* 2022; Epub ahead of print.
33. Liu T, Wu Y, Shi L, et al. Preclinical evaluation of [^{99m}Tc]Tc-labeled anti-EpCAM nanobody for EpCAM receptor expression imaging by immuno-SPECT/CT. *Eur J Nucl Med Mol Imaging.* 2022;49:1810–1821.
34. Demine S, Garcia Ribeiro R, Thevenet J, et al. A nanobody-based nuclear imaging tracer targeting dipeptidyl peptidase 6 to determine the mass of human beta cell grafts in mice. *Diabetologia.* 2020;63:825–836.
35. Balhuizen A, Massa S, Mathijs I, et al. A nanobody-based tracer targeting DPP6 for non-invasive imaging of human pancreatic endocrine cells. *Sci Rep.* 2017;7:15130.
36. Wei W, Jiang D, Ehlerding EB, Luo Q, Cai W. Noninvasive PET imaging of T cells. *Trends Cancer.* 2018;4:359–373.
37. Pandit-Taskar N, Postow MA, Hellmann MD, et al. First-in-humans imaging with ^{89}Zr-Df-IAB22M2C anti-CD8 minibody in patients with solid malignancies: preliminary pharmacokinetics, biodistribution, and lesion targeting. *J Nucl Med.* 2020;61:512–519.
38. Farwell MD, Gamache RF, Babazada H, et al. CD8-targeted PET imaging of tumor-infiltrating T cells in patients with cancer: a phase I first-in-humans study of ^{89}Zr-Df-IAB22M2C, a radiolabeled Anti-CD8 minibody. *J Nucl Med.* 2022;63:720–726.
39. Rashidian M, Ingram JR, Dougan M, et al. Predicting the response to CTLA-4 blockade by longitudinal noninvasive monitoring of CD8 T cells. *J Exp Med.* 2017;214:2243–2255.
40. Van Elssen CH, Rashidian M, Vrbanac V, et al. Noninvasive imaging of human immune responses in a human xenograft model of graft-versus-host disease. *J Nucl Med.* 2017;58:1003–1008.
41. Rothlauf PW, Li Z, Pishesha N, et al. Noninvasive immuno-PET imaging of CD8$^+$ T cell behavior in influenza a virus-infected mice. *Front Immunol.* 2021;12:777739.
42. Rashidian M, LaFleur MW, Verschoor VL, et al. Immuno-PET identifies the myeloid compartment as a key contributor to the outcome of the antitumor response under PD-1 blockade. *Proc Natl Acad Sci USA.* 2019;116:16971–16980.
43. Zhao H, Wang C, Yang Y, et al. ImmunoPET imaging of human CD8$^+$ T cells with novel ^{68}Ga-labeled nanobody companion diagnostic agents. *J Nanobiotechnology.* 2021;19:42.
44. Traenkle B, Kaiser PD, Pezzana S, et al. Single-domain antibodies for targeting, detection, and in vivo imaging of human CD4$^+$ cells. *Front Immunol.* 2021;12:799910.
45. Lecocq Q, Awad RM, De Vlaeminck Y, et al. Single-domain antibody nuclear imaging allows noninvasive quantification of LAG-3 expression by tumor-infiltrating leukocytes and predicts response of immune checkpoint blockade. *J Nucl Med.* 2021;62:1638–1644.
46. Blykers A, Schoonooghe S, Xavier C, et al. PET imaging of macrophage mannose receptor-expressing macrophages in tumor stroma using ^{18}F-radiolabeled camelid single-domain antibody fragments. *J Nucl Med.* 2015;56:1265–1271.
47. Xavier C, Blykers A, Laoui D, et al. Clinical translation of [^{68}Ga]Ga-NOTA-anti-MMR-sdAb for PET/CT imaging of protumorigenic macrophages. *Mol Imaging Biol.* 2019;21:898–906.
48. Varasteh Z, Mohanta S, Li Y, et al. Targeting mannose receptor expression on macrophages in atherosclerotic plaques of apolipoprotein E-knockout mice using ^{68}Ga-NOTA-anti-MMR nanobody: non-invasive imaging of atherosclerotic plaques. *EJNMMI Res.* 2019;9:5.
49. Broisat A, Hernot S, Toczek J, et al. Nanobodies targeting mouse/human VCAM1 for the nuclear imaging of atherosclerotic lesions. *Circ Res.* 2012;110:927–937.
50. De Vos J, Mathijs I, Xavier C, et al. Specific targeting of atherosclerotic plaques in ApoE(−/−) mice using a new camelid sdAb binding the vulnerable plaque marker LOX-1. *Mol Imaging Biol.* 2014;16:690–698.
51. Movahedi K, Schoonooghe S, Laoui D, et al. Nanobody-based targeting of the macrophage mannose receptor for effective in vivo imaging of tumor-associated macrophages. *Cancer Res.* 2012;72:4165–4177.
52. Senders ML, Hernot S, Carlucci G, et al. Nanobody-facilitated multiparametric PET/MRI phenotyping of atherosclerosis. *JACC Cardiovasc Imaging.* 2019;12:2015–2026.
53. Rashidian M, Keliher EJ, Bilate AM, et al. Noninvasive imaging of immune responses. *Proc Natl Acad Sci USA.* 2015;112:6146–6151.
54. Ackaert C, Smiejkowska N, Xavier C, et al. Immunogenicity risk profile of nanobodies. *Front Immunol.* 2021;12:632687.
55. Yang E, Liu Q, Huang G, Liu J, Wei W. Engineering nanobodies for next-generation molecular imaging. *Drug Discov Today.* 2022;27:1622–1638.
56. Molitoris BA, Sandoval RM, Yadav SPS, Wagner MC. Albumin uptake and processing by the proximal tubule: physiologic, pathologic and therapeutic implications. *Physiol Rev.* 2022;102:1625–1667.
57. Arano Y. Renal brush border strategy: a developing procedure to reduce renal radioactivity levels of radiolabeled polypeptides. *Nucl Med Biol.* 2021;92:149–155.
58. D'Huyvetter M, Vincke C, Xavier C, et al. Targeted radionuclide therapy with a ^{177}Lu-labeled anti-HER2 nanobody. *Theranostics.* 2014;4:708–720.
59. Hofstrom C, Orlova A, Altai M, Wangsell F, Graslund T, Tolmachev V. Use of a HEHEHE purification tag instead of a hexahistidine tag improves biodistribution of affibody molecules site-specifically labeled with ^{99m}Tc, ^{111}In, and ^{125}I. *J Med Chem.* 2011;54:3817–3826.
60. Gainkam LO, Caveliers V, Devoogdt N, et al. Localization, mechanism and reduction of renal retention of technetium-99m labeled epidermal growth factor receptor-specific nanobody in mice. *Contrast Media Mol Imaging.* 2011;6:85–92.
61. Baudhuin H, Van Bockstal PJ, De Beer T, et al. Lyophilization of NOTA-sdAbs: first step towards a cold diagnostic kit for ^{68}Ga-labeling. *Eur J Pharm Biopharm.* 2021;166:194–204.
62. Langbein T, Weber WA, Eiber M. Future of theranostics: an outlook on precision oncology in nuclear medicine. *J Nucl Med.* 2019;60(suppl 2):13S–19S.
63. Feng Y, Meshaw R, Zhao XG, Jannetti SA III, Vaidyanathan G, Zalutsky MR. Effective treatment of human breast carcinoma xenografts with single-dose ^{211}At-labeled Anti-HER2 single domain antibody fragment. *J Nucl Med.* May 26, 2022 [Epub ahead of print].

Role of Prostate-Specific Membrane Antigen PET in Metastatic Prostate Cancer: We Have the Answers

Kelsey L. Pomykala[1], Ken Herrmann[2], Anwar R. Padhani[3], Michael S. Hofman[4,5], Elisabetta Lalumera[6], and Stefano Fanti[7,8]

[1]*Institute for Artificial Intelligence in Medicine, University Hospital Essen, Essen, Germany;* [2]*Department of Nuclear Medicine, University of Duisburg–Essen and German Cancer Consortium (DKTK), University Hospital Essen, Essen, Germany;* [3]*Paul Strickland Scanner Centre, Mount Vernon Cancer Centre, Northwood, United Kingdom;* [4]*Prostate Cancer Theranostics and Imaging Centre of Excellence, Cancer Imaging, Peter MacCallum Cancer Centre, Melbourne, Australia;* [5]*Sir Peter MacCallum Department of Oncology, University of Melbourne, Melbourne, Australia;* [6]*Department for Life Quality Studies, University of Bologna, Rimini, Italy;* [7]*Department of Nuclear Medicine, Policlinico S. Orsola, University of Bologna, Bologna, Italy; and* [8]*IRCCS AOU di Bologna, Bologna, Italy*

Then He said to Thomas, "Put your finger here; see my hands. Reach out your hand and put it into my side. Stop doubting and believe."

—John 20:27

A recent commentary from Sartor et al. in *The Journal of Nuclear Medicine* (*1*) questions the use of prostate-specific membrane antigen (PSMA) PET imaging for selection criteria for PSMA-targeted therapy, commenting on the newly published outcome of patients with PSMA PET/CT screen failure by VISION trial criteria (*2*). In addition, comments by Hussain et al. in *Journal of Clinical Oncology* (*3*) regarding the role of PSMA PET in patients with metastatic hormone-sensitive prostate cancer have added to the controversy. Both commentaries require a response, with our main points of concern below.

PERSONALIZED MEDICINE

Targeted therapy intends to selectively hit tumor cells expressing the specific target. In contrast to many novel targeted therapies that rely on a single tissue sample, PSMA PET, which serves as a companion diagnostic for PSMA radioligand therapy, displays in vivo the presence of PSMA expression in all detected tumor lesions. The likelihood to benefit from PSMA radioligand therapy is clearly higher in patients with more PSMA-avid metastases (*4*). Although careful investigation of the benefit of PSMA radioligand therapy in PSMA PET–negative patients indeed warrants further formal testing, questioning the predictive value of PSMA PET in metastatic hormone-sensitive prostate cancer ridicules the concept of precision oncology.

MISGUIDED CONCLUSIONS

Many worthy points are made, including an emphasis on patient quality of life and that medicine is an art in which management decisions integrate physical examination, laboratory, imaging, and other data with clinical judgment. We also wholeheartedly agree with the statement that management discussions should be had with an interdisciplinary group, often including the image-interpreting physician (*3*). However, this does not tally with the conclusion of Hussain et al. (*3*) that, "Outside clinical trials, our shared recommendation is that there is little utility currently for the routine use of PSMA-PET in patients with detectable metastases on [conventional imaging] and recommendations regarding therapy should be based on [conventional imaging] findings." We do not see how this conclusion was drawn, nor do we see the methodology Hussain et al. used to build this recommendation after citing a work demonstrating that PSMA PET imaging is more sensitive than conventional imaging (*5*), with fewer false-positive and equivocal findings at a lower radiation dose, which are the relevant measures for a diagnostic test. Additionally, PSMA PET has a per-node specificity of 99% (*6*) and has been convincingly shown to lead to major patient management changes in the hands of experienced genitourinary oncologists (*7–10*). Furthermore, PSMA PET is predictive of freedom from progression in men undergoing salvage radiation therapy for biochemical recurrence after radical prostatectomy (*11*). Given these advantages and regulatory approval, it seems bizarre to use less accurate tests to guide therapy decisions. This is akin to managing lung cancers using chest radiographs instead of CT.

FEAR OF OVERDIAGNOSIS

One of the arguments made was that with a more sensitive imaging modality, more micrometastases will be found, leading to upstaging and overtreatment, with possible declines in quality of life and no proven survival benefit (*3*). We agree that longer-term studies evaluating survival differences with PSMA PET compared with conventional imaging are needed but are not without challenges (*12*). However, one must consider that a higher specificity leads to fewer harms caused by the false-positive results of conventional imaging. In the ProPSMA study sensitivity analysis, when equivocal imaging findings were considered positive, the false-positive rate of conventional imaging was an alarming 23% (*9*). Curiously, the authors then go on to contradict their first point of avoiding upstaging, by adding that despite the higher sensitivity of

Received May 10, 2022; revision accepted Jun. 2, 2022.
For correspondence or reprints, contact Kelsey L. Pomykala (Kelsey.herrmann@uk-essen.de).
Published online Jun. 9, 2022.

DOI: 10.2967/jnumed.122.264394

PSMA PET, micrometastases could be missed (false-negatives) and that curative adjuvant therapy should not be withheld on the basis of negative PET results (*3*). The claim, therefore, is that PSMA PET is both too sensitive and not sensitive enough.

STAGE MIGRATION

Hussain et al. (*3*) state that replacing conventional imaging with PSMA PET/CT is likely to cause stage migration. However, we believe that stage migration should be distinguished from the study biases it may produce (*13*). Stage migration is a consequence of the introduction of any new (and usually better) classification technique due to higher sensitivity. This is counterbalanced by improved specificity, with the overall impact being unknown, requiring further study. The authors do not make this distinction or note that biases potentially caused by stage migration need to be considered in trial designs, instead suggesting that the Will Rogers effect is a reason against replacing conventional imaging with new techniques (*3*).

CONCLUSION

For diagnosis of high-risk prostate cancer, localization of biochemical recurrence, and PSMA treatment selection, the most accurate diagnostic method should be used—PSMA PET/CT. This principle is accepted by multiple international guidelines. The opportunity to study both the benefits and the detriments of PSMA PET use remains open.

DISCLOSURE

Michael S. Hofman acknowledges philanthropic/government grant support from the Prostate Cancer Foundation (PCF) funded by CANICA Oslo Norway, Peter MacCallum Foundation, Medical Research Future Fund, NHMRC Investigator Grant, Movember, U.S. Department of Defense and the Prostate Cancer Foundation of Australia (PCFA). No other potential conflict of interest relevant to this article was reported.

ACKNOWLEDGMENTS

Ken Herrmann, Anwar R. Padhani, Michael S. Hofman, and Stefano Fanti are members of the Advanced Prostate Cancer Consensus Conference 2022 Imaging Expert Group, Lugano, Switzerland.

REFERENCES

1. Sartor O. Invited perspective, outcome of patients with PSMA-PET/CT screen failure by VISION criteria and treated with ^{177}Lu-PSMA therapy: a multicenter retrospective analysis. *J Nucl Med.* May 26, 2022 [Epub ahead of print].
2. Hotta M, Gafita A, Czernin J, Calais J. Outcome of patients with PSMA-PET/CT screen failure by VISION criteria treated with ^{177}Lu-PSMA therapy: a multicenter retrospective analysis. *J Nucl Med*. March 10, 2022 [Epub ahead of print].
3. Hussain M, Carducci MA, Clarke N, et al. Evolving role of prostate-specific membrane antigen-positron emission tomography in metastatic hormone-sensitive prostate cancer: more questions than answers? *J Clin Oncol.* April 19, 2022 [Epub ahead of print].
4. Buteau JP, Martin AJ, Emmett L, et al. PSMA PET and FDG PET as predictors of response and prognosis in a randomized phase 2 trial of ^{177}Lu-PSMA-617 (LuPSMA) versus cabazitaxel in metastatic, castration-resistant prostate cancer (mCRPC) progressing after docetaxel (TheraP ANZUP 1603) [abstract]. *J Clin Oncol*. 2022;40(suppl):10.
5. Calais J, Ceci F, Eiber M, et al. ^{18}F-fluciclovine PET-CT and ^{68}Ga-PSMA-11 PET-CT in patients with early biochemical recurrence after prostatectomy: a prospective, single-centre, single-arm, comparative imaging trial. *Lancet Oncol.* 2019; 20:1286–1294.
6. Perera M, Papa N, Roberts M, et al. Gallium-68 prostate-specific membrane antigen positron emission tomography in advanced prostate cancer: updated diagnostic utility, sensitivity, specificity, and distribution of prostate-specific membrane antigen-avid lesions—a systematic review and meta-analysis. *Eur Urol.* 2020;77: 403–417.
7. Donswijk ML, van Leeuwen PJ, Vegt E, et al. Clinical impact of PSMA PET/CT in primary prostate cancer compared to conventional nodal and distant staging: a retrospective single center study. *BMC Cancer.* 2020;20:723.
8. Hope TA, Aggarwal R, Chee B, et al. Impact of ^{68}Ga-PSMA-11 PET on management in patients with biochemically recurrent prostate cancer. *J Nucl Med.* 2017; 58:1956–1961.
9. Hofman MS, Lawrentschuk N, Francis RJ, et al. Prostate-specific membrane antigen PET-CT in patients with high-risk prostate cancer before curative-intent surgery or radiotherapy (proPSMA): a prospective, randomised, multicentre study. *Lancet.* 2020;395:1208–1216.
10. Pomykala KL, Czernin J, Grogan TR, Armstrong WR, Williams J, Calais J. Total-body ^{68}Ga-PSMA-11 PET/CT for bone metastasis detection in prostate cancer patients: potential impact on bone scan guidelines. *J Nucl Med.* 2020;61: 405–411.
11. Emmett L, Tang R, Nandurkar R, et al. 3-year freedom from progression after ^{68}Ga-PSMA PET/CT-triaged management in men with biochemical recurrence after radical prostatectomy: results of a prospective multicenter trial. *J Nucl Med.* 2020;61:866–872.
12. Lalumera E, Fanti S. Randomized controlled trials for diagnostic imaging: conceptual and practical problems. *Topoi (Dordr).* 2019;38:395–400.
13. Fanti S, Lalumera E, Hicks R. Facts and myths about stage migration: should the Will Rogers phenomenon ride off into the distance? *Eur Urol Oncol.* January 11, 2022 [Epub ahead of print].

Outcome of Patients with PSMA PET/CT Screening Failure by VISION Criteria and Treated with ^{177}Lu-PSMA: A Multicenter Retrospective Analysis

Oliver Sartor

Tulane University School of Medicine, New Orleans, Louisiana

See the associated article on page 1484.

Selection of patients for treatment with prostate-specific membrane antigen (PSMA)–targeted therapy is somewhat controversial. There are those who have suggested that no selection is necessary and those who have suggested that tight imaging-based selection criteria are required. What is optimal, what is required, and what is practical are all different questions.

Given the importance of the VISION trial (the only trial demonstrating overall survival benefit with PSMA-targeted therapy), findings in this trial will be examined in some detail (*1*). Of note, the VISION trial enrolled patients with at least 1 metastatic lesion present on baseline contrast-enhanced CT, MRI, or bone scanning obtained no more than 28 d before beginning study therapy. Thus, metastatic disease on conventional imaging was required. In addition, patients must have progressed after one or more androgen axis inhibitors (e.g., abiraterone, enzalutamide, darolutamide, or apalutamide) and at least one taxane-based chemotherapy. Approximately 41% of VISION participants were previously treated with 2 taxane regimens.

What were the eligibility criteria relative to PSMA PET/CT imaging in VISION? First, all patients must have had a centrally read ^{68}Ga-PSMA-11 PET/CT scan for trial entry. Second, a metastatic lesion (one or more) that was PSMA PET–positive was required. PSMA PET positivity was determined by uptake in the lesion at an intensity level greater than that in the liver. There was no SUV cutoff requirement; potential metastatic lesions in each patient were compared with liver uptake by a centralized PET reading. There were no size criteria for metastatic PSMA PET–positive lesions.

Importantly, the patients screened for the VISION trial had additional imaging-based exclusion criteria. Patients were excluded if there were PSMA PET–negative lesions (uptake less than in liver) measuring at least 1 cm in solid organs, at least 2.5 cm in lymph nodes, or at least 1 cm in a bone lesion with a soft-tissue component. Assessment was by contrast-enhanced CT combined with the PET/CT findings. These negative selection criteria are quite important and helped to exclude patients harboring lesions with low levels of PSMA expression.

During the VISION design phase, there was a strong desire to avoid using 2 PET scans as a requirement for trial entry, knowing that the VISION entry criteria would likely be cited by regulatory authorities considering ^{177}Lu-PSMA-617 as an approved therapy. In the United States, and many other areas of the world, obtaining reimbursement for 2 distinct types of PET scans was deemed potentially problematic. Thus, for practical reasons, ^{18}F-FDG PET scans were not used in the VISION entry criteria.

In the plenary session at the 2021 American Society of Clinical Oncology meeting, the discussant questioned whether PSMA-based imaging was required for selection of patients (*2*). This discussion followed the initial presentation of the VISION trial. Of the 1,003 patients screened with PET/CT, 49 (4.9%) had no PSMA-positive metastatic lesions. Of the 954 patients with PSMA PET metastatic lesions, 87 patients were excluded because PSMA-negative metastases were also detected. All told, only about 13% of patients were excluded because of PET imaging criteria. Given the overall survival benefit with a hazard ratio of 0.62 relative to control (hazard ratio, 0.62; 95% CI, 0.52–0.74), it is likely that had the VISION trial been conducted on non–PSMA PET-selected patients, the overall survival benefit would still have been statistically significant; that is, the CIs would not have crossed 1.0. Thus, questioning the requirement for PSMA PET selection for ^{177}Lu-PSMA-617 is reasonable.

Have any investigators used PSMA-targeted therapies without regard to PSMA PET selection? The answer is yes. Data on non–PSMA-selected patients have been presented from studies using ^{177}Lu J591, ^{225}Ac J591, PSMA bispecific antibodies, a PSMA antibody–drug conjugate, and PSMA-targeted chimeric antigen receptor T cells. J591 is a monoclonal antibody that binds to PSMA and has been used to target either ^{177}Lu or ^{225}Ac (*3,4*). The J591 radiopharmaceutical studies have not compared PSMA PET–selected and non–PSMA PET-selected patients; thus, it is not possible to determine how important selection might be to patient outcomes. The bispecific antibodies pasotuxizumab (also called AMG 212) and AMG 160 have also been studied in non–PSMA PET-selected patients (*5,6*). What is clearly noted is that many patients not selected by PSMA PET appear to respond to these treatments. Some meaningful responses have also been seen in the PSMA antibody–drug conjugate studies (*7*) and in patients treated with chimeric antigen receptor T cells (*8*). All in all, given the absence of long-term survival data and the absence of PSMA PET selection compared with non–PSMA PET selection, it is speculative to conclude that PSMA PET

Received May 6, 2022; revision accepted May 16, 2022.
For correspondence or reprints, contact Oliver Sartor (osartor@tulane.edu).
Published online May 26, 2022.

DOI: 10.2967/jnumed.122.264128

selection criteria improve outcomes in any of these studies. ICAR-T and bispecific antibodies may be very different from radioligands in terms of cellular PSMA expression requirements.

The TheraP Australian trial is a large phase II trial assessing prostate-specific antigen (PSA) responses to cabazitaxel or ^{177}Lu-PSMA-617 (*9*). The prior therapies administered to TheraP patients and the dosing of ^{177}Lu-PSMA-617 were distinct from VISION. The TheraP trial applied a double PET/CT selection using ^{68}Ga-PSMA-11 and ^{18}F-FDG criteria. PSMA-positive metastatic disease required an SUV_{max} of at least 20 at a disease site and greater than 10 at all other measurable sites of metastatic disease. In addition, ^{18}F-FDG PET positivity must be concordant. Patients with ^{18}F-FDG PET–positive lesions that were discordant by PSMA PET were deemed not eligible for ^{177}Lu-PSMA-617 treatment.

The data from TheraP suggest a high rate of PSA response to ^{177}Lu-PSMA-617 treatments; an unconfirmed PSA decline of at least 50% occurred in 66% of patients. Direct comparisons of the PSA response rate between TheraP and VISION can be made, but the patient populations are distinct in several ways. Not only were the imaging entry criteria distinct, but prior treatments were distinct (no cabazitaxel pretreatments were allowed in TheraP) and doses of ^{177}Lu-PSMA-617 differed between the trials. Thus, direct comparisons of PSA response rate in TheraP and VISION are problematic.

It is possible to compare exclusion rates between TheraP and VISION. As noted previously, approximately 13% of patients were excluded from VISION because of imaging issues. For TheraP, 291 patients were screened and 29 (10%) were excluded because PSMA uptake was insufficient and 51 (18%) were excluded because of imaging discordance between the ^{18}F-FDG PET and the PSMA PET findings. Thus, a total of 28% of the patients screened in TheraP were not treated because of PSMA PET criteria. Clearly, this exclusion rate was higher than in VISION.

Investigators had previously treated several patients on various protocols with ^{177}Lu-PSMA-617 (*10*). These clinical trials had entry criteria distinct from VISION, but all patients had undergone a baseline ^{68}Ga-PSMA PET/CT scan. A retrospective analysis of these findings is now available for analysis. There was a higher percentage of visceral disease in those not meeting VISION criteria (58.6% vs. 25.4%). Their findings indicated that treating patients who were excluded by using VISION criteria led to a lower PSA response rate (PSA decline of $\geq$50%) and a longer time to PSA progression. These data were striking in that a PSA decline rate of at least 50% was 50.3% versus 20.7%. Survival analyses were not properly powered and thus were not informative (however, survival trended favorably among those meeting VISION entry criteria). These data help to support the validity of the VISION criteria in patient selection and, to our knowledge, represent the only published experience addressing this issue.

What are the optimal PSMA PET criteria for selection of patients? This question is important for radioligands (both βs and αs), bispecific antibodies, antibody–drug conjugates, and chimeric antigen receptor T cells. Answers to this question are not yet clear, and trials with overall survival as an endpoint will likely be best to assess this question. It is intuitive to say that higher PSMA expression is better, but the different PSMA-targeted approaches may yield different answers. What is required? One can create an argument that no PSMA PET imaging is required for patient selection when using PSMA-targeted therapy. Little data are available to date. That said, administration of expensive therapies with potential toxicities to patients who stand little chance to benefit seems unwise. What is practical? Practicality depends on perspective and geography and economics. What is practical in one region may not be practical in another. In many respects, what is practical is what the regulators allow. There is much work to do before we can be definitive in our conclusions, especially now that PSMA-targeted therapy has many iterations.

DISCLOSURE

No potential conflict of interest relevant to this article was reported.

REFERENCES

1. Sartor O, de Bono J, Chi KN, et al. Lutetium-177-PSMA-617 for metastatic castration-resistant prostate cancer. *N Engl J Med.* 2021;385:1091–1103.
2. Morris MJ, De Bono JS, Chi KN, et al. Phase III study of lutetium-177-PSMA-6176 in patients with metastatic castrate resistant prostate cancer (VISION). *J Clin Oncol.* 2021;39:18s (LBA4).
3. Tagawa ST, Vallabhajosula S, Christos PJ, et al. Phase 1/2 study of fractionated dose lutetium-177-labeled anti-prostate-specific membrane antigen monoclonal antibody J591 (^{177}Lu-J591) for metastatic castration-resistant prostate cancer. *Cancer.* 2019;125:2561–2569.
4. Tagawa ST, Sun M, Sartor AO, et al. Phase I study of ^{225}Ac-J591 for men with metastatic castration-resistant prostate cancer (mCRPC) [abstract]. *J Clin Oncol.* 2021;39(suppl):5015.
5. Hummel HD, Kufer P, Grüllich C, et al. Pasotuxizumab, a BiTE® immune therapy for castration-resistant prostate cancer: phase I, dose-escalation study findings. *Immunotherapy.* 2021;13:125–141.
6. Tran B, Horvath L, Dorff, et al. Results from a phase I study of AMG 160, a half-life extended (HLE), PSMA-targeted, bispecific T-cell engager (BiTE®) immune therapy for metastatic castration-resistant prostate cancer (mCRPC) [abstract]. *Ann Oncol.* 2020;31(suppl 4):S507.
7. Petrylak DP, Vogelzang NJ, Chatta K, et al. PSMA ADC monotherapy in patients with progressive metastatic castration-resistant prostate cancer following abiraterone and/or enzalutamide: efficacy and safety in open-label single-arm phase 2 study. *Prostate.* 2020;80:99–108.
8. Slovin SF, Dorff TB, Falchook GS, et al. Phase 1 study of P-PSMA-101 CAR-T cells in patients with metastatic castration-resistant prostate cancer (mCRPC) [abstract]. *J Clin Oncol.* 2022;40(suppl):98.
9. Hofman MS, Emmett L, Sandhu S, et al. [^{177}Lu]Lu-PSMA-617 versus cabazitaxel in patients with metastatic castration-resistant prostate cancer (TheraP): a randomised, open-label, phase 2 trial. *Lancet.* 2021;397:797–804.
10. Hotta M, Gafita A, Czernin, Calais J. Outcome of patients with PSMA-PET/CT screen failure by VISION criteria and treated with ^{177}Lu-PSMA therapy: a multicenter retrospective analysis. *J Nucl Med.* March 10, 2022 [Epub ahead of print].

Outcome of Patients with PSMA PET/CT Screen Failure by VISION Criteria and Treated with ^{177}Lu-PSMA Therapy: A Multicenter Retrospective Analysis

Masatoshi Hotta, Andrei Gafita, Johannes Czernin, and Jeremie Calais

Ahmanson Translational Theranostics Division, Department of Molecular and Medical Pharmacology, UCLA, Los Angeles, California

See an invited perspective on this article on page 1482.

The aim of the study was to assess the outcome of patients with metastatic castration-resistant prostate cancer treated with ^{177}Lu-prostate-specific membrane antigen (PSMA) who would have been a screen failure (SF) in the VISION trial based on PSMA PET/CT criteria. **Methods:** We conducted a retrospective multicenter cohort study on 301 patients with metastatic castration-resistant prostate cancer treated with ^{177}Lu-PSMA. The patients were classified into eligible (VISION-PET-E) and SF (VISION-PET-SF) groups on the basis of the baseline PSMA PET/CT results. Prostate-specific antigen (PSA) response rates, PSA progression-free survival, and overall survival were compared. **Results:** Of 301 patients, 272 (90.4%) and 29 (9.6%) were VISION-PET-E and VISION-PET-SF, respectively. The VISION-PET-SF patients had a worse rate of ≥50% PSA decline (21% vs. 50%, $P = 0.005$) and PSA progression-free survival (2.1 vs. 4.1 mo, $P = 0.023$) and tended to have a shorter overall survival (9.6 vs. 14.2 mo. $P = 0.16$) than the VISION-PET-E patients. **Conclusion:** The VISION-PET-SF patients had worse outcomes than the VISION-PET-E patients. Our cohort did not include preexcluded patients (10%–15%) by local site assessments. Thus, 20%–25% of the patients may be SFs in unselected populations. Refinements in patient selection for ^{177}Lu-PSMA are needed to optimize outcomes.

Key Words: metastatic castration-resistant prostate cancer; radionuclide therapy; PSMA PET; ^{177}Lu; VISION trial

J Nucl Med 2022; 63:1484–1488
DOI: 10.2967/jnumed.121.263441

Men with metastatic castration-resistant prostate cancer have few alternative therapeutic options when the disease progresses after androgen-deprivation therapy, androgen receptor signaling inhibitors, and chemotherapy. Recently, the VISION trial, an international open-label, randomized phase 3 trial showed that prostate-specific membrane antigen (PSMA)–targeted molecular radionuclide therapy (MRT) with ^{177}Lu-PSMA can improve the outcome of patients with advanced metastatic castration-resistant prostate cancer. In this trial, 831 patients with metastatic castration-resistant prostate cancer previously treated with androgen receptor signaling inhibitor and taxane regimens were randomized in a 2:1 ratio to ^{177}Lu-PSMA (7.4 GBq every 6 wk × 6 cycles) plus the best standard of care ($n = 551$) or the standard of care alone ($n = 280$). The trial met both primary endpoints of overall survival (OS) and radiographic progression-free survival (PFS). The median OS was 15.3 mo in the ^{177}Lu-PSMA arm versus 11.3 mo in the standard-of-care–alone arm, resulting in a 38% reduction in the risk of death. The radiographic PFS was 8.7 versus 3.4 mo, respectively (*1*).

The VISION trial used PSMA PET/CT to select patients for inclusion. The screen failure (SF) rate was "only" 12.6% (126/1,003) (*1*), and some have argued that the trial could have been positive even in an unselected population (*2*). Eligibility by PSMA PET/CT results was determined by the sponsor's central readers (criteria initially not disclosed). The VISION PET selection criteria were released publicly at the American Society of Clinical Oncology 2021 meeting (*3*). It remains unknown whether the VISION PET criteria were appropriate to screen for and identify patients who will not benefit from ^{177}Lu-PSMA. Here, we exploited a database established retrospectively from multiple institutions to evaluate the outcome of patients treated with ^{177}Lu-PSMA who would have been a SF by VISION PET criteria.

MATERIALS AND METHODS

We conducted a retrospective cohort study in our institutional database of patients treated with at least 1 cycle of ^{177}Lu-PSMA between November 2017 and July 2021 ($n = 74$) and a multicenter dataset published previously ($n = 230$) (*4*). Patients were treated under compassionate use, an expanded access program, or clinical trials (Supplemental Table 1; supplemental materials are available at http://jnm.snmjournals.org). All patients underwent a baseline ^{68}Ga-PSMA-11 PET/CT scan before receiving ^{177}Lu-PSMA therapy. The eligibility criteria and institutional treatment protocols are described in Supplemental Tables 1 and 2. The presence of PSMA-positive disease by PET was not consistently predefined and was determined by the local clinical investigators at each institution.

One reader dually board-certified in radiology and nuclear medicine, and masked to the patient outcomes, reviewed the baseline PSMA PET/CT scan of each patient to apply the VISION PET criteria and determine eligible (VISION-PET-E) versus SF (VISION-PET-SF) patients. Patients were classified as VISION-PET-E if they had at least 1 PSMA-positive and no PSMA-negative metastatic lesions. The presence of PSMA-positive lesions was defined as PSMA uptake greater than uptake by liver parenchyma (*3*). The patients were classified as VISION-PET-SF if the baseline scan showed either of the following: absence of a metastatic lesion with uptake greater than in the liver background (i.e., low PSMA expression) or the presence of at least 1 metastatic lesion measurable by CT (≥1 cm for bone lesions with a soft-tissue component [M1b] or solid/visceral organ

Received Oct. 28, 2021; revision accepted Feb. 22, 2022.
For correspondence or reprints, contact Jeremie Calais (jcalais@mednet.ucla.edu).
Guest editor: Todd Peterson, Vanderbilt University.
Published online Mar. 10, 2022.

FIGURE 1. Baseline PSMA PET maximum-intensity projection of patient with metastatic castration-resistant prostate cancer categorized as VISION-PET-SF because of low PSMA expression (i.e., no PSMA-positive [>liver] metastatic lesion). SUV_{max} of liver and highest-uptake lesion were 9.6 and 6.4, respectively.

lesions [M1c], ≥2.5 cm for lymph node lesions [N1-M1a]) with uptake less than or equal to that in the liver background (i.e., PSMA-negative lesions) (*1*). Typical PSMA PET/CT images of low PSMA expression and PSMA-negative lesions are shown in Figures 1 and 2, respectively.

Outcome measures included prostate-specific antigen (PSA) response rates (≥50% PSA decline or any decline), PSA PFS, and OS. Kaplan–Meier curves with log-rank testing and Cox regression analysis were used to compare survival outcomes. The Fisher exact test and logistic regression analysis were used for categoric variable comparisons. The UCLA institutional review board waived written informed consent requirements because of the retrospective design of the analysis (waivers 19-000896 and 21-001565).

RESULTS

Overall, 3 of 304 (1.0%) men were lost to follow-up ($n = 2$) or had missing DICOM CT images ($n = 1$) and were excluded. Among 301 men, 272 (90.4%) and 29 (9.6%) were classified as VISION-PET-E and VISION-PET-SF, respectively. Cohort characteristics are provided in Table 1. The VISION-PET-SF patients had more visceral metastasis than VISION-PET-E patients (58.6% vs. 25.4%, $P < 0.001$). The median number of cycles was lower for VISION-PET-SF patients than for VISION-PET-E patients (2 cycles [interquartile range, 2–3] vs. 3 [interquartile range, 2–4], $P = 0.010$).

In the VISION-PET-SF group, 8 (2.7%) and 21 (7.0%) of 301 men were deemed to have low–PSMA-expressing or PSMA-negative lesions, respectively (summary images of these 29 patients are provided in Supplemental Figs. 1–29). The PSMA-negative lesions were in lymph nodes ($n = 7$), bone ($n = 1$), and visceral organs (liver, $n = 4$; lung, $n = 5$; pleura, $n = 2$; brain, $n = 1$; and muscle, $n = 1$).

Our cohort of VISION-PET-E patients was fairly comparable to the cohort included in the VISION trial (analysis set used for imaging-based PFS, Supplemental Table 3) (*1*). However, the treatment history differed. All VISION patients had been treated with a regimen of androgen receptor signaling inhibitor and taxane. In contrast, 94.5% and 80.1% of the current cohort underwent androgen receptor signaling inhibitor therapy and chemotherapy before MRT, respectively. Nevertheless, the PSA response and OS were comparable between the 2 cohorts (≥50% PSA decline, 50.3% vs. 46.0%; any PSA decline, 71.3% vs. 71.5%; OS, 14.2 mo vs. 14.6 mo).

The median follow-up time was 22.5 mo (interquartile range, 12.5–29.2 mo; range, 2.1–62.3 mo). The outcomes of the VISION-PET-E and VISION-PET-SF patients are shown in Table 2. The VISION-PET-SF patients had a significantly worse rate of ≥50% PSA decline, any PSA decline, and median PSA PFS than the VISION-PET-E patients. Although not statistically significant, median OS was 4.6 mo shorter in the VISION-PET-SF patients (Fig. 3).

In the VISION-PET-SF patients, the patients with PSMA-negative lesions ($n = 21$) had a shorter OS than those with low PSMA expression ($n = 8$) (Supplemental Table 4). However, there was no statistical difference in ≥50% PSA decline, any PSA decline, and median PSA PFS between the patients with PSMA-negative lesions and those with low PSMA expression (Fig. 4).

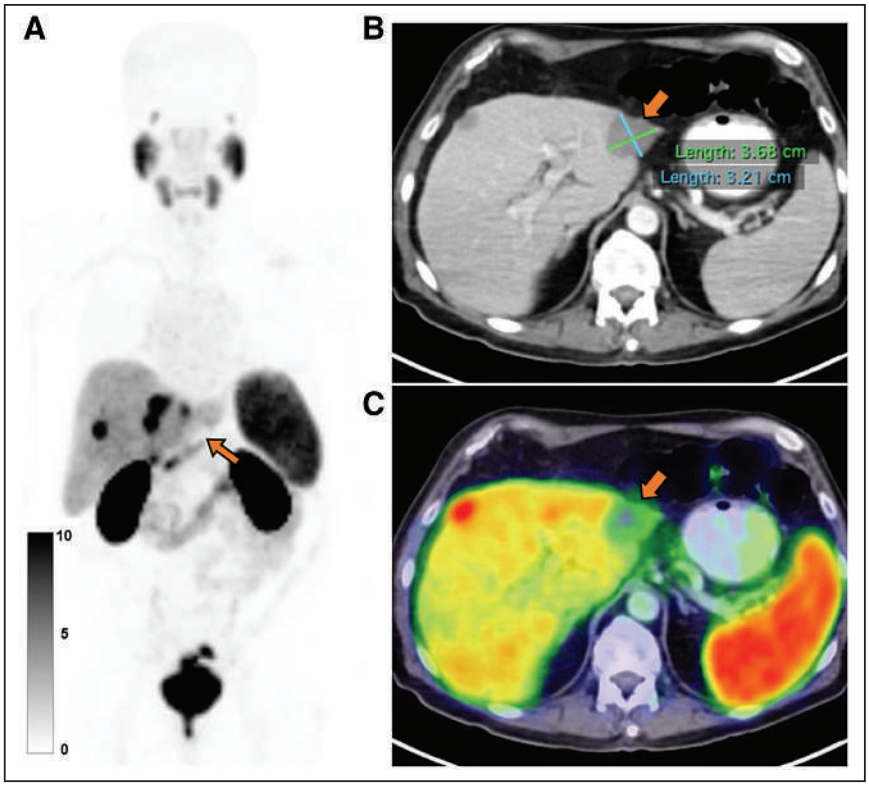

FIGURE 2. Baseline PSMA PET maximum-intensity projection (A), CT image (B), and PSMA PET/CT image (C) of patient with metastatic castration-resistant prostate cancer categorized as VISION-PET-SF because of PSMA-negative lesion (i.e., PSMA-negative metastatic lesion: liver metastasis ≥ 1.0 cm, uptake ≤ liver). One liver metastasis (arrow) showed lower uptake (SUV_{max}, 4.1) than liver parenchyma (SUV_{max}, 6.3).

DISCUSSION

The VISION trial used PSMA PET as a biomarker to select patients for ^{177}Lu-PSMA therapy. The VISION-PET-SF rate was "only" 12.6% (126/1,003) (*1*). Therefore, some have argued that the trial could have been positive even in an unselected population (*2*).

Here, we report that the VISION-PET-SF patients had worse outcomes than the

TABLE 1
Patient Characteristics

Characteristic	VISION-PET-E	VISION-PET-SF	*P*
n	272	29	
Median age (y)	72 (range, 66–76)	73 (range, 65–76)	0.91
Median PSA (ng/mL)	116.6 (interquartile range, 28.4–340.0)	74.0 (interquartile range, 17.5–198.3)	0.069
Treatment history			
Previous docetaxel	218 (80.1%)	25 (86.2%)	0.62
Second-line chemotherapy	95 (34.9%)	8 (27.6%)	0.54
Androgen receptor signaling inhibitor	257 (94.5%)	27 (93.1%)	0.67
Extent of disease on PSMA PET/CT			
Number of metastases ≥ 20	194 (71.3%)	16 (55.2%)	0.089
Number of metastases < 20	78 (28.7%)	13 (44.8%)	
Sites of disease on PSMA PET/CT			
Node only (N1 or M1a)	21 (7.7%)	1 (3.4%)	0.71
Bone only (M1b)	60 (22.1%)	3 (10.3%)	0.23
Node + bone (M1b and [N1 or M1a])	122 (44.9%)	8 (27.6%)	0.08
Viscera (any M1c)	69 (25.4%)	17 (58.6%)	<0.001
Number of cycles of ^{177}Lu-PSMA received			
1	38 (14.0%)	5 (17.2%)	0.065
2	68 (25.0%)	13 (44.8%)	
3	37 (13.6%)	5 (17.2%)	
4	91 (33.5%)	5 (17.2%)	
>4	38 (13.9%)	1 (3.4%)	
Median injected activity per cycle (GBq)	7.4 (interquartile range, 5.7–8.9)	7.4 (interquartile range, 6.0–8.5)	0.30

TABLE 2
Outcomes of VISION-PET-E and VISION-PET-SF Patients

Outcome	VISION-PET-E	VISION-PET-SF	*P*
n	272	29	
≥50% PSA decline			
n	131 (50.3%)	6 (20.7%)	0.005
Odds ratio	1	0.28 (95%CI, 0.11–0.71)	0.007
Any PSA decline			
n	194 (71.3%)	12 (41.4%)	0.003
Odds ratio	1	0.28 (95%CI, 0.13–0.62)	<0.001
PSA PFS			
Median months	4.9 (95%CI, 4.0–5.8)	2.1 (95%CI, 1.4–3.3)	0.023
Hazard ratio	1	1.6 (95%CI, 1.1–2.5)	0.025
OS			
Median months	14.2 (95%CI, 12.6–15.9)	9.6 (95%CI, 4.7–14.0)	0.16
Hazard ratio	1	1.4 (95%CI, 0.89–2.3)	0.16

VISION-PET-E patients in response to ^{177}Lu-PSMA therapy. We retrospectively identified a VISION-PET-SF rate of 9.6% in a cohort of 301 patients who were nevertheless deemed VISION-PET-E and treated with PSMA MRT on the basis of local assessments. Eligibility for treatment was determined by the local clinical investigators at each institution. The VISION PET criteria were released in June 2021 and were not available at the time of initial treatment. There are 2 main explanations for why patients with SF criteria by VISION PET criteria were still treated with ^{177}Lu-PSMA. First, VISION-PET-SF patients with PSMA-negative lesions also had PSMA-positive lesions. The local investigators may have considered that these PSMA-positive lesions were sufficiently suggestive of a treatment response. Second, in VISION-PET-SF patients with low PSMA expression, the local investigators may have considered the PSMA expression PET signal uptake as not sufficiently low to exclude patients from treatment, as there was no consistently predefined threshold to characterize PSMA positivity.

Our cohort did not include patients who were excluded upfront from PSMA MRT by the local clinical investigators. The local SF rate was estimated at around 10%–15% by contributing sites. Thus, SF numbers in our cohort are underestimated and can range from 20% to 25% in unselected populations. Including these patients in the analysis would further enhance the observed outcome differences.

Absent or low target expression limits the response to PSMA-targeted therapies (*5,6*). However, the key driving parameter of patient outcome seems to be the presence of PSMA-negative lesions that

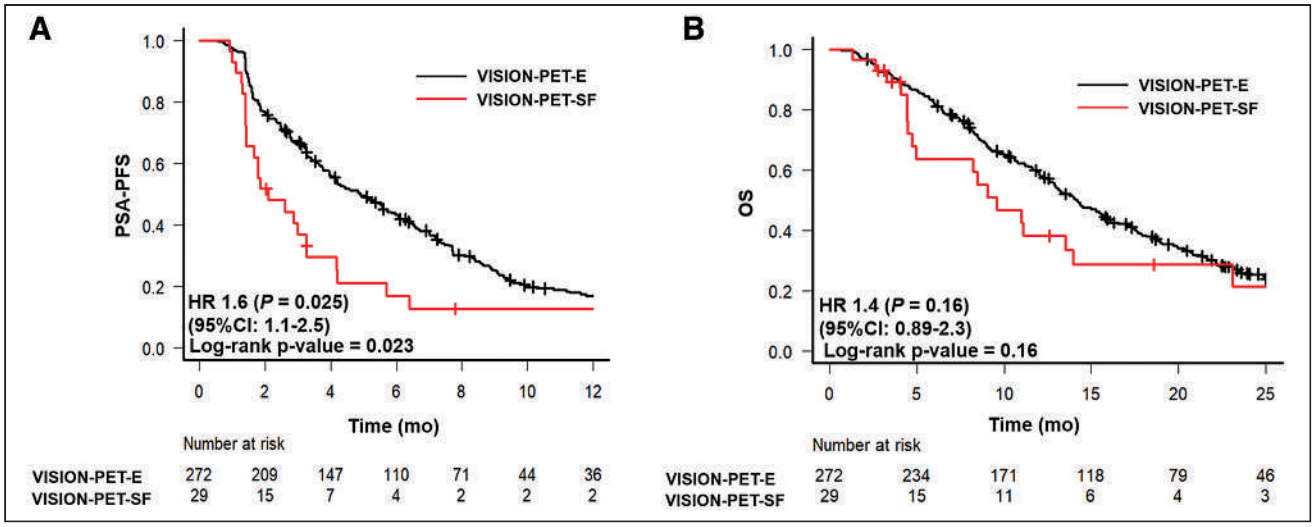

FIGURE 3. Kaplan–Meier curves of PSA PFS (A) and OS (B) comparing VISION-PET-E and VISION-PET-SF patients. HR = hazard ratio.

respond poorly to PSMA-targeted MRT and drive the prognostic of the patient (*7,8*). These lesions can be better identified with ^{18}F-FDG PET than with conventional imaging, as illustrated by the higher PSA response rates and PSA PFS observed in the Australian trials that used ^{18}F-FDG PET in addition to PSMA PET for patient selection (*9*).

Our results highlight the importance of using baseline PSMA PET/CT to identify patients unlikely to respond to PSMA-targeted therapies and stratify them toward other treatment options. However, the best management of patient with PSMA-negative lesions or with low–PSMA-expressing disease is unknown. Combination with stereotactic body radiation therapy to the largest or most glycolytic (i.e., aggressive) or non–PSMA-expressing lesions together with PSMA-targeted MRT may be one effective synergistic therapeutic approach. Use of this approach alternatively or in combination with other non–PSMA-targeted systemic therapies may be required.

Refinements in patient selection for PSMA MRT are needed to optimize patient outcomes. More comprehensive phenotyping via PET imaging may provide the road map to such refinements. Not characterizing target expression before PSMA-targeted treatment appears now nonethical, as a predictive whole-body imaging biomarker for response to PSMA-targeted therapies is available.

CONCLUSION

Patients with low or no PSMA-expressing lesions as assessed by PSMA PET/CT have a poor response profile to ^{177}Lu-PSMA therapy. Refinements in patient selection for ^{177}Lu-PSMA are needed to optimize patient outcomes.

DISCLOSURE

Jeremie Calais reports prior consulting activities outside the submitted work for Advanced Accelerator Applications, Blue Earth Diagnostics, Curium Pharma, GE Healthcare, Janssen, IBA RadioPharma, POINT Biopharma, Progenics, Radiomedix, and Telix Pharmaceuticals. Johannes Czernin is a founder and holds equity in Sofie Biosciences and Trethera Therapeutics. Intellectual property is class 99–patented by the University of California and licensed to Sofie Biosciences and Trethera Therapeutics. Johannes Czernin was a consultant for Endocyte Inc. (VISION trial steering

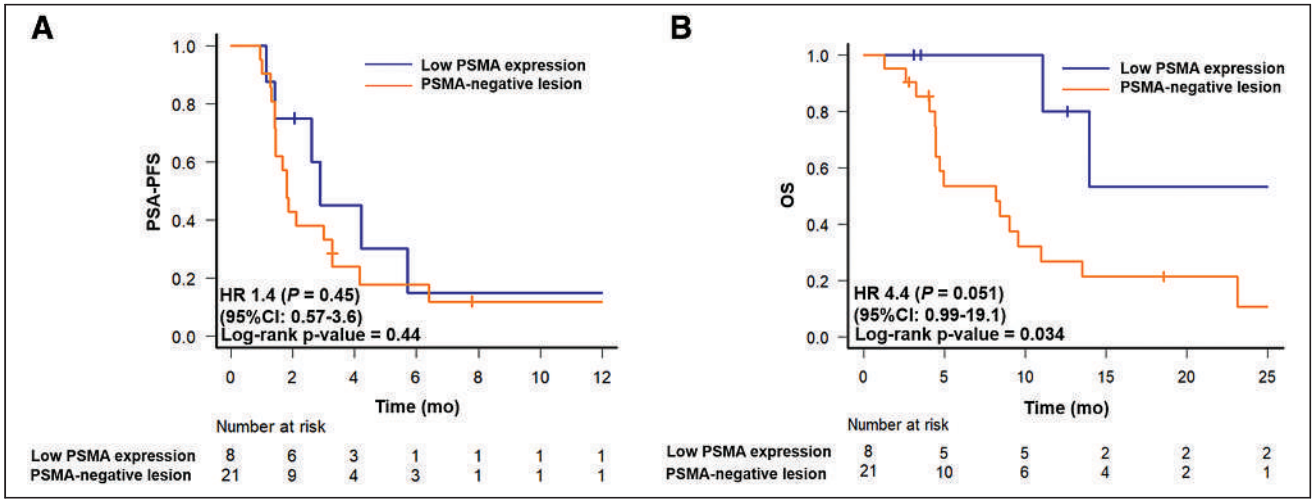

FIGURE 4. Kaplan–Meier curves of PSA PFS (A) and OS (B) comparing patients with low PSMA expression and PSMA-negative lesion. HR = hazard ratio.

committee), Actinium Pharmaceuticals, and Point Biopharma outside the submitted work. No other potential conflict of interest relevant to this article was reported.

ACKNOWLEDGMENTS

(We acknowledge the following individuals for their assistance with the creation of the multicenter study dataset, none of whom were compensated for their contributions and all of whom agreed to have us include their names here: Matthias Eiber (Technical University Munich), Michael Hofman (Peter MacCallum Cancer Center Melbourne), Ken Herrmann and Wolfgang Fendler (University Hospital Essen), Clemens Kratochwil and Uwe Haberkorn (University Hospital Heidelberg), and Ebrahim Delpassand (Excel Diagnostic Center Houston).

KEY POINTS

QUESTION: What is the outcome of patients who would have been VISION-PET-SF and who were still treated with ^{177}Lu-PSMA therapy?

PERTINENT FINDINGS: The patients who were VISION-PET-SF showed worse outcomes after ^{177}Lu-PSMA therapy than those who were VISION-PET-E.

IMPLICATIONS FOR PATIENT CARE: Pretherapy PSMA PET/CT is a biomarker of target expression that helps to predict patient response to ^{177}Lu-PSMA therapy. Refinements in patient selection for ^{177}Lu-PSMA are needed to optimize patient outcomes.

REFERENCES

1. Sartor O, de Bono J, Chi KN, et al. Lutetium-177-PSMA-617 for metastatic castration-resistant prostate cancer. *N Engl J Med.* 2021;385:1091–1103.
2. VISION: implementation of lutetium-177-PSMA-617 in metastatic castration-resistant prostate cancer approaches reality. ASCO Daily News website. https://dailynews.ascopubs.org/do/10.1200/ADN.21.200630/full. Published June 9, 2021. Accessed July 5, 2022.
3. Morris MJ, Bono JSD, Chi KN, et al. Phase III study of lutetium-177-PSMA-617 in patients with metastatic castration-resistant prostate cancer (VISION) [abstract]. *J Clin Oncol.* 2021;39(suppl):LBA4.
4. Gafita A, Calais J, Grogan TR, et al. Nomograms to predict outcomes after ^{177}Lu-PSMA therapy in men with metastatic castration-resistant prostate cancer: an international, multicentre, retrospective study. *Lancet Oncol.* 2021;22:1115–1125.
5. Current K, Meyer C, Magyar CE, et al. Investigating PSMA-targeted radioligand therapy efficacy as a function of cellular PSMA levels and intratumoral PSMA heterogeneity. *Clin Cancer Res.* 2020;26:2946–2955.
6. Vlachostergios PJ, Niaz MJ, Skafida M, et al. Imaging expression of prostate-specific membrane antigen and response to PSMA-targeted β-emitting radionuclide therapies in metastatic castration-resistant prostate cancer. *Prostate.* 2021;81:279–285.
7. Sandach P, Kersting D, Weber M, et al. PSMA- and FDG-PET mismatch assessment for optimized selection of PSMA radioligand therapy candidates [abstract]. *Nuklearmedizin.* 2021;60:48.
8. Michalski K, Ruf J, Goetz C, et al. Prognostic implications of dual tracer PET/CT: PSMA ligand and [^{18}F]FDG PET/CT in patients undergoing [^{177}Lu]PSMA radioligand therapy. *Eur J Nucl Med Mol Imaging.* 2021;48:2024–2030.
9. Hofman MS, Emmett L, Sandhu S, et al. [^{177}Lu]Lu-PSMA-617 versus cabazitaxel in patients with metastatic castration-resistant prostate cancer (TheraP): a randomised, open-label, phase 2 trial. *Lancet.* 2021;397:797–804.

Synthesis and Preclinical Evaluation of ^{177}Lu-Labeled Radiohybrid PSMA Ligands for Endoradiotherapy of Prostate Cancer

Alexander Wurzer*[1], Jan-Philip Kunert*[1], Sebastian Fischer[1], Veronika Felber[1], Roswitha Beck[1], Francesco de Rose[2], Calogero D'Alessandria[2], Wolfgang Weber[2], and Hans-Jürgen Wester[1]

[1]*Chair of Pharmaceutical Radiochemistry, Technical University of Munich, Garching, Germany; and* [2]*Department of Nuclear Medicine, Klinikum Rechts der Isar, Technical University of Munich, Munich, Germany*

The prostate-specific membrane antigen (PSMA)–targeted radiohybrid (rh) ligand [^{177}Lu]Lu-rhPSMA-7.3 has recently been assessed in a pretherapeutic dosimetry study on prostate cancer patients. In comparison to [^{177}Lu]Lu-PSMA I&T, application of [^{177}Lu]Lu-rhPSMA-7.3 resulted in a significantly improved tumor dose but also higher kidney accumulation. Although rhPSMA-7.3 has been initially selected as the lead compound for diagnostic application based on the characterization of its gallium complex, a systematic comparison of the most promising ^{177}Lu-labeled rhPSMA ligands is still missing. Thus, this study aimed to identify the rhPSMA ligand with the most favorable pharmacokinetics for ^{177}Lu-radioligand therapy. **Methods:** The 4 isomers of [^{177}Lu]Lu-rhPSMA-7 (namely [^{177}Lu]Lu-rhPSMA-7.1, -7.2, -7.3, and -7.4), along with the novel radiohybrid ligands [^{177}Lu]Lu-rhPSMA-10.1 and -10.2, were compared with the state-of-the-art compounds [^{177}Lu]Lu-PSMA I&T and [^{177}Lu]Lu-PSMA-617. The comparative evaluation comprised affinity studies (half-maximal inhibitory concentration) and internalization experiments on LNCaP cells, as well as lipophilicity measurements. In addition, we determined the apparent molecular weight (AMW) of each tracer as a parameter for human serum albumin (HSA) binding. Biodistribution studies and small-animal SPECT imaging were performed on LNCaP-tumor bearing mice at 24 h after injection. **Results:** ^{177}Lu labeling of the radiohybrids was performed according to the established procedures for the currently established PSMA-targeted ligands. All ligands showed potent binding to PSMA-expressing LNCaP cells, with affinities in the low nanomolar range and high internalization rates. Surprisingly, the most pronounced differences regarded the HSA-related AMW. Although [^{177}Lu]Lu-rhPSMA-7 isomers demonstrated the highest AMW and thus strongest HSA interactions, [^{177}Lu]Lu-rhPSMA-10.1 showed an AMW lower than for [^{177}Lu]Lu-rhPSMA-7.3 but higher than for the ^{177}Lu-labeled references PSMA I&T and PSMA-617. In biodistribution studies, [^{177}Lu]Lu-rhPSMA-10.1 exhibited the lowest kidney uptake and fastest excretion from the blood pool of all rhPSMA ligands while preserving a high tumor accumulation. **Conclusion:** Clinical investigation of [^{177}Lu]Lu-rhPSMA-10.1 is highly warranted to determine whether the favorable pharmacokinetics observed in mice will also result in high tumor uptake and decreased absorbed dose to kidneys and other nontarget tissues in patients.

Key Words: radiohybrid; rhPSMA; PSMA; radioligand therapy; prostate cancer

J Nucl Med 2022; 63:1489–1495
DOI: 10.2967/jnumed.121.263371

Radioligand therapy (RLT) of metastatic castration-resistant prostate cancer with ligands targeting prostate-specific membrane antigen (PSMA) holds great promise for patients who have exhausted conventional treatment regimens. Currently, ^{177}Lu-labeled PSMA-617 (*1*) and PSMA I&T (*2*) are the most extensively evaluated agents in this class and have demonstrated favorable safety and good treatment response rates (*3,4*). Although regulatory approval is still awaited for both agents, their application in compassionate-use programs has recently been reaffirmed by the European Association of Nuclear Medicine procedure guidelines for ^{177}Lu-PSMA therapy (*5*). [^{177}Lu]Lu-PSMA-617 has been evaluated by Novartis in a phase 3 clinical trial (NCT 03511664) on patients with metastatic castration-resistant prostate cancer. In that trial, [^{177}Lu]Lu-PSMA-617 was compared with the best standard of care. The investigators recently announced that both primary endpoints—overall and radiographic progression-free survival—were met (*6*). In addition, an ongoing phase 3 trial investigating [^{177}Lu]Lu-PSMA I&T (NCT 04647526) is evaluating its efficacy versus abiraterone or enzalutamide in delaying radiographic progression in patients with metastatic castration-resistant prostate cancer after second-line hormonal treatment. Retrospective clinical comparison of ^{177}Lu-labeled PSMA-617 and PSMA I&T point toward nearly identical pharmacokinetics for both tracers, and clinical efficacy is assumed to be similar, with no clear advantage to either compound (*7*).

Recently, the novel class of radiohybrid (rh) PSMA-targeted ligands was introduced by our group (*8*). These compounds combine a silicon-fluoride acceptor for ^{19}F/^{18}F-isotopic exchange radiolabeling and a chelator for complexation of a metal or radiometal (e.g., ^{177}Lu, ^{68}Ga, or ^{225}Ac). Respective ligand pairs of ^{18}F/nonradioactive metal and ^{19}F/radiometal, such as [^{18}F]Lu-rhPSMA and [^{177}Lu]Lu-rhPSMA, are chemically identical and thus display identical pharmacokinetics, offering unique possibilities for theranostic applications (Fig. 1).

For prostate cancer diagnosis, the first clinical evaluations were conducted with the ^{18}F-labeled ^{nat}Ga chelate of rhPSMA-7, which demonstrated a favorable biodistribution and indicated a high diagnostic performance for N-staging and localization of biochemical recurrence in patients with prostate cancer (*9–11*). Since rhPSMA-7

Received Oct. 12, 2021; revision accepted Jan. 18, 2022.
For correspondence or reprints, contact Alexander Wurzer (alexander.wurzer@tum.de).
*Contributed equally to this work.
Published online Jan. 27, 2022.

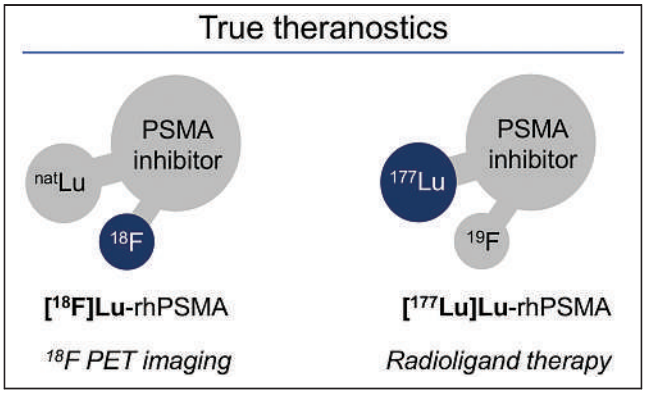

FIGURE 1. Theranostic radiohybrid concept applied to PSMA-targeted ligands. Molecules offer 2 labeling sites for radionuclides, silicon-fluorine acceptor site for ^{18}F labeling via isotopic exchange and chelator for radiometallation. ^{18}F-labeled cold lutetium–complexed ligand ([^{18}F]Lu-rhPSMA) is chemically identical to ^{177}Lu-labeled cold fluorine compound ([^{177}Lu]Lu-rhPSMA), therefore representing true theranostic agents for PET imaging and RLT.

was found to comprise 4 diastereoisomers (rhPSMA-7.1, -7.2, -7.3, and -7.4), a preclinical selection process was initiated that identified [^{18}F]Ga-rhPSMA-7.3 (often abbreviated as ^{18}F-rhPSMA-7.3) as the novel diagnostic lead compound (*12*) for current phase 3 clinical trials (NCT04186819 and NCT04186845).

For initial evaluation of the radiohybrid technology for therapeutic applications, rhPSMA-7.3 was labeled with ^{177}Lu and compared with [^{177}Lu]Lu-PSMA I&T in biodistribution and dosimetry studies on mice. Both ligands showed similar uptake in healthy organs, resulting in a similar dose to all major organs, including bone marrow and kidney (*13*). Compared with [^{177}Lu]Lu-PSMA I&T, [^{177}Lu]Lu-rhPSMA-7.3 exhibited a 2.8- and 4.7-fold higher tumor uptake at 1 and 168 h after injection, respectively, resulting in a significantly higher dose at the tumor and a superior treatment response (*13*).

In a pretherapeutic comparative dosimetry study of ^{177}Lu-labeled rhPSMA-7.3 and PSMA I&T on a small patient cohort ($n = 6$, intraindividual comparison), an approximately 2.4-fold higher mean absorbed dose for tumor lesions of the radiohybrid ligand was found, consistent with the preclinical observations (*14*). However, contradictory to animal studies, the mean absorbed dose to different healthy organs was also higher—for example, 2.3-fold higher doses to kidneys and 2.2-fold higher doses to bone marrow for [^{177}Lu]Lu-rhPSMA-7.3 versus [^{177}Lu]Lu-PSMA I&T. The authors concluded that the radiohybrid tracer holds promise for therapeutic effects similar to those obtained with [^{177}Lu]Lu-PSMA I&T while offering potential economic advantages by an approximately 2-fold reduction in the injected radioactive doses (*14*).

The selection of rhPSMA-7.3 as lead compound for diagnostic application was based on the evaluation of gallium chelates [^{18}F]Ga-rhPSMA-7.1, -7.2, -7.3, and -7.4 (*12*). Since it is known from the literature that the complex structure of the metal chelate (e.g., [Ga]DOTAGA and [Lu]DOTAGA) within a radioligand can influence its pharmacokinetic properties (*15,16*), all ^{177}Lu-labeled isomers of rhPSMA-7 have been included in this comparison. The isomers differ in the stereoconfiguration of the diaminopropionic acid branching unit (D-Dap or L-Dap) and the glutamic acid arm at the DOTAGA chelator (*R*- or *S*-DOTAGA: rhPSMA-7.1 [D-Dap–*R*-DOTAGA], rhPSMA-7.2 [L-Dap–*R*-DOTAGA], rhPSMA-7.3 [D-Dap–*S*-DOTAGA], rhPSMA-7.4 [L-Dap–*S*-DOTAGA]).

Given the promising initial data from ^{177}Lu-labeled rhPSMA-7.3, the aim of the present study was to evaluate whether other isomers of ^{177}Lu-labeled rhPSMA-7 or the closely related compounds [^{177}Lu]Lu-rhPSMA-10.1 (D-Dap) and -10.2 (L-Dap) (where DOTA replaces the DOTAGA chelator) might have further improved biodistribution kinetics in normal organs while maintaining the high tumor uptake found with [^{177}Lu]Lu-rhPSMA-7.3. We evaluated the ligands in comparison with reference ligands [^{177}Lu]Lu-PSMA-617 and [^{177}Lu]Lu-PSMA I&T (Fig. 2) in vitro (lipophilicity, half-maximal inhibitory concentration, internalization into LNCaP cells, binding to human serum albumin [HSA]) and in biodistribution studies on LNCaP tumor–bearing mice.

MATERIALS AND METHODS

A detailed description of the chemical synthesis of rhPSMA and the analytic instruments is provided in the supplemental materials (available at http://jnm.snmjournals.org).

Radiolabeling

Radiolabeling with no-carrier-added ^{177}Lu was performed according to the established procedures for PSMA-targeted ligands (*1,2*). Briefly, the precursor (1.0 nmol, 10 μL, 0.1 mM in dimethylsulfoxide) was added to 10 μL of 1.0 M aqueous NaOAc buffer (pH 5.5). Subsequently, 20–50 MBq of [^{177}Lu]$LuCl_3$ (specific activity > 3,000 GBq/mg at the time of radiolabeling, 740 MBq/mL, 0.04 M HCl; ITM) was added, and the mixture was filled up to 100 μL with 0.04 M HCl. The reaction mixture was heated for 20–30 min at 90°C, and the radiochemical purity was determined using radio-high-performance liquid chromatography and radio-thin-layer chromatography with 0.1 M sodium citrate buffer on instant thin-layer chromatography–silica gel chromatography paper (Agilent) and 1.0 M NH_4OAc/dimethylformamide buffer (1/1; *v*/*v*) on thin-layer chromatography silica gel 60 F_{254} plates (Merck Millipore).

Lipophilicity

Approximately 1 MBq of the ^{177}Lu-labeled PSMA ligand was dissolved in 1 mL of a 1:1 mixture (*v*/*v*) of phosphate-buffered saline (pH 7.4) and *n*-octanol ($n = 6$). After vigorous mixing of the suspension for 3 min, the vial was centrifuged at 15,000*g* for 3 min, and 100-μL aliquots of both layers were measured in a γ-counter. Finally, the ratio of the radioactivity detected in the *n*-octanol sample and the phosphate-buffered saline buffer was calculated and expressed as distribution ratio log $D_{7.4}$.

Binding to HSA

Binding of ^{177}Lu-labeled ligands to HSA was assessed by albumin-mediated size-exclusion chromatography (AMSEC), a novel method that has recently been developed by our group to determine the apparent molecular weight (AMW) of a compound in the presence of HSA. A dedicated and detailed description of the AMSEC method will be published elsewhere to cover the context and the development process of this method in its entirety. Briefly, a gel filtration size-exclusion column (Superdex 75 Increase 10/300 GL; fractionation range, 70–3 kDa; GE Healthcare) was calibrated as recommended by the manufacturer using a commercially available set of proteins (Gel Filtration LMW Calibration Kit; GE Healthcare). AMSEC experiments were performed by injection of the various radioligands using an HSA buffer at physiologic concentration (Biowest) as the mobile phase at room temperature. Depending on the strength of the HSA/ligand interaction during the chromatographic procedure, an injected radioligand (1.0 MBq, 10–20 GBq/μmol) can show a reduced retention time that correlates to AMWs higher than the actual, physical, molecular weight (the latter being for all investigated ligands < 2 kDa, and thus below the column fractionation range). The stronger this interaction, the longer the mean time the ligand is bound to HSA during the chromatographic process and the faster the ligand is

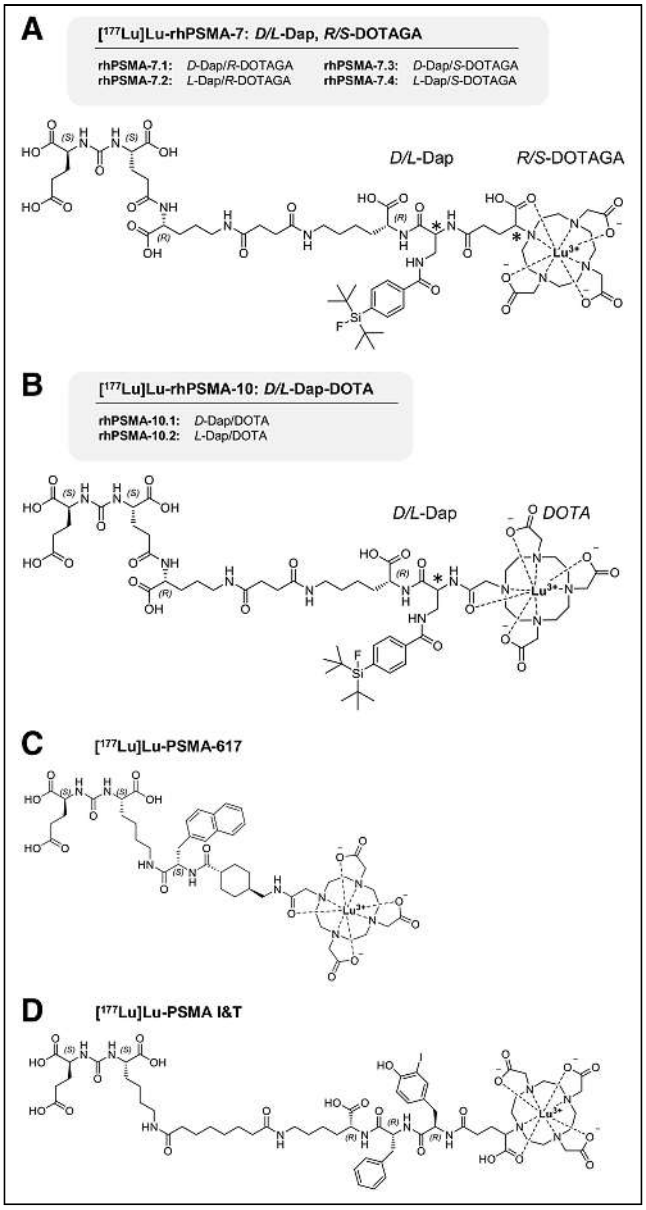

FIGURE 2. (A) rhPSMA-7 isomers differ in stereoconfiguration of diaminopropionic acid branching unit (D- or L-Dap) and glutamic acid arm at DOTAGA chelator (*R*- or *S*-DOTAGA). (B) rhPSMA-10.1 (D-Dap) and rhPSMA-10.2 (L-Dap), both equipped with DOTA chelator, also differ in stereoconfiguration of branching unit (D-or L-Dap). Well-established PSMA-addressing ligands PSMA-617 (C) and PSMA I&T (D) served as reference compounds (*1,2*).

eluted from the column. By means of calibration, the retention time can be translated into a ligand-specific AMW (expressed in kDa) as a parameter allowing quantification of the extent of HSA binding. The detection window ranges between 2.1 kDa (cutoff value, determined by [^{18}F]fluoride; no HSA interaction) and 70.2 kDa (experimental molecular weight of HSA; maximum HSA interaction). [^{177}Lu]Lu-rhPSMA-7.3 served as an internal standard during AMSEC studies (30.4 ± 0.5 kDa; n = 10).

Affinity Determinations (Half-Maximal Inhibitory Concentration) and Internalization Studies

Competitive binding studies were determined on LNCaP cells (1.5×10^5 cells in 0.25 mL/well) after incubation at 4°C for 1 h, using (((*S*)-1-carboxy-5-(4-([^{125}I]iodo)benzamido)pentyl)carbamoyl)-L-glutamic acid ([^{125}I]IBA)KuE; 0.2 nM/well) as the reference radioligand (n = 3). Internalization studies of the radiolabeled ligands (1.0 nM/well) were performed on LNCaP cells (1.25×10^5 cells in 0.25 mL/well) at 37°C for 1 h and accompanied by ([^{125}I]IBA)KuE (0.2 nM/well) as a reference. Data were corrected for nonspecific binding and normalized to the specific internalization observed for the reference (n = 3), as previously published (*8*).

In Vivo Experiments

All animal experiments were conducted in accordance with general animal welfare regulations in Germany (German animal protection act, as amended on May 18, 2018, article 141 G, version March 29, 2017, I 626, approval 55.2-1-54-2532-71-13) and the institutional guidelines for the care and use of animals. LNCaP tumor xenografts were established in 6- to 8-wk-old male CB-17 SCID mice as described previously (*8*).

Biodistribution Studies. The ^{177}Lu-labeled PSMA ligands (2–5 MBq; 0.1 nmol) were injected under isoflurane anesthesia into the tail vein of mice, which were euthanized 24 h after injection (n = 4–5). Selected organs were removed, weighed, and measured in a γ-counter. All rhPSMA ligands were evaluated during the same period (first quarter of 2020), whereas ^{177}Lu-labeled PSMA-617 and PSMA I&T (*17*) were assessed in 2016, using the identical cell line, mouse model, and experimental procedure.

Small-Animal SPECT/CT Imaging. Static images of ^{177}Lu-labeled ligands in euthanized mice were recorded 24 h after injection directly after blood collection, with an acquisition time of 45 min using a high-energy, general-purpose rat-and-mouse collimator and a stepwise multiplanar bed movement. For imaging studies, a VECTor4 small-animal SPECT/PET/optical imaging/CT device from MILabs was applied. Data were reconstructed using MILabs.Rec software (version 10.02) and PMOD software (version 4.0; PMOD Technologies LLC). After imaging, the mice underwent biodistribution studies.

RESULTS

Synthesis and Radiolabeling

Uncomplexed PSMA ligands were obtained via a solid-phase/solution-phase synthetic strategy with chemical purities of more than 97% as determined by high-performance liquid chromatography (absorbance at 220 nm). Identity was confirmed by mass spectrometry. Complexation with a 2.5-fold molar excess of $LuCl_3$ led to quantitative formation of the respective lutetium-PSMA ligands, which were used for in vitro studies. ^{177}Lu labeling of PSMA ligands according to standard manual procedures resulted in a radiochemical purity of more than 95%, determined by radio-high-performance liquid chromatography and radio-thin-layer chromatography (Supplemental Table 1).

In Vitro Characterization

Results of the in vitro evaluation of all rhPSMAs and the reference ligands PSMA-617 (*1*) and PSMA I&T (*2*) are summarized in Figure 3 and Supplemental Table 2. PSMA binding affinity (half-maximal inhibitory concentration; Fig. 3A) was high and in the low nanomolar range for all lutetium-rhPSMA ligands (range, 2.8 ± 0.5 to 3.6 ± 0.6 nM) and the 2 reference ligands ([^{177}Lu]Lu-PSMA I&T, 4.2 ± 0.8 nM; [^{177}Lu]Lu-PSMA-617, 3.3 ± 0.2 nM).

Slight differences between the ligands were found for the PSMA-mediated internalization into LNCaP cells (1 h, 37°C), which is expressed as a percentage of the specific internalization of the reference ligand ([^{125}I]IBA)KuE (Fig. 3B). Although [^{177}Lu]Lu-rhPSMA-7.1 and [^{177}Lu]Lu-PSMA I&T showed the lowest internalization rates, with values of 137% ± 6% and 145% ± 14%, respectively, the other rhPSMA compounds showed an approximately 1.4-fold higher

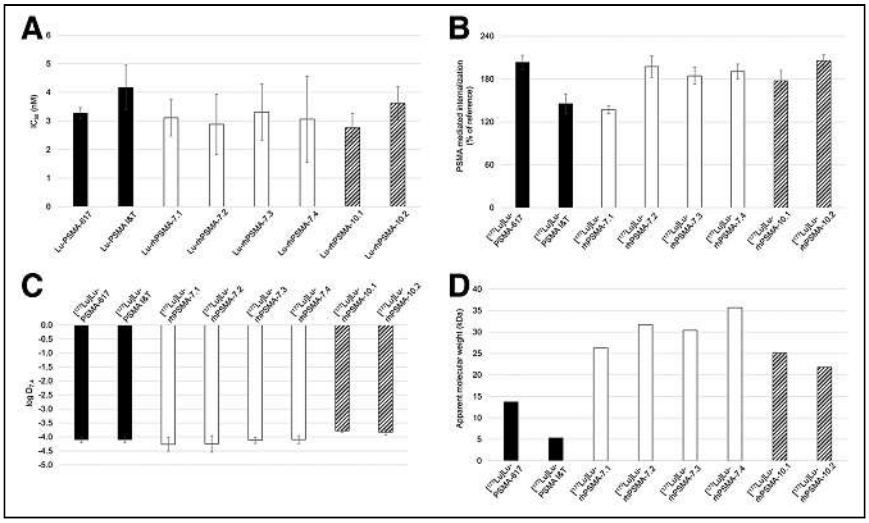

FIGURE 3. (A) Binding affinities (half-maximal inhibitory concentration [IC_{50}; nM], 1 h, 4°C) of [^{177}Lu]Lu-rhPSMA-7.1 to -7.4 (white; $n = 3$), [^{177}Lu]Lu-rhPSMA-10.1 and -10.2 (black/white stripes; $n = 3$), and references [^{177}Lu]Lu-PSMA-617 and [^{177}Lu]Lu-PSMA-I&T (black; $n = 3$). (B) PSMA-mediated internalization of [^{177}Lu]Lu-rhPSMA-7.1 to -7.4 (white; $n = 3$), [^{177}Lu]Lu-rhPSMA-10.1 and -10.2 (black/white stripes; $n = 3$), and references [^{177}Lu]Lu-PSMA-617 and [^{177}Lu]Lu-PSMA I&T (black; $n = 3$) by LNCaP cells (1 h, 37°C) as percentage of reference ligand ([^{125}I]IBA)KuE). (C) Lipophilicity of [^{177}Lu]Lu-rhPSMA-7.1 to -7.4 (white; $n = 6$), [^{177}Lu]Lu-rhPSMA-10.1 and -10.2 (black/white stripes; $n = 6$), and references [^{177}Lu]Lu-PSMA-617 and [^{177}Lu]Lu-PSMA I&T (black; $n = 6$), expressed as partition coefficient (log $D_{7.4}$ in *n*-octanol/phosphate-buffered saline, pH 7.4). (D) AMW of [^{177}Lu]Lu-rhPSMA-7.1 to -7.4 (white), [^{177}Lu]Lu-rhPSMA-10.1 and -10.2 (black/white stripes), and references [^{177}Lu]Lu-PSMA-617 and [^{177}Lu]Lu-PSMA I&T (black), as determined by HSA-mediated size-exclusion chromatography.

internalization (range, 177% ± 15% to 206% ± 8%), similar to that of [^{177}Lu]Lu-PSMA-617 (203% ± 10%).

The ^{177}Lu-labeled rhPSMA-7 isomers, as well as the references ([^{177}Lu]Lu-PSMA I&T and [^{177}Lu]Lu-PSMA-617), demonstrated a high and similar hydrophilicity, expressed as a partition coefficient (log $D_{7.4}$; *n*-octanol and phosphate-buffered saline, pH 7.4) with values between −4.1 ± 0.1 and −4.3 ± 0.3. The DOTA conjugates [^{177}Lu]Lu-rhPSMA-10.1 and -10.2 showed a slightly lower hydrophilicity, with a log $D_{7.4}$ of −3.8 (Fig. 3C).

The AMW of the tracers was determined to compare the relative HSA-binding strength of the ligands. Exemplary chromatograms of AMSEC experiments showing ligand-specific retention times are provided in Supplemental Figures 1–3. Interestingly, remarkable differences were found for the AMWs of the state-of-the-art references and even among the single isomers of ^{177}Lu-labeled rhPSMA-7 and rhPSMA-10 (Fig. 3D). Although [^{177}Lu]Lu-PSMA I&T showed the lowest HSA interaction (AMW, 5.3 kDa), followed by [^{177}Lu]Lu-PSMA-617 (AMW, 13.7 kDa), all radiohybrid ligands demonstrated an at least 1.5-fold higher AMW, with values between 21.8 and 35.7 kDa. Among the radiohybrids, the 2 DOTA conjugates, [^{177}Lu]Lu-rhPSMA-10.1 and -10.2, showed the lowest AMWs (25.1 and 21.8 kDa, respectively), whereas D-Dap–configured [^{177}Lu]Lu-rhPSMA-7.1 (molecular weight, 26.3 kDa) and [^{177}Lu]Lu-rhPSMA-7.3 (molecular weight, 30.4 kDa) showed the lowest AMWs within the rhPSMA-7 series (AMWs of L-Dap–comprising isomers: [^{177}Lu]Lu-rhPSMA-7.2, 31.7 kDa; [^{177}Lu]Lu-rhPSMA-7.4, 35.7 kDa).

In Vivo Characterization

Biodistribution Studies. Overall, the comparative biodistribution study of the ^{177}Lu-labeled PSMA ligands in LNCaP tumor–bearing mice at 24 h after injection revealed a quite similar distribution pattern with high tumor uptake, fast excretion from background organs, but a varying degree of activity retention in the kidneys (Fig. 4; Supplemental Tables 3 and 4).

At 24 h after injection, the highest activity retention in the kidneys was found for [^{177}Lu]Lu-PSMA I&T (34.7 ± 17.2 percentage injected dose [%ID]/g), whereas [^{177}Lu]Lu-PSMA-617 (1.4 ± 0.4 %ID/g) and [^{177}Lu]Lu-rhPSMA-10.1 (2.0 ± 0.8 %ID/g) demonstrated the fastest renal clearance. Kidney uptake of the former lead compound, [^{177}Lu]Lu-rhPSMA-7.3, was found to be 9.8 ± 2.7 %ID/g, thus showing slower renal clearance than [^{177}Lu]Lu-rhPSMA-7.1 (4.1 ± 0.8 %ID/g), [^{177}Lu]Lu-rhPSMA-10.1 (2.0 ± 0.8 %ID/g), and [^{177}Lu]Lu-rhPSMA-10.2 (8.1 ± 1.7 %ID/g). These differences are also well illustrated in the small-animal SPECT/CT images (Fig. 5). Tumor uptake was highest for all [^{177}Lu]Lu-rhPSMA-7 isomers and in the range of 11.6–12.7 %ID/g, followed by [^{177}Lu]Lu-rhPSMA-10.2 (10.5 ± 3.3 %ID/g) and -10.1 (9.8 ± 0.3 %ID/g), whereas the references, ^{177}Lu-labeled PSMA-617 (7.5 ± 0.9 %ID/g) and PSMA I&T (4.1 ± 1.1 %ID/g), exhibited a lower tumor uptake.

Tumor-to-Organ Ratios. Interestingly, all radiohybrid ligands are cleared from the blood pool and background tissues with a kinetic profile that resembles that of small molecules more than that of larger proteins, despite their extensive binding to HSA. Among all radiohybrids, the highest tumor-to-blood and tumor-to-kidney ratios were found for [^{177}Lu]Lu-rhPSMA-10.1 (tumor-to-blood, 11,498; tumor-to-kidney, 5.7), followed by [^{177}Lu]Lu-rhPSMA-7.1 (tumor-to-blood, 5,971; tumor-to-kidney, 3.2), whereas [^{177}Lu]Lu-rhPSMA-7.3 showed inferior values (tumor-to-blood, 3,843; tumor-to-kidney, 1.2). Although [^{177}Lu]Lu-PSMA I&T (tumor-to-blood, 408; tumor-to-kidney, 0.2) exhibited rather slow excretion in mice, [^{177}Lu]Lu-PSMA-617 showed the highest tumor-to-kidney ratio (tumor-to-blood, 1,424; tumor-to-kidney, 5.9), whereas its tumor-to-blood ratio was lower than all radiohybrid ligands (Supplemental Tables 5 and 6).

DISCUSSION

Although it has recently been demonstrated in patients that the uptake of [^{177}Lu]Lu-rhPSMA-7.3 in tumor lesions was on average 2- to 3-fold higher than that of [^{177}Lu]Lu-PSMA I&T, the slower clearance resulted in a comparatively higher dose to the kidney as the organ at risk (*14*). In retrospect, this result is hardly surprising, since the selection process of the best diagnostic rhPSMA-7 isomer was based on criteria that are considered suboptimal for therapy: fast blood clearance to reach high tumor-to-background ratios at early time points, predominantly renal clearance, and high kidney retention to ensure low activity in the bladder at early time points. In contrast, the selection criteria for the best therapeutic isomer are different. Compared with today's therapeutic ligands, a slightly delayed blood clearance is preferred. The ligand should be excreted renally while showing almost no retention in the kidneys.

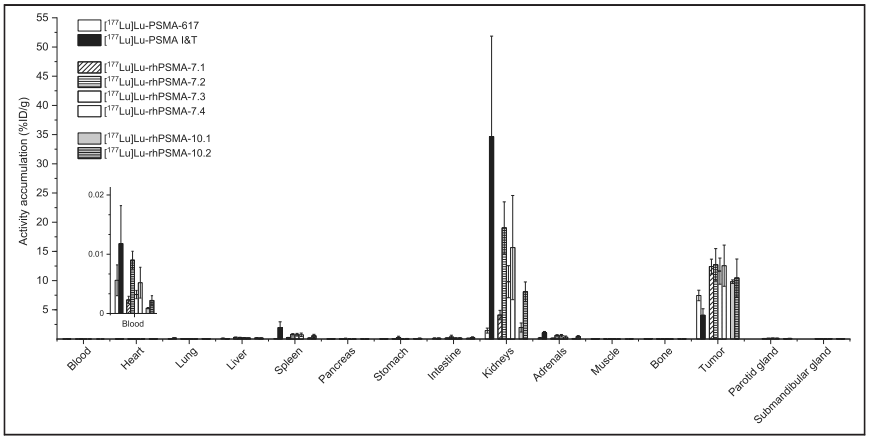

FIGURE 4. Biodistribution of [^{177}Lu]Lu-rhPSMA-7.1 to -7.4, [^{177}Lu]Lu-rhPSMA-10.1 and -10.2, and references [^{177}Lu]Lu-PSMA-617 and [^{177}Lu]Lu-PSMA I&T at 24 h after injection in male LNCaP tumor–bearing SCID mice. Data are expressed as %ID/g, mean ± SD (n = 4 − 5). Values of [^{177}Lu]Lu-PSMA I&T were taken from previously published study by our group (*17*) that was performed under identical conditions.

It must also be considered that the change in the isotope (lutetium for RLT instead of gallium for the diagnostic compound) results in a different structure and charge at the chelate–metal complex (gallium-DOTA: hexadentate, zwitterionic; lutetium-DOTA: octadentate, uncharged) (*15*). This matter obviously influences the pharmacokinetic properties of the entire ligand, as demonstrated by the prolonged clearance kinetics of the ^{177}Lu-labeled "best diagnostic isomer" rhPSMA-7.3 in patients (*14*).

With the aim of addressing these therapeutic criteria and of identifying a ^{177}Lu-labeled rhPSMA tracer with more favorable characteristics for RLT, we performed a coevaluation of 6 different rhPSMA ligands (4 rhPSMA-7 isomers and 2 rhPSMA-10 isomers) and compared the results with preclinical data on the 2 reference compounds, PSMA-617 and PSMA I&T.

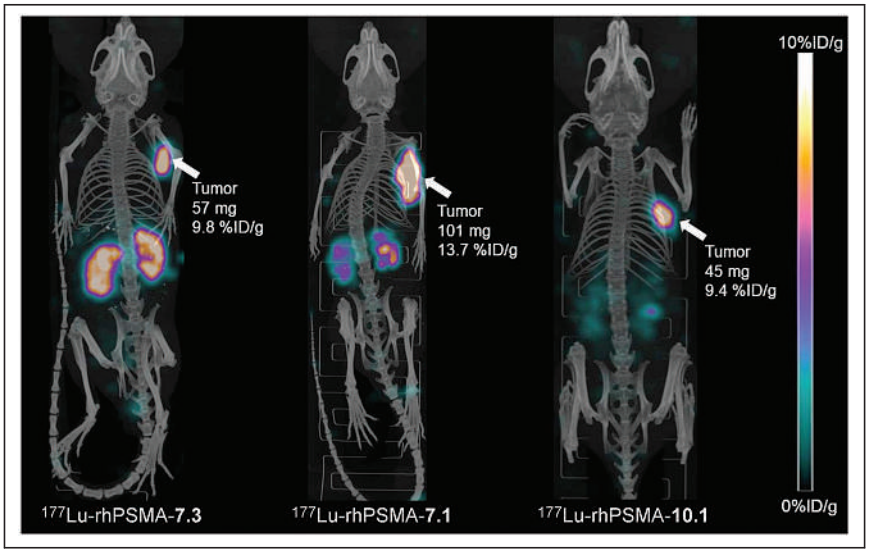

FIGURE 5. Static small-animal SPECT/CT images (maximum-intensity projections) of ^{177}Lu-labeled rhPSMA-7.3, -7.1, and -10.1 in LNCaP tumor–bearing mice, euthanized 24 h after injection and imaged directly after blood collection, with acquisition time of 45 min on VECTor4 small-animal SPECT/PET/optimal imaging/CT device. Tumor weight and tracer uptake in tumor (%ID/g) were determined from subsequent biodistribution studies.

All lutetium-complexed radiohybrid tracers and the external references, PSMA I&T and PSMA-617, demonstrated potent binding to LNCaP cells with an excellent affinity in the low-nanomolar range and high internalization rates, which did not allow prioritization of certain candidates for further evaluation.

In the context of PSMA-targeted RLT, the kidney and then the bone marrow are still considered the main organs at risk, and uptake in these should be carefully considered (*18*).

In our comparative biodistribution studies, pronounced differences in kidney uptake values were observed. Whereas our internal reference, D-Dap-*S*-DOTAGA–configured [^{177}Lu]Lu-rhPSMA-7.3, showed a kidney uptake of 9.8 ± 2.7 %ID/g at 24 h after injection, the uptake of the D-Dap-DOTA derivative, [^{177}Lu]Lu-rhPSMA-10.1, reached only 20% of that value (2.0 ± 0.8 %ID/g). Moreover, the stereoconfiguration of the Dap-branching unit (D-Dap or L-Dap) also resulted in a pronounced different kidney uptake, as shown for [^{177}Lu]Lu-rhPSMA-7.1 (D-Dap, 4.1 ± 0.8 %ID/g) and the 5-fold higher value of the corresponding L-Dap version, [^{177}Lu]Lu-rhPSMA-7.2 (19.0 ± 4.5 %ID/g). As already demonstrated in a previous study of [^{18}F]Ga-rhPSMA ligands (*12*), these results impressively demonstrate once more that even small modifications in the arene binding region of PSMA-targeted ligands can have a remarkable influence on the biodistribution. In this former study, the modification of the stereoconfiguration of the Dap branching unit and the DOTAGA chelator resulted in superior pharmacokinetics of [^{18}F]Ga-rhPSMA-7.3 in mice compared with the diastereomeric mixture [^{18}F]Ga-rhPSMA-7. This result was confirmed in patient studies, revealing a 5-fold lower excretion of [^{18}F]Ga-rhPSMA-7.3 into the bladder, a 1.6-fold lower kidney uptake, and a 1.6-fold higher tumor uptake than for the diastereomeric mixture [^{18}F]Ga-rhPSMA-7 (*19*).

Even though the results of our preclinical comparison are highly promising, there are many examples in the literature that question the direct transferability of the preclinical results to clinical studies, particularly with regard to kidney clearance and kidney retention. The low kidney uptake of [^{177}Lu]Lu-PSMA-617 (1.4 ± 0.4 %ID/g at 24 h after injection) in mice has often been highlighted as a major selection criterion that promoted its rapid clinical development and thus was considered a major advantage compared with [^{177}Lu]Lu-PSMA I&T (kidney uptake, 34.7 ± 17.2 %ID/g at 24 h after injection) (*20*). However, in contrast to preclinical results, head-to-head comparison of both ligands in patients has impressively demonstrated a nearly identical kidney uptake and clearance kinetic of both tracers (*7*). Moreover, a similar absorbed dose to the kidney was found in dosimetry studies: 0.4 ± 0.2 to 0.8 ± 0.3 Gy/GBq for [^{177}Lu]Lu-PSMA-617 (*21–23*) and

0.7 ± 0.2 Gy/GBq for [^{177}Lu]Lu-PSMA I&T (*24*). Until further investigations improve our understanding of species-dependent renal handling of PSMA tracers, and in the absence of alternative and more valid selection criteria, the evaluation of the biodistribution in mice, including the assessment of the different excretion behavior, will remain our only viable option—although we should treat such data with appropriate caution.

Regarding important nontarget organs such as liver, muscle, and heart, all ligands demonstrated almost identical and complete clearance 24 h after injection. Even though only low activity levels were found in the blood pool for all ligands, [^{177}Lu]Lu-rhPSMA-10.1 showed the best clearance of all investigated PSMA ligands, and this superior clearance is also expressed by the highest tumor-to-blood ratio (11,498): 3 times higher than for [^{177}Lu]Lu-rhPSMA-7.3 and 8 times higher than for [^{177}Lu]Lu-PSMA-617.

The tendency of both DOTA-conjugated [^{177}Lu]Lu-rhPSMA-10 isomers to clear more quickly can at least in part be explained by the HSA-binding experiments and our newly introduced in vitro parameter, AMW. The molecular weight of a molecule is known to have a direct implication in the glomerular sieving coefficient (GSC) (as a rule of thumb, the lower the molecular weight, the higher the GSC and the faster the excretion kinetics) (*25*). Thus, the stronger the interaction of a molecule with HSA or the higher the ratio of HSA-bound ligand to free ligand, the less ligand is subjected to glomerular filtration and thus the less ligand is excreted. In our assay, this ratio is indirectly determined by calculating the AMW of each compound (details on these methods will be described elsewhere).

Looking at the AMW of ^{177}Lu-labeled PSMA-617 (13.7 kDa) and PSMA-I&T (5.3 kDa) as key reference points, the 2.3-fold lower AMW of PSMA I&T appears prima facie unproportional: Kulkarni et al. could demonstrate that [^{177}Lu]Lu-PSMA-617 exhibits only a marginally slower clearance in patients than does [^{177}Lu]Lu-PSMA I&T (*7*). However, taking into account the nonlinear correlation of the molecular weight and GSC and the tiny changes in the GSC at low molecular weights, the differences in the AMW of PSMA I&T and PSMA-617 result in only slightly different GSCs, which explains the similar kidney excretion kinetics of these 2 ligands in patients (*25*). In contrast, the higher AMW of [^{177}Lu]Lu-rhPSMA-7.3 (molecular weight, 30.4) would translate into a markedly lower GSC and thus a delayed clearance, which has been confirmed by clinical results from Feuerecker et al. (*14*). On the basis of these results, we expect that the blood clearance kinetics of [^{177}Lu]Lu-rhPSMA-10.1 and -10.2 in humans will be somewhere between that of [^{177}Lu]Lu-rhPSMA-7.3 and [^{177}Lu]Lu-PSMA-617/PSMA-I&T. As demonstrated by Feuerecker et al. (*14*), the remarkable tumor uptake of [^{177}Lu]Lu-rhPSMA-7.3 found in our preclinical experiments (*13*) could also be observed in patients (effective dose of 6.4 ± 6.7 mGy/MBq for [^{177}Lu]Lu-rhPSMA-7.3 vs. 2.6 ± 2.4 mGy/MBq for [^{177}Lu]Lu-PSMA I&T). Thus, we are optimistic that we will be able to obtain a similarly improved tumor uptake in patients during the clinical assessment of [^{177}Lu]Lu-rhPSMA-10.1 and thus tumor doses higher than those currently obtained with the state-of-the art nonhybrid ligands (*14*).

Certainly there are also other effects determining different clearance kinetics of radiopharmaceuticals in mice and patients that must be considered—for example, species differences in drug binding to serum albumin (*26*) and differences in magnitude and binding affinities of the tracers to plasma proteins other than HSA, such as α-1-acid glycoprotein (*27*), transthyretin (*28*), or lipoproteins (*29*). Moreover, individual differences in uptake of PSMA ligands into the kidneys (*30*), varying relative proportions of hepatobiliary to renal clearance, and effects of species differences between mice and humans must be considered. In summary, however, we are optimistic that the promising biodistribution profile of [^{177}Lu]Lu-rhPSMA-10.1 observed in mice, together with its low AMW, will translate into improved tumor doses and tumor-to-kidney dose ratios of this isomer in patients.

CONCLUSION

On the basis of this preclinical comparison, [^{177}Lu]Lu-rhPSMA-10.1 seems to be a promising lead for the clinical development of an rhPSMA-targeted ligand for RLT. [^{177}Lu]Lu-rhPSMA-10.1 could have the potential to outperform the in vivo characteristics of the currently developed state-of-the-art PSMA targeted radioligands [^{177}Lu]Lu-PSMA-617 and [^{177}Lu]Lu-PSMA-I&T in men. Clinical studies are required to demonstrate whether our newly introduced additional preclinical selection criterion, the AMW, could be a valuable parameter for the future development of further therapeutic radiopharmaceuticals with optimally adjusted clearance kinetics.

DISCLOSURE

Hans-Jürgen Wester, Alexander Wurzer, Jan-Philip Kunert, Sebastian Fischer, and Veronika Felber are listed as inventors in patent applications for some types of therapeutic rhPSMA. Hans-Jürgen Wester receives funding from the SFB 824 (Deutsche Forschungsgemeinschaft, Bonn, Germany, Sonderforschungsbereich 824, project B11 and Z). Hans-Jürgen Wester is a founder and shareholder of, and a scientific advisor for, Scintomics GmbH, Fuerstenfeldbruck, Germany. Wolfgang Weber is a consultant for Blue Earth Diagnostics Ltd. No other potential conflict of interest relevant to this article was reported.

ACKNOWLEDGMENT

We thank Catriona Turnbull for carefully proofreading the manuscript.

KEY POINTS

QUESTION: Which ^{177}Lu-labeled rhPSMA ligand shows the best characteristics for RLT of prostate cancer?

PERTINENT FINDINGS: In preclinical experiments, [^{177}Lu]Lu-rhPSMA-10.1 demonstrated fast clearance kinetics from healthy tissues while preserving high tumor uptake.

IMPLICATIONS FOR PATIENT CARE: Preclinical data indicate more favorable pharmacokinetics for [^{177}Lu]Lu-rhPSMA-10.1 than for [^{177}Lu]Lu-PSMA-617 and [^{177}Lu]Lu-PSMA-I&T for RLT, a finding that has to be investigated in prospective clinical studies.

REFERENCES

1. Benešová M, Schafer M, Bauder-Wust U, et al. Preclinical evaluation of a tailor-made DOTA-conjugated PSMA inhibitor with optimized linker moiety for imaging and endoradiotherapy of prostate cancer. *J Nucl Med.* 2015;56:914–920.
2. Weineisen M, Schottelius M, Simecek J, et al. ^{68}Ga- and ^{177}Lu-labeled PSMA I&T: optimization of a PSMA-targeted theranostic concept and first proof-of-concept human studies. *J Nucl Med.* 2015;56:1169–1176.
3. Heck MM, Tauber R, Schwaiger S, et al. Treatment outcome, toxicity, and predictive factors for radioligand therapy with ^{177}Lu-PSMA-I&T in metastatic castration-resistant prostate cancer. *Eur Urol.* 2019;75:920–926.

4. Hofman MS, Violet J, Hicks RJ, et al. [^{177}Lu]-PSMA-617 radionuclide treatment in patients with metastatic castration-resistant prostate cancer (LuPSMA trial): a single-centre, single-arm, phase 2 study. *Lancet Oncol.* 2018;19:825–833.
5. Kratochwil C, Fendler WP, Eiber M, et al. EANM procedure guidelines for radionuclide therapy with ^{177}Lu-labelled PSMA-ligands (^{177}Lu-PSMA-RLT). *Eur J Nucl Med Mol Imaging.* 2019;46:2536–2544.
6. Morris MJ, Bono JSD, Chi KN, et al. Phase III study of lutetium-177-PSMA-617 in patients with metastatic castration-resistant prostate cancer (VISION) [abstract]. *J Clin Oncol.* 2021;39(suppl):LBA4.
7. Kulkarni HR, Singh A, Schuchardt C, et al. PSMA-based radioligand therapy for metastatic castration-resistant prostate cancer: the Bad Berka experience since 2013. *J Nucl Med.* 2016;57(suppl 3):97S–104S.
8. Wurzer A, Di Carlo D, Schmidt A, et al. Radiohybrid ligands: a novel tracer concept exemplified by ^{18}F- or ^{68}Ga-labeled rhPSMA inhibitors. *J Nucl Med.* 2020;61:735–742.
9. Kroenke M, Wurzer A, Schwamborn K, et al. Histologically confirmed diagnostic efficacy of ^{18}F-rhPSMA-7 PET for N-staging of patients with primary high-risk prostate cancer. *J Nucl Med.* 2020;61:710–715.
10. Eiber M, Kroenke M, Wurzer A, et al. ^{18}F-rhPSMA-7 PET for the detection of biochemical recurrence of prostate cancer after radical prostatectomy. *J Nucl Med.* 2020;61:696–701.
11. Oh SW, Wurzer A, Teoh EJ, et al. Quantitative and qualitative analyses of biodistribution and PET image quality of a novel radiohybrid PSMA, ^{18}F-rhPSMA-7, in patients with prostate cancer. *J Nucl Med.* 2020;61:702–709.
12. Wurzer A, Parzinger M, Konrad M, et al. Preclinical comparison of four [^{18}F, ^{nat}Ga]rhPSMA-7 isomers: influence of the stereoconfiguration on pharmacokinetics. *EJNMMI Res.* 2020;10:149.
13. Yusufi N, Wurzer A, Herz M, et al. Comparative preclinical biodistribution, dosimetry, and endoradiotherapy in metastatic castration-resistant prostate cancer using ^{19}F/^{166}Lu-rhPSMA-7.3 and ^{177}Lu-PSMA I&T. *J Nucl Med.* 2021;62:1106–1111.
14. Feuerecker B, Chantadisai M, Allmann A, et al. Pretherapeutic comparative dosimetry of ^{177}Lu-rhPSMA-7.3 and ^{177}Lu-PSMA I&T in patients with metastatic castration-resistant prostate cancer. *J Nucl Med.* 2022;63:833–839.
15. Wadas TJ, Wong EH, Weisman GR, Anderson CJ. Coordinating radiometals of copper, gallium, indium, yttrium, and zirconium for PET and SPECT imaging of disease. *Chem Rev.* 2010;110:2858–2902.
16. Umbricht CA, Benešová M, Schmid RM, et al. ^{44}Sc-PSMA-617 for radiotheragnostics in tandem with ^{177}Lu-PSMA-617: preclinical investigations in comparison with ^{68}Ga-PSMA-11 and ^{68}Ga-PSMA-617. *EJNMMI Res.* 2017;7:9.
17. Wirtz M, Schmidt A, Schottelius M, et al. Synthesis and in vitro and in vivo evaluation of urea-based PSMA inhibitors with increased lipophilicity. *EJNMMI Res.* 2018;8:84.
18. Yordanova A, Becker A, Eppard E, et al. The impact of repeated cycles of radioligand therapy using [^{177}Lu]Lu-PSMA-617 on renal function in patients with hormone refractory metastatic prostate cancer. *Eur J Nucl Med Mol Imaging.* 2017;44:1473–1479.
19. Oh SW, Wurzer A, Yusufi N, et al. Preclinical dosimetry and human biodistribution of ^{18}F-rhPSMA-7 and ^{18}F-rhPSMA-7.3 [abstract]. *J Nucl Med.* 2019;60(suppl 1):1635.
20. Wester HJ, Schottelius M. PSMA-targeted radiopharmaceuticals for imaging and therapy. *Semin Nucl Med.* 2019;49:302–312.
21. Delker A, Fendler WP, Kratochwil C, et al. Dosimetry for ^{177}Lu-DKFZ-PSMA-617: a new radiopharmaceutical for the treatment of metastatic prostate cancer. *Eur J Nucl Med Mol Imaging.* 2016;43:42–51.
22. Kabasakal L, Toklu T, Yeyin N, et al. Lu-177-PSMA-617 prostate-specific membrane antigen inhibitor therapy in patients with castration-resistant prostate cancer: stability, bio-distribution and dosimetry. *Mol Imaging Radionucl Ther.* 2017;26:62–68.
23. Violet J, Jackson P, Ferdinandus J, et al. Dosimetry of ^{177}Lu-PSMA-617 in metastatic castration-resistant prostate cancer: correlations between pretherapeutic imaging and whole-body tumor dosimetry with treatment outcomes. *J Nucl Med.* 2019;60:517–523.
24. Okamoto S, Thieme A, Allmann J, et al. Radiation dosimetry for ^{177}Lu-PSMA I&T in metastatic castration-resistant prostate cancer: absorbed dose in normal organs and tumor lesions. *J Nucl Med.* 2017;58:445–450.
25. Norden AG, Lapsley M, Lee PJ, et al. Glomerular protein sieving and implications for renal failure in Fanconi syndrome. *Kidney Int.* 2001;60:1885–1892.
26. Colclough N, Ruston L, Wood JM, MacFaul PA. Species differences in drug plasma protein binding. *MedChemComm.* 2014;5:963–967.
27. Smith SA, Waters NJ. Pharmacokinetic and pharmacodynamic considerations for drugs binding to alpha-1-acid glycoprotein. *Pharm Res.* 2018;36:30.
28. Buxbaum JN, Reixach N. Transthyretin: the servant of many masters. *Cell Mol Life Sci.* 2009;66:3095–3101.
29. Wasan KM, Brocks DR, Lee SD, Sachs-Barrable K, Thornton SJ. Impact of lipoproteins on the biological activity and disposition of hydrophobic drugs: implications for drug discovery. *Nat Rev Drug Discov.* 2008;7:84–99.
30. Begum NJ, Thieme A, Eberhardt N, et al. The effect of total tumor volume on the biologically effective dose to tumor and kidneys for ^{177}Lu-labeled PSMA peptides. *J Nucl Med.* 2018;59:929–933.

mCRPC Patients Receiving ^{225}Ac-PSMA-617 Therapy in the Post–Androgen Deprivation Therapy Setting: Response to Treatment and Survival Analysis

Mike Sathekge[1,2], Frank Bruchertseifer[3], Mariza Vorster[1], Ismaheel O. Lawal[1,2], Otto Knoesen[4], Johncy Mahapane[1], Cindy Davis[1], Amanda Mdlophane[2], Alex Maes[1,5], Kgomotso Mokoala[1], Kgomotso Mathabe[6], Christophe Van de Wiele*[1,7], and Alfred Morgenstern*[1,3]

[1]*Department of Nuclear Medicine; University of Pretoria and Steve Biko Academic Hospital, Pretoria, South Africa;* [2]*Nuclear Medicine Research Infrastructure, Pretoria, South Africa;* [3]*European Commission, Joint Research Centre, Karlsruhe, Germany;* [4]*Nuclear Technology Products, Pelindaba, South Africa;* [5]*Katholieke University Leuven, Kortrijk, Belgium;* [6]*Department of Urology; University of Pretoria and Steve Biko Academic Hospital, Pretoria, South Africa; and* [7]*Ghent University, Ghent, Belgium*

^{225}Ac-PSMA-617, targeting the prostate-specific membrane antigen (PSMA), which is overexpressed on prostate cancer cells, has shown a remarkable therapeutic efficacy in heavily pretreated patients with metastatic castration-resistant prostate carcinoma (mCRPC). Here, we report on treatment outcome and survival using this novel treatment modality in a series of 53 patients with mCRPC directly after their androgen deprivation treatment (ADT). **Methods:** ^{225}Ac-PSMA-617 was administered to 53 such patients. ^{68}Ga-PSMA PET/CT was obtained at baseline, before every treatment cycle, and on follow-up to select patients for treatment, determine the activity to be administered, and assess their response. Serial prostate-specific antigen (PSA) measurements were obtained for response assessment. **Results:** The median age of the patients was 63.4 y (range, 45–83 y). In total, 167 cycles were administered (median, 3; range, 1–7). Forty-eight patients (91%) had a PSA decline of at least 50%, and 51 patients (96%) had any decline in PSA. ^{68}Ga-PSMA PET findings became negative in 30 patients. In the multivariate analysis, a PSA decline of at least 50% proved predictive of both progression-free survival (PFS) and overall survival (OS), and platelet count also proved predictive for PFS. The median estimated OS was 9 mo for patients with a PSA decline of less than 50% but was not yet reached at the latest follow-up (55 mo) for patients with a PSA decline of 50% or more. The estimated median PFS was 22 mo for patients with a PSA decline of at least 50% and 4 mo for patients with a PSA decline of less than 50%. No severe hematotoxicity was noted, and only 3 patients had grade III–IV nephrotoxicity. The commonest toxicity seen was grade I–II xerostomia, observed in 81% of patients. **Conclusion:** In 91% of 53 patients with mCRPC, treatment with ^{225}Ac-PSMA-617 immediately after ADT resulted in at least a 50% decrease in PSA level. Furthermore, a PSA decline of at least 50% proved the single most important factor predicting PFS and OS after ^{225}Ac-PSMA-617 treatment. Of interest, median OS in patients with a PSA decline of at least 50% was not yet reached at the latest follow-up (55 mo). These favorable results suggest that it would be of major clinical relevance to perform a prospective randomized study comparing ^{225}Ac-PSMA-617 with current standard-of-care treatment options such as enzalutamide, abiraterone acetate, and docetaxel after ADT.

Key Words: ^{225}Ac-PSMA; ADT; therapy response; PSA response; prostate carcinoma

J Nucl Med 2022; 63:1496–1502
DOI: 10.2967/jnumed.121.263618

Prostate cancer is the second most frequent malignancy (after lung cancer) in men worldwide, accounting for approximately 4% of all deaths caused by cancer in men (*1,2*). Although the 5-y survival rate of localized prostate carcinoma is nearly 100%, the 5-y survival rate for patients with metastatic castration-resistant prostate carcinoma (mCRPC) is only about 30% (*3*). Standard-of-care treatment for mCRPC is androgen deprivation therapy (ADT), which normalizes serum levels of prostate-specific antigen (PSA) and produces an objective tumor response in over 90% of patients. However, despite an initial favorable response to ADT, most patients with mCRPC eventually experience disease progression within an average of 18–36 mo after treatment initiation (*4,5*). Once ADT-resistant or castration-resistant, mCRPC patients are treated with other options such as abiraterone acetate, enzalutamide, chemotherapy, ^{223}Ra-dichloride, or sipuleucel-T, the choice of which depends substantially on patient preference, current symptoms, burden of disease, and local availability (*5*).

Treatment of prostate carcinoma patients in low- to middle-income countries is challenging. Because of the lack of regular PSA screening, most prostate carcinoma patients in low- to middle-income countries present with metastatic disease at initial diagnosis (*6*). In addition, because of fear of associated side effects, some patients often refuse both ADT and chemotherapy. Furthermore, abiraterone and enzalutamide are not easily accessible to most patients.

^{225}Ac-PSMA-617, targeting the prostate-specific membrane antigen (PSMA), which is overexpressed on prostate cancer cells, has shown remarkable therapeutic efficacy in heavily pretreated mCRPC patients (*7–11*). When ^{225}Ac-PSMA-617 therapy is applied in dose-deescalation fashion, the most prevalent treatment-related toxicity is grade 1–2 xerostomia, making the therapy an acceptable

Received Nov. 30, 2021; revision accepted Jan. 20, 2022.
For correspondence or reprints, contact Mike Sathekge (mike.sathekge@up.ac.za).
*Contributed equally to this work.
Published online Feb. 17, 2022.

alternative for mCRPC patients in low- to middle-income countries who refuse chemotherapy because of fear of associated side effects or to whom novel treatment options such as enzalutamide or abiraterone are not readily available.

We previously reported on the favorable outcome and toxicity results from ^{225}Ac-PSMA-617 therapy in a small group (17 patients) with mCRPC (*12*). In this study, we report treatment outcome and survival in a larger series (53 patients) directly after ADT.

MATERIALS AND METHODS

This was a retrospective review of patients with histologically confirmed mCRPC treated with ^{225}Ac-PSMA-617 radioligand therapy. In patients who presented with early-stage disease, primary therapy was by radical prostatectomy, external-beam radiotherapy to the prostate gland, or brachytherapy. In patients who presented with metastatic disease, initial therapy was by ADT using surgical or medical castration. Eligibility for ^{225}Ac-PSMA-617 radioligand therapy was based on PSA progression: a minimum of 2 rising PSA values from a baseline measurement, with the measurements separated from one another by at least 1 wk. Inclusion criteria included mCRPC precluding treatment with localized therapy such as radiotherapy, patient refusal of chemotherapy, and lack of access to second-generation antiandrogen therapy such as abiraterone and enzalutamide (i.e., patients without medical insurance). Exclusion criteria included urinary tract obstruction and bone marrow suppression (Common Terminology Criteria for Adverse Events grade 3 or more). The decision to treat patients with ^{225}Ac-PSMA-617 was made in a multidisciplinary setting in our hospital for patients who eventually experienced disease progression despite an initial favorable response to ADT within an average of 18 mo after treatment initiation. At the time of treatment, all patients were aware that ^{225}Ac-PSMA-617 had not yet received regulatory approval for use in the routine care of patients with mCRPC. They understood that the treatment was applied on a compassionate basis for patients who refused available life-prolonging treatment options or had no access to these novel therapies. All patients therefore provided written informed consent to undergo treatment with ^{225}Ac-PSMA-617 with a full awareness of its possible complications, including xerostomia, bone marrow suppression, renal impairment, and potential currently unknown side effects. The institutional review board (Research Ethics Committee of the Faculty of Health Sciences, University of Pretoria, reference number 173/2021) approved this retrospective study, and the requirement to obtain informed consent was waived.

Patient Preparation

The patients first underwent ^{68}Ga-PSMA-11 PET/CT imaging and were deemed suitable candidates for therapy with ^{225}Ac-PSMA-617 if uptake by the tumor lesions was higher than physiologic uptake in the normal liver parenchyma. A full blood count, liver function tests, and measurements of electrolytes, urea, and creatinine were performed before treatment commencement and were repeated 2 wk before subsequent treatment cycles to determine patient fitness for them. ^{68}Ga-PSMA-11 PET/CT was repeated after each subsequent treatment cycle to determine the burden of residual tumor to guide dose deescalation.

Preparation and Administration of ^{225}Ac-PSMA-617

PSMA-617 was radiolabeled with ^{225}Ac as described previously (*8,12*). The initial administered activity of ^{225}Ac-PSMA-617 was 8 MBq for all patients. For subsequent treatment cycles, the administered activity was deescalated to 7, 6, or 4 MBq on the basis of the response to earlier treatments as assessed on repeat ^{68}Ga-PSMA-11 PET/CT as previously described (*12*). Treatments were repeated every 8 wk, provided that a continued response was demonstrated, no limiting toxicity developed, and residual tumor demonstrating ^{68}Ga-PSMA-11 avidity was shown on PET/CT imaging.

Safety

All patients were observed for a minimum of 4 h after ^{225}Ac-PSMA-617 administration to detect any immediate side effects. Within 2 wk before the first cycle of treatment, a baseline assessment was performed of hemoglobin level, leukocyte count, platelet count, glomerular filtration rate, and liver function. Except when the clinical situation warranted more frequent follow-up, these blood tests were repeated 2 wk before subsequent cycles of treatment (i.e., every 8 wk). After completion of all treatment cycles, these blood tests were repeated every 12 wk until disease progression or death. Patients who developed toxicity were followed up until resolution or death. In addition to undergoing the blood tests, patients reported any observed side effects during treatment or on follow-up. When the patients came for each cycle of treatment or follow-up, they were asked about side effects known to occur with PSMA-based radioligand therapy. Toxicity was defined according to the Common Terminology Criteria for Adverse Events, version 5.0.

Treatment Response Evaluation

Treatment response was evaluated using serial measurements of serum PSA values and ^{68}Ga-PSMA-11 PET/CT imaging. ^{68}Ga-PSMA-11 PET/CT was repeated every 8 wk (before each treatment cycle) and subsequently every 12 wk after treatment completion until disease progression or death. PSA response was defined as a PSA decline of at least 50% of the baseline value, according to the Prostate Cancer Working Group 3 criteria. Follow-up ^{68}Ga-PSMA-11 PET/CT was used to evaluate the status of initially identified metastatic lesions fulfilling the inclusion criteria on the baseline PET/CT scan. We used PSMA PET/CT criteria to categorize patients as responders or nonresponders. Favorable responders were categorized as showing stable disease, a partial response, or a complete response on PSMA PET/CT imaging; nonresponders were patients with progressive disease on PSMA PET/CT (*13*). The PSMA response was defined as complete if all lesions with tracer uptake disappeared; as partial if uptake lessened and tumor volume decreased by more than 30% on PET; as stable if there was a change in uptake and no more than a 30% change in tumor volume on PET, without evidence of new lesions; and as progressive if at least 2 new lesions appeared, uptake increased, or tumor volume increased by at least 30% on PET (*13–15*).

Statistical Analysis

Statistical analysis was performed using SPSS, version 28.0 (IBM). The Kolmogorov–Smirnov test was used to check whether data were normally distributed. Quantitative variables were compared using a paired Student *t* test and ANOVA when normally distributed or using a Mann–Whitney test and Kruskal–Wallis test when not normally distributed.

For univariate and regression analysis, we dichotomized values according to the median values in cases of continuous variables. We also dichotomized the following clinical covariates: Gleason score; number of treatment cycles; the presence of bone, visceral, and lymph node metastases; PSA response ($\leq$50% reduction or $>$50% reduction); undetectable PSA levels; and normalization of the ^{68}Ga-PSMA-11 PET findings. Progression-free survival (PFS) and overall survival (OS) were estimated by the Kaplan–Meier method and log rank testing to examine the predictive value of dichotomized variables and other clinical risk factors for disease control and OS. Multivariate analysis was performed using Cox regression and included, in sequential order of statistical significance, variables that were found to be significant in the univariate analysis followed by the interactive terms.

Finally, the χ^2 test was used to determine differences in proportion when appropriate.

TABLE 1
Patient Characteristics

Characteristic	Value
No. of patients included	53
Median age (y)	63.4
Eastern Cooperative Oncology Group score of 0 or 1 (*n*)	42
Eastern Cooperative Oncology Group score of 2 (*n*)	11
Median PSA level (ng/mL)	466
Median alkaline phosphatase level (IU/L)	188
Median hemoglobin value (g/dL)	11.5
Bone metastases (*n*)	47
Lymph node metastases (*n*)	36
Visceral metastases (*n*)	6
Lung	1
Liver	5
Brain	1
Local therapy to prostate (*n*)	
Prostatectomy	31
Radiotherapy	11
No local therapy	11

RESULTS

Patient Characteristics

Patient characteristics are shown in Table 1. Fifty-three mCRPC patients were included. Their median age was 63.4 y (range, 45–83 y). Twenty-three had an Eastern Cooperative Oncology Group score of 0, 19 had a score of 1, and 11 had a score of 2. Six patients had isolated lymph node involvement (stage IVA disease); the remaining patients all had bone metastases (stage IVB disease), and 6 of these patients also had visceral metastases (1 patient with both brain and liver metastases, 4 patients with liver metastases, and 1 patient with lung metastases). The median PSA level before treatment was 466 ng/mL (range, 102–4,405 ng/mL). The mean hemoglobin level was 11.5 g/dL (range, 6.1–16 g/dL), the median platelet count was 293,000/μL (range, 48,000–762,000/μL), the mean white blood cell count was 7,090/μL (range, 3,100–14,870/μL), and the median alkaline phosphatase level was 188 IU/L (range, 82–1796 IU/L).

In total, 167 cycles were administered (median, 3; range, 1–7). Seven patients received 1 cycle; 15 patients, 2 cycles; 11 patients, 3 cycles; 11 patients, 4 cycles; 2 patients, 5 cycles; 6 patients, 6 cycles; and 1 patient, 7 cycles. Eight patients continued with hormonal treatment despite progressive disease under these agents; their urologist or oncologist did not want to stop these medications because clinical benefit was still assumed.

Safety

Administration of ^{225}Ac-PSMA-617 was well tolerated. The commonest toxicity seen was grade I–II dry mouth, observed in 81% of patients. No patient with grade III dry mouth was seen, and no patient discontinued treatment because of this side effect. No patient with grade IV bone marrow toxicity was seen. Anemia was the most common manifestation of hematotoxicity, seen in 15% of patients (7 patients with grade I–II anemia and 1 patient with grade III). Any grade of renal failure was seen in 19% of patients (7 with grade I–II, 2 with grade III, and 1 with grade IV). Details on toxicity in the treated patients are in Table 2.

TABLE 2
Toxicity Profiles of 53 Patients Treated with ^{225}Ac-PSMA-617

Characteristic	Grade I–II	Grade III	Grade IV
Xerostomia	43 (81%)	0	0
Anemia	7 (13%)	1 (2%)	0
Leukopenia	4 (7%)	1 (2%)	0
Thrombocytopenia	5 (9%)	0	0
Renal failure	7 (13%)	2 (4%)	1 (2%)

Response to ^{225}Ac-PSMA-617 Therapy

After ^{225}Ac-PSMA-617 treatment, 48 patients (91%) had a PSA decline of at least 50%, and 51 patients (96%) had any decline in PSA (Fig. 1). PSA became undetectable in 19 patients (36%). ^{68}Ga-PSMA PET images became negative in 30 patients (57%); that is, avidity was similar to background blood-pool activity in all prostate cancer lesions after treatment with ^{225}Ac-PSMA-617.

OS

At the time of data analysis, 15 patients (28%) had died, and all deaths seemed directly related to their underlying mCRPC. In the univariate analysis, only a PSA decline of at least 50% proved significantly associated with a favorable OS ($P < 0.001$) (Table 3). When included in the multivariate analysis with age and Gleason score as covariates, the level of statistical significance was retained ($P < 0.001$). The median estimated OS was 9 mo for patients with a PSA decline of less than 50% but was not yet reached at the latest follow-up (55 mo) for patients with a PSA decline of 50% or more (Fig. 2). The OS of patients with stage III disease (lymph node involvement only, 6 patients) did not significantly differ from that of patients with stage IV disease (the remaining 47 patients) ($P = 0.186$).

PFS

During follow-up, 27 patients (51%) showed disease progression. In univariate analysis, the following parameters proved significantly related to PFS: a PSA decline of at least 50% ($P < 0.0001$), undetectable PSA ($P = 0.014$), platelet count ($P = 0.041$), ^{68}Ga-PSMA-11

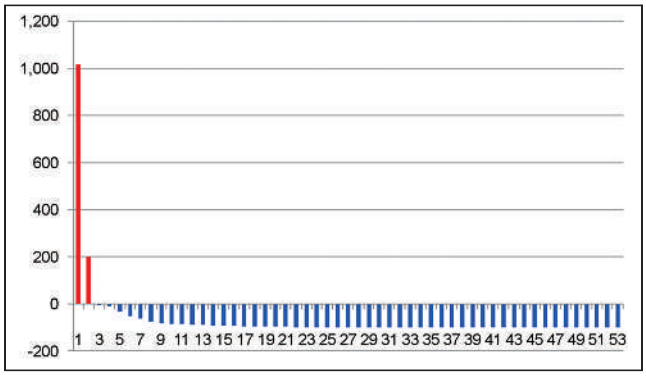

FIGURE 1. Waterfall plot demonstrating percentage change in PSA levels after treatment with ^{225}Ac-PSMA-617 in patient cohort (*x*-axis = number of patients; *y*-axis = percentage change).

TABLE 3
Univariate Analysis of Relationship Between Studied Variables and Survival

Variable	PFS	OS
Age	0.180	0.748
Eastern Cooperative Oncology Group score	0.077	0.772
Gleason score	0.596	0.774
Previous local radiotherapy	0.304	0.916
Baseline PSA level	0.972	0.888
PSA ≥ 50% decline	<0.001*	<0.001*
PSA undetectable	0.014*	0.132
Visceral metastases	0.937	0.772
Lymph node involvement	0.289	0.942
Bone metastases	0.459	0.186
No. of treatment cycles	0.650	0.097
ALP	0.727	0.886
Hemoglobin	0.090	0.132
Platelet count	0.041*	0.602
White blood cell count	0.373	0.605
Radiologic response	0.006*	0.407
PSMA-negative	0.026*	0.418

*$P < 0.05$.

PET/CT–based response ($P = 0.006$), and negative findings on ^{68}Ga-PSMA PET ($P = 0.026$), (Table 3; Fig. 2). When included in the multivariate analysis, only a PSA decline of at least 50% ($P = 0.002$) and platelet count ($P = 0.047$) retained statistical significance. The estimated median PFS for patients with a PSA decline of at least 50% was 22 mo, whereas that for patients with a PSA decline of less than 50% was 4 mo. The number of patients who relapsed but had negative PSMA PET findings after treatment (7 of 23) did not significantly differ from the number who relapsed but did not have negative PSMA PET findings after treatment (19/30) ($P = 0.027$).

DISCUSSION

Various early preclinical and clinical studies have provided a rationale for combining ADT with radiotherapy for the management of localized prostate cancer (*16*). For instance, in nude mice bearing Shionogi adenocarcinoma allografts, Zietman et al. demonstrated that ADT reduced the dose of radiotherapy necessary to control 50% of the tumor and that the timing of ADT is important for achieving this effect; orchidectomy was significantly more effective if performed 12 d before radiotherapy than if performed during or after radiotherapy (*17,18*). In Dunning prostate cancer–bearing rats, temporary ADT for 14 d before radiotherapy resulted in a significant lengthening of tumor growth (*19*). Furthermore, ADT was shown to downregulate vascular expression of growth factor, causing apoptosis of endothelial cells and normalization of tumor vascularization, thereby increasing oxygenation (*20*). Also, in a series of 237 prostate carcinoma patients, Milosevic et al. identified a broad heterogeneity in prostate cancer oxygenation, a prerequisite for radiotherapy efficacy, with the median partial pressure of O_2 ranging from 0 to 75 mm Hg (*20*). On the basis of these studies, various randomized phase III trials have been conducted that showed a significant clinical benefit from adding ADT to radiotherapy when treating intermediate-risk primary prostate carcinoma (*21*). As opposed to the beneficial radiotherapy-enhancing effects of short-term ADT administered in combination with radiotherapy for primary intermediate prostate carcinoma, long-term ADT administration in the metastatic setting resulting in androgen independence is often characterized by a remarkable resistance to treatment options that trigger apoptosis via the caspase cascade, including radiotherapy. Various factors responsible for radiation resistance in androgen-independent prostate carcinoma have been implicated, including increased levels of interleukin-6, neuroendocrine differentiation, Ack-1 androgen receptor phosphorylation, the existence of intrinsic cancer stem cells, and epithelial–mesenchymal transition, among others (*22–25*).

In the series presented, 91% of mCRPC patients had at least a 50% reduction in their initial PSA value after ^{225}Ac-PSMA-617 treatment, and neither baseline PSA nor alkaline phosphatase level significantly differed between responders and nonresponders. This percentage of patients exceeds by far those found in early clinical studies demonstrating at least a 50% PSA reduction: approximately 10% of patients treated with ipilimumab, sunitinib, cabozantinib, or ^{223}Ra-dichloride (Xofigo; Bayer) and approximately 30%, 40%, and 50% of patients treated with abiraterone, cabazitaxel, or enzalutamide (*26*). Our findings suggest that radiation resistance to α-emitting agents after ADT is not a significant issue, as is the case with, for instance, β-emitting agents in some patients. In this regard, reported response rates of mCRPC patients to ^{177}Lu-PSMA-617 have varied from 10.6% to 69% (*27*). Although these response rates were obtained in heterogeneous patient cohorts receiving

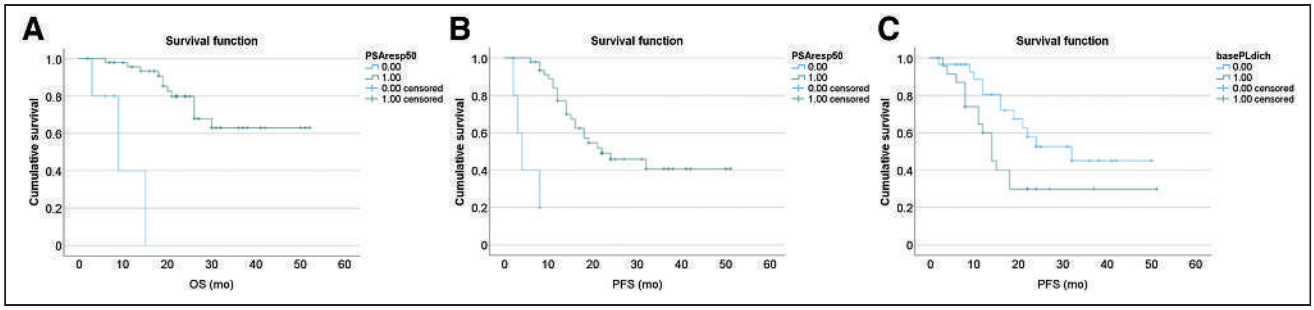

FIGURE 2. Kaplan–Meier curves of PSA-based OS of the entire cohort (PSA decline of ≥ 50% [green curve] and percentage of PSA decline < 50% [blue curve]) (A), PFS of the entire cohort (PSA decline of ≥ 50% [green curve] and percentage of PSA decline < 50% [blue curve]) (B), and PFS stratified by platelet counts (platelet counts < 293,000/mL [blue curve] and platelet counts > 293,000 [green curve]) (C).

various other treatments after ADT, lower response rates to ^{177}Lu-PSMA-617 as opposed to ^{225}Ac-PSMA-617 may be anticipated given the low linear-energy-transfer value of 0.7 keV/μm for ^{177}Lu when compared with 100 keV/μm for ^{225}Ac (*28*). The high linear-energy-transfer value of ^{225}Ac results in a high level of radiobiologic effectiveness when compared with β-radiation, requiring fewer particle tracks to induce cell death via induction of predominant DNA-strand breaks, among others, obviating cellular oxygen to induce its therapeutic effect (*27,29*). Although Xofigo is also an α-therapy targeting bone lesions only, it will most likely have less success than ^{225}Ac-PSMA-617, which targets both soft-tissue and bone lesions. This likelihood is also supported by recent information that both nodal and visceral metastases have been underestimated and understudied in patients with advanced prostate cancer and the fact that patients with visceral metastases invariably have a poorer prognosis than patients with bone-only metastases (*30*).

In our series, hemoglobin levels, a surrogate marker for molecular oxygen level, proved unrelated to treatment outcome. Furthermore, part of the high PSA response observed in our series may be due to the abscopal effect, attributed to irradiation-induced immune mechanisms such as exposure to tumor antigen, increased maturation of antigen-presenting cells taking up antigen released by dying cells, and production of interleukin-6 and tumor necrosis factor-α, as well as changes in the tumor microenvironment for improved recruitment of effector T cells (*31*). In this regard, Gorin et al., evaluating an α-emitting ^{231}Bi-labeled antibody for tumor cell irradiation of mouse xenografts, found that the treatment induced a protective antitumor effect by induction of tumor-specific T cells against a secondary tumor cell injection (*32*). Furthermore, Czernin et al. showed, in a mouse model of mCRPC, that a combination of ^{225}Ac-PSMA-617 and an inhibitor of programmed cell death protein 1 achieved better tumor control than monotherapy with either agent alone (*33*). In our series, 2 patients proved unresponsive to ^{225}Ac-PSMA-617 treatment despite high uptake of the ligand on the baseline scan. As shown by Kratochwil et al., in such patients mutations in DNA-damage-repair and checkpoint genes are frequently found. Future studies assessing the role of DNA-damage-repair–targeting agents in combination with ^{225}Ac-PSMA-617 therapy in overcoming radiation resistance in these patients are of interest (*34*).

A PSA decline of at least 50% to assess efficacy of treatment, as recommend by the Prostate Cancer Working Group 3, proved the single most important factor predicting PFS and OS after ^{225}Ac-PSMA-617 treatment in our patient cohort. The importance of PSA decline was also demonstrated in our previous study (*35*). The median estimated PFS was 4 mo for nonresponders and 22 mo for responders. Although median OS in the nonresponding group was 9 mo, median OS had not yet been reached at the last follow-up (55 mo) (Fig. 2). A first chemotherapy-naïve patient exceeding 5 y of complete remission after ^{225}Ac-PSMA-TAT was reported in Germany (*36*). Overall, our OS data in this small cohort suggest that ^{225}Ac-PSMA-617 has efficacy superior to that of chemotherapy (enzalutamide, abiraterone acetate, or docetaxel) administered in a comparable setting (post-ADT mCRPC patients having received no other treatment targeting their mCRPC) (*28–32*). Regarding the use of docetaxel in the mCRPC setting, 2 large phase 3 randomized, controlled trials published in 2004 (the TAX327 and SWOG9916 trials) found a median OS of 18.9 mo versus 16.5 mo and of 17.5 mo versus 15.6 mo for the control group receiving mitoxantrone, considered the standard of care at that moment (*37,38*). In the COU-AA-302 trial, comparing abiraterone acetate (1,000 mg once daily) plus prednisone or placebo plus prednisone in 1,048 patients randomly assigned to receive either of these treatment options, median OS for patients in the abiraterone acetate group was 34.7 mo (*39*). With regard to enzalutamide, in the double-blind phase 3 PREVAIL trial, in which 1,717 patients were randomly assigned to receive either enzalutamide at a dose of 160 mg or placebo once daily, the median estimated OS for the enzalutamide-treated group was 32.4 mo, versus 30.2 mo for the placebo group (median duration of follow-up for survival, ∼22 mo) (*40*). Recently, the TheraP trial demonstrated that ^{177}Lu-PSMA-617, compared with cabazitaxel, in men with mCRPC led to a higher PSA response and fewer grade 3 or 4 adverse events. ^{177}Lu-PSMA-617 is a new, effective class of therapy and a potential alternative to cabazitaxel (*41*). Although not directly comparable between earlier-stage and later-stage application of ^{225}Ac-PSMA-617 or ^{177}Lu-PSMA-617, a couple of studies have shown a better response from PSMA radioligand therapy with ^{177}Lu-PSMA-617 in chemotherapy-naïve patients (*42*). Furthermore, our group reported a unique cohort of chemotherapy-naïve men with mCRPC who had upfront treatment with ^{225}Ac-PSMA-617 (*12*) and demonstrated a remarkable 88% serum PSA decline by 50% or more after a median of 3 cycles of ^{225}Ac-PSMA-617, as is corroborated by this current series. This result is in contrast to an average of 65.4% serum PSA decline by 50% of patients in studies that had a later-stage application of ^{225}Ac-PSMA-617 or ^{177}Lu-PSMA-617 (*8–18, 30*). Although this remarkable response is exciting and holds much promise for ^{225}Ac-PSMA-617 in treating men with mCRPC, it may also represent a response achieved in less aggressive disease (*42*). mCRPC evolves, acquiring more aggressive behavior as different lines of treatment are applied to it. Additionally, of the patients presenting with liver metastasis, none presented with negative PSMA PET results after treatment, nor did any respond favorably to the treatment, as liver metastasis was also negatively correlated with OS in other studies (*30*). Thus, randomized controlled trials will be needed to stratify patients to either ^{177}Lu-PSMA-617 or ^{225}Ac-PSMA-617 so that the better therapy is administered at the moment in the treatment sequence when it is likely to have the best impact.

Finally, in our study, a high platelet count also proved significantly negatively related to PFS. Although the role of platelets is to stem blood loss after vascular injury, available data suggest that platelets may also interact with tumor cells and endothelial cells, enabling metastases and thereby worsening the prognosis of cancer patients (*43–45*). More specifically, platelets were shown to play a role in shielding tumor cells from immune elimination, in promoting arrest and extravasation of tumor cells, and in protecting cancer cells from undergoing apoptosis. Furthermore, experimental data suggest that thrombocytosis is induced by tumor-derived growth factors. Finally, a high pretreatment baseline platelet count has been previously associated with a poor prognosis in patients with ovarian, breast, lung, renal, colorectal, and pancreatic carcinoma (*46*).

In terms of the safety profile, xerostomia remains an adverse effect of concern, and most of our patients experienced dry mouth—commonly after the first cycle of treatment. To reduce the incidence and severity of treatment-induced xerostomia, we practiced the treatment deescalation strategy. Administered activity was reduced to 6 or 4 MBq in subsequent treatment cycles according to the volume of residual tumor load. This strategy is based on the principle of the tumor sink effect, in which more radioligand is available for binding in normal organs when tumor bulk is reduced by successful treatment (*47*). As we reported previously, we believe that this

strategy is partially successful because none of our patients has experienced grade III xerostomia or discontinued ^{225}Ac-PSMA-617 therapy because of dry mouth (*12,35*). Although anemia was also a relatively common toxicity (15%), no other grade 3 or 4 hematotoxicities were noted. Notably, only 3 patients experienced grade III–IV renal function impairment. All 3 of these patients presented with suboptimal renal function before the ^{225}Ac-PSMA-617 therapy. This finding warrants medium- to long-term monitoring of renal function of patients treated with ^{225}Ac-PSMA-617.

This study was retrospective and consequently bears all the disadvantages of such types of studies, including—in this specific setting—lack of a control group. However, the favorable results suggest that it would be of major clinical relevance to perform a prospective randomized study comparing ^{225}Ac-PSMA-617 with standard-of-care treatment options such as enzalutamide, abiraterone acetate, and docetaxel after ADT.

CONCLUSION

In 91% of this series of 53 mCRPC patients receiving ^{225}Ac-PSMA-617 therapy subsequent to ADT, the PSA level decreased by more than 50%. A PSA decline of at least 50% proved the single most important factor predicting PFS and OS after ^{225}Ac-PSMA-617 treatment. The median estimated PFS was 4 mo for nonresponders and 22 mo for responders, and the median OS was 9 mo in the nonresponding group and had not yet been reached at the last follow-up (55 mo) in the responding group. ^{225}Ac-PSMA-617 is a highly promising option for therapy of mCRPC directly after ADT and warrants further study in randomized trials.

DISCLOSURE

No potential conflict of interest relevant to this article was reported.

ACKNOWLEDGMENTS

We thank our patients for entrusting us with their care. We thank all members of the staff at the Department of Nuclear Medicine, Steve Biko Academic Hospital, for their various contributions to this work. We also specifically thank our colleagues Drs. Neo Mokgoro, Letjie Maserumule, Khanyinsile Hlongwa, Honest Ndlovu, Janet Reed, and Aisha Ismail, who cared for the patients whose data are included in this work.

KEY POINTS

QUESTION: What is the efficacy of ^{225}Ac-PSMA-617 in the post-ADT setting in men with mCRPC?

PERTINENT FINDINGS: ^{225}Ac-PSMA-617 administered in the post-ADT setting to men with mCRPC resulted in a PSA response in 91% of patients and produced an undetectable level of serum PSA in 36%. A decline in serum PSA by at least 50% was significantly associated with a longer OS. A PSA decline of at least 50%, a low pretreatment platelet level, and radiographic response on ^{68}Ga-PSMA-11 PET/CT were significant predictors of a longer PFS.

IMPLICATIONS FOR PATIENT CARE: ^{225}Ac-PSMA-617 is a viable treatment option that may be considered in men who develop mCRPC after ADT, especially if approved treatment options are not available or are contraindicated.

REFERENCES

1. Bray F, Ferlay J, Soerjomataram I, Siegel RL, Torre LA, Jemal A. Global cancer statistics 2018: GLOBOCAN estimates of incidence and mortality worldwide for 36 cancers in 185 countries. *CA Cancer J Clin.* 2018;68:394–424.
2. Ferlay J, Colombet M, Soerjomataram I, et al. Cancer statistics for the year 2020: an overview. *Int J Cancer.* April 5, 2021 [Epub ahead of print].
3. Center MM, Jemal A, Lortet-Tieulent J, et al. International variation in prostate cancer incidence and mortality rates. *Eur Urol.* 2012;61:1079–1092.
4. Gillessen S, Omlin A, Attard G, et al. Management of patients with advanced prostate cancer: recommendations of the St Gallen Advanced Prostate Cancer Consensus Conference (APCC). *Ann Oncol.* 2015;26:1589–1604.
5. Sumanasuriya S, De Bono J. Treatment of advanced prostate cancer: a review of current therapies and future promise. *Cold Spring Harb Perspect Med.* 2018;8: a030635.
6. Maphayi MR, Cassim N, Bello B, George JA. Mining laboratory data to describe prostate specific antigen testing and prostate cancer in Johannesburg, South Africa. *Pan Afr Med J.* 2020;35:61.
7. Kratochwil C, Bruchertseifer F, Rathke H, et al. Targeted α-therapy of metastatic castration-resistant prostate cancer with 225Ac-PSMA-617: swimmer-plot analysis suggests efficacy regarding duration of tumor control. *J Nucl Med.* 2018;59: 795–802.
8. Kratochwil C, Bruchertseifer F, Rathke H, et al. Targeted alpha therapy of mCRPC with ^{225}actinium-PSMA-617: dosimetry estimate and empirical dose finding. *J Nucl Med.* 2017;58:1624–1631.
9. Kratochwil C, Bruchertseifer F, Giesel F, et al. ^{225}Ac-PSMA-617 for PSMA targeting alpha-radiation therapy of patients with metastatic castration-resistant prostate cancer. *J Nucl Med.* 2016;57:1941–1944.
10. Yadav MP, Ballal S, Sahoo RK, Tripathi M, Seth A, Bal C. Efficacy and safety of ^{225}Ac-PSMA-617 targeted alpha therapy in metastatic castration-resistant prostate cancer patients. *Theranostics.* 2020;10:9364–9377.
11. van der Doelen MJ, Mehra N, van Oort IM, et al. Clinical outcomes and molecular profiling of advanced metastatic castration-resistant prostate cancer patients treated with ^{225}Ac-PSMA-617 targeted alpha-radiation therapy. *Urol Oncol.* 2021;39: 729.e7–729.e16.
12. Sathekge M, Bruchertseifer F, Knoesen O, et al. ^{225}Ac-PSMA-617 in chemotherapy-naive patients with advanced prostate cancer: a pilot study. *Eur J Nucl Med Mol Imaging.* 2019;46:129–138.
13. Fanti S, Goffin K, Hadaschik BA, et al. Consensus statements on PSMA PET/CT response assessment criteria in prostate cancer. *Eur J Nucl Med Mol Imaging.* 2021;48:469–476.
14. Fanti S, Hadaschik B, Herrmann K. Proposal of systemic therapy response assessment criteria in time of PSMA PET/CT imaging: PSMA PET Progression (PPP). *J Nucl Med.* 2020;61:678–682.
15. Grubmüller B, Senn D, Kramer G, et al. Response assessment using ^{68}Ga-PSMA ligand PET in patients undergoing ^{177}Lu-PSMA radioligand therapy for metastatic castration-resistant prostate cancer. *Eur J Nucl Med Mol Imaging.* 2019;46:1063–1072.
16. Dal Pra A, Cury F, Souhami L. Combining radiatiotherapy and androgen deprivation for localized prostate cancer: a critical review. *Curr Oncol.* 2010;17:28–38.
17. Zietman AL, Prince E, Nakfoor B, Park J. Androgen deprivation and radiation therapy: sequencing studies using the Shionogi in vivo tumor system. *Int J Radiat Oncol Biol Phys.* 1997;38:1067–1070.
18. Zietman AL, Prince E, Nakfoor B, Shipley W. Neoadjuvant androgen suppression with radiation in the management of locally advanced adenocarcinoma of the prostate: experimental and clinical results. *Urology.* 1997;49:74–83.
19. Kaminski JM, Hanlon A, Joon D, Meistreich M, Hachem P, Pollack A. Effect of sequencing of androgen deprivation and radiotherapy on prostate cancer growth. *Int J Radiat Oncol Biol Phys.* 2003;57:24–28.
20. Milosevic M, Chung P, Parker C, et al. Androgen withdrawal in patients reduces prostate cancer hypoxia: implications for disease progression and radiation response. *Cancer Res.* 2007;67:6022–6025.
21. Jiang T, Markovic D, Patel J, et al. Radiation therapy dose and androgen deprivation therapy in localized prostate cancer: a meta-regression of 5-year outcomes in phase III randomized controlled trials. *Prostate Cancer Prostatic Dis.* 2022;25:126–128.
22. Chaiswing L, Weiss H, Jayswal H, St. Clair D, Kypriamou N. Profiles of radioresistance mechanisms in prostate cancer. *Crit Rev Oncog.* 2018;23:39–67.
23. Mahajan K, Coppola D, Rawal B, et al. Ack-1 mediated androgen receptor phosphorylation modulates radiation resistance in castration-resistant prostate cancer. *J Biol Chem.* 2012;287:22112–22122.
24. Wu CT, Chen MF, Chen WC, Hsieh CC. The role of IL-6 in the radiation response of prostate cancer. *Radiat Oncol.* 2013;8:159.
25. Hu CD, Choo R, Huang J. Neuroendocrine differentiation in prostate cancer: a mechanism of radioresistance and treatment failure. *Front Oncol.* 2015;5:90.

26. Kratochwil C, Haberkorn U, Giesel F. Radionuclide therapy of metastatic prostate cancer. *Semin Nucl Med.* 2019;49:313–325.
27. Ahmadzadehfar H, Rahbar K, Essler M, Biersack HJ. PSMA-based theranostics: a step-by-step practical approach to diagnosis and therapy for mCRPC patients. *Semin Nucl Med.* 2020;50:98–109.
28. Morgenstern A, Apostolidis C, Kratochwil C, Sathekge M, Krolicki L, Bruchertseifer F. An overview of targeted alpha therapy with ^{225}actinium and ^{213}bismuth. *Curr Radiopharm.* 2018;11:200–208.
29. Parker C, Lewington V, Shore N, et al. Targeted alpha therapy, an emerging class of cancer agents: a review. *JAMA Oncol.* 2018;4:1765–1772.
30. Feuerecker B, Tauber R, Knorr K, et al. Activity and adverse events of actinium-225-PSMA-617 in advanced metastatic castration-resistant prostate cancer after failure of lutetium-177-PSMA. *Eur Urol.* 2021;79:343–350.
31. Haberkorn U, Giesel F, Morgenstern A, Kratochwil C. The future of radioligand therapy: α, β, or both? *J Nucl Med.* 2017;58:1017–1018.
32. Gorin JB, Ménager J, Gouard S, et al. Antitumor immunity induced after α irradiation. *Neoplasia.* 2014;16:319–328.
33. Czernin J, Current K, Mona CE, et al. Immune-checkpoint blockade enhances ^{225}Ac-PSMA617 efficacy in a mouse model of prostate cancer. *J Nucl Med.* 2021;62:228–231.
34. Kratochwil C, Giesel F, Heussel C, et al. Patients resistant against PSMA-targeting α-radiation therapy often harbor mutations in DNA damage-repair-associated genes. *J Nucl Med.* 2020;61:683–688.
35. Sathekge M, Bruchertseifer F, Vorster M, et al. Predictors of overall and disease-free survival in metastatic castration-resistant prostate cancer patients receiving ^{225}Ac-PSMA-617 radioligand therapy. *J Nucl Med.* 2020;61:62–69.
36. Rathke H, Bruchertseifer F, Kratochwil C, et al. First patient exceeding 5-year complete remission after ^{225}Ac-PSMA-TAT. *Eur J Nucl Med Mol Imaging.* 2021;48:311–312.
37. Tannock IF, De Wit R, Berry W, Horti J, Pluzasnka A, Chi K. Docetaxel plus prednisone of mitoxantrone plus prednisone for advanced prostate cancer. *N Engl J Med.* 2004;351:1502–1512.
38. Petrylak DP, Tangen C, Hussain M, Lara P, Jones J, Taplin M. Doxetaxel and estramustine compared with mitoxantrone and prednisone for advanced refractory prostate cancer. *N Engl J Med.* 2004;351:1513–1520.
39. Ryan CJ, Smith M, Fizazi K, et al. Abiraterone acetate plus prednisone versus placebo plus prednisone in chemotherapy-naive men with metastatic castration-resistant prostate cancer (COU-AA-302): final overall survival analysis of a randomised, double-blind, placebo-controlled phase 3 study. *Lancet Oncol.* 2015;16:152–160.
40. Armstrong AJ, Lin P, Tombal B, et al. Five-year survival prediction and safety outcomes with enzalutamide in men with chemotherapy-naïve metastatic castration-resistant prostate cancer from the PREVAIL trial. *Eur Urol.* 2020;78:347–357.
41. Hofman MS, Emmett L, Sandhu S, et al. [^{177}Lu]Lu-PSMA-617 versus cabazitaxel in patients with metastatic castration-resistant prostate cancer (TheraP): a randomised, open-label, phase 2 trial. *Lancet.* 2021;397:797–804.
42. Sathekge MM, Bruchertseifer F, Vorster M, Morgenstern A, Lawal IO. Global experience with PSMA-based alpha therapy in prostate cancer. *Eur J Nucl Med Mol Imaging.* 2021;49:30–46.
43. McCarty OJ, Mousa S, Bray P, Konstantopoulos K. Immobilized platelets support human colon carcinoma cell tethering, rolling, and firm adhesion under dynamic flow conditions. *Blood.* 2000;96:1789–1797.
44. Nieswandt B, Hafner M, Echtenacher A, Mannel D. Lysis of tumour cells by natural killer cells in mice is impeded by platelets. *Cancer Res.* 1999;59:1295–1300.
45. Kim YJ, Borstig L, Varki N, Varki M. P-selectin deficiency attenuates tumor growth and metastasis. *Proc Natl Acad Sci USA.* 1998;95:9325–9330.
46. Sylman JL, Boyce H, Mitrungo A, et al. A temporal examination of platelet counts as a predictor of prognosis in lung, prostate, and colon cancer patients. *Sci Rep.* 2018;8:6564.
47. Gaertner FC, Halabi K, Ahmadzadehfar H, et al. Uptake of PSMA-ligands in normal tissues is dependent on tumor load in patients with prostate cancer. *Oncotarget.* 2017;8:55094–55103.

Safety of Peptide Receptor Radionuclide Therapy with ^{177}Lu-DOTATATE in Neuroendocrine Tumor Patients with Chronic Kidney Disease

Shahad Alsadik[1], Gopinath Gnanasegaran[2], Luohai Chen[3,4], Dalvinder Mandair[1], Christos Toumpanakis[1], Martyn Caplin[1], and Shaunak Navalkissoor[2]

[1]Neuroendocrine Unit, Royal Free London NHS Foundation Trust, London, United Kingdom; [2]Department of Nuclear Medicine, Royal Free London NHS Foundation Trust, London, United Kingdom; [3]Department of Gastroenterology, Royal Free London NHS Foundation Trust, London, United Kingdom; and [4]First Affiliated Hospital, Sun Yat-Sen University, Guangzhou, China

Our purpose was to assess the efficacy and safety of ^{177}Lu-DOTATATE in neuroendocrine tumor patients with reduced renal function. **Methods:** A single-center retrospective analysis was performed on 33 patients with an estimated glomerular filtration rate (eGFR) of less than 60 mL/min/1.73 m^2. Of these, 26 had chronic kidney disease (CKD) stage 3a (eGFR, 45–60 mL/min/1.73 m^2) and 7 had CKD 3b (eGFR, 30–45 mL/min/1.73 m^2). Renal toxicity and temporal changes in eGFR were recorded. The association between potential risk factors and any kidney function deterioration (>10% reduction in eGFR) was evaluated. Data on survival, the radiologic response assessment, and quality of life were collected. **Results:** The incidence of permanent grade 3 or 4 nephrotoxicity was 3% (a single patient with grade 4 nephrotoxicity). The mean annual reduction in eGFR was estimated at 2.5%. A permanent decline of less than 10% in eGFR of any grade was recorded in 45% of patients (n = 15). Nine patients moved into higher CKD categories (8 patients who moved from CKD 3a to CKD 3b and 1 patient who moved from CKD 3b to CKD 5). No significant relationship was found between renal risk factors and a permanent reduction in renal function. Grade 3 or 4 bone marrow toxicity was observed in 9% of patients. The estimated median progression-free survival was 42 mo, and the median overall survival was 47 mo. At the end of treatment, the radiologic assessment showed a partial response in 33%, stable disease in 55%, and progressive disease in 12%. There was an improvement in global quality of life and endocrine score (European Organization for Research and Treatment of Cancer Quality-of-Life Questionnaire–Gastrointestinal NET-21) (P = 0.046 and 0.041, respectively). **Conclusion:** ^{177}Lu-DOTATATE appears to be generally well tolerated in patients with preexisting CKD 3, with a low incidence of permanent major nephrotoxicity. ^{177}Lu-DOTATATE appears to have a good therapeutic effect, with most patients reporting improvement in quality of life.

Key Words: neuroendocrine tumors; peptide receptor radionuclide therapy; PRRT; ^{177}Lu-DOTATATE; chronic kidney disease

J Nucl Med 2022; 63:1503–1508
DOI: 10.2967/jnumed.121.263056

Peptide receptor radionuclide therapy (PRRT) has been shown to be an effective treatment modality for somatostatin receptor–expressing neuroendocrine tumors (NETs), with ^{177}Lu-DOTATATE PRRT receiving marketing authorization by the U.S. and European Union regulators in 2018 and 2017, respectively, following the successful outcome of the NETTER-1 trial (*1*). The NETTER-1 study and other large-cohort studies have shown that ^{177}Lu-DOTATATE is an effective treatment in patients with somatostatin receptor–expressing NETs, with progression-free survival (PFS) of between 2 and 3 y (*1–4*). ^{177}Lu-DOTATATE is generally well tolerated, with a low incidence of significant grade 3 or 4 toxicities. The bone marrow and the kidneys have been considered the critical organs for PRRT (*5*).

The main mechanism of absorption of the PRRT radiation dose by the kidney is partial reabsorption of the radiopeptide in the proximal tubules after glomerular filtration and retention in the renal interstitium. This process is mediated by cubilin-dependent megalin receptor endocytosis at the proximal tubules (*6*). Renal radiopeptide retention can lead to excessive renal irradiation to the radiosensitive glomeruli, with potential subsequent deterioration in kidney function. Expression of somatostatin receptor on the proximal tubules is a minor mechanism that contributes to the total renal radiation dose (*7*).

In the early years of ^{90}Y-based PRRT, significant renal toxicity (grade 3 or 4) was recorded in up to 14% of patients who received a cumulative administered activity of more than 7,400 MBq/m^2 (*8,9*). The incidence of renal toxicity has significantly decreased with the coinfusion of positively charged amino acids such as L-lysine or L-arginine, which competitively inhibit the reabsorption of the radiopeptide. This amino acid coinfusion has reduced the renal radiation dose by up to 65% (*8,9*). There is lower renal toxicity with the shorter-ranged β-particles of ^{177}Lu than ^{90}Y, leading to reduced irradiation of the radiosensitive glomeruli. Despite amino acid–based renoprotection, ^{177}Lu-PRRT still results in an approximately 3.8% annual loss of kidney function, which is lower than the 7.3% yearly decline with ^{90}Y-PRRT described by the same group (*10*).

The ^{177}Lu-DOTATATE summary of product information had previously recommended ^{177}Lu-DOTATATE in patients with an estimated glomerular filtration rate (eGFR) of more than 50 mL/min/1.73 m^2 (*11*). The latest update of the summary of product information, in 2021, recommended a change in the cutoff of baseline creatinine clearance from at least 50 mL/min/1.73 m^2 to at least 40 mL/min/1.73 m^2, presumably based on feedback from treating clinicians (*5*).

Received Aug. 16, 2021; revision accepted Feb. 10, 2022.
For correspondence or reprints, contact Shaunak Navalkissoor (s.navalkissoor@nhs.net) or Shahad Alsadik (s.alsadik@nhs.net).
Published online Feb. 24, 2022.

There is no large dataset on PRRT toxicity in patients with stage 3 chronic kidney disease (CKD). Most of the currently published studies explore the renal toxicity of PRRT in patients with normal or mildly reduced renal function. It has been shown that patients with lower renal function have a higher renal absorbed dose per administered activity and thus are potentially at higher risk for renal toxicity (*12*). In this study, we set out to evaluate the incidence and clinical significance of hematologic and permanent renal toxicity after ^{177}Lu-DOTATATE in patients with reduced renal function (i.e., patients with an eGFR of 30–60 mL/min/1.73 m^2).

MATERIALS AND METHODS

All procedures involving human participants were in accordance with the ethical standards of the institutional or national research committee and with the 1964 Declaration of Helsinki. The institutional review board approved this retrospective study, and the requirement to obtain informed consent was waived.

We evaluated the baseline eGFR in all patients (n = 395) treated with ^{177}Lu-DOTATATE from May 2012 to August 2019 at the Royal Free London NHS Foundation Trust. Patients with CKD3 based on eGFR had a confirmatory ^{99m}Tc-diethylenetriaminepentaacetate glomerular filtration rate (GFR) determined at baseline as per routine clinical practice. We collected clinicopathologic, survival and health-related quality-of-life (HRQoL) data.

PRRT Protocol

The inclusion criteria included histologically confirmed, unresectable metastatic NETs with progressive disease. In addition, the pretherapy ^{68}Ga-DOTATATE study had to demonstrate sufficient tracer uptake (Kenning score, 2 or more). Patients had to have adequate bone marrow function and a GFR of more than 30 mL/min/1.73 m^2.

^{177}Lu-DOTATATE was administered at a target activity of 7.4 GBq per cycle to complete 4 cycles at an interval of 8–12 wk between cycles. Renal protection was implemented with standard amino acids (2.5% lysine and 2.5% arginine in 1 L of 0.9% NaCl; infusion rate, 250 mL/h) along with pretherapy antinausea medication (ondansetron, 30 mg).

Serum creatinine, eGFR, and full blood counts were calculated at baseline (on the day of the first cycle of PRRT), at 2- to 4-wk intervals between cycles, up to 8 wk after the last cycle, and at 3-month intervals thereafter.

CKD Classification

CKD was classified as CKD 1 (eGFR $\leq$ 90 mL/min/1.73 m^2, but with urine findings, structural abnormalities, or genetic traits pointing to kidney disease; for the purpose of this study, eGFR $\geq$ 90 counted as normal), CKD 2 (eGFR $\geq$ 60 to $<$ 90 mL/min/1.73 m^2), CKD 3a (eGFR $\geq$ 45 to $<$ 60 mL/min/1.73 m^2), CKD 3b (eGFR $\geq$ 30 to $<$ 45 mL/min/1.73 m^2), CKD 4 (eGFR $\geq$ 15 to $<$ 30 mL/min/1.73 m^2), or CKD 5 (eGFR $<$ 15 mL/min/1.73 m^2 or on dialysis) (*13*). Potential risk factors for renal toxicity, including age greater than 65 y, number of cycles, hypertension, diabetes, and previous chemotherapy or ^{90}Y, were identified and assessed.

HRQoL

Patients undergoing ^{177}Lu-DOTATATE treatment had HRQoL data prospectively collected as part of routine clinical practice. HRQoL was evaluated using the European Organization for Research and Treatment of Cancer Quality-of-Life Questionnaire–Gastrointestinal NET-21 (*14*). HRQoL was assessed before ^{177}Lu-DOTATATE and after each cycle of ^{177}Lu-DOTATATE. The scores were transformed to 0–100 scales, and the mean scores after each treatment were compared with the baseline scores.

Statistical Analysis

Median PFS and median overall survival with corresponding 95% CIs were estimated using the Kaplan–Meier method with the statistical software package SPSS (version 27.0; IBM). PFS was defined as the time from treatment initiation to tumor progression or death.

An objective tumor assessment on CT or MRI was performed at baseline, after cycle 2, and 3 mo after the final cycle. Afterward, CT or MRI was performed every 6 mo. We performed a radiologic response assessment after the last treatment cycle. Imaging consisted of CT or MRI and was compared with baseline imaging using RECIST, version 1.1 (*15*).

TABLE 1
Clinicopathologic Patient Characteristics

Characteristic	*n*
Sex	
Female	17 (52%)
Male	16 (48%)
Age group	
<65 y	17 (52%)
≥65 y	16 (48%)
Primary site of origin	
Gastrointestinal	21 (64%)
Pancreatic	6 (18%)
Other sites	2 (6%)
Unknown	4 (12%)
Grade	
1	14 (43%)
2	16 (48%)
3	1 (3%)
Unknown	2 (6%)
Pre-PRRT treatment	
Somatostatin receptor analogs	32 (97%)
Surgery	15 (45%)
Chemotherapy	8 (24%)
Locoregional	2 (6%)
Radiotherapy/^{90}Y-PRRT	4 (12%)
Sunitinib or everolimus	3 (9%)
Sites of metastasis	
Liver	31 (94%)
Bone	18 (55%)
Lymph nodes	24 (72%)
Peritoneum	8 (24%)
Risk factors for renal toxicity	
Hypertension	18 (22%)
Diabetes	9 (17.6%)
Chemotherapy	8 (24%)
^{90}Y-PRRT	3 (6%)
Number of ^{177}Lu cycles	
<4	7 (21%)
4	26 (79%)

Toxicity was assessed according to the Common Terminology Criteria for Adverse Events scoring system, version 5.0 (*16*). We also assessed the effect of PRRT on renal function by calculating the annual reduction in eGFR and by the change in CKD categories.

The Fisher exact test was used to test the relationship between potential risk factors (age > 65 y, hypertension, diabetes, pre-PRRT chemotherapy, age, and previous ^{90}Y-PRRT) and renal function deterioration (reduction in eGFR of >10%). *P* values of less than 0.05 were regarded as statistically significant.

Paired Wilcoxon signed-rank testing was used to compare the HRQoL before and during ^{177}Lu-DOTATATE treatment. The scores were transformed to 0–100 scales, and the average scores after each treatment were compared with baseline scores.

RESULTS

We identified 33 patients (8%) with CKD 3 (eGFR < 60 mL/min/1.73 m^2). Of these 33 patients, 26 patients had CKD 3a and 7 patients had CKD 3b. We followed these 33 patients for a median of 38 mo (range, 13–73 mo),

The clinicopathologic features are summarized in Table 1: 17 patients were female and 16 were male, with mean age of 65 y (range, 45–81 y).

The average administered activity of ^{177}Lu-DOTATATE was 7.2 GBq per cycle. Most patients (n = 26) completed 4 cycles of treatment, with 3 patients having 3 cycles and 4 patients having 2 cycles (Table 1). The reasons for stopping treatment early in the 7 patients who had fewer than 4 treatment cycles were radiologic progression in 4, clinical deterioration in 2, and prolonged bone marrow toxicity in 1.

Common Terminology Criteria for Adverse Events grade 3 or 4 renal toxicity was recorded in 3 (9%) patients, all of whom completed 4 treatment cycles. Two of these patients developed acute kidney injury due to acute terminal events (1 patient developed sepsis; the other developed acute clinical deterioration and dehydration). The eGFR of these 2 patients was stable before these acute events. One patient (3%) developed a gradual decline in kidney function and eventually began hemodialysis.

Permanent renal function deterioration (i.e., a reduction in eGFR of >10%) was seen in 15 patients (45%) by the end of the follow-up (Table 2). Kidney function improvement (eGFR increase by >10%) was seen in 2 (6%) patients. The remaining 16 (48%) patients had no significant change in their eGFR (Fig. 1).

The average annual eGFR reduction was 2.5% per year. Overall, 9 patients moved to a higher CKD category, with 8 patients moving from CKD 3a to CKD 3b and 1 patient from CKD 3b to CKD 5. There was no significant difference in toxicity profile between patients with baseline CKD 3a and CKD 3b.

We evaluated the role of known potential risk factors for renal toxicity (age > 65 y, hypertension, diabetes, previous chemotherapy, and previous ^{90}Y-PRRT) and found no statistically significant factor (P = 0.56, 0.56, 0.57, 0.24, and 0.20, respectively). The presence of multiple renal risk factors was also not a statistically significant predictor of renal toxicity (P = 0.27).

Bone marrow toxicity (excluding lymphopenia) of any grade was recorded in 16 patients (48%). Grade 3 or 4 bone marrow toxicity (excluding lymphopenia) was recorded in 3 patients (9%); grade 3 anemia, in 2 (6%); grade 3 leukopenia, in 1 (3%); grade 3 thrombocytopenia, in 1 (3%); and grade 3 or 4 lymphopenia, in 4 (12%) (Table 3).

TABLE 2
Risk Factors for Patients with Significant (>10%) Absolute Change in eGFR After Treatment with ^{177}Lu-DOTATATE

Patient no.	Age (y)	Treatment cycles (*n*)	Cumulative administered dose (MBq)	Risk factors for renal toxicity	Baseline eGFR (mL/min/1.73 m^2)	Last recorded eGFR (mL/min/1.73 m^2)	Follow-up (y)	Annual % eGFR loss
1	64	4	30,689	HTN, DM	43	36	2.16	7.55
2	49	4	30,291	—	49	39	2.68	5.48
3	70	4	30,000	Age > 65, HTN	48	41	1.66	8.78
4	46	2	15,200	Chemotherapy, ^{90}Y-PRRT	56	49	1.01	12.36
5	57	2	14,878	Age > 65,^{90}Y-PRRT	43	34	5.12	4.09
6	81	4	29,708	Age > 65, HTN	39	15*	2.93	21.01
7	76	4	29,708	Age > 65, HTN	53	37	2.78	10.88
8	62	4	29,309	—	48	35	3.08	8.80
9	69	4	29,901	Age > 65, HTN, DM	49	44	4.66	2.19
10	73	4	28,791	Age > 65, chemotherapy	53	38	3.26	8.69
11	59	4	28,424	HTM, DM, chemotherapy	58	51	3.20	3.77
12	79	4	29,761	Age > 65	56	39	3.64	8.33
13	57	4	29,793	Chemotherapy	48	33	3.99	7.84
14	68	4	30,970	Age > 65, HTN, chemotherapy	51	44	2.28	6.02
15	67	4	29,690	Age > 65	58	52	3.38	3.06

*Required hemodialysis.
HTN = hypertension; DM = diabetes mellitus.

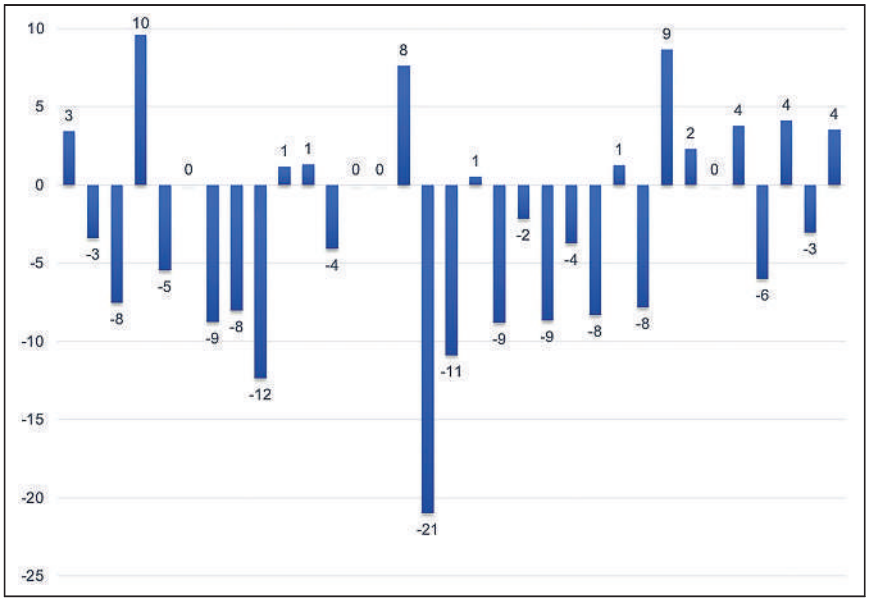

FIGURE 1. Clustered column graph representing annual percentage change in eGFR after ^{177}Lu-DOTATATE treatment.

Survival analysis showed that the estimated median PFS for the entire cohort (n = 33) was 42 mo (95% CI, 36–47 mo) and the estimated median overall survival was 47 mo (95% CI, 37–57 mo). The number of patients who died by the end of follow-up was 16 (49%). The median follow-up time was 38 mo (range, 13–73 mo).

End-of-treatment RECIST radiologic response assessment showed a partial response in 33% (n = 11), stable disease in 55% (n = 18), and progressive disease in 12% (n = 4).

HRQoL analysis in our cohort showed a significantly improved quality of life after ^{177}Lu-DOTATATE based on the European Organization for Research and Treatment of Cancer Quality-of-Life Questionnaire–Gastrointestinal NET-21.

The overall average score improved from a baseline of 29.36 to an average of 24.93 (P = 0.046) based on paired Wilcoxon signed-rank testing. The other main area of improvement was the endocrine score, which improved from 22.64 to 17.16 (P = 0.041). The gastrointestinal symptom score decreased from 22.82 to 20.79 (P = 0.440). The average disease-related worries score decreased from 50.42 to 44.55 (P = 0.082). The average social functioning score decreased from 41.88 to 38.28 (P = 0.337) (Fig. 2).

DISCUSSION

PRRT with ^{177}Lu-DOTATATE is an established therapeutic option for advanced, metastatic well-differentiated NETs. It has gained increasing popularity because of its efficacy and relatively favorable safety profile. However, safety data for PRRT in patients with reduced renal function are limited. Caution has been advised in treating patients with reduced renal function because of the possibility that permanent renal dysfunction will develop (*11*).

The main aim of this study was to assess the safety and efficacy of ^{177}Lu-DOTATATE in patients with baseline CKD 3. No acute radiation nephritis was noted in our cohort. Of the 3 patients with grade 3 or 4 nephrotoxicity after PRRT according to the Common Terminology Criteria for Adverse Events, 1 (3%) can potentially be attributed to PRRT. Kidney function gradually deteriorated in this patient, and CKD 5 eventually developed, requiring dialysis over 3 y. The decline in kidney function was attributed to persistent vomiting with poor oral intake, but we could not exclude a contributory role of PRRT. Our finding of 3% incidence of grade 3 or 4 nephrotoxicity is slightly higher than the 0%–1.5% found in other studies (*1–3,17–20*).

Less than half our patients (n = 15) developed a reduction in kidney function by the end of the study (>10% drop in eGFR). We did not find any statistically significant correlation between clinical risk factors and reduced renal function. Similarly, other studies have not found any consistent risk factors to identify an increased risk of reduced renal function in patients undergoing treatment with ^{177}Lu-DOTATATE (*21,22*). It would, however, be prudent to be cautious in treating patients with reduced renal function and multiple renal risk factors.

We found that 2 patients (6%) had an improvement in their kidney function. One of these patients had a mesenteric mass compressing a horseshoe kidney. The subsequent reduction in the size of the mesenteric mass reduced the renal compression and resulted in better renal perfusion, which is likely the cause of the improvement in function. The second patient's improvement in eGFR was likely related to improvement in general clinical condition after a PRRT-related tumor response. The patient's overall HRQoL score improved from 28.3 to 15.0.

TABLE 3
PRRT-Related Hematologic Toxicity in Patients with CKD 3

Grade	Anemia	Leukopenia	Thrombocytopenia	Lymphocytopenia
1	10 (30%)*	1 (3%)	7 (21%)	4 (12%)
2	4 (12%)	4 (12%)	2 (6%)	8 (24%)
3	2 (6%)	1 (3%)	1 (3%)	4 (12%)
4	0 (0%)	0 (%)	0 (0%)	0 (0%)

*Six patients with baseline hemoglobin < lower normal limit.

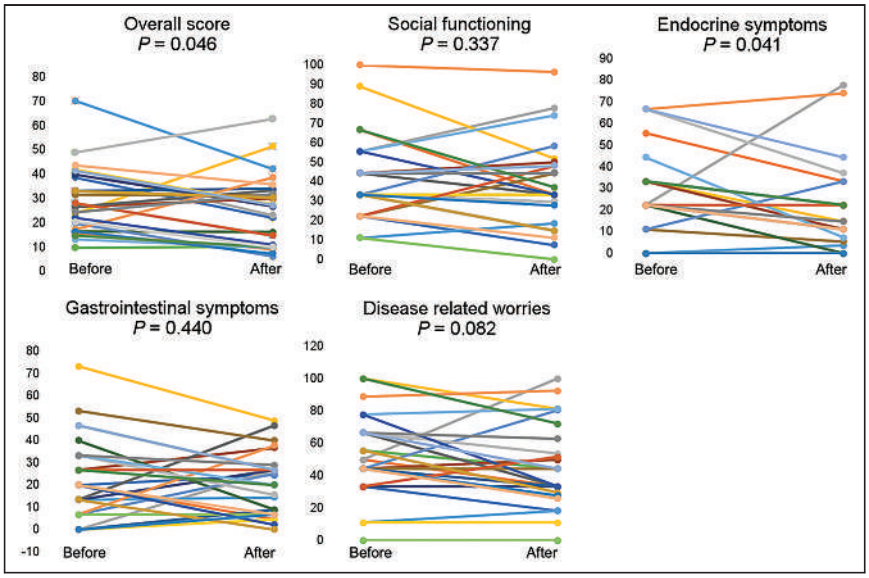

FIGURE 2. Comparison of HRQoL before and after ^{177}Lu-DOTATATE treatment.

The average annual eGFR drop was 2.5%. This result is in line with other ^{177}Lu-PRRT studies on patients with normal or mildly reduced eGFR. These studies reported an annual eGFR loss of less than 4% (*10,22*). Extrapolating these results, if we consider a hypothetical patient who had an average 2.5% eGFR loss per year and started at a baseline eGFR of 30 mL/min/1.73 m^2, this patient would need more than 10 y after ^{177}Lu-DOTATATE to reach CKD 5 and potentially require dialysis. However, if the patient were at the higher end (10%) of annual eGFR loss (which occurred in 3 patients; i.e., <10% of our cohort), the time to reach CKD 5 would decrease to approximately 6–7 y. In the worst-case scenario, if the patient lost more than 20% of baseline eGFR per year (which occurred in a single treated patient), the patient would reach CKD 5 in approximately 3 y (Fig. 3).

Longitudinal studies have shown that GFR declines steadily with age, beginning at age 30–40 y and further declining after age 65–70 y (*23*). The average GFR decline calculated in one study was estimated at approximately 0.75 mL/min/y. Some of the reduction in GFR may be due to the physiologic process of cellular senescence, which is more marked in older patients (*24*). However, in patients with more than a 10% reduction in GFR, physiologic decline alone would not explain the drop.

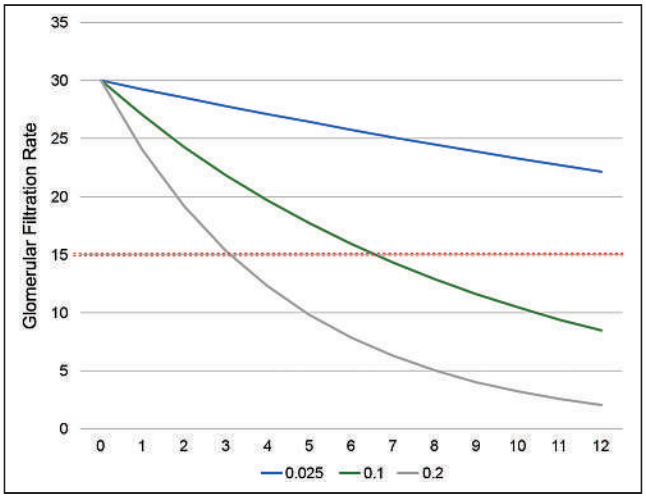

FIGURE 3. Hypothetical drop in GFR from baseline of 30 mL/min/1.73 m^2 at different percentages (2.5%, 10%, and 20%) over time after ^{177}Lu-DOTATATE treatment.

Grade 3 or 4 bone marrow toxicity in our cohort was 9%. This is slightly higher than in our overall cohort (7%) or in the NETTER-1 study (2%). This difference could probably represent a higher bone marrow dose due to prolonged radiation exposure from longer circulating radiopeptides in patients with reduced renal excretion. Similarly higher amounts of grade 3 or 4 bone marrow toxicity have been reported in other studies on patients with impaired renal function (*25,26*).

Survival analysis of our 33 patients showed that the estimated median PFS and median overall survival were 42 mo (95% CI, 36–47 mo) and 47 mo (95% CI, 37–57 mo), respectively. The PFS was greater than for the overall cohort of 395 patients at our center (PFS, 33 mo; 95% CI, 28–36 mo). The prolonged circulation time of radiopeptides may have resulted in a higher absorbed tumor dose, which potentially resulted in longer PFS. However, tumor dosimetry was not performed in this study.

The disease control rate was 88%, which is acceptable in patients with progressive advanced metastatic NETs, some of whom will have few other treatment options because of reduced renal function.

PRRT has been shown to improve the quality of life of patients with NETs (*1,27,28*). Similarly, our study showed a quality-of-life improvement in patients with CKD 3 after ^{177}Lu-DOTATATE treatment. ^{177}Lu-DOTATATE was shown to significantly improve the overall quality-of-life score ($P = 0.046$) and the endocrine symptom score ($P = 0.041$). These data further support the use of ^{177}Lu-DOTATATE in patients with reduced renal function.

There were a few limitations to this study; first, it was retrospective and thus had the associated inherent biases (e.g., selection bias and lack of follow-up). However, we felt it would be useful to report real-world data. Second, the sample size was relatively small. However, PRRT with ^{177}Lu-DOTATATE in patients with reduced renal function is considered a relative contraindication, and we feel these data may be valuable to other centers. Given that this was a retrospective study and of relatively small sample size, confirmation of these findings in a larger prospective, multicenter study with a formal sample-size calculation would be useful. Third, because of problems in obtaining funding, some patients were treated after a delay or as a later treatment line, potentially reducing PFS in PRRT patients with more extensive disease. Finally, our institution is a tertiary referral center, and some of our patients were followed up in their local hospitals. In some cases, it was difficult to retrieve patient follow-up information despite best efforts.

CONCLUSION

^{177}Lu-DOTATATE PRRT appears to be generally safe in NET patients with preexisting CKD 3. We found a low incidence of

grade 3 or 4 hematologic toxicity (9%) and permanent major nephrotoxicity (3%). The average annual eGFR loss was estimated at 2.5%. We found no significant risk factors for development of reduced renal function. In our cohort of CKD 3 NET patients, ^{177}Lu DOTATATE PRRT appears to have a good therapeutic effect, with PFS of 42 mo and overall survival of 47 mo. Most patients also had an improved quality of life.

DISCLOSURE

No potential conflict of interest relevant to this article was reported.

KEY POINTS

QUESTION: What are the efficacy and safety of ^{177}Lu-DOTATATE in patients with NETs and reduced renal function—that is, an eGFR below 60 mL/min/1.73 m^2?

PERTINENT FINDINGS: In this single-center retrospective analysis of 33 NET patients, a permanent reduction of more than 10% in eGFR of any grade was recorded in 45% of patients, with 1 patient (3%) developing grade 4 nephrotoxicity. No significant relationship was found between renal risk factors and a permanent reduction in renal function.

IMPLICATIONS FOR PATIENT CARE: There is a low incidence of grade 3 or 4 renal toxicity with ^{177}Lu-DOTATATE; therefore, patients with CKD 3 could be considered for treatment with ^{177}Lu-DOTATATE.

REFERENCES

1. Strosberg J, El-Haddad G, Wolin E, et al. Phase 3 trial of ^{177}Lu-Dotatate for midgut neuroendocrine tumors. *N Engl J Med.* 2017;376:125–135.
2. Brabander T, van der Zwan WA, Teunissen JJM, et al. Long-term efficacy, survival, and safety of [^{177}Lu-DOTA^0,Tyr^3]octreotate in patients with gastroenteropancreatic and bronchial neuroendocrine tumors. *Clin Cancer Res.* 2017;23:4617–4624.
3. Ezziddin S, Khalaf F, Vanezi M, et al. Outcome of peptide receptor radionuclide therapy with ^{177}Lu-octreotate in advanced grade 1/2 pancreatic neuroendocrine tumours. *Eur J Nucl Med Mol Imaging.* 2014;41:925–933.
4. Kwekkeboom DJ, de Herder WW, Kam BL, et al. Treatment with the radiolabeled somatostatin analog [^{177}Lu-DOTA^0,Tyr^3]octreotate: toxicity, efficacy, and survival. *J Clin Oncol.* 2008;26:2124–2130.
5. Annex I: summary of product characteristics. EMA website. https://www.ema.europa.eu/en/documents/product-information/lutathera-epar-product-information_en.pdf. Accessed July 7, 2022.
6. Rolleman EJ, Kooij PP, de Herder WW, Valkema R, Krenning EP, de Jong M. Somatostatin receptor subtype 2-mediated uptake of radiolabelled somatostatin analogues in the human kidney. *Eur J Nucl Med Mol Imaging.* 2007;34:1854–1860.
7. Bodei L, Mueller-Brand J, Baum RP, et al. The joint IAEA, EANM, and SNMMI practical guidance on peptide receptor radionuclide therapy (PRRNT) in neuroendocrine tumours. *Eur J Nucl Med Mol Imaging.* 2013;40:800–816.
8. Waldherr C, Pless M, Maecke HR, et al. Tumor response and clinical benefit in neuroendocrine tumors after 7.4 GBq ^{90}Y-DOTATOC. *J Nucl Med.* 2002;43:610–616.
9. Otte A, Herrmann R, Heppeler A, et al. Yttrium-90 DOTATOC: first clinical results. *Eur J Nucl Med.* 1999;26:1439–1447.
10. Valkema R, Pauwels SA, Kvols LK, et al. Long-term follow-up of renal function after peptide receptor radiation therapy with ^{90}Y-DOTA^0, Tyr^3-octreotide and ^{177}Lu-DOTA^0, Tyr^3-octreotate. *J Nucl Med.* 2005;46(suppl 1):83S–91S.
11. Annex I: summary of product characteristics. European Commission website. https://ec.europa.eu/health/documents/community-register/2017/20170926138665/anx_138665_en.pdf. Accessed July 7, 2022.
12. Svensson J, Berg G, Wängberg B, Larsson M, Forssell-Aronsson E, Bernhardt P. Renal function affects absorbed dose to the kidneys and haematological toxicity during ^{177}Lu-DOTATATE treatment. *Eur J Nucl Med Mol Imaging.* 2015;42:947–955.
13. CKD stages. UK Kidney Association website. https://renal.org/health-professionals/information-resources/uk-eckd-guide/ckd-stages. Accessed July 7, 2022.
14. EORTC QLQ – GI.NET21. EORTC website. https://www.eortc.org/app/uploads/sites/2/2018/08/Specimen-GI.NET21-English.pdf. Published 2004. Accessed July 7, 2022.
15. Eisenhauer EA, Therasse P, Bogaerts J, et al. New response evaluation criteria in solid tumours: revised RECIST guideline (version 1.1). *Eur J Cancer.* 2009;45:228–247.
16. Common Terminology Criteria for Adverse Events (CTCAE) version 5.0. NIH website. https://ctep.cancer.gov/protocoldevelopment/electronic_applications/docs/CTCAE_v5_Quick_Reference_8.5x11.pdf. Published November 27, 2017. Accessed July 7, 2022.
17. Ezziddin S, Attassi M, Yong-Hing CJ, et al. Predictors of long-term outcome in patients with well-differentiated gastroenteropancreatic neuroendocrine tumors after peptide receptor radionuclide therapy with ^{177}Lu-octreotate. *J Nucl Med.* 2014;55:183–190 .
18. Erbas B, Tuncel M. Renal function assessment during peptide receptor radionuclide therapy. *Semin Nucl Med.* 2016;46:462–478.
19. Frösss-Baron K, Garske-Roman U, Welin S, et al. ^{177}Lu-DOTATATE therapy of advanced pancreatic neuroendocrine tumors heavily pretreated with chemotherapy: analysis of outcome, safety, and their determinants. *Neuroendocrinology.* 2021;111:330–343.
20. Sansovini M, Severi S, Ianniello A, et al. Long-term follow-up and role of FDG PET in advanced pancreatic neuroendocrine patients treated with. *Eur J Nucl Med Mol Imaging.* 2017;44:490–499.
21. Bodei L, Kidd M, Paganelli G, et al. Long-term tolerability of PRRT in 807 patients with neuroendocrine tumours: the value and limitations of clinical factors. *Eur J Nucl Med Mol Imaging.* 2015;42:5–19.
22. Bergsma H, Konijnenberg MW, van der Zwan WA, et al. Nephrotoxicity after PRRT with ^{177}Lu-DOTA-octreotate. *Eur J Nucl Med Mol Imaging.* 2016;43:1802–1811.
23. Lindeman RD, Tobin J, Shock NW. Longitudinal studies on the rate of decline in renal function with age. *J Am Geriatr Soc.* 1985;33:278–285.
24. Glassock RJ, Winearls C. Ageing and the glomerular filtration rate: truths and consequences. *Trans Am Clin Climatol Assoc.* 2009;120:419–428.
25. Sundlöv A, Sjögreen-Gleisner K, Svensson J, et al. Individualised ^{177}Lu-DOTATATE treatment of neuroendocrine tumours based on kidney dosimetry. *Eur J Nucl Med Mol Imaging.* 2017;44:1480–1489.
26. Bergsma H, Konijnenberg MW, Kam BL, et al. Subacute haematotoxicity after PRRT with ^{177}Lu-DOTA-octreotate: prognostic factors, incidence and course. *Eur J Nucl Med Mol Imaging.* 2016;43:453–463.
27. Strosberg J, Wolin E, Chasen B, et al. Health-related quality of life in patients with progressive midgut neuroendocrine tumors treated with ^{177}Lu-Dotatate in the phase III NETTER-1 trial. *J Clin Oncol.* 2018;36:2578–2584.
28. Marinova M, Mücke M, Mahlberg L, et al. Improving quality of life in patients with pancreatic neuroendocrine tumor following peptide receptor radionuclide therapy assessed by EORTC QLQ-C30. *Eur J Nucl Med Mol Imaging.* 2018;45:38–46.

Heterogeneity of SSTR2 Expression Assessed by ^{68}Ga-DOTATOC PET/CT Using Coefficient of Variation in Patients with Neuroendocrine Tumors

Rosa Fonti[1,2], Mariarosaria Panico[1,2], Sara Pellegrino[2], Alessandro Pulcrano[2], Luisa Alessia Vastarella[2], Armin Hakkak Moghadam Torbati[2], Mario Giuliano[3,4], Giovannella Palmieri[4], Sabino De Placido[3,4], and Silvana Del Vecchio[2]

[1]*Institute of Biostructures and Bioimages, National Research Council, Naples, Italy;* [2]*Department of Advanced Biomedical Sciences, University of Naples "Federico II," Naples, Italy;* [3]*Department of Clinical Medicine and Surgery, University of Naples "Federico II," Naples, Italy; and* [4]*CRCTR Coordinating Rare Tumors Reference Center of Campania Region, AOU "Federico II," Naples, Italy*

High levels of somatostatin receptor subtype 2 (SSTR2) are a prerequisite for therapy with unlabeled or labeled somatostatin analogs. However, it is still unclear how the heterogeneity of SSTR2 expression may affect tumor response to therapy. The aim of our study was to test the ability of an imaging parameter such as coefficient of variation (CoV) derived from PET/CT with ^{68}Ga-peptides in the evaluation and quantification of the heterogeneity of SSTR2 expression within primary and metastatic lesions of patients with neuroendocrine tumors. **Methods:** Thirty-eight patients with pathologically proven neuroendocrine tumors who underwent ^{68}Ga-DOTATOC PET/CT were studied. Primary tumors were localized in the gastroenteropancreatic, bronchopulmonary, and other anatomic districts in 25, 7, and 6 patients, respectively. Malignant lesions were segmented using an automated contouring program and an SUV threshold of more than 2.5 or, in the case of liver lesions, a threshold of 30% of the SUV_{max}. The imaging parameters SUV_{mean}, CoV, SUV_{max}, receptor-expressing tumor volume, and total lesion receptor expression were obtained for each lesion. SUV_{mean}, CoV, and SUV_{max} were also obtained for representative volumes of normal liver and spleen, as well as for the whole pituitary gland. **Results:** In total, 107 lesions were analyzed, including 35 primary tumors, 32 metastatic lymph nodes, and 40 distant metastases. Average CoVs were 0.49 ± 0.20 for primary tumors, 0.57 ± 0.26 for lymph node metastases, and 0.44 ± 0.20 for distant metastases. The CoVs of malignant lesions were up to 4-fold higher than those of normal tissues ($P \leq 0.0001$). Among malignant lesions, the highest CoV was found for bone metastases (0.68 ± 0.20), and it was significantly greater than that of primary lesions ($P = 0.01$) and liver metastases ($P < 0.0001$). On the other hand, the lowest CoV was found for liver lesions (0.32 ± 0.07), probably because of the high background uptake. **Conclusion:** Our findings indicate that the heterogeneity of uptake, reflecting that of SSTR2, varies with the type and site of malignant lesions as assessed by CoVs obtained from ^{68}Ga-DOTATOC PET/CT scans. These observations may be related to different biologic characteristics of tumor lesions in the same patient—differences that may affect their response to treatment with both labeled and unlabeled somatostatin analogs.

Key Words: somatostatin receptor 2; heterogeneity; coefficient of variation; ^{68}Ga-peptide PET/CT; neuroendocrine tumors

J Nucl Med 2022; 63:1509–1514
DOI: 10.2967/jnumed.121.262928

Received Jul. 27, 2021; revision accepted Feb. 12, 2022.
For correspondence or reprints, contact Silvana Del Vecchio (delvecc@unina.it).
Published online Mar. 10, 2022.

Neuroendocrine neoplasms are a heterogeneous group of rare tumors arising from the diffuse neuroendocrine cell system and include both well-differentiated neuroendocrine tumors (NETs) and poorly differentiated carcinomas. Grading of NETs is essentially based on the rate of proliferation as assessed by Ki-67 staining (*1*). A common property of well-differentiated NETs is overexpression of somatostatin receptors (SSTRs), which constitute a target for therapy with unlabeled and β-emitter–conjugated somatostatin analogs (*2,3*).

SSTRs belong to the large family of G protein–coupled receptors that, on binding with their specific ligands, activate guanosine triphosphate–binding proteins, which, in turn, propagate a signaling cascade using different second-messenger systems (*4,5*). Of the 5 known SSTR subtypes, 1–5, the SSTR2 subtype is the most widely distributed in normal tissues and human tumors (*6*). High levels of SSTR2 have been found mainly in grade 1 and grade 2 NETs, for which a heterogeneous pattern of expression was also observed (*7,8*). Although previous studies showed that high levels of SSTR2 could predict a good response to therapy with somatostatin analogs and a prolonged survival (*7,8*), it is still unclear how the heterogeneity of SSTR2 expression within a lesion or among different lesions in the same patient may affect tumor response to therapy and clinical outcome.

SSTR2 displays a complex temporal and tissue-specific pattern of expression involving several growth and transcriptional factors, hormones, inflammatory cytokines, specific ligands, and microenviromental conditions (*4,9*). More recently, a growing body of evidence indicates that SSTR2 expression can be regulated by epigenetic mechanisms (*10,11*) such as DNA methylation and histone acetylation. Furthermore, upregulation of SSTR2 has been reported to occur through activation of NF-κB and MEK signaling pathways in a model of Epstein–Barr infection of nasopharyngeal carcinoma cells (*12*).

To test the predictive and prognostic value of intratumoral heterogeneity of SSTR2 expression and its possible role in the prediction and evaluation of peptide receptor radionuclide therapy response, some authors adopted a radiomic approach to extract several features from PET/CT scans acquired with ^{68}Ga-labeled analogs (*13–17*). In particular, one of these studies (*13*) found that 4 parameters—that is, entropy, correlation, short-zone emphasis, and homogeneity—were able to predict both progression-free survival and overall survival in patients who were candidates for peptide receptor radionuclide therapy. Furthermore, receptor-expressing tumor volume (RETV) could predict overall survival, whereas SUV_{max} and SUV_{mean} did not

correlate with survival. In another study (*16*), specific texture features derived from ^{68}Ga-DOTATOC and ^{18}F-FDG PET/CT, including intensity variability, size zone variability, zone percentage, entropy, homogeneity, dissimilarity, and coefficient of variation (CoV), were actually able to predict size, angioinvasion, and lymph node involvement in pancreatic NETs.

Among the texture features for the assessment of tumor heterogeneity, CoV is a simple and easy-to-calculate first-order parameter that indicates the percentage variability in SUV_{mean} within the tumor volume, reflecting the heterogeneity of tracer distribution and hence SSTR variability in ^{68}Ga-peptide examinations.

Although we are aware that radiomics is a powerful tool to characterize tumor heterogeneity and to extract clinically relevant subvisual information from PET images, the aim of the present study was to test the ability of a first-order parameter such as CoV derived from ^{68}Ga-peptide PET/CT scans to quantify the heterogeneity of SSTR2 expression within primary and metastatic lesions of NET patients.

MATERIALS AND METHODS

Patients

We studied 38 patients (25 men, 13 women; mean age, 60 ± 14 y; age range, 29–80 y) with pathologically proven NETs who underwent ^{68}Ga-DOTATOC PET/CT at our institution. The study was approved by the institutional review board, and all subjects signed an informed consent form. The patients were examined at the time of first diagnosis or during the course of disease, and 6 of them were reexamined during follow-up; in total, therefore, 44 ^{68}Ga-DOTATOC scans were obtained and evaluated. The primary tumor was localized in the gastroenteropancreatic district (25 patients: 16 pancreas, 6 midgut, and 3 mesentery), in the bronchopulmonary district (7 patients), or in other anatomic districts (6 patients). Tumor grade and Ki-67 proliferation index were available for 30 patients. Among them, 11 patients were classified as grade 1, 16 as grade 2, and 3 as grade 3; Ki-67 was less than 3% in 11 patients, between 3% and 20% in 16, and more than 20% in 3 (*1*). Ten patients had primary tumor only, 9 patients had lymph node but not distant metastases, and 19 patients had distant metastases with or without lymph node metastases. The patient characteristics are shown in Table 1. Seventeen ^{68}Ga-DOTATOC PET/CT scans were obtained for patients who had previously undergone surgery. When administered, previous treatments such as chemotherapy, temozolomide, or everolimus were discontinued at least 6 mo before the PET/CT scan. Furthermore, 18 scans were obtained for patients under treatment with somatostatin analogs using a standard regimen (30 mg intramuscularly once every 4 wk), because to avoid disease progression, discontinuation of therapy was not clinically recommended. In these patients, somatostatin analogs were administered on average 12.9 ± 7.6 (SD) days before the PET/CT scan, whereas the other patients receiving somatostatin analogs discontinued somatostatin analogs more than 1 mo before the scan.

TABLE 1
Patient Characteristics

Characteristic	Data
No. of patients	38
Age (y)	
Mean ± SD	60 ± 14
Range	29–80
Sex	
Female	13 (34%)
Male	25 (66%)
Type of NET	
Gastroenteropancreatic	25 (66%)
Bronchopulmonary	7 (18%)
Other	6 (16%)
Grade	
1	11 (29%)
2	16 (42%)
3	3 (8%)
Not determined	8 (21%)
Ki-67 (%)	
<3	11 (29%)
3–20	16 (42%)
>20	3 (8%)
Not determined	8 (21%)
Lesion sites per patient	
PT only	10 (26%)
PT + LNM	6 (16%)
PT + DM	6 (16%)
PT + LNM + DM	6 (16%)
LNM only	3 (8%)
DM only	3 (8%)
LNM + DM	4 (10%)

PT = primary tumor; LNM = lymph node metastases; DM = distant metastases.
Data are number, except for age.

^{68}Ga-DOTATOC Labeling

The radiopharmaceutical was prepared using a commercially available kit (SomaKit TOC; Advanced Accelerator Application) containing DOTATOC (edotreotide), a somatostatin analog with a high affinity for SSTR2. Edotreotide labeling was performed following the manufacturer's instructions. Briefly, ^{68}Ga-chloride eluted directly from a ^{68}Ge/^{68}Ga generator (Eckert and Ziegler Radiopharma GmbH) was added to 40 μg of peptide. The solution was immediately buffered and heated to 95°C for 7 min using a hot plate. Finally, the product was cooled at room temperature before use. All steps were performed under sterile conditions, and the final product was subjected to thin-layer chromatography to verify labeling efficiency. In all labeling procedures, the percentages of free and colloidal ^{68}Ga were no more than 2% and 3%, respectively.

^{68}Ga-DOTATOC PET/CT Study

Sixty minutes after intravenous administration of ^{68}Ga-DOTATOC (135 ± 25 MBq), patients underwent PET/CT using an Ingenuity TF scanner (Philips Healthcare). CT imaging was performed using the following parameters: 120 kV, 80 mA, a 0.8-s rotation time, and a pitch of 1.5. The PET scan was acquired in 3-dimensional mode, from the top of the skull to the upper thigh (3 min per bed position), at 6–8 bed positions per patient, depending on height. Images were iteratively reconstructed with ordered-subsets expectation maximization algorithm. Attenuation-corrected emission data were obtained using filtered backprojection of CT-reconstructed images. The resulting transaxial, sagittal, and coronal PET, CT, and fusion images were preliminarily examined using the Ingenuity TF software.

^{68}Ga-DOTATOC PET/CT Image Analysis

Images were transferred in DICOM format to a workstation equipped with the LIFEx program (*18*). All focal areas not attributable to physiologic uptake of ^{68}Ga-DOTATOC that showed morphologic or structural alterations on the corresponding CT images were considered positive. In cases of multiple liver or bone metastases, the lesion with the highest SUV_{max} was analyzed, whereas coalescent lymph nodes were considered a single lesion. A volume of interest (VOI) for each positive lesion was obtained by drawing a 3-dimensional region around the lesion using an automatic segmentation method (*19,20*) that groups all spatially connected voxels within a predefined threshold. In particular, an SUV threshold of more than 2.5 was used for all lesions on the basis of the mean SUV_{max} of the mediastinal blood pool plus 2 SDs. The exception was liver metastases, for which, because of the high physiologic liver uptake, a threshold of 30% of the SUV_{max} was used to avoid inclusion of normal parenchyma in the VOI (*21,22*). In addition, the accuracy of tumor delineation was confirmed on the corresponding CT images. By computed analysis of each VOI, the following parameters were obtained: SUV_{mean}, CoV (SD divided by SUV_{mean}), SUV_{max}, RETV, and total lesion receptor expression (TLRE), obtained by multiplying SUV_{mean} by RETV. In addition to tumor lesions, normal organs with high physiologic uptake were also analyzed, thus obtaining SUV_{mean}, CoV, and SUV_{max} in representative volumes of liver and spleen (using VOIs of the same size), as well as in the entire pituitary gland. Representative images of VOIs drawn around malignant lesions and within normal tissues are shown in Figure 1.

Statistical Analysis

Statistical analysis was performed using MedCalc software for Microsoft Windows, version 10.3.2.0. A P value of less than 0.05 was considered statistically significant. The Student t test was used to compare means of unpaired data.

RESULTS

Forty-four ^{68}Ga-DOTATOC PET/CT scans were acquired for 38 NET patients. In total, 107 lesions were analyzed, including 35 primary tumors (27 gastroenteropancreatic, 5 bronchopulmonary, and 3 in other anatomic districts), 32 lymph node metastases (20 regional and 12 nonregional), and 40 distant metastases (21 in the liver, 10 in the bones, and 9 in other anatomic sites [2 in the pancreas, 3 in the spleen, 2 in the peritoneum, 1 in the thyroid, and 1 in the retroperitoneum]) as shown in Table 2. The imaging parameters SUV_{mean}, CoV, SUV_{max}, RETV, and TLRE obtained for primary lesions, lymph node metastases, and distant metastases are shown in Table 3. In addition to tumor lesions, normal organs with high physiologic uptake such as liver, spleen, and pituitary gland were also analyzed, and the SUV_{mean}, CoV, and SUV_{max} are reported in Table 4.

We first examined the effects of treatment with somatostatin analogs on uptake in both tumor lesions and normal tissues by comparing the SUV_{max} obtained for patients undergoing ($n = 18$) or not undergoing ($n = 26$) therapy at the time of the ^{68}Ga-DOTATOC scan. As shown in Table 5, no statistically significant difference in the SUV_{max} for malignant lesions (primary tumors, lymph node metastases, and distant metastases) was found between treated and untreated patients. In contrast, uptake was significantly reduced in the normal liver ($P < 0.0001$), spleen ($P < 0.0001$), and pituitary gland ($P < 0.02$) of treated patients. These data indicate that administration of somatostatin analogs using a standard regimen reduces physiologic uptake of ^{68}Ga-DOTATOC in normal organs without affecting uptake in malignant lesions. Similarly, neither SUV_{mean} nor CoV in primary lesions ($P = 0.3515$ and 0.2718, respectively), lymph node metastases ($P = 0.4497$ and 0.0748, respectively), and distant metastases ($P = 0.1068$ and 0.2128, respectively) statistically differed between patients under treatment and those who were not. Therefore, the imaging parameters were analyzed in all patients as a whole group.

SUV_{mean} for primary lesions, lymph node metastases, and distant metastases was 8.70 ± 7.53, 8.38 ± 4.10, and 13.72 ± 9.90, respectively (Table 3). There was no statistically significant difference in SUV_{mean} between primary lesions and lymph node metastases ($P = 0.8507$), whereas both were significantly lower than distant metastases ($P = 0.0170$ and 0.0056, respectively). Moreover, CoVs for primary lesions, lymph node metastases, and distant metastases were 0.49 ± 0.20, 0.57 ± 0.26, and 0.44 ± 0.20, respectively (Table 3). There were no statistically significant differences in CoV between primary lesions and lymph node

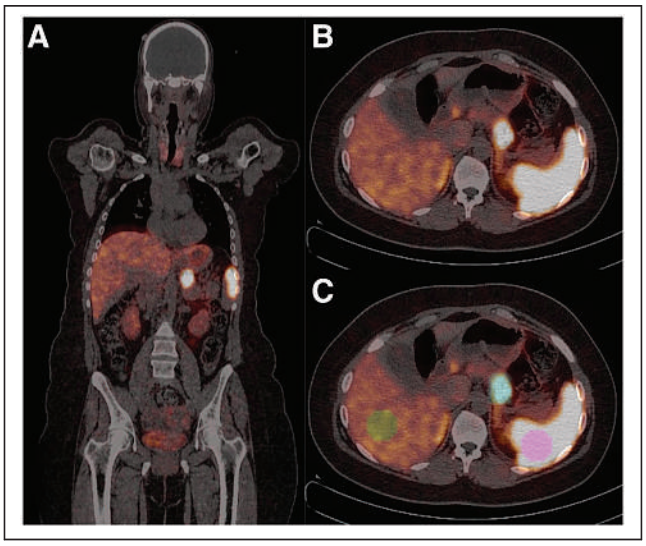

FIGURE 1. ^{68}Ga-DOTATOC PET/CT in patient with pancreatic NET. (A) Coronal image showing primary tumor. (B and C) Transaxial images of same section without (B) and with (C) overlay of VOIs drawn around primary tumor (blue VOI), within normal liver (green VOI), and within normal spleen (pink VOI).

TABLE 2
Type and Number of Lesions Analyzed on ^{68}Ga-DOTATOC PET/CT Images

Lesion type	*n*
Primary tumor	35
Gastroenteropancreatic tract	27
Bronchopulmonary tract	5
Other sites	3
Lymph node metastases	32
Regional basins	20
Nonregional basins	12
Distant metastases	40
Liver	21
Bone	10
Other sites	9
Total lesions	107

TABLE 3
Imaging Parameters Obtained by ^{68}Ga-DOTATOC PET/CT Analysis of Primary Tumors, Lymph Node Metastases, and Distant Metastases

Parameter	Mean ± SD	Median	Range	*P**
SUV_{max}				
Primary tumor	24.10 ± 19.51	16.60	4.78–88.31	T vs. N = 0.4559
Lymph node metastases	27.77 ± 20.51	21.51	3.00–82.04	N vs. M = 0.2256
Distant metastases	34.99 ± 27.89	28.26	3.98–115.55	M vs. T = 0.0573
SUV_{mean}				
Primary tumor	8.70 ± 7.53	6.86	3.29–42.72	T vs. N = 0.8507
Lymph node metastases	8.38 ± 4.10	8.05	1.41–18.31	N vs. M = 0.0056
Distant metastases	13.72 ± 9.90	12.44	1.68–43.41	M vs. T = 0.0170
CoV				
Primary tumor	0.49 ± 0.20	0.51	0.17–0.95	T vs. N = 0.1730
Lymph node metastases	0.57 ± 0.26	0.58	0.10–1.07	N vs. M = 0.0253
Distant metastases	0.44 ± 0.20	0.39	0.14–1.00	M vs. T = 0.3260
RETV (mL)				
Primary tumor	25.07 ± 34.75	10.69	2.43–178.24	T vs. N = 0.0879
Lymph node metastases	13.26 ± 17.42	7.04	0.80–82.04	N vs. M = 0.0044
Distant metastases	33.68 ± 36.04	18.97	2.11–136.25	M vs. T = 0.2972
TLRE (g)				
Primary tumor	309.83 ± 813.83	63.29	15.80–4766.19	T vs. N = 0.2616
Lymph node metastases	142.56 ± 195.34	71.25	2.99–766.21	N vs. M = 0.0028
Distant metastases	601.23 ± 816.25	258.38	3.56–2908.85	M vs. T = 0.1268

*Unpaired *t* test (T = primary tumor; N = lymph node metastases; M = distant metastases).

metastases ($P = 0.1730$) or distant metastases ($P = 0.3260$), whereas lymph node metastases had a significantly higher CoV than did distant metastases ($P = 0.0253$).

In a further analysis, distant metastases were divided into 3 subgroups, including liver, bone, and other metastatic lesions, and for each subgroup SUV_{mean} and CoVs were determined (Table 6). The average SUV_{mean} for liver, bone, and other metastatic lesions was 17.09 ± 11.61, 9.61 ± 6.40, and 10.45 ± 5.67, respectively. No statistically significant differences in SUV_{mean} were found among the 3 subgroups of distant metastases. The CoVs for liver, bone, and other metastatic lesions were 0.32 ± 0.07, 0.68 ± 0.20, and 0.47 ± 0.15, respectively. Bone metastases had a significantly higher CoV than either liver lesions ($P < 0.0001$) or metastases at

TABLE 4
Imaging Parameters Obtained by ^{68}Ga-DOTATOC PET/CT Analysis of Normal Organs with High Physiologic Tracer Uptake Such as Liver, Spleen, and Pituitary Gland

Parameter	Mean ± SD	Median	Range
SUV_{max}			
Liver	9.07 ± 3.45	9.37	3.12–19.90
Spleen	24.56 ± 11.61	21.89	5.23–46.35
Pituitary gland	6.03 ± 2.58	5.88	0.99–12.00
SUV_{mean}			
Liver	5.94 ± 2.60	5.82	1.84–11.27
Spleen	18.48 ± 9.71	18.89	3.00–35.63
Pituitary gland	3.95 ± 0.74	3.89	1.13–5.30
CoV			
Liver	0.16 ± 0.07	0.14	0.06–0.44
Spleen	0.16 ± 0.09	0.14	0.06–0.56
Pituitary gland	0.29 ± 0.11	0.26	0.09–0.63

TABLE 5
SUV_{max} in Malignant Lesions and Normal Tissues in Patients Treated or Not Treated with Somatostatin Analogs

Tissue type	No SSA therapy	SSA therapy	*P*
Primary lesion	25.08 ± 22.49	22.44 ± 13.75	NS
Lymph node metastasis	22.22 ± 22.25	31.57 ± 18.89	NS
Distant metastasis	22.49 ± 13.97	40.34 ± 30.74	NS
Normal liver	10.76 ± 3.11	6.55 ± 2.21	<0.0001
Normal spleen	32.40 ± 8.92	15.49 ± 6.69	<0.0001
Normal pituitary	7.03 ± 2.18	4.48 ± 2.43	<0.02

NS = not significant.
Data are mean ± SD.

TABLE 6
Imaging Parameters Obtained by ^{68}Ga-DOTATOC PET/CT Analysis of Liver, Bone, and Other Distant Metastases

Parameter	Mean ± SD	Median	Range	*P**
SUV_{max}				
Liver metastases	37.98 ± 31.13	28.49	6.87–115.55	L vs. B = 0.8234
Bone metastases	35.33 ± 29.61	18.83	3.98–94.90	B vs. O = 0.5038
Other metastases	27.61 ± 17.27	34.72	5.36–51.79	O vs. L = 0.3586
SUV_{mean}				
Liver metastases	17.09 ± 11.61	13.40	4.47–43.41	L vs. B = 0.0684
Bone metastases	9.61 ± 6.40	6.19	1.68–21.85	B vs. O = 0.7651
Other metastases	10.45 ± 5.67	14.23	3.43–16.54	O vs. L = 0.0600
CoV				
Liver metastases	0.32 ± 0.07	0.33	0.14–0.46	L vs. B < 0.0001
Bone metastases	0.68 ± 0.20	0.61	0.42–1.00	B vs. O = 0.0269
Other metastases	0.47 ± 0.15	0.50	0.20–0.65	O vs. L = 0.0006

*Unpaired *t* test (L = liver metastasis; B = bone metastases; O = other metastases).

other sites ($P = 0.0269$). A significant difference was also found between the CoVs for liver and the CoVs for other metastatic lesions ($P = 0.0006$). Therefore, the greatest heterogeneity of uptake reflecting SSTR expression was found in bone lesions, compared with the other distant metastases.

Furthermore, the CoV was significantly higher for bone metastases than for primary lesions ($P = 0.0132$) but did not significantly differ from that for lymph node metastases ($P = 0.2330$). In contrast, the CoV was significantly lower for liver metastases than for primary lesions ($P = 0.0005$) or lymph node metastases ($P = 0.0001$). On the other hand, no statistically significant differences in CoV were found between metastases at other sites and primitive lesions ($P = 0.8327$) or lymph node metastases ($P = 0.3138$). Finally, as expected, the mean CoV was significantly higher ($P \leq 0.0001$) for primary lesions, lymph node metastases, and distant metastases than for normal liver, spleen, and pituitary gland.

Values of conventional parameters such as SUV_{max} and volumetric parameters such as RETV and TLRE obtained for tumor lesions are shown in Table 3. SUV_{max} was 24.10 ± 19.51 for primary lesions, 27.77 ± 20.51 for lymph node metastases, and 34.99 ± 27.89 for distant metastases. No statistically significant differences in SUV_{max} were found among these 3 groups of lesions, although the SUV_{max} of distant metastases tended to be higher than that of primary lesions ($P = 0.0573$). RETV and TLRE were 25.07 ± 34.75 and 309.83 ± 813.83, respectively, for primary lesions; 13.26 ± 17.42 and 142.56 ± 195.34, respectively, for lymph node metastases; and 33.68 ± 36.04 and 601.23 ± 816.25, respectively, for distant metastases. RETV and TLRE were significantly greater for distant metastases than for lymph node metastases ($P = 0.0044$ and 0.0028, respectively), whereas RETV and TLRE did not significantly differ between primary lesions and lymph node metastases ($P = 0.0879$ and 0.2616, respectively) or distant metastases ($P = 0.2972$ and 0.1268, respectively).

DISCUSSION

Our study showed that all malignant lesions had up to a 4-fold higher CoV than normal tissues. In particular, the highest CoV was found for bone metastases, followed by lymph node metastases and primary lesions, reflecting the variable expression of SSTR depending on type and site of lesion. These findings suggest that, because of receptor heterogeneity among lesions, the biologic behavior of tumor cells may vary at different sites, leading to different patterns of tumor growth and progression and to different responses to targeted therapy with somatostatin analogs.

On the other hand, liver metastases, despite having the highest uptake, showed the lowest CoV among the 3 groups of distant metastases. The reason could be that metastatic cells infiltrate and proliferate within a tissue with a high and homogeneous physiologic uptake such as normal liver. In fact, to avoid inclusion of normal parenchyma in the tumor VOI, we used a percentage segmentation threshold different from that of all other lesions, and the accuracy of the tumor-contouring procedure was carefully checked on the corresponding CT images. However, it cannot be ruled out that normal liver parenchyma may be interspersed with clusters of metastatic cells within the lesion.

Previous studies evaluated the heterogeneity of SSTR expression by texture analysis determining the prognostic value of several texture parameters such as entropy and homogeneity in NET patients (*23,24*). In our study, we used a simple first-order parameter such as CoV that was able to reveal and quantitate the heterogeneity of receptor expression in malignant lesions, depending on their type and site. Furthermore, our observations may provide methodologic clues for texture analysis of NETs since metastatic lesions in different districts cannot be analyzed together because they can have a different predictive value on tumor response and final outcome due to significantly different heterogeneity. Moreover, using a texture analysis approach, the repeatability and reproducibility of texture features are a major issue. In this respect, CoV measurements depend on the same factors as those that affect conventional parameters such as SUV_{max} and SUV_{mean}, and we used an automated contouring program to standardize the procedure as much as possible.

The site-dependent pattern of SSTR2 heterogeneity in malignant lesions may be caused by the different microenvironmental conditions at the various sites. Accumulating evidence indeed indicates that a dynamic cross-talk exists between NET cells and tumor stroma, since NET cells produce a large spectrum of proangiogenic

and profibrotic factors inducing a high intratumoral microvascular density and fibrotic complications whereas stromal cells such as fibroblasts, endothelial cells, and inflammatory cells produce several growth factors and cytokines that can modulate proliferation and likely receptor expression in NET cells (*9*).

In our study, we also evaluated the possible effect of therapy with somatostatin analogs on the uptake of ^{68}Ga-peptide in tumor lesions and normal tissues. We showed that, between treated and untreated patients, there were no significant differences in SUV_{max} for primary lesions, lymph node metastases, and distant metastases, whereas SUV_{max} was significantly lower for normal liver, spleen, and pituitary gland in treated patients than in untreated patients. These findings indicate that administration of standard doses of somatostatin analogs reduces uptake of ^{68}Ga-peptide in high-capacity, low-affinity compartments such as normal liver and spleen but has no detectable effects on uptake in low-capacity, high-affinity compartments such as malignant lesions. It is likely that the standard doses of peptide usually prescribed to NET patients do not reach the large excess of cold peptide probably needed to compete with ^{68}Ga-peptide for receptor binding in tumor cells. On the other hand, it is well known that binding of somatostatin analogs to SSTR2 is followed by receptor internalization and that this process may reduce receptor density on the plasma membrane. However, there is evidence that prolonged treatment with somatostatin analogs may cause receptor upregulation (*5*), probably depending on cell context and microenviromental conditions. These findings taken together may be useful in clinical practice, as discontinuation of therapy with somatostatin analogs in patients undergoing PET/CT with ^{68}Ga peptides might be avoided without affecting the results of the diagnostic scan.

CONCLUSION

Our study showed that a simple parameter obtained by ^{68}Ga-DOTATOC PET/CT image analysis such as CoV allows the evaluation of uptake heterogeneity in tumor lesions in different anatomic districts. The heterogeneity of uptake reflects that of SSTR expression and may therefore be related to different biologic characteristics of tumor lesions in the same patient, potentially predicting a differential tumor response to treatment with both labeled and unlabeled somatostatin analogs.

DISCLOSURE

No potential conflict of interest relevant to this article was reported.

KEY POINTS

QUESTION: Can heterogeneity of SSTR2 expression easily be evaluated by ^{68}Ga-peptide PET/CT in a clinical context?

PERTINENT FINDINGS: Heterogeneity of SSTR2 was measured by CoV derived from ^{68}Ga-peptide PET/CT performed on NET patients. The highest CoV was found for bone metastases, followed by lymph node metastases and primary lesions.

IMPLICATIONS FOR PATIENT CARE: The heterogeneity of ^{68}Ga-DOTATOC uptake, reflecting that of SSTR2, varies with the type and site of malignant lesions and may affect the response to treatment with both labeled and unlabeled somatostatin analogs.

REFERENCES

1. Pavel M, Öberg K, Falconi M, et al. Gastroenteropancreatic neuroendocrine neoplasms: ESMO clinical practice guidelines for diagnosis, treatment and follow-up. *Ann Oncol.* 2020;31:844–860.
2. Strosberg J, El-Haddad G, Wolin E, et al. Phase 3 trial of ^{177}Lu-Dotatate for midgut neuroendocrine tumors. *N Engl J Med.* 2017;376:125–135.
3. Kong G, Hicks RJ. Peptide receptor radiotherapy: current approaches and future directions. *Curr Treat Options Oncol.* 2019;20:77.
4. Barnett P. Somatostatin and somatostatin receptor physiology. *Endocrine.* 2003;20:255–264.
5. Olias G, Viollet C, Kusserow H, Epelbaum J, Meyerhof W. Regulation and function of somatostatin receptors. *J Neurochem.* 2004;89:1057–1091.
6. Reubi JC, Waser B. Concomitant expression of several peptide receptors in neuroendocrine tumours: molecular basis for in vivo multireceptor tumour targeting. *Eur J Nucl Med Mol Imaging.* 2003;30:781–793.
7. Qian ZR, Li T, Ter-Minassian M, et al. Association between somatostatin receptor expression and clinical outcomes in neuroendocrine tumors. *Pancreas.* 2016;45:1386–1393.
8. Hu Y, Ye Z, Wang F, et al. Role of somatostatin receptor in pancreatic neuroendocrine tumor development, diagnosis, and therapy. *Front Endocrinol (Lausanne).* 2021;12:679000.
9. Cives M, Pelle' E, Quaresmini D, Rizzo FM, Tucci M, Silvestris F. The tumor microenvironment in neuroendocrine tumors: biology and therapeutic implications. *Neuroendocrinology.* 2019;109:83–99.
10. Klomp MJ, Dalm SU, de Jong M, Feelders RA. Hofland, Hofland LJ. Epigenetic regulation of somatostatin and somatostatin receptors in neuroendocrine tumors and other types of cancer. *Rev Endocr Metab Disord.* 2021;22:495–510.
11. Taelman VF, Radojewski P, Marincek N, et al. Upregulation of key molecules for targeted imaging and therapy. *J Nucl Med.* 2016;57:1805–1810.
12. Lechner M, Schartinger VH, Steele CD, et al. Somatostatin receptor 2 expression in nasopharyngeal cancer is induced by Epstein Barr virus infection: impact on prognosis, imaging and therapy. *Nat Commun.* 2021;12:117.
13. Werner RA, Lapa C, Ilhan H, et al. Survival prediction in patients undergoing radionuclide therapy based on intratumoral somatostatin-receptor heterogeneity. *Oncotarget.* 2017;8:7039–7049.
14. Önner H, Abdülrezzak U, Tutuş A. Could the skewness and kurtosis texture parameters of lesions obtained from pretreatment Ga-68 DOTA-TATE PET/CT images predict receptor radionuclide therapy response in patients with gastroenteropancreatic neuroendocrine tumors? *Nucl Med Commun.* 2020;41:1034–1039.
15. Weber M, Kessler L, Schaarschmidt B, et al. Treatment-related changes in neuroendocrine tumors as assessed by textural features derived from ^{68}Ga-DOTATOC PET/MRI with simultaneous acquisition of apparent diffusion coefficient. *BMC Cancer.* 2020;20:326.
16. Mapelli P, Partelli S, Salgarello M, et al. Dual tracer ^{68}Ga-DOTATOC and ^{18}F-FDG PET/computed tomography radiomics in pancreatic neuroendocrine neoplasms: an endearing tool for preoperative risk assessment. *Nucl Med Commun.* 2020;41:896–905.
17. Liberini V, Rampado O, Gallio E, et al. ^{68}Ga-DOTATOC-PET/CT-based radiomic analysis and PRRT outcome: a preliminary evaluation based on an exploratory radiomic analysis on two patients. *Front Med (Lausanne).* 2021;7:601853.
18. Nioche C, Orlhac F, Boughdad S, et al. LIFEx: a freeware for radiomic feature calculation in multimodality imaging to accelerate advances in the characterization of tumor heterogeneity. *Cancer Res.* 2018;78:4786–4789.
19. Fonti R, Larobina M, Del Vecchio S, et al. Metabolic tumor volume assessed by ^{18}F-FDG PET/CT for the prediction of outcome in patients with multiple myeloma. *J Nucl Med.* 2012;53:1829–1835.
20. Pellegrino S, Fonti R, Mazziotti E, et al. Total metabolic tumor volume by ^{18}F-FDG PET/CT for the prediction of outcome in patients with non-small cell lung cancer. *Ann Nucl Med.* 2019;33:937–944.
21. Fonti R, Conson M, Del Vecchio S. PET/CT in radiation oncology. *Semin Oncol.* 2019;46:202–209.
22. Liberini V, De Santi B, Rampado O, et al. Impact of segmentation and discretization on radiomic features in ^{68}Ga-DOTA-TOC PET/CT images of neuroendocrine tumor. *EJNMMI Phys.* 2021;8:21.
23. Bezzi C, Mapelli P, Presotto L, et al. Radiomics in pancreatic neuroendocrine tumors: methodological issues and clinical significance. *Eur J Nucl Med Mol Imaging.* 2021;48:4002–4015.
24. Saleh M, Bhosale PR, Yano M, et al. New frontiers in imaging including radiomics updates for pancreatic neuroendocrine neoplasms. *Abdom Radiol (NY).* October 23, 2020 [Epub ahead of print].

Analysis of Short-Term and Stable DNA Damage in Patients with Differentiated Thyroid Cancer Treated with ^{131}I in Hypothyroidism or with Recombinant Human Thyroid-Stimulating Hormone for Remnant Ablation

Alberto Signore[1], Giuseppe Campagna[1], Jessica Marinaccio[2], Marco de Vitis[2], Chiara Lauri[1], Francesco Berardinelli[2], Anna Tofani[1], Marco Chianelli[3], Marina Borro[4], Giovanna Gentile[4], Maurizio Simmaco[4], Francesco Colombini[5], Anna Giovanetti[6], and Antonella Sgura[2]

[1]*Nuclear Medicine Unit, Department of Medical-Surgical Sciences and of Translational Medicine, Faculty of Medicine and Psychology, University of Rome "Sapienza," Rome, Italy;* [2]*Department of Science, University of Rome "Roma Tre," Rome, Italy;* [3]*Unit of Endocrinology, Regina Apostolorum Hospital, Rome, Italy;* [4]*Department of Neurosciences, Mental Health, and Sensory Organs, Faculty of Medicine and Psychology, University of Rome "Sapienza," Rome, Italy;* [5]*Diacron International SRL, Grosseto, Italy; and* [6]*ENEA, Division of Health Protection Technologies, Casaccia Research Centre, Rome, Italy*

It is well known that ionizing radiation can induce genetic damage and that oxidative stress is a major factor inducing it. Our aim was to investigate whether thyroid remnant ablation with low activities of ^{131}I (1,850 MBq) is associated with DNA damage by evaluating the CometAssay, micronuclei, and chromosome aberrations with multicolor fluorescent in situ hybridization. **Methods:** We studied 62 patients prepared with recombinant human thyroid-stimulating hormone (rhTSH) or by thyroid hormone withdrawal. In both groups, we analyzed stable and unstable genetic alterations before ^{131}I therapy and 1 wk and 3 mo after ^{131}I administration. We also correlated the genetic damage with several variables, including the degree of radiation-induced oxidative stress, genetic polymorphisms of enzymes involved in DNA repair, and antioxidative stress. **Results:** We found a comparable amount of DNA breaks evaluated by CometAssay and micronuclei testing in both groups of patients at different time points, but there was a significant increase in stable chromosome aberrations evaluated by multicolor fluorescent in situ hybridization (breaks and translocations) in patients prepared with thyroid hormone withdrawal. Overall, high chromosome damage was associated with higher retained body radioactivity and unfavorable gene polymorphism. A high level of free oxygen radicals and a low level of antioxidants were found in all patients at any time point. In particular, patients prepared with thyroid hormone withdrawal, at 3 mo, had significantly higher levels of free oxygen radicals than those prepared with rhTSH. **Conclusion:** An increase in stable chromosome aberrations with respect to baseline is detectable after administration of low doses of ^{131}I in patients prepared with thyroid hormone withdrawal but not in patients prepared with rhTSH. The clinical significance of these chromosomal alterations remains to be determined.

Key Words: ^{131}I; radiation-induced genetic damage; hypothyroidism; rhTSH; gene polymorphism; free oxygen radicals

Received Oct. 27, 2021; revision accepted Jan. 12, 2022.

For correspondence or reprints, contact Alberto Signore (alberto.signore@uniroma1.it).

Published online Feb. 3, 2022.

J Nucl Med 2022; 63:1515–1522
DOI: 10.2967/jnumed.121.263442

In clinical practice, ^{131}I is used for thyroid remnant ablation in patients who undergo thyroidectomy for differentiated thyroid carcinoma. Radionuclide therapy has been reported to induce harmful effects on cells and tissues (*1–7*). Indeed, several reports have shown chromosomal damage induced by ^{131}I, although only chromosomes 1, 2, 4, 8, and 10 have been analyzed (*8–12*). Despite this controversial issue (*3,5,13–19*), a significant reduction in ablative treatments has been observed in the last decade. Therefore, it is important to better elucidate the possible presence of stable genetic damage and of radioinduced oxidative stress after treatment with ^{131}I. Furthermore, gene polymorphisms that alter the repair of DNA damage should also be investigated (*20*).

Recombinant human thyroid-stimulating hormone (rhTSH) has effectively been used for exogenous stimulation before ^{131}I ablation therapy, although it is not yet widely used for preparation of patients receiving high therapeutic amounts of radioiodine (*5*). The main aim of this study was to investigate whether the relatively low administered activities of ^{131}I for thyroid remnant ablation are associated with some stable chromosome damage. Secondary aims were to analyze the level of baseline (i.e., before remnant ablation) genetic damage and oxidative stress in patients with differentiated thyroid carcinoma; to evaluate the role of different DNA repair and antioxidative genes in the occurrence of genetic damage and oxidative stress by analyzing genetic polymorphisms in patients; and to evaluate whether the yield of damage is comparable in patients prepared by rhTSH or by hypothyroidism.

MATERIALS AND METHODS

Patients

A group of 62 patients to be treated with 1,850 MBq (50 mCi) of ^{131}I were randomly assigned to 2 cohorts: 31 patients in hypothyroidism (HYPO group) (40-d suspension of levothyroxine and replacement with triiodothyronine for the first 25 d) and 31 patients in euthyroidism

injected with rhTSH (rhTSH group) (1 mg 2 d before ^{131}I and 1 mg 1 d before ^{131}I).

Patients were matched for age, sex, pathologies, and lifestyle habits; were nonsmokers; and were being administered no drugs. Patients with other primary tumors or previously treated with radiotherapy or receiving drugs with an effect on oxidative status or on the immune system were excluded. All patients were on a low-iodine diet for 10 d before therapy. The study was approved by local Ethics Committee (approvals 736/2014 and 241 SA_2017), and all subjects gave written informed consent. Patient recruitment lasted 15 mo; the study was completed in 2 y.

The radiation exposure rate was measured at a 1-m distance at the time of ^{131}I administration (baseline), after 24 h, and after 48 h, as an indirect measurement of residual body activity. Patients with less than 20 μSv/h at 48 h were discharged from the hospital. Those with more than 20 μSv/h were counted again after 72 h.

Sampling

In all patient cohorts, 10 mL of blood were withdrawn in lithium heparin.

Before treatment with ^{131}I in euthyroidism (when sampling for therapeutic purposes was scheduled), blood was immediately processed for micronuclei, translocations, DNA breaks (CometAssay; Bio-Techne Corp.), thyroglobulin levels, creatinine, glomerular filtration rate estimated with the Chronic Kidney Disease Epidemiology Collaboration formula (epi-GFR) (*21*), thyroid stimulating hormone (TSH), plasma reactive oxygen metabolite-derived compounds (d-ROMs), plasma anti–reactive oxygen metabolite potential (anti-ROMs), and single-nucleotide polymorphisms (SNPs).

One week after ^{131}I treatment (when sampling for therapeutic purposes was scheduled), blood was immediately processed for micronuclei, CometAssay, d-ROMs, and anti-ROMs.

Three months after ^{131}I treatment (when sampling for follow-up purposes was scheduled), blood was processed for micronuclei, translocations, CometAssay, thyroglobulin, TSH, d-ROMs, and anti-ROMs.

Cell Culture Conditions

Half-milliliter blood samples from patients were diluted with 4.5 mL of complete medium in a culture flask and incubated at 37°C in a humidified atmosphere with 5% CO_2. The culture medium was RPMI 1640 (Euroclone) supplemented with 20% heat-inactivated fetal bovine serum (Euroclone), penicillin (10,000 units/mL) and streptomycin (10 mg/mL) (Biologic Industries), and 1% L-glutamine (Euroclone). T lymphocytes were stimulated to divide for 72 h using 2% phytohemagglutinin (Gibco) in the culture medium.

Micronucleus Assay

To obtain binucleated cells, cytochalasin B (6 μg/mL) (Sigma Aldrich) was added to the culture medium 24 h before harvesting, as previously described (*22*). Briefly, cells were pelleted by centrifugation (8 min at 12,000 rpm), resuspended in 0.075 M KCl, and incubated for 2 min at 37°C. The suspension was fixed 3 times in freshly prepared modified Carnoy solution (5:1 v/v methanol/acetic acid). Binucleated cells were dropped onto slides, air-dried, and counterstained with 4,6-diamidino-2 phenylindole (Sigma Aldrich) in Vectashield antifade (Vector Laboratories). Micronuclei were identified according to the following criteria: the micronuclei were in cytoplasm and had a diameter of less than a third of the whole nucleus; they were circular or oval, and their staining and refractivity were in accordance with that of the whole nucleus; and their structures were similar to those of the whole nucleus, with complete separation and no other nearby fragments or impurities. Images were captured with the Metacyte module of Metafer automated capture software (MetaSystems) at ×40 magnification using an Axio Imager Z1 microscope (Zeiss) equipped with a Cool Cube 1 (charge-coupled device) camera (MetaSystems). At least 1,000 binucleated cells for each patient were analyzed under each experimental condition.

CometAssay

The CometAssay technique was used to evaluate the frequency of double-strand breaks and single-strand breaks induced by ^{131}I.

The alkaline CometAssay was performed as described by Giovanetti et al. (*23*). Twenty microliters of whole blood were gently resuspended in 180 μL of 0.7% low-melting-point agarose in phosphate-buffered saline (calcium- and magnesium-free) at 38°C and immediately pipetted onto a warm frosted glass microscope slide precoated with a layer of 1% normal-melting-point agarose in phosphate-buffered saline. Coverslips were applied, and the slides were set at 4°C to solidify the agarose. The coverslips were then removed, and the slides were incubated in a lysis solution (2.5 M NaCl, 10 mM Tris-HCl, 100 mM Na_2 ethylenediaminetetraacetic acid, NaOH to pH 10, 1% Triton X-100 (Thermo Fisher Scientific), and 10% dimethyl sulfoxide) for 45 min. After this step, all the operations were performed at 4°C under dim light. After lysis, the slides were rinsed for 10 min with electrophoresis buffer (1 mM Na_2-ethylenediaminetetraacetic acid, 300 mM NaOH, pH 13) and placed for 20 min onto a horizontal electrophoresis unit containing the same electrophoresis buffer to allow DNA unwinding. Electrophoresis was conducted with the Sub-Cell GT System (15 Å to ~25 cm) equipped with Power Pack 300 (Bio-Rad Laboratories Inc.) for 15 min (25 V, 300 mA). Subsequently, the slides were gently washed in neutralization buffer solution for 5 min (0.4 M Tris-HCl, pH 7.5), dehydrated with an ethanol series (70%, 85%, and 100%), dried at room temperature, and stored. When not otherwise indicated, all chemicals were purchased from Sigma Aldrich.

For microscopy analysis, the slides were stained with ethidium bromide (10 μg/mL) immediately before being analyzed at ×400 magnification by a fluorescent Axiolab Zeiss microscope (Carl Zeiss AG).

The slides were analyzed using a fluorescence microscope (Leica) equipped with a camera. On each slide, coded and (with masking) scored, 200 comets were acquired using the I.A.S. software automatic image analysis system (Delta Sistemi).

Collection of Chromosome Spreads and Multicolor Fluorescent In Situ Hybridization (M-FISH)

The M-FISH analysis was used to quantify stable genomic damage due to ^{131}I. We analyzed the following in particular: exchanges (both simple exchanges, caused by 2 breaks on 2 different chromosomes [reciprocal and nonreciprocal], and complex exchanges, due to 3 or more breaks on 2 or more chromosomes); acentric fragments; and total breaks (as the total number of breakpoints involved in simple and complex exchanges and acentric fragment observed).

Chromosome spreads were obtained after 3 h of incubation in 5×10^6 M colchicine (Sigma Aldrich). Metaphase spreads were prepared following standard cytogenetic procedures, consisting of treatment with a hypotonic solution (0.075 M KCl) for 20 min at 37°C followed by fixation in freshly prepared Carnoy solution (3:1 v/v methanol/acetic acid).

Fixed cells were dropped onto glass slides and hybridized with the 24XCyte Human M-FISH Probe Kit (MetaSystems), as previously reported (*24,25*). Briefly, the slides were denatured in 0.07N NaOH and then rinsed in a graded ethanol series. Meanwhile, the probe mix was denatured using an MJ mini personal thermal cycler (Bio-Rad Laboratories) with the following program: 5 min at 75°C, 30 s at 10°C, and 30 min at 37°C. Probes were added to the slides, and a coverslip was added and sealed using rubber cement. Samples were then hybridized in a humidified chamber at 37°C for 48 h, washed in saline–sodium citrate buffer for 5 min at 75°C, and counterstained with 4,6-diamidino-2 phenylindole (Sigma Aldrich) in Vectashield antifade (Vector Laboratories). Finally, images were captured with the M-search module of

Metafer software (MetaSystems) at ×63 magnification using an Axio Imager Z1 microscope (Zeiss) equipped with a Cool Cube 1 camera (MetaSystems). At least 100 metaphases were analyzed for each patient under each experimental condition. The karyotyping and cytogenetic analyses of each single chromosome were performed using the ISIS software (MetaSystems).

Genotyping (SNPs)

Genomic DNA was isolated from blood samples using the X-tractor Gene system (Corbett Life Science). Reference sequences for each gene were obtained from NCBI GenBank database. The sequences of selected primers are reported in Supplemental Tables 1 and 2 (supplemental materials are available at http://jnm.snmjournals.org). Locus-specific PCR and extension primers were designed by Genotyping Tools and the MassArray Assay Design 4.0 software (Sequenom Inc.).

The SNPs analyzed were XRCC1 G28152A (rs25487), XRCC3 A4541G (rs1799794), XRCC3 C18067T (rs861539), and RAD51 G315C (rs1801320) for enzymes used to repair single-strand DNA breaks (DNA1 package) and CAT C-262T (rs1001179), OGG1 Ser326Cys (rs1052133), NOS3 Glu298Asp (rs1799983), PON1 A575G (rs662), PON1 C-108T (rs705379), and MPO G-463A (rs2333227) for enzymes used to scavenger activity of free oxygen (DNA2 package).

Genotyping of XRCC1 G28152A (rs25487), XRCC3 A4541G (rs1799794), XRCC3 C18067T (rs861539), and RAD51 G315C (rs1801320) was performed by pyrosequencing technology, using the PyroMark Q48 Autoprep system (Qiagen) according to manufacturer directions. Both the amplification and the sequencing primers were obtained by the PSQ Assay Design software (Qiagen).

The region covering the SNPs of interest was amplified by polymerase chain reaction (PCR). The PCR conditions were 95°C for 3 min, 40 cycles with denaturation at 95°C for 30 s, annealing at 56°C for 30 s, elongation at 72°C for 30 s, and a final extension step at 72°C for 5 min. PCR was performed in a final volume of 25 μL, containing 70 ng of genomic DNA, 10 pmol of each primer, 0.2 mM dNTPs, PCR buffer, 1 U of Taq DNA polymerase (Takara Bio Inc.), and 1 mM $MgCl_2$ for XRCC1 G28152A, XRCC3 C18067T, and RAD51 G315C, whereas 1.5 mM $MgCl_2$ was used for XRCC3 A4541G amplification (*26*).

The other SNPs were genotyped by the Sequenom MassArray iPLEX platform (Sequenom). Twenty nanograms of genomic DNA were standardized for genotyping of each sample. According to the manufacturer's instructions, the DNA samples were amplified by a multiplex PCR and treated with shrimp alkaline phosphate. The PCR products were then used for locus-specific single-base extension reaction. The resulting products were desalted and transferred to a 96-SpectroCHIP array. The alleles were discriminated by matrix-assisted laser desorption ionization time-of-flight mass spectrometry. Data were processed and analyzed by Sequenom MassArray TYPER 4.0 software.

For each heterozygote mutation, we assigned a score of 0.5, and for each homozygote mutation, we assigned a score of 1. The total mutation score for DNA-1 and DNA-2 enzyme packages was calculated for each patient.

Oxidative Stress and Antioxidant Capacity

d-ROMs and anti-ROMs were measured with Diacron kits (Diacron International). The d-ROMs test measures the oxidant ability of a plasma sample toward a particular substance (modified aromatic amine) used as an indicator (chromogen). The change in absorbance per unit time (calculated on the basis of a serum with known title) is expressed in conventional units (CARR U). The reference range is less than 300 CARR U (*27*).

The anti-ROMs test measures the antioxidant capacity of plasma, expressed as iron-reducing activity. The method has been engineered to have 2 phases: the first phase (first minute) provides the value of the so-called fast antioxidants (anti-ROMsF) (i.e., those that act quickly, such as vitamin C or vitamin E), and the second phase provides the value of the so-called slow antioxidants (anti-ROMsS) (such as thiol groups, sulfhydryl groups [-SH], uric acid, or polyphenols). The test reference values in a healthy population are more than 200 μEq/L for fast antioxidants and more than 1,000 μEq/L for slow antioxidants (*28*).

Statistical Analysis

Sample size was calculated on the basis of the results of M-FISH translocations observed in an unpublished previous pilot study on 10 patients. We hypothesized a clinically meaningful difference of 0.8 for $\mu_{HYPO} - \mu_{rhTSH}$, with an SD of 1.1 and setting α to 0.05 with 80% power. The calculated total sample size was 62 patients, namely 31 per group.

Continuous variables are presented as mean ± SD when data were normally distributed or as median and 95% CI otherwise. Categoric variables are expressed as absolute frequencies and percentages.

The association of group (HYPO vs. rhTSH) with sex, pT1, pT3, and papillary and follicular histologic type was evaluated by the χ^2 test, whereas the association with pT2, pT4, and N1 was evaluated by the Fisher exact test because the expected frequencies were less than 5. The Shapiro–Wilk test was used to test the normality of the continuous variables and of the residuals, whereas homoscedasticity was verified by checking the studentized residuals. For continuous variables, differences between groups (HYPO vs. rhTSH) were compared by the Student *t* or Mann–Whitney test. A generalized linear mixed model for repeated measures with a gaussian distribution and an identity link was used to verify differences in d-ROMs, anti-ROMsS, and anti-ROMsF at baseline, 1 wk, and 3 mo in the HYPO group versus the rhTSH group. The Tukey method was used to correct the *P* values for multiple comparisons.

To understand which variables may influence the break or total exchange at the 3-mo time point in HYPO and rhTSH patients, we used a generalized linear mixed model with a negative binomial function and a logarithmic link, with independent variables consisting of age; sex; breaks or total exchanges at baseline; radiation exposure rate at 48 h; anti-ROMsF, anti-ROMsS, and d-ROMs at baseline and 3 mo; and DNA-1, DNA-2, and epi-GFR at baseline.

To evaluate differences in micronuclei and CometAssay between the 3 temporal points (baseline, 1 wk, and 3 mo) relative to HYPO versus rhTSH, we applied a generalized linear mixed model for repeated measures with a negative binomial/gaussian distribution and a logarithmic/identity link (respectively), and the Tukey method was used to correct for multiple comparisons.

Finally, a generalized linear mixed model with a negative binomial distribution and a logarithmic link was used to assess differences in breaks and total exchanges between baseline and 1 wk in the HYPO group versus the rhTSH group. The Tukey method was used to correct for multiple comparisons.

A *P* value of less than 0.05 was considered statistically significant. Data were analyzed by SAS, version 9.4 (SAS Institute Inc.).

RESULTS

All patients completed the 1-y follow-up. None dropped out, but 2 patients did not consent to analysis of DNA polymorphisms, and in 3 patients of the rhTSH group we did not measure d-ROMs and anti-ROMs. The mean age of the 2 groups did not significantly differ (Table 1), but a significant difference was seen in the levels of TSH, thyroglobulin at the time of ^{131}I, creatinine, and epi-GFR.

Administration of rhTSH was well tolerated. All patients had efficient ablation as evaluated by unstimulated thyroglobulin levels at 3 mo after therapy and by rhTSH-stimulated thyroglobulin levels at the 12-mo follow-up.

TABLE 1
Differences in Clinical and Biochemical Variables Between HYPO and rhTSH Groups

Variable	HYPO	rhTSH	*P*
Age (y)	47.64 ± 11.18 (43.54–51.75)	48.64 ± 11.53 (44.42–52.87)	0.73
Sex			0.32
Male	4 (12.90%)	7 (22.58%)	
Female	27 (87.10%)	24 (77.42%)	
pT1	18 (58.06%)	20 (64.52%)	0.60
pT2	5 (16.13%)	1 (3.23%)	0.19
pT3	7 (22.58%)	10 (32.26%)	0.39
pT4	1 (3.23%)	0 (0.00%)	1.00
Papillary histologic type	20 (64.52%)	19 (61.29%)	0.79
Follicular histologic type	11 (35.48%)	12 (38.71%)	0.79
N1	2 (6.45%)	4 (12.90%)	0.67
TSH at ^{131}I (μU/mL)	87.37 (76.62–99.72)	112.80 (98.84–135.80)	0.01
Thyroglobulin at ^{131}I (ng/mL)	0.79 (0.25–2.77)	0.25 (0.20–0.34)	0.008
Thyroglobulin at 3 mo (ng/mL)	0.10 (0.10–0.10)	0.10 (0.10–0.10)	0.53
Exposure rate at 24 h (mSv/h)	33 (28–37)	24 (20–28)	<0.0001
Exposure rate at 48 h (mSv/h)	16 (12–18)	9 (8–9)	<0.0001
Creatinine (mg/mL)	0.98 (0.85–1.05)	0.76 (0.72–0.80)	<0.0001
Epi-GFR (mL/min)	74.77 ± 17.50 (68.36–81.19)	97.61 ± 12.50 (93.03–102.20)	<0.0001

Qualitative data are number and percentage; continuous data are mean ± SD or median and 95% CI.

The radiation exposure rate at 1 m was higher in HYPO patients on days 1 and 2 than in rhTSH patients (median, 36 vs. 24 μSv/h on day 1 and 16 vs. 9 μSv/h on day 2; both $P < 0.0001$; Table 1). Most patients were dismissed on day 2, but 4 patients from the HYPO group were dismissed on day 3 and 11 patients from the rhTSH group were dismissed on day 1, confirming the lower residual body activity in rhTSH patients than in HYPO patients. The calculated area under the curve for the exposure rate through 120 h was 27% lower in rhTSH patients than in HYPO patients, reflecting lower residual body activity (Fig. 1).

Micronucleus and CometAssay

Micronucleus values did not differ between the HYPO and rhTSH group or between the same group at 1 wk and 3 mo after treatment (Fig. 2).

The CometAssay showed no differences between the HYPO and rhTSH groups. However, all patients showed a statistically significant increase in damage at 1 wk ($P < 0.0001$), followed by a reduction at 3 mo ($P < 0.0001$), although not yet reaching the basal values (Fig. 3).

M-FISH

Results are reported in Figure 4 and Table 2. In particular, breaks and total exchanges in patients belonging to the HYPO group significantly increased from the basal sample to the 3-mo sample (in both, $P = 0.004$). By contrast, in patients belonging to the rhTSH group, no significant increase in breaks or total exchanges was found between the basal sample and the 3-mo sample. Overall, 19 of 32 patients from the rhTSH group had no increase or even a reduction in the number of chromosome breaks, as compared with 8 of 32 patients from the HYPO group. If we consider the total exchanges, 23 of 32 patients from the rhTSH group had no increase or even a reduction in the number of chromosome exchanges, as compared with 11 of 32 patients from the HYPO group.

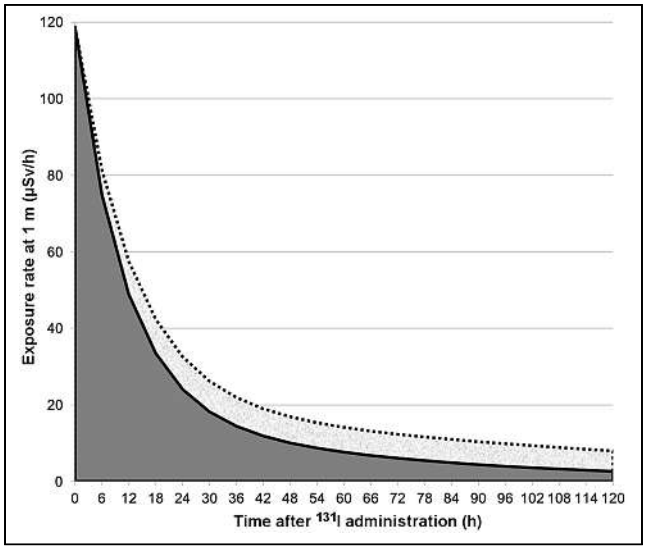

FIGURE 1. Results of fitted radiation exposure rate in patients, up to 120 h, measured at 1-m distance. Dotted line represents HYPO patients; solid line represents rhTSH patients. In HYPO patients, there is increased retained body activity with respect to rhTSH patients, with 27% higher exposure rate, calculated comparing 2 areas under curves.

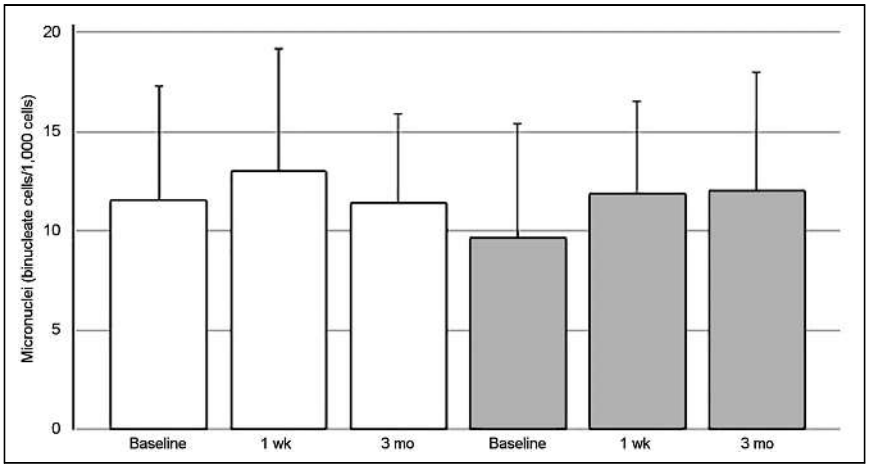

FIGURE 2. Results of micronucleus measurement (white bars, HYPO; gray bars, rhTSH). No differences exist between or within groups. Tukey method was used to correct for multiple comparisons.

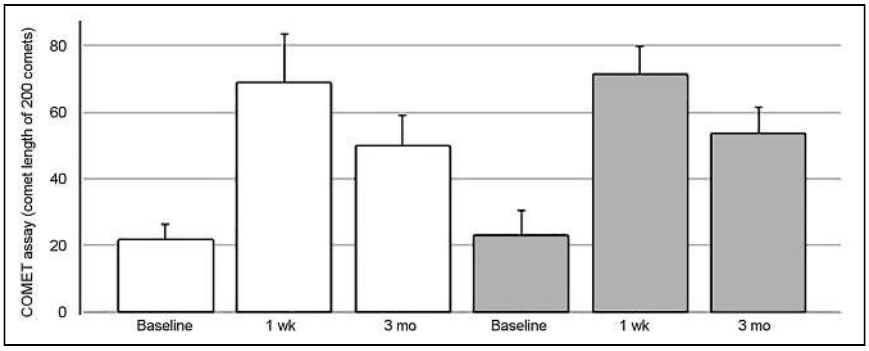

FIGURE 3. Results of CometAssay (white bars, HYPO; gray bars, rhTSH). Significant differences were found between baseline and 1 wk, between 1 wk and 3 mo, and between baseline and 3 mo in both groups (all $P < 0.0001$). Tukey method was used to correct for multiple comparisons.

Table 2 shows the results of the generalized linear mixed model of breaks and total exchanges at 3 mo in HYPO and rhTSH patients. In the HYPO group, anti-ROMs at 1 wk were negatively associated with breaks at 3 mo (with a reduction of 0.3%; $P = 0.046$), whereas the exposure rate at 48 h was positively associated with the response variable, with an increase of 6.2% ($P = 0.016$). Total chromosome exchanges at 3 mo in the HYPO group were negatively associated with anti-ROMs at 1 wk, with a reduction of 0.9% ($P = 0.015$), and were positively associated with DNA-1, with an increase of 127.5% ($P = 0.027$). The exposure rate at 48 h was positively associated with the response variable, with an increase of 0.2% ($P = 0.046$). Finally, in the rhTSH group, only exposure rate at 48 h was positively associated with breaks at 3 mo in the rhTSH group, with an increase of 95.4% ($P = 0.04$).

No association was observed between total exchanges at 3 mo in the rhTSH group and the analyzed covariates.

Genotyping (SNPs)

In the HYPO patient group, 11 patients had a total DNA score (DNA-1 + DNA-2) of 3 or higher, but in the rhTSH patient group, 17 patients had a total DNA mutation score of 3 or higher, indicating a higher frequency of mutations in rhTSH patients. These polymorphisms were observed predominantly in genes of the DNA-2 package (for the antioxidative stress enzymes) and, indeed, positively influenced the number of chromosome breaks at 3 mo in rhTSH patients.

Nevertheless, in the HYPO subgroup with a DNA mutation score of at least 3, chromosome breaks measured by the M-FISH technique increased from 2.3 ± 2.2 (mean basal sample) to 5.5 ± 2.8 (3-mo sample) ($P = 0.01$), as compared with rhTSH patients (with DNA mutation score ≥ 3), in whom the frequency of chromosome exchange breaks increased from 6.6 ± 8.1 (basal sample) to 8.5 ± 8.6 (3-mo sample) ($P =$ not statistically significant).

Chromosome total exchanges in these HYPO patients also significantly increased from 1.0 ± 1.1 to 2.1 ± 1.1 (basal vs. 3-mo sample) ($P = 0.03$), as compared with rhTSH patients, in whom the frequency of chromosome exchange breaks increased from 2.1 ± 3.0 to 3.3 ± 4.6 (basal vs. 3-mo sample) ($P =$ not statistically significant).

Oxidative Stress

Overall, most patients had high levels of d-ROMs and low levels of anti-ROMs at any time point, with no significant differences between HYPO patients and rhTSH patients at baseline and 1 wk but higher values in HYPO patients at 3 mo ($P = 0.03$) (Table 3). Only 3 HYPO patients and 4 rhTSH patients had normal d-ROM values at entry, highlighting the high level of stress induced by cancer, surgery, and the postsurgical period (including hypothyroidism in HYPO patients) or supraphysiologic thyroxine replacement.

In HYPO patients, we observed a reduction in oxidative stress at 1 wk, with a statistically significant decrease in d-ROMs versus baseline ($P = 0.0001$). However, at 3 mo, HYPO patients had a new significant increase in d-ROMs as compared with values at 1 wk ($P < 0.0001$). These differences were not observed in rhTSH patients.

As far as anti-ROMsF and anti-ROMsS are concerned, we did not observe significant differences between HYPO and rhTSH patients or significant modifications over time. However, most patients had anti-ROM values below the level of reference ranges at any time, presumably as a result of the high stress level in these patients.

DISCUSSION

Several papers have been published on the potential genetic damage and on the increased risk of secondary cancer in patients treated with ^{131}I, even if with low activities (*1–20*), although the causative association between ^{131}I therapy and an increased risk of secondary cancers has not yet been definitively established. Indeed, no longitudinal study has been published indicating that an increase in chromosome breaks or translocations after ^{131}I therapy is associated with an increased risk of malignancies. Nevertheless, there is a worldwide tendency to reduce ^{131}I ablation in patients with a low or intermediate risk after total thyroidectomy for differentiated thyroid carcinoma.

Structural aberrations generated by DNA double-strand breaks can be classified as stable or unstable according to their ability to

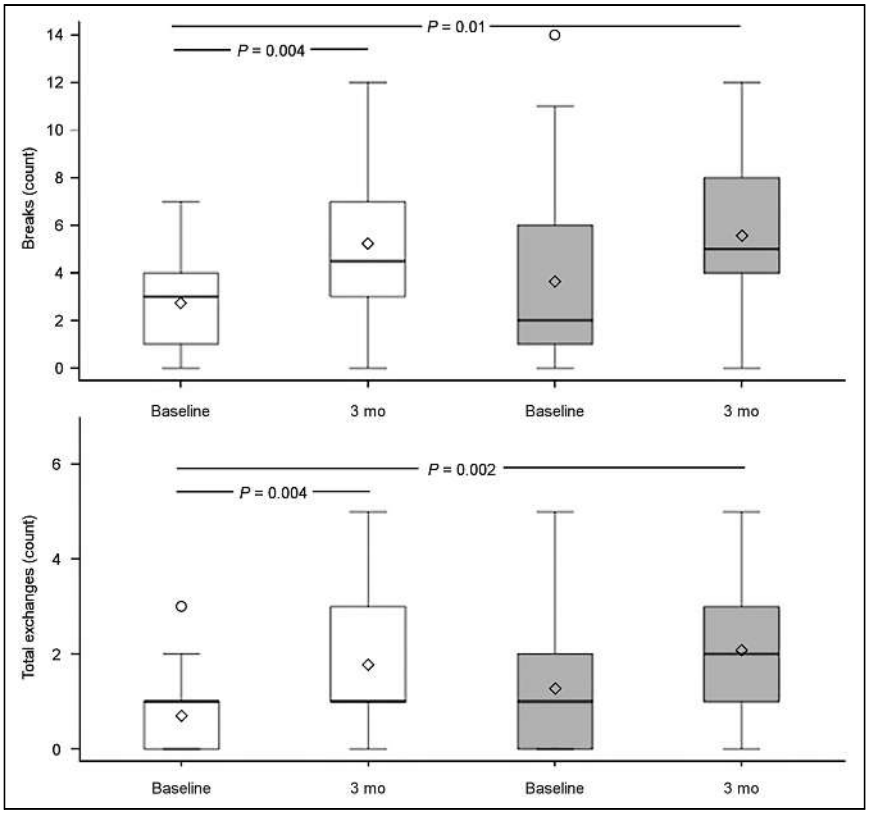

FIGURE 4. Stable chromosome damage (total exchanges and chromosome breaks) in patients before and 3 mo after ^{131}I therapy (white bars, HYPO; gray bars, rhTSH). Tukey method was used to correct for multiple comparisons.

persist in cellular progeny. Unstable aberrations include deletions, dicentric chromosomes, ring chromosomes, and acentric or otherwise asymmetric rearrangements that are normally not tolerated (i.e., lethal) in dividing cells and are, therefore, not transmitted with subsequent cell divisions. Stable aberrations, on the other hand, are generally tolerated by the cells and transmitted to the following cellular generations. It is believed that stable and unstable aberrations are induced with the same frequency, but unstable aberrations seem to be less frequent precisely because they are lost at each cell division.

We investigated whether 1,850 MBq (50 mCi) of ^{131}I for ablation therapy could cause stable genetic damage in patients who undergo surgery for differentiated thyroid carcinoma with low and intermediate risk. Moreover, we investigated whether patients prepared with thyroid hormone withdrawal or with rhTSH display similar levels of chromosome damage. We found transient unstable DNA damage in both groups and modest stable DNA damage only in HYPO patients.

Indeed, micronuclei are a sign of early unstable damage, and we expected normal levels at 1 wk and 3 mo after therapy. The trend of DNA damage measured by CometAssay after 1 wk and 3 mo suggests that the observed DNA damage consists mainly of single-strand breaks, a sensitive biomarker induced by reactive oxygen species and reversible over time (*29*). Indeed, cancer, chronic inflammation, and oxidative stress are closely related, and numerous agents, such as ionizing radiation, have been proven to interfere with redox cell signaling pathways (*30*). Since several studies have shown that unstable DNA damage can also manifest several cellular generations after radiation exposure, generating what is

TABLE 2
Parameter Estimates by Generalized Linear Mixed Model of Chromosome Breaks and Exchanges at 3 Months in HYPO and rhTSH Groups

Variable	Mean ± SE	95% CI	Exp (mean)	% chance	*P*
Chromosome breaks at 3 mo in HYPO patients*					
Anti-ROMsS at 1 wk	−0.003 ± 0.001	−0.005 to −0.00005	1.00	−0.3	0.046
Exposure rate at 48 h	0.06 ± 0.02	0.01 to 0.10	1.06	6.2	0.016
Chromosome exchanges at 3 mo in HYPO patients†					
Anti-ROMsS at 1 wk	−0.009 ± 0.003	−0.02 to −0.002	0.99	−0.9	0.015
DNA-1	0.82 ± 0.34	0.10 to 1.54	2.28	127.5	0.027
Exposure rate at 48 h	0.06 ± 0.03	0.002 to 0.12	1.06	6.2	0.046
Chromosome breaks at 3 mo in rhTSH patients‡					
DNA-2	0.67 ± 0.25	0.03 to 1.31	1.95	95.4	0.04

*Covariate: age, sex, breaks at baseline, d-ROMs at baseline and 1 wk, anti-ROMsF at baseline and 1 wk, anti-ROMsS at baseline, DNA-1, DNA-2, and epi-GFR.

†Covariate: age, sex, exchanges at baseline, d-ROMs at baseline and 1 wk, anti-ROMsF at baseline and 1 wk, anti-ROMsS at baseline, DNA-2, and epi-GFR.

‡Covariate: age, sex, breaks at baseline, d-ROMs at baseline and 1 wk, anti-ROMsF at baseline and 1 wk, anti-ROMsS at baseline and 1 wk, DNA-1, dosimetry at 48 h, and epi-GFR.

Exp (mean) = exponential of the mean.

TABLE 3
Differences in Longitudinal Data of d-ROMs and Anti-ROMsS/F Between HYPO and rhTSH Groups

	HYPO				rhTSH			
Variable	Baseline	1 wk	3 mo	*P*	Baseline	1 wk	3 mo	*P*
d-ROMs	399.75 ± 86.51 (368.02–431.48)	333.46 ± 71.07 (307.39–359.53)	402.93 ± 72.60* (375.82–430.04)	<0.0001	374.22 ± 75.56 (345.72–402.72)	355.20 ± 93.50 (319.93–390.47)	363.62 ± 66.84* (338.20–389.04)	0.29
Anti-ROMsF	209.15 ± 50.53 (190.61–227.68)	215.13 ± 47.25 (197.80–232.46)	212.13 ± 52.46 (192.89–231.37)	0.83	211.49 ± 35.75 (197.63–225.36	219.53 ± 36.46 (205.39–233.67)	202.81 ± 30.95 (191.46–214.16)	0.07
Anti-ROMsS	727.15 ± 121.06 (682.75–771.55)	731.30 ± 172.46 (668.04–794.56)	727.31 ± 134.85 (677.85–776.77)	0.99	681.79 ± 116.81 (636.50–727.09)	720.57 ± 96.55 (683.13–758.01)	665.52 ± 105.12 (626.96–704.08)	0.09

*HYPO vs. rhTSH: d-ROMs: *P* (3 mo vs. 3 mo) = 0.03.

Post hoc analysis: HYPO. d-ROMs: *P* (baseline vs. 1 wk) = 0.0001; *P* (1 wk vs. 3 mo) < 0.0001. Normal values are <300 CARR U for d-ROMs, >200 μEq/L for anti-ROMsF, and >1,000 μEq/L for anti-ROMsS. Data are mean ± SD and 95%CI.

called delayed damage, this study also assessed the unstable damage at 3 mo after therapy, by CometAssay, but we found no significant difference between the 2 groups.

Stable aberrations, by contrast, are a marker of radiation exposure, and the results of the M-FISH analysis showed a statistically significant increase in the frequency of chromosome breaks between the basal sample and the 3-mo sample only in HYPO patients, suggesting that in these patients, not prepared with rhTSH, genomic instability occurs after treatment and persists with time. These data could be partially explained by the reduced renal clearance of ^{131}I (due to a reduced glomerular filtration rate) and higher retained total-body activity (due to the hypothyroidism induced in HYPO patients by withdrawal of levothyroxine), but genetic and metabolic factors could also play a role.

Use of rhTSH, by maintaining euthyroidism and a normal renal clearance (epi-GFR and creatinine values), reduced by 27% the radiation exposure rate over a period of 120 h, an indirect measurement of the retained body activity, and reduced the genomic instability.

SNPs represent different variants of the same gene present in the population. In each individual, the type and combination of polymorphisms of genes involved in DNA repair, and for enzymes acting as free oxygen radical scavengers, influenced the amount of DNA damage observed. Thus, analysis of gene polymorphism allowed us to identify a subgroup of HYPO and rhTSH patients more susceptible to chromosome damage induced by ^{131}I because of mutations in enzymes deputed to DNA repair (DNA-1) or enzymes involved in scavenging of free oxygen radicals (DNA-2). It was interesting to note that among these patients, the HYPO group showed a greater increase in chromosome damage after ^{131}I than did the rhTSH group. Indeed, polymorphism of the gene regulating the redox status has been involved in several other malignancies, mainly breast cancer (*31*).

Overall, in HYPO patients the number of chromosome breaks at 3 mo was associated with the level of breaks at baseline, residual body activity at 48 h, and levels of anti-ROMs (Table 2). As far as the anti-ROMs are concerned, we found a significant positive association with anti-ROMsF at 1 wk and a negative association with anti-ROMsS at 1 wk. An explanation for this finding could be that a high level of dROMs (as observed in these patients) induces an increase in anti-ROMs and that, among these, anti-ROMsF rises quickly and is positively associated with an increase in chromosome damage, whereas anti-ROMsS may require more time to rise and is negatively associated with an increase in chromosome damage.

Patients prepared with rhTSH showed no significant increase in either breaks or total exchanges after ^{131}I, suggesting that these patients have less radiation-induced chromosome damage, even in the presence of mutations in several enzymes. Interestingly, the number of chromosome breaks at 3 mo in rhTSH patients was positively associated with polymorphisms of genes for DNA-repairing enzymes (DNA-2 group).

These data confirm previously published findings that ^{131}I therapy can induce stable DNA damage, but for the first time (to our knowledge) we were able to demonstrate that rhTSH may significantly reduce this damage, particularly in patients with unfavorable polymorphisms of genes involved in DNA repair. Whether chromosome damage in peripheral lymphocytes relates to an increased risk of secondary malignancies remains a matter of debate. In addition, data obtained by measurement of d-ROMs and anti-ROMs demonstrate a crucial role of oxidative stress. In this regard, patients with high levels of d-ROMs and low levels of anti-ROMs, or with an unfavorable genotype for DNA-repairing enzymes or for free oxygen radical scavengers, might be more susceptible to radiation-induced DNA damage.

CONCLUSION

Administered activity, DNA polymorphisms, glomerular filtration rate, and oxidant/antioxidant homeostasis are all parameters that may influence DNA damage in patients treated with ^{131}I. Our study highlighted the importance of rhTSH in preventing radiation-induced stable chromosome damage, even if an unfavorable genetic background is present. Even if stable DNA damage is considered particularly important for involvement in tumor cell clonal evolution, our study showed no evidence that stable DNA damage has clinical consequences or induces secondary tumors. To evaluate these specific endpoints, larger longitudinal studies are warranted.

DISCLOSURE

This study was partially supported by funds from the University of Rome "Sapienza." Genzyme-Sanofi supports research on thyroid cancer at our institution but did not sponsor this specific study. rhTSH was regularly purchased for all patients. No other potential conflict of interest relevant to this article was reported.

ACKNOWLEDGMENTS

We thank Drs. Patrizia Pizzichini, Gabriela Capriotti, Anna Festa, and Daniela Prosperi for recruiting patients.

KEY POINTS

QUESTION: Is there transient DNA damage after ^{131}I ablation therapy, is there detectable permanent ^{131}I-induced chromosome damage, and to what extent is permanent chromosome damage due to ^{131}I dose or to oxidative stress in the patient and gene polymorphism?

PERTINENT FINDINGS: DNA damage after ^{131}I ablation therapy occurred in most patients treated with 1,850 MBq and disappeared after 3 mo. Some chromosome breaks and exchanges occurred after ^{131}I therapy, particularly in HYPO patients, possibly because of higher retained activity or high oxidative stress. Most patients had a reduction in anti–free oxygen radical scavengers and an increase in free oxygen radicals. An unfavorable genotype exposed patients to higher radiation-induced damage. When patients were matched for severity of gene mutations, hypothyroid patients had higher levels of chromosome damage.

IMPLICATIONS FOR PATIENT CARE: Transient chromosome damage is not relevant in patients treated with 1,850 MBq of ^{131}I. Candidates for ^{131}I ablation therapy should be prepared with rhTSH, avoiding discomfort and symptoms of hypothyroidism and chromosome damage. Genes that control oxidative stress might influence induction of DNA damage in patients treated with ^{131}I.

REFERENCES

1. Watanabe N, Yokoyama K, Kinuya S, et al. Radiotoxicity after iodine-131 therapy for thyroid cancer using the micronucleus assay. *J Nucl Med.* 1998;39:436–440.
2. de Vathaire F, Schlumberger M, Delisle MJ, et al. Leukaemias and cancers following iodine-131 administration for thyroid cancer. *Br J Cancer.* 1997;75:734–739.
3. Tulchinsky M, Binse I, Campennì A, et al. Radioactive iodine therapy for differentiated thyroid cancer: lessons from confronting controversial literature on risks for secondary malignancy. *J Nucl Med.* 2018;59:723–725.
4. Brown AP, Chen J, Hitchcock YJ, Szabo A, Shrieve DC, Tward JD. The risk of second primary malignancies up to three decades after the treatment of differentiated thyroid cancer. *J Clin Endocrinol Metab.* 2008;93:504–515.
5. Iyer NG, Morris LG, Tuttle RM, Shaha AR, Ganly I. Rising incidence of second cancers in patients with low-risk (T1N0) thyroid cancer who receive radioactive iodine therapy. *Cancer.* 2011;117:4439–4446.
6. Molenaar RJ, Pleyer C, Radivoyevitch T, et al. Risk of developing chronic myeloid neoplasms in well-differentiated thyroid cancer patients treated with radioactive iodine. *Leukemia.* 2018;32:952–959.
7. Rubino C, de Vathaire F, Dottorini ME, et al. Second primary malignancies in thyroid cancer patients. *Br J Cancer.* 2003;89:1638–1644.
8. Frigo A, Dardano A, Danese E, et al. Chromosome translocation frequency after radioiodine thyroid remnant ablation: a comparison between recombinant human thyrotropin stimulation and prolonged levothyroxine withdrawal. *J Clin Endocrinol Metab.* 2009;94:3472–3476.
9. Puerto S, Marcos R, Ramírez MJ, Galofrè P, Creus A, Surralle's J. Equal induction and persistence of chromosome aberrations involving chromosomes 1, 4 and 10 in thyroid cancer patients treated with radioactive iodine. *Mutat Res.* 2000;469:147–158.
10. Lambert V, Thierens H, Monsieurs M, Roncancio C, Laurent C. Translocation frequencies measured in patients one year after radioactive iodine therapy for thyrotoxicosis. *Int J Radiat Biol.* 2001;77:679–685.
11. M'Kacher R, Legal JD, Schlumberger M, et al. Biological dosimetry in patients treated with iodine-131 for differentiated thyroid carcinoma. *J Nucl Med.* 1996;37:1860–1864.
12. Baugnet-Mahieu L, Lemaire M, Leonard E, Leonard A, Gerber G. Chromosome aberrations after treatment with radioactive iodine for thyroid cancer. *Radiat Res.* 1994;140:429–431.
13. Buscombe J. Radioiodine and its relationship to hematologic malignancy: the confounding role of supraphysiologic thyroxine. *J Clin Oncol.* 2018;36:1884–1885.
14. Fisher R. Questionable relevance of leukaemia risk after radioiodine ablation of thyroid cancer. *J Clin Oncol.* 2018;36:1885.
15. Hindié E, Recher C, Zerdoud S, Leenhardt L, Avram AM. Risk of hematologic malignancies after radioactive iodine treatment of thyroid cancer: an unjustified warning. *J Clin Oncol.* 2018;36:1881–1882.
16. Kreissl MC, Grande E. Inconclusive analysis of the connection between secondary hematologic malignancies and radioiodine treatment. *J Clin Oncol.* 2018;36:1882–1883.
17. Molenaar RJ, Sidana S, Radivoyevitch T, et al. Risk of hematologic malignancies after radioiodine treatment of well-differentiated thyroid cancer. *J Clin Oncol.* 2018;36:1831–1839.
18. Piccardo A, Puntoni M, Verburg FA, Luster M, Giovanella L. Power of absolute values to avoid data misinterpretations: the case of radioiodine-induced leukemia and myelodysplasia. *J Clin Oncol.* 2018;36:1880–1881.
19. Sollini M, Chiti A. Concerns about the risk of myeloid malignancies after radioiodine therapy in thyroid cancer. *J Clin Oncol.* 2018;36:1885–1886.
20. García-Quispes WA, Pastor S, Galofré P, et al. Influence of DNA-repair gene variants on the micronucleus frequency in thyroid cancer patients. *Mutat Res.* 2013;750:34–39.
21. Levey AS, Stevens LA, Schmid CH, et al. A new equation to estimate glomerular filtration rate. *Ann Intern Med.* 2009;150:604–612.
22. Franchini V, De Sanctis S, Marinaccio J, et al. Study of the effects of 0.15 terahertz radiation on genome integrity of adult fibroblasts. *Environ Mol Mutagen.* 2018;59:476–487.
23. Giovanetti A, Deshpande T, Basso E. Persistence of genetic damage in mice exposed to low dose of x rays. *Int J Radiat Biol.* 2008;84:227–235.
24. Nieri D, Berardinelli F, Sgura A, et al. Cyogenetics effects in AG01522 human primary fibroblasts exposed to low doses of radiations with different quality. *Int J Radiat Biol.* 2013;89:698–707.
25. Berardinelli F, Nieri D, Tanzarella C, et al. mFISH analysis of irradiated human fibroblasts: a comparison among radiations with different quality in the low-dose range. *Radiat Prot Dosimetry.* 2015;166:302–305.
26. Osti MF, Nicosia L, Agolli L, et al. Potential role of single nucleotide polymorphisms of XRCC1, XRCC3, and RAD51 in predicting acute toxicity in rectal cancer patients treated with preoperative radiochemotherapy. *Am J Clin Oncol.* 2017;40:535–542.
27. Colombini F, Carratelli M, Alberti A. Oxidative stress, d-ROMs test and ceruloplasmin. *Free Radic Res.* 2016;50:447–453.
28. Pizza V, Agresta A, Iorio EL, Capasso A. Oxidative stress and aging: a clinical and biochemical study. *Pharmacologyonline.* 2013;2:28–37.
29. Kucharová M, Hronek M, Rybáková K, et al. Comet assay and its use for evaluating oxidative DNA damage in some pathological states. *Physiol Res.* 2019;68:1–15.
30. Reuter S, Gupta SC, Chaturvedi MM, Aggarwal BB. Oxidative stress, inflammation, and cancer: how are they linked? *Free Radic Biol Med.* 2010;49:1603–1616.
31. Al Zoubi MS, Zavaglia K, Mazanti C, et al. Polymorphisms and mutations in GSTP1, RAD51, XRCC1 and XRCC3 genes in breast cancer patients. *Int J Biol Markers.* 2017;32:e337–e343.

^{89}Zr-DFO-Durvalumab PET/CT Before Durvalumab Treatment in Patients with Recurrent or Metastatic Head and Neck Cancer

Sarah R. Verhoeff[1], Pim P. van de Donk[2], Erik H.J.G. Aarntzen[3], Sjoukje F. Oosting[2], Adrienne H. Brouwers[4], Iris H.C. Miedema[5], Jens Voortman[5], Willemien C. Menke-van der Houven van Oordt[5], Ronald Boellaard[3,6], Dennis Vriens[7], Marije Slingerland[8], Rick Hermsen[9], Ilse van Engen-van Grunsven[10], Sandra Heskamp*[3], and Carla M.L. van Herpen*[1]

[1]Department of Medical Oncology, Radboud University Medical Center, Nijmegen, The Netherlands; [2]Department of Medical Oncology, University Medical Center Groningen, University of Groningen, Groningen, The Netherlands; [3]Department of Radiology and Nuclear Medicine, Radboud University Medical Center, Nijmegen, The Netherlands; [4]Department of Nuclear Medicine and Molecular Imaging, University Medical Center Groningen, University of Groningen, Groningen, The Netherlands; [5]Department of Medical Oncology, Cancer Center Amsterdam, Amsterdam UMC, Vrije Universiteit Amsterdam, Amsterdam, The Netherlands; [6]Department of Radiology and Nuclear Medicine, Cancer Center Amsterdam, Amsterdam UMC, Vrije Universiteit Amsterdam, Amsterdam, The Netherlands; [7]Department of Radiology, Section of Nuclear Medicine, Leiden University Medical Center, Leiden, The Netherlands; [8]Department of Medical Oncology, Leiden University Medical Center, Leiden, The Netherlands; [9]Department of Nuclear Medicine, Canisius Wilhelmina Hospital, Nijmegen, The Netherlands; and [10]Department of Pathology, Radboud University Medical Center, Nijmegen, The Netherlands

In this PD-L1 ImagiNg to prediCt durvalumab treatment response in SCCHN (PINCH) study, we performed ^{89}Zr-DFO-durvalumab (anti–PD-L1 [programmed death ligand 1]) PET/CT in patients with recurrent or metastatic (R/M) squamous cell carcinoma of the head and neck (SCCHN) before monotherapy durvalumab treatment. The primary aims were to assess safety and feasibility of ^{89}Zr-DFO-durvalumab PET imaging and predict disease control rate during durvalumab treatment. Secondary aims were to correlate ^{89}Zr-DFO-durvalumab uptake to tumor PD-L1 expression, ^{18}F-FDG uptake, and treatment response of individual lesions. **Methods:** In this prospective multicenter phase I–II study (NCT03829007), patients with incurable R/M SCCHN underwent baseline ^{18}F-FDG PET and CT or MRI. Subsequently, PD-L1 PET imaging was performed 5 d after administration of 37 MBq of ^{89}Zr-DFO-durvalumab. To optimize imaging conditions, dose finding was performed in the first 14 patients. For all patients (n = 33), durvalumab treatment (1,500 mg/4 wk, intravenously) was started within 1 wk after PD-L1 PET imaging and continued until disease progression or unacceptable toxicity (maximum, 24 mo). CT evaluation was assessed according to RECIST 1.1 every 8 wk. PD-L1 expression was determined by combined positive score on (archival) tumor tissue. ^{89}Zr-DFO-durvalumab uptake was measured in ^{18}F-FDG–positive lesions, primary and secondary lymphoid organs, and blood pool. **Results:** In total, 33 patients with locoregional recurrent (n = 12) or metastatic SCCHN (n = 21) were enrolled. ^{89}Zr-DFO-durvalumab injection was safe. A dose of 10 mg of durvalumab resulted in highest tumor-to-blood ratios. After a median follow-up of 12.6 mo, overall response rate was 26%. The disease control rate at 16 wk was 48%, with a mean duration of 7.8 mo (range, 1.7–21.1). On a patient level, ^{89}Zr-DFO-durvalumab SUV_{peak} or tumor-to-blood ratio could not predict treatment response (hazard ratio, 1.5 [95% CI, 0.5–3.9; P = 0.45] and 1.3 [95% CI, 0.5–3.3; P = 0.60], respectively). Also, on a lesion level, ^{89}Zr-DFO-durvalumab SUV_{peak} showed no substantial correlation to treatment response (Spearman ρ, 0.45; P = 0.051). Lesional ^{89}Zr-DFO-durvalumab uptake did not correlate to PD-L1 combined positive score but did correlate to ^{18}F-FDG SUV_{peak} (Spearman ρ, 0.391; P = 0.005). **Conclusion:** PINCH is the first, to our knowledge, PD-L1 PET/CT study in patients with R/M SCCHN and has shown the feasibility and safety of ^{89}Zr-DFO-durvalumab PET/CT in a multicenter trial. ^{89}Zr-DFO-durvalumab uptake did not correlate to durvalumab treatment response.

Key Words: PD-L1; immuno-PET; head and neck cancer; immune checkpoint inhibitors; durvalumab

J Nucl Med 2022; 63:1523–1530
DOI: 10.2967/jnumed.121.263470

Squamous cell carcinoma of the head and neck (SCCHN) is the seventh most common cancer worldwide, with up to 900,000 new diagnoses in 2020 (*1*). Patients with recurrent or metastatic (R/M) SCCHN with no curative options have a poor prognosis (*2*). However, a subset of patients derives durable responses from immune checkpoint inhibitors (ICI) targeting programmed cell death 1 (PD-1) or its ligand (PD-L1) (*3–5*), although selecting those patients up front remains challenging.

Patients who benefit most from ICI often express high levels of tumor PD-L1 as analyzed by immunohistochemistry, using different assays, scoring protocols, and cut-offs (*5–8*). Since June 2019, pembrolizumab has received Food and Drug Administration and European Medicines Agency approval as first-line treatment of R/M SCCHN patients with an immunohistochemistry combined positive score (CPS) of at least ≥1. Thus, pretreatment assessment of PD-L1 has major clinical implication, although there are also patients with a PD-L1–negative tumor biopsy who benefit from ICI (*9–11*).

Received Nov. 14, 2021; revision accepted Jan. 26, 2022.
For correspondence or reprints, contact C.M.L. van Herpen (Carla.vanherpen@radboudumc.nl).
*Contributed equally to this work.
Published online May 5, 2022.

Therefore, there is a clinical need to better understand ICI responses and the caveats that remain with selection based on PD-L1 expression in tumor biopsies. The role and expression of PD-L1 in anticancer immune responses is complex and warrants a biomarker that enables monitoring its heterogeneous and dynamic expression in different (tumor) tissues (*12*). Molecular imaging with radiolabeled tracers targeting PD-1 and PD-L1 allows noninvasive visualization of all accessible PD-1/PD-L1 (*13,14*). This approach overcomes important limitations of immunohistochemistry analyses, including invasive biopsies and sampling errors (*15,16*). It is a complementary tool for blood and tissue sampling, potentially providing relevant information for selecting patients and steering drug development (*17*).

The first clinical PD-1/PD-L1 imaging studies were performed with ^{89}Zr-labeled atezolizumab (anti–PD-L1) and nivolumab (anti–PD-1) in patients with metastatic breast cancer, bladder cancer, and non–small cell lung cancer (NSCLC), demonstrating a correlation between tracer uptake and treatment response (*18,19*). To date, to our knowledge, no PD-L1 PET imaging studies have been performed in patients with R/M SCCHN.

The primary aim of this PD-L1 ImagiNg to prediCt durvalumab treatment response in SCCHN (PINCH) study was to assess the safety and feasibility of ^{89}Zr-DFO-durvalumab PD-L1 PET imaging and to predict durvalumab disease control rate in patients with R/M SCCHN. Secondary aims were to investigate the correlation of ^{89}Zr-DFO-durvalumab uptake to PD-L1 expression measured on tumor biopsies, ^{18}F-FDG uptake, and treatment response of individual tumor lesions.

MATERIALS AND METHODS

Patients

Eligible patients were aged 18 y or older, had an Eastern Cooperative Oncology Group performance status of 0 or 1, and had a life expectancy of at least 12 wk. Patients had histologically or cytologically confirmed R/M SCCHN of the oral cavity, oropharynx, hypopharynx, or larynx not amenable to curative therapy, with no prior systemic treatment for R/M SCCHN. Patients with known leptomeningeal carcinomatosis, symptomatic or uncontrolled brain metastases requiring treatment, were excluded. Patient recruitment was performed at 4 university medical centers in The Netherlands (Radboudumc, UMC Groningen, Amsterdam UMC, and Leiden UMC). The study was performed in accordance with the Declaration of Helsinki and approved by the institutional review board of each participating center.

Procedures

Contrast-Enhanced (ce) CT or MRI, ^{18}F-FDG PET/CT, and ^{89}Zr-DFO-Durvalumab PET/CT. At baseline, all patients underwent ceCT or MRI of the head and neck, chest, and abdomen, combined with whole-body ^{18}F-FDG PET/CT and ^{89}Zr-DFO-durvalumab PET/CT. ^{18}F-FDG PET/CT was performed according to European Association of Nuclear Medicine guidelines, version 1.0 (*20*), and the ^{89}Zr-imaging procedure was harmonized between participating EARL (EANM Research GmbH)-accredited centers (PET/CT systems) (*21*). Patients underwent ^{89}Zr-DFO-durvalumab PET/CT 5 d after intravenous injection of approximately 37 MBq of ^{89}Zr-DFO-durvalumab. Details on the conjugation, radiolabeling, and quality control of ^{89}Zr-DFO-durvalumab and image acquisition and reconstruction are described in the supplemental material (supplemental materials are available at http://jnm.snmjournals.org) (*21–24*).

After baseline imaging, all patients were planned for durvalumab treatment (fixed dose of 1,500 mg intravenously once every 4 wk) starting within 1 wk after PET imaging until disease progression or unacceptable toxicity, for a maximum of 24 mo. Data on adverse events were collected up to 90 d after the last treatment dose and graded according to the National Cancer Institute Common Terminology Criteria for Adverse Events (version 4.0). Treatment evaluation was performed with ceCT of the head and neck, chest, and abdomen at baseline and every 8 wk during treatment, using RECIST (version 1.1). Participants were contacted every 3 mo to assess survival after discontinuation of durvalumab treatment.

^{89}Zr-DFO-Durvalumab PET/CT

Dose Finding. On the basis of prior dose-finding studies with ^{89}Zr-labeled antibodies, we aimed to enroll a minimum of 3 patients per dose cohort (2, 10, or 50 mg of durvalumab) (*25*). All patients received an intravenous injection of 2 mg of ^{89}Zr-DFO-durvalumab. For the 10- and 50-mg cohorts, ^{89}Zr-DFO-durvalumab was complemented with 8 and 48 mg of unlabeled durvalumab, respectively. For pharmacokinetic purposes, blood plasma samples were drawn within 10 min after injection and 5 d later (day of the PET scan). Plasma radioactivity was measured in a γ-counter and reported as the percentage injected dose per gram (%ID/g). The optimal dose for ^{89}Zr-DFO-durvalumab PET imaging was determined based on pharmacokinetic blood analyses and visual and quantitative PET analyses.

After dose finding, we aimed to include an additional 43 patients receiving the optimal dose of ^{89}Zr-DFO-durvalumab. However, the study was closed early for enrollment in December 2020 due to the registration of pembrolizumab as first-line treatment for R/M SCCHN patients in The Netherlands (June 2020). In total, we enrolled an additional 19 patients who underwent the same procedures as described above, except for the collection of blood samples for pharmacokinetic analyses.

Imaging Assessment

ceCT or MRI and ^{18}F-FDG PET/CT. Baseline ceCT/MRI and ^{18}F-FDG PET/CT scans were centrally reviewed by 2 independent radiology and nuclear medicine physicians according to standard clinical practice. The evaluation of CT lesions was performed according to RECIST 1.1 (*26*). Lesion size was defined as the mean size in millimeters (mm) as determined by 2 reviewers.

The ^{18}F-FDG PET/CT scans were assessed using PERCIST (*27*). A tumor lesion was defined as visually positive based on anatomic substrate on low-dose CT in combination with higher than surrounding ^{18}F-FDG uptake and a diameter on ceCT or MRI of ≥10 or ≥15 mm in lymph nodes (*26*). The maximum and peak SUVs (SUV_{max} and SUV_{peak}) based on body weight were obtained, as well as metabolic tumor volume (MTV) and total lesion glycolysis (TLG).

^{89}Zr-DFO-Durvalumab PET/CT. The quantification of tumor lesions was performed by placing a 3-dimensional sphere in an ^{18}F-FDG–positive lesion using Accurate tool software developed in IDL [Interactive Data Language], version 8.4 (Harris Geospatial Solutions) (*28*). This was done for all ^{18}F-FDG–positive lesions, irrespective of visual ^{89}Zr-DFO-durvalumab uptake. This volume of interest was manually delineated around the entire lesion if this could be distinguished from the background. In tumor lesions without evident visual ^{89}Zr uptake, a spheric volume of interest of 1 cm^3 was drawn at the anatomic location of the tumor lesion, based on the low-dose CT, diagnostic CT, and ^{18}F-FDG PET/CT. On a lesion level, the SUV_{peak} of individual lesions was determined to report tumor tracer uptake. For healthy organs and blood pool, SUV_{mean} was reported. To correct for variable concentrations of circulating ^{89}Zr-DFO-durvalumab, tumor-to-blood (TTB) ratios were reported as SUV_{peak} tumor/SUV_{mean} blood. The blood-pool activity was measured in a spheric volume of interest in the descending aorta. To correct for differences in number of lesions per patient, the lesional SUV_{peak} and ^{18}F-FDG TLG values of 1 individual patient were summarized as geometric mean (gm) values. This gm was used to correlate tracer accumulation to treatment response. Furthermore, to correct for partial-volume effect, subgroup analyses were performed for lesions ≥ 20m (reported in the supplemental material)

PD-L1 Immunohistochemistry

Fresh or archival cytologic or histologic samples suitable for PD-L1 staining were available for 27 patients. This involved tumor tissue from recurrent disease ($n = 12$) or metastases in lung ($n = 7$), lymph node ($n = 7$), or bone ($n = 1$). PD-L1 staining was performed using VENTANA (Roche) PD-L1 (SP263) assay and evaluated by a certified pathologist in head and neck cancer masked to clinical information. As an internal control, staining for PD-L1 was performed with the clinically validated 22C3 antibody using the Dako stainer in histologic samples of 8 patients (*8*). In all samples, PD-L1 expression was assessed according to the CPS, which describes the number of PD-L1–positive tumor cells plus immune cells per 100 tumor cells, showing positive cell membrane staining or a score of <1, 1–20, or >20.

Statistical Analysis

Clinical outcome was evaluated according to intention-to-treat analyses on a patient and lesion level and visualized in a waterfall plot. Furthermore, we assessed the disease control rate, overall response rate, progression-free survival (PFS), and overall survival. A log-rank test was performed to correlate PD-L1 CPS to PFS. A Cox regression model was used to report hazard ratios (HR) for progressive disease.

In the dose-finding study, we compared differences in tracer-uptake and TTB ratios between the 3 dose groups, testing for significance using a 2-sided Kruskal–Wallis test.

On a patient level, the relation between ^{89}Zr-DFO-durvalumab, patient gm SUV_{peak}, and SUV_{peak} of the hottest lesion with durvalumab response was explored by Kaplan–Meier survival plots. Similar analyses were performed for gm ^{18}F-FDG SUV_{peak}, TLG, and MTV. Patients were grouped in a below-median and above-median group to evaluate a difference in survival using the log-rank test. The relation between these groups was tested by additional Cox regression models, reporting HRs for progressive disease or survival.

We correlated ^{89}Zr-DFO-durvalumab uptake with ^{18}F-FDG SUV_{peak} and ^{18}F-FDG TLG on a lesion level. Additional descriptive analyses were performed to evaluate the per-lesion PD-L1 expression to tracer accumulation. For these correlations, we report the Spearman correlation coefficient (ρ). Statistical analyses were performed using SPSS Statistics (IBM) for Windows, version 22.0. Differences with a P value of 0.05 or less were considered statistically significant.

RESULTS

Baseline Characteristics

Between April 2019 and December 2020, 37 patients were screened, 3 were considered ineligible, and 1 declined to participate. ^{89}Zr-DFO-durvalumab PET dose finding was performed in 14 patients (Supplemental Fig. 1). Twenty-one of 33 (64%) patients presented with metastatic disease, most frequently located in lung (45%) and lymph nodes (39%). PD-L1 CPS could be determined in 27 patients (82%), including 17 patients with only archival tumor tissue available. Baseline characteristics are reported in Table 1.

Durvalumab Treatment

In total, 31 of 33 patients started durvalumab treatment. Two patients showed rapid disease progression before treatment initiation and were offered best supportive care. One other patient showed rapid disease progression before first disease evaluation at 8 wk. After a median follow-up of 12.6 mo, the median time on durvalumab treatment was 5.3 mo (range, 1.2–26.5 mo).

The median PFS was 5.3 mo (95% CI, 2.96–7.62 mo), and median overall survival was 13.1 mo (95% CI, 7.88–18.40 mo). The survival rate at 12 and 24 mo was 58% (95% CI, 8.82–11.28) and 45% (95% CI, 8.91–24.87), respectively (Supplemental Fig. 2). The overall response rate was 26%, including 3 patients with complete

TABLE 1
Baseline Characteristics

Parameter	Patients ($n = 33$)
Age (y)	Median, 64.5; range, 49–80
Sex (*n*)	
Male	26, 79%
ECOG PS (*n*)	
0	10, 30%
1	23, 70%
Smoking (*n*)	
Current	4, 12%
Never or former	29, 88%
Alcohol (*n*)	
Current	24, 73%
Never or former	9, 27%
Primary tumor location (*n*)	
Hypopharynx	4, 13%
Larynx	7, 22%
Oral cavity	10, 30%
Oropharynx	8, 24%
Unknown	3, 10%
Disease extent at baseline (*n*)	
Loco/regional recurrence	12, 36%
Metastatic disease	21, 64%
Location metastases	
Lung	28, 45%
Lymph node	24, 39%
Bone	5, 8%
Other (liver, adrenal gland, muscle)	4, 8%
Prior treatments with curative intent* (*n*)	
Surgery alone	3, 9%
Surgery with adjuvant radiation	8, 24%
Surgery with adjuvant chemoradiation	9, 27%
Radiation alone	5, 15%
Chemoradiation	8, 24%
Time from last platinum therapy (*n*)	
≤6 mo	1, 6%
>6 mo	16, 94%
Histologic/cytologic biopsy†	
Archival	17, 52%
Fresh	16, 48%
PD-L1 status‡ (*n*)	
PD-L1 CPS < 1	13, 40%
PD-L1 CPS 1–20	8, 24%
PD-L1 CPS ≥ 20	6, 18%
No assessment possible	6, 18%

*Chemotherapy regimen included monotherapy cisplatin or carboplatin, or combination regimens, for example, docetaxel, cisplatin and 5-fluorouracil or carboplatin and 5-fluorouracil.

†A fresh biopsy was defined as histologic or cytologic tumor biopsy performed at study enrollment up to < 1 mo before study enrollment.

‡PD-L1 assessment was performed on biopsy tissue from R/M disease. PD-L1 staining was performed using VENTANA SP263.

ECOG PS = Eastern Cooperative Oncology Group performance status.

Data are median and range, or *n* and %.

response and 5 patients with partial response. The best response to durvalumab treatment per patient is depicted in Figure 1. The disease control rate at 16 wk was 48%, with a mean response duration of 7.8 mo (range, 1.7–21.1 mo). The most frequent reported grade 3–4 treatment-related adverse events were elevated alanine transaminase and aspartate transaminase caused by hepatitis and pneumonitis (Supplemental Table 1). PD-L1 CPS showed no association with PFS (PFS of 4.6 vs. 12.9 vs. 3.5 mo with CPS < 1, 1–20 and > 20, respectively; P = 0.259; Supplemental Fig. 3).

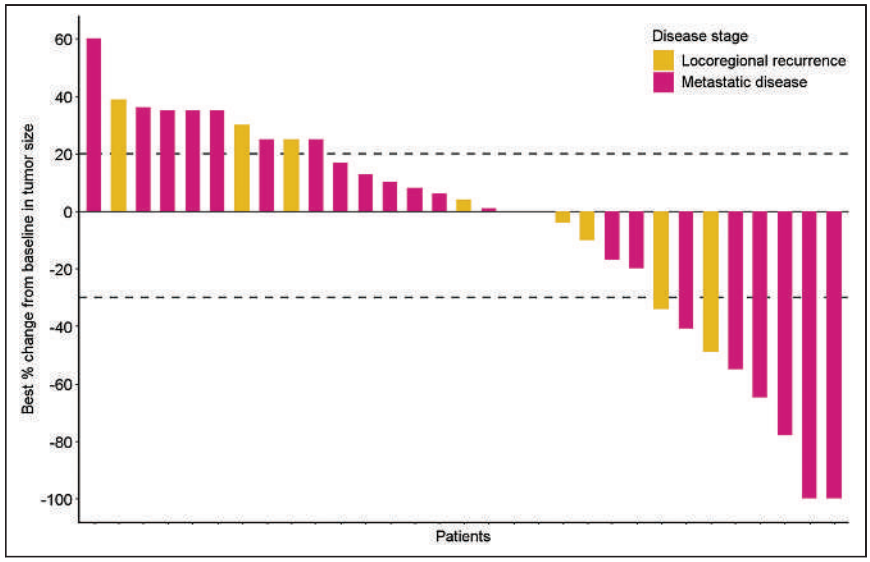

FIGURE 1. Each bar of waterfall plot depicts best response according to RECIST, version 1.1, of single patient during durvalumab treatment. Blue bars represent patients with metastatic disease, pink bars patients with locoregional recurrent disease. Dotted lines reflect RECIST for disease progression (+20% change) and partial response (−30%).

^{89}Zr-DFO-Durvalumab PET/CT

Dose Finding

In total, 14 patients were assigned to 1 of 3 dose cohorts: 2 mg (n = 4), 10 mg (n = 6), or 50 mg (n = 4) of durvalumab. No clinically relevant infusion-related reactions for the injection with ^{89}Zr-DFO-durvalumab were reported.

Example ^{89}Zr-DFO-durvalumab PET/CT scans are shown in Figure 2. The pharmacokinetic analysis at day 5 showed the lowest ^{89}Zr-DFO-durvalumab (%ID/g) plasma concentration in the 2-mg cohort (Supplemental Fig. 4), whereas highest concentrations were measured in the 50-mg cohort (P = 0.077). The 10-mg dose cohort showed variable plasma concentrations between patients. In the 2-mg cohort, tumor lesions could not be visualized properly and high tracer retention was observed in the liver and spleen. At higher antibody doses, liver and spleen uptake decreased and tumor uptake increased. Also, increasing antibody dose resulted in visually prolonged ^{89}Zr-DFO-durvalumab circulation time. Quantitative analyses showed that the mean TTB ratio was highest in the 10-mg cohort and lowest in the 50-mg cohort (2-mg cohort: 2.28 ± 0.61; 10-mg cohort: 3.75 ± 0.93; 50-mg cohort: 1.48 ± 1.64; P = 0.019; Supplemental Fig. 5).

On the basis of the highest TTB ratios and tumor visualization, we selected 10 mg for subsequent ^{89}Zr-DFO-durvalumab PET/CT imaging.

PET Imaging Analyses

In total, 24 patients underwent ^{89}Zr-DFO-durvalumab PET/CT imaging using an antibody dose of 10 mg. In these patients, ^{89}Zr-DFO-durvalumab tumor accumulation was measured for all ^{18}F-FDG–positive tumor lesions (n = 53). The ^{89}Zr-DFO-durvalumab uptake, lesion size, and lesion location are displayed in Figure 3. An overview of all lesions can be found in Supplemental Table 2.

^{89}Zr-DFO-Durvalumab PET Imaging. For quantitative analyses of ^{89}Zr-DFO-durvalumab, 53 lesions were included. No significant differences were observed between lesions in different organ sites. However, accumulation of ^{89}Zr-DFO-durvalumab was highly variable in tumor lesions within and between patients (Figs. 3 and 4. The largest heterogeneity in 1 patient was observed between a lung (SUV_{peak}, 3.3) and liver (SUV_{peak}, 9.8) metastasis. The highest SUV_{peak} was reported in

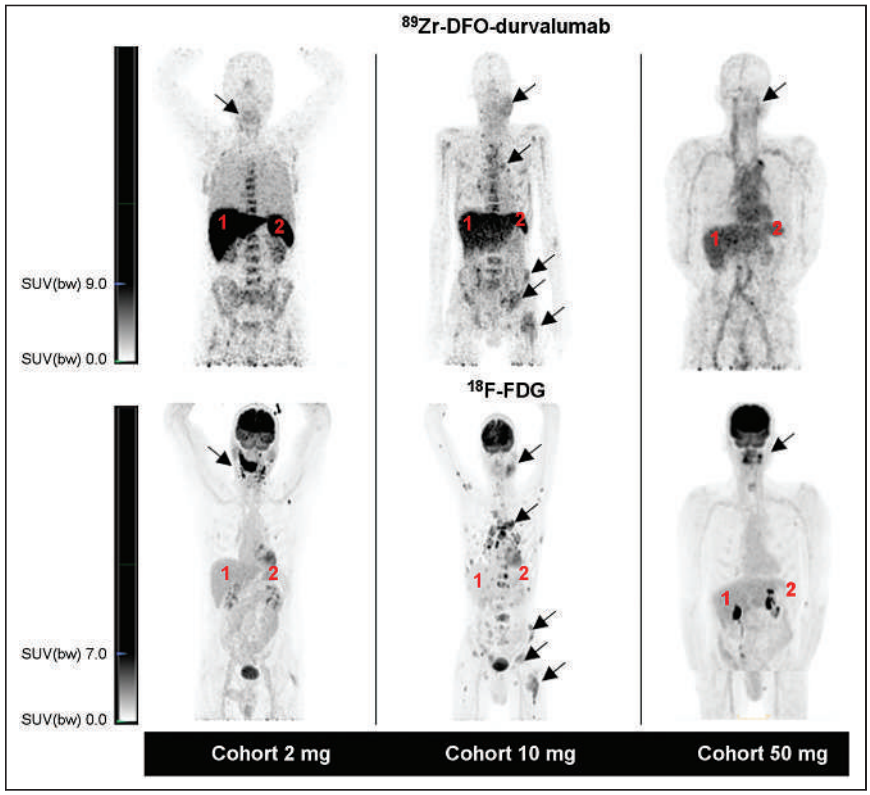

FIGURE 2. Representative example images of 1 patient per dose cohort. For each cohort, ^{89}Zr-DFO-durvalumab PET/CT (top) and ^{18}F-FDG PET/CT (bottom) are presented. Physiologic ^{89}Zr-DFO-durvalumab is visualized in lymphoid organs (e.g., liver [1], spleen [2]). Arrows identify tumor lesions. SUV(bw) = SUV based on body weight.

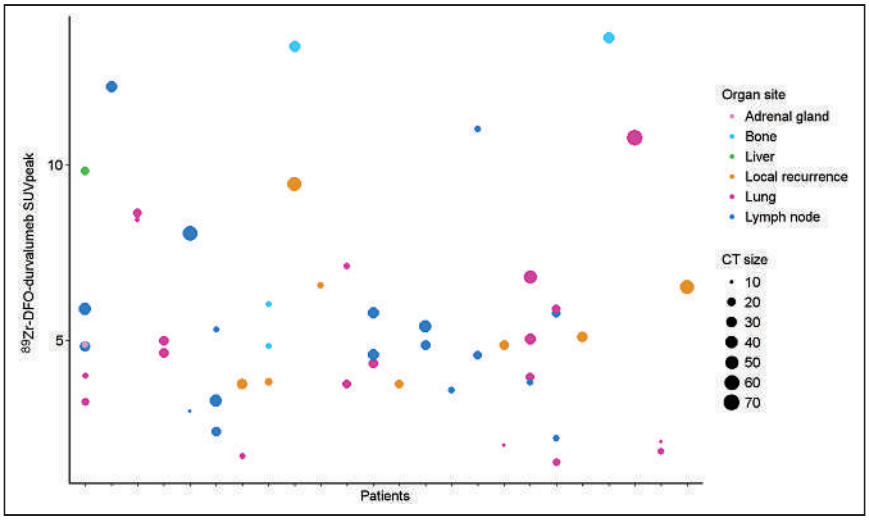

FIGURE 3. Scatterplot of all ^{18}F-FDG–positive lesions (n = 53) measuring ≥ 10 mm (or 15 mm in lymph node) and the lesions' corresponding ^{89}Zr-DFO-durvalumab uptake. Lesions were distributed over lung (n = 20), lymph nodes (n = 18), local recurrence (n = 8), bone (n = 5), and liver (n = 1).

2 bone lesions (SUV_{peak}, 13.4 and 13.6) and 1 locoregional lymph node (SUV_{peak}, 12.2). ^{89}Zr-DFO-durvalumab SUV_{peak} was correlated with lesion size (Spearman ρ, 0.359; P = 0.09) and ^{18}F-FDG SUV_{peak} (Spearman ρ, 0.391; P = 0.005), but not with organ site (Spearman ρ, 0.15; P = 0.28). The overall mean gm ^{89}Zr-DFO-durvalumab SUV_{peak} was 6.0 (95% CI, 4.6–7.3).

^{18}F-FDG PET Imaging. In 33 patients, 70 ^{18}F-FDG–positive lesions were identified according to PERCIST used for quantitative analyses. The ^{18}F-FDG uptake was highly variable within and between patients, with an overall gm ^{18}F-FDG SUV_{peak} of 7.7 (range, 2.0–18.2) and ^{18}F-FDG TLG of 70.3 mL (range, 2.7–659.0 mL).

Correlation Between Tracer Uptake and Treatment Response or PD-L1 Expression

^{89}Zr-DFO-Durvalumab PET/CT. The median PFS of patients with an above-median ^{89}Zr-DFO-durvalumab SUV_{peak} was 5.7 mo compared with 3.5 mo in the below-median group (HR, 1.5 [95% CI, 0.5–3.9; P = 0.45]; Fig. 5A). Also, gm ^{89}Zr-DFO-durvalumab TTB ratio did not correlate with survival (HR, 1.3 [95% CI, 0.5–3.3; P = 0.60]; Fig. 5B). Patients grouped based on the hottest lesion showed a similar PFS of 5.7 mo (SUV_{peak} ≥ 6.22) versus 3.5 mo (SUV_{peak} < 6.22) (HR, 1.1 [95% CI, 0.4–3.0; P = 0.84]).

To correct for partial-volume effect, the correlation of ^{89}Zr-DFO-durvalumab SUV_{peak} and TTB ratio with PFS was also performed after correcting for lesions less than 20 mm, showing no essential differences between results described for all lesions (Supplemental Fig. 6).

In total, 35 lesions were visible on evaluation CT scans during treatment. On a lesion level, ^{89}Zr-DFO-durvalumab accumulation and treatment response was variable (Fig. 6). There was no substantial correlation between lesional ^{89}Zr-DFO-durvalumab SUV_{peak} or TTB ratio with the change in lesion size at 12 wk (Spearman ρ, 0.45; P = 0.051 and Spearman ρ, −0.669; P = 0.78, respectively). A cutoff of the median SUV_{peak} of these lesions did not improve the correlation of ^{89}Zr-DFO-durvalumab SUV_{peak} with treatment response (Spearman ρ, 0.67; P = 0.855).

^{18}F-FDG PET/CT

Patients with an above-median ^{18}F-FDG TLG showed a significantly worse outcome than di patients with a low ^{18}F-FDG TLG (median PFS, 1.8 vs. 7.3 mo; HR, 2.4 [95% CI, 1.1–5.4; P = 0.04; Fig. 7]). Patients with above-median ^{18}F-FDG SUV_{peak} showed a median PFS of 5.3 compared with 5.7 mo in the below-median group (HR, 1.5 [95% CI, 0.7–3.4; P = 0.30]). The ^{18}F-FDG MTV was not associated with PFS (P = 0.69; not shown).

The correlation between ^{18}F-FDG SUV_{peak} and ^{18}F-FDG TLG ratio with PFS after correcting for lesions less than 20 mm is reported in the supplemental materials and showed similar results as described for all lesions (Supplemental Fig. 7).

On a lesion level, PD-L1 CPS did not correlate to ^{89}Zr-DFO-durvalumab SUV_{peak} (Spearman ρ, 0.38; P = 0.20), ^{89}Zr-DFO-durvalumab TTB ratio (Spearman ρ, −0.06; P = 0.85), ^{18}F-FDG TLG (Spearman ρ, 0.40; P = 0.90), or ^{18}F-FDG SUV_{peak} (Spearman ρ, −0.12; P = 0.70).

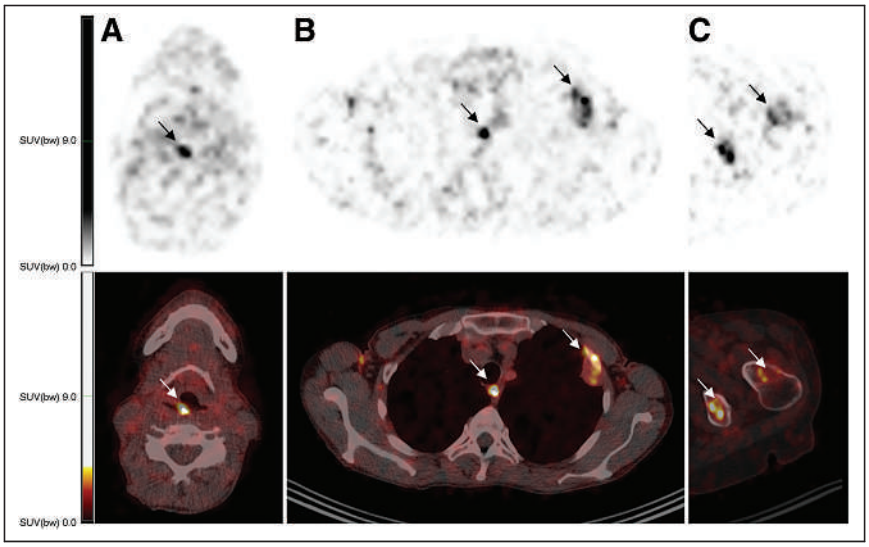

FIGURE 4. Example fused images of ^{89}Zr-DFO-durvalumab (10 mg) PET/CT images showing tracer uptake in known tumor locations. Axial sections in 2 different patients are displayed. Arrows highlight tumor lesions in local recurrence (A), lymph node and pleural lesion (B), and 2 other bone lesions (C). SUV(bw) = SUV based on body weight.

DISCUSSION

The PINCH study reported ^{89}Zr-DFO-durvalumab PET/CT in R/M SCCHN patients treated with durvalumab to address current caveats in the predictive role of PD-L1 expression on tumor biopsies. ^{89}Zr-DFO-durvalumab PET/CT was considered safe and feasible in a multicenter setting. Heterogeneous ^{89}Zr-DFO-durvalumab tumor accumulation was detected within and between

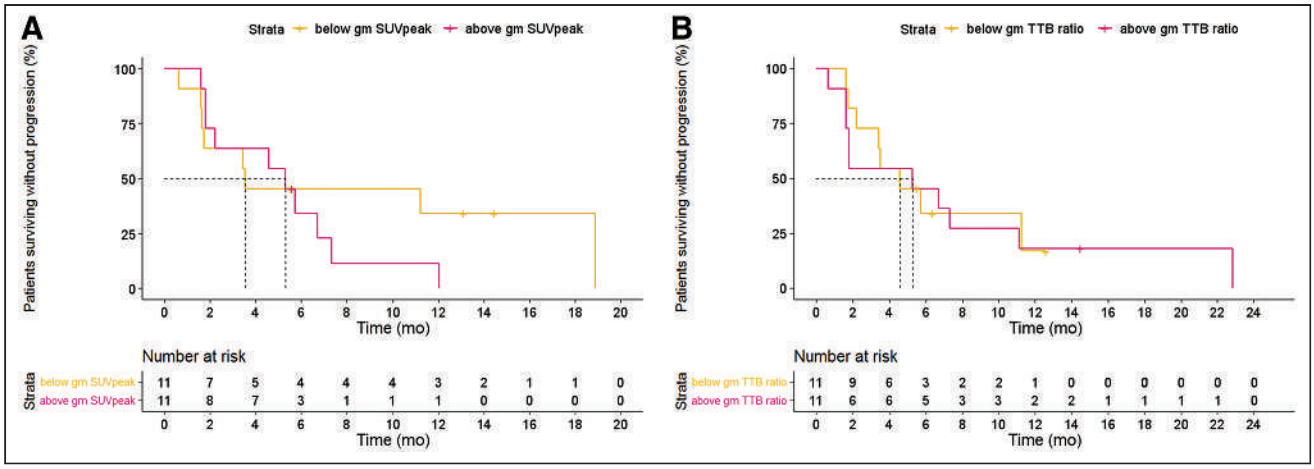

FIGURE 5. Kaplan–Meier estimates of PFS based on ^{89}Zr-DFO-durvalumab SUV_{peak} (A) and TTB ratios (B) dichotomized at median value.

patients. ^{89}Zr-DFO-durvalumab uptake could not predict durvalumab treatment response.

To achieve optimal tumor-to-background contrast, selection of proper antibody dose and imaging timing is essential. The PINCH study showed superior TTB ratios when performing PET/CT 5 d after ^{89}Zr-DFO-durvalumab administration using 10 mg of durvalumab, compared with 2 and 50 mg. In agreement with previous studies, increasing the dose of unlabeled antibody saturates the spleen uptake and results in higher concentrations of circulating ^{89}Zr-labeled antibodies and increased tumor uptake (*24,25*). At 50 mg, TTB ratio decreased, most likely explained by a decrease in available binding sites for ^{89}Zr-DFO-durvalumab. In line with this, low or absent tumor accumulation was also reported for ^{89}Zr-DFO-durvalumab PET imaging with 750 mg of unlabeled durvalumab (*22*).

Preclinical studies have demonstrated a relation between the accumulation of radiolabeled PD-1 and PD-L1 antibodies with PD-L1 expression, thereby distinguishing between tumors with different PD-L1 expression levels (*13,14*). The first 2 clinical trials also reported an association between radiolabeled PD-L1 antibody uptake and PD-L1 expression (*18,19*). However, we did not find such a correlation. Of note, our analysis was performed on a subset of patients using archival tissue biopsies, as fresh histologic proof was not mandatory for study inclusion. Besides sampling error due to small tumor samples, correlating (archival) biopsies to PET imaging remains challenging because of the heterogeneous and dynamic expression levels of PD-L1. Also, in comparison to previous studies, the PD-L1 staining and scoring procedures differed (*29,30*).

A previous study in 22 patients with metastatic NSCLC, triple-negative breast cancer, and bladder cancer treated with atezolizumab, above-median gm ^{89}Zr-atezolizumab SUV_{max} was associated with improved overall survival and PFS (*18*). Furthermore, both ^{89}Zr-nivolumab (anti–PD-1) and ^{18}F-BMS-986192 (anti–PD-L1) SUV_{peak} were correlated to nivolumab treatment response in 13 NSCLC patients. However, 2 other studies using ^{89}Zr-durvalumab and ^{89}Zr-pembrolizumab in NSCLC patients showed a trend but no significant correlation between tracer uptake and durvalumab, respectively, and pembrolizumab treatment efficacy (*22,31*), which is more in line with our data. The early termination of the study resulted in a lower number of included patients. Potentially, more patients could have resulted in a significant correlation. We also evaluated the correlation between tumor metabolism and ICI response, as performed in previous studies (*32,33*). Our data suggest that, in particular,^{18}F-FDG TLG may identify poor durvalumab responders upfront. A potential explanation could be that patients with more extensive disease have already undergone extra steps in the immune escape route.

Altogether, PET imaging with ^{89}Zr-labeled PD-L1 antibodies has not consistently shown a correlation between tracer uptake and treatment response. Potential explanations are the different characteristics

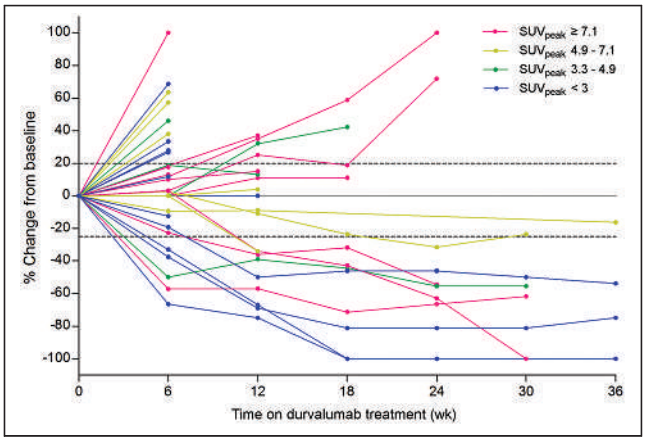

FIGURE 6. Spaghetti plot reporting lesional ^{89}Zr-DFO-durvalumab SUV_{peak} and lesional response of 17 lesions where colors identify corresponding ^{89}Zr-DFO-durvalumab uptake by distribution over quartiles.

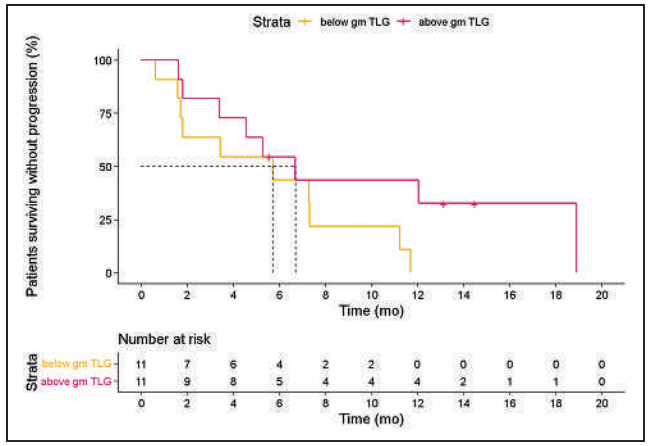

FIGURE 7. Kaplan–Meier estimates of PFS based on ^{18}F-FDG TLG dichotomized at population median.

of the antibodies used, which include affinity for PD-L1, which could influence tumor retention; Fc-tail modification/glycosylation, which could affect circulation time and effector functions; and nonspecific antibody uptake due to enhanced permeability and retention (EPR) effect (*34–36*). As a result of the EPR effect, there is always a (low) PET signal in the tumor, although the PET signal is not PD-L1–mediated. This EPR effect may hamper the detection of small amounts of tumor PD-L1, which can be clinically relevant as low PD-L1 expression (1% positive cells) has been associated with ICI response. To limit the nonspecific uptake and thereby increase the potential to measure low PD-L1 expression levels, small molecules or peptides with rapid blood clearance can be used (*37,38*). Finally, other mechanisms within the immune suppressive microenvironment beyond PD-L1, such as the activation and promoting of CD8+ T cell priming in tumor-draining lymph nodes, determining ICI response could have influenced the correlation between tracer uptake and ICI response (*39*).

Despite the fact that ^{89}Zr-DFO-durvalumab did not correlate to treatment outcome, we do see potential of ^{89}Zr-labeled antibodies in optimizing the ICI treatment efficacy in patients with R/M SCCHN (*40*). Besides a unique insight into antibody biodistribution, the in vivo visualization of ^{89}Zr-labeled antibodies highlights essential local effector mechanisms, reveals the complexity of dose–response relations, and may shed a new light on the role of nontumor located PD-L1 expression in the anticancer immune responses (*39*). Ultimately, this teaches us how to use (and combine) these drugs to improve response rates, an essential step in early drug development suitable for phase 1 and 2 clinical trials.

CONCLUSION

The PINCH study is the first, to our knowledge, to perform PD-L1 PET/CT in patients with R/M SCCHN. It has shown that ^{89}Zr-DFO-durvalumab PET/CT imaging is feasible and safe. However, ^{89}Zr-DFO-durvalumab uptake did not correlate to PD-L1 expression on a patient level and could not predict durvalumab treatment response.

DISCLOSURE

This study was supported by AstraZeneca, Radboud Institute for Health Sciences, and NWO (91617039, KWF [10099]). This study was supported by Astrazeneca. Carla M.L. van Herpen received research grants from AstraZeneca, Bristol-Myers Squibb, MSD, Merck, Ipsen, Novartis, and Sanofi and has been on advisory boards for Bayer, Bristol-Myers Squibb, Ipsen, MSD, and Regeneron. Erik H.J.G. Aarntzen received a research grant from AstraZeneca. No other potential conflict of interest relevant to this article was reported.

KEY POINTS

QUESTION: Can ^{89}Zr-DFO-durvalumab PET/CT predict durvalumab treatment response in patients with R/M head and neck cancer?

PERTINENT FINDINGS: This multicenter clinical trial studies the feasibility and safety of ^{89}Zr-DFO-durvalumab PET/CT and its ability to predict durvalumab treatment response. ^{89}Zr-DFO-durvalumab PET/CT was safe and feasible but was unable to predict durvalumab treatment response.

IMPLICATIONS FOR PATIENT CARE: Our findings indicate that an approach other than radiolabeled antibody–based PET imaging to predict treatment response to ICIs using molecular imaging is needed.

REFERENCES

1. Sung H, Ferlay J, Siegel RL, et al. Global cancer statistics 2020: GLOBOCAN estimates of incidence and mortality worldwide for 36 cancers in 185 countries. *CA Cancer J Clin.* 2021;71:209–249.
2. Ferlay J, Colombet M, Soerjomataram I, et al. Estimating the global cancer incidence and mortality in 2018: GLOBOCAN sources and methods. *Int J Cancer.* 2019;144:1941–1953.
3. Harrington KJ, Ferris RL, Blumenschein G Jr, et al. Nivolumab versus standard, single-agent therapy of investigator's choice in recurrent or metastatic squamous cell carcinoma of the head and neck (CheckMate 141): health-related quality-of-life results from a randomised, phase 3 trial. *Lancet Oncol.* 2017;18:1104–1115.
4. Cohen EEW, Bell RB, Bifulco CB, et al. The Society for Immunotherapy of Cancer consensus statement on immunotherapy for the treatment of squamous cell carcinoma of the head and neck (HNSCC). *J Immunother Cancer.* 2019;7:184.
5. Burtness B, Harrington KJ, Greil R, et al. Pembrolizumab alone or with chemotherapy versus cetuximab with chemotherapy for recurrent or metastatic squamous cell carcinoma of the head and neck (KEYNOTE-048): a randomised, open-label, phase 3 study. *Lancet.* 2019;394:1915–1928.
6. Fridman WH, Pagès F, Sautès-Fridman C, Galon J. The immune contexture in human tumours: impact on clinical outcome. *Nat Rev Cancer.* 2012;12:298.
7. Cohen EEW, Soulières D, Le Tourneau C, et al. Pembrolizumab versus methotrexate, docetaxel, or cetuximab for recurrent or metastatic head-and-neck squamous cell carcinoma (KEYNOTE-040): a randomised, open-label, phase 3 study. *Lancet.* 2019;393:156–167.
8. de Ruiter EJ, Mulder FJ, Koomen BM, et al. Comparison of three PD-L1 immunohistochemical assays in head and neck squamous cell carcinoma (HNSCC). *Mod Pathol.* 2021;34:1125–1132.
9. Reck M, Rodriguez-Abreu D, Robinson AG, et al. Pembrolizumab versus chemotherapy for PD-L1-positive non-small-cell lung cancer. *N Engl J Med.* 2016;375:1823–1833.
10. Rittmeyer A, Barlesi F, Waterkamp D, et al. Atezolizumab versus docetaxel in patients with previously treated non-small-cell lung cancer (OAK): a phase 3, open-label, multicentre randomised controlled trial. *Lancet.* 2017;389:255–265.
11. Siu L, Even C, Mesía R, et al. A randomized, open-label, multicenter, global phase 2 study of durvalumab (D), tremelimumab (T), or D plus T, in patients with PD-L1 low/negative recurrent or metastatic head and neck squamous cell carcinoma: CONDOR. *Int J Radiat Oncol Biol Phys.* 2018;100:1307.
12. Verhoeff SR, van den Heuvel MM, van Herpen CML, Piet B, Aarntzen E, Heskamp S. Programmed cell death-1/ligand-1 PET imaging: a novel tool to optimize immunotherapy? *PET Clin.* 2020;15:35–43.
13. Heskamp S, Wierstra PJ, Molkenboer-Kuenen JDM, et al. PD-L1 microSPECT/CT imaging for longitudinal monitoring of PD-L1 expression in syngeneic and humanized mouse models for cancer. *Cancer Immunol Res.* 2019;7:150–161.
14. Hettich M, Braun F, Bartholoma MD, Schirmbeck R, Niedermann G. High-resolution PET imaging with therapeutic antibody-based PD-1/PD-L1 checkpoint tracers. *Theranostics.* 2016;6:1629–1640.
15. Hofman P. The challenges of evaluating predictive biomarkers using small biopsy tissue samples and liquid biopsies from non-small cell lung cancer patients. *J Thorac Dis.* 2019;11:S57–S64.
16. Kluger HM, Zito CR, Turcu G, et al. PD-L1 studies across tumor types, its differential expression and predictive value in patients treated with immune checkpoint inhibitors. *Clin Cancer Res.* 2017;23:4270–4279.
17. Waaijer SJH, Kok IC, Eisses B, et al. Molecular imaging in cancer drug development. *J Nucl Med.* 2018;59:726–732.
18. Bensch F, van der Veen EL, Lub-de Hooge MN, et al. ^{89}Zr-atezolizumab imaging as a non-invasive approach to assess clinical response to PD-L1 blockade in cancer. *Nat Med.* 2018;24:1852–1858.
19. Niemeijer AN, Leung D, Huisman MC, et al. Whole body PD-1 and PD-L1 positron emission tomography in patients with non-small-cell lung cancer. *Nat Commun.* 2018;9:4664.
20. Boellaard R, Delgado-Bolton R, Oyen WJ, et al. FDG PET/CT: EANM procedure guidelines for tumour imaging: version 2.0. *Eur J Nucl Med Mol Imaging.* 2015;42:328–354.
21. Makris NE, Boellaard R, Visser EP, et al. Multicenter harmonization of ^{89}Zr PET/CT performance. *J Nucl Med.* 2014;55:264–267.
22. Smit J, Borm FJ, Niemeijer A-LN, et al. PD-L1 PET/CT imaging with radiolabeled durvalumab in patients with advanced stage non-small cell lung cancer. *J Nucl Med.* 2022;63:686–693.
23. Verel I, Visser GW, Boellaard R, Stigter-van Walsum M, Snow GB, van Dongen GA. ^{89}Zr immuno-PET: comprehensive procedures for the production of ^{89}Zr-labeled monoclonal antibodies. *J Nucl Med.* 2003;44:1271–1281.
24. Jauw YW, Menke-van der Houven van Oordt CW, Hoekstra OS, et al. Immuno-positron emission tomography with zirconium-89-labeled monoclonal antibodies

in oncology: what can we learn from initial clinical trials? *Front Pharmacol.* 2016; 7:131.
25. Dijkers EC, Oude Munnink TH, Kosterink JG, et al. Biodistribution of ^{89}Zr-trastuzumab and PET imaging of HER2-positive lesions in patients with metastatic breast cancer. *Clin Pharmacol Ther.* 2010;87:586–592.
26. Eisenhauer EA, Therasse P, Bogaerts J, et al. New response evaluation criteria in solid tumours: revised RECIST guideline (version 1.1). *Eur J Cancer.* 2009;45: 228–247.
27. Pinker K, Riedl C, Weber WA. Evaluating tumor response with FDG PET: updates on PERCIST, comparison with EORTC criteria and clues to future developments. *Eur J Nucl Med Mol Imaging.* 2017;44:55–66.
28. Boellaard R. Quantitative oncology molecular analysis suite: ACCURATE. *J Nucl Med.* 2018;59(suppl 1):1753.
29. Madore J, Vilain RE, Menzies AM, et al. PD-L1 expression in melanoma shows marked heterogeneity within and between patients: implications for anti-PD-1/PD-L1 clinical trials. *Pigment Cell Melanoma Res.* 2015;28:245–253.
30. Ilie M, Long-Mira E, Bence C, et al. Comparative study of the PD-L1 status between surgically resected specimens and matched biopsies of NSCLC patients reveal major discordances: a potential issue for anti-PD-L1 therapeutic strategies. *Ann Oncol.* 2016;27:147–153.
31. Niemeijer AN, Oprea Lager DE, Huisman MC, et al. First-in-human study of ^{89}Zr-pembrolizumab PET/CT in patients with advanced stage non-small-cell lung cancer. *J Nucl Med.* July 16, 2021 [Epub ahead of print].
32. Dall'Olio FG, Calabro D, Conci N, et al. Baseline total metabolic tumour volume on 2-deoxy-2-[^{18}F]fluoro-d-glucose positron emission tomography-computed tomography as a promising biomarker in patients with advanced non-small cell lung cancer treated with first-line pembrolizumab. *Eur J Cancer.* 2021;150: 99–107.
33. Ito K, Schoder H, Teng R, et al. Prognostic value of baseline metabolic tumor volume measured on ^{8}F-fluorodeoxyglucose positron emission tomography/computed tomography in melanoma patients treated with ipilimumab therapy. *Eur J Nucl Med Mol Imaging.* 2019;46:930–939.
34. Boussiotis VA. Molecular and biochemical aspects of the PD-1 checkpoint pathway. *N Engl J Med.* 2016;375:1767–1778.
35. Arce Vargas F, Furness AJS, Litchfield K, et al. Fc effector function contributes to the activity of human anti-CTLA-4 antibodies. *Cancer Cell.* 2018;33: 649–663.e4.
36. Shi Y, van der Meel R, Chen X, Lammers T. The EPR effect and beyond: strategies to improve tumor targeting and cancer nanomedicine treatment efficacy. *Theranostics.* 2020;10:7921–7924.
37. Stutvoet TS, van der Veen EL, Kol A, et al. Molecular imaging of PD-L1 expression and dynamics with the adnectin-based PET tracer ^{18}F-BMS-986192. *J Nucl Med.* 2020;61:1839–1844.
38. Leung D, Bonacorsi S, Smith RA, Weber W, Hayes W. Molecular imaging and the PD-L1 pathway: from bench to clinic. *Front Oncol.* 2021;11:698425.
39. Borst J, Busselaar J, Bosma DMT, Ossendorp F. Mechanism of action of PD-1 receptor/ligand targeted cancer immunotherapy. *Eur J Immunol.* 2021;51:1911–1920.
40. Canning M, Guo G, Yu M, et al. Heterogeneity of the head and neck squamous cell carcinoma immune landscape and its impact on immunotherapy. *Front Cell Dev Biol.* 2019;7:52.

Reproducibility of PSMA PET/CT Imaging for Primary Staging of Treatment-Naïve Prostate Cancer Patients Depends on the Applied Radiotracer: A Retrospective Study

Marinus J. Hagens[1–3], Daniela E. Oprea-Lager[4], André N. Vis[2,3], Maurits Wondergem[5], Maarten L. Donswijk[5], Dennie Meijer[2,3], Louise Emmett[6], Pim J. van Leeuwen[1,3], and Henk G. van der Poel[1–3]

[1]Department of Urology, Netherlands Cancer Institute–Antoni van Leeuwenhoek Hospital, Amsterdam, The Netherlands; [2]Department of Urology, Amsterdam University Medical Centers Location VUmc, Amsterdam, The Netherlands; [3]Prostate Cancer Network Netherlands, Amsterdam, The Netherlands; [4]Department of Radiology and Nuclear Medicine, Amsterdam University Medical Centers Location VUmc, Amsterdam, The Netherlands; [5]Department of Nuclear Medicine, Netherlands Cancer Institute–Antoni van Leeuwenhoek Hospital, Amsterdam, The Netherlands; and [6]Department of Diagnostic Imaging, St. Vincent's Public Hospital, and Australia University of New South Wales, Sydney, New South Wales, Australia

Our purpose was to determine and compare the interobserver variability of 3 clinically frequently used radiotracers targeting the prostate-specific membrane antigen (PSMA), namely ^{18}F-DCFPyL, ^{18}F-PSMA-1007, and ^{68}Ga-PSMA-11, in primary prostate cancer (PCa) staging. **Methods:** Patients with newly diagnosed PCa in whom PSMA PET/CT was performed for primary staging purposes were retrospectively included. All PSMA PET/CT images were centrally overread within a high-volume PCa center, and original reports (from referring hospitals) were compared with overread reports (from the overreading hospital). To assess the interobserver variability, a Cohen κ analysis was used. To study possible differences in interobserver variability between the 3 applied PSMA radiotracers, multivariate logistic regression analyses were used. **Results:** In total, 584 patients with newly diagnosed PCa were included in the analysis. ^{18}F-DCFPyL, ^{18}F-PSMA-1007, and ^{68}Ga-PSMA-11 were used in 205 (35.1%), 168 (28.8%), and 211 (36.1%) patients, respectively. The overall agreement (Cohen κ analysis) for locoregional lymph node metastases, distant lymph node metastases, bone metastases, and visceral metastases was 0.86, 0.86, 0.80, and 0.46, respectively. ^{18}F-PSMA-1007 showed a significantly increased interobserver variability regarding bone metastases, compared with ^{18}F-DCFPyL and ^{68}Ga-PSMA-11 ($P = 0.001$ and 0.03, respectively). Additionally, ^{18}F-PSMA-1007 showed a significantly increased interobserver variability regarding overall agreement and locoregional lymph node metastases, compared with ^{18}F-DCFPyL ($P < 0.001$ and $P = 0.01$, respectively). **Conclusion:** Interobserver variability differs among the 3 clinically frequently used PSMA radiotracers (^{18}F-DCFPyL, ^{18}F-PSMA-1007, and ^{68}Ga-PSMA-11) in patients with newly diagnosed PCa. The agreement in bone metastases is significantly worse for ^{18}F-PSMA-1007, mainly due to nonspecific tracer uptake in osseous structures. On the basis of our findings, PSMA PET/CT scans undertaken with ^{18}F-PSMA-1007 in primary staging should be interpreted carefully, and training on interpreting this specific PSMA radiotracer is strongly advised.

Key Words: PSMA PET; prostate cancer; staging; radiotracers; interobserver variability

J Nucl Med 2022; 63:1531–1536
DOI: 10.2967/jnumed.121.263139

Prostate cancer (PCa) is the second most common malignancy in men worldwide. Imaging has a pivotal role in staging and selection of the appropriate management strategy in men with primary diagnosed PCa. After its clinical introduction in 2011, PET/CT imaging with agents targeting the prostate-specific membrane antigen (PSMA), a transmembrane folate hydrolase on the surface of PCa cells, has shown increasing adoption for use in staging and restaging of PCa (*1,2*). Compared with conventional imaging using CT and bone scans, PSMA PET/CT has shown superior accuracy; higher sensitivity and specificity, more frequent management changes, fewer equivocal findings, and lower radiation exposure (*3*).

The interobserver variability, defined as the absence of consensus among nuclear medicine physicians regarding oncologic staging, gives an indication of the reliability and reproducibility of the assessment and is an essential indicator of the clinical value of PSMA PET/CT scans. Interobserver variability is affected by the ability of nuclear medicine physicians to recognize potential false-positive sources of uptake, such as false-positive bone findings, already frequently described with PSMA radiotracers (*4–12*). Forestalling these false-positive findings and consequently limiting the interobserver variability are dependent on tracer and training and crucial to ensuring high-quality diagnostics.

Currently, several PSMA radiotracers, including ^{18}F-DCFPyL, ^{18}F-PSMA-1007, and ^{68}Ga-PSMA-11, are being used for PET/CT imaging. Even though these PSMA radiotracers are well established, agreement on which tracer is optimal in primary PCa staging is lacking. Few studies have been published regarding the interobserver variability of PET imaging with PSMA radiotracers, and these studies have focused primarily on ^{68}Ga-PSMA-11 (*1,13–15*). No large studies have compared interobserver variabilities of different PSMA radiotracers for staging purposes. The aim of this study was to determine the interobserver variability in primary PCa staging among the 3 clinically most frequently used PSMA radiotracers (i.e., ^{18}F-DCFPyL, ^{18}F-PSMA-1007, and ^{68}Ga-PSMA-11) and identify the PSMA radiotracer with the least interobserver variability for use in PCa staging.

Received Aug. 30, 2021; revision accepted Feb. 10, 2022.
For correspondence or reprints, contact Marinus J. Hagens (m.hagens@nki.nl).
Published online Aug. 25, 2022.

MATERIALS AND METHODS

Study Design and Patient Population

A retrospective cohort study was performed at The Netherlands Cancer Institute (NCI) on the interobserver variability of PSMA PET/CT scans in patients with newly diagnosed PCa.

Patients who had been referred to the NCI between January 2018 and December 2020, and whose PSMA PET/CT scans were overread (defined as a secondary interpretation) by 1 of 3 nuclear medicine physicians of the NCI, were retrospectively included. Patients were excluded from analysis when staging was performed using tracers other than ^{18}F-DCFPyL, ^{18}F-PSMA-1007, or ^{68}Ga-PSMA-11 and when PSMA PET/CT scans were not performed for primary staging purposes (Fig. 1). The institutional review board approved this retrospective study, and the requirement to obtain informed consent was waived.

Being a high-volume PCa center, the NCI received patient referrals on a case-by-case basis, either for treatment or treatment advice, from 44 hospitals in The Netherlands (academic or nonacademic and high- or low-volume). Together with the referral letter, DICOM images were securely sent to the NCI using CD-ROMs. After uploading the DICOM images to the electronic system, we destroyed the CD-ROMs. All PSMA PET/CT scans, initially performed, interpreted, and reported in referring hospitals, were overread in the NCI for clinical purposes and in line with the PROMISE criteria (*16*). Given the clinical purpose of the overreads, data were not anonymized. The assessments of nuclear medicine physicians from both referring hospitals and overreading hospitals were performed in a nonmasked manner. All PSMA PET/CT scans were discussed within a multidisciplinary consultation in the NCI with radiologists, nuclear medicine physicians, urologists, radiation oncologists, and medical oncologists. Overreads were considered the reference to be followed.

Patient characteristics were collected from patient charts, and PSMA PET/CT results were collected from nuclear medicine reports. According to the PROMISE criteria, a scan was reported as positive when the lesion was consistent with or suggestive of being PCa (*16*). Original reports (from referring hospitals) were compared with overread reports (from the overreading hospital—i.e., NCI) regarding molecular imaging TNM (miTNM) classification. Agreement scoring was based on the miTNM classification irrespective of the number or location of lesions per patient. Overall agreement was defined as complete agreement in miTNM classification irrespective of the number or location of lesions per patient.

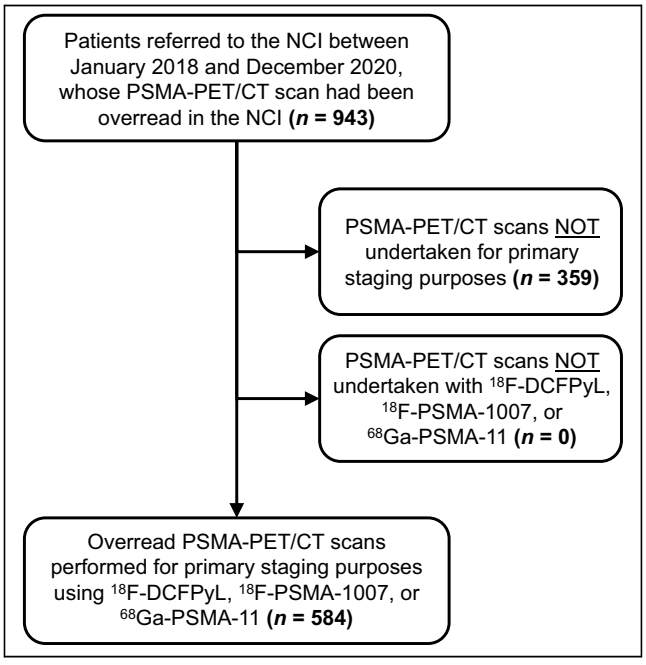

FIGURE 1. Flowchart of study design.

PET Imaging and Analysis

All PET images were acquired from mid thigh to skull base or vertex. Most patients selected for PSMA PET/CT had a biopsy Gleason score of at least 4 + 3 = 7 (International Society of Urological Pathology [ISUP] ≥ 3), an initial prostate-specific antigen (PSA) value of at least 20 ng/mL, or clinical or radiologic disease that was at least T3.

Different tracer incubation times and doses were used for different tracers; a median of 60 min (interquartile range [IQR], 60–120 min) after a median dose of 217 MBq (IQR, 205–305 MBq) for ^{18}F-DCFPyL, a median of 90 min (IQR, 89–120 min) after a median dose of 271 MBq (IQR, 231–301 MBq) for ^{18}F-PSMA-1007, and a median of 60 min (IQR, 59–60 min) after a median dose of 137 MBq (IQR, 117–156 MBq) for ^{68}Ga-PSMA-11. PET images were combined with either a low-dose CT scan (120–140 kV, 40–80 mAs) or a diagnostic CT scan (130 kV, 110 mAs) for anatomic correlation and attenuation correction.

Statistical Analysis

Categoric variables were reported as frequency distributions and percentages, and continuous variables were reported as medians with IQR.

First, the characteristics of the 3 different patient populations staged with 1 of the 3 PSMA radiotracers were compared to check for case-mix variation, using a χ^2 test for dichotomous and categoric variables or a Mann–Whitney U test for continuous variables. To assess the interobserver variability of the 3 clinically most frequently used PSMA radiotracers, a Cohen κ analysis was performed for each miTNM category. As conventionally classified, κ values of 0–0.20 defined poor agreement; 0.21–0.40, fair agreement; 0.41–0.60, moderate agreement; 0.61–0.80, substantial agreement; and 0.81–1.0, nearly perfect agreement (*17*). To study possible differences in interobserver variability between the 3 applied PSMA radiotracers, multivariate logistic regression analyses were used, taking into account potential differences in initial PSA level, cT stage, cN stage, and biopsy ISUP grade. For this analysis, the degree of agreement was dichotomized.

A P value of less than 0.05 was considered to indicate statistical significance. All statistical analyses were performed with the statistical package SPSS (version 27; IBM) for MacOS (Apple).

RESULTS

In total, 584 patients staged with PSMA PET/CT for primary, untreated PCa were included in the analysis. Their characteristics are presented in Table 1. ^{18}F-DCFPyL, ^{18}F-PSMA-1007, and ^{68}Ga-PSMA-11 were applied in 205 (35.1%), 168 (28.8%), and 211 (36.1%) of the 584 patients and in 15 (34.1%), 27 (61.4%), and 17 (38.6%) of 44 hospitals, respectively. A comparison among radiotracers showed a case-mix variation in clinical tumor stage (cT stage) and clinical nodal stage (cN stage); ^{18}F-DCFPyL was applied in patients with significantly lower cT and cN stages than was ^{18}F-PSMA-1007 ($P = 0.01$ and $P < 0.001$, respectively) or ^{68}Ga-PSMA-11 ($P = 0.01$ and 0.01, respectively).

Interobserver Variability

According to the local PSMA PET/CT interpretation, 99.0% (578/584) of patients were considered positive, of whom 31.8% (186/584) had locoregional lymph nodes metastases (miN1), 9.1% (53/584) had distant lymph node metastases (miM1a), 12.0% (70/584) had bone metastases (miM1b), and 0.5% (3/584) had visceral metastases (miM1c; lung, liver, and pleura). After overreading all

TABLE 1
Patient Characteristics

Characteristic	Overall (n = 584)	^{18}F-DCFPyL (n = 205)	^{18}F-PSMA-1007 (n = 168)	^{68}Ga-PSMA-11 (n = 211)	Case-mix variation		
					^{18}F-DCFPyL vs. ^{18}F-PSMA-1007	^{18}F-DCFPyL vs. ^{68}Ga-PSMA-11	^{18}F-PSMA-1007 vs. ^{68}Ga-PSMA-11
Age (y)	68 (63–72)	68 (63–71)	67 (63–72)	68 (62–73)	0.63	0.47	0.84
Initial PSA (μg/L)	14.0 (8.0–29.2)	12.2 (7.8–25.3)	16.6 (8.3–33.8)	14.0 (8.4–31.0)	0.08	0.14	0.76
Clinical T stage							
T1	109 (18.7%)	40 (19.5%)	27 (16.1%)	42 (19.9%)	0.01	0.01	0.78
T2	250 (42.8%)	101 (49.3%)	68 (40.5%)	81 (38.4%)			
T3	212 (36.3%)	64 (31.2%)	67 (39.9%)	81 (38.4%)			
T4	13 (2.2%)	— (0.0%)	6 (3.6%)	7 (3.3%)			
Clinical N stage							
N0	393 (67.3%)	159 (77.6%)	101 (60.1%)	133 (63.0%)	<0.001	0.01	0.54
N1	191 (32.7%)	46 (22.4%)	67 (39.9%)	78 (37.0%)			
Biopsy ISUP grade							
1	31 (5.3%)	8 (3.9%)	14 (8.3%)	9 (4.3%)	0.22	0.15	0.45
2	95 (16.3%)	43 (21.0%)	25 (14.9%)	27 (12.8%)			
3	157 (26.9%)	47 (22.9%)	45 (26.8%)	65 (30.8%)			
4	143 (24.5%)	51 (24.9%)	38 (22.6%)	54 (25.6%)			
5	154 (26.4%)	56 (27.3%)	44 (26.2%)	54 (25.6%)			
Missing	4 (0.7%)	— (0.0%)	2 (1.2%)	2 (0.9%)			

Categoric data are number and percentage; continuous data are median and IQR.

scans, 98.6% (576/584) were considered positive, of which 32.7% (191/584) had miN1, 9.8% (57/584) had miM1a, 10.6% (62/584) had miM1b, and 1.0% (6/584) had miM1c (lung and liver, Table 2).

The overall agreement for all tracers combined for the assessment of a positive scan, miN1 status, miM1a status, miM1b status, and miM1c status was 0.71, 0.86, 0.86, 0.80, and 0.46, respectively (Cohen κ analysis, Table 3). For ^{18}F-DCFPyL, the Cohen κ for a positive scan, miN1 status, miM1a status, and miM1b status was 0.66, 0.89, 0.81, and 0.88, respectively. No κ for miM1c status could be calculated within the ^{18}F-DCFPyL cohort, since no visceral metastases were found by nuclear medicine physicians from referring hospitals. For ^{18}F-PSMA-1007, the Cohen κ for a positive scan, miN1 status, miM1a status, miM1b status, and miM1c status was 0.66, 0.82, 0.79, 0.73, and 0.50, respectively. For ^{68}Ga-PSMA-11, the Cohen κ for a positive scan, miN1 status, miM1a status, miM1b status, and miM1c status was 1.00, 0.86, 0.91, 0.82, and 0.49, respectively.

TABLE 2
PSMA PET/CT Results

Result	Referring hospital	Overreading hospital
Positive scan	578 (99.0%)	576 (98.6%)
Locoregional lymph node metastases (miN)	186 (31.8%)	191 (32.7%)
Distant metastases		
miM1a	53 (9.1%)	57 (9.8%)
miM1b	70 (12.0%)	62 (10.6%)
miM1c	3 (0.5%)	6 (1.0%)

miM1a = Distant lymph node metastases; miM1b = bone metastases; miM1c = visceral metastases.

Positive scan was defined as agreement in PSMA avidity. Data are number of patients for whom referring or overreading nuclear medicine physician considers respective miTNM classification as positive and are reported as numbers of patients and percentages with respect to total number of patients.

When comparing the interobserver variability of the 3 clinically frequently used radiotracers, significant differences were found regarding overall agreement, miN status, and miM1b status (Table 4). ^{18}F-PSMA-1007 showed a significantly higher interobserver variability regarding miM1b status than did ^{18}F-DCFPyL or ^{68}Ga-PSMA-11 (P = 0.001 and 0.03, respectively). Additionally, ^{18}F-PSMA-1007 showed a significantly higher interobserver variability regarding overall agreement and miN status than did ^{18}F-DCFPyL ($P < 0.001$ and $P = 0.01$, respectively).

Clinical Confirmation

In 29 (5.0%) patients, referred from 18 different academic or nonacademic and high- or low-volume centers, no agreement regarding miM1b status was observed between the original report and the overread report. ^{18}F-PSMA-1007 was used in 17 of these 29 (58.6%), of whom 7 underwent a robot-assisted radical prostatectomy with pelvic lymph node dissection. After surgery, 6 of the 7

TABLE 3
PSMA PET/CT Interobserver Variability

Parameter	Cohen κ			
	Overall	^{18}F-DCFPyL (n = 205)	^{18}F-PSMA-1007 (n = 168)	^{68}Ga-PSMA-11 (n = 211)
Positive scan	0.71 (0.14)	0.66 (0.18)	0.66 (0.32)	1.00 (0.00)
Locoregional lymph nodes (miN)	0.86 (0.02)	0.89 (0.04)	0.82 (0.04)	0.86 (0.04)
Distant metastasis				
miM1a	0.86 (0.04)	0.81 (0.09)	0.79 (0.07)	0.91 (0.04)
miM1b	0.80 (0.04)	0.88 (0.06)	0.73 (0.06)	0.82 (0.06)
miM1c*	0.46 (0.15)	—	0.50 (0.31)	0.49 (0.18)

*No Cohen κ could be calculated for miM1c of ^{18}F-DCFPyL, since miM1c of referring nuclear medicine physicians was constant; all scans were initially reported as no miM1c.

miM1a = distant lymph node metastases; miM1b = bone metastases; miM1c = visceral metastases.

Data in parentheses are SE. Positive scan was defined as agreement in PSMA avidity. Interobserver variability represents agreement of nuclear medicine physicians regarding miTNM classification, irrespective of number or location of lesions per patient.

patients had undetectable PSA levels, making the presence of bone metastases unlikely. In 1 patient, PSA levels remained detectable (0.12 μg/L). Pathology reports showed a pT3aN1 tumor with 3 of 19 positive locoregional lymph nodes and a clear margin. In this patient, PSMA PET/CT reported 3 locoregional lymph nodes but also a dubious paraaortic lymph node. Consequently, in this patient, the presence of bone metastases remains equivocal.

DISCUSSION

Since the introduction of PSMA PET/CT in clinical practice, various types of PSMA radiotracers have been developed, implemented, and used in parallel. However, these interchangeable applications are prone to bias and may impact the therapeutic management of patients with PCa at initial staging. To the best of our knowledge, this was the first study comparing the interobserver variability of the 3 clinically most frequently used radiotracers in PSMA PET/CT imaging. We observed superior interobserver agreement for the radiotracers ^{18}F-DCFPyL and ^{68}Ga-PSMA-11 compared with ^{18}F-PSMA-1007 in regard to miN status, miM1b status, and overall agreement.

No studies comprising large patient cohorts have been conducted yet on the interobserver variability of ^{18}F-PSMA-1007 and ^{18}F-DCFPyL for use in patients with newly diagnosed PCa. Studies on the interobserver variability of ^{68}Ga-PSMA-11, on the other hand, have been conducted. Basha et al. (*13*), Derwael et al. (*14*), Demirci et al. (*18*), and Gültekin et al. (*19*) described substantial to nearly perfect agreement for miN, miM1a, miM1b, and miM1c status (κ values of 0.63–0.94). Compared with the aforementioned

TABLE 4
PSMA PET/CT Interobserver Variability

Parameter	Agreement (%)			*P*		
	^{18}F-DCFPyL (n = 205)	^{18}F-PSMA-1007 (n = 168)	^{68}Ga-PSMA-11 (n = 211)	^{18}F-DCFPyL vs. ^{18}F-PSMA-1007	^{18}F-DCFPyL vs. ^{68}Ga-PSMA-11	^{18}F-PSMA-1007 vs. ^{68}Ga-PSMA-11
Positive scan	98.5	99.4	100.0	0.91	0.99	0.99
Locoregional lymph nodes (miN)	96.1	90.5	93.4	0.03	0.18	0.41
Distant metastasis						
miM1a	98.0	95.2	98.1	0.16	0.77	0.18
miM1b	98.0	89.9	96.2	0.001	0.29	0.03
miM1c	99.5	98.8	97.6	0.74	0.18	0.43
Overall agreement	91.2	77.4	84.8	<0.001	0.08	0.14

miM1a = distant lymph node metastases; miM1b = bone metastases; miM1c = visceral metastases.

Positive scan was defined as agreement in PSMA avidity. Agreement scoring was based on miTNM classification, irrespective of number or location of lesions per patient, with respect to total number of patients scanned with tracer above column. Overall agreement was defined as complete agreement in PCa staging irrespective of number or location of lesions per patient, with respect to total number of patients scanned with tracer above column. Data on agreement are percentages. Degree of significance is corrected for possible confounding variables (initial PSA level, cT stage, cN stage, and biopsy ISUP grade).

studies, we found better interobserver agreement for ^{68}Ga-PSMA-11; only nearly perfect agreement was found (κ values of 0.82–1.00). Notably, we found a relatively low Cohen κ for the assessment of a positive scan and miM1c status using PSMA PET/CT imaging, whereas a high interobserver agreement was observed. This is due to a previously described κ paradox: the higher the agreement, the higher the possibility of finding agreement by chance. Since the Cohen κ corrects for chance, a higher agreement can create a smaller Cohen κ (*20*).

The overall agreement for the clinically used PSMA radiotracers regarding miN1, miM1a, and miM1b status was moderate to high. Accordingly, a nearly perfect interobserver agreement was found for both miN and miM1a status (both κ values of 0.86). This is in contrast to the interobserver agreement of other diagnostic modalities frequently used in PCa staging, such as MRI. Regarding locoregional and distant lymph node staging, Johnston et al. found decreased κ values for N and M1a status using whole-body MRI (κ = 0.79 and 0.68, respectively) compared with our κ values for miN and miM1a status (*21*). This higher interobserver variability relative to PSMA PET/CT may be explained by the multiple sequences of MRI (dynamic contrast-enhanced/diffusion-weighted/T2-weighted) and the lower specificity of MRI than of PSMA PET/CT for the detection of distant PCa metastases.

This higher interobserver variability of ^{18}F-PSMA-1007 is at least partly caused by nonspecific uptake of this tracer, most frequently seen in osseous structures, as illustrated in Figure 2; increased uptake of ^{18}F-PSMA-1007 is observed, whereas a clear correlation on CT images is missing. Initially, ^{18}F-PSMA-1007 was a promising PSMA radiotracer because of its hepatobiliary clearance. This is different from ^{18}F-DCFPyL and ^{68}Ga-PSMA-11, since both tracers are excreted in the urine, resulting in physiologic biodistribution in the ureters and bladder. Because of the absence of urinary excretion in ^{18}F-PSMA-1007, detection of local disease or recurrent disease might be improved (*22,23*). However, increasing evidence points to a major disadvantage of using ^{18}F-PSMA-1007 in primary staging. Significantly higher numbers of lesions with increased tracer uptake, attributed to a benign (i.e., fibrous dysplasia, posttraumatic, or degenerative change) or physiologic origin, are found for ^{18}F-PSMA-1007 (*24–28*). Although nonspecific skeletal uptake is described more often in the literature with regard to ^{18}F-PSMA-1007 (*27*), it is also seen in ^{18}F-DCFPyL and ^{68}Ga-PSMA-11 (*4–9*). The exact mechanism of this nonspecific skeletal ^{18}F-PSMA-1007 uptake is yet unknown. However, it is hypothesized that the higher affinity of ^{18}F-PSMA-1007 for the PSMA receptor, which was shown in preclinical studies, may result in a higher signal from benign skeletal lesions (*25*).

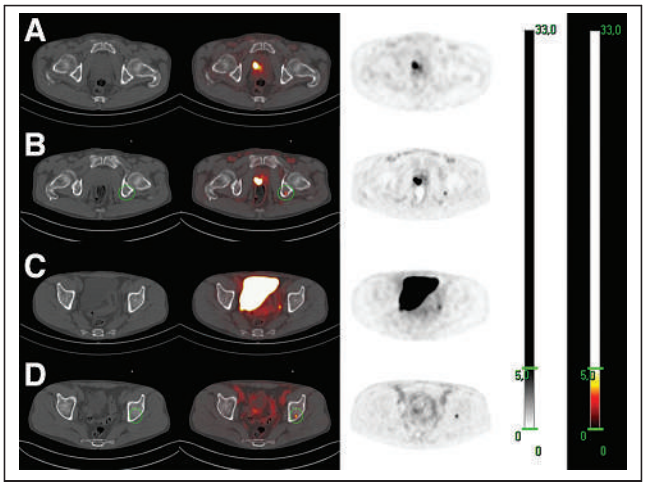

FIGURE 2. Comparison of ^{18}F-DCFPyL (A and C) and ^{18}F-PSMA-1007 (B and D) in single patient. ^{18}F-DCFPyL images were acquired 48 d after ^{18}F-PSMA-1007 PET/CT scan. No suspected skeletal lesions were found using ^{18}F-DCFPyL, whereas suspected skeletal lesions were found in os ischium and acetabulum dome using ^{18}F-PSMA-1007 (B and D, respectively). After robot-assisted radical prostatectomy with extended pelvic lymph node dissection, pT2N0 ISUP 3 was found. Postoperative PSA levels were undetectable, making presence of bone metastases unlikely and indicating presence of nonspecific uptake of ^{18}F-PSMA-1007 in bone.

Our study was not devoid of limitations. First, it was a retrospective study in which the presence of selection bias cannot be ruled out. Although we performed multivariate logistic regression analyses, patients assessed and staged by ^{18}F-PSMA-1007 could have had a significantly higher interobserver variability in miM1b status, due to overall more aggressive disease features. Second, we conducted a retrospective cohort study in which overreads were conducted as part of a second opinion or treatment advice. The results may be affected by this selection, since hospitals may refer patients with doubtful PSMA PET/CT scans more frequently. In addition, assessments were performed in a nonmasked manner by only 2 nuclear medicine physicians. In contrast to a multiple-reader method, the use of only 2 nuclear medicine physicians could have affected the interobserver variability. Another important limitation of our study was the lack of uniform systematic interpretation criteria. During the original report in referring hospitals, different interpretation criteria were used. The presence and clinical use of different interpretation criteria may impact the interobserver variability since each criterion focuses on slightly different aspects of PSMA PET/CT scans. However, recent introduction of the E-PSMA, the European Association of Nuclear Medicine standardized reporting guidelines for PSMA PET, will enable harmonization of diagnostic interpretation criteria by combining the PSMA visual with the quantitative and semiquantitative expression (*23*). This combination will facilitate data reproducibility and thus support therapeutic management decisions. Lastly, not only the PSMA radiotracer but also the nuclear medicine physician may impact interobserver variability. Especially in questionable situations, in which the presence of metastases is doubted, experience is important. One could argue that less experienced nuclear medicine physicians are more likely to misinterpret PSMA PET/CT scans (i.e., misinterpret the ^{18}F-PSMA-1007 uptake in benign [skeletal] lesions as being compatible with bone metastases). Considering the fact that ^{18}F-PSMA-1007 has been introduced more recently, experience in reporting PSMA PET/CT scans made with this tracer is likely less than for ^{18}F-DCFPyL or ^{68}Ga-PSMA-11. Therefore, lack of experience with this tracer cannot be excluded as a cause of the higher interobserver variability.

Unlike other studies on the interobserver variability of PSMA PET/CT scans, our study was based on a considerably larger cohort. In addition, patients were referred from different hospitals throughout The Netherlands, and overreads were conducted by several experienced nuclear medicine physicians. The interobserver variability therefore cannot be attributed to individual interpretations.

CONCLUSION

Interobserver agreement on PSMA PET/CT for use in PCa staging was moderate to high. However, agreement on assessment of PSMA

PET/CT imaging by 2 nuclear medicine physicians regarding staging of newly diagnosed PCa differs among 3 frequently used PSMA radiotracers (^{18}F-DCFPyL, ^{18}F-PSMA-1007, and ^{68}Ga-PSMA-11). Agreement on miM1b status is significantly worse for ^{18}F-PSMA-1007 than for ^{18}F-DCFPyL or ^{68}Ga-PSMA-11, mainly because of nonspecific tracer uptake in osseous structures. On the basis of our findings, bone lesions seen on PSMA PET/CT scans with ^{18}F-PSMA-1007 in primary staging should be interpreted carefully, and training—to gain experience in interpreting this specific PSMA radiotracer—is strongly advised.

DISCLOSURE

No potential conflict of interest relevant to this article was reported.

ACKNOWLEDGMENT

We thank Drs. Zing J. Cheung and Marcel P.M. Stokkel for overreading the PSMA PET/CT scans used for this retrospective study.

KEY POINTS

QUESTION: Does the interobserver variability differ among the 3 clinically frequently used PSMA radiotracers (^{18}F-DCFPyL, ^{18}F-PSMA-1007, and ^{68}Ga-PSMA-11) in primary-PCa staging?

PERTINENT FINDINGS: In a retrospective analysis with 584 patients staged with PSMA PET/CT for primary untreated PCa, a significantly higher interobserver variability regarding assessment of bone metastasis was observed in patients assessed and staged by ^{18}F-PSMA-1007.

IMPLICATIONS FOR PATIENT CARE: Bone lesions seen on PSMA PET/CT scans with ^{18}F-PSMA-1007 in primary staging should be interpreted carefully, and training—to gain experience in interpreting this specific PSMA radiotracer—is strongly advised.

REFERENCES

1. Jansen BHE, Jansen RW, Wondergem M, et al. Lesion detection and interobserver agreement with advanced image reconstruction for ^{18}F-DCFPyL PET/CT in patients with biochemically recurrent prostate cancer. *J Nucl Med.* 2020;61:210–216.
2. Mottet N, van den Bergh RCN, Briers E, et al. EAU-EANM-ESTRO-ESUR-SIOG guidelines on prostate cancer: 2020 update. Part 1: screening, diagnosis, and local treatment with curative intent. *Eur Urol.* 2021;79:243–262.
3. Hofman MS, Lawrentschuk N, Francis RJ, et al. Prostate-specific membrane antigen PET-CT in patients with high-risk prostate cancer before curative-intent surgery or radiotherapy (proPSMA): a prospective, randomised, multicentre study. *Lancet.* 2020;395:1208–1216.
4. Artigas C, Alexiou J, Garcia C, et al. Paget bone disease demonstrated on ^{68}Ga-PSMA ligand PET/CT. *Eur J Nucl Med Mol Imaging.* 2016;43:195–196.
5. Sasikumar A, Joy A, Pillai MR, et al. A rare case of rectal carcinoma and prostate carcinoma with coexistent Paget's disease mimicking bone metastases in both ^{18}F-FDG and ^{68}Ga PSMA PET/CT. *Eur J Nucl Med Mol Imaging.* 2017;44:738–739.
6. Jochumsen MR, Dias AH, Bouchelouche K. Benign traumatic rib fracture: a potential pitfall on ^{68}Ga-prostate-specific membrane antigen PET/CT for prostate cancer. *Clin Nucl Med.* 2018;43:38–40.
7. Torga G, Yin Y, Pomper MG, et al. Uptake of prostate-specific membrane antigen-targeted ^{18}F-DCFPyL in avascular necrosis of the femoral head. *World J Nucl Med.* 2019;18:416–419.
8. De Coster L, Sciot R, Everaerts W, et al. Fibrous dysplasia mimicking bone metastasis on ^{68}GA-PSMA PET/MRI. *Eur J Nucl Med Mol Imaging.* 2017;44:1607–1608.
9. Artigas C, Otte FX, Lemort M, et al. Vertebral hemangioma mimicking bone metastasis in ^{68}Ga-PSMA ligand PET/CT. *Clin Nucl Med.* 2017;42:368–370.
10. Sasikumar A, Joy A, Pillai MR, et al. ^{68}Ga-PSMA PET/CT imaging in multiple myeloma. *Clin Nucl Med.* 2017;42:e126–e127.
11. Snow HA, Hofman MS, Mitchell CA, et al. Incidental metastatic melanoma identified on ^{68}Ga-prostate-specific membrane antigen PET/CT for metastatic prostate cancer. *Clin Nucl Med.* 2018;43:509–511.
12. Junqueira MZ, Rocha NH, Sapienza MT. ^{68}Ga-prostate-specific membrane antigen PET/CT uptake in intraventricular meningioma in the choroid plexus. *Clin Nucl Med.* 2021;46:58–59.
13. Basha MA, Hamed MA, Hussein O, et al. ^{68}Ga-PSMA-11 PET/CT in newly diagnosed prostate cancer: diagnostic sensitivity and interobserver agreement. *Abdom Radiol (NY).* 2019;44:2545–2556.
14. Derwael C, Lavergne O, Lovinfosse P, et al. Interobserver agreement of ^{68}Ga-PSMA-11 PET/CT images interpretation in men with newly diagnosed prostate cancer. *EJNMMI Res.* 2020;10:15.
15. Toriihara A, Nobashi T, Baratto L, et al. Comparison of 3 interpretation criteria for ^{68}Ga-PSMA11 PET based on inter- and intrareader agreement. *J Nucl Med.* 2020; 61:533–539.
16. Eiber M, Herrmann K, Calais J, et al. Prostate Cancer Molecular Imaging Standardized Evaluation (PROMISE): proposed miTNM classification for the interpretation of PSMA-ligand PET/CT. *J Nucl Med.* 2018;59:469–478.
17. Landis JR, Koch GG. The measurement of observer agreement for categorical data. *Biometrics.* 1977;33:159–174.
18. Demirci E, Akyel R, Caner B, et al. Interobserver and intraobserver agreement on prostate-specific membrane antigen PET/CT images according to the miTNM and PSMA-RADS criteria. *Nucl Med Commun.* 2020;41:759–767.
19. Gültekin A, Yaylalı O, Şengöz T, et al. Intraobserver and interobserver agreement for the interpretation of ^{68}Ga–prostate-specific membrane antigen-I&T positron emission tomography/computed tomography imaging. *Nucl Med Commun.* 2019; 40:1250–1255.
20. Feinstein AR, Cicchetti DV. High agreement but low kappa: I. The problems of two paradoxes. *J Clin Epidemiol.* 1990;43:543–549.
21. Johnston EW, Latifoltojar A, Sidhu HS, et al. Multiparametric whole-body 3.0-T MRI in newly diagnosed intermediate- and high-risk prostate cancer: diagnostic accuracy and interobserver agreement for nodal and metastatic staging. *Eur Radiol.* 2019;29:3159–3169.
22. Giesel FL, Will L, Lawal I, et al. Intraindividual comparison of ^{18}F-PSMA-1007 and ^{18}F-DCFPyL PET/CT in the prospective evaluation of patients with newly diagnosed prostate carcinoma: a pilot study. *J Nucl Med.* 2018;59:1076–1080.
23. Ceci F, Oprea-Lager DE, Emmett L, et al. E-PSMA: the EANM standardized reporting guidelines v1.0 for PSMA-PET. *Eur J Nucl Med Mol Imaging.* 2021;48:1626–1638.
24. Rauscher I, Krönke M, König M, et al. Matched-pair comparison of ^{68}Ga-PSMA-11 PET/CT and ^{18}F-PSMA-1007 PET/CT: frequency of pitfalls and detection efficacy in biochemical recurrence after radical prostatectomy. *J Nucl Med.* 2020;61:51–57.
25. Cardinale J, Schäfer M, Benešová M, et al. Preclinical evaluation of ^{18}F-PSMA-1007, a new prostate-specific membrane antigen ligand for prostate cancer imaging. *J Nucl Med.* 2017;58:425–431.
26. Pattison DA, Debowski M, Gulhane B, et al. Prospective intra-individual blinded comparison of ^{18}F-PSMA-1007 and [^{68}Ga]Ga-PSMA-11 PET/CT imaging in patients with confirmed prostate cancer. *Eur J Nucl Med Mol Imaging.* 2022;49:763–776.
27. Wondergem M, van der Zant FM, Broos WAM, et al. Matched-pair comparison of ^{18}F-DCFPyL PET/CT and ^{18}F-PSMA-1007 PET/CT in 240 prostate cancer patients: interreader agreement and lesion detection rate of suspected lesions. *J Nucl Med.* 2021;62:1422–1429.
28. Grünig H, Maurer A, Thali Y, et al. Focal unspecific bone uptake on [^{18}F]-PSMA-1007 PET: a multicenter retrospective evaluation of the distribution, frequency, and quantitative parameters of a potential pitfall in prostate cancer imaging. *Eur J Nucl Med Mol Imaging.* 2021;48:4483–4494.

^{18}F-PFPN PET: A New and Attractive Imaging Modality for Patients with Malignant Melanoma

Xiao Zhang*[1,2], Mengting Li*[1,2], Yongkang Gai[1,2], Jing Chen[3], Juan Tao[4], Liu Yang[4], Fan Hu[1,2], Wenyu Song[1,2], Tzu-Chen Yen[5,6], and Xiaoli Lan[1,2]

[1]*Department of Nuclear Medicine, Union Hospital, Tongji Medical College, Huazhong University of Science and Technology, Wuhan, China;* [2]*Hubei Key Laboratory of Molecular Imaging, Wuhan, China;* [3]*Cancer Center, Union Hospital, Tongji Medical College, Huazhong University of Science and Technology, Wuhan, China;* [4]*Department of Dermatology, Union Hospital, Tongji Medical College, Huazhong University of Science and Technology, Wuhan, China;* [5]*Department of Medicine and Molecular Imaging Center, Linkou Chang Gung Memorial Hospital and Chang Gung University, Taoyuan City, Taiwan; and* [6]*Aprinoia Therapeutics Co., Ltd., Suzhou, China*

^{18}F-FDG PET has limited diagnostic applications in malignant melanoma (MM). ^{18}F-*N*-(2-(diethylamino)ethyl)-5-(2-(2-(2-fluoroethoxy)ethoxy)ethoxy)picolinamide (^{18}F-PFPN) is a novel PET probe with high affinity and selectivity for melanin. We conducted a clinical study with 2 aims, first to investigate the biodistribution and radiation dosimetry of ^{18}F-PFPN in healthy volunteers, and second, to examine the diagnostic utility of ^{18}F-PFPN PET imaging in patients with MM. **Methods:** ^{18}F-PFPN was synthesized through a fluoro-for-tosyl exchange reaction. Five healthy volunteers were enrolled to investigate the biodistribution, pharmacokinetics, radiation dosimetry, and safety of the tracer. Subsequently, a total of 21 patients with clinically suspected or confirmed MM underwent both ^{18}F-PFPN PET/MRI and ^{18}F-FDG PET/CT scans. The normalized SUV_{max} of selected lesions was determined for both tracers and compared in patient- and lesion-based analyses. **Results:** ^{18}F-PFPN has an elevated radiochemical yield and was highly stable in vivo. In healthy volunteers, ^{18}F-PFPN was safe and well tolerated, and its effective absorbed dose was comparable to that of ^{18}F-FDG. In patient-based analysis, ^{18}F-PFPN uptake was higher than ^{18}F-FDG for both primary tumors and nodal metastases. In lesion-based analysis,^{18}F-PFPN PET imaging could detect 365 metastases that were missed on ^{18}F-FDG PET. Additionally, ^{18}F-PFPN PET imaging had clinical value in distinguishing false-positive lesions on ^{18}F-FDG PET. **Conclusion:** ^{18}F-PFPN is a safe and well-tolerated melanin PET tracer. In a pilot clinical study, ^{18}F-PFPN PET imaging outperformed traditional ^{18}F-FDG PET in identifying both primary MM and its distant spread.

Key Words: ^{18}F-PFPN; ^{18}F-FDG; malignant melanoma; PET; diagnosis

J Nucl Med 2022; 63:1537–1543
DOI: 10.2967/jnumed.121.263179

Malignant melanoma (MM) is a highly aggressive tumor that poses a significant public health burden (*1*). The 5-y overall survival rates of patients with nodal and distant spread are as low as 65% and 25%, respectively. However, early surgical excision of localized MM portends favorable outcomes (5-y overall survival, 98%). In this scenario, both prompt diagnosis and accurate disease staging are paramount to reduce mortality.

Traditional ^{18}F-FDG PET may be clinically useful for staging and therapeutic monitoring of advanced (stage III−IV) MM (*2*). However, the value of ^{18}F-FDG PET imaging in this malignancy is limited by uptake in the liver and brain (*3*), which may ultimately compromise reliable detection of primary or metastatic melanoma lesions at these anatomic sites. Additionally, ^{18}F-FDG PET does not have sufficient sensitivity to diagnose stage I−II MM (*4*) and is generally unable to identify small (<1 cm) metastases to the lung, liver, and brain (*5*).

Recent advances in specific PET tracers, including MM-selective antibodies (*6,7*), α-melanocyte–stimulating hormone receptor ligands (*5,8*), and peptides (*9,10*), have fostered our ability to identify MM lesions. Unfortunately, several caveats, including slow and limited tumor uptake, suboptimal in vivo stability, and elevated liver accumulation, still hamper their routine clinical application. One of the most promising molecular targets for the imaging of MM is melanin, which exists in most melanomas (>90%) (*11*). Several melanin-targeted radiopharmaceuticals, including ^{123}I-MEL008 (*12*), ^{18}F-FBZA (*13*), ^{18}F-MEL050 (*14*), and 4-^{11}C-MBZA (*15*), have been synthesized from benzamide, quinoxaline, or picolinamide and applied as PET and SPECT tracers. We have previously designed and synthesized an ^{18}F-labeled benzamide analog as a melanin-imaging tracer, termed ^{18}F-5-fluoro-*N*-(2-[diethylamino]ethyl)picolinamide (^{18}F-5-FPN). This probe, characterized by high melanin affinity and favorable pharmacokinetic properties (*16,17*), has shown promising preclinical value for the identification of small (<2 mm) nodal and distant metastases from MM in mice (*18*). However, the relatively elevated hepatic tracer uptake of ^{18}F-5-FPN hindered its clinical applications. Subsequently, we optimized this probe to have a higher tumor–to–normal-liver ratio and radiochemical yield, named ^{18}F-*N*-(2-(diethylamino)ethyl)-5-(2-(2-(2-fluoroethoxy)ethoxy)ethoxy)picolinamide (^{18}F-PFPN) (*19*).

To shed further light on the translational value of ^{18}F-PFPN as a melanin-targeted PET probe for MM imaging, we designed the current study with 2 principal aims. First, we sought to investigate the biodistribution and radiation dosimetry of ^{18}F-PFPN in healthy volunteers. Second, we examined, for the first time, the clinical utility of ^{18}F-PFPN PET imaging in patients with suspected or pathologically confirmed MM.

Received Sep. 8, 2021; revision accepted Jan. 14, 2022.
For correspondence or reprints, contact Xiaoli Lan (LXL730724@hotmail.com).
*Contributed equally to this work.
Published online Feb. 3, 2022.

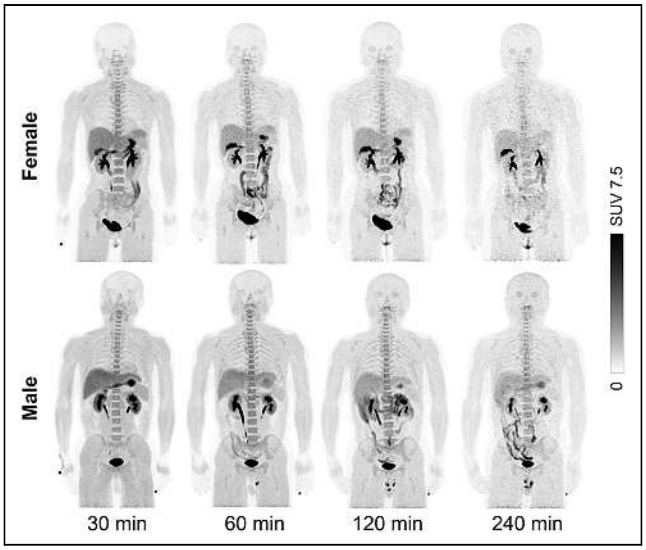

FIGURE 1. Maximum-intensity-projection PET images obtained from female and male volunteers at different time points after intravenous ^{18}F-PFPN injection.

MATERIALS AND METHODS

Healthy Volunteers and Patients

The institutional review board approved this study, and all subjects gave written informed consent. Five healthy volunteers (3 women and 2 men; age range, 28–48 y; Supplemental Table 1 [supplemental materials are available at http://jnm.snmjournals.org]) were enrolled to investigate the biodistribution, pharmacokinetics, radiation dosimetry, and safety of ^{18}F-PFPN. Between January 19, 2021, and June 19, 2021, the patients with clinically suspected or confirmed MM were recruited. All patients underwent ^{18}F-FDG PET/CT and ^{18}F-PFPN PET/MRI within 1 wk. CT was performed when MRI was contraindicated (1 patient because of a metal implant). Patients with acute systemic diseases, electrolyte disorders, other known malignancies, an age of less than 18 y, or pregnancy or lactation were then excluded.

Biodistribution and Radiation Dosimetry of ^{18}F-PFPN in Healthy Volunteers

^{18}F-PFPN was synthesized using the procedural steps outlined in Supplemental Figure 1 (*19*). The procedures for determining the tracer biodistribution and the radiation dosimetry are described in Supplemental Figure 2. In healthy volunteers, serial whole-body PET/MRI scans were subsequently acquired on an integrated PET/MRI scanner (Signa; GE

TABLE 1
General Characteristics of Patients with Clinically Suspected or Confirmed MM

Patient no.	Sex	Age (y)	Weight (kg)	^{18}F-PFPN dose (MBq)	^{18}F-FDG dose (MBq)	Clinical role of PET	Primary tumor location	Confirmed metastases*	Clinical stage/ final diagnosis
1	M	70	76	358.9	318.2	IS	Right plantar region	LNM, LM, BM, SM	T4bN3cM1, 4
2	F	55	54	270.1	244.2	IS	Left plantar region	LNM	T4bN3cM0, IIIc
3	M	40	73	344.1	314.5	IS	Left plantar region	—	T2bN0M0, IIa
4	M	47	55	214.6	259	RD	Occipital skin	LNM, GM	PD
5	M	67	59	196.1	266.4	IS	Right plantar region	LNM, LM, BM	T4bN3cM1, 4
6	M	59	69	266.4	281.2	RD	Left choroid (eye)	LM	PD
7	M	55	60	321.9	266.4	IS	Right plantar region	LNM, LM, BM	T4bN3cM1, 4
8	M	47	75	381.1	340.4	RD	Left choroid (eye)	LNM, LM, BM	PD
9	F	73	50	247.9	260.1	IS	Rectum	LNM, LM, BM, SM, PM	T4bN3cM1, 4
10	F	49	52	255.3	255.3	IS	Left isovarvas	LNM, BM	T3bN2bM1, 4
11	F	39	94	296	366.3	RD	Left pollex	LNM	PD
12	F	39	64	196.5	266.4	RD	Left plantar region	LNM	PD
13	F	63	60	303.4	273.8	RD	Right heel	LNM	PD
14	M	50	85	392.2	323.4	RD	Right plantar region	LNM, LM, BM, AM	PD
15	F	33	48	218.3	210.9	IS	Left arm	—	T4bN0M0, IIc
16	M	63	50	236.8	247.9	RD	Left heel	LNM, BM, PM, AM, CM, GM, CUM	PD
17	M	66	82	310.8	344.1	IS	Right forehead (skin)	LNM	T2aN2bM0, IIIb
18	F	54	60	247.9	259	RD	Perineum	LNM	PD
19	M	70	72	270.1	307.1	RD	Left plantar region	LNM	PD
20	F	50	67	270.1	254.2	RD	Left toe	LNM, PM, CUM	PD
21	F	63	67	314.5	259	RD	Perineum	LNM	PD

*Confirmed after thorough review of imaging and pathologic findings.

IS = initial staging; LNM = lymph node metastases; LM = liver metastases; BM = bone metastases; SM = spleen metastases; RD = recurrence detection; GM = gastric metastases; PD = progression of disease; PM = pulmonary metastases; AM = adrenal gland metastasis; CM = cerebral metastasis; CUM = cutaneous metastasis.

TABLE 2
Patient- and Lesion-Based Analyses of ^{18}F-PFPN and ^{18}F-FDG PET Imaging Findings

Analysis	Parameter	Primary tumor	Lymph node metastases	Bone metastases	Liver metastases	Metastases to other sites
Patient-based analysis		8	18	8	7	6
Number of patients	^{18}F-FDG	8	17	7	5	4
	^{18}F-PFPN	8	18	8	7	6
	P		1.0*	1.0*	0.462*	
Normalized SUV_{max}	^{18}F-FDG	4.42 ± 3.43	7.36 ± 6.08	6.18 ± 4.06	4.94 ± 4.36	13.92 ± 10.97
	^{18}F-PFPN, 1 h	10.27 ± 6.09	15.14 ± 14.07	18.21 ± 21.00	23.56 ± 25.66	20.32 ± 19.29
	^{18}F-PFPN, 3 h	17.82 ± 10.29	21.10 ± 17.66	28.47 ± 36.08	37.03 ± 48.64	29.87 ± 27.1
	P (1 h/3 h)	0.022*/0.008*	0.043/0.005	0.161/0.130	0.144/0.178	0.496/0.211
Lesion-based analysis			124	394	141	33
Number of lesions	^{18}F-FDG		98	151	49	29
	^{18}F-PFPN		124	394	141	33
	P		0.000	0.000	0.000	0.114†
Normalized SUV_{max}	^{18}F-FDG		5.36 ± 4.08	5.01 ± 2.33	5.08 ± 2.11	7.93 ± 7.70
	^{18}F-PFPN, 1 h		10.88 ± 9.49	20.14 ± 21.83	19.17 ± 17.29	11.97 ± 11.59
	^{18}F-PFPN, 3 h		16.35 ± 13.55	31.83 ± 37.09	31.55 ± 31.52	17.52 ± 16.56
	P (1 h/3 h)		0.000/0.000	0.000/0.000	0.000/0.000	0.117/0.006

*Paired *t* test.
†Fisher exact test.
1 h/3 h = *P* value calculated for ^{18}F-FDG SUV_{max} vs. ^{18}F-PFPN SUV_{max} at 1 or 3 h.

Healthcare) at 30, 60, 120, and 240 min after tracer injection. At each time point, images were acquired immediately after collection of biologic specimens (blood and urine). The tracer uptake in each major organ was determined by calculating the SUV_{mean}. The pharmacokinetic profile of ^{18}F-PFPN was investigated by determining the radioactive count of blood, plasma samples, and urine specimens collected at different time points using an automatic well-type automatic γ-counter (WIZARD 2470; PerkinElmer). The absorbed radiation dose for each major organ was calculated using the OLINDA/EXM software, version 2.1. The healthy volunteers were asked to report any subjective abnormality within 1 h from the completion of the study procedures. Vital signs were determined in the preprocedural phase and 4 h after tracer injection.

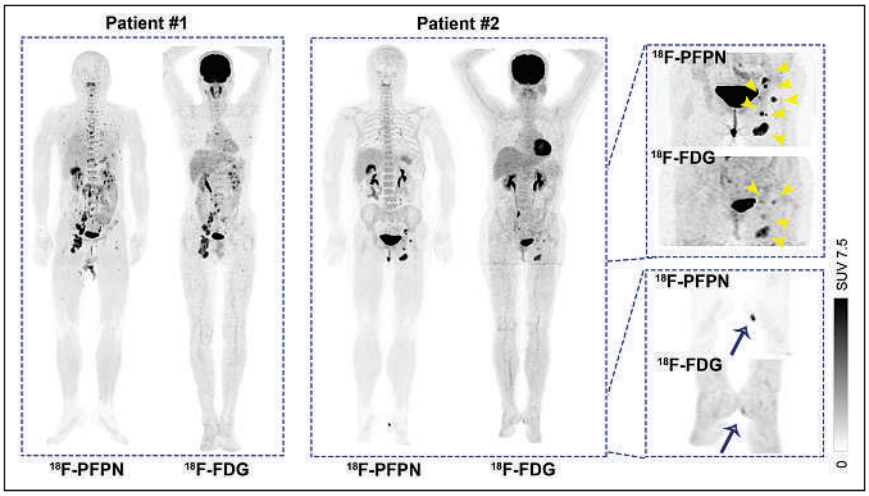

FIGURE 2. Representative images of patients with MM who underwent ^{18}F-PFPN and ^{18}F-FDG PET scans for disease staging. ^{18}F-PFPN PET outperformed traditional ^{18}F-FDG PET for identifying both primary tumors and distant metastases. Blue arrows indicate primary lesions, whereas yellow arrowheads denote lymph node metastases.

PET Imaging in Patients with Suspected or Pathologically Confirmed MM

^{18}F-PFPN PET/MR images were acquired approximately 1 and 3 h after the intravenous injection of ^{18}F-PFPN (dose, 3.0–5.4 MBq/kg). ^{18}F-FDG PET/CT images were acquired approximately 60 min after the intravenous injection of ^{18}F-FDG (dose, 3.7–5.4 MBq/kg). All scans were from the brain to the upper thigh (or the foot when required).

Image Interpretation

Images were uploaded on an Advantage Workstation (version AW4.6; GE Healthcare) for registration, fusion, and interpretation.

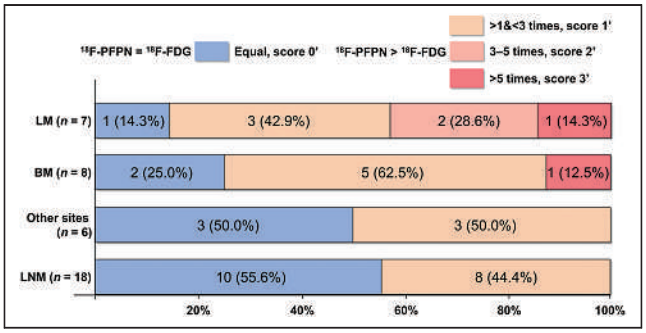

FIGURE 3. Comparative findings obtained from visual assessment of ^{18}F-PFPN and ^{18}F-FDG PET images. LM = liver metastases; BM = bone metastases; LNM = lymph node metastases. n (%) in each bar refers to patient number (patient number as a percentage of the total population).

^{18}F-PFPN and ^{18}F-FDG PET images were independently reviewed by 2 experienced nuclear medicine physicians who were not aware of patient clinical data and conventional imaging results. All discrepancies were resolved by consensus.

Regions of interest were drawn on transaxial slices, and the raw SUV_{max} was automatically calculated to quantify ^{18}F-FDG and ^{18}F-PFPN uptake within each lesion. To improve the comparability of SUV_{max}, raw data were normalized using the following formula:

$$\text{Normalized } SUV_{max} = \text{Raw } SUV_{max}/SUV_{bkgd},$$

where SUV_{bkgd} indicates the SUV_{mean} of the descending aorta.

Both patient- and lesion-based quantitative assessments were performed. Patient-based analysis included either the primary tumor or the single lesion showing the highest tracer uptake at each metastatic site. Lesion-based analysis for each site was performed either on all lesions (when their count was ≤10) or the 10 lesions that showed the highest tracer uptake (when their count was >10). A visual scoring system was also applied and is described in the supplemental materials.

Statistical Analysis

Continuous variables are presented as means ± SD. SUV_{max} was compared between groups using the Student *t* test. Categoric variables were compared using the χ^2 test. All analyses were undertaken in SPSS, version 22 (IBM). Two-tailed *P* values of less than 0.05 were considered statistically significant.

RESULTS

Quality Control and Radiochemistry of the ^{18}F-PFPN Tracer

^{18}F-PFPN was successfully synthesized. The radiochemical purity and specific activity of ^{18}F-PFPN (n = 5) was 97.38% ± 1.99% and 101–165 GBq/mmol, respectively. This probe's in vivo stability measured at 4 h after injection was more than 95%. An illustrative high-performance liquid chromatography image of the tracer in the urine is shown in Supplemental Figure 3.

Biodistribution, Dosimetry, and Safety of ^{18}F-PFPN in Healthy Volunteers

For healthy volunteers, the ^{18}F-PFPN maximum-intensity-projection images are shown in Figure 1. ^{18}F-PFPN uptake was visible in the renal pelvis and calices, ureters, gallbladder, urinary bladder, stomach, and liver. Hepatic SUV_{mean} decreased over time, being 4.51 ± 0.75, 3.26 ± 0.62, 2.45 ± 0.40, and 1.74 ± 0.28 at 30, 60, 120, and 240 min after injection, respectively (Supplemental Fig. 4). A similar pattern was observed for blood uptake, which gradually decreased from (2.65 ± 0.20) × 10^{-3} percentage injected dose [%ID]/g at 30 min after injection to (1.35 ± 0.67) × 10^{-3} %ID/g at 240 min (Supplemental Fig. 5). Comparable results were evident for most organs, except the gallbladder, eyes, and urine. The tracer activity in the urine was 0.15 ± 0.05 %ID/g at 30 min after injection and reached a peak of 0.35 ± 0.14 %ID/g at 60 min, suggesting rapid renal clearance. Concerning the eyes, we observed an SUV_{mean} increase from 0.79 ± 0.07 at 30 min after injection to 1.32 ± 0.30 at 240 min due to the presence of choroidal melanocytes and retinal pigment cells.

The estimated absorbed-radiation dosimetry for different organs is depicted in Supplemental Table. 2. The urinary bladder wall showed the highest dose activity (1.73 × 10^{-1} mSv/MBq), followed by the kidneys. A mean absorbed dose of 7.37 × 10^{-3} mSv/MBq was observed in the eyes. The total effective dose was 2.01 × 10^{-2} mSv/MBq.

Neither immediate adverse reactions nor significant changes in vital signs were observed after tracer injection. Similarly, follow-up laboratory examinations did not reveal any abnormal changes in liver and kidney function tests.

Characteristics of Patients with MM

In total, 21 patients (mean age, 54.86 ± 11.58 y) with clinically suspected or confirmed MM were included in the study (Table 1). Nine patients underwent imaging for initial disease staging, whereas investigations in the remaining 12 were aimed at detecting recurrences. Most primary MMs were in the skin, followed by choroid membranes. One patient had an occult primary MM located in the rectum.

Comparison of ^{18}F-PFPN and ^{18}F-FDG PET Imaging in Patients with MM

We subsequently compared ^{18}F-PFPN and ^{18}F-FDG PET imaging in MM patients (Table 2; Fig. 2). ^{18}F-PFPN PET could clearly delineate lesions, with an excellent

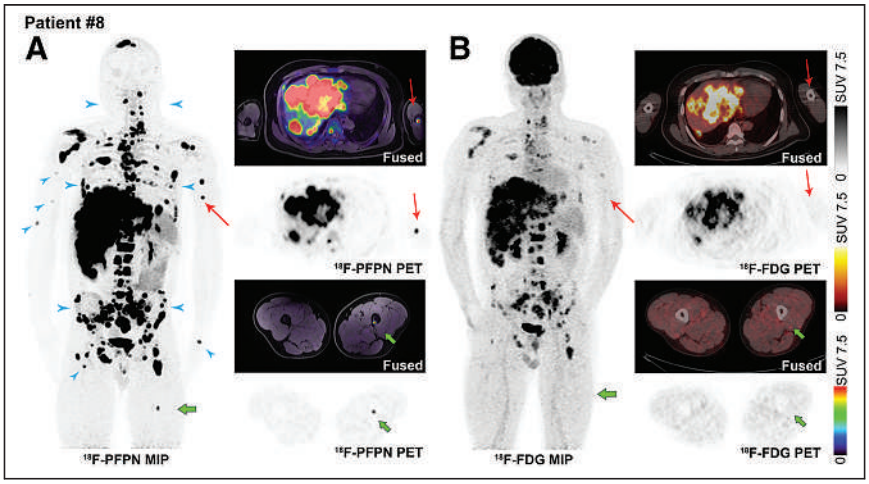

FIGURE 4. A 47-y-old man who underwent surgical removal of choroidal MM 19 mo before imaging. On maximum-intensity-projection (MIP) images, ^{18}F-PFPN PET (A) was able to identify higher number of lesions (blue arrowheads) than ^{18}F-FDG PET could (B). ^{18}F-PFPN PET/MRI identified hyperintense T1-weighted focus of increased tracer uptake in left arm (SUV_{max}, 8.4; red arrows) and left femur (SUV_{max}, 6.8; <2 mm, green arrows), which had normal uptake and density on ^{18}F-FDG PET/CT images.

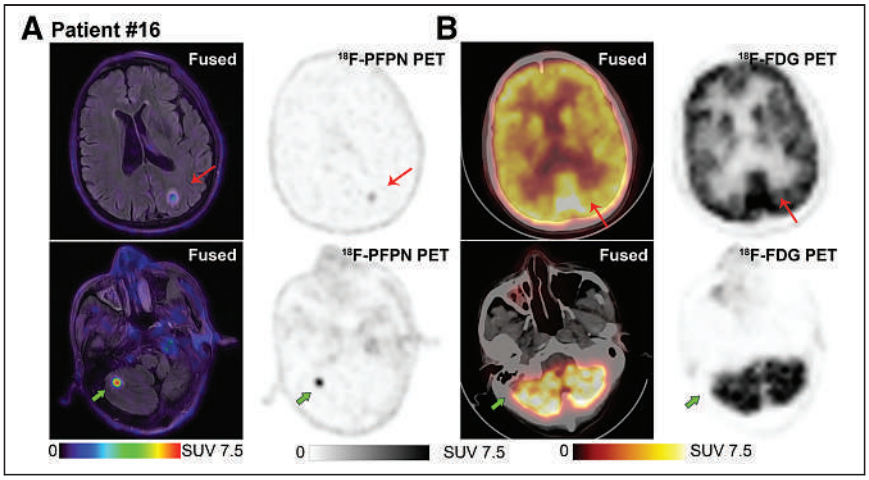

FIGURE 5. A 63-y-old man who underwent surgical removal of plantar melanoma 2 y before PET imaging. (A) Craniocerebral ^{18}F-PFPN PET/MRI revealed avid tracer uptake in left parietal lobe (SUV_{max}, 1.8; red arrows) and right cerebellum (SUV_{max}, 4.3; green arrows). (B) Conversely, no malignant lesions were visible on ^{18}F-FDG PET; notably, these images were characterized by high background activity caused by elevated physiologic tracer uptake in brain.

contrast due to low background uptake, especially in the brain and liver. On a patient-based analysis, both ^{18}F-PFPN and ^{18}F-FDG PET showed the same diagnostic performance (100%) for the detection of primary lesions; in addition, these 2 techniques performed similarly for identifying metastases (100.00% vs. 94.44% in lymph nodes, 100.00% vs. 87.50% in bone, 100.00% vs. 71.43% in liver, 100.00% vs. 66.67% in other sites, respectively). Significant differences were observed between SUV_{max} for ^{18}F-PFPN and SUV_{max} for ^{18}F-FDG measured at 1 and 3 h for both primary lesions ($P = 0.022$ and 0.008, respectively) and lymph node metastases ($P = 0.043$ and 0.005, respectively), with the former tracer showing the higher uptake.

On a lesion-based analysis, ^{18}F-PFPN PET/MRI detected a higher number of lesions than did ^{18}F-FDG PET (365 additional lesions); the detection rates according to the anatomic distribution were as follows: lymph nodes (100.00% vs. 79.03%, respectively), bone (100.00% vs. 38.32%, respectively), liver (100.00% vs. 34.75%, respectively), and other sites (100.00% vs. 87.88%, respectively). The SUV_{max} for ^{18}F-PFPN in the primary lesions, as well as in nodal, bone, and hepatic metastases, significantly increased from 1 to 3 h after injection ($P < 0.05$); conversely, a significant decrease was observed for most tissues and organs. A similar increase in normalized SUV_{max} for ^{18}F-PFPN was evident between 1 and 3 h. Notably, normalized SUV_{max} for ^{18}F-PFPN at 3 h was higher than that for ^{18}F-FDG for most lesions ($P < 0.01$). The original SUV_{max} data are shown in Supplemental Table 3.

On the visual scoring system (Fig. 3), ^{18}F-PFPN outperformed ^{18}F-FDG for the detection of distant metastases to the liver (10′ vs. 0′), bone (8′ vs. 0′), other distant sites (3′ vs. 0′) and lymph nodes (8′ vs. 0′). The total scores for ^{18}F-PFPN and ^{18}F-FDG PET were 29′ and 0′, respectively.

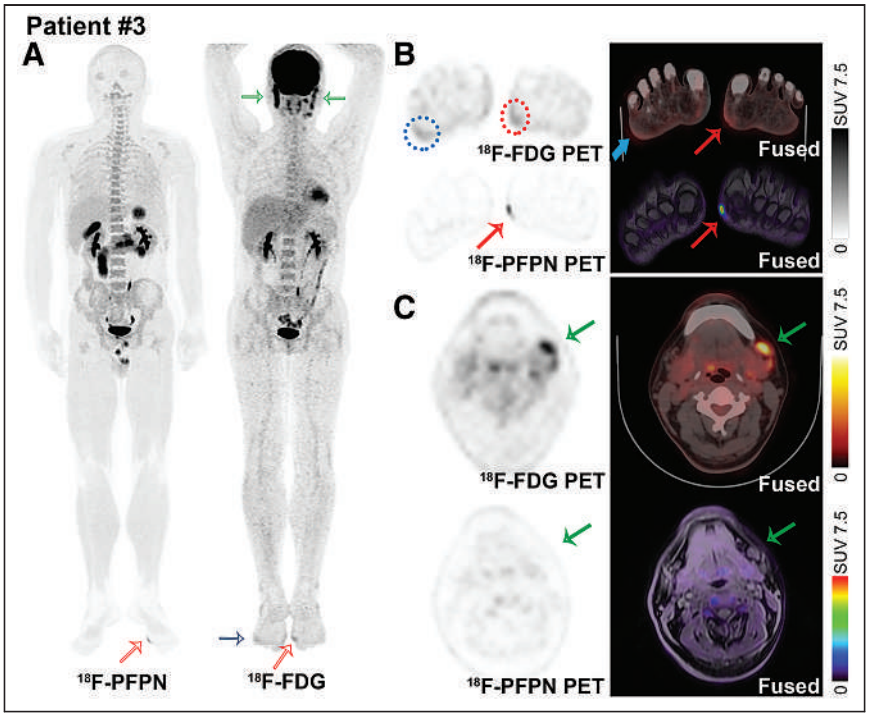

FIGURE 6. A 40-y-old man who sought medical attention for growing pigmented lesion on arch of left foot. ^{18}F-FDG PET images (A and B) revealed mild tracer accumulations in left anterior arch (red circle and red arrows; SUV_{max}, 3.3) and lateral margin of right foot (blue circle and blue arrows; SUV_{max}, 2.7). ^{18}F-PFPN PET clearly delineated left-foot lesion, which showed avid tracer uptake (SUV_{max}, 5.0), but ^{18}F-PFPN PET did not identify any lesion in right foot. Results of pathologic examination identified left-foot lesion as nodular ulcerated MM (thickness, 1.2 mm; pathologic T stage, pT2b). Interestingly, there was intense ^{18}F-FDG uptake in cervical lymph nodes (C, green arrows: SUV_{max}, 3.0–12.6), which, however, did not show significant ^{18}F-PFPN uptake. Collectively, these findings ruled out possibility that these lesions were metastases from MM; ^{18}F-FDG PET–positive nodes likely had reactive inflammatory nature.

Illustrative Case Reports

A 47-y-old man (patient 8, Fig. 4) underwent ^{18}F-PFPN PET for the detection of MM recurrences. ^{18}F-PFPN PET identified more lesions than ^{18}F-FDG PET did (fold-change in lesion detection for ^{18}F-PFPN PET: 2-fold higher for nodal metastases, 3-fold higher for hepatic metastases, and 2.5-fold higher for bone metastases). Notably, ^{18}F-PFPN PET successfully detected lesions smaller than 2 mm.

In patient 16 (Fig. 5), high background activity caused by elevated physiologic tracer uptake in the brain prevented the identification of cerebral metastases on ^{18}F-FDG PET imaging; however, the lesions were clearly visible on ^{18}F-PFPN PET images. Besides, MRI sequences provided diagnostic confirmation.

In patient 3 (Fig. 6), ^{18}F-PFPN PET, but not ^{18}F-FDG PET, correctly identified the

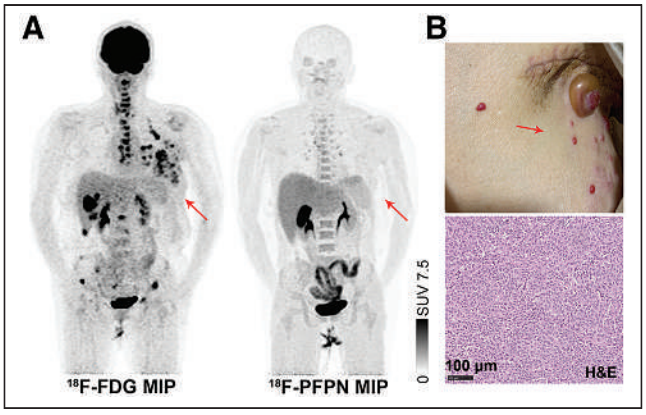

FIGURE 7. A 51-y-old woman who underwent partial excision of MM in left breast 1 y before PET imaging. She was regularly followed up; marked increase in serum CA 19-9 level (>1,200 U/mL; reference range, 0–35 U/mL) was evident over last 4 mo. (A) On ^{18}F-FDG PET imaging, avid tracer uptake was evident in operated breast (SUV_{max}, 3.7–10.4), axillary lymph nodes (SUV_{max}, 3.8–9.6), and bone (SUV_{max}, 3.2–10.2), indicating recurrent disease. Unexpectedly, ^{18}F-PFPN PET imaging findings were negative. (B) Visual examination of operated breast showed nonpigmented recurrent lesions. Pathology examination (hematoxylin and eosin [H&E] staining) of axillary lymph nodes identified metastases from MM; however, these metastatic cells were proven to be nonpigmented (unable to produce melanin). Red arrows indicate breast lesion.

primary lesion located in the left foot as an early-stage melanoma. Interestingly, the cervical lymph nodes showed intense ^{18}F-FDG uptake, whereas there was no ^{18}F-PFPN accumulation in these areas. The follow-up results suggested the findings to be inflammatory but not metastasis lesions and false-positive on ^{18}F-FDG PET.

Figure 7 shows an illustrative case of ^{18}F-PFPN PET and ^{18}F-FDG PET findings in a woman with distant amelanotic lesions from MM. Melanoma cells unable to produce melanin were missed on ^{18}F-PFPN PET, which further confirmed the specificity of ^{18}F-PFPN as a melanin PET tracer.

DISCUSSION

There are 2 principal findings from this study. First, on analyzing the biodistribution, pharmacokinetics, radiation dosimetry, and safety of ^{18}F-PFPN in 5 healthy volunteers, we found that this melanin PET tracer was safe and well tolerated; also, its absorbed radiation dose was comparable to ^{18}F-FDG. Second, in a pilot clinical investigation on suspected or confirmed MM patients, ^{18}F-PFPN showed higher uptake than ^{18}F-FDG for both primary tumors and distant metastases. In a lesion-based analysis,^{18}F-PFPN PET imaging could detect 365 metastases that were missed on ^{18}F-FDG PET. Collectively, these data represent a promising step in understanding the clinical value of ^{18}F-PFPN PET imaging for diagnosing and detecting disease recurrences in MM.

Although ^{18}F-FDG PET imaging has extensive applications in patients with solid malignancies (*20*), its clinical value in MM is beset by high false-positive rates (100% in early-stage MM) (*21*). In this scenario, there have been increasing efforts to develop novel PET tracers capable of recognizing and binding to melanin with high affinity and specificity. The melanin PET tracer used in this study (^{18}F-PFPN) was optimized and improved on the basis of our previous nicotinamide probe, ^{18}F-5-FPN (*17*). Compared with the parent molecule, ^{18}F-PFPN is characterized by a more favorable pharmacokinetic profile—importantly, the negligible hepatic accumulation and rapid renal clearance (*19*)—thus endowing this tracer with the capacity to be safely applied for clinical imaging studies.

However, partial excretion may occur through the hepatobiliary system, which may at least in part account for both gallbladder and intestinal wall uptake. On another note, the annular tracer accumulation in the eyes can be explained by the presence of choroidal melanocytes and retinal pigment cells. In terms of radiation safety, the total effective dose of ^{18}F-PFPN was 0.020 mSv/MBq, which is comparable to the whole-body effective dose of ^{18}F-FDG (0.019 mSv/MBq) (*22*). Collectively, these results prompted us to conduct the first clinical ^{18}F-PFPN PET imaging study in patients with MM.

First, on analyzing diagnostic performance for the detection of primary MM, we found that ^{18}F-PFPN PET could identify early T-stage lesions (e.g., T2b). Additionally, significant differences were observed between SUV_{max} for ^{18}F-PFPN and SUV_{max} for ^{18}F-FDG measured at 3 h for primary lesions, with the former tracer showing the highest uptake (3.92-fold higher uptake than that of ^{18}F-FDG). In view of these findings, we subsequently examined the role of ^{18}F-PFPN PET imaging to identify distant metastases. Although the results of ^{18}F-PFPN PET imaging led to modifications in disease staging for one patient only (1/9), this may be related to the high proportion of patients with advanced disease stages. Interestingly, ^{18}F-PFPN showed low background activity, ultimately allowing reliable delineation of a higher number of distant lesions from MM, including those at nodal, bone, and hepatic sites. Pigmented lesions can appear hyperintense on T1-weighted MR images because of the high number of negative melanin charges, which ultimately facilitate iron binding. In this scenario, the combination of ^{18}F-PFPN PET with MRI can increase image interpretation accuracy. Immune checkpoint inhibitions could enhance immune cells to kill tumors, which had been one of the main treatments for metastatic melanoma (*23*). ^{18}F-PFPN may provide an excellent possibility to distinguish between inflammatory processes and melanotic lesions through specific binding to melanin. Benefitting from this capacity, ^{18}F-PFPN imaging could be a valuable tool to evaluate immune checkpoint inhibition efficacy by reflecting the changes in melanoma tumor cells. However, ^{18}F-PFPN PET may underperform traditional ^{18}F-FDG PET in less common amelanotic or hypomelanotic subtypes of MM, which comprise 2%−8% of all cases. These lesions, whose appearance can mimic several benign and malignant conditions, continue to pose significant diagnostic challenges (*11*).

Our findings need to be interpreted in the context of some limitations. First, it would have been interesting to include patients with early-stage (I−II) MM; more research is necessary to confirm our findings and to evaluate the role of ^{18}F-PFPN PET imaging in this patient group. Second, our study focused on the clinical value of this imaging modality in patients with pigmented MM. One of the study patients had her distant amelanotic lesions missed on ^{18}F-PFPN PET; therefore, the possibility of nonpigmented lesions in patients with MM should be based on a comprehensive consideration of thorough clinical and imaging investigations. Finally, the single-center design may have limited the external validity of our results. Despite these limitations, our data represent a promising step in understanding the potential utility of ^{18}F-PFPN as a melanin tracer and may open new research directions. For example, labeling ^{18}F-PFPN with therapeutic radioisotopes may warrant further scrutiny as a potential therapeutic strategy in metastatic MM (*24*).

CONCLUSION

^{18}F-PFPN is a safe and well-tolerated melanin PET tracer. In a pilot clinical study, ^{18}F-PFPN PET outperformed traditional ^{18}F-FDG PET in identifying both primary MM and distant metastases. Further research is needed to verify these results in a larger sample and investigate the clinical value of ^{18}F-PFPN PET imaging in early-stage MM.

DISCLOSURE

This work was financially supported by the National Natural Science Foundation of China (grants 81901783 and 82030052). Tzu-Chen Yen is an employee of Aprinoia Therapeutics Co., Ltd. No other potential conflict of interest relevant to this article was reported.

ACKNOWLEDGMENT

We thank Chunxia Qin for technical assistance.

KEY POINTS

QUESTION: ^{18}F-PFPN is a novel PET probe with high affinity and selectivity for melanin; it may have clinical utility in patients with MM.

PERTINENT FINDINGS: In MM patients, uptake of ^{18}F-PFPN was higher than that of ^{18}F-FDG for both primary tumors and metastases, and ^{18}F-PFPN PET could detect 365 metastases missed on ^{18}F-FDG PET. Additionally, ^{18}F-PFPN PET had clinical value in distinguishing false-positive lesions on ^{18}F-FDG PET.

IMPLICATIONS FOR PATIENT CARE: ^{18}F-PFPN PET may outperform traditional ^{18}F-FDG PET in identifying both primary melanoma and its distant spread.

REFERENCES

1. Siegel RL, Miller KD, Fuchs HE, Jemal A. Cancer statistics, 2021. *CA Cancer J Clin.* 2021;71:7–33.
2. Schüle SC, Eigentler TK, Garbe C, la Fougere C, Nikolaou K, Pfannenberg C. Influence of ^{18}F-FDG PET/CT on therapy management in patients with stage III/IV malignant melanoma. *Eur J Nucl Med Mol Imaging.* 2016;43:482–488.
3. Stelter L, Evans MJ, Jungbluth AA, et al. Novel mechanistic insights into arginine deiminase pharmacology suggest ^{18}F-FDG is not suitable to evaluate clinical response in melanoma. *J Nucl Med.* 2012;53:281–286.
4. Wagner JD, Schauwecker D, Davidson D, et al. Inefficacy of F-18 fluorodeoxy-D-glucose-positron emission tomography scans for initial evaluation in early-stage cutaneous melanoma. *Cancer.* 2005;104:570–579.
5. Cheng Z, Zhang L, Graves E, et al. Small-animal PET of melanocortin 1 receptor expression using a ^{18}F-labeled α-melanocyte-stimulating hormone analog. *J Nucl Med.* 2007;48:987–994.
6. Revskaya E, Jongco AM, Sellers RS, et al. Radioimmunotherapy of experimental human metastatic melanoma with melanin-binding antibodies and in combination with dacarbazine. *Clin Cancer Res.* 2009;15:2373–2379.
7. Jandl T, Revskaya E, Jiang Z, Bryan RA, Casadevall A, Dadachova E. Complement-dependent cytotoxicity of an antibody to melanin in radioimmunotherapy of metastatic melanoma. *Immunotherapy.* 2013;5:357–364.
8. Gao F, Sihver W, Jurischka C, et al. Radiopharmacological characterization of ^{64}Cu-labeled α-MSH analogs for potential use in imaging of malignant melanoma. *Amino Acids.* 2016;48:833–847.
9. Beaino W, Anderson CJ. PET imaging of very late antigen-4 in melanoma: comparison of ^{68}Ga- and ^{64}Cu-labeled NODAGA and CB-TE1A1P-LLP2A conjugates. *J Nucl Med.* 2014;55:1856–1863.
10. Wei W, Ehlerding EB, Lan X, Luo Q, Cai W. PET and SPECT imaging of melanoma: the state of the art. *Eur J Nucl Med Mol Imaging.* 2018;45:132–150.
11. Thomas NE, Kricker A, Waxweiler WT, et al. Comparison of clinicopathologic features and survival of histopathologically amelanotic and pigmented melanomas: a population-based study. *JAMA Dermatol.* 2014;150:1306–1314.
12. Liu X, Pham TQ, Berghofer P, et al. Synthesis and evaluation of novel radioiodinated nicotinamides for malignant melanoma. *Nucl Med Biol.* 2008;35:769–781.
13. Ma X, Wang S, Wang S, et al. Biodistribution, radiation dosimetry, and clinical application of a melanin-targeted PET probe, ^{18}F-P3BZA, in patients. *J Nucl Med.* 2019;60:16–22.
14. Rizzo-Padoin N, Chaussard M, Vignal N, et al. [^{18}F]MEL050 as a melanin-targeted PET tracer: fully automated radiosynthesis and comparison to ^{18}F-FDG for the detection of pigmented melanoma in mice primary subcutaneous tumors and pulmonary metastases. *Nucl Med Biol.* 2016;43:773–780.
15. Garg PK, Nazih R, Wu Y, Singh R, Garg S. 4-^{11}C-methoxy *N*-(2-diethylaminoethyl) benzamide: a novel probe to selectively target melanoma. *J Nucl Med.* 2017;58:827–832.
16. Liu M, Wang Y, Li M, et al. Using tyrosinase as a tri-modality reporter gene to monitor transplanted stem cells in acute myocardial infarction. *Exp Mol Med.* 2018;50:1–10.
17. Feng H, Xia X, Li C, et al. Imaging malignant melanoma with ^{18}F-5-FPN. *Eur J Nucl Med Mol Imaging.* 2016;43:113–122.
18. Wang Y, Li M, Zhang Y, et al. Detection of melanoma metastases with PET: comparison of ^{18}F-5-FPN with ^{18}F-FDG. *Nucl Med Biol.* 2017;50:33–38.
19. Xu X, Yuan L, Yin L, et al. Synthesis and preclinical evaluation of ^{18}F-PEG$_3$-FPN for the detection of metastatic pigmented melanoma. *Mol Pharm.* 2017;14:3896–3905.
20. Groheux D, Cochet A, Humbert O, Alberini JL, Hindié E, Mankoff D. ^{18}F-FDG PET/CT for staging and restaging of breast cancer. *J Nucl Med.* 2016;57(suppl 1):17S–26S.
21. Acland KM, Healy C, Calonje E, et al. Comparison of positron emission tomography scanning and sentinel node biopsy in the detection of micrometastases of primary cutaneous malignant melanoma. *J Clin Oncol.* 2001;19:2674–2678.
22. Liu T, Liu C, Zhang Z, et al. ^{64}Cu-PSMA-BCH: a new radiotracer for delayed PET imaging of prostate cancer. *Eur J Nucl Med Mol Imaging.* 2021;48:4508–4516.
23. Dummer R, Lebbé C, Atkinson V, et al. Combined PD-1, BRAF and MEK inhibition in advanced BRAF-mutant melanoma: safety run-in and biomarker cohorts of COMBI-i. *Nat Med.* 2020;26:1557–1563.
24. Xu X, Yuan L, Gai Y, et al. Targeted radiotherapy of pigmented melanoma with ^{131}I-5-IPN. *J Exp Clin Cancer Res.* 2018;37:306.

^{223}Ra Induces Transient Functional Bone Marrow Toxicity

Maria Parlani*[1], Francesco Boccalatte*[2], Anna Yeaton[2], Feng Wang[3], Jianhua Zhang[3], Iannis Aifantis[2], and Eleonora Dondossola[1]

[1]*Genitourinary Medical Oncology Department and David H. Koch Center for Applied Research of Genitourinary Cancers, University of Texas M.D. Anderson Cancer Center, Houston, Texas;* [2]*Department of Pathology and Laura and Isaac Perlmutter Cancer Center, New York University School of Medicine, New York, New York; and* [3]*Department of Genomic Medicine, University of Texas M.D. Anderson Cancer Center, Houston, Texas*

^{223}Ra is a bone-seeking, α-particle–emitting radionuclide approved for the treatment of patients with metastatic prostate cancer and is currently being tested in a variety of clinical trials for primary and metastatic cancers to bone. Clinical evaluation of ^{223}Ra hematologic safety showed a significantly increased rate of neutropenia and thrombocytopenia in patients, hinting at myelosuppression as a side effect. **Methods:** In this study, we investigated the consequences of ^{223}Ra treatment on bone marrow biology by combining flow cytometry, single-cell RNA sequencing, three-dimensional multiphoton microscopy and bone marrow transplantation analyses. **Results:** ^{223}Ra accumulated in bones and induced zonal radiation damage confined to the bone interface, followed by replacement of the impaired areas with adipocyte infiltration, as monitored by 3-dimensional multiphoton microscopy ex vivo. Flow cytometry and single-cell transcriptomic analyses on bone marrow hematopoietic populations revealed transient, nonspecific ^{223}Ra-mediated cytotoxicity on resident populations, including stem, progenitor, and mature leukocytes. This toxicity was paralleled by a significant decrease in white blood cells and platelets in peripheral blood—an effect that was overcome within 40 d after treatment. ^{223}Ra exposure did not impair full hematopoietic reconstitution, suggesting that bone marrow function is not permanently hampered. **Conclusion:** Our results provide a comprehensive explanation of ^{223}Ra reversible effects on bone marrow cells and exclude long-term myelotoxicity, supporting safety for patients.

Key Words: ^{223}Ra; myelotoxicity; bone marrow

J Nucl Med 2022; 63:1544–1550
DOI: 10.2967/jnumed.121.263310

The radioisotope ^{223}Ra is an α-particle emitter that accumulates in bone after in vivo administration (*1,2*). ^{223}Ra was originally tested as targeted radiotherapy for prostate cancer metastasis in bone (*1*), which represents a major site for distant colonization (*3*). The high-energy radiation of ^{223}Ra, coupled with limited penetrance in tissues (<100 μm), mediates zonal toxicity at the bone interface toward osteoblasts, osteoclasts, and tumor cells (*4–7*). ^{223}Ra prolonged the median overall survival (3.6 mo) and delayed the time to first symptomatic skeletal event (5.8 mo) in men with prostate cancer metastatic to bone (*8,9*). These results led to the approval of ^{223}Ra for the treatment of metastatic prostate cancer patients with symptomatic bone lesions and no visceral involvement (*8,9*). On the basis of this positive outcome, the use of ^{223}Ra is now being clinically investigated for other tumor types that colonize the bone, including multiple myeloma, hormone-positive breast cancer, renal cell carcinoma, non–small cell lung cancer, and differentiated thyroid cancer (*10–12*).

Follow-up studies on patients excluded long-term emergence of secondary malignancies associated with ^{223}Ra treatment (such as other primary bone cancers or acute myelogenous leukemia) for up to 3 y (*13,14*). Hematologic safety analyses instead showed an impact by ^{223}Ra on bone marrow function (*15*). Accordingly, median absolute neutrophil counts and platelet number, which remained constant for placebo-treated patients, significantly decreased in ^{223}Ra-treated men, with a rebound after the end of the treatment. Hemoglobin levels were not significantly affected over the treatment period in either the ^{223}Ra group or the placebo group. In comparison, antitumor radiation levels of β-emitting agents such as ^{89}Sr- or ^{153}Sm-ethylenediamine-tetra-methylene-phosphonic acid, which displays abundant γ-emission, are associated with more severe bone marrow toxicity, limiting their usefulness for treating patients (*1*).

Neutropenia and thrombocytopenia currently represent the most common adverse reactions and hint at significant levels of bone marrow toxicity (*15*). Therefore, understanding the biologic determinants of ^{223}Ra-mediated myelosuppression and the medium- to long-term consequences on bone marrow function is critical to support a more meaningful and rational application of this agent in current and future patients. Furthermore, ruling out major toxic effects could further prompt ^{223}Ra use in early-stage patients.

In this study, we investigated the effects of ^{223}Ra on bone marrow biology, including topology and function. We applied preclinical murine models combined with 3-dimensional multiphoton microscopy, flow cytometry analysis, bone marrow transplantation experiments, and single-cell RNA sequencing to elucidate ^{223}Ra-mediated myelotoxicity over time.

MATERIALS AND METHODS

Animal Studies

Animal studies were approved by the Institutional Animal Care and Use Committee of the University of Texas M.D. Anderson Cancer Center and were performed according to the institutional guidelines for animal care and handling. More details on the in vivo studies are provided in the supplemental materials (available at http://jnm.snmjournals.org).

Statistical Analysis

Statistical analysis was performed using GraphPad Prism 8 by unpaired 2-tailed Student *t* testing or 1-way ANOVA followed by

Received Oct. 13, 2021; revision accepted Feb. 10, 2022.
For correspondence or reprints, contact Eleonora Dondossola (edondossola@mdanderson.org) or Francesco Boccalatte (francesco.boccalatte@nyulangone.org).
*Contributed equally to this work.
Published online Feb. 17, 2022.

Tukey post hoc testing. Data are mean ± SD. For single-cell RNA sequencing, differential expression analysis was determined using the Wilcoxon rank sum test.

Further experimental methods are detailed in the supplemental materials.

RESULTS

^{223}Ra Accumulates in Bones and Affects the Bone Marrow Compartment

To study the effects of ^{223}Ra on bone marrow biology, C57BL/6 mice were administered a single dose of 7.5 kBq, according to the therapeutic dose used in other preclinical analyses on mice (*2,4,6*). Radiation emission was monitored for up to 40 d in femur, tibia, humerus, skull, and spine. ^{223}Ra accumulated in different bones and significantly decayed over time to a similar extent, with limited radiation emission (≤15% of the initial amount) detectable by day 40 after injection, in line with its half-life of 11.4 d (Fig. 1A) (*1*). Bone matrix showed localized radioactivity, whereas no signal was detected within bone marrow cells (Fig. 1A). These results confirm that ^{223}Ra accumulates in calcified bone tissues but not in the bone marrow cavity, as previously reported (*2*). Interestingly, ^{223}Ra induced a significant decrease in white blood cells in bone, whereas levels of red blood cells and platelets did not significantly change (Fig. 1B). These results suggest that ^{223}Ra incorporates in the calcified component of bone and induces cellular changes in bone marrow cells.

^{223}Ra Induces Topologic Changes Within the Bone Marrow Cavity

Next, we investigated the topologic effects that ^{223}Ra exerts over time on bone marrow cells by applying infrared-excited nonlinear microscopy. We focused on tibia, which recapitulates the complexity of bone architecture, including areas of cancellous bone at the distal epiphysis/metaphysis (where ^{223}Ra effects should be maximized (*2*)), and a trabecula-free cavity at the diaphysis (where the impact of ^{223}Ra should be minimal (*2*)). Tibiae were processed, cut at the vibratome to generate 3-dimensional slices, stained, and analyzed by multiphoton microscopy. We acquired 3-dimensional stacks (up to 4.5 mm × 1.2 mm × 200 mm) at different time points and monitored bone marrow cells (CD45, a marker expressed by all nucleated hematopoietic cells (*16*), and 4′,6-diamidino-2-phenylindole), together with second- and third-harmonic generation label-free nonlinear imaging techniques. Second-harmonic generation is elicited by noncentrosymmetric structures, such as collagen deposited in the bone matrix (*4*), whereas third-harmonic generation is engendered at different interfaces, such the water-lipid interface in adipocytes (*17*). Bone marrow at the baseline showed a homogeneous distribution of CD45$^+$ cells, intercalated within bone trabeculae at the epiphysis and metaphysis, with no evidence of adipocytes, as expected for healthy adult mice younger than 2 y (Fig. 2A; Supplemental Fig. 1A) (*20*). By day 4 after ^{223}Ra injection, bone marrow at the epiphysis and metaphysis showed major damage, with CD45-positive cells alternated to strongly fluorescent circular structures, negative for third-harmonic generation (Fig. 2A; Supplemental Fig. 1B). These events preferentially localized at 36.6 ± 36 μm from bone, either trabecular or cortical, and were distributed mostly at the epiphysis or metaphysis, within 1.39 mm (Fig. 2B) from the growth plate. By day 11, active damage persisted near cancellous and cortical bone, with preferential distribution 2,247 ± 700 μm from the growth plate, paralleled by the emergence

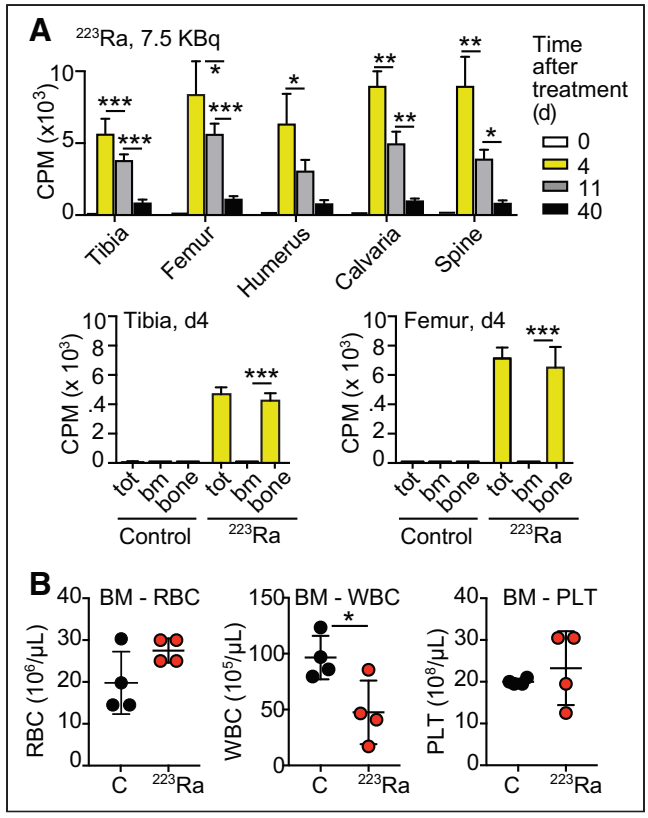

FIGURE 1. ^{23}Ra accumulates in bones and affects bone marrow compartment. (A, top) Measurement of radiation emission by ^{223}Ra-treated bones over time. Tibia, femur, humerus, calvaria, and spine were removed at 0, 4, 11, or 40 d after ^{223}Ra treatment, and counts per minute were measured. Mean ± SD is shown (3–6 bones per group). *$P < 0.05$. **$P < 0.01$. ***$P < 0.001$. Significance was tested on 1-way ANOVA followed by Tukey honestly-significant-difference post hoc test. (A, bottom) Tibia and femur from control mice or 4 d after ^{223}Ra treatment were removed, and counts per minute were measured for total bone or mineralized bone and bone marrow separately, after bone marrow flushing. Mean ± SD is shown (4 bones per group). ***$P < 0.001$ by unpaired 2-tailed Student *t* test. (B) Bone marrow hematologic analysis of control and ^{223}Ra (day 4)-treated mice by ABX Micros 60 hematology analyzer. Mean ± SD is shown (4 mice per group). *$P < 0.05$ by unpaired 2-tailed Student *t* test. bm and BM = bone marrow; bone = mineralized bone; CPM = counts per minute; PLT = platelets; RBC = red blood cells; tot = total bone; WBC = white blood cells.

of third-harmonic generation-positive adipocytes at the epiphysis and metaphysis (Fig. 2; Supplemental Fig. 1C). This trend increased until up to day 40 (Fig. 2A; Supplemental Fig. 1D), with a significantly higher number of third-harmonic generation–positive adipocytes at the epiphysis and metaphysis and some damage still persisting at the metaphysis (Fig. 2B). By day 60, fewer than 5 areas of damage per slice were still visible, with a significant infiltration of adipocytes at the epiphysis and metaphysis (Fig. 2B; Supplemental Fig. 1E). The bone marrow at the diaphysis instead did not show any sign of perturbation, even on day 4 after treatment, when the damage was more evident in other areas (Fig. 2; Supplemental Figs. 1A–1E). The progressive adipocyte increase at the epiphysis and metaphysis, with no involvement of the diaphysis, was further confirmed by histology (Supplemental Fig. 2).

These results suggest that ^{223}Ra induces extensive bone marrow remodeling at the epiphysis and metaphysis, which are more

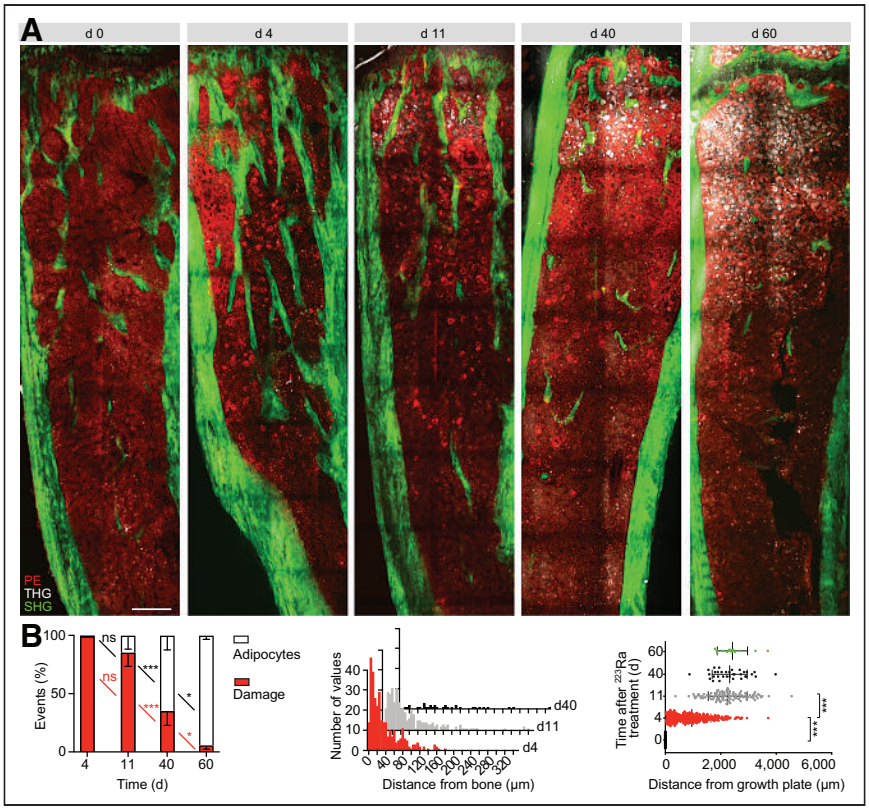

FIGURE 2. ^{223}Ra induces topologic changes within bone marrow cavity. (A) Immunofluorescence analysis of 4.5 mm × 1.2 mm × 200 μm tibia slices retrieved from mice before and 4, 11, 40, and 60 d after ^{223}Ra treatment. Red indicates CD45-positive cells, PE; gray indicates adipocytes, third-harmonic generation; green indicates bone, second-harmonic generation. Scale bar is 300 μm. (B, left) Percentage of radiation damage events and adipocytes in tibia slices on days 0–60 after ^{223}Ra treatment. Mean ± SD is shown, with total number of events reported for 1 slice per tibia, 1 tibia per mouse, and 3 mice per group. (B, middle) Frequency distribution of radiation-damage-event distance from bone on days 4, 11, and 40 for 1 slice per tibia, 1 tibia per mouse, and 3 mice per group. (B, right) Distance of radiation damage events from growth plate on days 0–60 after ^{223}Ra treatment. Mean ± SD is shown, with total number of events reported for 1 slice per tibia, 1 tibia per mouse, and 3 mice per group. $^{*}P < 0.05$. $^{***}P < 0.001$. Significance was tested on 1-way ANOVA followed by Tukey honestly-significant-difference post hoc test. ns = not statistically significant; PE = R-phycoerythrin; SHG = second-harmonic generation; THG = third-harmonic generation.

exposed to its radiation, possibly because of the presence of cancellous bone, but leaves the diaphysis morphologically unperturbed.

^{223}Ra Induces Transient, Nonspecific Myelotoxicity in Bone Marrow-Derived Cells

To evaluate the effects of ^{223}Ra on specific bone marrow populations, mice were treated with ^{223}Ra and their bone marrow collected either before (day 0) or at 4, 11, and 40 d after treatment. Then, the impact of ^{223}Ra on stem, progenitor, mature leukocyte, and erythroid cells was evaluated by flow cytometry (Supplemental Fig. 3; Supplemental Table 1). To further evaluate the long-term toxicity, we monitored hematopoietic stem and progenitor cells at various stages of differentiation. ^{223}Ra treatment significantly depleted total CD45-positive bone marrow leukocytes at 4 and 11 d after treatment, whereas their number returned to baseline after 40 d, indicating a transient effect (Fig. 3A; Supplemental Fig. 4A). When we monitored hematopoietic stem and progenitor cells at various stages of differentiation, we found that the early myeloid and lymphoid lineages were affected to a similar extent (Fig. 3A; Supplemental Figs. 4B and 4C). Notably, the long-term hematopoietic stem cell (HSC) population (Lin-negative Kit-positive Sca-positive CD135-negative CD150-positive CD40-negative) was also significantly reduced by ^{223}Ra but fully recovered by 40 d after treatment, suggesting restoration of the hematopoiesis and reversible myelotoxicity. This was further confirmed by the evaluation of mature myeloid and lymphoid cells, which reached normal levels by 40 d after treatment (Fig. 3A; Supplemental Fig. 4D). The only cell type not significantly affected by ^{223}Ra treatment was mature erythrocytes. To better understand the nature of this phenomenon, we further dissected this population according to the maturation stages and identified depletion of the more immature precursors and erythroblasts by early ^{223}Ra treatment, whereas the mature, nonnucleated erythrocytes (which are the most abundant population) were unaffected by ^{223}Ra (Fig. 3A; Supplemental Fig. 4E). The absence of splenomegaly for up to day 40 after treatment suggests that no extramedullary hematopoiesis emerged to compensate the bone marrow functional damage (Fig. 3B). Analysis of peripheral blood at different time points after ^{223}Ra treatment showed a significant decrease in white blood cells until up to day 28 after treatment, as well as a significant decrease in platelets until up to day 16 after treatment, and no significant reduction in red blood cells, hemoglobin, or hematocrit (Fig. 3C), in agreement with the outcome observed in patients (*15*).

These results indicate that in multiple bone marrow populations, treatment with ^{223}Ra has widespread toxicity that resolves over time. To evaluate the global effects of ^{223}Ra on bone marrow in early hematopoietic populations, we conducted single-cell RNA sequencing on Kit-positive hematopoietic stem and progenitor cells from the bone marrow of C57BL/6 mice over time (days 0, 4, 11, and 40 after treatment with ^{223}Ra; 3 mice per time point). We obtained high-quality transcriptomic data from a total of 10,501 single cells followed by analysis using Seurat, an R package designed for single-cell RNA sequencing data (*18*). The distribution of all the transcriptomes over time was visualized using uniform manifold approximation and projection (Fig. 4A). To define similarity clusters, we applied unsupervised clustering based on the differential expression analysis for specific genes with a resolution of 0.8 and resolved 26 separate clusters (Supplemental Figs. 5 and 6). On the basis of previous studies on single-cell gene expression (*19*), we manually curated population-specific genes in each cluster and defined 16 distinct populations, comprising all major stem, progenitor, and mature bone marrow cell types (Fig. 4A). In particular, to guide a reliable cell type assignment, we examined the expression of specific genes correlating with a more primitive (CD34, Flt3) or more lineage-primed (Dntt, Elane, Ly6g) phenotype (Fig. 4B; Supplemental Fig. 7). By comparing the bone marrow composition at baseline and after ^{223}Ra treatment over time, we observed that the most primitive cluster of hematopoietic stem

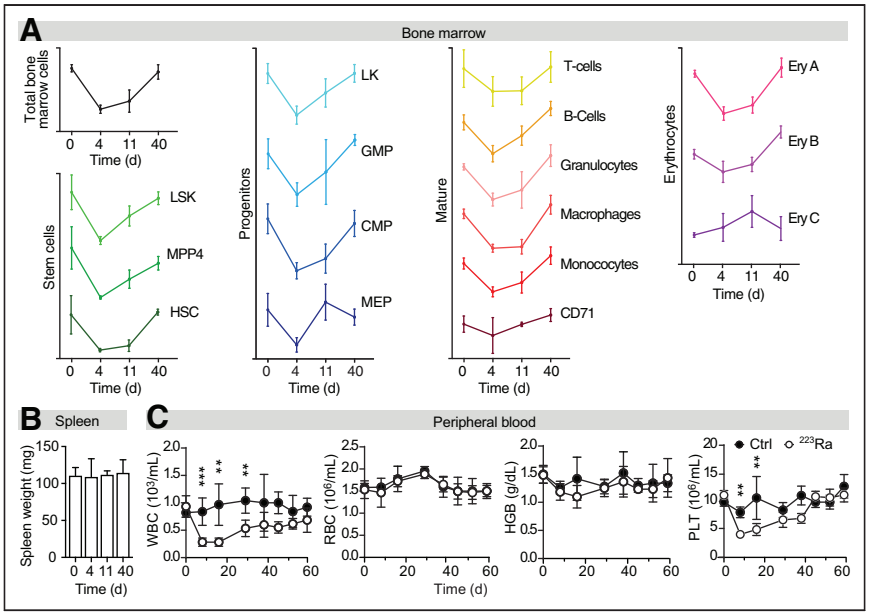

FIGURE 3. ^{223}Ra causes significant but transient myelotoxicity. (A) Effects of ^{223}Ra treatment at baseline and after 4, 11, and 40 d on total bone marrow leukocytes; hematopoietic stem and progenitor cells (based on LSK, MPP4, or HSC markers); early progenitor cells (based on LK, granulocyte-macrophage progenitor, common myeloid progenitor, and megakaryocyte-erythrocyte progenitor markers); B, T, myeloid, and erythroid markers; and erythroid cells at different stages of maturation for 3–4 mice/group. One representative experiment is shown, and experiment was repeated twice. Absolute numbers for each graph and statistical analysis are reported in Supplemental Figure 4. (B) Spleen weight (4 spleens per group). (C) Hematologic analysis of control and ^{223}Ra-treated mice on days 0–60 after treatment for 5–6 mice per group. One representative experiment is shown, and experiment was repeated twice. $^{**}P < 0.01$. $^{***}P < 0.001$. Significance was tested on unpaired 2-tailed Student *t* test. CMP = common myeloid progenitor; Ctrl = control; Ery A = basophilic erythroblasts; Ery B = basophilic and polychromatic erythroblasts; Ery C = orthochromatic erythroblasts; GMP = granulocyte-monocyte progenitors; HGB = hemoglobin; LK = Lin$^-$ c-Kit$^+$; HSCs = hematopoietic stem cells; LSK = Lin-negative Sca-1–positive c-Kit–positive; MEP = megakaryocyte-erythrocyte progenitor; MPP4 = multipotent progenitor population 4; PLT = platelets; RBC = red blood cells; WBC = white blood cells.

and progenitor cells (made of 796 single cells and quite homogeneous in terms of differential gene expression) underwent a limited proportional skewing, whereas lineage-primed precursors showed either a contraction (e.g., granulocytic and neutrophil precursors) or an expansion (e.g., common myeloid progenitor, B-cell precursors, and progenitors). These adaptations were limited primarily to the initial time points after ^{223}Ra treatment, whereas the reciprocal proportions were reestablished within 40 d from treatment (Fig. 4C), in line with flow cytometry data. To leverage the power of single-cell transcriptome data, we then examined differentially expressed genes from the clusters representing stem and early progenitors by comparing each posttreatment time point (days 4, 11, and 40) with the baseline (day 0). Gene ontology and pathway search via Gene Set Enrichment Analysis (*21–23*) on day 4 after treatment showed upregulation of genes related to apoptosis, radiation response, and double-strand break repair, reflecting an ionizing insult and need to react, which in hematopoietic stem and progenitor cell was overcome by day 40. An enrichment for terms related to metabolism, DNA replication, cell cycle, and hematopoietic stem/progenitor cell differentiation was also evident in most populations at early time points (Fig. 4D), indicating that the acute irradiation insult prompted progenitor cells to activate a mitogenic program to restore all hematopoietic types to their baseline levels. Interestingly, very few differences were identifiable at baseline and 40 d after treatment (Fig. 4D; Supplemental Fig. 8) in more immature populations, indicating that most perturbations at the transcriptomic level are fully resolved.

Overall, the data obtained at the single-cell level indicate that in all bone marrow populations. ^{223}Ra has an acute toxicity that is overcome by 40 d after treatment. This finding supports the notion that ^{223}Ra administration, although acutely toxic, does not permanently damage the hematopoietic system.

^{223}Ra Exposure Does Not Impair Full Hematopoietic Reconstitution

Given the transient myelotoxicity that affects all the hematopoietic compartments, we further investigated whether HSCs were able to fully reconstitute a functional steady-state hematopoiesis after acute exposure to ^{223}Ra. To this purpose, we performed bone marrow transplantation experiments using bone marrow from donors that were exposed to ^{223}Ra treatment. C57BL/6 GFP mice were treated with saline (as control) or ^{223}Ra; after 30 d their bone marrow was recovered and implanted in lethally irradiated wild-type C57BL/6 mice. Three-dimensional reconstruction of femurs at the multiphoton microscope 1 mo after treatment showed repopulation of the bone marrow cavity by GFP cells in both control and ^{223}Ra-exposed mice, whereas wild-type C57BL/6 mice did not show any specific fluorescence (Fig. 5A). Hematologic parameters (white blood cells, red blood cells, hemoglobin, platelets) were monitored as an index of functional bone marrow reconstitution 1 mo after transplantation, showing no differences between mice that were previously exposed to ^{223}Ra and those exposed to control treatment (Fig. 5B). Finally, both control and ^{223}Ra-exposed mice survived 40 wk after transplantation (Fig. 5C).

These results show that the acute ^{223}Ra insult to HSCs does not impair full hematopoietic reconstitution, thus indicating that the treatment does not subvert bone marrow function over the long term.

DISCUSSION

Among the limited treatments currently available for patients with castration-resistant prostate cancer metastatic to bone, ^{223}Ra is a viable option that improves overall survival coupled with a good therapeutic index and relatively low toxicity (*8*). Such results prompted further clinical testing of ^{223}Ra for the treatment of other primary cancers and cancers metastatic to bone, with an increasing number of patients who could benefit from this drug (*10–12*).

^{223}Ra exerts zonal cancer cell killing and efficiently reduces tumor mass in vivo, especially in the case of small lesions (*4,7*), and its preventive application decreases tumor burden in preclinical models of disseminated breast cancer (*10*). In addition, retrospective clinical analyses showed that overall survival is improved in men with metastatic bone disease and a low bone scan index

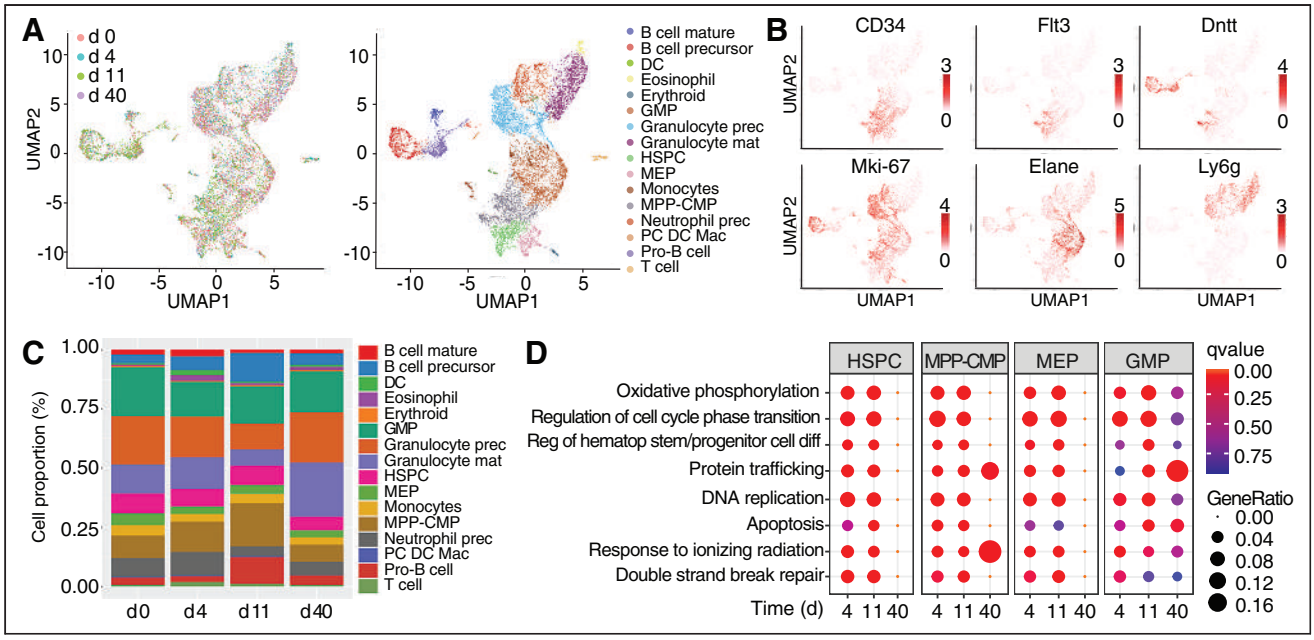

FIGURE 4. ^{223}Ra treatment induces temporary changes in bone marrow cell transcriptome. (A) Uniform manifold approximation and projection of single-cell RNA-sequencing data collected from Kit-positive bone marrow cells of C57/BL6 mice before treatment (day 0) and after 4, 11, and 40 d of treatment with ^{223}Ra in 3 mice per group. (B) Uniform manifold approximation and projection of color-coded hematopoietic populations, based on single-cell transcriptomic profiles. (C) Expression pattern of selected key marker genes. Color scale indicates log-normalized expression levels of indicated genes. (D) Relative proportion of 16 individual cell populations over time after treatment with ^{223}Ra for 0 (untreated), 4, 11, and 40 d. (E) Dot plots showing most representative gene sets from top differentially expressed genes in mice treated with ^{223}Ra for 4, 11, and 40 d vs. untreated. Size of dots represents proportion of differential expressed genes in each term, and color indicates significance of enrichment. DC = dendritic cells; diff = differentiation; GMP = granulocyte-monocyte progenitors; hematop = hematopoietic; HSPC = hematopoietic stem and progenitor cell; MEP = megakaryocyte/erythroid progenitors; MPP-CMP = multipotent progenitors-common myeloid progenitors; PC DC Mac = plasma cell dendritic cell macrophage mixed markers; reg = regulation; UMAP = uniform manifold approximation and projection.

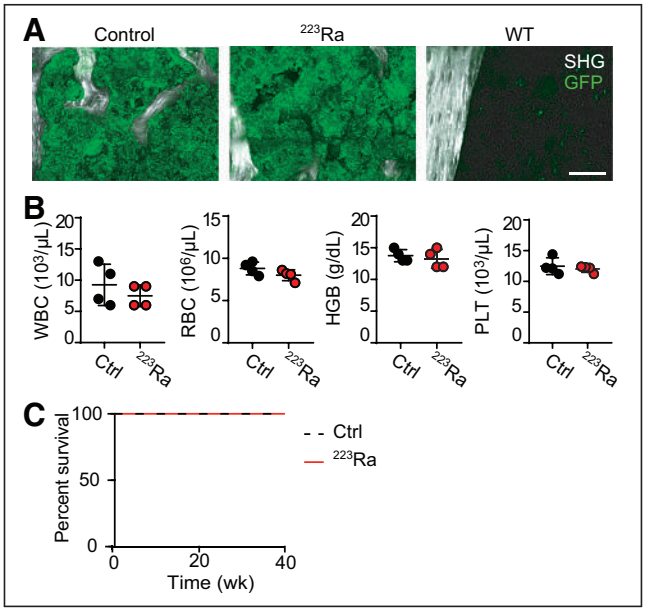

FIGURE 5. ^{223}Ra does not affect long-term functionality of HSCs. (A) Bone marrow reconstitution in mice administered control or ^{223}Ra-exposed bone marrow cells monitored by immunofluorescence analysis 1 mo after transplantation. Wild-type GFP mouse tibia is shown as negative control. Scale bar is 100 μm. (B) Hematologic analysis of transplanted mice. Mean ± SD is shown for 4 mice per group. (C) Survival of control or ^{223}Ra-exposed transplanted mice (n = 4). Ctrl = control; HGB = hemoglobin; PLT = platelets; RBC = red blood cells; SHG = second-harmonic generation; WBC = white blood cells; WT = wild type.

(*24*), whereas preliminary clinical observations suggest that ^{223}Ra has higher efficiency in individuals with fewer circulating tumor cells (<5 circulating tumor cells/7.5 mL of blood) (*25*). Altogether, this evidence supports ^{223}Ra application for secondary prevention of bone metastasis and treatment of oligometastatic bone disease to achieve maximal efficacy, extending the benefits of this treatment to patients at early stages.

Recent clinical observations showed that ^{223}Ra does not induce the emergence of secondary malignancies (*13,14*), and neutropenia and thrombocytopenia are among the most common side effects (*15*). To exclude long-term myelotoxicity, which is particularly relevant when considering a larger cohort of patients with longer survival expectancy, we tested the global effects of ^{223}Ra exposure on hematopoiesis in preclinical models. We confirmed that ^{223}Ra incorporation within bone-calcified matrix induces cellular changes in the bone marrow. Topologic alterations were induced in the bone marrow cavity, where zonal radiologic damage emerged 4 d after treatment and decreased over time up to day 40 after treatment, paralleled by an increment of adipocytes. Cytotoxicity, which extended among all hematopoietic cell lineages, was overcome by 6 wk from ^{223}Ra administration and was paralleled by a significant, transient decrease in circulating white blood cells, with a 50% reduction 28 d after treatment compared with control-treated mice. In patients 4 wk after the first dose of ^{223}Ra, the levels of circulating neutrophils significantly decreased by approximately 25% (*15*). The higher cytotoxic impact in mouse models might be explained by the smaller scale of mouse bones compared with human ones, which in proportion are exposed to higher levels of α-radiation (that travels for <100 μm of distance (*8*)).

Blood cells are formed in a complex microenvironment in which several different stromal cell types (such as endothelial, osteoblastic, and adipogenic progenitors) foster hematopoiesis through mutual interactions. This delicate balance is compromised by external insults, such as chemotherapy or radiation (*18*), which impact the hematopoietic compartment both directly (by arresting its proliferation) and indirectly (by compromising its niche (*26–28*)). ^{223}Ra induces zonal bone marrow injury at the tibia epiphysis and metaphysis, paralleled by the transient change in the number of peripheral blood cells. This early damage is followed by a marked increase in adipocytes, which usually accompanies the restoration of normal hematopoiesis. This increase is in line with recent studies showing that irradiation or fluorouracil treatment causes differentiation of stromal cells into adipocytes, which in turn produce cytokines that stimulate HSCs to regenerate hematopoiesis (*20*). Bone marrow alterations were evident at the epiphysis or metaphysis, where dense trabecular areas are present, and more prominent remodeling of cancellous bone (*29*) may further increase ^{223}Ra incorporation, enhancing zonal toxicity. In contrast, the diaphysis was relatively unaltered. Consistently, high-resolution analysis of bone by α-camera autoradiography showed a predominant ^{223}Ra localization at the growth plate, with little activity at the diaphysis and no signal from the bone marrow (*2*). Interestingly, most quiescent long-term HSCs preferentially reside in the diaphysis, and in particular within perivascular rather than osteoblastic niches (*30*), suggesting a potential role for the region-specific distribution of ^{223}Ra in sparing some niches that host HSCs.

Importantly, our results show no major differences in lineage commitment at baseline and 40 d after ^{223}Ra treatment—neither in the transcriptional programs of the hematopoietic stem and progenitor cells nor in their mature progeny. The bone marrow of mice exposed to ^{223}Ra efficiently restores full hematopoiesis in irradiated hosts, with no significant differences from control-treated mice. This finding suggests that, despite transient bone marrow damage, HSC functionality and normal hematopoietic reconstitution processes are not permanently impaired by ^{223}Ra. Our study addressed these effects after exposure to 1 therapeutic dose of ^{223}Ra, and follow-up work can be performed to exclude a potential increased cytotoxicity by repeated cycles of treatment or by exposure to higher doses.

CONCLUSION

Our results provide a comprehensive explanation of the effects of ^{223}Ra on bone marrow cells and suggest their reversibility, excluding long-term myelotoxicity.

DISCLOSURE

This work was supported by the University of Texas M.D. Anderson Cancer Center Prostate Cancer SPORE (P50 CA140388-09) and Moonshots Initiative; Bayer HealthCare Pharmaceuticals (57440); the U.S. National Institutes of Health (R01CA202025, R01CA202027, R01CA216421, R01CA228135; P01CA229086, and P30 CA016672); the Leukemia & Lymphoma Society (TRP 6580); Alex's Lemonade Stand Foundation for Childhood Cancer; and St. Baldrick's Cancer Research Foundation. ^{223}Ra was received from Bayer. No other potential conflict of interest relevant to this article was reported.

ACKNOWLEDGMENTS

We thank Drs. Maria Guillamot-Ruano and Lara Brambilla (NYU Langone Health) for critical reading of the manuscript and the Leukemia Sample Bank at University of Texas M.D. Anderson Cancer Center for sharing the ABX Micros 60 instrument.

KEY POINTS

QUESTION: Does ^{223}Ra induce permanent bone marrow damage?

PERTINENT FINDINGS: ^{223}Ra prolongs survival in bone-metastasis patients but induces significant neutropenia. Three-dimensional multiphoton microscopy, fluorescence-activated cell sorting analysis, single-cell RNA sequencing, and bone marrow transplantation reveal reversible ^{223}Ra-mediated functional myelotoxicity.

IMPLICATIONS FOR PATIENT CARE: Our results provide a comprehensive explanation of ^{223}Ra reversible effects on bone marrow cells and exclude long-term myelotoxicity, supporting safety for patients.

REFERENCES

1. Bruland ØS, Nilsson S, Fisher DR, Larsen RH. High-linear energy transfer irradiation targeted to skeletal metastases by the alpha-emitter ^{223}Ra: adjuvant or alternative to conventional modalities? *Clin Cancer Res.* 2006;12:6250s–6257s.
2. Abou DS, Ulmert D, Doucet M, Hobbs RF, Riddle RC, Thorek DL. Whole-body and microenvironmental localization of radium-223 in naive and mouse models of prostate cancer metastasis. *J Natl Cancer Inst.* 2015;108:djv380.
3. Gandaglia G, Abdollah F, Schiffmann J, et al. Distribution of metastatic sites in patients with prostate cancer: a population-based analysis. *Prostate.* 2014;74:210–216.
4. Dondossola E, Casarin S, Paindelli C, et al. Radium 223-mediated zonal cytotoxicity of prostate cancer in bone. *J Natl Cancer Inst.* 2019;111:1042–1050.
5. Paindelli C, Navone N, Logothetis CJ, Friedl P, Dondossola E. Engineered bone for probing organotypic growth and therapy response of prostate cancer tumoroids in vitro. *Biomaterials.* 2019;197:296–304.
6. Suominen MI, Fagerlund KM, Rissanen JP, et al. Radium-223 inhibits osseous prostate cancer growth by dual targeting of cancer cells and bone microenvironment in mouse models. *Clin Cancer Res.* 2017;23:4335–4346.
7. Paindelli C, Casarin S, Wang F, et al. Enhancing radium 223 treatment efficacy by anti-beta 1 integrin targeting. *J Nucl Med.* October 28, 2021 [Epub ahead of print].
8. Parker C, Nilsson S, Heinrich D, et al. Alpha emitter radium-223 and survival in metastatic prostate cancer. *N Engl J Med.* 2013;369:213–223.
9. Sartor O, Coleman R, Nilsson S, et al. Effect of radium-223 dichloride on symptomatic skeletal events in patients with castration-resistant prostate cancer and bone metastases: results from a phase 3, double-blind, randomised trial. *Lancet Oncol.* 2014;15:738–746.
10. Suominen MI, Rissanen JP, Kakonen R, et al. Survival benefit with radium-223 dichloride in a mouse model of breast cancer bone metastasis. *J Natl Cancer Inst.* 2013;105:908–916.
11. Ueno NT, Tahara RK, Fujii T, et al. Phase II study of radium-223 dichloride combined with hormonal therapy for hormone receptor-positive, bone-dominant metastatic breast cancer. *Cancer Med.* 2020;9:1025–1032.
12. Morris MJ, Corey E, Guise TA, et al. Radium-223 mechanism of action: implications for use in treatment combinations. *Nat Rev Urol.* 2019;16:745–756.
13. Parker CC, Coleman RE, Sartor O, et al. Three-year safety of radium-223 dichloride in patients with castration-resistant prostate cancer and symptomatic bone metastases from phase 3 randomized Alpharadin in Symptomatic Prostate Cancer trial. *Eur Urol.* 2018;73:427–435.
14. Dizdarevic S, Petersen PM, Essler M, et al. Interim analysis of the reassure (radium-223 alpha emitter agent in non-intervention safety study in mCRPC population for long-term evaluation) study: patient characteristics and safety according to prior use of chemotherapy in routine clinical practice. *Eur J Nucl Med Mol Imaging.* 2019;46:1102–1110.
15. Vogelzang NJ, Coleman RE, Michalski JM, et al. Hematologic safety of radium-223 dichloride: baseline prognostic factors associated with myelosuppression in the ALSYMPCA trial. *Clin Genitourin Cancer.* 2017;15:42–52.e8.
16. Hermiston ML, Zikherman J, Zhu JW. CD45, CD148, and Lyp/Pep: critical phosphatases regulating SRC family kinase signaling networks in immune cells. *Immunol Rev.* 2009;228:288–311.
17. Tsai C-K, Wang T-D, Lin J-W, et al. Virtual optical biopsy of human adipocytes with third harmonic generation microscopy. *Biomed Opt Express.* 2013;4:178–186.

18. Butler A, Hoffman P, Smibert P, Papalexi E, Satija R. Integrating single-cell transcriptomic data across different conditions, technologies, and species. *Nat Biotechnol.* 2018;36:411–420.
19. Giladi A, Paul F, Herzog Y, et al. Single-cell characterization of haematopoietic progenitors and their trajectories in homeostasis and perturbed haematopoiesis. *Nat Cell Biol.* 2018;20:836–846.
20. Naveiras O, Nardi V, Wenzel PL, Hauschka PV, Fahey F, Daley GQ. Bone-marrow adipocytes as negative regulators of the haematopoietic microenvironment. *Nature.* 2009;460:259–263.
21. Hänzelmann S, Castelo R, Guinney J. GSVA: Gene set variation analysis for microarray and RNA-seq data. *BMC Bioinformatics.* 2013;14:7.
22. Liberzon A, Birger C, Thorvaldsdóttir H, Ghandi M, Mesirov JP, Tamayo P. The molecular signatures database (MSigDB) hallmark gene set collection. *Cell Syst.* 2015;1:417–425.
23. Barbie DA, Tamayo P, Boehm JS, et al. Systematic RNA interference reveals that oncogenic KRAS-driven cancers require TBK1. *Nature.* 2009;462:108–112.
24. Alva A, Nordquist L, Daignault S, et al. Clinical correlates of benefit from radium-223 therapy in metastatic castration resistant prostate cancer. *Prostate.* 2017;77:479–488.
25. Carles J, Castellano D, Méndez-Vidal MJ, et al. Circulating tumor cells as a biomarker of survival and response to radium-223 therapy: experience in a cohort of patients with metastatic castration-resistant prostate cancer. *Clin Genitourin Cancer.* 2018;16:e1133–e1139.
26. McCulloch EA, Till JE. The radiation sensitivity of normal mouse bone marrow cells, determined by quantitative marrow transplantation into irradiated mice. *Radiat Res.* 1960;13:115–125.
27. Xie Y, Yin T, Wiegraebe W, et al. Detection of functional haematopoietic stem cell niche using real-time imaging. *Nature.* 2009;457:97–101.
28. Otsuka K, Hirabayashi Y, Tsuboi I, Inoue T. Regeneration capability of Lin-/*Kit*+/Sca-1+ cells with or without radiation exposure for repopulation of peripheral blood in lethally irradiated mice monitored using Ly5.1 isotype on days 35, 90, and 270 after transplantation. *Exp Hematol.* 2010;38:417–425.
29. Langdahl B, Ferrari S, Dempster DW. Bone modeling and remodeling: potential as therapeutic targets for the treatment of osteoporosis. *Ther Adv Musculoskelet Dis.* 2016;8:225–235.
30. Acar M, Kocherlakota KS, Murphy MM, et al. Deep imaging of bone marrow shows non-dividing stem cells are mainly perisinusoidal. *Nature.* 2015;526:126–130.

First-in-Humans Evaluation of ^{18}F-SMBT-1, a Novel ^{18}F-Labeled Monoamine Oxidase-B PET Tracer for Imaging Reactive Astrogliosis

Victor L. Villemagne[1,2], Ryuichi Harada[3,4], Vincent Doré[2,5], Shozo Furumoto[6], Rachel Mulligan[2], Yukitsuka Kudo[4], Samantha Burnham[5], Natasha Krishnadas[2], Svetlana Bozinovski[2], Kun Huang[2], Brian J. Lopresti[7], Kazuhiko Yanai[3], Christopher C. Rowe[2,8,9], and Nobuyuki Okamura[10]

[1]Department of Psychiatry, University of Pittsburgh, Pittsburgh, Pennsylvania; [2]Department of Molecular Imaging and Therapy, Austin Health, Melbourne, Victoria, Australia; [3]Department of Pharmacology, Tohoku University School of Medicine, Sendai, Japan; [4]Institute of Development of Aging and Cancer, Tohoku University, Sendai, Japan; [5]CSIRO Health and Biosecurity Flagship: Australian e-Health Research Centre, Melbourne, Victoria, Australia; [6]Cyclotron and Radioisotope Center, Tohoku University, Sendai, Japan; [7]Department of Radiology, University of Pittsburgh, Pittsburgh, Pennsylvania; [8]Florey Institute of Neuroscience and Mental Health, University of Melbourne, Melbourne, Victoria, Australia; [9]Australian Dementia Network, Melbourne, Victoria, Australia; and [10]Division of Pharmacology, Faculty of Medicine, Tohoku Medical and Pharmaceutical University, Sendai, Japan

Reactive gliosis, characterized by reactive astrocytes and activated microglia, contributes greatly to neurodegeneration throughout the course of Alzheimer disease (AD). Reactive astrocytes overexpress monoamine oxidase B (MAO-B). We characterized the clinical performance of ^{18}F-(*S*)-(2-methylpyrid-5-yl)-6-[(3-fluoro-2-hydroxy)propoxy]-quinoline (^{18}F-SMBT-1), a novel MAO-B PET tracer as a potential surrogate marker of reactive astrogliosis. **Methods:** Seventy-seven participants—53 who were elderly and cognitively normal, 7 with mild cognitive impairment, 7 with AD, and 10 who were young and cognitively normal—were recruited for the different aspects of the study. Older participants underwent 3-dimensional magnetization-prepared rapid gradient-echo MRI and amyloid-β, tau, and ^{18}F-SMBT-1 PET. To ascertain ^{18}F-SMBT-1 selectivity to MAO-B, 9 participants underwent 2 ^{18}F-SMBT-1 scans, before and after receiving 5 mg of selegiline twice daily for 5 d. To compare selectivity, ^{18}F-THK5351 studies were also conducted before and after selegiline. Amyloid-β burden was expressed in centiloids. ^{18}F-SMBT-1 outcomes were expressed as SUV, as well as tissue ratios and binding parameters using the subcortical white matter as a reference region. **Results:** ^{18}F-SMBT-1 showed robust entry into the brain and reversible binding kinetics, with high tracer retention in basal ganglia, intermediate retention in cortical regions, and the lowest retention in cerebellum and white matter, which tightly follows the known regional brain distribution of MAO-B (R^2 = 0.84). More than 85% of ^{18}F-SMBT-1 signal was blocked by selegiline across the brain, and in contrast to ^{18}F-THK5351, no residual cortical activity was observed after the selegiline regimen, indicating high selectivity for MAO-B and low nonspecific binding. ^{18}F-SMBT-1 also captured the known MAO-B increases with age, with an annual rate of change (~2.6%/y) similar to the in vitro rates of change (~1.9%/y). Quantitative and semiquantitative measures of ^{18}F-SMBT-1 binding were strongly associated ($R^2 > 0.94$), suggesting that a simplified tissue-ratio approach could be used to generate outcome measures. **Conclusion:** ^{18}F-SMBT-1 is a highly selective MAO-B tracer, with low nonspecific binding, high entry into the brain, and reversible kinetics. Moreover, ^{18}F-SMBT-1 brain distribution matches the reported in vitro distribution and captures the known MAO-B increases with age, suggesting that ^{18}F-SMBT-1 can potentially be used as a surrogate marker of reactive astrogliosis. Further validation of these findings with ^{18}F-SMBT-1 will require examination of a much larger series, including participants with mild cognitive impairment and AD.

Key Words: reactive astrogliosis; MAO-B; Alzheimer disease; amyloid; brain imaging

J Nucl Med 2022; 63:1551–1559
DOI: 10.2967/jnumed.121.263254

The neuropathologic hallmarks of Alzheimer disease (AD)—neurofibrillary tangles of tau protein and amyloid-β (Aβ) plaques—are accompanied by reactive gliosis, cellular degeneration, and diffuse synaptic and neuronal loss (*1*).

In recent years, there has been increased interest in the study of astrocytes (*2*). Astrocytes are the most abundant glial cells in the brain and are involved in several functions critical for the normal functioning and preservation of brain homeostasis (*3,4*), such as synaptic plasticity and formation of memory (*5,6*), regulation of γ-aminobutyric acid and glutamatergic neurotransmission (*7–9*), regulation of cerebral blood flow (*10,11*), and both Aβ production (*12*) and Aβ clearance (*13*). Astrocytes are also essential components of the neuroglial vascular unit, where they play a key neuroprotective role in cerebrovascular disease (*10,11*). Astrocytes do not constitute a homogeneous population and have been morphologically classified into protoplasmic, fibrous, and interlaminar or by their state: resting or activated (*14*). Although reactive astrocytes have also been classified as neurotoxic (A1), characterized by the expression of complement fraction 3, and neuroprotective (A2), expressing the S100A10 protein (*15,16*), reactive astrogliosis constitutes a much more complex spectrum of toxic and protective pathways (*2,17*), playing a crucial role in the pathophysiology of AD (*9,18*). Astrogliosis is an early neuroinflammatory event in several neurodegenerative conditions (*19*) such as AD (*7,9,18*), making it a target for the in vivo assessment of neuroinflammatory processes and their potential synergistic or independent contribution to the

Received Sep. 22, 2021; revision accepted Jan. 14, 2022.
For correspondence or reprints, contact Victor L. Villemagne (victor.villemagne@pitt.edu).
Published online Jan. 27, 2022.

development of AD dementia. In AD, reactive astrogliosis and microgliosis have been observed around both dense-core Aβ plaques and neurofibrillary tangles, and they are believed to contribute greatly to neurodegeneration throughout the course of the disease (*18,20*). In contrast to microgliosis, which is not detected by imaging at early disease stages (*21*), reactive astrogliosis occurs early (*22*), making it a particularly attractive target for understanding its contribution to AD pathogenesis and the development of dementia and, as such, is a potential therapeutic target for AD (*23*).

Reactive astrocytes overexpress monoamine oxidase B (MAO-B) (*24*), and molecular neuroimaging studies have used MAO-B tracers such as ^{11}C-L-deprenyl-D_2 (^{11}C-DED) as surrogate markers of astrogliosis (*22,25–28*). Some of these studies have shown that reactive astrogliosis is observed at the prodromal stages in both sporadic and familial AD (*22,25*). Historically, ^{11}C-DED has been used as a surrogate PET tracer for reactive astrogliosis; however, several issues limit the use of ^{11}C-DED, such as difficulty with quantification due to its irreversible kinetics, the existence of radiolabeled metabolites that can cross the blood–brain barrier and bind to monoamine transporters, poor image quality, and low selectivity for MAO-B (*29*). More recently another MAO-B tracer, ^{11}C-SL25.1188, with more favorable tracer kinetics than ^{11}C-DED was developed (*30,31*). ^{11}C-BU99008, a tracer for the imidazoline 2 binding sites, has also been proposed as a surrogate marker of astrogliosis (*32–35*). Unfortunately, like ^{11}C-DED, these tracers are labeled with ^{11}C, which has a 20-min half-life, preventing widespread clinical or research applications.

Recently, an analog of the PET radiotracer ^{18}F-THK5351, which was developed as a putative tau imaging radiotracer (*36*) but was later shown to have significant MAO-B binding (*37,38*), has been found to be highly selective for MAO-B (*39*). Preclinical assessment showed that ^{18}F-(*S*)-(2-methylpyrid-5-yl)-6-[(3-fluoro-2-hydroxy)propoxy]quinoline (^{18}F-SMBT-1) binds with high affinity (dissociation constant, 3.5 nM) and selectivity to MAO-B in human brain homogenates (*39*). Comparison of in vitro ^{18}F-SMBT-1 binding against MAO-B regional activity expressed as relative luminescence showed ^{18}F-SMBT-1 binding to correlate strongly with regional activity of MAO-B in the brain (*39*). Autoradiography studies showed significantly higher specific binding in the frontal cortex of an AD patient than in a control subject (*39*). Specific binding of ^{18}F-SMBT-1 was completely displaced after incubation with 1 μM of the selective MAO-B inhibitor lazabemide (*39*), showing high selectivity and low nonspecific binding. Receptor-binding screening assays showed no significant ^{18}F-SMBT-1 binding to 60 common neurotransmitter receptors, ion channels, and transporters (*39*). Radiation exposure was extrapolated to be 21.3 μSv/MBq for women and 12.2 μSv/MBq for men (*39*). Toxicity studies of ^{18}F-SMBT-1 in animals, including acute pharmacology and toxicity at doses 1,000–10,000 times higher than those expected in a PET study, demonstrated no toxic effects related to the drug treatment.

The aim of this first-in-humans study was to characterize ^{18}F-SMBT-1 binding, assessing its relation to age, regional brain distribution, and selectivity for MAO-B. We also examined ^{18}F-SMBT-1 tracer kinetics and explored potential quantification approaches.

MATERIALS AND METHODS

Participants

In total, 77 nonsmoking participants—53 who were elderly and cognitively normal (CN), 7 with mild cognitive impairment (MCI), 7 with AD, and 10 young and CN (YCN)—were recruited for the different aspects of the study. All participants were screened for unstable medical or psychiatric disease and concomitant medication. Participants with known use of antidepressants, cold and flu tablets, or opiate or opioid agonist medication were excluded because of the possibility of interactions with selegiline. For participants with a recognized memory impairment, this information was collected from a next of kin or caregiver. The study protocol was approved by the Austin Health Human Research Ethics Committee, and all participants gave written informed consent.

Image Acquisition

PET scans were acquired on 1 of 2 scanners, a Philips TF64 PET/CT or a Siemens Biograph mCT. A low-dose CT scan was obtained for attenuation correction. Partial-volume correction was not performed in any of the studies.

^{18}F-SMBT-1 PET. ^{18}F-SMBT-1 was synthesized in-house in the Department of Molecular Imaging and Therapy, Austin Health, using an ORA Neptis radiosynthesiser. The ^{18}F-SMBT-1 synthesis is detailed in the supplemental materials (available at http://jnm.snmjournals.org). Sixty-nine adults (10 YCN, 49 CN, 6 MCI, and 4 AD) participated in the assessment of ^{18}F-SMBT-1. All were administered 186 ± 6 MBq (range, 177–194 MBq). The average administered mass was 1.0 ± 0.8 μg (range 0.10–2.60 μg). Of the 69, 10 nondemented participants (4 CN and 6 MCI) underwent a 90-min dynamic scan after an intravenous bolus injection of ^{18}F-SMBT-1. The remaining 59 participants (10 YCN, 45 CN, and 4 AD) underwent a 20-min emission scan (4 × 5 min) starting at 60 min after injection of ^{18}F-SMBT-1. A second ^{18}F-SMBT-1 PET scan was acquired for 9 participants (5 CN and 4 AD) after completion of a 5-d regimen of oral selegiline.

Aβ PET. All 67 older adults underwent Aβ PET imaging with ^{18}F-flutemetamol (n = 3), ^{18}F-florbetapir (n = 2), or ^{18}F-NAV4694 (n = 62) to ascertain Aβ status. ^{18}F-NAV4694 and ^{18}F-florbetapir were synthesized in-house in the Department of Molecular Imaging and Therapy, Austin Health, as previously reported (*40–42*). ^{18}F-flutemetamol was manufactured by Cyclotek Pty Ltd. The ^{18}F-NAV4694 and ^{18}F-florbetapir PET acquisitions consisted of 20-min (4 × 5 min) dynamic scans obtained at 50 min after an intravenous bolus injection of 185 MBq (±10%) of ^{18}F-NAV4694 or ^{18}F-florbetapir. Similarly, the participants who received ^{18}F-flutemetamol also underwent a 20-min (4 × 5 min) PET acquisition starting at 90 min after injection of 185 MBq (±10%) of ^{18}F-flutemetamol. All Aβ imaging results were expressed in centiloids (*40,41,43,44*).

Tau PET. Nine older adults who were enrolled in the selegiline assessments with ^{18}F-SMBT-1 also underwent tau imaging with either 6-(fluoro-^{18}F)-3-(^{1}H-pyr- rolo[2,3-C]pyridin-1-yl)isoquinolin-5-amine (^{18}F-MK-6240) (n = 7) (*45*) or ^{18}F-PI2620 (n = 2) (*46*). Both tau imaging tracers were synthesized in-house in the Department of Molecular Imaging and Therapy, Austin Health, as previously reported (*47*). The ^{18}F-MK6240 PET acquisition consisted of a 20-min (4 × 5 min) dynamic scan acquired at 90 min after an intravenous bolus injection of 185 MBq (±10%) of ^{18}F-MK6240. The ^{18}F-PI2620 PET acquisition consisted of a 20-min (4 × 5 min) dynamic scan acquired at 80 min after an intravenous bolus injection of 200 MBq (±10%) of ^{18}F-PI2620. All tau imaging results were expressed as SUV ratios (SUVRs) using the cerebellar cortex as a reference region.

^{18}F-THK5351 PET. Eight older adults (4 CN, 1 MCI, and 3 AD) underwent 2 ^{18}F-THK5351 PET scans. ^{18}F-THK5351 was synthesized in-house in the Department of Molecular Imaging and Therapy, Austin Health, as previously described (*48*). Participants received an intravenous bolus injection of 185 MBq (±10%) of ^{18}F-THK5351, and a 30-min emission scan (4 × 5 min) was acquired starting at 50 min after injection. A second ^{18}F-THK5351 PET scan was acquired after completion of a 5-d regimen of oral selegiline.

MRI. Participants were also asked to undergo structural MRI on a 3-T TIM Trio scanner (Siemens Medical Solutions) to obtain

high-resolution T1-weighted anatomic magnetization-prepared rapid gradient-echo sequences.

Image Analysis

Aβ and tau PET scans were spatially normalized using CapAIBL (*44*). The standard centiloid method was applied to determine Aβ burden (*43*). A centiloid value of more than 20 was selected to determine a high-Aβ (Aβ+) scan (*49*). A 1.19 SUVR in the temporal composite region (*50*) was used to discriminate between high tau (tau-positive) and low tau (tau-negative). ^{18}F-THK5351 scans were spatially normalized using CapAIBL and expressed as SUVs. ^{18}F-SMBT-1 PET images were also spatially normalized using CapAIBL. ^{18}F-SMBT-1 PET volumes of interest were sampled to assess tracer selectivity, regional distribution, effect of age, and kinetic analysis. SUV values for the selegiline studies were estimated in 4 composite gray matter volumes of interest: neocortex (comprising frontal cortex, superior parietal lobe, lateral temporal lobe, lateral occipital lobe, anterior and posterior cingulate gyri, and precuneus), mesial temporal lobe (comprising hippocampus, entorhinal cortex, parahippocampus, and amygdala), basal ganglia (comprising caudate nuclei, putamen, globus pallidus, and thalamus), and cerebellar cortex. Several brain regions were evaluated as potential reference tissue, before generation of semiquantitative tissue ratios/SUVRs and graphical analysis of the data. Kinetic analysis was performed using PMOD (PMOD Technologies).

Assessing Tracer Selectivity Using Selegiline

Seventeen volunteers participated in the selegiline study. After a baseline ^{18}F-THK5351 or ^{18}F-SMBT-1 PET scan, the participants were supplied with oral selegiline tablets and instructed to follow a 5-d regimen at the standard therapeutic dose of 10 mg daily (5 mg at breakfast and 5 mg at lunch). At the completion of the regimen, the participants were invited back for a repeat PET scan.

Statistical Analysis

All statistical analyses were performed with JMP Pro (version 16.0; SAS Institute Inc.) for Macintosh (Apple). Data are presented as mean ± SD unless otherwise stated. Groups were compared using paired or unpaired Student *t* tests. Effect size was measured with Cohen *d*. Correlations were assessed by Spearman and Pearson correlation coefficients. Changes in tracer retention between pre- and postselegiline ^{18}F-THK5351 studies were expressed as percentage reduction from baseline. Significance was set at a *P* value of less than 0.05, uncorrected for multiple comparisons.

RESULTS

No significant changes in vital signs or in immediate or delayed adverse events related to the study drug were observed or reported by any of the participants during or after the ^{18}F-SMBT-1 scan.

Tracer Selectivity Studies

The irreversible MAO-B inhibitor selegiline was used to evaluate the selectivity of ^{18}F-SMBT. All participants underwent an Aβ and tau imaging scan, in addition to the 2 ^{18}F-SMBT-1 scans before and after selegiline. The same study was repeated with a different cohort of participants using ^{18}F-THK5351 to assess the validity of the selegiline regimen.

Table 1 shows the demographics of both groups. Tracer selectivity was assessed in 17 participants; 8 of them (4 CN, 3 Aβ+ AD, and 1 Aβ+ MCI) underwent assessment with ^{18}F-THK5351, whereas 9 (5 CN and 4 Aβ+ AD) underwent assessment with ^{18}F-SMBT-1.

For the selectivity study with ^{18}F-THK5351, 8 participants underwent Aβ PET and 2 ^{18}F-THK5351 PET scans, one at baseline and one after a 5-d regimen of 5 mg of oral selegiline twice daily. Figure 1A shows Aβ imaging studies performed with ^{18}F-flutemetamol in a CN subject and with ^{18}F-NAV4694 in an AD patient, as well as baseline ^{18}F-THK5351 PET images of the same individuals before and after the selegiline regimen, indicating a variable degree of blockade of the ^{18}F-THK5351. Given that there is a significant reduction in tracer retention in the cerebellar cortex, usually used as a reference region, all images are displayed in SUV units. Importantly, there is residual neocortical signal in the follow-up scan of the Aβ+ AD patient that is likely attributable to tau. Figure 1B shows a variable decrease in baseline ^{18}F-THK5351 signal in the neocortex (~63% decrease), mesial temporal lobe (~71% decrease), basal ganglia (~82% decrease), and cerebellar cortex (~54% decrease), although there were no significant differences in the degree of signal reduction between CN and AD subjects.

For the selectivity study with ^{18}F-SMBT-1, 9 participants (5 CN and 4 Aβ+ tau-positive AD) underwent Aβ and tau imaging and

TABLE 1
Demographics of ^{18}F-THK5351 and ^{18}F-SMBT-1 Selectivity Evaluations

	^{18}F-THK5351		^{18}F-SMBT-1	
Demographic	CN	AD/MCI	CN	AD
Total subjects (*n*)	4	4	5	4
Age (y)	79.1 ± 6.7	74.9 ± 7.0	78.5 ± 6.0	76.7 ± 1.5
Sex (*n*)	3 M/1 F	2 M/2 F	2 M/3 F	1 M/3 F
APOE4	25%	50%	60%	67%
MMSE	29.3 ± 0.5	25.7 ± 2.8*	29.2 ± 0.8	22.8 ± 4.8*
CDR SoB	0.0 ± 0.0	2.2 ± 0.4*	0.0 ± 0.0	7.6 ± 2.1*
Aβ (centiloids)	28.3 ± 54.7	82.7 ± 12.7	17.4 ± 10.2	127.6 ± 47.1
Aβ+	25%	100%	60%	100%

*Statistically significant ($P < 0.05$).
MMSE = Mini Mental State Examination; CDR SoB = clinical dementia rating sum of boxes.
Continuous data are mean ± SD.

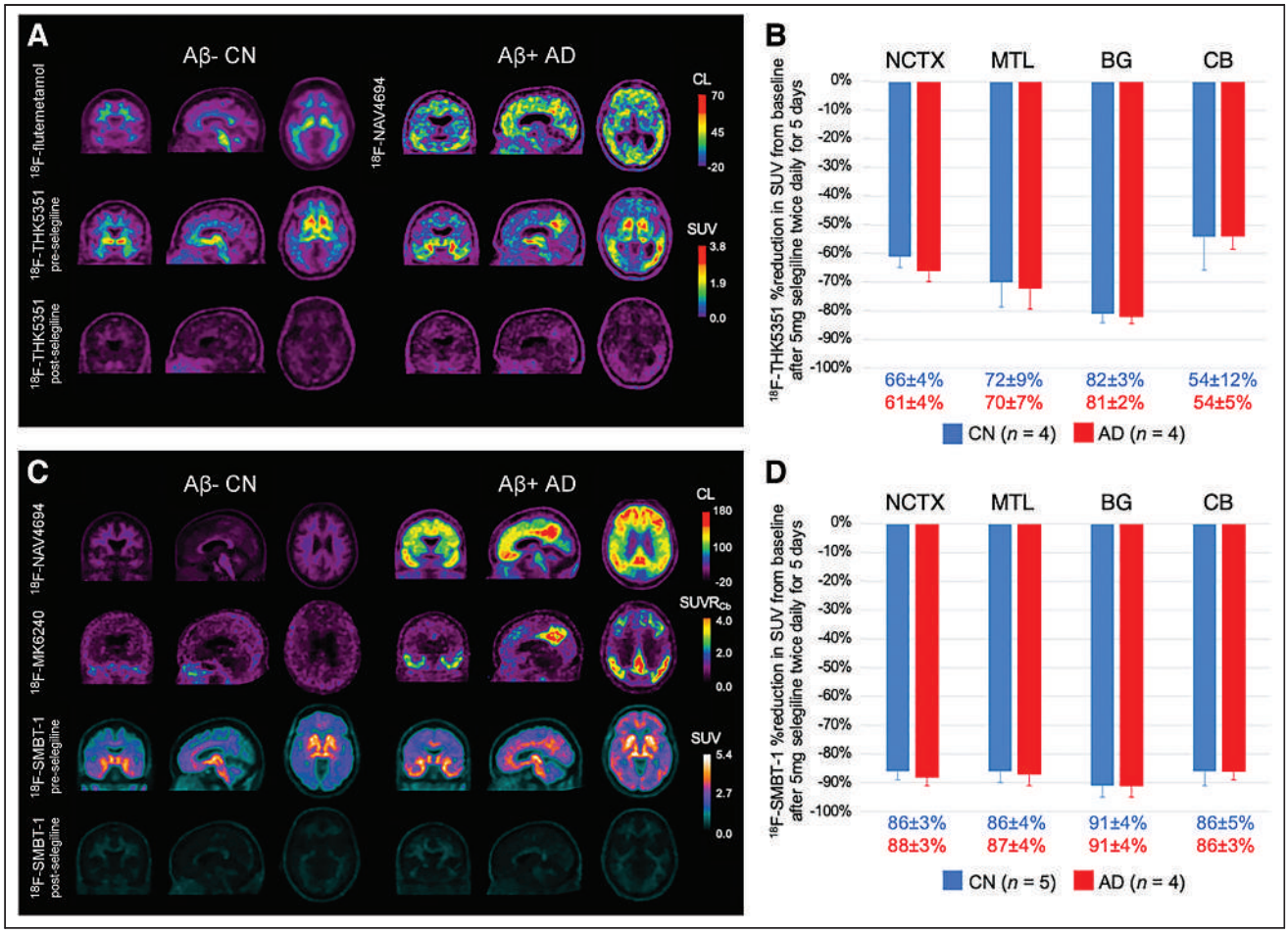

FIGURE 1. Effect of selegiline on ^{18}F-THK5351 and ^{18}F-SMBT-1. (A) Representative coronal, sagittal, and transaxial PET images in Aβ-negative CN subject (79-y-old man; MMSE, 29) and in Aβ+ AD subject (72-y-old man; MMSE, 24). Aβ imaging studies are expressed in centiloids (top row) and were performed with ^{18}F-flutemetamol or ^{18}F-NAV4694. Baseline ^{18}F-THK5351 PET images (middle row) of same individuals before and after (bottom row) selegiline regimen indicate variable degree of regional blockade of ^{18}F-THK5351, most noticeable in basal ganglia, mesial temporal lobe, and neocortex. Given that there is significant reduction in tracer retention in cerebellar cortex, images are displayed in SUV units. Although in CN participants there is significant reduction of ^{18}F-THK5351 retention throughout brain, in AD patients there is residual cortical retention likely due to ^{18}F-THK5351 binding to tau. (B) Bar graphs showing percentage of selegiline ^{18}F-THK5351 regional blockade in neocortex (~63% decrease), mesial temporal lobe (~71% decrease), basal ganglia (~82% decrease), and cerebellum (~54% decrease). Reduction of signal was greater in basal ganglia and mesial temporal lobe than in neocortex and cerebellum, although there were no significant differences in degree of signal reduction between CN and AD subjects. (C) Representative coronal, sagittal, and transaxial PET images in Aβ-negative, tau-negative CN subject (78-y-old woman; MMSE, 29) and in Aβ+, tau-positive AD subjects (75-y-old woman; MMSE, 21). Aβ imaging studies performed with ^{18}F-NAV4694 are expressed in centiloids (top row). Second row shows tau imaging studies expressed in SUVR using cerebellar cortex as reference region, performed with either ^{18}F-MK6240 or ^{18}F-PI2620. Baseline ^{18}F-SMBT-1 PET images (third row) of same individuals before and after (bottom row) selegiline regimen indicate high degree of regional blockade of ^{18}F-SMBT-1 across all regions of brain. Images are displayed in SUV units. In contrast to ^{18}F-THK5351 (Fig. 1A), there was no residual cortical retention in CN or AD subjects. (D) Bar graphs showing high percentage of blocking of ^{18}F-SMBT-1 by selegiline, with more than 85% blockade across all regions of brain, indicating selective binding of ^{18}F-SMBT-1 to MAO-B as well as low nonspecific binding. There were no significant differences in degree of signal reduction between regions or between CN and AD subjects. BG = basal ganglia; CB = cerebellum; CL = centiloids; MTL = mesial temporal lobe; NCTX = neocortex.

2 ^{18}F-SMBT-1 PET scans, one at baseline and one after the same 5-d regimen of 5 mg of oral selegiline twice daily. Figure 1C shows Aβ imaging studies with ^{18}F-NAV4694 and tau imaging studies with ^{18}F-MK6240, using the cerebellar cortex as a reference region, in a CN subject and an AD subject. The ^{18}F-SMBT-1 SUV images before and after the selegiline regimen indicate a very high degree of reduction in ^{18}F-SMBT-1 signal, with no residual activity attributable to Aβ or tau. Figure 1D shows a more than 85% decrease in baseline ^{18}F-SMBT-1 signal in the neocortex, mesial temporal lobe, basal ganglia, and cerebellum, with the same degree of signal reduction in CN and AD subjects. A more detailed brain regional blockade by selegiline is provided in Table 2.

Regional Brain Distribution of ^{18}F-SMBT-1

We also assessed the in vivo regional brain distribution of ^{18}F-SMBT-1. Figure 2 shows ^{18}F-SMBT-1 SUV at 60–80 min after injection in 44 low-Aβ (Aβ-negative) CN subjects, against the reported in vitro ^{11}C-DED autoradiography regional concentrations (*51*). There was a strong correlation ($R^2 = 0.84$, $P = 0.0002$) between the in vivo regional ^{18}F-SMBT-1 signal and the in vitro concentrations in several regions of the brain.

Increase in MAO-B with Age

To further evaluate ^{18}F-SMBT-1, we scanned 10 YCN subjects (5 women, 5 men; 31.3 ± 4.0 y old) (Table 3) to assess whether

TABLE 2
Percentage Reduction in Regional ^{18}F-THK5351 and ^{18}F-SMBT-1 SUV by Selegiline

Region	^{18}F-THK-5351		^{18}F-SMBT-1	
	CN	AD	CN	AD
Caudate	−86%	−84%	93%	95%
Thalamus	−83%	−82%	93%	95%
Putamen	−80%	−78%	92%	92%
Anterior cingulate	−76%	−74%	88%	90%
Hippocampus	−69%	−64%	88%	90%
Frontal cortex	−67%	−63%	87%	89%
Temporal	−67%	−67%	87%	88%
Posterior cingulate	−66%	−63%	86%	88%
Parietal	−63%	−56%	85%	86%
Cerebellar cortex	−54%	−54%	86%	86%
Whole cerebellum	−72%	−68%	83%	83%
Pons	−73%	−68%	82%	82%
Midbrain	−66%	−63%	82%	81%
Occipital	−61%	−56%	80%	83%
Cerebellar white matter	−65%	−56%	69%	69%
SWM + corpus callosum	−64%	−57%	62%	65%
SWM	−54%	−54%	60%	63%

No *P* values were statistically significant for CN ≠ AD.

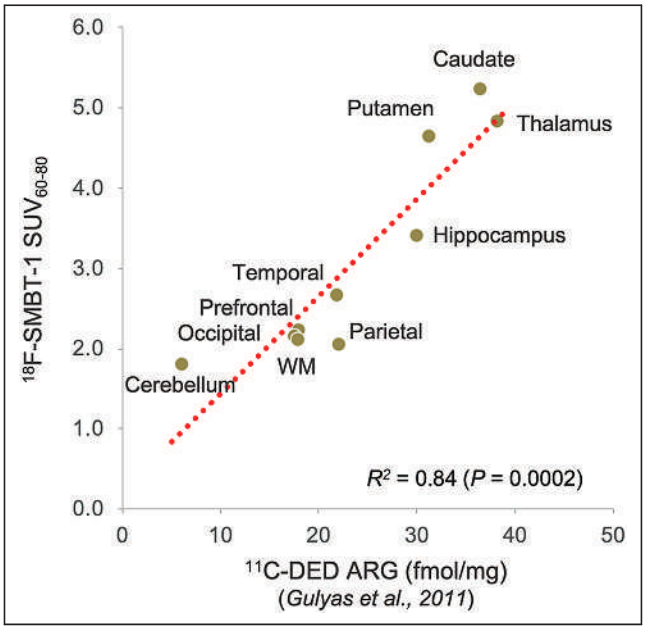

FIGURE 2. Regional distribution of MAO-B in brain: correlation between in vitro autoradiography with ^{11}C-DED and ^{18}F-SMBT-1 retention in Aβ-negative CN subjects. There was high correlation (R^2 = 0.84) between known in vitro regional distribution of MAO-B in brain (*51*), expressed in fmol/mg, and regional SMBT-1 retention at 60–80 min after injection. ARG = autoradiography; WM = white matter.

^{18}F-SMBT-1 was able to capture the age-related increases of MAO-B in the frontal cortex as previously reported by in vitro studies (*52*). ^{18}F-SMBT-1 SUV in the frontal cortex of 10 YCN and 44 Aβ-negative tau-negative CN subjects (Fig. 3A) demonstrated a significant age-related increase in MAO-B (R^2 = 0.44, $P < 0.0001$). Figure 3B shows coronal, sagittal, and transaxial

TABLE 3
Demographics for Assessment of Effect of Age

Demographic	YCN	Aβ-negative CN
Total subjects (*n*)	10	44
Age (y)	31.3 ± 4.0*	76.0 ± 4.8
Female	50%	57%
Education (y)		14.8 ± 2.7
APOE4		30%
MMSE		28.6 ± 1.5
CDR SoB		0.07 ± 0.2
Aβ burden (centiloids)		0.80 ± 6.9

*Statistically significant association ($P < 0.05$).
MMSE = Mini Mental State Examination; CDR SoB = clinical dementia rating sum of boxes.

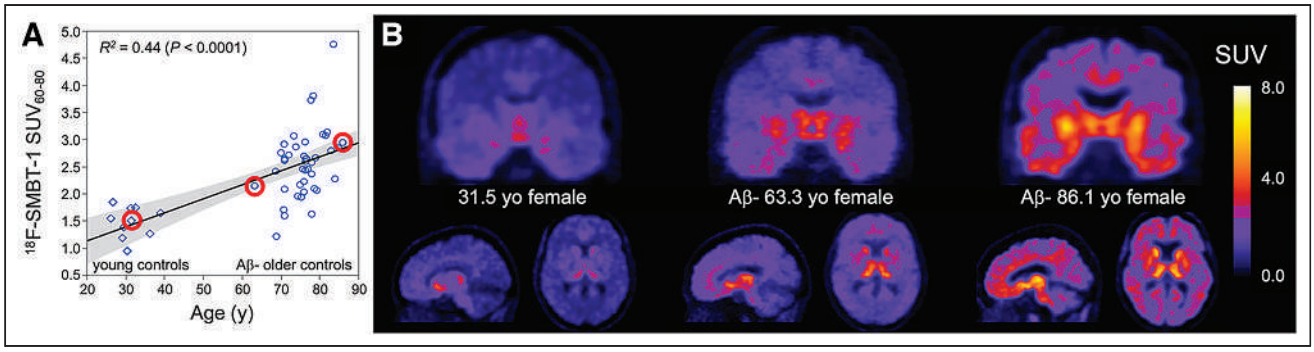

FIGURE 3. Effect of age. (A) ^{18}F-SMBT-1 SUV at 60–80 min after injection in frontal cortex of 10 YCN subjects (5 women, 5 men; 31.3 ± 4.0 y old) and 44 Aβ-negative CN subjects (25 women, 19 men; 76.0 ± 4.8 y old) was able to capture reported age-related increases of MAO-B in frontal cortex as previously reported by in vitro studies (*52*) and in vivo with PET (*62*). (B) Coronal, sagittal, and transaxial ^{18}F-SMBT-1 images illustrating age-related regional increases in ^{18}F-SMBT-1 signal in 3 women, whose ages ranged from 31 to 86 y (red circles in A).

images illustrating the age-related regional increases in ^{18}F-SMBT-1 signal in 3 women, whose ages ranged from 31 to 86 y old.

^{18}F-SMBT-1 Kinetics

We characterized the in vivo ^{18}F-SMBT-1 kinetics in 10 elderly participants (6 MCI and 4 CN, Table 4). Time–activity curves revealed that ^{18}F-SMBT-1 has robust entry into the brain (SUV, 4–7 at ~3–5 min after injection) and displays reversible kinetics (Fig. 4A). ^{18}F-SMBT-1 retention was highest in the basal ganglia and thalamus; intermediate in the anterior cingulate, gyrus rectus, and hippocampus; low in neocortical areas; and lowest in the cerebellum and in the subcortical white matter (SWM).

Before generating SUVRs over time, we compared the SUVs in several potential reference regions—cerebellum, cerebellar white matter, SWM (*53*), SWM, and corpus callosum (*54*)—to be used in a simplified reference tissue model (*55*). The SUVR generated with the SWM as a reference region had the strongest correlation with the in vitro regional distribution of MAO-B (Table 5) (*51*).

SUVRs were shown to approach an apparent steady state in high-binding areas approximately 50 min after injection (Fig. 4B), suggesting the possibility of using a simplified ^{18}F-SMBT-1 imaging protocol with SUVR as the outcome. ^{18}F-SMBT-1 reversible kinetics were further validated by graphical analysis of the 90-min dynamic scans, using the same regions as used for generating SUVRs. ^{18}F-SMBT-1 specific binding measures of distribution volume derived from the noninvasive Logan plot (*56*), as well as nondisplaceable binding potential estimated using the Ichise multilinear reference tissue model, MRTM (*57*), showed high correlations with late-scan SUVR (R^2 = 0.97 and 0.94 for nondisplaceable binding potential and distribution volume, respectively) and with the known distribution of MAO-B in the human brain (R^2 = 0.78 and 0.72 for nondisplaceable binding potential and distribution volume, respectively) (*51*).

TABLE 4
Demographics for Assessing ^{18}F-SMBT-1 Tracer Kinetics

Demographic	CN/MCI
Total subjects (*n*)	10
Age (y)	73.2 ± 7.2
Female	30%
APOE4	60%
MMSE	27.7 ± 1.6
CDR SoB	0.3 ± 0.4
Aβ burden (centiloids)	15.8 ± 31.0
Aβ+	30%

MMSE = Mini Mental State Examination; CDR SoB = clinical dementia rating sum of boxes.

DISCUSSION

To the best of our knowledge, ^{18}F-SMBT-1 represents the first available ^{18}F MAO-B radiotracer to be used in a clinical study. Because preclinical evaluation demonstrated ^{18}F-SMBT-1 to have an in vitro binding profile well suited for an MAO-B PET tracer (*39*), the study aimed at characterizing the ^{18}F-SMBT-1 binding profile in vivo with PET. The study was divided into 4 main areas or substudies. We first assessed ^{18}F-SMBT-1 selectivity for MAO-B before and after a 5-d regimen of oral selegiline. ^{18}F-SMBT-1 is an analog of the PET radiotracer ^{18}F-THK5351, which was developed as a putative tau imaging radiotracer (*39*) but was later shown to have significant MAO-B binding (*37,38*). Therefore, we compared the ^{18}F-SMBT-1 results with studies performed with ^{18}F-THK5351 under the same selegiline regimen. For these studies, given that there is a significant widespread reduction in tracer retention even in regions usually used as an internal reference, all images were displayed in SUV units. In the ^{18}F-THK5351 studies, the degree of blockade by selegiline in gray matter areas was variable, ranging from 54% in the cerebellar cortex to more than 80% in the basal ganglia. Moreover, there was some residual ^{18}F-THK5351 signal in the cortex, likely representing ^{18}F-THK5351 binding to tau. In the ^{18}F-SMBT-1 studies, the degree of blockade by selegiline in gray matter areas was more than 85%, and most importantly, there was no residual cortical signal. There were no significant differences in the degree of signal reduction between CN and AD subjects with either ^{18}F-THK5351 or ^{18}F-SMBT-1. This study also demonstrated the low degree of nonspecific binding with ^{18}F-SMBT-1. This is important because it enables ^{18}F-SMBT-1 to accurately detect incipient early cortical changes in MAO-B concentrations as well as small changes over time. The low nonspecific binding is also evident in the high-contrast images (Fig. 1C) even at 60–80 min after injection. We then assessed the regional brain distribution of ^{18}F-SMBT-1 and compared the results with in vitro autoradiography performed with ^{11}C-DED (*51*), showing a high correlation between the two.

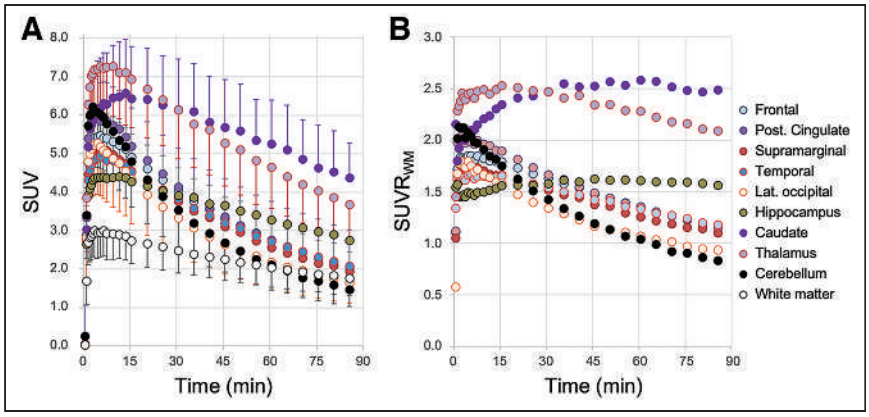

FIGURE 4. ^{18}F-SMBT-1 time–activity and total binding curves. (A) Time–activity curves reveal that ^{18}F-SMBT-1 has robust entry into brain (SUV, 5–7 at ~5 min after injection) and reversible kinetics. ^{18}F-SMBT-1 clearance was slower in areas of high concentrations of MAO-B, such as basal ganglia and hippocampus, and faster in regions with lower MAO-B concentrations, such as frontal cortex, temporal lobe, and cerebellum. (B) Tissue ratios—using SWM as reference region—over time show SWM SUVR approaching apparent steady state in high binding areas ~50 min after injection. SWM was more stable reference region across clinical groups and across Aβ status.

The competition studies with selegiline and the regional distribution studies indicate that ^{18}F-SMBT-1 is a highly selective ^{18}F-labeled MAO-B tracer (*7*).

^{18}F-SMBT-1 was also able to capture the known increases in MAO-B with age. The estimated yearly signal increase for ^{18}F-SMBT-1 in the frontal cortex is about 2.5%/y, similar to the approximately 1.9%/y estimates from in vitro studies (*52*).

Finally, we evaluated the tracer kinetic characteristics of ^{18}F-SMBT-1. The time–activity curves showed high initial entry into the brain, followed by clearance of the tracer. Clearance was slower in areas with very high MAO-B concentrations such as the basal ganglia, intermediate in areas with high MAO-B concentrations such as the hippocampus and anterior cingulate gyrus, and faster in cortical areas with low concentrations of MAO-B such as the neocortical areas. The lowest retention was observed in SWM. The reversible binding kinetics suggested that ^{18}F-SMBT-1 binding could be quantified using graphical analysis (*56,57*) and a simplified reference tissue model (*55*).

Before embarking on the generation of tissue ratios and graphical analysis of the data, we explored several potential reference regions. We correlated the tissue ratios generated with each of them against the known regional distribution of MAO-B in the brain. SWM SUVR yielded the strongest correlation. Moreover, the SWM was the region least affected by selegiline (Table 2) and one of the least atrophic regions across the AD continuum (*58*). Graphical analysis outcomes, either multilinear reference tissue model or Logan plot, also generated using the SWM as reference region, correlated strongly with SWM SUVR and with the in vitro brain distribution of MAO-B. The small number of MCI and AD patients precludes drawing any conclusion regarding group differences in the ^{18}F-SMBT-1 signal. A larger sample size of MCI and AD patients, with their corresponding Aβ and tau status, will be required to examine whether ^{18}F-SMBT-1 can capture the reported increases in MAO-B in AD.

Although most of the recently developed specific neuroimaging and biofluid markers of disease have focused on the pathologic hallmarks of AD, such as Aβ plaques and tau tangles, the most prevalent markers identified in genomewide association studies of AD are related to neuroinflammation (*59*). The introduction of biomarker-based approaches to identifying brain pathology has informed new strategies for the design of preventative clinical trials aimed at preventing the onset of cognitive impairment and dementia. Markers of Aβ and tau pathology and markers of neurodegeneration have been incorporated into a recently proposed biomarker-based framework (*60*). In view of the advantage of the modular design of the framework, and considering that reactive gliosis is a critical aspect of the neuropathology of AD, the biomarker framework might be expanded to include reactive gliosis.

There are several limitations to the study. There is no validation of the semiquantitative or simplified reference region approach by full kinetic analysis with metabolite-corrected arterial input function. The same applies to the selection of the reference region. Initial semiquantitative and quantitative examinations used the SWM as the reference region. Although SWM was affected significantly less by the selegiline regimen than were the cortical, subcortical, or cerebellar regions (~60% vs. >85% blockade), the selegiline study clearly indicates that there is substantial specific binding in SWM. This, in principle, would preclude the use of SWM as a reference region. It could be argued that SWM represents a brain region that is not likely to be involved in the early disease process; although there is SWM atrophy in AD, atrophy is more prevalent around mesial temporal lobe structures (*58*). Another issue to consider is that SWM, *stricto sensu*, does not truly fulfill the criteria for a reference region (*55*) given that it has a completely different cellular

TABLE 5
Correlation Between MAO-B In Vitro Distribution and ^{18}F-SMBT-1 Binding Parameters and Tissue Ratios Generated with Different Reference Regions

Parameter	*r*	95% CI	*P*
SWM SUVR	0.914	0.62–0.98	0.0002
SUVR	0.904	0.61–0.98	0.0007
Cerebellum			
SWM + corpus callosum	0.889	0.55–0.98	0.0013
Cerebellar white matter	0.888	0.55–0.98	0.0014
Ichise nondisplaceable binding potential	0.885	0.54–0.98	0.0015
Logan total distribution volume ratio	0.849	0.42–0.97	0.0038

Correlation between in vitro MAO-B brain distribution assessed with autoradiography (*51*) and quantitative and semiquantitative measures of ^{18}F-SMBT-1 binding, ranked by correlation coefficients (*r*). Tissue ratios and graphical analysis results using SWM as reference region yielded highest correlation with in vitro measures of MAO-B.

composition, has about half the regional cerebral blood flow of gray matter, and is likely to have a completely different degree of nonspecific binding. A more appropriate term for it might be *internal brain scaling region.* The kinetic analysis was performed pooling CN and MCI subjects, with 30% being deemed Aβ+. Probably because of the small numbers, there were no significant kinetic differences between CN and MCI subjects, nor were there significant kinetic differences when comparing Aβ-negative with Aβ+.

CONCLUSION

Our first-in-humans studies confirmed that ^{18}F-SMBT-1 is a selective MAO-B tracer. Although the main goal was to characterize an MAO-B tracer to be used as a surrogate marker of astrogliosis in neurodegenerative conditions, the potential applications of an MAO-B tracer are much wider, extending from neuropsychiatric conditions such as depression (*30*) to movement disorders (*61*). In the particular case of assessing astrogliosis, ^{18}F-SMBT-1 will allow a better understanding of the pathophysiology of AD while examining its potential direct or indirect effect over neurodegeneration, cognitive decline, and clinical progression, enabling more accurate staging and prognosis at earlier stages of the disease.

DISCLOSURE

The study was supported in part by National Health Medical Research Council (NHMRC) of Australia grants G1005121 and 19KK0212 from Japan. Yukitsuka Kudo and Nobuyuki Okamura own stock in Clino Ltd., licensing SMBT-1. Ryuichi Harada, Shozo Furumoto, Yukitsuka Kudo, and Nobuyuki Okamura have a patent pending for the technology described in this article. No other potential conflict of interest relevant to this article was reported.

ACKNOWLEDGMENTS

We thank the Brain Research Institute for support in acquiring the MRI data. We thank Drs. Chester Mathis, William E. Klunk, Milos Ikonomovic, Oscar Lopez, Ann Cohen, Howard Aizenstein, Scott Mason, Beth Snitz, and Beth Shaaban at the University of Pittsburgh for extremely fruitful discussions around ^{18}F-SMBT-1, MAO-B, and reactive astrogliosis. We thank the participants who took part in the study and their families.

KEY POINTS

QUESTION: Is ^{18}F-SMBT-1 a selective MAO-B tracer?

PERTINENT FINDINGS: A clinical study in 59 elderly and 10 young participants showed that ^{18}F-SMBT-1 is a highly selective MAO-B tracer, with reversible kinetics and low specific signal that follows the known regional distribution of MAO-B in the brain and captures the known increases in MAO-B with age.

IMPLICATIONS FOR PATIENT CARE: ^{18}F-SMBT-1 can be used as a surrogate marker of reactive astrogliosis

REFERENCES

1. Masters CL, Beyreuther K. The neuropathology of Alzheimer's disease in the year 2005. In: Beal MF, Lang AE, Ludolph AC, eds. *Neurodegenerative Diseases: Neurobiology, Pathogenesis and Therapeutics.* Cambridge University Press; 2005: 433–440.
2. Escartin C, Galea E, Lakatos A, et al. Reactive astrocyte nomenclature, definitions, and future directions. *Nat Neurosci.* 2021;24:312–325.
3. Fakhoury M. Microglia and astrocytes in Alzheimer's disease: implications for therapy. *Curr Neuropharmacol.* 2018;16:508–518.
4. Vasile F, Dossi E, Rouach N. Human astrocytes: structure and functions in the healthy brain. *Brain Struct Funct.* 2017;222:2017–2029.
5. Adamsky A, Kol A, Kreisel T, et al. Astrocytic activation generates de novo neuronal potentiation and memory enhancement. *Cell.* 2018;174:59–71 e14.
6. Kol A, Adamsky A, Groysman M, Kreisel T, London M, Goshen I. Astrocytes contribute to remote memory formation by modulating hippocampal-cortical communication during learning. *Nat Neurosci.* 2020;23:1229–1239.
7. Osborn LM, Kamphuis W, Wadman WJ, Hol EM. Astrogliosis: an integral player in the pathogenesis of Alzheimer's disease. *Prog Neurobiol.* 2016;144:121–141.
8. Danbolt NC, Furness DN, Zhou Y. Neuronal vs glial glutamate uptake: resolving the conundrum. *Neurochem Int.* 2016;98:29–45.
9. Carter SF, Herholz K, Rosa-Neto P, Pellerin L, Nordberg A, Zimmer ER. Astrocyte biomarkers in Alzheimer's disease. *Trends Mol Med.* 2019;25:77–95.
10. Iadecola C, Nedergaard M. Glial regulation of the cerebral microvasculature. *Nat Neurosci.* 2007;10:1369–1376.
11. Koehler RC, Roman RJ, Harder DR. Astrocytes and the regulation of cerebral blood flow. *Trends Neurosci.* 2009;32:160–169.
12. Zhao J, O'Connor T, Vassar R. The contribution of activated astrocytes to Abeta production: implications for Alzheimer's disease pathogenesis. *J Neuroinflammation.* 2011;8:150.
13. Thal DR. The role of astrocytes in amyloid beta-protein toxicity and clearance. *Exp Neurol.* 2012;236:1–5.
14. Perez-Nievas BG, Serrano-Pozo A. Deciphering the astrocyte reaction in Alzheimer's disease. *Front Aging Neurosci.* 2018;10:114.
15. Zamanian JL, Xu L, Foo LC, et al. Genomic analysis of reactive astrogliosis. *J Neurosci.* 2012;32:6391–6410.
16. Liddelow SA, Barres BA. Reactive astrocytes: production, function, and therapeutic potential. *Immunity.* 2017;46:957–967.
17. Sofroniew MV. Astrogliosis. *Cold Spring Harb Perspect Biol.* 2014;7:a020420.
18. Birch AM. The contribution of astrocytes to Alzheimer's disease. *Biochem Soc Trans.* 2014;42:1316–1320.
19. Acioglu C, Li L, Elkabes S. Contribution of astrocytes to neuropathology of neurodegenerative diseases. *Brain Res.* 2021;1758:147291.
20. Ingelsson M, Fukumoto H, Newell KL, et al. Early Abeta accumulation and progressive synaptic loss, gliosis, and tangle formation in AD brain. *Neurology.* 2004; 62:925–931.
21. Kreisl WC, Lyoo CH, Liow JS, et al. ^{11}C-PBR28 binding to translocator protein increases with progression of Alzheimer's disease. *Neurobiol Aging.* 2016; 44:53–61.
22. Carter SF, Scholl M, Almkvist O, et al. Evidence for astrocytosis in prodromal Alzheimer disease provided by ^{11}C-deuterium-L-deprenyl: a multitracer PET paradigm combining ^{11}C-Pittsburgh compound B and ^{18}F-FDG. *J Nucl Med.* 2012;53:37–46.
23. Assefa BT, Gebre AK, Altaye BM. Reactive astrocytes as drug target in Alzheimer's disease. *BioMed Res Int.* 2018;2018:4160247.
24. Ekblom J, Jossan SS, Bergstrom M, Oreland L, Walum E, Aquilonius SM. Monoamine oxidase-B in astrocytes. *Glia.* 1993;8:122–132.
25. Rodriguez-Vieitez E, Ni R, Gulyas B, et al. Astrocytosis precedes amyloid plaque deposition in Alzheimer APPswe transgenic mouse brain: a correlative positron emission tomography and in vitro imaging study. *Eur J Nucl Med Mol Imaging.* 2015;42:1119–1132.
26. Rodriguez-Vieitez E, Saint-Aubert L, Carter SF, et al. Diverging longitudinal changes in astrocytosis and amyloid PET in autosomal dominant Alzheimer's disease. *Brain.* 2016;139:922–936.
27. Schöll M, Carter SF, Westman E, et al. Early astrocytosis in autosomal dominant Alzheimer's disease measured in vivo by multi-tracer positron emission tomography. *Sci Rep.* 2015;5:16404.
28. Engler H, Nennesmo I, Kumlien E, et al. Imaging astrocytosis with PET in Creutzfeldt-Jakob disease: case report with histopathological findings. *Int J Clin Exp Med.* 2012;5:201–207.
29. Jevtić II, Lai TH, Penjišević JZ, et al. Newly synthesized fluorinated cinnamylpiperazines possessing low in vitro MAO-B binding. *Molecules.* 2020;25:4941.
30. Moriguchi S, Wilson AA, Miler L, et al. Monoamine oxidase B total distribution volume in the prefrontal cortex of major depressive disorder: an [^{11}C]SL25.1188 positron emission tomography study. *JAMA Psychiatry.* 2019;76:634–641.
31. Saba W, Valette H, Peyronneau MA, et al. [^{11}C]SL25.1188, a new reversible radioligand to study the monoamine oxidase type B with PET: preclinical characterisation in nonhuman primate. *Synapse.* 2010;64:61–69.
32. Tyacke RJ, Myers JFM, Venkataraman A, et al. Evaluation of ^{11}C-BU99008, a PET ligand for the imidazoline2 binding site in human brain. *J Nucl Med.* 2018;59: 1597–1602.

33. Venkataraman AV, Keat N, Myers JF, et al. First evaluation of PET-based human biodistribution and radiation dosimetry of ^{11}C-BU99008, a tracer for imaging the imidazoline2 binding site. *EJNMMI Res.* 2018;8:71.
34. Kumar A, Koistinen NA, Malarte ML, et al. Astroglial tracer BU99008 detects multiple binding sites in Alzheimer's disease brain. *Mol Psychiatry.* 2021;26:5833–5847.
35. Calsolaro V, Matthews PM, Donat CK, et al. Astrocyte reactivity with late-onset cognitive impairment assessed in vivo using ^{11}C-BU99008 PET and its relationship with amyloid load. *Mol Psychiatry.* 2021;26:5848–5855.
36. Harada R, Okamura N, Furumoto S, et al. ^{18}F-THK5351: a novel PET radiotracer for imaging neurofibrillary pathology in Alzheimer disease. *J Nucl Med.* 2016;57:208–214.
37. Ng KP, Pascoal TA, Mathotaarachchi S, et al. Monoamine oxidase B inhibitor, selegiline, reduces ^{18}F-THK5351 uptake in the human brain. *Alzheimers Res Ther.* 2017;9:25.
38. Harada R, Ishiki A, Kai H, et al. Correlations of ^{18}F-THK5351 PET with postmortem burden of tau and astrogliosis in Alzheimer disease. *J Nucl Med.* 2018;59:671–674.
39. Harada R, Hayakawa Y, Ezura M, et al. ^{18}F-SMBT-1: a selective and reversible PET tracer for monoamine oxidase-B imaging. *J Nucl Med.* 2021;62:253–258.
40. Battle MR, Pillay LC, Lowe VJ, et al. Centiloid scaling for quantification of brain amyloid with [^{18}F]flutemetamol using multiple processing methods. *EJNMMI Res.* 2018;8:107.
41. Rowe CC, Jones G, Dore V, et al. Standardized expression of ^{18}F-NAV4694 and ^{11}C-PiB beta-amyloid PET results with the centiloid scale. *J Nucl Med.* 2016;57:1233–1237.
42. Navitsky M, Joshi AD, Kennedy I, et al. Standardization of amyloid quantitation with florbetapir standardized uptake value ratios to the centiloid scale. *Alzheimers Dement.* 2018;14:1565–1571.
43. Klunk WE, Koeppe RA, Price JC, et al. The centiloid project: standardizing quantitative amyloid plaque estimation by PET. *Alzheimers Dement.* 2015;11:1-15.e4.
44. Bourgeat P, Dore V, Fripp J, et al. Implementing the centiloid transformation for ^{11}C-PiB and beta-amyloid ^{18}F-PET tracers using CapAIBL. *Neuroimage.* 2018;183:387–393.
45. Walji AM, Hostetler ED, Selnick H, et al. Discovery of 6-(fluoro-^{18}F)-3-(^{1}H-pyrrolo[2,3-C]pyridin-1-yl)isoquinolin-5-amine (^{18}F-MK-6240): a positron emission tomography (PET) imaging agent for quantification of neurofibrillary tangles (NFTs). *J Med Chem.* 2016;59:4778–4789.
46. Brendel M, Barthel H, van Eimeren T, et al. Assessment of 18F-PI-2620 as a biomarker in progressive supranuclear palsy. *JAMA Neurol.* 2020;77:1408–1419.
47. Krishnadas N, Dore V, Lamb F, et al. Case report: ^{18}F-MK6240 tau positron emission tomography pattern resembling chronic traumatic encephalopathy in a retired Australian rules football player. *Front Neurol.* 2020;11:598980.
48. Ishiki A, Harada R, Okamura N, et al. Tau imaging with [^{18}F]THK-5351 in progressive supranuclear palsy. *Eur J Neurol.* 2017;24:130–136.
49. Jack CR Jr, Wiste HJ, Weigand SD, et al. Defining imaging biomarker cut points for brain aging and Alzheimer's disease. *Alzheimers Dement.* 2017;13:205–216.
50. Jack CR Jr, Wiste HJ, Schwarz CG, et al. Longitudinal tau PET in ageing and Alzheimer's disease. *Brain.* 2018;141:1517–1528.
51. Gulyás B, Pavlova E, Kasa P, et al. Activated MAO-B in the brain of Alzheimer patients, demonstrated by [^{11}C]-L-deprenyl using whole hemisphere autoradiography. *Neurochem Int.* 2011;58:60–68.
52. Galva MD, Bondiolotti GP, Olasmaa M, Picotti GB. Effect of aging on lazabemide binding, monoamine oxidase activity and monoamine metabolites in human frontal cortex. *J Neural Transm Gen Sect.* 1995;101:83–94.
53. Fleisher AS, Joshi AD, Sundell KL, et al. Use of white matter reference regions for detection of change in florbetapir positron emission tomography from completed phase 3 solanezumab trials. *Alzheimers Dement.* 2017;13:1117–1124.
54. Chen K, Roontiva A, Thiyyagura P, et al. Improved power for characterizing longitudinal amyloid-beta PET changes and evaluating amyloid-modifying treatments with a cerebral white matter reference region. *J Nucl Med.* 2015;56:560–566.
55. Lammertsma AA, Hume SP. Simplified reference tissue model for PET receptor studies. *Neuroimage.* 1996;4:153–158.
56. Logan J, Fowler JS, Volkow ND, Wang GJ, Ding YS, Alexoff DL. Distribution volume ratios without blood sampling from graphical analysis of PET data. *J Cereb Blood Flow Metab.* 1996;16:834–840.
57. Ichise M, Ballinger JR, Golan H, et al. Noninvasive quantification of dopamine D2 receptors with iodine-123-IBF SPECT. *J Nucl Med.* 1996;37:513–520.
58. Li J, Pan P, Huang R, Shang H. A meta-analysis of voxel-based morphometry studies of white matter volume alterations in Alzheimer's disease. *Neurosci Biobehav Rev.* 2012;36:757–763.
59. Hammond TR, Marsh SE, Stevens B. Immune signaling in neurodegeneration. *Immunity.* 2019;50:955–974.
60. Jack CR Jr, Bennett DA, Blennow K, et al. A/T/N: an unbiased descriptive classification scheme for Alzheimer disease biomarkers. *Neurology.* 2016;87:539–547.
61. Cohen G, Farooqui R, Kesler N. Parkinson disease: a new link between monoamine oxidase and mitochondrial electron flow. *Proc Natl Acad Sci USA.* 1997;94:4890–4894.
62. Fowler JS, Volkow ND, Wang GJ, et al. Age-related increases in brain monoamine oxidase B in living healthy human subjects. *Neurobiol Aging.* 1997;18:431–435.

Assessing Reactive Astrogliosis with ^{18}F-SMBT-1 Across the Alzheimer Disease Spectrum

Victor L. Villemagne[1,2], Ryuichi Harada[3,4], Vincent Doré[1,5], Shozo Furumoto[6], Rachel Mulligan[1], Yukitsuka Kudo[4], Samantha Burnham[5], Natasha Krishnadas[1], Pierrick Bourgeat[7], Ying Xia[7], Simon Laws[8], Svetlana Bozinovski[1], Kun Huang[1], Milos D. Ikonomovic[2,9,10], Jürgen Fripp[7], Kazuhiko Yanai[3], Nobuyuki Okamura[11], and Christopher C. Rowe[1,12,13]

[1]Department of Molecular Imaging and Therapy, Austin Health, Melbourne, Victoria, Australia; [2]Department of Psychiatry, University of Pittsburgh, Pittsburgh, Pennsylvania; [3]Department of Pharmacology, School of Medicine, Tohoku University, Sendai, Japan; [4]Institute of Development of Aging and Cancer, Tohoku University, Sendai, Japan; [5]CSIRO Health and Biosecurity Flagship: Australian e-Health Research Centre, Melbourne, Victoria, Australia; [6]Cyclotron and Radioisotope Center, Tohoku University, Sendai, Japan; [7]CSIRO: Australian e-Health Research Centre, Brisbane, Queensland, Australia; [8]School of Medical and Health Sciences, Edith Cowan University, Perth, Western Australia, Australia; [9]Department of Neurology, University of Pittsburgh, Pittsburgh, Pennsylvania; [10]Geriatric Research Education and Clinical Center, VA Pittsburgh Healthcare System, Pittsburgh, Pennsylvania; [11]Division of Pharmacology, Faculty of Medicine, Tohoku Medical and Pharmaceutical University, Sendai, Japan; [12]Florey Institute of Neurosciences and Mental Health, University of Melbourne, Melbourne, Victoria, Australia; and [13]Australian Dementia Network, Melbourne, Victoria, Australia

A neuroinflammatory reaction in Alzheimer disease (AD) brains involves reactive astrocytes that overexpress monoamine oxidase-B (MAO-B). ^{18}F-(*S*)-(2-methylpyrid-5-yl)-6-[(3-fluoro-2-hydroxy)propoxy]quinoline (^{18}F-SMBT-1) is a novel ^{18}F PET tracer highly selective for MAO-B. We characterized the clinical performance of ^{18}F-SMBT-1 PET across the AD continuum as a potential surrogate marker of reactive astrogliosis. **Methods:** We assessed ^{18}F-SMBT-1 PET regional binding in 77 volunteers (76 ± 5.5 y old; 41 women, 36 men) across the AD continuum: 57 who were cognitively normal (CN) (44 amyloid-β [Aβ]–negative [Aβ−] and 13 Aβ-positive [Aβ+]), 12 who had mild cognitive impairment (9 Aβ− and 3 Aβ+), and 8 who had AD dementia (6 Aβ+ and 2 Aβ−). All participants also underwent Aβ and tau PET imaging, 3-T MRI, and neuropsychologic evaluation. Tau imaging results were expressed in SUV ratios using the cerebellar cortex as a reference region, whereas Aβ burden was expressed in centiloids. ^{18}F-SMBT-1 outcomes were expressed as SUV ratio using the subcortical white matter as a reference region. **Results:** ^{18}F-SMBT-1 yielded high-contrast images at steady state (60–80 min after injection). When compared with the Aβ− CN group, there were no significant differences in ^{18}F-SMBT-1 binding in the group with Aβ− mild cognitive impairment. Conversely, ^{18}F-SMBT-1 binding was significantly higher in several cortical regions in the Aβ+ AD group but also was significantly lower in the mesial temporal lobe and basal ganglia. Most importantly, ^{18}F-SMBT-1 binding was significantly higher in the same regions in the Aβ+ CN group as in the Aβ− CN group. When all clinical groups were considered together, ^{18}F-SMBT-1 correlated strongly with Aβ burden and much less with tau burden. Although in most cortical regions ^{18}F-SMBT-1 did not correlate with brain volumetrics, regions known for high MAO-B concentrations presented a direct association with hippocampal and gray matter volumes, whereas the occipital lobe was directly associated with white matter hyperintensity. ^{18}F-SMBT-1 binding was inversely correlated with Mini Mental State Examination and the Australian Imaging Biomarkers and Lifestyle's Preclinical Alzheimer Cognitive Composite in some neocortical regions such as the frontal cortex, lateral temporal lobe, and supramarginal gyrus. **Conclusion:** Cross-sectional human PET studies with ^{18}F-SMBT-1 showed that Aβ+ AD patients, but most importantly, Aβ+ CN individuals, had significantly higher regional ^{18}F-SMBT-1 binding than Aβ− CN individuals. Moreover, in several regions in the brain, ^{18}F-SMBT-1 retention was highly associated with Aβ load. These findings suggest that increased ^{18}F-SMBT-1 binding is detectable at the preclinical stages of Aβ accumulation, providing strong support for its use as a surrogate marker of astrogliosis in the AD continuum.

Key Words: reactive astrogliosis; MAO-B; Alzheimer disease; amyloid; tau; brain imaging

J Nucl Med 2022; 63:1560–1569
DOI: 10.2967/jnumed.121.263255

The neuropathologic hallmarks of Alzheimer disease (AD)—neurofibrillary tangles (NFT) of tau protein and amyloid-β (Aβ) plaques—are accompanied by reactive gliosis, cellular degeneration, and diffuse synaptic and neuronal loss (*1*). Astrocytes are the most abundant glial cells in the brain and are involved in several functions critical for the normal functioning and preservation of brain homeostasis (*2,3*). Loss of these regulatory and compensatory mechanisms in astrogliosis likely translates into increased vasculature-related vulnerability (*4*), affecting the brain's ability to compensate for the accumulating Aβ and tau burden and impaired cerebrovascular function in AD. The complex spectrum of toxic and protective pathways (*5,6*) of reactive astrogliosis plays a crucial role in the pathophysiology of AD (*7–9*) and other neurodegenerative conditions (*10–16*). Reactive astrogliosis and microgliosis have been observed around both dense-core Aβ plaques and neurofibrillary tangles, and they are believed to contribute greatly to neurodegeneration throughout the course of AD (*9,17*). In contrast to microgliosis (*18*), reactive astrogliosis occurs early in the disease (*19*), and is a particularly attractive target for understanding its contribution to

Received Sep. 22, 2021; revision accepted Jan. 14, 2022.
For correspondence or reprints, contact Victor L. Villemagne (victor.villemagne@pitt.edu).
Published online Jan. 27, 2022.

the development of AD dementia, and, as such, is a potential therapeutic target for AD (*20*).

Reactive astrocytes overexpress monoamine oxidase B (MAO-B) (*21*), and molecular neuroimaging studies have used MAO-B tracers such as ^{11}C-L-deprenyl-D_2 and ^{11}C-SL25.1188 (*22,23*) as surrogate markers of astrogliosis (*15,19,24–26*). Some of these studies have shown that reactive astrogliosis is observed at the prodromal stages in both sporadic and familial AD (*19,24*). ^{11}C-BU99008—a tracer for the imidazoline 2 binding sites, with some partial binding to MAO-B (*27*)—has also been proposed as a surrogate marker of astrogliosis (*28,29*). Unfortunately, these tracers are labeled with ^{11}C, which has a 20-min half-life, preventing widespread clinical or research applications.

A novel ^{18}F MAO-B tracer, ^{18}F-(*S*)-(2-methylpyrid-5-yl)-6-[(3-fluoro-2-hydroxy)propoxy]quinoline (^{18}F-SMBT-1), with high in vitro binding affinity (dissociation constant, 3.5 nM) and selectivity to MAO-B has recently been developed (*30*). Comparison of in vitro ^{18}F-SMBT-1 binding against MAO-B activity showed SMBT-1 binding to be highly correlated with the regional activity of MAO-B in AD brain tissue homogenates (*30*). Autoradiography analysis showed significantly higher specific binding in the frontal cortex tissue section from an AD patient than in a control (*30*), and this binding was completely displaced by the selective MAO-B inhibitor lazabemide (*30*).

In a first-in-humans study (*31*), ^{18}F-SMBT-1 showed robust entry into the brain and reversible binding kinetics, with quantitative and semiquantitative measures of ^{18}F-SMBT-1 binding being strongly associated. More than 85% of ^{18}F-SMBT-1 signal was blocked by selegiline across the brain, indicating high selectivity for MAO-B and low nonspecific binding. ^{18}F-SMBT-1 regional binding followed the known regional brain distribution of MAO-B ($R^2 = 0.84$) while also capturing the known MAO-B increases with age ($R^2 > 0.94$), suggesting that ^{18}F-SMBT-1 can potentially be used as a surrogate marker of reactive astrogliosis in AD.

The aim of this study was to characterize ^{18}F-SMBT-1 binding across the AD continuum, assessing its relation to Aβ and tau pathology burden, as well as brain volumetrics, white matter hyperintensity, and cognitive performance.

MATERIALS AND METHODS

Participants

In total, 77 nonsmoking elderly participants (76 ± 5.5 y old; age range, 58–89 y; 40 women, 35 men) were included in the study: 57 cognitively normal (CN) controls, 12 subjects meeting the criteria for mild cognitive impairment (MCI) (*32*), and 8 subjects meeting the NINDS-ADRDA and NIAA-AA criteria for AD (*33*). Subjects with AD and MCI were recruited from memory disorder clinics. CN subjects were recruited by advertisement in the community. Some participants (46 CN, 6 MCI, and 4 AD) were included in a previous study (*31*).

All participants were screened for unstable medical or psychiatric disease and concomitant medication. Participants with known use of MAO-B inhibitors or with a diagnosis of a psychiatric disorder were excluded. For participants with a recognized memory impairment, this information was collected from the next of kin or a caregiver. The study protocol was approved by the Austin Health Human Research Ethics Committee, and all participants gave written informed consent.

A detailed neuropsychologic evaluation is provided in the supplemental materials (available at http://jnm.snmjournals.org).

Image Acquisition

All SMBT-1 PET scans were acquired on a Philips TF64 PET/CT device. Aβ and tau PET scans were acquired on 1 of 2 scanners, a Philips TF64 PET/CT or a Siemens Biograph mCT. A low-dose CT scan was obtained for attenuation correction.

^{18}F-SMBT-1 PET. All 77 participants underwent ^{18}F-SMBT-1 PET. As previously reported (*31*), 10 nondemented participants (4 CN and 6 MCI) underwent a 90-min dynamic scan after receiving an intravenous bolus injection of 185 MBq (±10%) of ^{18}F-SMBT-1. The remaining 67 participants received an intravenous bolus injection of 185 MBq (±10%) of ^{18}F-SMBT-1 and underwent a 20-min emission scan (4 × 5 min) starting at 60 min after injection.

^{18}F-SMBT-1 was synthesized in-house in the Department of Molecular Imaging and Therapy, Austin Health, as previously described (*31*). ^{18}F-SMBT-1 yielded more than 95% radiochemical purity after high-performance liquid chromatography purification, with an average decay-corrected radiochemical yield of 40%. The molar activity at the end of ^{18}F-SMBT-1 synthesis was more than 400 GBq/μmol.

Aβ PET. All 77 participants underwent Aβ PET imaging with ^{18}F-flutemetamol ($n = 3$), ^{18}F-florbetapir ($n = 2$), or ^{18}F-NAV4694 ($n = 72$) to ascertain Aβ status. ^{18}F-NAV4694 and ^{18}F-florbetapir were synthesized in-house in the Department of Molecular Imaging and Therapy, Austin Health, as previously described (*34,35*). ^{18}F-flutemetamol was manufactured by Cyclotek Pty Ltd. The ^{18}F-NAV4694 and ^{18}F-florbetapir PET acquisitions consisted of 20-min (4 × 5 min) dynamic scans obtained at 50 min after an intravenous bolus injection of 200 MBq (±10%) of the tracers. Similarly, the^{18}F-flutemetamol PET acquisition also was a 20-min (4 × 5 min) scan starting at 90 min after injection of 185 MBq (±10%) of the tracer. All Aβ imaging results were expressed in centiloids (*34–38*). In a subset of participants ($n = 31$) who had available longitudinal Aβ imaging data, rates of Aβ accumulation—expressed as centiloids/y—were generated from the linear regression of the data as previously described (*39*).

Tau PET. Seventy-four participants underwent tau imaging with either ^{18}F-MK6240 ($n = 70$) or ^{18}F-PI2620 ($n = 2$). Both tau imaging tracers were synthesized in-house in the Department of Molecular Imaging and Therapy, Austin Health, as previously reported (*40,41*). The ^{18}F-MK6240 PET acquisition consisted of a 20-min (4 × 5 min) dynamic scan obtained at 90 min after an intravenous bolus injection of 185 MBq (±10%) of the tracer. The ^{18}F-PI2620 PET acquisition consisted of a 20-min (4 × 5 min) dynamic scan acquired at 80 min after an intravenous bolus injection of 200 MBq (±10%) of the tracer. All tau imaging results were expressed as SUV ratios using the cerebellar cortex as a reference region. A metatemporal region comprising the entorhinal cortex, amygdala, hippocampus, parahippocampal gyrus, fusiform gyrus, and inferior and middle temporal gyri—as adapted from a previous publication (*42*)—was used to determine tau status and for correlational analysis.

MRI. Seventy-three participants underwent structural MRI on a 3-T TIM Trio scanner (Siemens Medical Solutions) to obtain high-resolution T1-weighted anatomic magnetization-prepared rapid gradient-echo and fluid-attenuated inversion recovery sequences.

Image Analysis

Aβ and tau PET scans were spatially normalized using CapAIBL (*38*). The standard centiloid method was applied to determine Aβ burden (*36*). A threshold of 20 centiloids was used to categorize participants as high Aβ (Aβ-positive [Aβ+]) or low Aβ (Aβ-negative [Aβ−]) (*43*). Thresholds of 1.19 SUV ratio for ^{18}F-MK6240 and 1.20 SUV ratio for ^{18}F-PI2620 in the metatemporal composite region (*42*) were used to categorize participants as high tau (tau-positive) or low tau (tau-negative). As previously described (*31*), assessment of the stability of potential reference regions for ^{18}F-SMBT-1 across age and across groups showed no associations with age, but the cerebellar cortex was significantly higher in Aβ+ CN subjects than in Aβ− CN subjects, precluding its use as a reference region. Therefore, ^{18}F-SMBT-1 regional SUVs at 60–80 min after injection were normalized using the subcortical

white matter as a reference region to generate SUV ratios. ^{18}F-SMBT-1 PET images were spatially normalized using CapAIBL, and no correction for partial-volume effects was applied.

The T1-weighted magnetization-prepared rapid gradient-echo images for all participants were first segmented into gray matter, white matter, and cerebrospinal fluid using an expectation maximization algorithm (*44*) and subsequently used to measure hippocampal, gray matter, white matter, and ventricular volumes. The hippocampus region of interest was extracted using a multiatlas approach based on the Harmonized Hippocampus Protocol (*45*). Cortical volumes were normalized by total intracranial volume. The white matter hyperintensity volume was quantified from fluid-attenuated inversion recovery images using the HyperIntensity Segmentation Tool (*46*).

Statistical Analyses

All statistical analyses were performed with JMP Pro (version 16.0; SAS Institute Inc.) for Macintosh (Apple). Data are presented as mean ± SD unless otherwise stated. Groups were compared using the Tukey honest significance test followed by a Dunnett test against Aβ− CN. Effect size was measured with Cohen *d*. Correlations were assessed by Spearman and Pearson correlation coefficients. Vertexwise correlations between ^{18}F-SMBT-1 and Aβ and tau imaging were performed with CapAIBL. The 2 participants who underwent tau imaging with ^{18}F-PI2620 were excluded from the correlational analysis. Group comparisons of ^{18}F-SMBT-1 and correlations between SMBT-1 and Aβ or tau burdens were adjusted for age and sex. Correlations between ^{18}F-SMBT-1 and brain volumes were adjusted for age, sex, and Aβ and tau burdens. Correlations between ^{18}F-SMBT-1 and cognitive parameters were also adjusted for age, sex, hippocampal volume, and Aβ and tau burdens. Significance was set at a P value of less than 0.05, uncorrected for multiple comparisons.

RESULTS

Table 1 shows the demographics of the clinical groups. There were no significant differences in age between groups. The MCI group had twice as many men as women, in contrast to the CN and AD groups, which had more women than men. The MCI and AD groups had significantly fewer years of education. As expected, the MCI and AD groups had cognitive performance significantly worse than the CN group (Table 1). The AD group had significantly more atrophic hippocampi and cortical gray matter, more extensive white matter hyperintensity, higher Aβ and tau burdens, and a higher prevalence of APOE4 (Table 1). The demographics of participants classified by Aβ status is provided in Supplemental Table 1.

TABLE 1
Demographics

Demographic	CN	MCI	AD
Total subjects (*n*)	57	12	8
Age (y)	76.8 ± 5.1	73.4 ± 5.8	76.4 ± 7.6
Sex (*n*)	32F/25 M	4F/8 M*	5F/3 M
Education (y)	14.8 ± 2.7	10.0 ± 1.7*	10.3 ± 1.3*
APOE4	39%	25%	57%*
MMSE	28.6 ± 1.5	27.9 ± 1.7	24.1 ± 4.1*
Clinical dementia rating	0.03 ± 0.1	0.33 ± 0.3*	0.69 ± 0.3*
Clinical dementia rating sum of boxes	0.05 ± 0.2	0.46 ± 0.3	6.00 ± 2.3*
Episodic memory	0.16 ± 0.8	−1.08 ± 0.5*	−3.40 ± 1.5*
Nonmemory	−0.06 ± 0.6	−0.86 ± 0.5*	−2.61 ± 1.8*
AIBL PACC	0.09 ± 0.6	−0.85 ± 0.7*	−4.25 ± 2.0*
Hippocampus (cm^3)	5.91 ± 0.5	5.80 ± 0.8	4.84 ± 0.7*
Cortical gray matter (cm^3)	467 ± 35	467 ± 10	429 ± 22*
White matter (cm^3)	388 ± 26	388 ± 17	387 ± 28
Ventricles (cm^3)	33.8 ± 13	37.0 ± 25	43.5 ± 13
White matter hyperintensity (cm^3)	5.15 ± 6.6	4.60 ± 7.1	17.8 ± 19*
Aβ burden (centiloids)	13.7 ± 33	20.3 ± 43	85.8 ± 66*
Aβ accumulation (centiloids/y, n = 31)	2.35 ± 4.1	0.22 ± 0.1	4.08
Tau SUV ratio			
Mesial temporal	0.95 ± 0.2	1.14 ± 0.3	1.58 ± 1.0*
Temporoparietal	1.05 ± 0.2	1.20 ± 0.2	1.93 ± 1.2*
Rest of neocortex	0.90 ± 0.1	1.01 ± 0.1	1.49 ± 0.7*
Metatemporal	1.03 ± 0.2	1.21 ± 0.3	1.83 ± 1.2*
Aβ+	23%	25%	75%*
Tau+	18%	42%	67%*

*Significantly different from CN group ($P < 0.05$).
Continuous data are mean ± SD.

^{18}F-SMBT-1 yielded high-contrast SUV images at steady state (60–80 min after injection). Figure 1 shows representative ^{18}F-SMBT-1 images from Aβ− CN, Aβ+ CN, Aβ− MCI, Aβ+ MCI, and Aβ+ AD subjects. When the clinical groups were compared with the CN group, ^{18}F-SMBT-1 binding was significantly higher in several regions in the AD group (including the 2 Aβ− "AD" subjects), namely the posterior cingulate gyrus, supramarginal gyrus, and lateral occipital lobe, but also was significantly lower in the globus pallidus, hippocampus, and parahippocampal gyrus.

Then, the clinical groups were classified on the basis of their Aβ status. Of the 57 CN subjects, 44 were Aβ− and 13 Aβ+. Of the 12 MCI subjects, 9 were Aβ− and 3 Aβ+, whereas of the 8 patients with probable AD, 6 were Aβ+ and 2 Aβ−. When compared with the Aβ− CN group, there were no significant differences in ^{18}F-SMBT-1 binding in either the Aβ− MCI group or the Aβ− AD group (Supplemental Table 2). In contrast, when compared with the Aβ− CN group, ^{18}F-SMBT-1 binding was significantly higher in several cortical regions in the Aβ+ AD group (Fig. 2), namely the posterior cingulate gyrus, supramarginal gyrus, lateral occipital lobe, gyrus angularis, and primary visual cortex, but also was significantly lower in the globus pallidus and hippocampus, with Cohen effect sizes (*d*) ranging from 2.65 and 2.36 in the lateral occipital lobe and supramarginal gyrus, respectively, to −1.66 and −1.88 in the hippocampus and globus pallidus, respectively (Supplemental Table 2). Several regions were also significantly higher in the Aβ+ CN group than in the Aβ− CN group (Fig. 2). In addition to the posterior cingulate gyrus, supramarginal gyrus, and lateral occipital lobe—the same regions as those with high binding in the Aβ+ AD group—^{18}F-SMBT-1 binding was also significantly higher in the orbitofrontal, lateral, and inferior temporal gyri. ^{18}F-SMBT-1 binding was also significantly lower in the globus pallidus (Supplemental Table 2). The effect sizes (*d*) ranged from 1.21 and 1.00 in the supramarginal gyrus and lateral temporal lobe, respectively, to −1.29 in the globus pallidus (Supplemental Table 2). Similar regions, such as the supramarginal gyrus, showed higher ^{18}F-SMBT-1 binding in the Aβ+ MCI group, but none reached significance (Fig. 2).

When all clinical groups were considered together, ^{18}F-SMBT-1 PET correlated strongly with Aβ burden and much less with tau burden (Table 2). Figure 3A shows that this close regional relationship between Aβ deposition and astrogliosis was present in only some regions of the brain, such as the supramarginal gyrus, posterior cingulate gyrus, lateral occipital lobe, and inferior and middle temporal gyri, but was much lower in other regions also characterized by high Aβ deposition, such as the frontal cortex, and relatively absent in the superior temporal gyrus. When further exploring the relationship between ^{18}F-SMBT-1 and Aβ, we observed that a nonlinear fit seemed to better describe the relationship between ^{18}F-SMBT-1 and Aβ in, for example, the supramarginal gyrus, where the ^{18}F-SMBT-1 signal seems to be increasing before Aβ becomes abnormal (Supplemental Fig. 1). This relationship was not affected by adjustment for age, white matter hyperintensity, and hippocampal volume. There were no correlations between ^{18}F-SMBT-1 and Aβ in brain regions with a high density of MAO-B, such as the anterior cingulate gyrus and the mesial temporal lobe. Further, in the basal ganglia, the region with the highest density of MAO-B in the brain, ^{18}F-SMBT-1 correlated inversely with Aβ (Table 2). A similar picture was observed for the correlation between ^{18}F-SMBT-1 and tau in the metatemporal region, although the associations were less extensive (Fig. 3B) and were less significant than for Aβ (Table 2). When examining the relationship between ^{18}F-SMBT-1 and Aβ accumulation in a subset of participants ($n = 31$) who had available longitudinal Aβ imaging data, we observed a significant association in the temporal lobe (lateral and inferior temporal) (Table 2). Trend levels ($P < 0.09$) were also observed in the parahippocampus, temporooccipital region, and supramarginal gyrus region (Table 2).

When all clinical groups were considered together, Aβ and tau burdens were highly associated with hippocampal volume and gray matter volume (Supplemental Table 3). Overall, sex was the major contributor to the variation in gray matter volume, whereas age was the major contributor to the variation in white matter hyperintensity. A few associations survived after covariate adjustment. ^{18}F-SMBT-1 binding in the supramarginal gyrus and lateral occipital lobe was inversely associated with gray matter ($r = -0.28$, $P = 0.017$) and hippocampal volume ($r = -0.28$, $P = 0.016$), respectively (Supplemental Table 3). Conversely, ^{18}F-SMBT-1 binding in the hippocampus was significantly associated with hippocampal volume ($r = 0.34$,

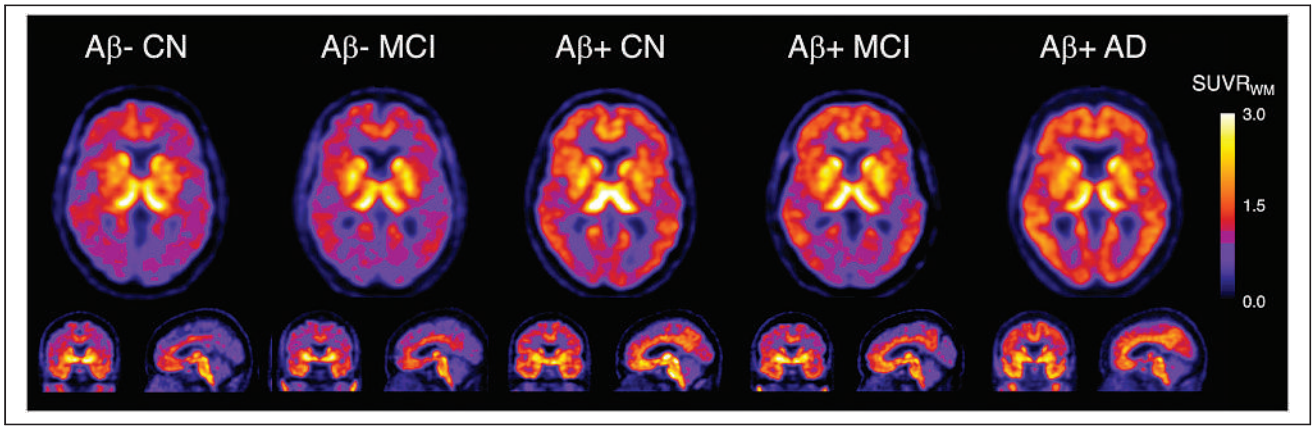

FIGURE 1. Representative transaxial, coronal, and sagittal ^{18}F-SMBT-1 PET images in Aβ− CN subject (84-y-old man; MMSE, 28; CDR, 0; 7 centiloids); Aβ− MCI subject (69-y-old woman; MMSE, 27; CDR, 0.5; 9 centiloids); Aβ+ CN subject (72-y-old man; MMSE, 29; CDR, 0; 24 centiloids); Aβ+ MCI subject (72-y-old man; MMSE, 27; CDR, 0.5; 144 centiloids); and Aβ+ AD subject (78-y-old woman; MMSE, 25; CDR, 1; 173 centiloids). Aβ− CN and MCI participants show normal distribution of ^{18}F-SMBT-1 in brain, highlighting cortical areas with high concentration of MAO-B such as basal ganglia, thalamus, mesial temporal lobe, and anterior cingulate gyrus, as well as different nuclei in brain stem. Higher cortical ^{18}F-SMBT-1 binding is observed in Aβ+ CN, MCI, and AD participants, with binding extending to frontal cortex, temporal lobe, occipital lobe, and posterior cingulate gyrus. SUVR$_{WM}$ = SUV ratio using white matter as reference region.

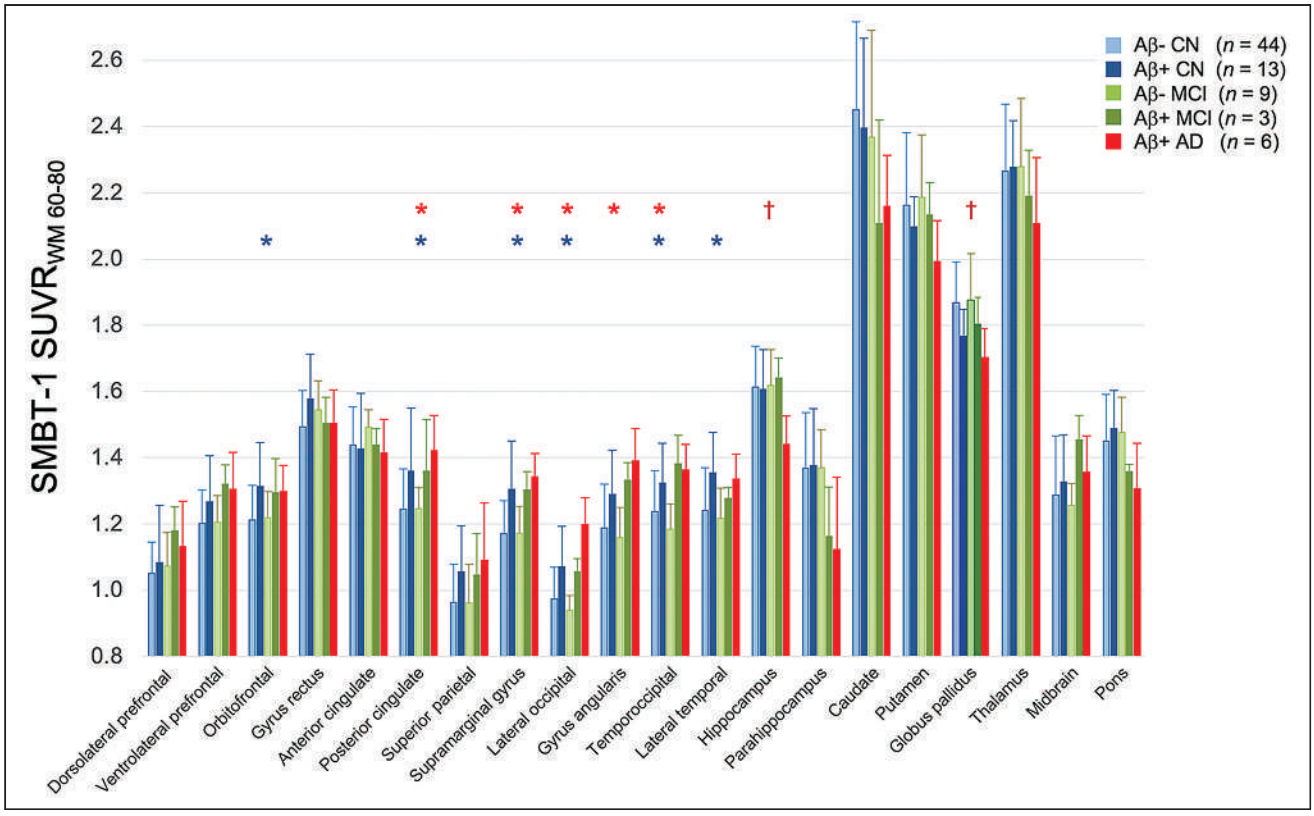

FIGURE 2. Bar graphs showing that regional ^{18}F-SMBT-1 SUV ratios were significantly higher in posterior cingulate gyrus, supramarginal gyrus, lateral occipital lobe, gyrus angularis, and primary visual cortex in Aβ+ AD group but also were significantly lower in globus pallidus and hippocampus. In addition, ^{18}F-SMBT-1 binding was significantly higher in orbitofrontal, lateral, and inferior temporal gyri and significantly lower in globus pallidus. Similar regions, such as supramarginal gyrus, showed higher ^{18}F-SMBT-1 binding in Aβ+ MCI group, but none reached significance. *Significantly higher than in Aβ− CN group ($P < 0.05$). †Significantly lower than in Aβ− CN group ($P < 0.05$). $SUVR_{WM}$ = SUV ratio using white matter as reference region.

$P = 0.003$), cortical gray matter volume ($r = 0.34$, $P = 0.004$), and white matter volume ($r = 0.23$, $P = 0.048$), but theirs was a direct relationship—in other words, the lower the ^{18}F-SMBT-1 binding, the lower the respective volume (Supplemental Table 2). Similar findings were observed in the caudate nuclei, pallidus, thalamus, and pons, where ^{18}F-SMBT-1 binding was also directly associated with gray matter volume (Supplemental Table 3). In contrast to the findings in the mesial temporal lobe, no atrophy was detected in these regions. ^{18}F-SMBT-1 binding in the occipital lobe was significantly associated with white matter hyperintensity (Supplemental Table 3).

When all groups were considered together, and after adjusting for age, sex, Aβ, tau, and hippocampal volume, ^{18}F-SMBT-1 binding correlated with Mini Mental State Examination (MMSE) and the Australian Imaging Biomarkers and Lifestyle's Preclinical Alzheimer Cognitive Composite (AIBL PACC) in some neocortical regions such as the frontal cortex, lateral temporal lobe, supramarginal gyrus, and angular gyrus, contributing 24%–35% of the variance in MMSE and 18%–28% of the variance in AIBL PACC (Table 3). Overall, all cognitive domains were driven by tau, with hippocampal volume contributing to CDR SoB, nonmemory, and AIBL PACC and sex contributing to episodic memory and AIBL PACC.

DISCUSSION

To the best of our knowledge, ^{18}F-SMBT-1 represents the first available ^{18}F MAO-B radiotracer to be used in a clinical study to assess reactive astrogliosis. In the present clinical study, we evaluated the performance of ^{18}F-SMBT-1 PET across the AD spectrum.

When comparing clinical groups, we found that the AD group had both significantly higher (posterior cingulate gyrus, supramarginal gyrus) and lower (hippocampus, globus pallidus) SMBT-1 binding than the CN elderly controls. This difference was better defined when the clinical groups were separated according to high or low Aβ PET burden. It became clear that in regions such as the posterior cingulate gyrus, supramarginal gyrus, and lateral occipital lobe, the Aβ+ CN and Aβ+ AD groups became better separated from the Aβ− CN group but also that the globus pallidus and hippocampus remained significantly lower. Interestingly, the same regions tended to be higher in the Aβ+ MCI group, but it was a group with only 3 participants and none of the regions achieved significance. Most importantly, the Aβ+ CN group had significantly higher ^{18}F-SMBT-1 binding than the Aβ− CN group in the same regions as those that were significantly higher in the AD group (posterior cingulate gyrus, supramarginal gyrus, and lateral occipital lobe), but ^{18}F-SMBT-1 binding was also significantly higher in the orbitofrontal, lateral, and inferior temporal gyri. These findings match recent reports from fluid biomarker studies that found plasma levels of glial fibrillary acidic protein, an astrocytic marker, to be higher in Aβ+ CN subjects than in Aβ− CN subjects (*47*), as well as predicting future conversion to AD in MCI subjects (*48*).

As in the AD group, when compared with the Aβ− CN group the Aβ+ CN group had significantly lower ^{18}F-SMBT-1 binding in the globus pallidus. The first thing to consider when looking at the mesial temporal structures is that the PET results are not

TABLE 2
Association Between Regional ^{18}F-SMBT-1 Binding and Global Aβ Burden, Metatemporal Tau, and Aβ Accumulation

	Centiloids (n = 77)		Metatemporal tau SUV ratio (n = 72)		Aβ accumulation (centiloids/y) (n = 31)	
SMBT-1 region	r	P	r	P	r	P
Ventrolateral prefrontal	0.180	0.117	0.130	0.281	0.177	0.341
Orbitofrontal	0.233	0.042*	0.137	0.254	0.240	0.193
Anterior cingulate	−0.127	0.270	0.079	0.513	−0.017	0.926
Posterior cingulate	0.339	0.003*	0.339	0.004*	0.212	0.253
Superior parietal	0.230	0.044*	0.283	0.017*	0.159	0.393
Supramarginal gyrus	0.477	<0.0001*	0.365	0.002*	0.315	0.084
Lateral occipital	0.484	<0.0001*	0.308	0.009*	0.297	0.105
Primary visual cortex	0.322	0.004*	0.229	0.055	0.049	0.794
Gyrus angularis	0.382	0.001*	0.280	0.018*	0.271	0.141
Temporooccipital	0.334	0.003*	0.306	0.010*	0.340	0.061
Lateral temporal	0.275	0.015*	0.194	0.106	0.431	0.016*
Inferior temporal	0.233	0.042*	−0.073	0.543	0.668	<0.0001*
Amygdala	−0.081	0.482	−0.145	0.229	0.290	0.114
Hippocampus	−0.170	0.140	−0.114	0.343	0.240	0.193
Parahippocampus	−0.161	0.161	−0.122	0.310	0.363	0.051
Entorhinal cortex	−0.062	0.595	−0.119	0.323	−0.035	0.850
Caudate nuclei	−0.248	0.030*	−0.262	0.027*	0.172	0.356
Putamen	−0.235	0.040*	−0.211	0.078	−0.100	0.593
Globus pallidus	−0.432	<0.0001*	−0.391	0.001*	−0.249	0.176
Thalamus	−0.179	0.120	−0.215	0.072	−0.139	0.457
Midbrain	0.185	0.108	0.183	0.128	0.086	0.644
Pons	−0.146	0.205	−0.203	0.090	0.310	0.090

*Statistically significant association ($P < 0.05$).

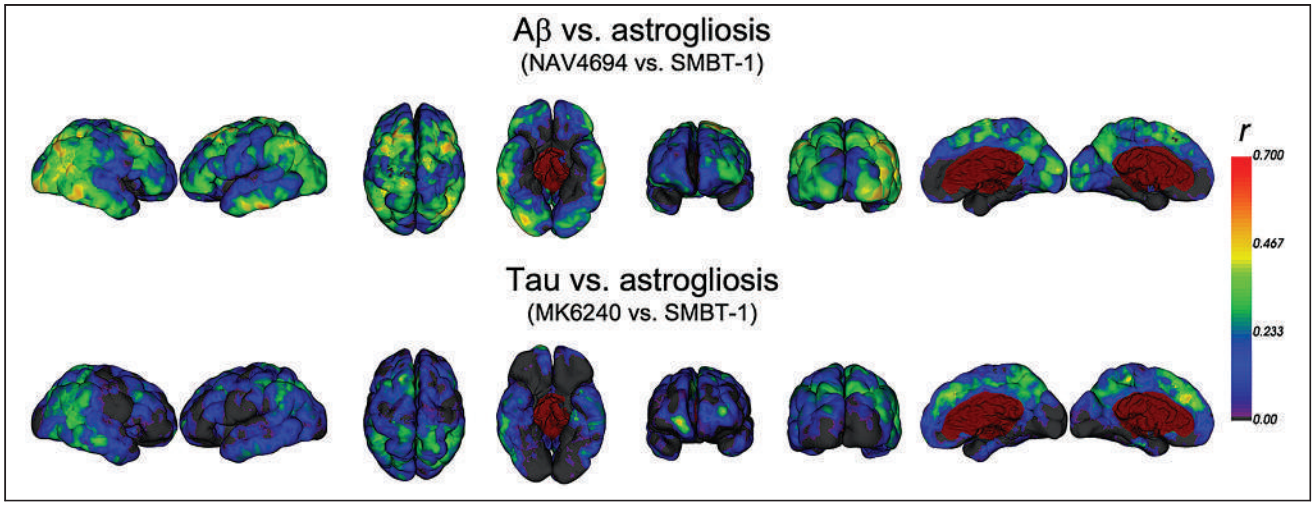

FIGURE 3. (A) There were high regional vertexwise associations between ^{18}F-SMBT-1 binding and Aβ across brain areas of early Aβ deposition such as temporoparietal junction, supramarginal gyrus, and posterior cingulate gyrus, but also much lower associations were observed in areas also characterized by high Aβ, such as frontal cortex and superior temporal gyrus. Some areas, particularly those characterized by high MAO-B concentrations in Aβ− CN subjects, such as basal ganglia, mesial temporal lobe, and anterior cingulate gyrus, presented negative correlations (not shown). (B) Much less extensive regional associations were observed with tau. Color scale represents regression coefficients (r).

TABLE 3
Association Between Regional ^{18}F-SMBT-1 Binding and Cognitive Performance

	MMSE		CDR SoB		Episodic memory		Nonmemory		AIBL PACC	
SMBT-1 region	β	*P*	β	*P*	β	*P*	β	*P*	β	*P*
Ventrolateral prefrontal	−0.27	0.025*	0.16	0.109	−0.12	0.240	−0.12	0.286	−0.21	0.032*
Orbitofrontal	−0.35	0.004*	0.14	0.168	−0.11	0.313	−0.12	0.285	−0.22	0.027*
Anterior cingulate	−0.25	0.036*	0.06	0.545	−0.21	0.040*	−0.19	0.084	−0.26	0.005*
Posterior cingulate	−0.22	0.082	0.15	0.150	−0.07	0.529	−0.17	0.136	−0.19	0.060
Superior parietal	−0.19	0.124	0.14	0.175	−0.00	0.979	−0.20	0.072	−0.15	0.138
Supramarginal gyrus	−0.29	0.025*	0.08	0.479	−0.09	0.450	−0.18	0.127	−0.17	0.099
Lateral occipital	−0.17	0.188	0.24	0.026*	−0.13	0.252	−0.14	0.226	−0.21	0.046*
Gyrus angularis	−0.30	0.018*	0.16	0.125	−0.12	0.266	−0.14	0.230	−0.20	0.051
Temporooccipital	−0.17	0.196	0.01	0.963	−0.09	0.422	−0.03	0.780	−0.09	0.406
Lateral temporal	−0.35	0.003*	0.04	0.689	−0.14	0.169	−0.11	0.293	−0.19	0.048*
Inferior temporal	−0.22	0.102	0.20	0.068	−0.25	0.023*	−0.08	0.487	−0.28	0.007*
Amygdala	−0.24	0.037*	0.10	0.305	−0.12	0.240	−0.20	0.056	−0.20	0.032*
Hippocampus	−0.22	0.072	0.11	0.304	−0.17	0.115	−0.19	0.092	−0.18	0.073
Parahippocampus	−0.10	0.420	0.12	0.217	−0.01	0.912	−0.01	0.922	−0.07	0.451
Caudate nuclei	−0.01	0.945	−0.01	0.912	0.06	0.604	0.10	0.358	0.07	0.518
Putamen	−0.16	0.207	−0.07	0.535	−0.00	0.996	0.09	0.240	0.05	0. 652
Globus pallidus	−0.02	0.856	−0.01	0.904	−0.20	0.068	−0.17	0.150	−0.14	0.179
Thalamus	−0.09	0.473	0.05	0.657	−0.06	0.601	−0.05	0.631	−0.09	0.388

*Statistically significant association ($P < 0.05$).
CDR SoB = clinical dementia rating sum of boxes.

corrected for partial-volume effects, and as expected, the hippocampi were significantly more atrophic in the Aβ+ AD group than in the Aβ− CN group (5.94 ± 0.5 vs. 4.50 ± 0.5, $P < 0.0001$)—likely the best explanation for lower ^{18}F-SMBT-1 binding in a region that otherwise has a high density of MAO-B. On the other hand, partial-volume effects are not likely to explain the lower ^{18}F-SMBT-1 binding in the region with the highest density of MAO-B in the brain. Although only the globus pallidus reached significance, all basal ganglia regions showed lower ^{18}F-SMBT-1 binding (Fig. 2). An alternative explanation might be that, as in vitro studies using autoradiography and ^{11}C-L-deprenyl-D_2 showed, MAO-B presented an inverse correlation with Braak and Braak stages in AD brains (*49*), suggesting that as the neurodegeneration progresses, the expression of MAO-B decreases, most noticeably in those areas with a high density of MAO-B such as the mesial temporal lobe and basal ganglia, while also reflecting the regional loss of astrocytes similar to what is observed in neurons (*50*) associated with progressive Aβ deposition.

Early Aβ deposition is known to occur in brain regions with significantly higher SMBT-1 binding in Aβ+ CN and Aβ+ AD subjects, such as the supramarginal gyrus (identified as the "temporoparietal junction" in 2012 (*51*) and recently rebranded as the "banks of the superior temporal sulcus" (*52*)) along with the orbitofrontal and the posterior cingulate gyri (*51*) . This fact suggests that reactive astrogliosis, as detected with ^{18}F-SMBT-1, is associated with early Aβ deposition at the preclinical stages of AD and likely plays a moderating or modulating role over neurodegeneration, cognitive trajectories, and clinical progression. This possibility was further confirmed by the correlational and vertexwise analysis in which ^{18}F-SMBT-1 binding in the same regions correlated strongly with Aβ. But the association between ^{18}F-SMBT-1 binding and Aβ merits closer examination. The highest correlations were in areas of early Aβ deposition, whereas other areas, characterized by high Aβ such as the frontal cortex, had much lower correlations. In contrast, brain areas known for a high density of MAO-B either lacked correlation or had even an inverse correlation, as observed in the mesial temporal lobe, anterior cingulate gyrus, and basal ganglia. And although the association between ^{18}F-SMBT-1 binding and Aβ accumulation in areas such as the inferior temporal lobe followed a linear relationship (Supplemental Fig. 2), the association between ^{18}F-SMBT-1 binding and Aβ was better described by a nonlinear fit. This finding suggests that the increase in ^{18}F-SMBT-1 signal likely precedes the time that Aβ becomes abnormal (Supplemental Fig. 1), in agreement with the hypothesis that reactive astrogliosis precedes the significant build-up of Aβ plaques in the brain (*24,53*). The consequent suggestion is that astrocytes could be reactive and increase MAO-B expression or activity in response to Aβ changes that precede plaque deposition (e.g., an increased brain concentration of Aβ oligomers and protofibrils). The high association of reactive astrogliosis with insoluble Aβ, coupled with its early manifestation, has prompted the postulation that the neuroinflammatory reaction is driven by soluble Aβ oligomers (*24,25*). Astrocytes do not constitute a homogeneous population and have—and adopt—different morphologic, biochemical, and functional properties reflecting a complex mix of toxic and protective pathways (*6*). Thus, the relationship with Aβ and tau, given the diverse morphologic and biochemical diversity of

astrocytes, is not likely to be straightforward or the same across different brain regions, indicating a complex regional relationship rather than a global response.

The associations between ^{18}F-SMBT-1 binding and brain volumetrics or white matter hyperintensity were not strong. Hippocampal and parahippocampal ^{18}F-SMBT-1 binding was associated with hippocampal volume, as ^{18}F-SMBT-1 binding in the caudate nuclei, pallidus, thalamus, and pons was also associated with gray matter volume, but these were all direct associations, with lower ^{18}F-SMBT-1 binding being associated with smaller volumes. The expedient explanation would be that these regions—regions with normally high concentrations of MAO-B—are atrophic. As explained in the section dealing with the correlations with Aβ, the hippocampi in the Aβ+ AD group were significantly more atrophic. Therefore, the lower ^{18}F-SMBT-1 binding in the hippocampus and parahippocampal gyrus can be explained by partial-volume effects. But the basal ganglia were not atrophic, and there were no significant differences across the groups; partial-volume effects thus cannot explain the lower ^{18}F-SMBT-1 binding. We believe that the results in the basal ganglia truly reflect a reduction in ^{18}F-SMBT-1 binding in these areas, especially in AD, a condition in which, as neurodegeneration progresses, the expression of MAO-B likely decreases, most noticeably in those areas with a high density of MAO-B such as the basal ganglia.

In regard to the associations between ^{18}F-SMBT-1 binding and cognitive parameters, the main driver of cognitive impairment across all domains was tau burden, contributing more than 50% of the variance, followed by hippocampal volume. Sex was also a contributor to episodic memory and AIBL PACC, with women performing worse than men. ^{18}F-SMBT-1 binding correlated mainly with MMSE and AIBL PACC in some neocortical regions such as the frontal cortex, with the lateral temporal lobe, supramarginal gyrus, and angular gyrus contributing 24%–35% of the variance of MMSE and 18%–28% of the variance of AIBL PACC. These findings suggest that reactive astrogliosis makes a detrimental contribution to general cognition and some memory tasks that are independent of tau, Aβ, or hippocampal atrophy and that early amelioration of neuroinflammation might be a complementary therapeutic avenue for AD (*20*).

There are several limitations and caveats to this study. Similarly to microglial activation, only surrogate markers are available to assess reactive astrogliosis. In contrast to neuroreceptor PET studies using tracers that bind directly to the receptor, the study of neuroinflammation is based on using surrogate markers to assess their change of state from resting to activated. Thus, microglial activation has been studied for decades by assessing overexpression of mitochondrial translocator protein 18 kDa (*18*) and, more recently, by using tracers for macrophage colony-stimulating factor 1 receptor (*54*) or purinergic receptors (*55*), whereas reactive astrogliosis has been assessed with markers of MAO-B (*19*) and imidazoline 2 binding sites (*29*). It needs to be clearly understood that ^{18}F-SMBT-1 is a MAO-B tracer, and as such, several factors and conditions that affect MAO-B can affect ^{18}F-SMBT-1 binding. Besides the obvious effect of MAO-B inhibitors, MAO-B also increases with age (*56*), is affected by smoking (*57*), and has been found to be altered in psychiatric conditions such as major depression (*22*). Therefore, careful clinical anamnesis and an itemized listing of exclusionary criteria are required before participants undergo ^{18}F-SMBT-1 PET. Although MAO-B is present mainly in astrocytes, it is also found, in a much smaller concentration, in neurons (*58*). ^{18}F-SMBT-1 can detect increases and decreases in MAO-B in the brain but cannot discriminate between the fluid change or transition of reactive astrocytes from a protective to a toxic state, and not all reactive astrocytes overexpress MAO-B (*58*). The small number of Aβ+ MCI subjects precludes drawing any conclusion on group differences in the SMBT-1 signal. A larger sample size, especially Aβ+ MCI and Aβ+ AD patients, will be required to further validate the finding that ^{18}F-SMBT-1 captures the reported increases in MAO-B across the AD continuum. There is also a chance of spurious correlations from analyses of subgroups. These analyses were undertaken to dissect the relation between the different aspects of ^{18}F-SMBT-1 binding in the presence or absence of Aβ and tau and how ^{18}F-SMBT-1 binding relates to other variables. Finally, the participants were volunteers who were not randomly selected from the community and were generally well educated and had high scores on cognitive tests; thus, these findings might not apply to the general population.

The introduction of biomarker-based approaches for the identification of brain pathology has informed new strategies for the design of clinical trials aimed at preventing the onset of cognitive impairment and dementia. Markers of Aβ and tau pathology and markers of neurodegeneration have been incorporated into a recently proposed biomarker-based framework (*59*). The advantage of the modular design of the framework, and considering that reactive gliosis is a critical aspect of the neuropathology of AD, is that the biomarker framework might be expanded to include reactive gliosis.

Our studies showed that ^{18}F-SMBT-1 can be used as a surrogate marker of reactive astrogliosis. Despite the limited sample size in some of the groups, there was a distinctive degree and pattern of tracer binding across the AD continuum that was associated mainly with the presence of Aβ burden in the brain. ^{18}F-SMBT-1 will allow a better understanding of the pathophysiology of AD, enabling more accurate staging and determination of prognosis at earlier stages of the disease. It will also be necessary to examine the relationship between ^{18}F-SMBT-1 binding in the brain and plasma glial fibrillary acidic protein. Longitudinal studies will be required to assess the effects of reactive astrogliosis over the clinical expression of AD and also, given the intimate relationship between astrocytes and blood vessels, of cerebrovascular disease. Longitudinal studies will also be required to fully elucidate the complex interaction between reactive astrogliosis, AD pathology, and cerebrovascular disease and their moderating or modulating impact over neurodegeneration, cognitive decline, and clinical progression.

CONCLUSION

Cross-sectional human PET studies with ^{18}F-SMBT-1, a highly selective ^{18}F-labeled MAO-B tracer, showed that Aβ+ AD subjects but, most importantly, Aβ+ CN subjects have significantly higher regional ^{18}F-SMBT-1 binding than Aβ− CN subjects. Moreover, in several regions of the brain, ^{18}F-SMBT-1 retention was highly associated with Aβ burden. These findings suggest that increased ^{18}F-SMBT-1 binding occurs at the preclinical stages of Aβ accumulation, providing strong support for its use as a surrogate marker of astrogliosis and a biomarker of early stages in the AD continuum.

DISCLOSURE

The study was supported in part by National Health Medical Research Council (NHMRC) of Australia grants G1005121 and 19KK0212 from Japan. Yukitsuka Kudo and Nobuyuki Okamura own stock in Clino Ltd., licensing SMBT-1. Ryuichi Harada, Shozo Furumoto, Yukitsuka Kudo, and Nobuyuki Okamura have a patent pending for the technology described in this article.

No other potential conflict of interest relevant to this article was reported.

ACKNOWLEDGMENTS

We thank the Brain Research Institute for support in acquiring the MRI data. We thank Drs. Chester Mathis, William E. Klunk, Oscar Lopez, Ann Cohen, Brian Lopresti, Howard Aizenstein, Scott Mason, Beth Snitz, and Beth Shaaban at the University of Pittsburgh for extremely fruitful discussions about SMBT-1, MAO-B, and reactive astrogliosis. We thank the participants in this study and their families. This paper is dedicated to the first author's father, Victor E. Villemagne (January 8, 1935–May 7, 2021).

KEY POINTS

QUESTION: Can ^{18}F-SMBT-1 be used to assess reactive astrogliosis in vivo?

PERTINENT FINDINGS: A clinical study on 77 elderly participants showed that ^{18}F-SMBT-1, a novel ^{18}F MAO-B tracer used as a surrogate marker of reactive astrogliosis, was significantly higher in AD patients and, most importantly, in elderly CN controls with high Aβ in the brain.

IMPLICATIONS FOR PATIENT CARE: ^{18}F-SMBT-1 can be used as a surrogate and early marker of reactive astrogliosis across the AD continuum.

REFERENCES

1. Masters CL. Neuropathology of Alzheimer's disease. In: Burns A, O'Brien J, Ames D, eds. *Dementia.* 3rd ed. Hodder Arnold; 2005:393–407.
2. Fakhoury M. Microglia and astrocytes in Alzheimer's disease: implications for therapy. *Curr Neuropharmacol.* 2018;16:508–518.
3. Vasile F, Dossi E, Rouach N. Human astrocytes: structure and functions in the healthy brain. *Brain Struct Funct.* 2017;222:2017–2029.
4. McConnell HL, Li Z, Woltjer RL, Mishra A. Astrocyte dysfunction and neurovascular impairment in neurological disorders: correlation or causation? *Neurochem Int.* 2019;128:70–84.
5. Sofroniew MV. Astrogliosis. *Cold Spring Harb Perspect Biol.* 2014;7:a020420.
6. Escartin C, Galea E, Lakatos A, et al. Reactive astrocyte nomenclature, definitions, and future directions. *Nat Neurosci.* 2021;24:312–325.
7. Osborn LM, Kamphuis W, Wadman WJ, Hol EM. Astrogliosis: an integral player in the pathogenesis of Alzheimer's disease. *Prog Neurobiol.* 2016;144:121–141.
8. Carter SF, Herholz K, Rosa-Neto P, Pellerin L, Nordberg A, Zimmer ER. Astrocyte biomarkers in Alzheimer's disease. *Trends Mol Med.* 2019;25:77–95.
9. Birch AM. The contribution of astrocytes to Alzheimer's disease. *Biochem Soc Trans.* 2014;42:1316–1320.
10. Acioglu C, Li L, Elkabes S. Contribution of astrocytes to neuropathology of neurodegenerative diseases. *Brain Res.* 2021;1758:147291.
11. Kovacs GG, Xie SX, Robinson JL, et al. Sequential stages and distribution patterns of aging-related tau astrogliopathy (ARTAG) in the human brain. *Acta Neuropathol Commun.* 2018;6:50.
12. Nelson PT, Dickson DW, Trojanowski JQ, et al. Limbic-predominant age-related TDP-43 encephalopathy (LATE): consensus working group report. *Brain.* 2019; 142:1503–1527.
13. Yamanaka K, Komine O. The multi-dimensional roles of astrocytes in ALS. *Neurosci Res.* 2018;126:31–38.
14. Radford RA, Morsch M, Rayner SL, Cole NJ, Pountney DL, Chung RS. The established and emerging roles of astrocytes and microglia in amyotrophic lateral sclerosis and frontotemporal dementia. *Front Cell Neurosci.* 2015;9:414.
15. Engler H, Nennesmo I, Kumlien E, et al. Imaging astrocytosis with PET in Creutzfeldt-Jakob disease: case report with histopathological findings. *Int J Clin Exp Med.* 2012;5:201–207.
16. Diniz LP, Araujo APB, Matias I, et al. Astrocyte glutamate transporters are increased in an early sporadic model of synucleinopathy. *Neurochem Int.* 2020; 138:104758.
17. Ingelsson M, Fukumoto H, Newell KL, et al. Early Abeta accumulation and progressive synaptic loss, gliosis, and tangle formation in AD brain. *Neurology.* 2004; 62:925–931.
18. Kreisl WC, Lyoo CH, Liow JS, et al. ^{11}C-PBR28 binding to translocator protein increases with progression of Alzheimer's disease. *Neurobiol Aging.* 2016;44: 53–61.
19. Carter SF, Scholl M, Almkvist O, et al. Evidence for astrocytosis in prodromal Alzheimer disease provided by ^{11}C-deuterium-L-deprenyl: a multitracer PET paradigm combining ^{11}C-Pittsburgh compound B and ^{18}F-FDG. *J Nucl Med.* 2012;53:37–46.
20. Assefa BT, Gebre AK, Altaye BM. Reactive astrocytes as drug target in Alzheimer's disease. *BioMed Res Int.* 2018;2018:4160247.
21. Ekblom J, Jossan SS, Bergstrom M, Oreland L, Walum E, Aquilonius SM. Monoamine oxidase-B in astrocytes. *Glia.* 1993;8:122–132.
22. Moriguchi S, Wilson AA, Miler L, et al. Monoamine oxidase B total distribution volume in the prefrontal cortex of major depressive disorder: an [^{11}C]SL25.1188 positron emission tomography study. *JAMA Psychiatry.* 2019;76:634–641.
23. Saba W, Valette H, Peyronneau MA, et al. [^{11}C]SL25.1188, a new reversible radioligand to study the monoamine oxidase type B with PET: preclinical characterisation in nonhuman primate. *Synapse.* 2010;64:61–69.
24. Rodriguez-Vieitez E, Ni R, Gulyas B, et al. Astrocytosis precedes amyloid plaque deposition in Alzheimer APPswe transgenic mouse brain: a correlative positron emission tomography and in vitro imaging study. *Eur J Nucl Med Mol Imaging.* 2015;42:1119–1132.
25. Rodriguez-Vieitez E, Saint-Aubert L, Carter SF, et al. Diverging longitudinal changes in astrocytosis and amyloid PET in autosomal dominant Alzheimer's disease. *Brain.* 2016;139:922–936.
26. Schöll M, Carter SF, Westman E, et al. Early astrocytosis in autosomal dominant Alzheimer's disease measured in vivo by multi-tracer positron emission tomography. *Sci Rep.* 2015;5:16404.
27. Kumar A, Koistinen NA, Malarte ML, et al. Astroglial tracer BU99008 detects multiple binding sites in Alzheimer's disease brain. *Mol Psychiatry.* 2021;26: 5833–5847.
28. Venkataraman AV, Keat N, Myers JF, et al. First evaluation of PET-based human biodistribution and radiation dosimetry of ^{11}C-BU99008, a tracer for imaging the imidazoline2 binding site. *EJNMMI Res.* 2018;8:71.
29. Calsolaro V, Matthews PM, Donat CK, et al. Astrocyte reactivity with late-onset cognitive impairment assessed in vivo using ^{11}C-BU99008 PET and its relationship with amyloid load. *Mol Psychiatry.* 2021;26:5848–5855.
30. Harada R, Hayakawa Y, Ezura M, et al. ^{18}F-SMBT-1: a selective and reversible PET tracer for monoamine oxidase-B imaging. *J Nucl Med.* 2021;62:253–258.
31. Villemagne VL, Harada H, Doré V, et al. First-in-human evaluation of ^{18}F-SMBT-1, a novel ^{18}F-labeled MAO-B PET tracer for imaging reactive astrogliosis. *J Nucl Med.* January 27, 2022 [Epub ahead of print].
32. Petersen RC, Smith GE, Waring SC, Ivnik RJ, Tangalos EG, Kokmen E. Mild cognitive impairment: clinical characterization and outcome. *Arch Neurol.* 1999;56: 303–308.
33. McKhann GM, Knopman DS, Chertkow H, et al. The diagnosis of dementia due to Alzheimer's disease: recommendations from the National Institute on Aging-Alzheimer's Association workgroups on diagnostic guidelines for Alzheimer's disease. *Alzheimers Dement.* 2011;7:263–269.
34. Rowe CC, Jones G, Dore V, et al. Standardized expression of ^{18}F-NAV4694 and ^{11}C-PiB beta-amyloid PET results with the centiloid scale. *J Nucl Med.* 2016;57: 1233–1237.
35. Navitsky M, Joshi AD, Kennedy I, et al. Standardization of amyloid quantitation with florbetapir standardized uptake value ratios to the centiloid scale. *Alzheimers Dement.* 2018;14:1565–1571.
36. Klunk WE, Koeppe RA, Price JC, et al. The centiloid project: standardizing quantitative amyloid plaque estimation by PET. *Alzheimers Dement.* 2015;11: 1–15.e1–4.
37. Battle MR, Pillay LC, Lowe VJ, et al. Centiloid scaling for quantification of brain amyloid with [^{18}F]flutemetamol using multiple processing methods. *EJNMMI Res.* 2018;8:107.
38. Bourgeat P, Dore V, Fripp J, et al. Implementing the centiloid transformation for ^{11}C-PiB and beta-amyloid ^{18}F-PET tracers using CapAIBL. *Neuroimage.* 2018; 183:387–393.
39. Villemagne VL, Burnham S, Bourgeat P, et al. Amyloid beta deposition, neurodegeneration, and cognitive decline in sporadic Alzheimer's disease: a prospective cohort study. *Lancet Neurol.* 2013;12:357–367.
40. Krishnadas N, Dore V, Lamb F, et al. Case report: ^{18}F-MK6240 tau positron emission tomography pattern resembling chronic traumatic encephalopathy in a retired Australian rules football player. *Front Neurol.* 2020;11:598980.
41. Brendel M, Barthel H, van Eimeren T, et al. Assessment of ^{18}F-PI-2620 as a biomarker in progressive supranuclear palsy. *JAMA Neurol.* 2020;77:1408–1419.

42. Jack CR Jr, Wiste HJ, Schwarz CG, et al. Longitudinal tau PET in ageing and Alzheimer's disease. *Brain.* 2018;141:1517–1528.
43. Jack CR Jr, Wiste HJ, Weigand SD, et al. Defining imaging biomarker cut points for brain aging and Alzheimer's disease. *Alzheimers Dement.* 2017;13:205–216.
44. Van Leemput K, Maes F, Vandermeulen D, Suetens P. Automated model-based tissue classification of MR images of the brain. *IEEE Trans Med Imaging.* 1999;18:897–908.
45. Boccardi M, Bocchetta M, Apostolova LG, et al. Delphi definition of the EADC-ADNI harmonized protocol for hippocampal segmentation on magnetic resonance. *Alzheimers Dement.* 2015;11:126–138.
46. Manjón JV, Coupé P, Raniga P, Xia Y, Fripp J, Salvado O. HIST: hyperintensity segmentation tool. In: Wu G, Coupé P, Zhan Y, Munsell BC, Rueckert D, eds. *Patch-Based Techniques in Medical Imaging.* Springer; 2016:92–99.
47. Chatterjee P, Pedrini S, Stoops E, et al. Plasma glial fibrillary acidic protein is elevated in cognitively normal older adults at risk of Alzheimer's disease. *Transl Psychiatry.* 2021;11:27.
48. Cicognola C, Janelidze S, Hertze J, et al. Plasma glial fibrillary acidic protein detects Alzheimer pathology and predicts future conversion to Alzheimer dementia in patients with mild cognitive impairment. *Alzheimers Res Ther.* 2021;13:68.
49. Gulyás B, Pavlova E, Kasa P, et al. Activated MAO-B in the brain of Alzheimer patients, demonstrated by [^{11}C]-L-deprenyl using whole hemisphere autoradiography. *Neurochem Int.* 2011;58:60–68.
50. Smale G, Nichols NR, Brady DR, Finch CE, Horton WE Jr. Evidence for apoptotic cell death in Alzheimer's disease. *Exp Neurol.* 1995;133:225–230.
51. Villain N, Chetelat G, Grassiot B, et al. Regional dynamics of amyloid-beta deposition in healthy elderly, mild cognitive impairment and Alzheimer's disease: a voxelwise PiB-PET longitudinal study. *Brain.* 2012;135:2126–2139.
52. Guo T, Landau SM, Jagust WJ; Alzheimer's Disease Neuroimaging Initiative. Detecting earlier stages of amyloid deposition using PET in cognitively normal elderly adults. *Neurology.* 2020;94:e1512–e1524.
53. Leclerc B, Abulrob A. Perspectives in molecular imaging using staging biomarkers and immunotherapies in Alzheimer's disease. *ScientificWorldJournal.* 2013;2013:589308.
54. Horti AG, Naik R, Foss CA, et al. PET imaging of microglia by targeting macrophage colony-stimulating factor 1 receptor (CSF1R). *Proc Natl Acad Sci USA.* 2019;116:1686–1691.
55. Beaino W, Janssen B, Kooij G, et al. Purinergic receptors P2Y12R and P2X7R: potential targets for PET imaging of microglia phenotypes in multiple sclerosis. *J Neuroinflammation.* 2017;14:259.
56. Galva MD, Bondiolotti GP, Olasmaa M, Picotti GB. Effect of aging on lazabemide binding, monoamine oxidase activity and monoamine metabolites in human frontal cortex. *J Neural Transm Gen Sect.* 1995;101:83–94.
57. Fowler JS, Volkow ND, Wang GJ, et al. Neuropharmacological actions of cigarette smoke: brain monoamine oxidase B (MAO B) inhibition. *J Addict Dis.* 1998;17:23–34.
58. Perez-Nievas BG, Serrano-Pozo A. Deciphering the astrocyte reaction in Alzheimer's disease. *Front Aging Neurosci.* 2018;10:114.
59. Jack CR Jr, Bennett DA, Blennow K, et al. A/T/N: an unbiased descriptive classification scheme for Alzheimer disease biomarkers. *Neurology.* 2016;87:539–547.

Tracking Innate Immune Activation in a Mouse Model of Parkinson's Disease Using TREM1 and TSPO PET Tracers

Katherine L. Lucot[1], Marc Y. Stevens[2], T. Adam Bonham[3], E. Carmen Azevedo[2], Aisling M. Chaney[2], Ebony D. Webber[3], Poorva Jain[2], Jessica L. Klockow[4], Isaac M. Jackson[2], Mackenzie L. Carlson[5], Edward E. Graves[4], Thomas J. Montine[1], and Michelle L. James[2,6]

[1]Department of Pathology, Stanford University, Stanford, California; [2]Department of Radiology, Molecular Imaging Program at Stanford, Stanford University, Stanford, California; [3]Department of Comparative Medicine, Stanford University, Stanford, California; [4]Department of Radiation Oncology, Molecular Imaging Program at Stanford, Stanford University, Stanford, California; [5]Department of Bioengineering, Stanford University, Stanford, California; and [6]Department of Neurology and Neurological Sciences, Stanford University, Stanford, California

Parkinson's disease (PD) is associated with aberrant innate immune responses, including microglial activation and infiltration of peripheral myeloid cells into the central nervous system (CNS). Methods to investigate innate immune activation in PD are limited and have not yet elucidated key interactions between neuroinflammation and peripheral inflammation. Translocator protein 18 kDa (TSPO) PET is a widely evaluated imaging approach for studying activated microglia and peripheral myeloid lineage cells in vivo but has yet to be fully explored in PD. Here, we investigate the utility of TSPO PET in addition to PET imaging of triggering receptor expressed on myeloid cells 1 (TREM1)—a novel biomarker of proinflammatory innate immune cells—for detecting innate immune responses in the 6-hydroxydopamine mouse model of dopaminergic neuron degeneration. **Methods:** C57/BL6J and *TREM1* knockout mice were stereotactically injected with 6-hydroxydopamine in the left striatum; control mice were injected with saline. At day 7 or 14 after surgery, mice were administered ^{18}F-GE-180, ^{64}Cu-TREM1 monoclonal antibody (mAb), or ^{64}Cu-isotype control mAb and imaged by PET/CT. Ex vivo autoradiography was performed to obtain high-resolution images of tracer binding within the brain. Immunohistochemistry was conducted to verify myeloid cell activation and dopaminergic cell death, and quantitative polymerase chain reaction and flow cytometry were completed to assess levels of target in the brain. **Results:** PET/CT images of both tracers showed elevated signal within the striatum of 6-hydroxydopamine–injected mice compared with those injected with saline. Autoradiography afforded higher-resolution brain images and revealed significant TSPO and TREM1 tracer binding within the ipsilateral striatum of 6-hydroxydopamine mice compared with saline mice at both 7 and 14 d after toxin. Interestingly, ^{18}F-GE-180 enabled detection of inflammation in the brain and peripheral tissues (blood and spleen) of 6-hydroxydopamine mice, whereas ^{64}Cu-TREM1 mAb appeared to be more sensitive and specific for detecting neuroinflammation, in particular infiltrating myeloid cells, in these mice, as demonstrated by flow cytometry findings and higher tracer binding signal-to-background ratios in brain. **Conclusion:** TSPO and TREM1 PET tracers are promising tools for investigating different cell types involved in innate immune activation in the context of dopaminergic neurodegeneration, thus warranting further investigation in other PD rodent models and human postmortem tissue to assess their clinical potential.

Received Aug. 16, 2021; revision accepted Feb. 10, 2022.

For correspondence or reprints, contact Michelle L. James (mljames@stanford.edu).

Published online Feb. 17, 2022.

Key Words: Parkinson's disease; neuroinflammation; molecular imaging; TSPO PET; TREM1 PET

J Nucl Med 2022; 63:1570–1578
DOI: 10.2967/jnumed.121.263039

Parkinson's disease (PD) is the most common movement disorder and the second most common neurodegenerative disease. Affecting nearly 7 million people worldwide (*1–3*), PD encompasses a wide spectrum of motor, cognitive, autonomic, and psychiatric symptoms. PD is characterized pathologically by dopaminergic neuron loss in the substantia nigra and accumulation of Lewy bodies and neurites, which contain misfolded α-synuclein protein, within neurons. Neuroinflammation is intimately tied to both dopaminergic neuron loss and α-synuclein accumulation, indicating this to be an early event in PD pathogenesis (*4*). Activated microglial cells, peripheral myeloid-mediated proinflammatory innate immune responses, and neurotoxic adaptive immune activity in the central nervous system (CNS) are also specifically involved in PD pathogenesis (*5,6*).

Methods to investigate inflammatory processes in PD brain are restricted mainly to postmortem tissue or cerebrospinal fluid. Although these studies have yielded useful insights on the presence of activated microglia and altered proinflammatory cytokine concentrations in the substantia nigra and cerebrospinal fluid of PD patients (*7–15*), they are often obtained at a single time point and are therefore limited in the information they can provide on highly dynamic immune responses.

PET imaging of translocator protein 18 kDa (TSPO)—an established imaging biomarker of inflammation, predominately upregulated in activated microglia and peripheral myeloid lineage cells (e.g., macrophages, monocytes, and neutrophils)—is a useful method to visualize neuroinflammation in living subjects. ^{18}F-GE-180 is one of the most sensitive and specific TSPO PET tracers for imaging rodent models of neuroinflammation (*16–20*) because of its high signal-to-background ratio as demonstrated through head-to-head comparison studies with ^{18}F-PBR06 (*19*), ^{11}C-(*R*)-PK11195 (*20*), and ^{18}F-DPA-714 (*21*); however, it has not yet been evaluated in PD mouse models (*22,23*). Additionally, triggering receptor expressed on myeloid cells 1 (TREM1) (*24*) was recently identified as a novel, highly specific imaging biomarker of proinflammatory innate immune cells: our laboratory reported the first TREM1 PET tracer, ^{64}Cu-TREM1

monoclonal antibody (mAb), and demonstrated its ability to detect peripheral CNS-infiltrating TREM1-positive myeloid cells in mouse models of stroke and multiple sclerosis (2.5–3.5 percentage injected dose per gram in brain regions of interest) (*25–27*).

Here, we set out to assess the potential of these 2 promising PET imaging biomarkers for providing unique insights into the spatiotemporal dynamics of innate immune responses in the context of PD and neuroinflammation. We hypothesized that detection of TSPO and TREM1 PET by ^{18}F-GE-180 and ^{64}Cu-TREM1 mAb, respectively, can track different aspects of innate immune activation in a mouse model of dopaminergic neurodegeneration.

MATERIALS AND METHODS

Study Design

6-Hydroxydopamine hydrobromide (6-hydroxydopamine) selectively damages dopaminergic neurons and protracts degeneration of the nigrostriatal system when injected into the striatum unilaterally (*28*). We performed TSPO and TREM1 PET imaging 7 and 14 d after intrastriatal injection of 6-hydroxydopamine or vehicle (saline). TSPO and TREM1 tracer specificity was assessed using PK-11195, a TSPO ligand, and an appropriate isotype control antibody, respectively. Since the unlabeled TREM1 tracer and other available TREM1 antibodies are agonists, they cannot be used for mass-level blocking experiments without perturbing the molecular pathways of interest in our mouse model; therefore, *TREM1* knockout mice were imaged 7 d after 6-hydroxydopamine injection to further assess specificity of the TREM1 PET agent. Binding and spatial distribution of each tracer were confirmed by ex vivo γ-counting and high-resolution autoradiography. Alterations in immune activation were confirmed using flow cytometry, immunohistochemistry, and reverse-transcription quantitative polymerase chain reaction (PCR). Figure 1 summarizes the study time line, and Supplemental Table 1 shows the numbers of mice and tissue samples used for each experiment (supplemental materials are available at http://jnm.snmjournals.org).

Animals

All experiments involving animals were completed in accordance with the Stanford Administrative Panel on Laboratory Animal Care, which is accredited by the Association for the Assessment and Accreditation of Laboratory Animal Care International. Male 8- to 12-wk-old C57BL/6J wild-type mice (Jackson Laboratories) and *TREM1* knockout littermates (*29*), a kind gift from the laboratory of Professor Katrin Andreasson (Stanford University, original breeders provided by Dr. Christoph Mueller, University of Bern), were housed in a temperature-controlled environment under a 12-h light/dark schedule with unrestricted access to food and water. When indicated, anesthetization was performed using isoflurane.

6-Hydroxydopamine Model Induction

6-Hydroxydopamine (10 μg/μL; Sigma) or saline was injected (1 μL) into the striatum of anesthetized mice during stereotactic surgery (coordinates: anterior/posterior = 0.5, lateral = 1.8, dorsal/ventral = −3.5) using established methods (*30,31*).

^{18}F-GE-180 Radiolabeling

^{18}F-GE-180 was radiosynthesized according to standard methods (*22*). The tracer was formulated in phosphate-buffered saline (0.1 M NaCl, 0.05 M sodium phosphate, pH 7.4) containing 10% ethanol. A molar activity of 44.4 GBq/μmol and high radiochemical purity (>95%) were achieved.

TREM1 DOTA Conjugation

Mouse TREM1 mAb (R&D Systems) was conjugated with DOTA-*N*-hydroxysuccinimide (Macrocyclics) using metal-free buffers and previously published procedures (*25,32*). The average number of chelator molecules per antibody was determined to be 0.8–1.9 using electrospray ionization mass spectrometry and matrix-assisted laser desorption/ionization time of flight. The average was determined after performing 3 independent reactions.

^{64}Cu-TREM1 mAb and Isotype Control Radiolabeling

TREM1 mAb and isotype control mAb were radiolabeled using previously reported general copper-labeling methods (*25,33,34*). Briefly, immunoconjugate (80 ± 11 μg, n = 4) in NH_4OAc (pH 5.5) was added to $^{64}CuCl_2$ (0.06 GBq) in NH_4OAc under gentle agitation at 37°C. The reaction was monitored via radio–thin-layer chromatography until a labeling efficiency of more than 99% was observed (15–30 min), at which point 2 μL of ethylenediaminetetraacetic acid (50 mM) were added. Reactions were analyzed by radio–thin-layer chromatography and size-exclusion high-performance liquid chromatography (Phenomenex 00H-2146-K0, 5 μm SEC-s3000 400 Å, 300 × 7.8 mm). Pure fractions (>99%) of ^{64}Cu-TREM1 mAb and isotype control mAb were combined and diluted with saline. The molar activity of each tracer was determined to be more than 70 GBq/μmol, and high radiochemical purity (>97%) was achieved.

In Vivo PET/CT Acquisition

Mice were imaged using a dual small-animal PET/CT scanner (GNEXT; Sophie) 7 or 14 d after stereotactic injection of 6-hydroxydopamine. Isotype control, blocking, *TREM1* knockout, and saline studies were conducted on day 7. Mice were anesthetized and intravenously injected (3.7–5.55 MBq) with their respective tracer (Supplemental Table 1).

CT images were acquired as previously described (*35*) for anatomic reference before a 10-min static PET acquisition 50 min after administration of ^{18}F-GE-180 or 19 h after intravenous injection of ^{64}Cu-TREM1 mAb or ^{64}Cu-isotype control mAb. A calibration factor was calculated each imaging day on the basis of a reference standard consisting of a 20-mL syringe containing a known amount of ^{18}F or ^{64}Cu. PET data were acquired and reconstructed as previously described by our laboratory (*25*).

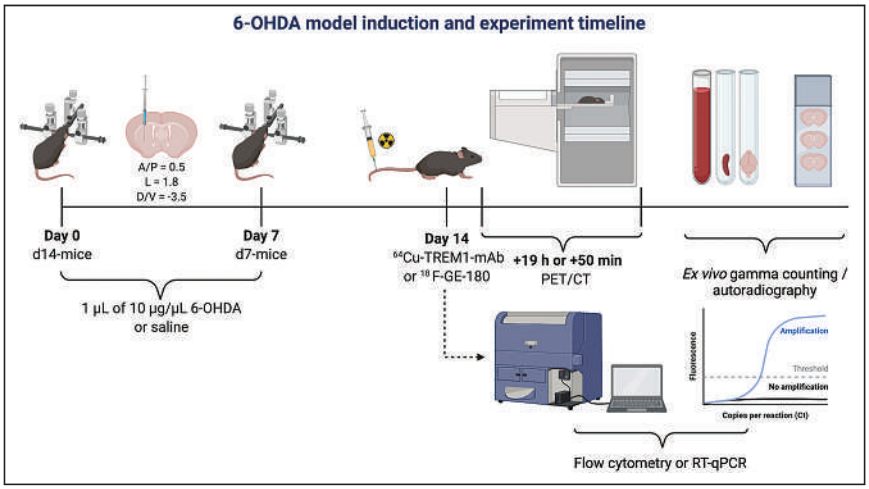

FIGURE 1. Study design of 6-hydroxydopamine model induction and imaging time line. d7- and d14-mice refer to mice injected with 6-hydroxydopamine or saline 7 or 14 d, respectively, before imaging or flow cytometry. A/P = anterior/posterior; D/V = dorsal/ventral; L = lateral; OHDA = hydroxydopamine; RT-qPCR = reverse transcription-quantitative polymerase chain reaction.

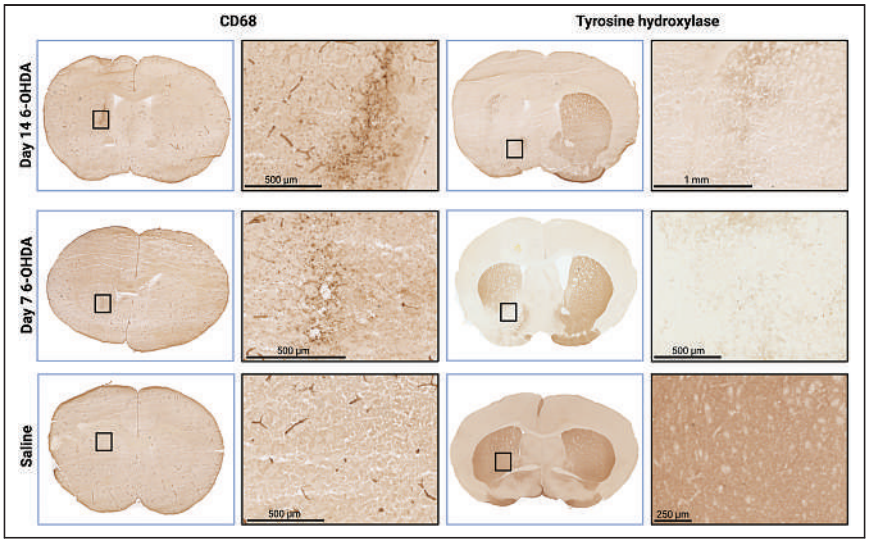

FIGURE 2. Immunohistochemistry of representative mouse brains injected with either 6-hydroxydopamine or saline. (Left) CD68 immunohistochemistry in brains of 6-hydroxydopamine or saline mice, with zoomed images beside their respective coronal brain images. CD68-positive immunostaining was present in slightly different regions of brain because of small variations in injection site. (Right) Tyrosine hydroxylase staining of dopaminergic processes in ipsilateral and contralateral striata of mice injected with 6-hydroxydopamine or saline. Ice crystals, or bubbles (freezing artifacts), due to rapid freezing can be seen in zoomed images. OHDA = hydroxydopamine.

PET Analysis and Quantitation

PET and CT images were coregistered and analyzed using VivoQuant (version 4.0; inviCRO) and Inveon Research Workspace software (Siemens) to quantify tracer uptake in specific regions of interest. For striatum quantitation, a 3-dimensional mouse brain atlas was fit to the PET/CT images via alignment of the atlas with the skull of each mouse (as determined by CT).

^{18}F-GE-180 Blocking Studies

Blocking studies were conducted 7 d after stereotactic 6-hydroxydopamine injection. The TSPO ligand PK-11195 (3 mg/kg; Sigma-Aldrich) was administered intravenously 15 min before ^{18}F-GE-180 injection, and a subsequent 10-min static PET scan was acquired at 50–60 min after tracer injection.

γ-Counting and Autoradiography

On scan completion, cardiac puncture was performed under anesthesia, and the mice were subsequently perfused with 30 mL of phosphate-buffered saline, pH 7.4 (1 time), to assess tracer uptake and spatial distribution in tissues while eliminating the contribution of tracer signal in blood. Brain, blood, and spleen were harvested, weighed, and counted using an automatic γ-counter (Hidex). Brains were immediately submerged in phosphate-buffered saline before being counted to reduce the likelihood of drying before subsequent freezing for ex vivo autoradiography. Percentage injected dose per gram was calculated for each organ of interest. Immediately after γ-counting, brains were frozen in optimal-cutting-temperature compound, and 40-μm-thick sections were cut for autoradiography (Microm HM550 Microtome; Leica Biosystems) and exposed to digital films for a minimum of 10 half-lives. Films were scanned using a Typhoon phosphor scanner (Cytiva), and the mean pixel intensity in the ipsilateral versus contralateral striatum was quantified using Image J (version 1.53a).

Immunohistochemistry

The same brain sections as used for autoradiography were probed with antibodies to CD68 (marker for microglia and other myeloid lineage cells) and tyrosine hydroxylase (marker for dopaminergic cells) using standard procedures (*36*).

Briefly, sections were fixed in acetone for 10 min, thoroughly washed in tris-buffered saline, and pretreated with 0.6% H_2O_2 in 0.3% Triton X (Union Carbide)–tris-buffered saline before overnight 4°C incubation with anti-CD68 (rat, 1:500; Bio Rad) and anti–tyrosine hydroxylase (rabbit, 1:3,000; Abcam) antibodies. The following day, sections were washed with tris-buffered saline, incubated for 1 h with ImmPRESS horseradish peroxidase antirat IgG polymer detection kit (Vector Laboratories) and ImmPRESS horse antirabbit IgG PLUS polymer kit (Vector Laboratories), and subsequently exposed to 0.05% 3,3-diaminobenzidine (Sigma-Aldrich) in 0.1 M TrisHCl (pH 7.4) with 0.03% H_2O_2 for 1–3 min. Sections were washed with 0.1 M TrisHCl before application of a coverslip. Images were captured using a Nanozoomer 2.0-RS (Hamamatsu).

RNA Isolation and Gene Expression Analysis

Ipsilateral brain sections were harvested from anesthetized mice after perfusion, immediately flash-frozen in TRIzol (Invitrogen), and stored at −80°C until use. RNA was extracted

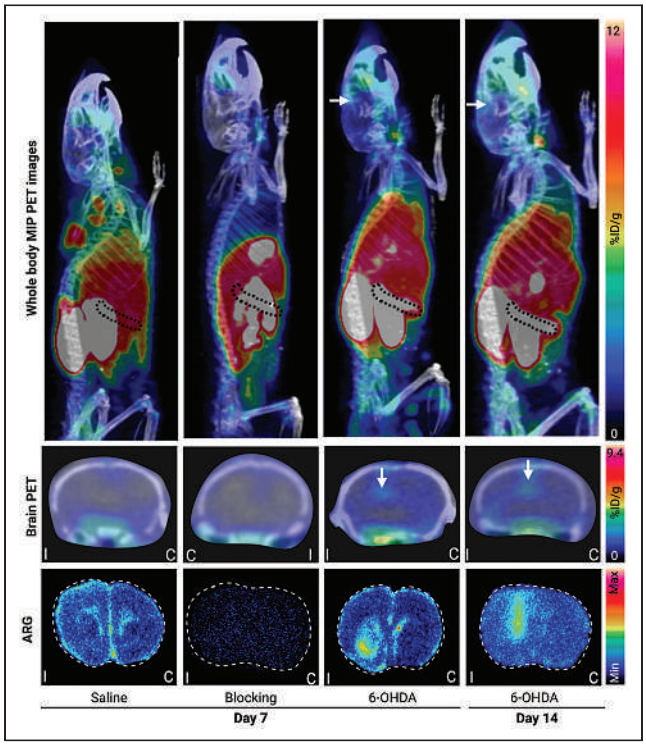

FIGURE 3. Representative ^{18}F-GE-180 PET/CT whole-body maximum-intensity-projection images, coronal brain images, and autoradiography of 40-μm-thick coronal mouse brain sections. Black and white dashed outlines indicate spleen and coronal brain sections, respectively. Arrows point to areas of increased TSPO PET signal around site of 6-hydroxydopamine injection. %ID = percentage injected dose; ARG = autoradiography; C = contralateral brain hemisphere; I = ipsilateral brain hemisphere; MIP = maximum-intensity projection; OHDA = hydroxydopamine.

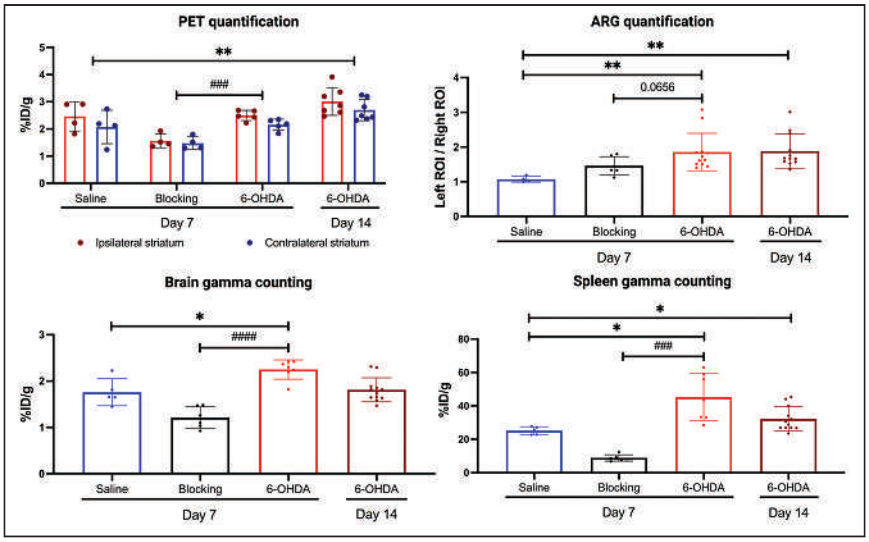

FIGURE 4. Quantification of TSPO PET tracer signal (saline ipsilateral, 2.5 ± 0.53; saline contralateral, 2.1 ± 0.61; blocking ipsilateral, 1.6 ± 0.25; blocking contralateral, 1.5 ± 0.24; day 7 6-hydroxydopamine ipsilateral, 2.5 ± 0.19; day 7 6-hydroxydopamine contralateral, 2.2 ± 0.20; day 14 6-hydroxydopamine ipsilateral, 3.0 ± 0.51; day 14 6-hydroxydopamine contralateral, 2.7 ± 0.39), ex vivo autoradiography (saline, 1.1 ± 0.09; blocking, 1.5 ± 0.26; day 7 6-hydroxydopamine, 1.9 ± 0.49; day 14 6-hydroxydopamine, 1.9 ± 0.54), and γ-counting quantification (brain: saline, 1.8 ± 0.29; blocking, 1.2 ± 0.23; day 7 6-hydroxydopamine, 2.3 ± 0.21; day 14 6-hydroxydopamine, 1.8 ± 0.26; spleen: saline, 25.2 ± 2.33; blocking, 8.9 ± 1.89; day 7 6-hydroxydopamine, 45.2 ± 14.13; day 14 6-hydroxydopamine, 32.2 ± 7.26) in saline, blocking, and 6-hydroxydopamine mice. All groups were compared with saline control (significance denoted by *); day 7 6-hydroxydopamine and blocking were compared (significance denoted by #). Data are mean ± SD percentage injected dose per gram. $^{*}P < 0.05$. $^{**}P < 0.01$. $^{\#\#\#}P < 0.001$. $^{\#\#\#\#}P < 0.0001$. %ID = percentage injected dose; ARG = autoradiography; OHDA = hydroxydopamine; ROI = region of interest.

following the TRIzol reagent RNA isolation standard operating procedure (Invitrogen). Briefly, tissues were homogenized, and RNA was isolated using chloroform (Sigma-Aldrich). Messenger RNA was precipitated and then purified in isopropanol and 75% EtOH, and the product was suspended in nuclease-free water. All messenger RNA was assessed for concentration and quality using an Eppendorf BioSpectrometer.

Complementary DNA was synthesized using the RT^2 First Strand kit (Qiagen), and incubation steps were completed in the Thermal Cycler Mini Amp (Applied Biosystems), per kit protocol. PCR was performed with SYBR green polymerase (Qiagen), reverse-transcription PCR Qiagen-specified primers (*TSPO, TREM1,* and *GAPDH*), and complementary DNA. *GAPDH* was used as a housekeeping gene. Reactions were completed in the Applied Biosystems QuantStudio 6 Real-Time PCR machine. Each sample was run with 3 technical replicates, and fold-change for each gene was calculated by deriving $2^{\Delta\Delta CT}$. Transcripts with undetectable values were assigned a cycle threshold of 38 for analysis (*37*). Samples with high variation between technical replicates (SD > 0.70) were excluded from analysis.

Flow Cytometry

Day 7 6-hydroxydopamine and saline mice were perfused, and brains (ipsilateral and contralateral hemispheres) and spleens were harvested and processed into single-cell suspensions for flow cytometric analysis. Briefly, brain and spleen tissues were mechanically homogenized in CNS buffer (2.5% HEPES [2-[4-(2-hydroxyethyl)piperazin-1-yl]ethanesulfonic acid], pH 7.5 [Invitrogen] in Hanks balanced salt solution without calcium or magnesium [Gibco]) and fluorescent activated cell sorting buffer (2% fetal bovine serum in phosphate-buffered saline), respectively. Myelin was removed from brain samples using a Percoll (GE Healthcare) gradient (25% Percoll in CNS buffer). Resulting single-cell suspensions were stained for live/dead (Aqua; ThermoFisher Scientific), TREM1 (APC; R&D Systems), CD11c (PAC-Blue; Biolegend), Ly-6G (PE-Cy7; Biolegend), CD11b (APC-Cy7; Biolegend), CD3 (PE; Biolegend), and CD45 (PerCP-Cy5.5; Biolegend) to isolate immune cell populations. Cells were fixed in 2% paraformaldehyde (Santa Cruz Biotechnology) before analysis. Data were gated (Supplemental Fig. 1) and analyzed using FlowJo (version 10.7.1).

Statistics

Statistical analyses were performed using GraphPad Prism (version 9.1.1). Data were assessed for normalization, and parametric/nonparametric tests were applied as appropriate before 2-way (PET and flow cytometry) or 1-way (autoradiography, γ-counting, and gene expression) ANOVA. *P* values of less than 0.05 were considered statistically significant.

RESULTS

Injection of 6-Hydroxydopamine Induces Dopaminergic Neurodegeneration and Myeloid Cell Activation

To confirm dopaminergic neurodegeneration and immune response in our PD rodent model, immunohistochemistry was performed on brain slices 7 and 14 d after striatal injection of 6-hydroxydopamine or saline, at which time activation of microglial/macrophages and dopaminergic cell loss is expected to be greatest (*38*). CD68 immunohistochemistry of striatum showed activated microglia/macrophages in and around the site of toxin injection (Fig. 2; Supplemental Fig. 2). Importantly, this marker did not detect significant levels of activated microglia/macrophages in the saline mice, indicating that the immune activation was specific to 6-hydroxydopamine injection. Tyrosine hydroxylase immunohistochemistry confirmed both the loss of dopaminergic processes at the toxin injection site and the presence of intact cells in the saline mice (Fig. 2). Unfortunately, accurate quantitation of our immunostaining was not possible because of the presence of freezing artifacts. These artifacts arose due to staining of the same tissue as used for autoradiography, which was not able to undergo extensive fixation protocols (i.e., sectioning and exposure to autoradiography films was performed 30–60 min after removal of brain tissue to minimize radioactive decay). Importantly, immunostaining of the same tissues as used for autoradiography enabled accurate quantitation of tracer signal in autoradiography images and provided clear, qualitative evidence of innate immune activation associated with dopaminergic cell loss, which appeared to be more pronounced 14 d after 6-hydroxydopamine, aligning with the results from a similar study performed by Cicchetti et al. (Fig. 2; Supplemental Fig. 2) (*38*).

TSPO PET Imaging Enables Visualization of Innate Immune Activation in Brain, Spleen, and Blood of 6-Hydroxydopamine–Injected Mice

To investigate the ability of TSPO PET to detect innate immune activation in the 6-hydroxydopamine model, in vivo PET images were acquired at 50–60 min after injection of ^{18}F-GE-180 (Fig. 3; Supplemental Fig. 3). Whole-body images revealed increased tracer uptake in the brains of day 7 and day 14 6-hydroxydopamine mice

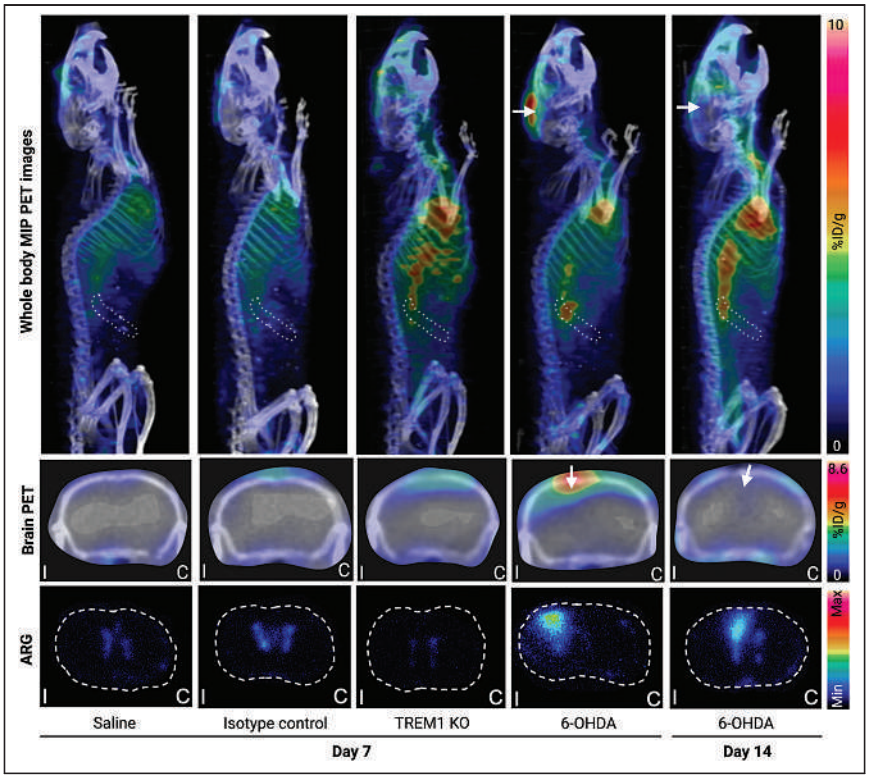

FIGURE 5. Representative ^{64}Cu-TREM1 PET/CT whole-body maximum-intensity-projection images, coronal brain images, and autoradiography of 40-μm-thick coronal mouse brain sections. Dashed outlines indicate spleen and coronal brain sections. %ID = percentage injected dose; ARG = autoradiography; C = contralateral brain hemisphere; I = ipsilateral brain hemisphere; KO = knockout; MIP = maximum-intensity projection; OHDA = hydroxydopamine.

compared with saline mice and day 7 6-hydroxydopamine mice pretreated with PK1119. In the periphery, we observed increased signal in adipose tissue (brown and white), kidneys, spleen, liver, and lungs (all tissues known to express TSPO (*39*)) of day 7 and day 14 6-hydroxydopamine mice, whereas, preblocked mice contained signal only in the gastrointestinal tract (indicative of tracer excretion), thus proving the specificity of ^{18}F-GE-180 in this model. PET signal was quantified in the ipsilateral and contralateral striata (Fig. 4). Quantitation of PET images confirmed there was a significant increase in tracer binding in the ipsilateral striatum of day 14 6-hydroxydopamine mice compared with saline mice ($P < 0.01$), in addition to significant attenuation of signal in 6-hydroxydopamine–injected mice preblocked with PK-11195 ($P < 0.001$), confirming tracer specificity.

Ex vivo autoradiography of both day 7 and day 14 6-hydroxydopamine mouse brains exhibited significantly elevated tracer binding compared with saline mice ($P < 0.01$), with striatal tracer uptake ratios (ipsilateral to contralateral striatum) determined to be 1.9 for day 7 6-hydroxydopamine, 1.9 for day 14 6-hydroxydopamine, 1.1 for saline, and 1.5 for blocking mice (Figs. 3 and 4). γ-counting of whole brain, spleen, and peripheral blood (Fig. 4; Supplemental Fig. 4A) revealed significantly increased tracer uptake in all 3 tissues of day 7 6-hydroxydopamine mice ($P < 0.05$ for all 3 tissues). Day 14 6-hydroxydopamine mice showed a significant difference only in spleen ($P < 0.05$), when compared with saline animals. Importantly, γ-counting of brain tissue was performed using whole-brain tissue (as opposed to ipsilateral vs. contralateral hemisphere), which could have diluted the differences in signal observed in injured versus uninjured striata within autoradiography images. PK-11195 blocking significantly decreased tracer uptake in the brain ($P < 0.0001$) and spleen ($P < 0.001$) of day 7 6-hydroxydopamine mice. The increased TSPO PET and autoradiography signal was supported by reverse-transcription quantitative PCR findings, which revealed a strong trend that ipsilateral striatal *TSPO* messenger RNA levels trended toward significance in day 7 6-hydroxydopamine mice ($P < 0.0598$) and were significantly increased in day 14 6-hydroxydopamine mice ($P < 0.01$, Supplemental Fig. 5A). Taken together, these data indicate that TSPO PET shows promise for visualizing inflammation in the brain, spleen, and blood of this rodent model of dopaminergic degeneration.

TREM1 Imaging Reveals Infiltrating Innate Immune Cells in the Brain of 6-Hydroxydopamine–Injected Mice

To assess the ability of TREM1 PET to detect activated myeloid cells in 6-hydroxydopamine mice, whole-body PET/CT images were acquired (Fig. 5; Supplemental Fig. 6) and signal quantified in the ipsilateral versus contralateral striatum (Fig. 6). Whole-body images showed that in the spleen, signal was higher in day 7 and day 14 6-hydroxydopamine mice than in isotype control, knockout, and saline mice. There also appeared to be higher blood signal in day 7 and day 14 6-hydroxydopamine mice (in addition to knockout mice) than in isotype control and saline mice. Quantitation of PET data confirmed that day 7 6-hydroxydopamine mice had significantly higher tracer binding in the ipsilateral striatum than did isotype control injected mice ($P < 0.01$). Though not statistically significant, PET quantitation trended toward higher tracer binding in the striatum of day 7 6-hydroxydopamine mice than in saline controls ($P < 0.08$). Of note, TREM1 PET signal in the ipsilateral striata of knockout mice was not significantly different from that in wild-type mice 7 d after 6-hydroxydopamine injection ($P < 0.32$), most likely due to the presence of unbound tracer residing in the blood of knockout mice since they lack TREM1 (and thus more tracer remains in the blood pool as opposed to binding to target-containing tissues). In particular, there appeared to be elevated signal in the cortex of knockout mice close to the surgical site, where a hole was drilled to allow injection of 6-hydroxydopamine. After removal of unbound tracer in blood via perfusion, brain tissues were further evaluated using ex vivo autoradiography (Figs. 5 and 6). Autoradiography showed that TREM1 tracer binding was significantly elevated in the injured brain tissue of day 7 ($P < 0.05$) and day 14 ($P < 0.01$) 6-hydroxydopamine mice compared with saline mice. Importantly, day 7 6-hydroxydopamine mice had significantly increased tracer binding compared with the knockout mice ($P < 0.01$), and knockout mouse brains no longer contained any signal, confirming tracer specificity. Ratios of autoradiography signal in the injured to uninjured brain were as follows: 2.2 for day 7 6-hydroxydopamine, 3.3 for day 14 6-hydroxydopamine, 1.1 for saline, 1.7 for isotype control, and 1.0 for *TREM1* knockout mice.

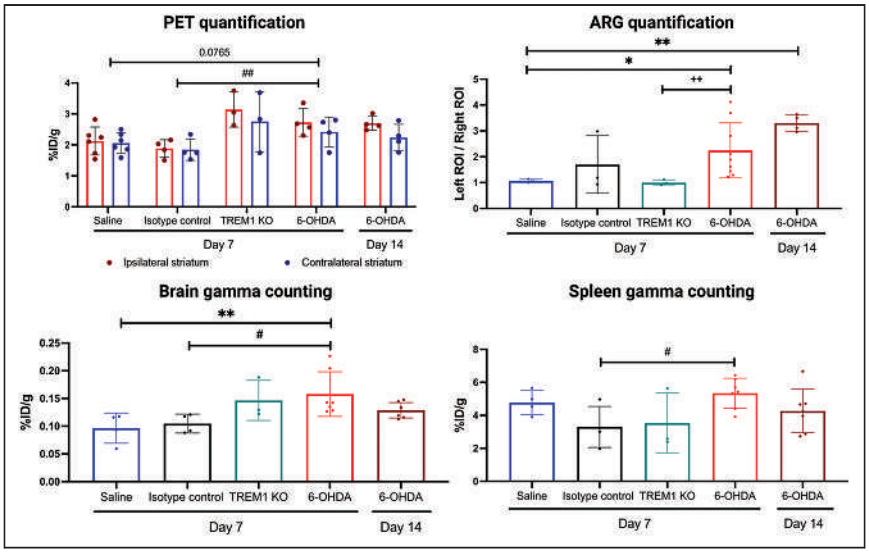

FIGURE 6. Quantification of TREM1 PET tracer signal (saline ipsilateral, 2.1 ± 0.45; saline contralateral, 2.1 ± 0.33; isotype control ipsilateral, 1.9 ± 0.29; isotype control contralateral, 1.8 ± 0.35; *TREM1* knockout ipsilateral, 3.1 ± 0.57; *TREM1* knockout contralateral, 2.8 ± 0.97; day 7 6-hydroxydopamine ipsilateral, 2.7 ± 0.45; day 7 6-hydroxydopamine contralateral, 2.4 ± 0.48; day 14 6-hydroxydopamine ipsilateral, 2.7 ± 0.23; day 14 6-hydroxydopamine contralateral, 2.2 ± 0.43), ex vivo autoradiography (saline, 1.1 ± 0.07; isotype control, 1.7 ± 1.12; *TREM1* knockout, 1.0 ± 0.17; day 7 6-hydroxydopamine, 2.2 ± 1.07; day 14 6-hydroxydopamine, 3.3 ± 0.32), and γ-counting quantification (brain: saline, 0.1 ± 0.03; isotype control, 0.1 ± 0.02; *TREM1* knockout, 0.15 ± 0.04; day 7 6-hydroxydopamine, 0.16 ± 0.04; day 14 6-hydroxydopamine, 0.13 ± 0.01; spleen: saline, 4.8 ± 0.74; isotype control, 3.3 ± 1.2; *TREM1* knockout, 3.5 ± 1.82; day 7 6-hydroxydopamine, 5.4 ± 0.91; day 14 6-hydroxydopamine, 4.3 ± 1.32) in saline, isotype control, and 6-hydroxydopamine mice. All groups were compared with saline control (significance denoted by *); day 7 6-hydroxydopamine and isotype control were compared (significance denoted by #) as well as day 7 6-hydroxydopamine and *TREM1* knockout (significance denoted by +). Data are mean ± SD percentage injected dose per gram. $^{*/\#}P < 0.05$. $^{**/\#\#/++}P < 0.01$. %ID = percentage injected dose; ARG = autoradiography; KO = knockout; OHDA = hydroxydopamine; ROI = region of interest.

Ex vivo γ-counting was performed on whole brain, spleen, and peripheral blood (from cardiac puncture; Fig. 6; Supplemental Fig. 4B). Tracer binding was significantly increased in the whole brain of day 7 6-hydroxydopamine mice ($P < 0.01$) and trended higher in the peripheral blood of day 14 6-hydroxydopamine mice ($P < 0.13$) than in saline mice. Additionally, tracer signal was significantly increased in all organs of day 7 6-hydroxydopamine mice compared with isotype control ($P < 0.01$ for brain and < 0.05 for spleen and blood). Reverse-transcription quantitative PCR analysis revealed that *TREM1* expression was markedly increased in day 14 6-hydroxydopamine mice ($P < 0.05$), whereas increases in day 7 6-hydroxydopamine mice trended toward significance ($P < 0.08$, Supplemental Fig. 4B).

To confirm the presence of TREM1-positive immune cells after dopaminergic neuron damage, flow cytometry was performed on ipsilateral and contralateral brain regions (Fig. 7). A significant increase in the infiltration (expressed as percentage live singlets) of peripheral myeloid ($CD45^{hi}$ [hi = high] CD11b-positive) cells was observed in the ipsilateral hemisphere of day 7 6-hydroxydopamine mice compared with the contralateral hemisphere of day 7 6-hydroxydopamine mice ($P < 0.0001$) and the ipsilateral hemisphere of saline mice ($P < 0.001$, Fig. 7A). Increased lymphoid (CD45-positive CD11b-negative) cell infiltration was also observed in the ipsilateral versus contralateral region of day 7 6-hydroxydopamine mice ($P < 0.0001$). In contrast, microglia populations ($CD45^{int}$ [int= intermediate] CD11b-positive) were unchanged by 6-hydroxydopamine treatment. No significant changes in myeloid or lymphoid cell populations were observed in the spleens of day 7 6-hydroxydopamine or saline mice (Supplemental Fig. 7). Phenotyping of immune cell subtypes revealed significantly elevated TREM1-positive myeloid cells in the ipsilateral brain of day 7 6-hydroxydopamine mice (vs. contralateral in day 7 6-hydroxydopamine mice [$P < 0.0001$] and ipsilateral in saline mice [$P = 0.01$], Fig. 7B). TREM1 expression was not observed on infiltrating lymphoid cells and did not significantly change on microglial cells, confirming that the increased signal observed in PET and autoradiography images is due primarily to infiltration of TREM1-positive peripheral myeloid lineage cells.

Further characterization of infiltrating myeloid cells revealed an increased frequency of neutrophils ($CD45^{hi}$ CD11b-positive Ly6G-positive) compared with monocyte/macrophage/dendritic cells ($CD45^{hi}$ CD11b-positive Ly6G-negative) (Supplemental Fig. 8A). A large number of neutrophils compared with monocytes/macrophages/dendritic cells were found to infiltrate the ipsilateral brain of day 7 6-hydroxydopamine mice ($P < 0.001$). Moreover, a higher frequency of neutrophils were TREM1-positive ($P < 0.01$, Supplemental Fig. 8B), suggesting that most TREM1 PET signal observed after 6-hydroxydopamine treatment represents TREM1-positive neutrophils. Together, these data indicate that TREM1 PET is a highly specific approach for visualizing the presence of early proinflammatory innate immune activation in the 6-hydroxydopamine model of dopaminergic neurodegeneration.

DISCUSSION

The utility of ^{18}F-GE-180 and ^{64}Cu-TREM1 mAb to enable quantification of whole-body innate immune responses was evaluated in the 6-hydroxydopamine mouse model. We understand that PD is a highly complex chronic, progressive neurodegenerative disorder and that there is no mouse model that recapitulates this disease. Importantly, the rodent model we chose has been extensively studied and is known to contain selective dopaminergic degeneration in addition to innate immune activation, making it a suitable starting point to study the ability of TREM1 and TSPO PET to detect activated myeloid cells in the context of PD pathology (*30*). Better understanding the inflammatory responses in PD may enable more accurate monitoring of disease progression and response to novel therapies and, ultimately, help to prevent or reset the chronic neuroinflammation that exacerbates disease (*40*).

Here, we have shown that TSPO and TREM1 tracers enabled detection of complementary molecular information in the 6-hydroxydopamine mouse model through detecting 2 distinct immune cell types involved in innate immune responses associated with dopaminergic degeneration. Because of the current limitations of small-animal PET (i.e., relatively low spatial resolution and the partial-volume effect), our in vivo imaging data were

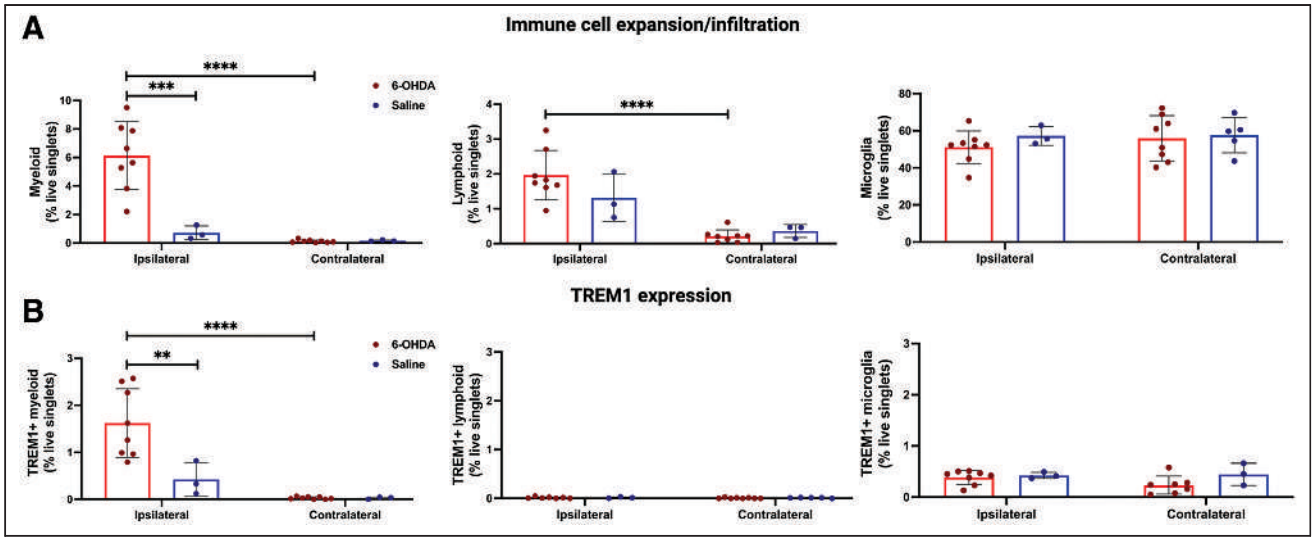

FIGURE 7. Flow cytometry analysis of 6-hydroxydopamine and saline brains. (A) Flow cytometry analysis demonstrating frequency of peripheral myeloid ($CD45^{hi}$ [hi = high] CD11b-positive), lymphoid (CD45-positive CD11b-negative), and microglial ($CD45^{int}$ [int= intermediate] CD11b-positive) cells in brains of 6-hydroxydopamine and saline mice 7 d after stereotactic injection (myeloid: day 7 6-hydroxydopamine ipsilateral, 6.1 ± 0.72; day 7 6-hydroxydopamine contralateral, 0.12 ± 0.09; saline ipsilateral, 0.72 ± 0.48; saline contralateral, 0.16 ± 0.05; lymphoid: day 7 6-hydroxydopamine ipsilateral, 2.0 ± 0.71; day 7 6-hydroxydopamine contralateral, 0.21 ± 0.18; saline ipsilateral, 1.3 ± 0.67; saline contralateral, 0.36 ± 0.18; microglia: day 7 6-hydroxydopamine ipsilateral, 51.1 ± 8.76; day 7 6-hydroxydopamine contralateral, 55.9 ± 12.18; saline ipsilateral, 57.2 ± 5.12; saline contralateral, 57.6 ± 9.54). (B) Frequency of TREM1-positive myeloid, lymphoid, and microglial cells (TREM1-positive myeloid: day 7 6-hydroxydopamine ipsilateral, 1.6 ± 0.73; day 7 6-hydroxydopamine contralateral, 0.03 ± 0.025; saline ipsilateral, 0.42 ± 0.36; saline contralateral, 0.026 ± 0.023; TREM1-positive lymphoid: day 7 6-hydroxydopamine ipsilateral, 0.014 ± 0.016; day 7 6-hydroxydopamine contralateral, 0.0068 ± 0.01; saline ipsilateral, 0.016 ± 0.014; saline contralateral, 0.011 ± 0.0065; TREM1-positive microglia: day 7 6-hydroxydopamine ipsilateral, 0.39 ± 0.14; day 7 6-hydroxydopamine contralateral, 0.23 ± 0.18; saline ipsilateral, 0.42 ± 0.061; saline contralateral, 0.45 ± 0.22). Data are mean ± SD percentage total live singlets. $^{**}P < 0.01$. $^{***}P < 0.001$. $^{****}P < 0.0001$. OHDA = hydroxydopamine.

corroborated by additional ex vivo methods. Specifically, we performed high-resolution ex vivo autoradiography together with immunostaining of the same tissue slices and confirmed the specific correspondence of ^{18}F-GE180 and ^{64}Cu-TREM1 mAb binding in regions containing activated myeloid cells in 6-hydroxydopamine mice. Importantly, we did not observe the exact same results using γ-counting since we used whole brain as opposed to ipsilateral versus contralateral brain tissue, which likely dilutes the differences found using autoradiography. Since autoradiography affords high-resolution images depicting spatial distribution and binding of tracers, it permits more accurate quantitation. Thus, the results from our autoradiography analyses more reliably represent the extent of tracer binding and its correspondence with immunostaining.

Interestingly, there was significantly elevated ^{18}F-GE180 signal in both the CNS and peripheral tissues (i.e., spleen and blood), indicating that TSPO PET might be useful for investigating inflammation throughout the whole body in the context of PD. Conversely, ^{64}Cu-TREM1 mAb may be more suitable for examining subtle alterations in innate immune activation in the CNS because of its increased signal-to-background ratio compared with ^{18}F-GE180, as demonstrated by brain autoradiography.

Our autoradiography findings were supported by gene expression data using tissue from the ipsilateral striatum. That is, we found that *TSPO* and *TREM1* were both significantly upregulated in ipsilateral striatum of day 14 6-hydroxydopamine mice compared with saline mice and that there was a strong trend toward significant elevation of both genes in day 7 6-hydroxydopamine animals (*TSPO,* $P < 0.0598$, and *TREM1,* $P < 0.0776$). Importantly, the fold change in *TREM1* expression was nearly 30 times greater than for *TSPO,* reiterating that *TREM1* is likely a more sensitive biomarker for neuroinflammation in this model than is *TSPO*. Importantly, mouse and human RNA-sequencing data (https://www.brainrnaseq.org) (*41*) for TSPO and TREM1 show that cellular expression of these proteins is quite different. In mice, for example, basal TSPO levels are about 20-fold higher in resting microglia/macrophages than are TREM1 levels. Crucially, TREM1 is specifically expressed on myeloid lineage cells, whereas TSPO is found not only in microglia/macrophages but also in astrocytes or endothelial cells for both mice and humans (Supplemental Fig. 9). The stark differences in expression of these 2 genes, as well as differences in their basal levels, indicates that TREM1 PET might be a more sensitive and specific technique for monitoring aberrant innate immune activation in the CNS. Flow cytometry allowed further investigation of the molecular changes underpinning a positive TREM1 PET/autoradiography image. Our data suggest that peripheral infiltrating myeloid cells (e.g., neutrophils) are likely the predominant cell type expressing TREM1 in the ipsilateral brain tissue of 6-hydroxydopamine mice (and not brain-resident microglia); however, further studies are needed to confirm this possibility at different time points throughout the course of disease in this model. Images acquired using ^{18}F-GE180, on the other hand, most likely reflect a combination of TSPO-expressing microglia, macrophages, astrocytes, and endothelial cells, reinforcing the importance of understanding the cellular specificity of an imaging biomarker in a given context or disease when interpreting imaging data. Accordingly, our future studies will involve additional flow cytometry comparing TSPO- and TREM1-expressing cells in different tissues in this mouse model (and other PD-like models) in addition to immunohistochemistry or multiplexed methods of probing the expression and spatial distribution of TSPO and TREM1 in human postmortem PD versus healthy control brain tissue. Such studies will help to further parse out the various cell types that express TSPO or TREM1 in different contexts.

CONCLUSION

Here, we showed that both TSPO and TREM1 PET enabled detection of innate immune activation after selective dopaminergic degeneration in a rodent model of PD-like pathology; however, there were some key differences in the molecular information these techniques afforded. That is, our data provided definitive evidence of the high specificity and sensitivity of TREM1 PET for imaging peripheral CNS-infiltrating myeloid cells in the brain of mice injected with 6-hydroxydopamine, whereas TSPO PET provided information on a larger array of cell types in the CNS and may be more useful for detecting inflammatory changes in both the brain and peripheral tissues of these mice, highlighting the potential of whole-body imaging using TSPO tracers. The current availability of TSPO PET (*42*) for clinical use allows for immediate testing of whole-body molecular imaging of PD patients. TREM1 PET, on the other hand, may help reveal unprecedented insights into the role of peripheral CNS-infiltrating myeloid cells in the pathogenesis of PD, both in rodent models and in patients after successful translation.

DISCLOSURE

This work was generously supported by the Smart Foundation. Michelle James is a cofounder and board member of Willow Neuroscience. No other potential conflict of interest relevant to this article was reported.

ACKNOWLEDGMENTS

We are very grateful to Dr. Jason Thanh Lee from the Sci^3 small-animal imaging facility at Stanford University for his continual support and gracious assistance with PET/CT imaging. We also want to thank Theresa McLaughlin at the Vincent Coates Foundation Mass Spectrometry Laboratory and Stanford University Mass Spectrometry (SUMS) for her help with the liquid chromatography–mass spectrometry data. We are truly grateful to Dr. Emily M. Deal for her assistance with editing and assembling the manuscript. Lastly, figures were assembled/created with BioRender.com.

KEY POINTS

QUESTION: Can ^{18}F-GE-180 (TSPO PET) and ^{64}Cu-TREM1 mAb (TREM1 PET) detect different types of cells involved in innate immune activation in a mouse model of PD-like pathology?

PERTINENT FINDINGS: TSPO and TREM1 PET enabled visualization and monitoring of innate immune cell activation and infiltration in a mouse model of PD-like pathology, with significant tracer binding observed in animals with dopaminergic cell degeneration compared with controls. In vivo findings were corroborated by ex vivo autoradiography, flow cytometry, and immunohistochemistry.

IMPLICATIONS FOR PATIENT CARE: The future translation of ^{64}Cu-TREM1 mAb and immediate availability of multiple TSPO PET radiotracers for clinical research could permit noninvasive biomarker-driven disease staging and monitoring of the inflammatory component of PD while facilitating the development and real-time assessment of novel immunomodulatory therapeutics for this disease.

REFERENCES

1. Holmqvist S, Chutna O, Bousset L, et al. Direct evidence of Parkinson pathology spread from the gastrointestinal tract to the brain in rats. *Acta Neuropathol (Berl).* 2014;128:805–820.
2. Blanz J, Saftig P. Parkinson's disease: acid-glucocerebrosidase activity and alpha-synuclein clearance. *J Neurochem.* 2016;139(suppl 1):198–215.
3. Moore DJ, West AB, Dawson VL, Dawson TM. Molecular pathophysiology of Parkinson's disease. *Annu Rev Neurosci.* 2005;28:57–87.
4. Grozdanov V, Bousset L, Hoffmeister M, et al. Increased immune activation by pathologic alpha-synuclein in Parkinson's disease. *Ann Neurol.* 2019;86:593–606.
5. Tan EK, Chao YX, West A, Chan LL, Poewe W, Jankovic J. Parkinson disease and the immune system: associations, mechanisms and therapeutics. *Nat Rev Neurol.* 2020;16:303–318.
6. Kam TI, Hinkle JT, Dawson TM, Dawson VL. Microglia and astrocyte dysfunction in Parkinson's disease. *Neurobiol Dis.* 2020;144:105028.
7. McGeer PL, Itagaki S, Boyes BE, McGeer EG. Reactive microglia are positive for HLA-DR in the substantia nigra of Parkinson's and Alzheimer's disease brains. *Neurology.* 1988;38:1285–1291.
8. Liu B, Gao HM, Hong JS. Parkinson's disease and exposure to infectious agents and pesticides and the occurrence of brain injuries: role of neuroinflammation. *Environ Health Perspect.* 2003;111:1065–1073.
9. Mogi M, Harada M, Riederer P, Narabayashi H, Fujita K, Nagatsu T. Tumor necrosis factor-α (TNF-α) increases both in the brain and in the cerebrospinal fluid from parkinsonian patients. *Neurosci Lett.* 1994;165:208–210.
10. Mogi M, Harada M, Kondo T, et al. Interleukin-1β, interleukin-6, epidermal growth factor and transforming growth factor-α are elevated in the brain from parkinsonian patients. *Neurosci Lett.* 1994;180:147–150.
11. Boka G, Anglade P, Wallach D, Javoy-Agid F, Agid Y, Hirsch EC. Immunocytochemical analysis of tumor necrosis factor and its receptors in Parkinson's disease. *Neurosci Lett.* 1994;172:151–154.
12. Mogi M, Kondo T, Mizuno Y, Nagatsu T. p53 protein, interferon-gamma, and NF-κB levels are elevated in the parkinsonian brain. *Neurosci Lett.* 2007;414:94–97.
13. Hirsch EC, Hunot S. Neuroinflammation in Parkinson's disease: a target for neuroprotection? *Lancet Neurol.* 2009;8:382–397.
14. Tansey MG, McCoy MK, Frank-Cannon TC. Neuroinflammatory mechanisms in Parkinson's disease: potential environmental triggers, pathways, and targets for early therapeutic intervention. *Exp Neurol.* 2007;208:1–25.
15. McGeer PL, Itagaki S, Akiyama H, McGreer EG. Rate of cell death in parkinsonism indicates active neuropathological process. *Ann Neurol.* 1988;24:574–576.
16. Brendel M, Probst F, Jaworska A, et al. Glial activation and glucose metabolism in a transgenic amyloid mouse model: a triple-tracer PET study. *J Nucl Med.* 2016;57:954–960.
17. Liu B, Le KX, Park MA, et al. In vivo detection of age- and disease-related increases in neuroinflammation by ^{18}F-GE180 TSPO microPET imaging in wild-type and Alzheimer's transgenic mice. *J Neurosci.* 2015;35:15716–15730.
18. Chaney A, Cropper HC, Johnson EM, et al. ^{11}C-DPA-713 versus ^{18}F-GE-180: a preclinical comparison of translocator protein 18 kDa PET tracers to visualize acute and chronic neuroinflammation in a mouse model of ischemic stroke. *J Nucl Med.* 2019;60:122–128.
19. James ML, Belichenko NP, Shuhendler AJ, et al. [^{18}F]GE-180 PET detects reduced microglia activation after LM11A-31 therapy in a mouse model of Alzheimer's disease. *Theranostics.* 2017;7:1422–1436.
20. Boutin H, Murray K, Pradillo J, et al. ^{18}F-GE-180: a novel TSPO radiotracer compared to ^{11}C-R-PK11195 in a preclinical model of stroke. *Eur J Nucl Med Mol Imaging.* 2015;42:503–511.
21. Sridharan S, Lepelletier FX, Trigg W, et al. Comparative evaluation of three TSPO PET radiotracers in a LPS-induced model of mild neuroinflammation in rats. *Mol Imaging Biol.* 2017;19:77–89.
22. Wadsworth H, Jones PA, Chau WF, et al. [^{18}F]GE-180: a novel fluorine-18 labelled PET tracer for imaging translocator protein 18 kDa (TSPO). *Bioorg Med Chem Lett.* 2012;22:1308–1313.
23. Werry EL, Bright FM, Piguet O, et al. Recent developments in TSPO PET imaging as a biomarker of neuroinflammation in neurodegenerative disorders. *Int J Mol Sci.* 2019;20:3161.
24. Bouchon A, Dietrich J, Colonna M. Cutting edge: inflammatory responses can be triggered by TREM-1, a novel receptor expressed on neutrophils and monocytes. *J Immunol.* 2000;164:4991–4995.
25. Liu Q, Johnson EM, Lam RK, et al. Peripheral TREM1 responses to brain and intestinal immunogens amplify stroke severity. *Nat Immunol.* 2019;20:1023–1034.
26. Chaney A, Cropper H, Johnson E, Stevens M, James M. Imaging the invaders: TREM1 as a novel PET imaging biomarker of peripheral infiltrating myeloid cells

and potential therapeutic target in multiple sclerosis [abstract]. *J Nucl Med.* 2019; 60(suppl 1):1506b.
27. Chaney A, Wilson E, Jain P, et al. TREM1-PET imaging of pro-inflammatory myeloid cells distinguishes active disease from remission in multiple sclerosis [abstract]. *J Nucl Med.* 2020;61(suppl 1):199.
28. Bové J, Prou D, Perier C, Przedborski S. Toxin-induced models of Parkinson's disease. *NeuroRx.* 2005;2:484–494.
29. Weber B, Schuster S, Zysset D, et al. TREM-1 deficiency can attenuate disease severity without affecting pathogen clearance. *PLoS Pathog.* 2014;10:e1003900.
30. Park SE, Song KI, Kim H, Chung S, Youn I. Graded 6-OHDA-induced dopamine depletion in the nigrostriatal pathway evokes progressive pathological neuronal activities in the subthalamic nucleus of a hemi-parkinsonian mouse. *Behav Brain Res.* 2018;344:42–47.
31. Boix J, Padel T, Paul G. A partial lesion model of Parkinson's disease in mice: characterization of a 6-OHDA-induced medial forebrain bundle lesion. *Behav Brain Res.* 2015;284:196–206.
32. Verel I, Visser GWM, Boellaard R, Stigter-van Walsum M, Snow GB, van Dongen GA. ^{89}Zr immuno-PET: comprehensive procedures for the production of ^{89}Zr-labeled monoclonal antibodies. *J Nucl Med.* 2003;44:1271–1281.
33. Cree BAC, Bennett JL, Kim HJ, et al. Inebilizumab for the treatment of neuromyelitis optica spectrum disorder (N-MOmentum): a double-blind, randomised placebo-controlled phase 2/3 trial. *Lancet.* 2019;394:1352–1363.
34. Hartung DM. Economics and cost-effectiveness of multiple sclerosis therapies in the USA. *Neurotherapeutics.* 2017;14:1018–1026.
35. Chaney AM, Johnson EM, Cropper HC, James ML. PET imaging of neuroinflammation using [^{11}C]DPA-713 in a mouse model of ischemic stroke. *J Vis Exp.* 2018; 136:57243.
36. Cropper HC, Johnson EM, Haight ES, et al. Longitudinal translocator protein-18 kDa-positron emission tomography imaging of peripheral and central myeloid cells in a mouse model of complex regional pain syndrome. *Pain.* 2019; 160:2136–2148.
37. Nicol LS, Dawes JM, La Russa F, et al. The role of G-protein receptor 84 in experimental neuropathic pain. *J Neurosci.* 2015;35:8959–8969.
38. Cicchetti F, Brownell AL, Williams K, Chen YI, Livni E, Isacson O. Neuroinflammation of the nigrostriatal pathway during progressive 6-OHDA dopamine degeneration in rats monitored by immunohistochemistry and PET imaging. *Eur J Neurosci.* 2002;15:991–998.
39. Tu LN, Zhao AH, Hussein M, Stocco DM, Selvaraj V. Translocator protein (TSPO) affects mitochondrial fatty acid oxidation in steroidogenic cells. *Endocrinology.* 2016;157:1110–1121.
40. Joshi N, Singh S. Updates on immunity and inflammation in Parkinson disease pathology. *J Neurosci Res.* 2018;96:379–390.
41. Zhang Y, Chen K, Sloan SA, et al. An RNA-sequencing transcriptome and splicing database of glia, neurons, and vascular cells of the cerebral cortex. *J Neurosci.* 2014;34:11929–11947.
42. Endres CJ, Pomper MG, James M, et al. Initial evaluation of ^{11}C-DPA-713, a novel TSPO PET ligand, in humans. *J Nucl Med.* 2009;50:1276–1282.

Total-Body ^{18}F-FDG PET/CT in Autoimmune Inflammatory Arthritis at Ultra-Low Dose: Initial Observations

Yasser Abdelhafez[1,2], Siba P. Raychaudhuri*[3,4], Dario Mazza[1], Soumajyoti Sarkar[3], Heather L. Hunt[1], Kristin McBride[1], Mike Nguyen[1], Denise T. Caudle[1], Benjamin A. Spencer[1,5], Negar Omidvari[1,5], Heejung Bang[6], Simon R. Cherry[1,5], Lorenzo Nardo[1], Ramsey D. Badawi[1,5], and Abhijit J. Chaudhari*[1]

[1]*Department of Radiology, University of California Davis, Davis, California;* [2]*Nuclear Medicine Unit, South Egypt Cancer Institute, Assiut University, Assiut, Egypt;* [3]*Department of Internal Medicine-Rheumatology, University of California Davis, Davis, California;* [4]*Northern California Veterans Affairs Medical Center, Mather, California;* [5]*Department of Biomedical Engineering, University of California Davis, Davis, California; and* [6]*Department of Public Health Sciences, University of California Davis, Davis, California*

Autoimmune inflammatory arthritides (AIA), such as psoriatic arthritis and rheumatoid arthritis, are chronic systemic conditions that affect multiple joints of the body. Recently, total-body (TB) PET/CT scanners exhibiting superior technical characteristics (total-body coverage, geometric sensitivity) that could benefit AIA evaluation, compared with conventional PET/CT systems, have become available. The objectives of this work were to assess the performance of an ultra-low-dose, ^{18}F-FDG TB PET/CT acquisition protocol for evaluating systemic joint involvement in AIA and to report the association of TB PET/CT measures with joint-by-joint rheumatologic examination and standardized rheumatologic outcome measures. **Methods:** Thirty participants (24 with AIA and 6 with osteoarthritis) were prospectively enrolled in this single-center, observational study. All participants underwent a TB PET/CT scan for 20 min starting at 40 min after intravenous injection of 78.1 ± 4.7 MBq of ^{18}F-FDG. Qualitative and quantitative evaluation of ^{18}F-FDG uptake and joint involvement were performed from the resulting images and compared with the rheumatologic assessments. **Results:** TB PET/CT enabled the visualization of ^{18}F-FDG uptake at joints of the entire body, including those of the hands and feet, in a single bed position, and in the same phase of radiotracer uptake. A range of pathologies consistent with AIA (and non-AIA in the osteoarthritis group) were visualized, and the feasibility of extracting PET measures from joints examined by rheumatologic assessments was demonstrated. Of 1,997 evaluable joints, there was concordance between TB PET qualitative assessments and joint-by-joint rheumatologic evaluation in the AIA and non-AIA cohorts for 69.9% and 91.1% joints, respectively, and an additional 20.1% and 8.8% joints, respectively, deemed negative on rheumatologic examination showed PET positivity. On the other hand, 10.0% and 0% joints in the AIA and non-AIA cohorts, respectively, were positive on rheumatologic evaluation but negative on TB PET. Quantitative measures from TB PET in the AIA cohort demonstrated a moderate-to-strong correlation (Spearman $\rho = 0.53$–0.70, $P < 0.05$) with the rheumatologic outcome measures. **Conclusion:** Systemic joint evaluation in AIA (and non-AIA) is feasible with a TB PET/CT system and an ultra-low-dose protocol. Our results provide the foundation for future larger studies to evaluate the possible improvements in AIA joint assessment via the TB PET/CT technology.

Key Words: total-body PET/CT; autoimmune arthritis; rheumatoid arthritis; psoriatic arthritis; osteoarthritis

Received Dec. 30, 2021; revision accepted Apr. 18, 2022.

For correspondence or reprints, contact Abhijit J. Chaudhari (ajchaudhari@ucdavis.edu).

*Contributed equally to this work.

Published online May 19, 2022.

J Nucl Med 2022; 63:1579–1585
DOI: 10.2967/jnumed.121.263774

Autoimmune inflammatory arthritides (AIA), such as psoriatic arthritis (PsA) and rheumatoid arthritis (RA), are chronic, systemic conditions with articular and extraarticular manifestation. Joint inflammation is regarded as the hallmark of AIA and is considered a bellwether for downstream joint destruction and pain (*1*). Consequently, disease activity and treatment response assessments in AIA have relied primarily on the physical evaluation of joints (e.g., tenderness and swelling) and composite scores from joint examination, joint pain and activity, and laboratory inflammatory markers. These assessments, however, are subjective (*2*) and lack the sensitivity required to detect early or subclinical disease (*3*).

To address this limitation, PET/CT scanning using the radiotracer ^{18}F-FDG has been proposed, with results demonstrating the ability to assess joint inflammation (*4–8*), considered a precursor to AIA-associated joint damage. Despite these advantages, concerns about using ^{18}F-FDG PET/CT on current systems in the AIA population have been expressed. These include the significant cumulative dose to the patient for chronic disease activity monitoring or measuring treatment response (*9,10*) and the assessment of only portions of the body (e.g., just large joints (*11*)), given the limited PET sensitivity and spatial resolution characteristics of systems used for quantifying radiotracer uptake in small joints of the hands and feet that are affected early in AIA (*7,12*).

Recently, long-axial field-of-view (FOV) PET/CT systems capable of imaging either the entire adult human body (*13*) or large portions of the body (*14,15*) have become available. Their sensitivity characteristics are far superior to state-of-the-art conventional whole-body PET/CT systems, and early studies have shown that dose reduction is possible (*16*). These systems have a spatial resolution comparable to or better than conventional whole-body PET/CT scanners (*13*). To date, however, these total-body (TB) PET/CT systems have not been evaluated for assessing systemic autoimmune diseases, such as AIA.

In this article we present the first-in-humans evaluation of a TB PET/CT scanner to document the head-to-toe articular manifestations of AIA. The objectives of this work were to assess the performance of an ultra-low-dose ^{18}F-FDG TB PET/CT acquisition protocol to evaluate joint involvement in AIA and to report the association of rheumatologic measures of AIA joint and disease activity with those evaluated from TB PET/CT.

TABLE 1
Characteristics of the Study Participants and Summary of Their Rheumatologic Assessments

Characteristic	Non-AIA ($n = 6$)	AIA ($n = 24$)	P	AIA		P
				PsA ($n = 15$)	RA ($n = 9$)	
Age (y)	54.5 ± 14.5 (36–72)	58.5 ± 13.9 (28–77)	0.63	56.8 ± 16.3 (28–77)	61.4 ± 8.3 (47–71)	0.79
BMI (kg/m^2)	28.6 ± 8.4 (19.8–40)	31.3 ± 6.3 (20–46.6)	0.49	32.3 ± 7.1 (20–46.6)	29.6 ± 4.5 (23.1–36.4)	0.36
TJC (68 joints)	0.5 ± 0.8 (0–2)	12.5 ± 14 (0–55)	<0.001	10.5 ± 13.7 (0–55)	16 ± 14.4 (4–45)	0.22
SJC (68 joints)	0	1.6 ± 2.4 (0–9)	—	1.9 ± 2.7 (0–9)	1.2 ± 2.0 (0–6)	0.67
TJC (28 joints)	0	8.7 ± 7.1 (0–25)	—	7 ± 6.8 (0–25)	11.6 ± 7.1 (4–23)	0.13
SJC (28 joints)	0	1.2 ± 1.7 (0–6)	—	1.1 ± 1.6 (0–5)	1.2 ± 2.0 (0–6)	0.92
DAS-28-CRP*	—	3.7 ± 1.1 (2.1–5.4)	—	3.7 ± 1.1 (2.1–5.4)	3.7 ± 1.0 (2.4–5.1)	0.93

*DAS-28-CRP is not a validated outcome measure for non-AIA (OA) so was not calculated.
Values are reported as mean ± SD (minimum–maximum).
BMI = body mass index; TJC = tender joint count; SJC = swollen joint count; CRP = C-reactive protein.

MATERIALS AND METHODS

Study Participants

This prospective study was approved by Institutional Review Board of the University of California Davis, and all participants provided written informed consent before study procedures began. The recruited participants had a confirmed diagnosis, according to established criteria, of 1 of 2 subtypes of AIA (PsA or RA) (*17,18*) or osteoarthritis (OA), a non-AIA (*19*).

All study participants underwent rheumatologic evaluation by a fellowship-trained, board-certified rheumatologist and dermatologist with over 25 y of posttraining experience in AIA within 2 wk before the TB PET/CT scan. Rheumatologic assessments included the evaluation of 68 joints using the Disease Activity in Psoriatic Arthritis (DAPSA) outcome measure (*20*) and Disease Activity Score (based on the assessment of 28 joints [DAS-28] (*21*), which are subset of the 68 joints). Blood samples were drawn on the day of the scan for assessing serum C-reactive protein (CRP), used to calculate DAPSA score and DAS-28-CRP. The swollen and tender joint counts (swollen joint count, tender joint count) were recorded. A joint was considered positive if it was tender, swollen, or both.

Total-Body ^{18}F-FDG PET/CT

All participants underwent scanning on a TB PET/CT scanner (uEXPLORER; United Imaging Health Care) at a single time point for 20 min starting at 40 ± 1 min after an intravenous injection of 78.1 ± 4.7 MBq of ^{18}F-FDG. Details of

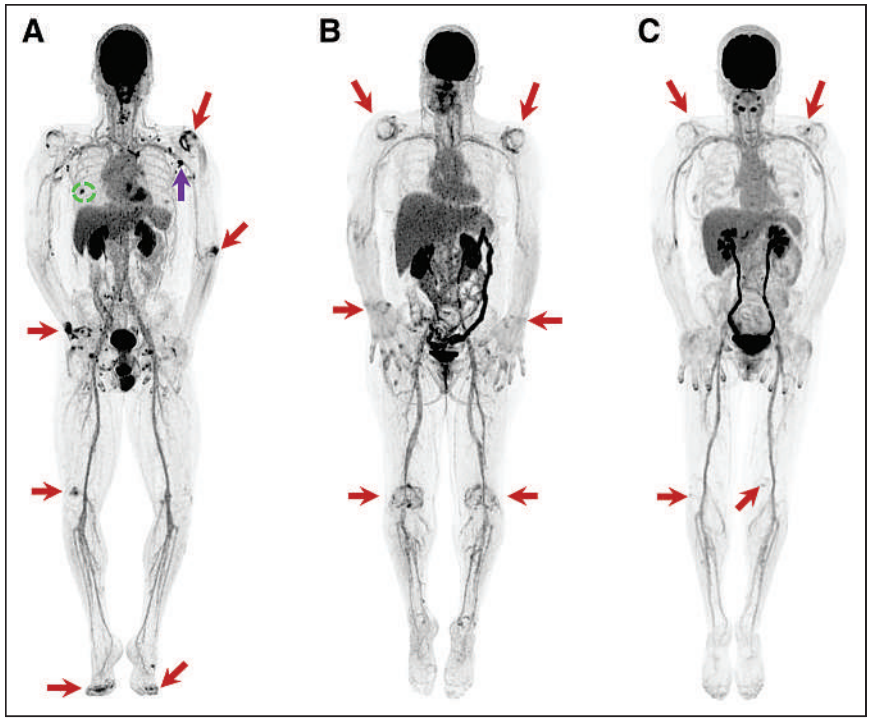

FIGURE 1. Total-body ^{18}F-FDG PET uptake in participants with AIA compared with those with OA, shown as maximum-intensity projections (MIPs). (A) A 33-y-old man with PsA, showing asymmetric polyarthritis involving left shoulder, left elbow, right wrist, right knee, and small joints of the hands and feet (arrows). (B) A 59-y-old woman with RA, showing mostly bilateral symmetric joint involvement of the shoulders and knees, and to lesser extent the wrist joints. (C) A 64-y-old woman with OA, presenting primarily mild-to-moderate uptake at fewer joints (shoulders and knees) commonly involved in this condition. Several extraarticular findings are noted in A, including ^{18}F-FDG–avid bilateral axillary and left supraclavicular lymph nodes. Left side uptake is secondary to COVID vaccination (purple arrow), and the active spot (dashed circle) seen opposite the inferior angle of the scapula corresponds to inflamed scapulothoracic bursa.

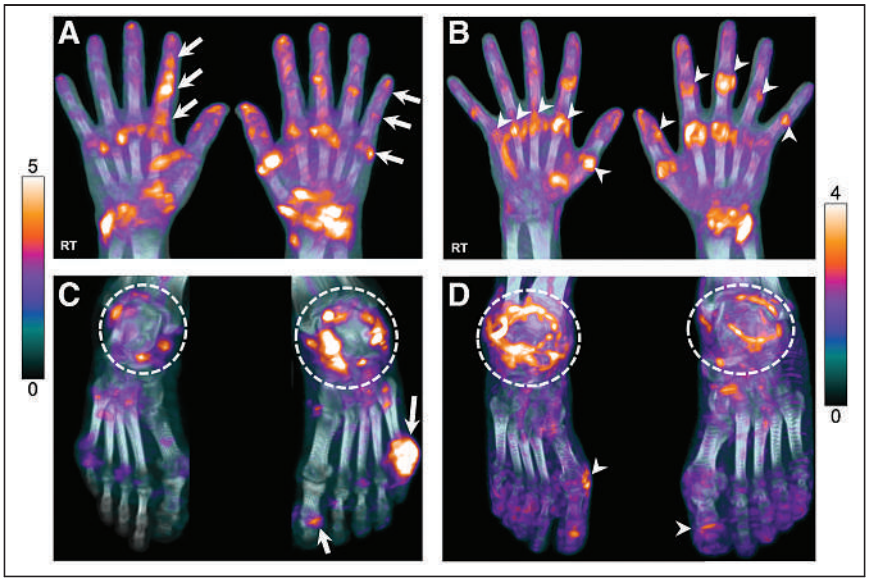

FIGURE 2. ^{18}F-FDG uptake in hands and feet of participants with AIA. (A) A 54-y-old man with PsA showing elevated uptake at multiple hand joints. Raylike distribution, as indicated by arrows, in metacarpophalangeal (MCP), proximal interphalangeal (PIP), and distal interphalangeal (DIP) joints in sequence, attributed to involvement of flexor or extensor tendons. (B) A 47-y-old woman with RA, showing involvement of entire row of MCP (arrowheads, right hand) and PIP/interphalangeal (IP) joints (arrowheads, left hand). (C) Feet images of same PsA participant in A, demonstrating increased uptake at ankle joints (dashed circles), more intense on the left side, and left first IP and fifth metatarsophalangeal (MTP) joints (arrows). (D) Feet images of a 71-y-old man with RA, demonstrating bilateral, rather symmetric, uptake around ankles as well as right first MTP and left first IP joints, suggestive of synovitis (arrowheads).

participant positioning, acquisition, reconstruction, and image assessment are provided in the supplemental materials (supplemental materials are available at http://jnm.snmjournals.org). TB PET/CT image assessments were reported qualitatively for each of the 68 joints using a modified 4-point Likert scale (*5*): 0, no uptake; 1, mild uptake comparable to the surrounding background; 2, moderate uptake higher than the surrounding background and comparable to blood pool (BP) at the ascending aorta; and 3, marked uptake higher than BP. For binary analyses, any uptake with a score of ≥ 2 was considered positive. SUV_{max} was measured on 2.344-mm isotropic voxel reconstructions with no point-spread function modeling or postprocessing smoothing. Measurements were performed only for joints that scored ≥ 1. Values were reported as a ratio ($rSUV_{max}$) between the joint SUV_{max} normalized by the BP SUV_{mean}. Positive joint count, summed qualitative scores, and summed $rSUV_{max}$ were derived for each scan. Further, a composite measure (PET_{comp}) was calculated analogous to the DAPSA score (*20*) as the sum of positive joints from PET, patient-reported outcomes of joint pain and activity (each between 1 to 10), and serum CRP level in mg/dL.

Statistical Analysis

Continuous variables were compared between 2 independent categoric groups using the Mann–Whitney *U* test. Association between categoric variables was assessed using the Fisher exact test. Correlation between 2 continuous measures was calculated using Spearman ρ. All analyses were performed using SPSS, version 21 (IBM Corp.).

RESULTS

Participant Characteristics

Thirty participants (24 with established AIA [15 PsA and 9 RA], and 6 with non-AIA [OA]; 7 women and 23 men), with a median age of 63.5 y (age range: 28–77 y), were evaluated. Characteristics of the participants and outcomes of their rheumatologic assessments are presented in Table 1. As expected, participants with AIA had higher positive joint counts than those without AIA. There was no difference in participant characteristics or rheumatologic assessments between individuals with PsA and RA.

TB PET/CT Systemic Joint Evaluation

All participants completed their TB PET/CT scans. Figure 1 shows PET maximum-intensity-projection (MIP) images for representative participants. Of a total of 2,040 joints (30 participants × 68 joints per participant), 43 (~2%) joints from 6 participants with AIA could not be adequately evaluated from the scans (due to prosthesis [8 joints], significant motion [30 joints], or being outside the PET and CT FOV [5 elbow joints]). Thus, the analysis presented is for 1,997 evaluable joints.

Most participants with AIA (23/24, 95.8%) presented with peripheral polyarthritis apparent on TB PET/CT. Figure 2 shows images of the hands and feet of representative study participants with AIA. Table 2 provides details of joints with positive TB PET/CT findings.

Comparison of TB PET/CT Assessments with Rheumatologic Outcome Measures

Qualitative Evaluation. In the AIA cohort, of 1,589 joints evaluated, 69.9% showed concordance between the TB PET and joint-by-joint rheumatologic evaluation (Table 3). An additional 20.1% were positive on TB PET but negative on rheumatologic examination. Finally, 10.0% were negative on TB PET but positive on rheumatologic evaluation. Supplemental Table 1 summarizes the distribution of the 159 joints in the latter category. Of these joints, 148 (93.0%) were small joints of the hands or feet, and 136 of the 148 joints (91.9%) were just tender on physical examination with no objective evidence of swelling or redness. In OA participants, concordance between TB PET and joint-by-joint rheumatologic evaluation was 91.2%. An additional 8.8% of joints were positive on TB PET but negative on rheumatologic examination, whereas no joints were negative on TB PET and positive on rheumatologic examination (Table 3).

Quantitative Evaluation. Quantitative ^{18}F-FDG TB PET/CT findings in joints are summarized in Table 4. Imaging metrics were higher in AIA participants than in non-AIA participants. Systemic ^{18}F-FDG TB PET metrics showed moderate-to-strong correlation with the DAPSA and DAS-28 scores (Table 5). The correlation coefficient was higher with DAS-28 because the measure does not involve assessment of the hand DIP or any foot joints.

DISCUSSION

We report articular findings from first-in-humans ^{18}F-FDG TB PET/CT scans in an AIA and non-AIA (OA) population. The entire adult human body was imaged in a single bed position in the same phase of radiotracer uptake. An ultra-low-dose protocol was implemented. The ability of assessing ^{18}F-FDG uptake for both large and small joints across the body was demonstrated.

Early diagnosis of AIA and initiation of treatment at its onset is essential to achieve clinical remission or at least low or minimal

TABLE 2
Frequency and Distribution of Positive Joints on ^{18}F-FDG TB PET/CT

Joint group	Specific joint(s)	Positive joint count/no. of participants (average)	
		Non-AIA	AIA
Hand joints	First IP and 2-fifth PIP	6/2 (3.0)	82/17 (4.8)
	1st-5th MCP	1/1 (1.0)	71/15 (4.7)
	2nd-5th DIP	0/0 (0)	38/10 (3.8)
	Sum	7/2 (3.5)	191/20 (9.6)
Feet joints	First IP, 2nd-5th PIP and DIP	0/0 (0)	15/5 (3.0)
	1st-5th MTP	4/3 (1.3)	41/10 (4.1)
	Sum	4/3 (1.3)	56/11 (5.1)
Upper limb joints	Gleno-humeral	6/4 (1.5)	37/21 (1.8)
	Acromio-clavicular	3/2 (1.5)	23/13 (1.8)
	Sterno-clavicular	3/3 (1.0)	26/17 (1.5)
	Elbows	3/2 (1.5)	11/8 (1.4)
	Wrists	4/2 (2.0)	31/19 (1.6)
	Sum	19/5 (3.8)	128/22 (5.8)
Lower limb joints	Hips	5/3 (1.7)	22/13 (1.7)
	Knees	1/1 (1.0)	20/14 (1.4)
	Talo-tibial	3/2 (1.5)	20/12 (1.7)
	Midtarsal and subtalar	0/0 (0)	17/12 (1.4)
	Sum	9/4 (2.3)	79/21 (3.8)
Temporomandibular joints		0/0 (0)	9/6 (1.5)
Sum of all positive joints/participants (average)		39/6 (6.5)	463/23 (20.1)

Data in parentheses are percentages.
IP = interphalangeal; PIP = proximal interphalangeal; MCP = metacarpophalangeal; DIP = distal interphalangeal; MTP = metatarsophalangeal.

disease activity (*22,23*). There is currently no validated diagnostic test for PsA (*24*), and clinical assessments for AIA are suboptimal (*2*). Therefore, the ability to perform a systemic evaluation of AIA-associated joint inflammatory activity in a quantitative manner on a per-patient basis via TB PET/CT, as demonstrated by our study, could offer an important tool to the rheumatology community. Furthermore, TB PET/CT could be useful to monitor response to therapies on a personalized basis and justify cessation, reduction or switching to another line of treatment (*24–26*). Beyond joints, TB PET/CT provides the visualization of other tissues that AIA may impact, such as the axial skeleton, entheses, digits (dactylitis), and nail and skin, as well as organs such as heart, brain, liver, kidneys, and skeletal muscle (*27,28*). Future investigations in assessing the impact of AIA on these tissues could further expand our understanding of the disease process.

Our findings indicate that 20.1% of AIA joints deemed negative on rheumatologic examination were PET-positive. This mismatch has also been reported by other PET studies (*4,8,29*). It is plausible

TABLE 3
Qualitative ^{18}F-FDG TB PET/CT Findings in Joints in Comparison with Rheumatologic Examination

^{18}F-FDG TB PET evaluation	Rheumatologic examination			
	AIA		Non-AIA	
	Negative	Positive (T/S/TS)	Negative	Positive (T/S/TS)
Negative	967	159 (146/4/9)	369	0
Positive	320	143 (117/3/23)	36	3 (3/0/0)
Total (n = 1997)*	1287	302	405	3

*Forty-three joints in AIA participants were unevaluable on PET; 6 of them were tender on rheumatologic examination.
T = only tender; S = only swollen; TS = tender and swollen.

TABLE 4
Quantitative Findings from ^{18}F-FDG TB PET/CT–Positive Joints

^{18}F-FDG PET metrics derived from …	Non-AIA (n = 6)	AIA (n = 24)	P
68 Joints			
Positive count	6.5 ± 4.9 (2–14)	19.3 ± 12.6 (0–49)	0.01
Summed scores	14.2 ± 10.7 (4–30)	44.5 ± 30.2 (0–124)	0.01
Summed $rSUV_{max}$	10.7 ± 8.7 (2.9–25.2)	28.6 ± 19.3 (1.5–90.2)	0.001
28 Joints			
Positive count	3.5 ± 2.7 (0–7)	10.7 ± 7.6 (0–26)	0.02
Summed scores	7.7 ± 5.9 (0–14)	24.1 ± 17.1 (0–64)	0.02
Summed $rSUV_{max}$	6.7 ± 4.1 (1.8–12.5)	16.3 ± 11.1 (4.2–50.3)	0.001

Values are reported as mean ± SD (minimum–maximum).
$rSUV_{max}$ = ratio between joint SUV_{max} and blood pool SUV_{mean}.

to hypothesize that ^{18}F-FDG PET, due to its ability to detect cellular metabolic activity, is sensitive to subclinical AIA inflammation that may be occult on rheumatologic evaluation but may play a role in joint damage (*30*). Future studies with short- and long-term follow-up will be needed to test this hypothesis. On the other hand, 10.0% joints that were positive on rheumatologic evaluation were PET-negative. There could be 3 possible reasons for this discrepancy. First, 93.6% of these joints were assessed as being tender on rheumatologic evaluation. Tenderness alone in established AIA may not reflect active inflammation (*31–33*). Furthermore, inclusion of the tender joint count in rheumatologic assessment may confound evaluation of AIA inflammatory activity (*34*). Our results support this premise and could help better establish the clinical value of tenderness in AIA evaluation, with or without synovitis or swelling. The second reason could be the limited TB PET spatial resolution (~3 mm (*13*)) for the small joints of the hand and feet. The reconstructed radiotracer uptake was likely underestimated for the small joints; data suggest that the contrast recovery coefficient for a 10-mm sphere with 4-to-1 source-to-background ratio and using the same reconstruction method used here is approximately 50% (*13*). The quantification of small lesion activity could likely be improved with the implementation of advanced image reconstruction methods developed specifically for TB PET/CT (*35*). Spatial resolution is particularly important in AIA imaging, as AIA may coexist with OA or another musculoskeletal condition in the same anatomic region (e.g., small joints of the hand (*7*)), and defining the pattern may be critical for differential diagnosis (*22*). Finally, despite the use of positioning aids, intrascan motion likely confounded the evaluation of the small joints of the hand and feet. Impact of motion could be mitigated by shortening image acquisition time or retrospective temporal binning of the data into shorter frames and either software-driven motion correction or choosing frames with the least intrascan motion (*36*). For shortening the image acquisition time while maintaining the signal-to-noise ratio, an increase in the injected dose may be necessary. On the other hand, advanced low-count image reconstruction methods (*35*) will be essential when using short frames.

TABLE 5
Spearman Correlation (ρ) Between Systemic Joint Measures from ^{18}F-FDG TB PET/CT and Rheumatologic Assessments

	Rheumatologic assessments	
^{18}F-FDG PET metrics	DAPSA score (n = 15 with PsA)	DAS-28-CRP (n = 24 with AIA)
68 Joints		
Positive count	0.61* (0.10–0.88)	0.62† (0.30–0.82)
Summed scores	0.61* (0.08–0.89)	0.61† (0.27–0.83)
Summed $rSUV_{max}$	0.56* (0.03–0.86)	0.53† (0.18–0.77)
PET_{comp}‡	0.63* (0.17–0.87)	0.70* (0.40–0.86)
28 Joints		
Positive count	0.55* (0.06–0.89)	0.68† (0.40–0.86)
Summed scores	0.57* (0.09–0.89)	0.68† (0.39–0.87)
Summed $rSUV_{max}$	0.53* (0.01–0.87)	0.60† (0.29–0.84)

*$P < 0.05$.
†$P < 0.01$.
‡PET_{comp} = positive joint count + patient-reported joint activity + patient-reported joint pain + CRP.
Values are given as Spearman ρ-coefficient (with 95% CIs in parentheses). Because DAPSA score is not validated for evaluating RA, data under the DAPSA column are extracted from participants with PsA, whereas data under DAS-28-CRP are extracted from all the 24 participants with AIA.

Because of the high sensitivity of the TB PET/CT system (*13*), an ultra-low-dose protocol was implemented. Our findings are overall consistent with documented patterns of joint involvement in AIA, and with the findings of previous studies (*4–6,8,37,38*), though those studies used a 3- to 5-times higher injected dose than that used in our study. Dose is a significant limitation for the broader adoption of PET/CT technology in AIA (*9,10*), given its chronic nature and the potential need for monitoring disease activity in both treatment responders and nonresponders. Low-dose approaches such as those used in our work could therefore provide means for the rheumatology community to capitalize on the benefits offered by TB PET/CT.

A 40-min ^{18}F-FDG uptake time was used based on the tracer's arterial blood clearance characteristics (*39,40*), with a 20-min scan time, and data were reconstructed into a single frame matching our current clinical protocols (*41*). Our pilot data recently showed that shorter scans may provide reasonable image quality (*42*). These shorter scans need further validation; however, they could motivate

the creation of more practical scanning protocols suitable for the AIA population that experiences significant difficulty in tolerating long scan times. The shorter frames could also enable future classification of ^{18}F-FDG kinetics in lesions over the 20-min window and provide additional biomarkers, such as those from relative Patlak plots (*43*). Furthermore, the 40- to 60-min scanning window used will allow future exploration of optimizing the scan start time within that window.

Our study has limitations. First, this was a feasibility study with a modest sample size. Second, this was a cross-sectional study with participants enrolled with different levels of AIA disease activity, and the treatments they were receiving could have affected the PET findings. Follow-up TB PET imaging will be essential to establish the test–retest reliability in this patient population. Third, semiquantitative SUV_{max}-based measures were used and other measures, such as metabolically active volume, can be considered in the future. Fourth, our ultra-low-dose CT protocol, while supporting PET attenuation correction and anatomic localization, resulted in an overall low CT image quality. An increase in dose and deployment of recently developed machine-learning–based methods for low-dose CT reconstruction (*44*) could be helpful to address this limitation and to assess the added value of CT-based joint findings. Fifth, the transaxial FOV was not sufficient to capture the elbows consistently. Positioning schemes that would enable the capture of all joints of the body will be helpful to implement in the future. Sixth, the study was not powered to assess differences in PET uptake patterns between the AIA subtypes. Finally, we did not compare our findings with those from other imaging modalities such as ultrasound or MRI. These studies could help define the future role of TB PET/CT for AIA assessment compared with other imaging modalities.

CONCLUSION

The feasibility of acquiring ^{18}F-FDG TB PET/CT scans in participants with AIA, and a non-AIA comparator group, at an ultra-low dose was demonstrated. TB PET/CT enabled the acquisition of joints of the entire body, including hands and feet, in a single bed position, and in the same phase of radiotracer uptake. A range of pathologies consistent with AIA (and non-AIA) were visualized, and the feasibility of extracting PET measures from anatomic sites commonly examined clinically (68 and 28 joints) was demonstrated. Quantitative measures from TB PET/CT demonstrated a moderate-to-strong correlation with outcomes of AIA rheumatologic assessments. These results provide the foundation for future studies to substantiate these findings and quantitatively evaluate the improvements possible in AIA assessment via the TB PET/CT technology.

DISCLOSURE

University of California Davis has a research and a revenue-sharing agreement with United Imaging Health Care. Ramsey D. Badawi, Simon R. Cherry, and Lorenzo Nardo are investigators on a research grant funded by United Imaging Health Care, the manufacturer of the scanner used in this article. The work is supported in part by the National Institutes of Health (NIH R01 AR076088 and R01 CA206187) and the National Psoriasis Foundation. No other potential conflict of interest relevant to this article was reported.

ACKNOWLEDGMENTS

We thank Dr. Fatma Sen, Mr. John Brock, Mr. Ofilio Vigil, Ms. Lynda Painting, and Ms. Dana Little from the University of California, Davis for their support.

KEY POINTS

QUESTION: Is it feasible to assess joint involvement in autoimmune arthritis using ^{18}F-FDG and an ultra-low-dose protocol on a TB PET/CT scanner?

PERTINENT FINDINGS: In this prospective study, systemic joint involvement in participants with autoimmune arthritis was successfully visualized and ^{18}F-FDG uptake per joint was quantified. Results showed a high concordance of TB PET/CT measures with joint-by-joint rheumatologic evaluation and moderate-to-strong correlation with rheumatologic outcome measures. ^{18}F-FDG TB PET/CT was positive for 20% of joints deemed negative on rheumatologic examination, suggestive of its ability to potentially detect subclinical disease activity.

IMPLICATIONS FOR PATIENT CARE: Evaluation of autoimmune arthritis is feasible using ultra-low-dose, ^{18}F-FDG TB PET/CT scans.

REFERENCES

1. Sweeney SE, Firestein GS. Rheumatoid arthritis: regulation of synovial inflammation. *Int J Biochem Cell Biol.* 2004;36:372–378.
2. Pincus T. Limitations of a quantitative swollen and tender joint count to assess and monitor patients with rheumatoid arthritis. *Bull NYU Hosp Jt Dis.* 2008;66:216–223.
3. Hensor EMA, Conaghan PG. Time to modify the DAS28 to make it fit for purpose(s) in rheumatoid arthritis? *Expert Rev Clin Immunol.* 2020;16:1–4.
4. Beckers C, Ribbens C, Andre B, et al. Assessment of disease activity in rheumatoid arthritis with ^{18}F-FDG PET. *J Nucl Med.* 2004;45:956–964.
5. Goerres GW, Forster A, Uebelhart D, et al. F-18 FDG whole-body PET for the assessment of disease activity in patients with rheumatoid arthritis. *Clin Nucl Med.* 2006;31:386–390.
6. Yamashita H, Kubota K, Mimori A. Clinical value of whole-body PET/CT in patients with active rheumatic diseases. *Arthritis Res Ther.* 2014;16:423.
7. Chaudhari AJ, Ferrero A, Godinez F, et al. High-resolution ^{18}F-FDG PET/CT for assessing disease activity in rheumatoid and psoriatic arthritis: findings of a prospective pilot study. *Br J Radiol.* 2016;89:20160138.
8. Lee SJ, Jeong JH, Lee CH, et al. Development and validation of an ^{18}F-fluorodeoxyglucose-positron emission tomography with computed tomography-based tool for the evaluation of joint counts and disease activity in patients with rheumatoid arthritis. *Arthritis Rheumatol.* 2019;71:1232–1240.
9. McQueen FM. Imaging in early rheumatoid arthritis. *Best Pract Res Clin Rheumatol.* 2013;27:499–522.
10. Bruijnen ST, Gent YY, Voskuyl AE, Hoekstra OS, van der Laken CJ. Present role of positron emission tomography in the diagnosis and monitoring of peripheral inflammatory arthritis: a systematic review. *Arthritis Care Res (Hoboken).* 2014;66:120–130.
11. Kubota K, Ito K, Morooka M, et al. FDG PET for rheumatoid arthritis: basic considerations and whole-body PET/CT. *Ann N Y Acad Sci.* 2011;1228:29–38.
12. Narayan N, Owen DR, Taylor PC. Advances in positron emission tomography for the imaging of rheumatoid arthritis. *Rheumatology (Oxford).* 2017;56:1837–1846.
13. Spencer BA, Berg E, Schmall JP, et al. Performance evaluation of the uEXPLORER total-body PET/CT scanner based on NEMA NU 2-2018 with additional tests to characterize PET scanners with a long axial field of view. *J Nucl Med.* 2021;62:861–870.
14. Karp JS, Viswanath V, Geagan MJ, et al. PennPET Explorer: design and preliminary performance of a whole-body imager. *J Nucl Med.* 2020;61:136–143.
15. Prenosil GA, Sari H, Fürstner M, et al. Performance characteristics of the Biograph Vision Quadra PET/CT system with a long axial field of view using the NEMA NU 2-2018 standard. *J Nucl Med.* 2022;63:476–484.
16. Hu Y, Liu G, Yu H, et al. Feasibility of ultra-low ^{18}F-FDG activity acquisitions using total-body PET/CT. *J Nucl Med.* 2022;63:959–965.
17. Taylor W, Gladman D, Helliwell P, et al. Classification criteria for psoriatic arthritis: development of new criteria from a large international study. *Arthritis Rheum.* 2006;54:2665–2673.
18. Aletaha D, Neogi T, Silman AJ, et al. 2010 Rheumatoid arthritis classification criteria: an American College of Rheumatology/European League Against Rheumatism collaborative initiative. *Arthritis Rheum.* 2010;62:2569–2581.

19. Kolasinski SL, Neogi T, Hochberg MC, et al. 2019 American College of Rheumatology/Arthritis Foundation guideline for the management of osteoarthritis of the hand, hip, and knee. *Arthritis Care Res (Hoboken).* 2020;72:149–162.
20. Smolen JS, Breedveld FC, Burmester GR, et al. Treating rheumatoid arthritis to target: 2014 update of the recommendations of an international task force. *Ann Rheum Dis.* 2016;75:3–15.
21. Prevoo ML, van 't Hof MA, Kuper HH, van Leeuwen MA, van de Putte LB, van Riel PL. Modified disease activity scores that include twenty-eight-joint counts. Development and validation in a prospective longitudinal study of patients with rheumatoid arthritis. *Arthritis Rheum.* 1995;38:44–48.
22. Gossec L, Smolen JS, Ramiro S, et al. European League Against Rheumatism (EULAR) recommendations for the management of psoriatic arthritis with pharmacological therapies: 2015 update. *Ann Rheum Dis.* 2016;75:499–510.
23. Smolen JS, Landewe RBM, Bijlsma JWJ, et al. EULAR recommendations for the management of rheumatoid arthritis with synthetic and biological disease-modifying antirheumatic drugs: 2019 update. *Ann Rheum Dis.* 2020;79:685–699.
24. Ng BCK, Jadon DR. Unmet needs in psoriatic arthritis. *Best Pract Res Clin Rheumatol.* 2021;35:101693.
25. Bouman CA, van Herwaarden N, van den Hoogen FH, et al. Long-term outcomes after disease activity-guided dose reduction of TNF inhibition in rheumatoid arthritis: 3-year data of the DRESS study—a randomised controlled pragmatic non-inferiority strategy trial. *Ann Rheum Dis.* 2017;76:1716–1722.
26. Merola JF, Lockshin B, Mody EA. Switching biologics in the treatment of psoriatic arthritis. *Semin Arthritis Rheum.* 2017;47:29–37.
27. Figus FA, Piga M, Azzolin I, McConnell R, Iagnocco A. Rheumatoid arthritis: extra-articular manifestations and comorbidities. *Autoimmun Rev.* 2021;20:102776.
28. Van den Bosch F, Coates L. Clinical management of psoriatic arthritis. *Lancet.* 2018;391:2285–2294.
29. Kothekar E, Revheim ME, Borja AJ, et al. Utility of FDG-PET/CT in clinical psoriasis grading: the PET-PASI scoring system . *Am J Nucl Med Mol Imaging.* 2020;10:265–271.
30. Suto T, Okamura K, Yonemoto Y, Okura C, Tsushima Y, Takagishi K. Prediction of large joint destruction in patients with rheumatoid arthritis using ^{18}F-FDG PET/CT and disease activity score. *Medicine (Baltimore).* 2016;95:e2841.
31. Collison J. Tender joints might not indicate inflammation. *Nat Rev Rheumatol.* 2019;15:2.
32. Gessl I, Popescu M, Schimpl V, et al. Role of joint damage, malalignment and inflammation in articular tenderness in rheumatoid arthritis, psoriatic arthritis and osteoarthritis. *Ann Rheum Dis.* 2021;80:884–890.
33. Felbo SK, Wiell C, Østergaard M, et al. Do tender joints in active psoriatic arthritis reflect inflammation assessed by ultrasound and magnetic resonance imaging? *Rheumatology (Oxford).* 2022;61:723–733.
34. Hammer HB, Michelsen B, Provan SA, et al. Tender Joint count and inflammatory activity in patients with established rheumatoid arthritis: results from a longitudinal study. *Arthritis Care Res (Hoboken).* 2020;72:27–35.
35. Qi J, Matej S, Wang G, Zhang X. 3D/4D reconstruction and quantitative total body imaging. *PET Clin.* 2021;16:41–54.
36. Berg E, Revilla EM, Abdelhafez YG, et al. Framework design for comprehensive patient motion compensation in total-body PET [abstract]. Presented at: the virtual meeting of the IEEE Nuclear Science Symposium & Medical Imaging Conference, November 4–8, 2020. https://www.eventclass.org/contxt_ieee2020/online-program/session?s=M-10. Accessed September 2, 2022.
37. Roivainen A, Parkkola R, Yli-Kerttula T, et al. Use of positron emission tomography with methyl-^{11}C-choline and 2-^{18}F-fluoro-2-deoxy-D-glucose in comparison with magnetic resonance imaging for the assessment of inflammatory proliferation of synovium. *Arthritis Rheum.* 2003;48:3077–3084.
38. Kubota K, Ito K, Morooka M, et al. Whole-body FDG-PET/CT on rheumatoid arthritis of large joints. *Ann Nucl Med.* 2009;23:783–791.
39. Vriens D, de Geus-Oei LF, Oyen WJ, Visser EP. A curve-fitting approach to estimate the arterial plasma input function for the assessment of glucose metabolic rate and response to treatment. *J Nucl Med.* 2009;50:1933–1939.
40. Keramida G, Anagnostopoulos CD, Peters AM. The extent to which standardized uptake values reflect FDG phosphorylation in the liver and spleen as functions of time after injection of ^{18}F-fluorodeoxyglucose. *EJNMMI Res.* 2017;7:13.
41. Ng QK, Triumbari EKA, Omidvari N, Cherry SR, Badawi RD, Nardo L. Total-body PET/CT: first clinical experiences and future perspectives. *Semin Nucl Med.* 2022;52:330–339.
42. Abdelhafez Y, Hunt H, Caudle D, et al. Ultra-low-dose total-body ^{18}F-FDG PET/CT in patients with autoimmune inflammatory arthritis: evaluation of image quality with shorter scan time. *J Nucl Med.* 2021;62:1697.
43. Zuo Y, Qi J, Wang G. Relative Patlak plot for dynamic PET parametric imaging without the need for early-time input function. *Phys Med Biol.* 2018;63:165004.
44. Wu D, Kim K, El Fakhri G, Li Q. Iterative low-dose CT reconstruction with priors trained by artificial neural network. *IEEE Trans Med Imaging.* 2017;36:2479–2486.

PET Imaging of System x_C^- in Immune Cells for Assessment of Disease Activity in Mice and Patients with Inflammatory Bowel Disease

Minjung Seo*[1], Yeji Kim*[2], Byong Duk Ye*[3], Sang Hyoung Park[3], Seog-Young Kim[2], Jin Hwa Jung[2], Sung Wook Hwang[3], Sun Young Chae[4], Dong Yun Lee[4], Sang Ju Lee[4], Seung Jun Oh[4], Jihun Kim[5], Ji Young Kim[6], Sae Jung Na[7], Misung Kim[8], Sang-Yeob Kim[2], Norman Koglin[9], Andrew W. Stephens[9], Mi-Na Kweon[2], and Dae Hyuk Moon[4]

[1]*Department of Nuclear Medicine, Ulsan University Hospital, University of Ulsan College of Medicine, Ulsan, Republic of Korea;* [2]*Department of Convergence Medicine, Asan Medical Center, University of Ulsan College of Medicine, Seoul, Republic of Korea;* [3]*Department of Gastroenterology, Asan Medical Center, University of Ulsan College of Medicine, Seoul, Republic of Korea;* [4]*Department of Nuclear Medicine, Asan Medical Center, University of Ulsan College of Medicine, Seoul, Republic of Korea;* [5]*Department of Pathology, Asan Medical Center, University of Ulsan College of Medicine, Seoul, Republic of Korea;* [6]*Department of Nuclear Medicine, Hanyang University Medical Center, Hanyang University College of Medicine, Seoul, Republic of Korea;* [7]*Department of Radiology, Uijeongbu St. Mary's Hospital, College of Medicine, Catholic University of Korea, Seoul, Republic of Korea;* [8]*Department of Pathology, Ulsan University Hospital, Ulsan, Republic of Korea; and* [9]*Life Molecular Imaging GmbH, Berlin, Germany*

We aimed to explore whether the imaging of antiporter system x_C^- of immune cells with (4*S*)-4-(3-^{18}F-fluoropropyl)-L-glutamate (^{18}F-FSPG) PET can assess inflammatory bowel disease (IBD) activity in murine models and patients (NCT03546868). **Methods:** ^{18}F-FSPG PET imaging was performed to assess IBD activity in mice with dextran sulfate sodium-induced and adoptive T-cell transfer–induced IBD and a cohort of 20 patients at a tertiary care center in South Korea. Immunohistochemical analysis of system x_C^- and cell surface markers was also studied. **Results:** Mice with experimental IBD showed increased intestinal ^{18}F-FSPG uptake and xCT expression in cells positive (+) for CD11c, F4/80, and CD3 in the lamina propria, increases positively associated with clinical and pathologic disease activity. ^{18}F-FSPG PET studies in patients, most of whom were clinically in remission or had mildly active IBD, showed that PET imaging was sufficiently accurate in diagnosing endoscopically active IBD and remission in patients and bowel segments. ^{18}F-FSPG PET correctly identified all 9 patients with superficial or deep ulcers. Quantitative intestinal ^{18}F-FSPG uptake was strongly associated with endoscopic indices of IBD activity. The number of $CD68^+xCT^+$ and $CD3^+xCT^+$ cells in 22 bowel segments from patients with ulcerative colitis and the number of $CD68^+xCT^+$ cells in 7 bowel segments from patients with Crohn disease showed a significant positive association with endoscopic indices of IBD activity. **Conclusion:** The assessment of system x_C^- in immune cells may provide diagnostic information on the immune responses responsible for chronic active inflammation in IBD. ^{18}F-FSPG PET imaging of system x_C^- activity may noninvasively assess the IBD activity.

Key Words: system x_C^-; immune cells; PET; inflammatory bowel disease

J Nucl Med 2022; 63:1586–1591
DOI: 10.2967/jnumed.121.263289

Inflammatory bowel disease (IBD) consists of 2 types of chronic incurable intestinal disorders, ulcerative colitis (UC) and Crohn disease (CD). Tight monitoring of disease activity is essential throughout the course of the disease to guide therapeutic decisions and assess response to therapy and relapse (*1,2*). Although endoscopic mucosal healing is a long-term goal of therapy, endoscopic evaluation may not always be feasible because of lack of immediate availability, cost, need for bowel preparation, relatively poor patient acceptance, and complications. Less invasive markers of disease activity are therefore needed.

Key immune processes involved in the pathogenesis of IBD include cytokine production by activated dendritic cells and macrophages, and the development of effector T lymphocyte subsets (*3*). Targeting dysfunctional immune cells and their products has led to the development of new therapies that have benefited patients (*3*). Similarly, a noninvasive method that targets dysfunctional immune cells, distinguishing between active cell subsets and quiescent cell populations, may allow specific assessment of disease activity, rather than relying on nonspecific indicators of disease activity (*4*).

System x_C^- plays an important role in the regulation of the innate and adaptive immune systems (*5*) and is upregulated in activated macrophages (*6,7*). On antigen stimulation, proliferating T cells require sufficient glutathione levels to ensure proper reactive oxygen species balance, resulting in the induction of high levels of xCT for cystine uptake (*8,9*). An *ex vivo* study on patients with IBD has shown that intestinal lamina propria macrophages expressed xCT, which resulted in high glutathione levels and full T-cell receptor reactivity (*10*). All these results suggest that system x_C^- could be a specific indicator of disease activity in IBD. Research designed to characterize the functional relevance of system x_C^- in disease states with oxidative stress and inflammation might pave the way for diagnosing and treating IBD (*5*).

(4*S*)-4-(3-^{18}F-fluoropropyl)-L-glutamate (^{18}F-FSPG) is a ^{18}F-labeled L-glutamate derivative that is specifically taken up by system x_C^- (*11*). An exploratory clinical study has shown that ^{18}F-FSPG PET can detect inflammation of the lungs and sarcoidosis (*12*). The low

Received Oct. 6, 2021; revision accepted Jan. 18, 2022.
For correspondence or reprints, contact Dae Hyuk Moon (dhmoon@amc.seoul.kr) or Mi-Na Kweon (mnkweon@amc.seoul.kr).
*Contributed equally to this work.
Published online Jan. 27, 2022.

background uptake of ^{18}F-FSPG would be especially advantageous in detecting inflammatory lesions in the intestine (*12,13*), an organ in which the use of conventional ^{18}F-FDG imaging may be limited because of physiologic uptake. ^{18}F-FDG PET may also be limited in differentiating mildly active IBD from endoscopic remission (*14,15*), showing an adequate accuracy only for detecting moderate-to-severe endoscopic disease (*16,17*). The objective of this study was to evaluate whether the *in vivo* assessment of system x_C^- in immune cells provides information on the dysregulated immune responses responsible for chronic active inflammation in IBD, thereby assessing the disease activity. We first conducted animal experiments to investigate whether ^{18}F-FSPG would have increased accumulation associated with xCT expression in immune cells. Second, we aimed to explore the diagnostic validity of ^{18}F-FSPG PET/CT in patients. Finally, we assessed the association of ^{18}F-FSPG uptake and xCT expression in immune cells with endoscopic markers.

MATERIALS AND METHODS

Experimental IBD Models, ^{18}F-FSPG PET Imaging, and *Ex Vivo* Analysis

The research protocol was approved by the Institutional Animal Care and Use Committee (registration numbers 2016-12-153 and 2017-12-017). All animal experiments conformed to the institutional guidelines. Experimental details are reported in accordance with the ARRIVE guidelines, version 2.0 (Animal Research: Reporting of In Vivo Experiments). Dextran sulfate sodium (DSS)–induced and adoptive T-cell transfer–induced IBD models were evaluated. Details of clinical disease activity, *ex vivo* analysis, and immunohistochemical staining for expression of xCT and cell surface markers are provided in the supplemental methods (supplemental materials are available at http://jnm.snmjournals.org).

Clinical Study Design and Patients

This was a prospective, nonrandomized, single-center cohort study. The study protocol, provided in the supplemental materials, was approved by the Ministry of Food and Drug Safety of the Republic of Korea and the institutional review board of Asan Medical Center (approval 2018-0262). This trial was conducted in accordance with the Declaration of Helsinki and institutional guidelines. All patients provided written informed consent before participation. The primary objective was to explore the validity of ^{18}F-FSPG PET/CT for the diagnosis of patients with active IBD. The secondary objectives were to explore the validity of ^{18}F-FSPG PET/CT for detecting bowel segments with active IBD; to assess the correlation of ^{18}F-FSPG activity with clinical, endoscopic, and biologic markers of disease activity; to assess the interreader variability of visual ^{18}F-FSPG PET/CT interpretation, and to evaluate the safety of ^{18}F-FSPG PET/CT. Intended enrollment included 10 patients with UC and 10 with CD, numbers regarded as sufficient to obtain PET/CT imaging information while avoiding unnecessary exposure to ionizing radiation. The trial was registered at http://clinicaltrials.gov as NCT03546868.

Patients eligible for inclusion were consecutive adults aged between 19 and 79 y who had UC or CD, as diagnosed clinically, endoscopically, and histologically. The complete inclusion and exclusion criteria are listed in the supplemental methods. All cases were identified on the basis of presenting symptoms, as evaluated by 3 of the authors at the Department of Gastroenterology.

^{18}F-FSPG PET/CT Imaging of Patients

Patients were asked to fast for at least 4 h before being administered ^{18}F-FSPG (8 h if they were on a high-protein diet). A dose of 200 ± 20 MBq of ^{18}F-FSPG was administered as a slow intravenous bolus injection for up to 60 s. Sixty minutes later, PET/CT was performed from the abdomen to the pelvis, with an acquisition time of 3 min per bed position, using a PET/CT scanner (Discovery PET/CT 690; GE Healthcare). The total radiation exposure from the CT examination did not exceed 1 mSv. Hyoscine butylbromide was administered intravenously before or during the PET/CT to reduce peristaltic movement. The safety assessment of ^{18}F-FSPG is provided in the supplemental methods.

Images were interpreted independently by 2 board-certified nuclear medicine physicians who were masked to clinical and endoscopic data. ^{18}F-FSPG intensity moderately higher than in the liver was considered positive for active disease. The SUV_{max} of each bowel segment was also determined, with the summed SUV_{max} being the sum of all segments. Disagreements between the 2 physicians were resolved by consensus. Details are provided in the supplemental methods (*12,13*).

Assessment of Disease Activity

Endoscopic assessment was considered a valid reference standard for disease activity and extent. Sigmoidoscopy or colonoscopy was performed by an experienced gastroenterologist masked to ^{18}F-FSPG PET/CT results. The severity and extent of inflammatory lesions were evaluated using the UC Endoscopic Index of Severity (UCEIS) in UC patients and the CD Endoscopic Index of Severity (CDEIS) in CD patients (*18*). Segmental scores were determined in 5 bowel segments per patient using the UCEIS or CDEIS. For segmental CDEIS, the score for ulcerated or nonulcerated stenosis was imputed to the affected segment. Endoscopic evidence of active UC was defined as a UCEIS score of at least 2, whereas endoscopic evidence of active CD was defined as a CDEIS score of at least 3. Bowel segments with a superficial or deep ulcer were considered severe disease. Clinical and pathologic assessment are summarized as the supplemental methods (*18*).

Immunohistochemical Staining of Human xCT, GLUT1, and Cell Surface Markers

The immunohistochemistry study was approved by the institutional review board of Asan Medical Center (approval 2019-0260). Written informed consent was obtained again from all participants. The details are summarized in the supplemental methods (*19*) and Supplemental Table 1.

Statistical Analysis

The sensitivity of ^{18}F-FSPG PET/CT for the diagnosis of endoscopic evidence of active disease was calculated as the probability of positive ^{18}F-FSPG uptake in patients with active disease, as defined by the UCEIS or CDEIS. Specificity was defined as the probability of negative ^{18}F-FSPG uptake when the disease was not present. Bowel segment–level sensitivity and specificity were determined according to segmental UCEIS and CDEIS scores. Bowel segments that were not assessed by endoscopy were excluded from the analysis. The details are provided in the supplemental methods.

RESULTS

In Vivo Animal Studies

Twelve of 15 DSS-treated mice and 11 of 15 mice that underwent adoptive T-cell transfer met the eligibility criteria and completed the study. The control groups consisted of 6 and 10 mice, respectively. Clinical disease activity of DSS-treated mice on day 7 (median, 1.8; range, 0.7–3.3) and T-cell–transferred mice 8–12 wk after transfer (median, 2.5; range, 1.0–4.0) was significantly higher than that of their respective control groups ($P < 0.001$; Supplemental Fig. 1).

In DSS-treated mice, an increased ^{18}F-FSPG uptake in the colon was observed (Fig. 1). The SUV_{max} of ^{18}F-FSPG was significantly higher in the colons of DSS-treated than control mice (median, 2.1 [range, 0.5–3.9] vs. 0.7 [range, 0.5–1.9]; $P = 0.018$), as was the pathologic score derived from colon tissue (median, 14.2 [range,

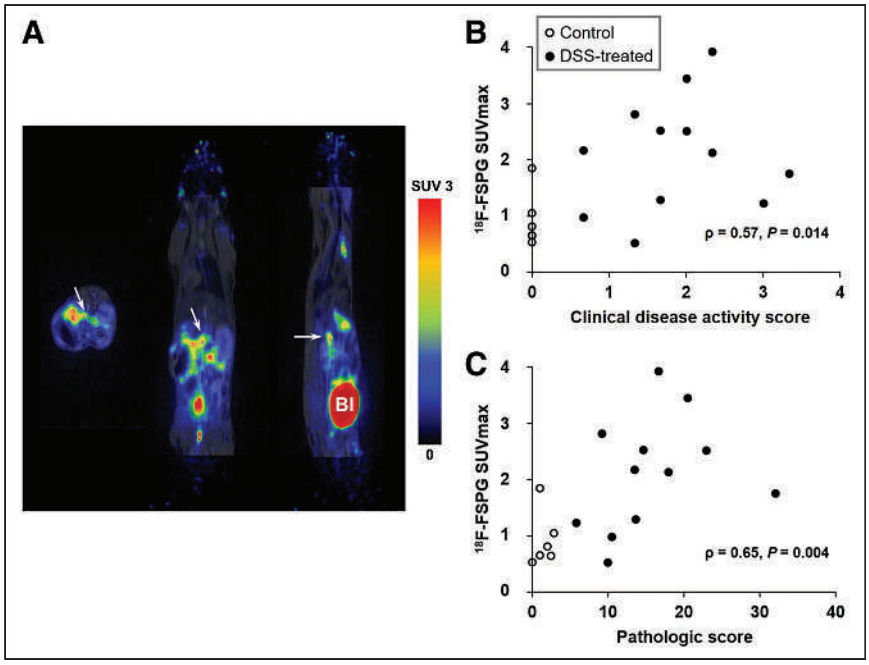

FIGURE 1. ^{18}F-FSPG imaging in DSS-treated mice. (A) Representative transaxial, coronal, and sagittal ^{18}F-FSPG PET/MR images of murine DSS-induced IBD model. Arrows indicate positive ^{18}F-FSPG uptake along colon. (B and C) Associations of colonic SUV_{max} with clinical disease activity (B) and pathologic score (C). Bl = bladder.

5.8–32.0] vs. 1.5 [range, 0–2.8]; $P < 0.001$). The SUV_{max} of ^{18}F-FSPG uptake was positively associated with clinical disease activity ($\rho = 0.57$, $P = 0.014$) and pathologic scores ($\rho = 0.65$, $P = 0.004$; Fig. 1; Supplemental Fig. 2).

Similarly, the SUV_{max} of colonic ^{18}F-FSPG uptake (median, 4.5 [range, 2.9–6.8] vs. 0.7 [range, 0.5–0.9]; $P < 0.001$) and the pathologic score derived from colon tissue (median, 8.3 [range, 6.4–14.8] vs. 0.8 [range, 0.4–1.6]; $P < 0.001$) were significantly higher in T-cell–transferred than in control mice (Fig. 2). The SUV_{max} of ^{18}F-FSPG uptake showed positive associations with clinical disease activity ($\rho = 0.74$, $P < 0.001$) and pathologic scores ($\rho = 0.74$, $P < 0.001$; Fig. 2; Supplemental Fig. 3).

Immunohistochemical staining of colon tissues revealed that xCT and GLUT1 were highly expressed in dendritic cells positive (+) for CD11c, in F4/80$^+$ macrophages, and in CD3$^+$ T cells in the lamina propria from mice with experimental colitis (Supplemental Fig. 4). In addition, immunohistochemical staining showed that xCT and GLUT1 were expressed in the epithelial cells of normal and inflamed mucosa.

Patients and ^{18}F-FSPG PET/CT Procedure

Between August 2018 and January 2019, 23 patients with IBD were assessed for initial eligibility and invited to participate in this prospective study. Three patients withdrew their consent before the injection of ^{18}F-FSPG. Finally, 10 patients with UC and 10 with CD were enrolled. All 20 patients completed ^{18}F-FSPG PET/CT as planned. The median administered activity per patient was 199.8 MBq (range, 192.4–214.6 MBq), and the median administered mass dose was 0.82 μg (range, 0.21–1.86 μg). Nineteen patients underwent colonoscopy, and 1 underwent sigmoidoscopy 1 d after ^{18}F-FSPG PET/CT. The demographic and baseline clinical characteristics are listed in Table 1. Six patients with UC (60%) and 8 with CD (80%) showed endoscopic evidence of active disease. Twelve (26%) of 47 bowel segments in patients with UC and 24 (59%) of 41 segments in patients with CD showed active inflammatory lesions.

^{18}F-FSPG Uptake in Patients

Readers determined that overall image quality was adequate for interpretation in all patients. The interreader agreements of visual assessment of ^{18}F-FSPG accumulation had κ-values of 0.70 (95% CI, 0.49–0.92) for patient-level analysis and 0.65 (95% CI, 0.57–0.73) for bowel segment–level analysis. Two readers disagreed on the presence of ^{18}F-FSPG accumulation in 2 (10%) of 20 patients and 10 (11%) of 95 bowels segments.

^{18}F-FSPG PET/CT was positive in 4 (67%) of the 6 UC patients with endoscopically active inflammation (Fig. 3) and correctly diagnosed endoscopic remission in 2 (50%) of the 4 patients (Supplemental Table 2). The 2 false-negative patients had scores of

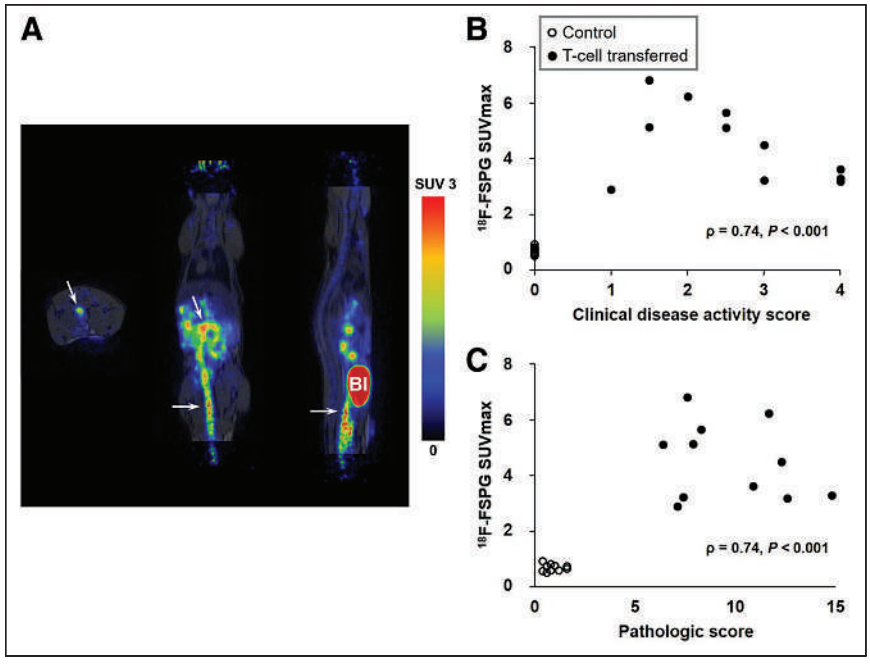

FIGURE 2. ^{18}F-FSPG imaging in T-cell–transferred mice. (A) Representative transaxial, coronal, and sagittal ^{18}F-FSPG PET/MR images of T-cell transfer–induced IBD model. Arrows indicate increased ^{18}F-FSPG uptake in colon. (B and C) Associations of colonic SUV_{max} with clinical disease activity (B) and pathologic score (C). Bl = bladder.

TABLE 1
Demographic and Clinical Characteristics

Characteristic	UC	CD
Asian (Korean)	10 (100%)	10 (100%)
Age (y)	42 (22–56)	28 (21–34)
Male	6 (60%)	9 (90%)
Body mass index (kg/m^2)	24.9 (17.1–36.9)	23.4 (18.7–30.0)
Smoking status		
Never	6 (60%)	6 (60%)
Former	3 (30%)	3 (30%)
Every day	1 (10%)	1 (10%)
Disease duration (mo)	40.2 (5.2–91.0)	55.8 (50.3–99.4)
Partial Mayo score	2 (0–4)	NA
Remission, 0–2	7 (70%)	
Mildly active, 3–5	3 (30%)	
CDAI	NA	91.89 (26.09–265.56)
Remission, <150		7 (70%)
Mildly active, 150–219		2 (20%)
Moderately active, 220–450		1 (10%)
Harvey–Bradshaw Index	NA	2 (1–12)
Remission, 0–4		8 (80%)
Mildly active, 5–7		1 (10%)
Moderately active, 8–16		1 (10%)
Hemoglobin (g/dL)	14.2 (10.5–15.2)	14.2 (9.4–17.5)
White blood cells ($\times 10^3/\mu L$)	7.7 (3.9–12.9)	6.9 (4.0–10.0)
Platelets ($\times 10^3/\mu L$)	310 (233–405)	287 (223–521)
Erythrocyte sedimentation (mm/h)	15 (3–53)	17 (2–105)
C-reactive protein (mg/dL)	0.11 (0.10–0.99)	0.43 (0.10–3.83)
Fecal calprotectin (μg/g)	65.1 (30.0–721)	116 (36.1–2,810)
UCEIS	2 (0–5)	NA
CDEIS	NA	9.8 (0.8–28.5)

NA = not applicable; CDAI = Crohn's Disease Activity Index.
Qualitative data are number and percentage; continuous data are median and range.

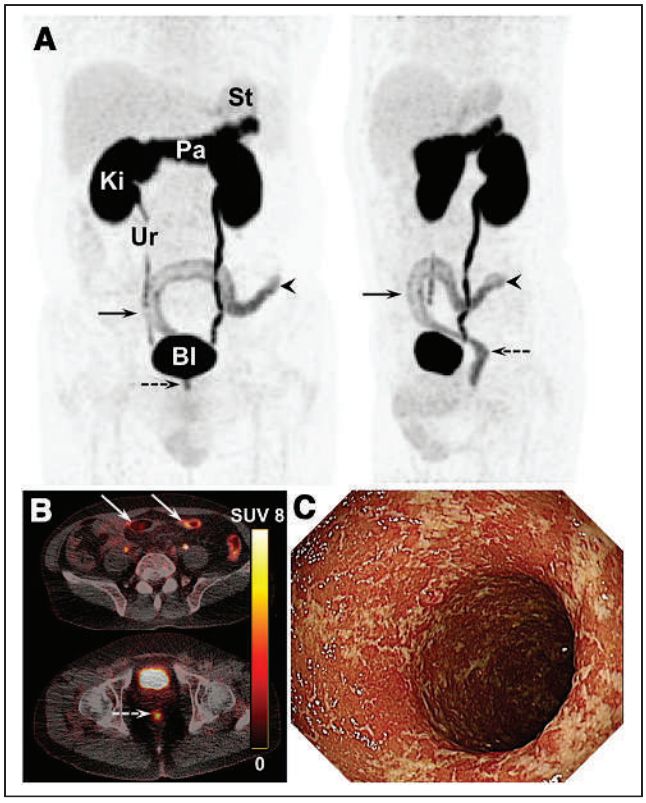

FIGURE 3. ^{18}F-FSPG PET/CT and endoscopic images of 55-y-old man with UC who presented with increased stool frequency, loose stools, hematochezia, and mild leukocytosis. His partial Mayo score was 4. (A and B) Maximum-intensity projection (A) and axial ^{18}F-FSPG (B) PET show increased ^{18}F-FSPG uptake along distal descending colon (arrowheads), sigmoid colon (arrows), and rectum (dashed arrows), with endoscopically active inflammation. (C) Endoscopic image of descending colon. Segmental UCEIS of ascending and transverse colon was 0, and that of descending colon, sigmoid colon, and rectum was 5. St = stomach; Pa = pancreas; Ki = kidneys; Ur = ureter; Bl = bladder.

3 (Supplemental Fig. 5), and the 2 false-positives had scores of 4 (Supplemental Fig. 6). The sensitivity and specificity of ^{18}F-FSPG PET/CT in identifying active bowel segments were 75% (9/12) and 86% (30/35), respectively. All patients ($n = 2$) and bowel segments ($n = 5$) with superficial or deep ulcers were correctly identified.

All 8 CD patients with active inflammation (Fig. 4) and 2 with endoscopic remission were correctly diagnosed by ^{18}F-FSPG PET/CT (Supplemental Table 3). In a segment-based analysis, ^{18}F-FSPG PET/CT had a sensitivity of 71% (17/24) and a specificity of 94% (16/17), respectively. All 7 patients and 16 of 20 segments with superficial or deep ulcerations were correctly diagnosed.

Association Between ^{18}F-FSPG Uptake and Disease Activity

In patients with UC, the median SUV_{max} was 3.1 (range, 1.8–8.2). The summed SUV_{max} was strongly associated with the UCEIS ($\rho = 0.79$, $P = 0.006$) but not with the partial Mayo score, C-reactive protein, and fecal calprotectin (Supplemental Fig. 7). The segmental SUV_{max} (median, 2.2; range, 0.8–8.2) also showed strong associations with UCEIS ($n = 47$, $\rho = 0.66$; $P < 0.001$) and the Robarts Histopathology Index ($n = 23$, $\rho = 0.64$; $P = 0.001$).

The median SUV_{max} in patients with CD was 5.6 (range, 2.8–7.6). The summed SUV_{max} was strongly associated with the Crohn's Disease Activity Index (CDAI), C-reactive protein, fecal calprotectin, and the CDEIS (Supplemental Fig. 8). The segmental SUV_{max} (median, 2.9; range, 1.5–7.6) also showed a strong association with CDEIS ($n = 41$, $\rho = 0.61$; $P < 0.001$) but not with the Colonic and Ileal Global Histologic Disease Activity Score ($n = 7$, $\rho = 0.33$; $P = 0.47$).

Safety of ^{18}F-FSPG PET/CT

No adverse events were observed in patients with UC. However, 4 patients (40%) with CD had adverse events with mild

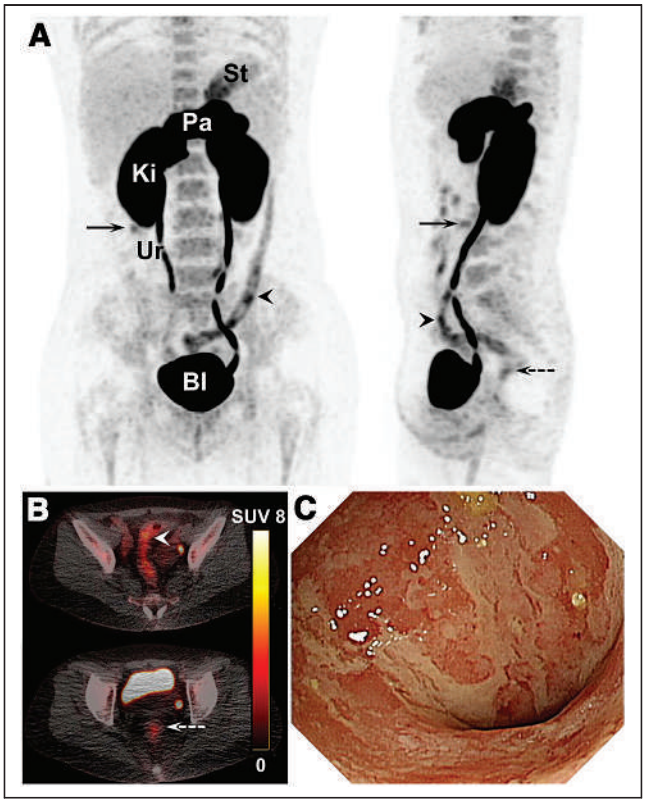

FIGURE 4. ^{18}F-FSPG PET/CT and endoscopic images of 26-y-old woman with CD who presented with abdominal pain and elevated C-reactive protein. Her CDAI was 102.47. (A and B) Maximum-intensity projection (A) and axial ^{18}F-FSPG (B) PET show increased ^{18}F-FSPG uptake in ileum (arrows), sigmoid and descending colon (arrowheads), and rectum (dashed arrows), which correlated well with endoscopic findings. Segmental CDEIS scores were 12 for ascending colon, 0 for transverse colon, 24 for descending and sigmoid colon, and 23 for rectum. Ileum was not assessed by colonoscopy. (C) Endoscopic image of rectum shows geographic and superficial ulcers, exudates, and streaks of coagulated blood. St = stomach; Pa = pancreas; Ki = kidneys; Ur = ureter; Bl = bladder.

intensity, including diarrhea, upper respiratory infection, arthritis, and dizziness. No adverse events were related to the study drug, and none of the patients experienced any serious adverse events or any clinically relevant changes in safety parameters.

Association Between xCT Expression and Disease Activity

Immunohistochemical staining showed that CD68$^+$, CD3$^+$, or CD66b$^+$ cells were present in the lamina propria of intestinal mucosa affected by UC (Supplemental Fig. 9) or CD (Supplemental Fig. 10). In addition, xCT was found to be expressed in the inflammatory and epithelial cells of all bowel segments. In patients with UC, the numbers of CD68$^+$xCT$^+$, CD3$^+$xCT$^+$, and CD66b$^+$xCT-negative cells in 22 bowel segments showed positive associations with UCEIS and SUV_{max} (Supplemental Table 4). By contrast, cytokeratin$^+$xCT$^+$ was negatively associated with UCEIS and SUV. In patients with CD, only the number of CD68$^+$xCT$^+$ cells in 7 bowel segments showed a significant association with CDEIS (Supplemental Table 5). Other cell populations showed no association with CDEIS or SUV.

DISCUSSION

Using mice with experimental IBD, we found that ^{18}F-FSPG accumulation in the colon was associated with disease activity indices and xCT expression in immune cells. Expansion of this study to patients, most of whom were clinically in remission or had mildly active IBD, showed that ^{18}F-FSPG PET/CT was accurate in diagnosing endoscopically active IBD and remission in patients and bowel segments. All patients with superficial or deep ulcers were correctly identified. Quantitative ^{18}F-FSPG uptake and xCT expression in immune cells were associated with endoscopic disease activity indices. ^{18}F-FSPG PET/CT was well tolerated, with no study drug–related adverse events. Our results suggest that ^{18}F-FSPG PET/CT can assess disease activity and distinguish between active IBD and mucosal healing, as determined endoscopically.

Although this study did not include participants across the entire range of disease activity, the subjects of this study may constitute a representative sample of those who would likely be the intended-use population for ^{18}F-FSPG PET/CT. All patients were evaluated by endoscopy after ^{18}F-FSPG PET/CT, with masked readers interpreting ^{18}F-FSPG PET/CT. Thus, there are no potential risks of bias or applicability regarding the accuracy of data. False-positives and false-negatives were likely due to an indeterminate zone for decision making. Greater experience with refined classification criteria may reduce the likelihood of patient misclassification. The positive association between quantitative ^{18}F-FSPG uptake and endoscopic assessment further supports the validity of ^{18}F-FSPG PET/CT. In patients with UC, the absence of a significant association between ^{18}F-FSPG uptake and conventional markers may be due to the inclusion of patients with mildly active disease and the small study sample.

We found that endoscopic assessment was positively associated with xCT expression by CD68$^+$ and CD3$^+$ immune cells in patients with UC and with xCT expression by CD68$^+$ cells in CD but not with xCT$^+$CD66b$^+$ cells. Although the small number of assessed bowel segments with CD may have precluded a consistent association, these results confirm the role of CD68$^+$xCT$^+$ macrophages in the antioxidative microenvironment of IBD (*10*). Our results also demonstrate that xCT expression is upregulated in human CD3$^+$ T cells, further strengthening the evidence for xCT expression and cystine uptake as regulators of T-cell function. These findings are consistent with results showing high initial rates of cystine and ^{18}F-FSPG uptake followed by decreases during a later phase of inflammation (*6,11,12*). xCT expression and cystine uptake in immune cells might mirror cellular concentrations of reactive oxygen species as well as metabolic activity (*20*). Taken together, these findings suggest that *in vivo* ^{18}F-FSPG PET/CT results may indicate broad changes in immune metabolism. Understanding of xCT in immune cells may also provide a pathologic tool to assess IBD activity.

Interestingly, the endoscopic assessment was negatively associated with xCT expression by cytokeratin$^+$ cells in patients with UC. xCT was expressed on the apical surfaces of the epithelial cells (Supplemental Figs. 9 and 10), where absorption occurs (*10,21*). This localization to absorptive sites suggests that system x_C^- plays a role in intestinal cystine transport (*21*) but does not involve ^{18}F-FSPG transport into the epithelial cells. The reason for the lack of association between GLUT1$^+$ immune cells and endoscopic assessment is not apparent but may be related to the persistent glucose hypermetabolism in healing tissue after inflammation (*22,23*).

Radiation exposure is an important limitation in using ^{18}F-FSPG PET/CT to assess disease activity, mainly because most of these patients are relatively young. Current guidelines recommend using cross-sectional imaging modalities that do not entail exposure to ionizing radiation when it is likely that serial examinations are required (*1*). A per-patient dose of 200 MBq of ^{18}F-FSPG would result in a mean effective dose of 4.0 ± 0.2 mSv, including the dose from CT (*24*). These doses can be significantly reduced using

highly sensitive PET/CT systems (*25*). Study protocols that allow a low dose of ^{18}F-FSPG can reduce the radiation dose by as much as 75% without clinical detriment (*26*).

This study had several limitations. First, the diagnostic validity should be interpreted with caution because of the small number of included patients and the exploratory nature of the study. Additional studies on larger numbers of patients are required to validate our initial results. Second, the assessment of IBD activity was based on endoscopic findings. Thus, comparisons between endoscopy and ^{18}F-FSPG PET/CT may be limited because the actual sites of endoscopic evaluation may not precisely match those of ^{18}F-FSPG uptake, thereby underestimating the accuracy of ^{18}F-FSPG PET/CT for evaluating bowel segments.

CONCLUSION

^{18}F-FSPG PET/CT imaging of system x_C^- in immune cells can noninvasively assess IBD activity and remission of the entire bowel without the need for bowel preparation and safety issues related to invasive endoscopic procedures. Assessment of system x_C^- expression by immune cells may provide diagnostic information on the dysregulated immune responses responsible for chronic active inflammation.

DISCLOSURE

This research was sponsored by the Asan Foundation (Seoul, Republic of Korea) and financially supported by National Research Foundation grants NRF-2016M2A2A7A03913219 and NRF-2019R1A2C209022213 funded by the Korea Ministry of Science and ICT, Republic of Korea, and by the Korea Health Technology R&D Project through the Korea Health Industry Development Institute, funded by the Ministry of Health and Welfare, Republic of Korea (grant HI18C2383). The funders had no role in the conceptualization or design of the study; in the collection, analysis, and interpretation of the data; in the writing of the manuscript; or in the decision to submit the manuscript for publication. Norman Koglin and Andrew Stephens report personal fees from Life Molecular Imaging GmbH (employment) during the conduct of the study and are listed as coinventors on a patent application entitled "[F-18]-labeled L-glutamic acid and L-glutamine derivatives (I), their use and processes for their preparation; US 9,308,282", which is owned by Life Molecular Imaging. Dae Hyuk Moon reports receiving grants from the National Research Foundation of Korea, the Korea Health Industry Development Institute, and Life Molecular Imaging GmbH. No other potential conflict of interest relevant to this article was reported.

KEY POINTS

QUESTION: Does *in vivo* assessment of system x_C^- in immune cells provide information on the dysregulated immune responses responsible for chronic active inflammation in IBD, thereby assessing the disease activity?

PERTINENT FINDINGS: System x_C^- expression in immune cells was associated with endoscopic disease activity indices. PET imaging of system x_C^- was accurate in diagnosing endoscopically active disease and remission in patients and bowel segments.

IMPLICATIONS FOR PATIENT CARE: PET imaging of system x_C^- may noninvasively assess disease activity and remission without the need for bowel preparation or the safety issues related to endoscopic procedures.

REFERENCES

1. Lichtenstein GR, Loftus EV, Isaacs KL, Regueiro MD, Gerson LB, Sands BE. ACG clinical guideline: management of Crohn's disease in adults. *Am J Gastroenterol.* 2018;113:481–517.
2. Rubin DT, Ananthakrishnan AN, Siegel CA, Sauer BG, Long MD. ACG clinical guideline: ulcerative colitis in adults. *Am J Gastroenterol.* 2019;114:384–413.
3. de Souza HS, Fiocchi C. Immunopathogenesis of IBD: current state of the art. *Nat Rev Gastroenterol Hepatol.* 2016;13:13–27.
4. Dearling JL, Daka A, Veiga N, Peer D, Packard AB. Colitis immunoPET: defining target cell populations and optimizing pharmacokinetics. *Inflamm Bowel Dis.* 2016;22:529–538.
5. Lewerenz J, Hewett SJ, Huang Y, et al. The cystine/glutamate antiporter system x_C^- in health and disease: from molecular mechanisms to novel therapeutic opportunities. *Antioxid Redox Signal.* 2013;18:522–555.
6. Sato H, Fujiwara K, Sagara J, Bannai S. Induction of cystine transport activity in mouse peritoneal macrophages by bacterial lipopolysaccharide. *Biochem J.* 1995; 310:547–551.
7. Nabeyama A, Kurita A, Asano K, et al. xCT deficiency accelerates chemically induced tumorigenesis. *Proc Natl Acad Sci USA.* 2010;107:6436–6441.
8. Garg SK, Yan Z, Vitvitsky V, Banerjee R. Differential dependence on cysteine from transsulfuration versus transport during T cell activation. *Antioxid Redox Signal.* 2011;15:39–47.
9. Levring TB, Hansen AK, Nielsen BL, et al. Activated human CD4+ T cells express transporters for both cysteine and cystine. *Sci Rep.* 2012;2:266.
10. Sido B, Lasitschka F, Giese T, et al. A prominent role for mucosal cystine/cysteine metabolism in intestinal immunoregulation. *Gastroenterology.* 2008;134:179–191.
11. Koglin N, Mueller A, Berndt M, et al. Specific PET imaging of x_C^- transporter activity using a ^{18}F-labeled glutamate derivative reveals a dominant pathway in tumor metabolism. *Clin Cancer Res.* 2011;17:6000–6011.
12. Chae SY, Choi CM, Shim TS, et al. Exploratory clinical investigation of (4*S*)-4-(3-^{18}F-fluoropropyl)-L-glutamate PET of inflammatory and infectious lesions. *J Nucl Med.* 2016;57:67–69.
13. Baek S, Mueller A, Lim YS, et al. (4*S*)-4-(3-^{18}F-fluoropropyl)-L-glutamate for imaging of x_C^- transporter activity in hepatocellular carcinoma using PET: preclinical and exploratory clinical studies. *J Nucl Med.* 2013;54:117–123.
14. Li Y, Beiderwellen K, Nensa F, et al. [^{18}F]FDG PET/MR enterography for the assessment of inflammatory activity in Crohn's disease: comparison of different MRI and PET parameters. *Eur J Nucl Med Mol Imaging.* 2018;45:1382–1393.
15. Tenhami M, Virtanen J, Kauhanen S, et al. The value of combined positron emission tomography/magnetic resonance imaging to diagnose inflammatory bowel disease: a prospective study. *Acta Radiol.* 2021;62:851–857.
16. Shih IL, Wei SC, Yen RF, et al. PET/MRI for evaluating subclinical inflammation of ulcerative colitis. *J Magn Reson Imaging.* 2018;47:737–745.
17. Li Y, Khamou M, Schaarschmidt BM, et al. Comparison of ^{18}F-FDG PET-MR and fecal biomarkers in the assessment of disease activity in patients with ulcerative colitis. *Br J Radiol.* 2020;93:20200167.
18. Walsh AJ, Bryant RV, Travis SP. Current best practice for disease activity assessment in IBD. *Nat Rev Gastroenterol Hepatol.* 2016;13:567–579.
19. Ahn J, Jin M, Song E, et al. Immune profiling of advanced thyroid cancers using fluorescent multiplex immunohistochemistry. *Thyroid.* 2021;31:61–67.
20. Siska PJ, Kim B, Ji X, et al. Fluorescence-based measurement of cystine uptake through xCT shows requirement for ROS detoxification in activated lymphocytes. *J Immunol Methods.* 2016;438:51–58.
21. Burdo J, Dargusch R, Schubert D. Distribution of the cystine/glutamate antiporter system x_C^- in the brain, kidney, and duodenum. *J Histochem Cytochem.* 2006;54: 549–557.
22. Lazzeri E, Bozzao A, Cataldo MA, et al. Joint EANM/ESNR and ESCMID-endorsed consensus document for the diagnosis of spine infection (spondylodiscitis) in adults. *Eur J Nucl Med Mol Imaging.* 2019;46:2464–2487.
23. Priftakis D, Riaz S, Zumla A, Bomanji J. Towards more accurate ^{18}F-fluorodeoxyglucose positron emission tomography (^{18}F-FDG PET) imaging in active and latent tuberculosis. *Int J Infect Dis.* 2020;92(suppl):S85–S90.
24. Smolarz K, Krause BJ, Graner FP, et al. (*S*)-4-(3-^{18}F-fluoropropyl)-L-glutamic acid: an ^{18}F-labeled tumor-specific probe for PET/CT imaging: dosimetry. *J Nucl Med.* 2013;54:861–866.
25. Surti S, Viswanath V, Daube-Witherspoon ME, Conti M, Casey ME, Karp JS. Benefit of improved performance with state-of-the art digital PET/CT for lesion detection in oncology. *J Nucl Med.* 2020;61:1684–1690.
26. Alberts I, Sachpekidis C, Prenosil G, et al. Digital PET/CT allows for shorter acquisition protocols or reduced radiopharmaceutical dose in [^{18}F]-FDG PET/CT. *Ann Nucl Med.* 2021;35:485–492.

^{18}F-FDG Fetal Dosimetry Calculated with PET/MRI

Paolo Zanotti-Fregonara[1], Tatsuya Ishiguro[2], Kosuke Yoshihara[2], Shiro Ishii[3], and Takayuki Enomoto[2]

[1]Molecular Imaging Branch, National Institute of Mental Health, Bethesda, Maryland; [2]Department of Obstetrics and Gynecology, Niigata University Medical & Dental Hospital, Niigata, Japan; and [3]Department of Radiology and Nuclear Medicine, Fukushima Medical University Hospital, Fukushima, Japan

The fetal absorbed dose from ^{18}F-FDG administration to the mother is an essential piece of information when considering the use of PET to stage cancers during pregnancy. However, the few existing human case reports were obtained using either PET-only or PET/CT machines, which may not accurately identify the soft tissues of the fetus for dosimetric calculations. This study presents data from 11 women injected with ^{18}F-FDG for cancer staging during the first 2 trimesters of pregnancy and is, to our knowledge, the first to be entirely acquired with PET/MRI. **Methods:** Eleven pregnant women (12 scans) with cervical cancer were imaged with ^{18}F-FDG PET/MRI, and their images were retrospectively analyzed for this study. The fraction of injected activity concentrated by the fetus was derived from manually drawing regions of interest on the MRI slices. From the activity fraction, the fetal time-integrated coefficients were derived and combined with the standard coefficients of the mothers' organs from the ICRP publication 106. The fetal absorbed doses were calculated with OLINDA/EXM 1.1 and a dynamic bladder model. **Results:** All fetuses after early pregnancy could be accurately delineated because of the coregistered MRI scans. ^{18}F-FDG activity was unevenly distributed in the fetal body: the hearts and urinary bladders were generally visible, whereas the brain showed lower uptake. The estimated fetal doses were 2.21E−02 mGy/MBq for 1 woman imaged in early pregnancy, 7.38 ± 0.25 E−03 mGy/MBq for 3 women imaged at the end of the first trimester, and 4.92 ± 1.53 E−03 mGy/MBq for 8 women imaged during the second trimester. **Conclusion:** PET/MR images of pregnant women injected with ^{18}F-FDG confirm that the fetal ^{18}F-FDG dose is very low. Therefore, clinically appropriate ^{18}F-FDG scans in women with cancer should not be withheld because of pregnancy.

Key Words: ^{18}F-FDG; pregnancy; fetal dosimetry; PET/MRI

J Nucl Med 2022; 63:1592–1597
DOI: 10.2967/jnumed.121.263561

Given the critical role of ^{18}F-FDG in staging most types of cancer and the worldwide diffusion of PET machines, the number of pregnant women injected with ^{18}F-FDG—either by mistake or by clinical necessity—is bound to increase. In this context, the dose to the fetus is essential to reach an informed clinical decision. Until relatively recently, fetal biokinetic data for ^{18}F-FDG were unknown. When Russell et al. compiled the first extensive database of fetal doses from different radiopharmaceuticals in 1997, no biologic data were available; thus, the ^{18}F-FDG dose was calculated by considering only irradiation from maternal organs (*1*). Stabin revised these doses in 2004 on the basis of newly acquired monkey data (*2*), but the first case report of ^{18}F-FDG use in a pregnant woman was only published in 2008 (*3*). Since then, at least 20 different case reports have become available (*4*), and new dosimetric estimates based on human data have been proposed (*5*).

Although these advances allow a clearer picture of ^{18}F-FDG fetal uptake and dosimetry at different stages of pregnancy, more cases are needed to refine these values and to fill gaps during those periods of pregnancy where case data are not yet available. In addition, almost all previous dose estimates were derived from PET-only or PET/CT images, where the soft tissues can sometimes be difficult to delineate. This study presents data from 11 pregnant women (12 scans) who were injected with ^{18}F-FDG for cancer staging during the first 2 trimesters of pregnancy and imaged with PET/MRI.

MATERIALS AND METHODS

Patients

Eleven pregnant women with cervical cancer were imaged with ^{18}F-FDG PET/MRI, and their images were retrospectively analyzed for this study. The gestational age ranged from 9 to 24 wk and was determined by measuring the crown-rump length by ultrasound examination at 9–10 gestational wk, calculated from the last menstrual period. One woman was imaged twice at 18 and 24 wk. Data for 7 of these 11 women were previously published in a study that sought to assess the clinical utility of ^{18}F-FDG PET in cervical cancer (*6*). The patients were treated at the Niigata University Medical and Dental Hospital, Niigata, Japan, and the imaging was performed at the Fukushima Medical University Hospital using a Biograph mMR PET/MRI device equipped with a 3-T MRI (Siemens Healthcare). Acquisition details were previously published (*6*). The women were injected with approximately 4 MBq of ^{18}F-FDG per kg (average injected activity, 213 ± 52 MBq). The institutional ethics board of the National Institute of Mental Health approved this retrospective study, and the requirement to obtain informed consent was waived.

Dosimetry Calculations

The dosimetric calculations in this study closely followed the methodology proposed by Zanotti-Fregonara et al. (*4*), according to which pregnancy was divided into periods: early pregnancy (0–10 wk) where, given the small size of the fetus, the fetal dose was approximated to that of the uterus of a nonpregnant woman; the rest of the first trimester (11–13 wk); and the second trimester (14–26 wk). For these last 2 periods, the digital phantoms representing pregnant women at the first and second trimester were used (*7*). None of the women was in the third trimester.

The fraction of injected activity concentrated by the fetus (or by the uterus for the only participant who was imaged during early pregnancy) was derived from manually drawing regions of interest on all MRI slices in which the fetus was visible (or around the whole uterus). All fetal

Received Nov. 20, 2021; revision accepted Jan. 18, 2022.
For correspondence or reprints, contact Paolo Zanotti-Fregonara (zanottifregonp@nih.gov).
Published online Feb. 3, 2022.

TABLE 1
Time-Integrated Activities for Mothers' Organs, Taken from ICRP 106 (*8*)

Organ	Time-integrated activity (Bq h/Bq)
Brain	0.21
Heart wall	0.11
Lungs	0.079
Liver	0.13
Rest of the body	1.7

regions of interest were drawn by an experienced imaging specialist, who also analyzed most of the cases reported in the literature. The results of this study are therefore directly comparable to those previously published. From the activity fraction, the time-integrated coefficients were derived by considering the physical half-life of ^{18}F (1.83 h) as the effective half-life of ^{18}F-FDG. The time-integrated activities were combined with those of the mothers' organs reported in publication 106 of the International Commission on Radiological Protection (ICRP) (Table 1 (*8*). Maternal bladder voiding was simulated with the following parameters: first fraction of 0.075 with a half-life of 0.2 h, and second fraction of 0.225 with a half-life of 1.5 h. The bladder-voiding interval was set at 1 h. The absorbed doses were calculated by entering the time-integrated coefficients of both the mothers and the fetuses into OLINDA/EXM 1.1 (*9*).

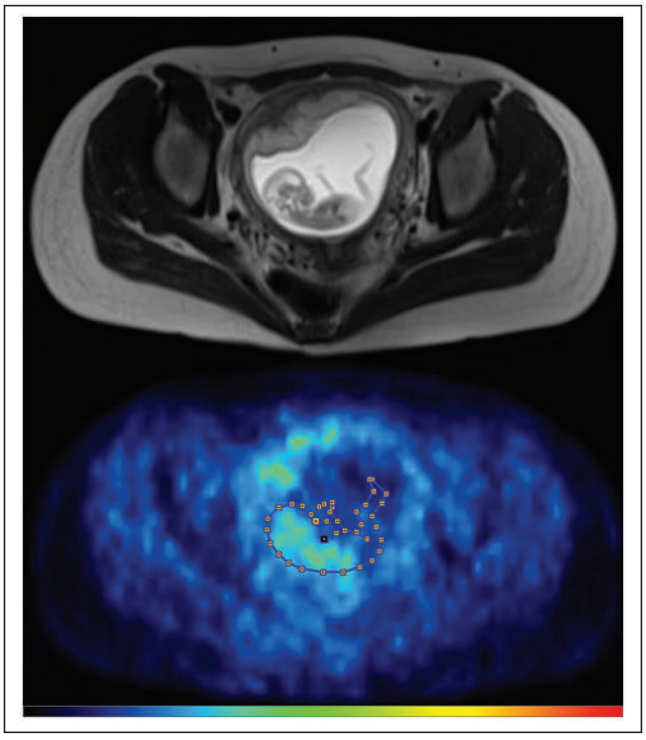

FIGURE 1. Transaxial images of MRI (top) and PET (bottom) in a woman at 13 wk of pregnancy. Fetus is visible in minute detail on MRI, including body parts, such as limbs, that are cold on PET images. Figure demonstrates how region of interest drawn around fetal body, shown superimposed to PET scan, would not have been drawn with this shape if only PET images had been available. It is thus reasonable to hypothesize that fetal dosimetry obtained with PET/MRI is more accurate than that obtained with PET-only or PET/CT scans.

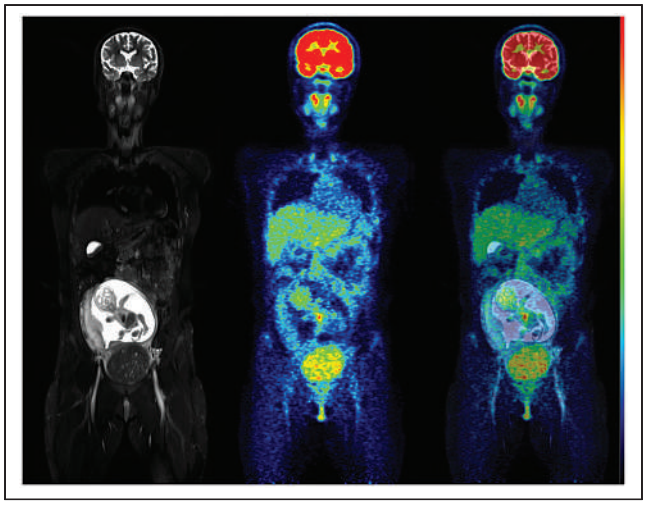

FIGURE 2. Coronal slices of MRI (left), PET (center), and fused PET/MRI (right) of a woman in 18th week of pregnancy. Of particular interest is level of uptake in fetal organs. Although heart showed high ^{18}F-FDG uptake, brain had only a low level of glucose consumption, especially compared with brain uptake of mother. This pattern of low glucose consumption has previously been noted even in mature fetuses (*4*).

The dose calculated with individual image-derived time-integrated coefficients was also compared with those extrapolated with the mathematic function proposed Zanotti-Fregonara and Stabin (*10*). This function was obtained by fitting a sigmoid curve through the time-integrated coefficients of the cases available at the time of publication (*4*).

RESULTS

All fetuses were visible in detail on the MRI scans, which allowed the delineation of their body contours (Fig. 1). ^{18}F-FDG activity was unevenly distributed in the fetal body. The hearts were generally visible, whereas the brain showed low uptake (Figs. 2 and 3). The estimated fetal doses were 2.21E−02 mGy/MBq for the woman imaged during early pregnancy, 7.38 ± 0.25 E−03 mGy/MBq for the 3 women imaged at the end of the first trimester, and 4.92 ± 1.53 E−03 mGy/MBq for the 8 women imaged during the second trimester (Table 2).

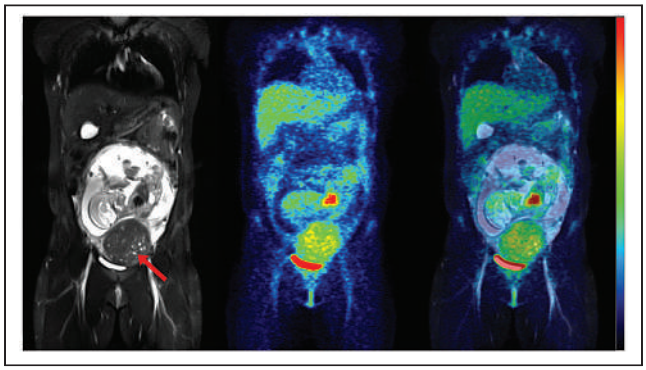

FIGURE 3. Coronal slices of MRI (left), PET (center), and fused PET/MRI (right) of same woman as in Figure 2 but at 24 wk of pregnancy. Fetus has visibly increased in mass, but pattern of ^{18}F-FDG uptake in organs has not changed, with heart showing high glucose consumption but brain still largely silent. Red arrow points to uterine fibroid.

TABLE 2
Dosimetry Results for Fetuses in Present Study Compared with Cases Previously Reported in the Literature

Fetus	Stage of gestation	Mother's weight (kg)	Injected activity (MBq)	Machine	Phantom (trimester)	Fraction	Time-integrated activity (Bq h/Bq)	Dose (mGy/MBq)	Reference
1	5 wk	86	296	PET/CT	Nonpregnant	0.0012	0.0030	1.73E–02	(*21*)
2	6 wk	68	583	PET	Nonpregnant	0.0036	0.0095	3.14E–02	(*22*)
3	8 wk	60	320	PET/CT	Nonpregnant	0.0020	0.0053	2.23E–02	(*3*)
4	*9 wk*	*50*	*144*	*PET/MRI*	*Nonpregnant*	*0.0019*	*0.0052*	*2.21E–02*	*This study*
5	10 wk	71	296	PET/CT	Nonpregnant	0.0018	0.0046	2.08E–02	(*23*)
6	12 wk	58	385	PET/CT	1	0.0006	0.0016	7.25E–03	(*21*)
7	~12 wk	77	350	PET	1	0.0010	0.0026	7.70E–03	(*21*)
8	*13 wk*	*64*	*178*	*PET/MRI*	*1*	*0.0005*	*0.0013*	*7.11E–03*	*This study*
9	*13 wk*	*53*	*209*	*PET/MRI*	*1*	*0.0007*	*0.0020*	*7.43E–03*	*This study*
10	*13 wk*	*52*	*205*	*PET/MRI*	*1*	*0.0009*	*0.0024*	*7.61E–03*	*This study*
11	*14 wk*	*86*	*333*	*PET/MRI*	*2*	*0.0013*	*0.0035*	*3.69E–03*	*This study*
12	*14 wk*	*48*	*187*	*PET/MRI*	*2*	*0.0018*	*0.0047*	*3.87E–03*	*This study*
13	*14 wk*	*49*	*199*	*PET/MRI*	*2*	*0.0018*	*0.0048*	*3.88E–03*	*This study*
14	*15 wk*	*59*	*235*	*PET/MRI*	*2*	*0.0028*	*0.0063*	*4.10E–03*	*This study*
15	*18 wk**	*67*	*189*	*PET/MRI*	*2*	*0.0040*	*0.0106*	*4.72E–03*	*This study*
16	18 wk†	88	200	PET	2	0.0009	0.0023	3.52E–03	(*22*)
17	19 wk	51	348	PET/MRI	2	0.0024	0.0063	4.10E–03	(*21*)
18	19 wk	70	296	PET/MRI	2	0.0037	0.0097	4.59E–03	(*21*)
19	*19 wk*	*50*	*197*	*PET/MRI*	*2*	*0.0059*	*0.0157*	*5.46E–03*	*This study*
20	*19 wk*	*48*	*187*	*PET/MRI*	*2*	*0.0055*	*0.0145*	*5.28E–03*	*This study*
21	21 wk	53	181	PET/CT	2	0.0049	0.0129	5.05E–03	(*24*)
22	23 wk	59	181	PET	2	0.0078	0.0206	6.17E–03	(*22*)
23	*24 wk**	*70*	*291*	*PET/MRI*	*2*	*0.0135*	*0.0356*	*8.33E–03*	*This study*
24	25 wk	67	337	PET	2	0.0084	0.0222	6.40E–03	(*22*)
25	25 wk‡	76	188	PET/CT	2	0.0156	0.0412	9.14E–03	(*4*)
26	25 wk‡	76	188	PET/CT	2	0.0164	0.0434	9.46E–03	(*4*)
27	26 wk	81	242	PET/CT	2	0.0129	0.0340	8.10E–03	(*25*)
28	28 wk	82	174	PET	3	0.0071	0.0187	3.38E–03	(*22*)
29	~28 wk	66	296	PET	3	0.0195	0.0515	6.22E–03	(*21*)
30	30 wk†	89	229	PET	3	0.0196	0.0518	6.24E–03	(*22*)
31	34 wk	95	555	PET/CT	3	0.0192	0.0507	6.15E–03	(*26*)

*, † = Women imaged twice during pregnancy.
‡Twin pregnancy.
Dosimetry results for fetuses in present study are italicized; cases previously reported in the literature are not italicized. References show publication in which the cases were originally described. Doses may differ from those reported in original publication, when they were reanalyzed in a standardized way (*4*).

The doses extrapolated with the sigmoid function predicted the measured doses in the first 15 wk of pregnancy well (within 10%). Starting from the 15th week, however, the extrapolated time-integrated coefficients were lower than the measured coefficients (Fig. 4; the measured doses were thus underestimated by up to 25% (Table 3).

DISCUSSION

This study, which contains the largest population ever published of pregnant patients imaged with ^{18}F-FDG, significantly expands the pool of available human dosimetric data. The available cases now cover the duration of pregnancy until the 34th week, with an approximate frequency of at least 1 case every 2 wk (Table 2). Notably, previously available case reports left a gap between the 12th and the 18th weeks. Because the present study includes 8 scans acquired between the 13th and the 18th weeks, a more complete picture of ^{18}F-FDG uptake during pregnancy is now available. It is also important to note that, after the 34th week, dosimetry is not likely to change significantly because ^{18}F-FDG uptake by the fetus tends to plateau (Fig. 4). In addition, late-pregnancy dosimetry might be clinically less valuable, because scans can more easily be

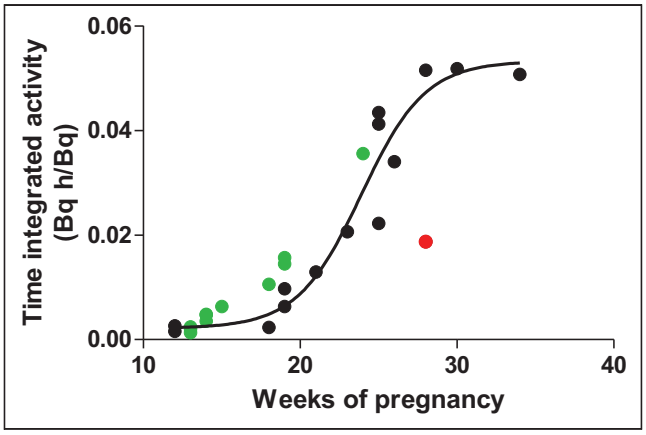

FIGURE 4. Sigmoid function fitted through the measured time-integrated activity data points (black dots), as reported in Zanotti-Fregonara and Stabin (*10*). During fitting of original curve, automatic detection of outliers (ROUT [robust regression and outlier removal] Q coefficient, 1.0%) removed 1 point (in red). This outlying red point came from a PET-only study, which raises the possibility of inaccurate segmentation of fetal body on PET images. Data points of the patients in the present study (in green) tended to be higher than extrapolated values. Although difference was modest, this points to possibility of systematic group difference (see text for discussion).

postponed until delivery or labor can be induced, since the fetus is already viable.

Importantly, all women in this study were scanned with PET/MRI, which allowed a detailed delineation of the fetal body contours and hence dose estimations were arguably more accurate. Such accuracy cannot be achieved by coregistering the PET to an MRI acquired separately because the fetus would have moved in the meantime. In the present study, fetal movements were likely to be minimal because excellent coregistration of MRI and PET was observed in all cases; an example of this is visible in the superposition of the fetal heart on MRI and myocardial ^{18}F-FDG activity in Figures 2 and 3. In addition to providing an excellent visualization of the fetal body, PET/MRI machines do not deliver to the fetus the additional dose of a CT scan or of a transmission source and therefore, if available, should preferentially be used to image pregnant women.

The MR images allowed drawing of the fetal regions of interest with a high level of confidence, so that inaccuracies due to manual segmentation could be minimized. Of course, because there is no gold standard against which the segmentations can be compared, residual segmentation errors cannot be quantified. However, it is reasonable to assume that fetal regions of interest drawn on an MRI are more accurate than those drawn directly from PET, where fetal contours are not visible (Fig. 1), or CT, where fetal soft tissues are difficult to delineate. The present dose estimates confirmed the low level of radiation absorbed by the fetus when the mother is injected with ^{18}F-FDG. The highest estimate was observed in early pregnancy (3.2 mGy), but the average of the remaining cases was 1.1 ± 0.5 mGy. The fetus of the woman who had 2 examinations received a cumulative dose of 3.3 mGy. These values would not significantly change if different anthropomorphic phantoms were used (*4,11,12*) and are more than 1 order of magnitude lower than the threshold for deterministic effects. Although stochastic effects cannot technically be ruled out, no effects have ever been observed for doses this low (*13*). Taken together, these data suggest that the benefits for both mother and fetus of a clinically appropriate ^{18}F-FDG PET scan outweigh the hypothetical risks to the fetus theorized by the linear no-threshold model (*14,15*). Notably, in the case of cervical cancers, the primary tumor size may be evaluated with MRI, but to assess lymph-node involvement the alternative to PET/MRI may be an invasive histologic verification.

To compensate for the incomplete data coming from sparse published case reports, we previously used mathematic modeling

TABLE 3
Comparison Between Doses Extrapolated from Mathematic Function Described in Zanotti-Fregonara and Stabin (*10*) and Doses Measured in This Study, Starting After Early Pregnancy

Stage of gestation	Phantom (trimester)	Measured time-integrated activity (Bq h/Bq)	Extrapolated time-integrated activity (Bq h/Bq)	Measured dose (mGy/MBq)	Extrapolated dose (mGy/MBq)	% Difference between the measured and extrapolated doses
13 wk	1	0.0013	0.00241	7.11E−03	7.61E−03	7.0
13 wk	1	0.0020	0.00241	7.43E−03	7.61E−03	2.4
13 wk	1	0.0024	0.00241	7.61E−03	7.61E−03	0.0
14 wk	2	0.0035	0.00256	3.69E−03	3.56E−03	−3.5
14 wk	2	0.0047	0.00256	3.87E−03	3.56E−03	−8.0
14 wk	2	0.0048	0.00256	3.88E−03	3.56E−03	−8.2
15 wk	2	0.0063	0.00281	4.10E−03	3.59E−03	−12.4
18 wk*	2	0.0106	0.00485	4.72E−03	3.89E−03	−17.6
19 wk	2	0.0157	0.00641	5.46E−03	4.11E−03	−24.7
19 wk	2	0.0145	0.00641	5.28E−03	4.11E−03	−22.2
24 wk*	2	0.0356	0.02836	8.33E−03	7.29E−03	−12.5

*Woman imaged twice during pregnancy.

to extrapolate the time-integrated coefficients for the whole duration of pregnancy from available human cases (*10*). We found that the variation of the fetal time-integrated coefficients follows a sigmoid function: after a rapid increase in the second trimester and the beginning of the third, when the fetal mass rapidly increases, the function eventually tends to plateau when the fetus reaches maturity (Fig. 4). Building on that work, the present study prospectively tested whether the doses extrapolated by the function could predict the calculated doses. Our findings demonstrated that the extrapolated doses closely match the calculated doses until the 15th week of pregnancy but underestimate the doses by up to 25% between the 14th and 25th weeks (Table 3). An error of up to 25% could be considered minor compared with the uncertainties in internal dose estimations (*16,17*) and, indeed, larger differences are observed between the measured values in different fetuses at the same week of pregnancy (Table 2). On the other hand, the actual dose was underestimated in 8 of 11 fetuses, including all the fetuses starting at the 14th week (Table 3), which suggests the possibility of a systematic group difference. One possible source of this difference is ethnicity; specifically, this study comprised Japanese women (average weight, 59 ± 12 kg), whereas the populations used to build the mathematic function comprised American and European women (average weight, 73 ± 13 kg). Another possible reason for a systematic group difference is that previously published cases were acquired mostly with PET, where fetal contours were not visible, or PET/CT, where fetal soft tissues were sometimes difficult to delineate or to differentiate from placental uptake (*18*); in contrast, all the fetuses in this study were visible in detail thanks to the simultaneous MRI. For example, when creating the original sigmoid curve, 1 data point was automatically eliminated as an outlier during the fitting process (Fig. 4). Because this point was from a PET-only study, it is possible that the segmentation of that fetal body was inaccurate.

Finally, it should be noted that the cases in the present paper, as well as all the other cases published in the literature to date, consist of static images. In consequence, some (conservative) assumptions must be made to calculate the dose, such as considering the physical half-life of ^{18}F equal to the effective half-life of ^{18}F-FDG. It is likely that the fetal dose calculated with measured time-integrated coefficients will be slightly lower. If the PET scan of a pregnant woman is planned, we encourage nuclear medicine departments to acquire dynamic images. These would not increase the radiation dose but would allow an even more accurate assessment of fetal dosimetry as well as enable, for the first time, calculation in vivo of the metabolic rate of glucose in the various fetal tissues with full kinetic modeling. Given the absence of radiometabolites, ^{18}F-FDG activity in the mother's aorta would provide an excellent image-derived input function. Recent scanners—which allow fast dynamic images of excellent quality to be obtained over the whole body even with lower injected activities (*19*)—may yield input functions of such quality that they could reliably be used in conjunction with the gold standard of compartmental modeling rather than only with graphical analyses (*20*). This would enable a deeper understanding of the physiology of glucose utilization in the fetus and its evolution over the duration of pregnancy.

CONCLUSION

PET/MR images of pregnant women injected with ^{18}F-FDG confirm that the fetal ^{18}F-FDG dose is very low. Therefore, clinically appropriate ^{18}F-FDG scans in women with cancer should not be withheld because of pregnancy.

DISCLOSURE

This work was supported in part by the Intramural Research Program of the National Institute of Mental Health, National Institutes of Health (project number ZIAMH002852). The views expressed in this commentary do not necessarily represent the views of the National Institutes of Health, the Department of Health and Human Services, or the United States Government. No other potential conflict of interest relevant to this article was reported.

ACKNOWLEDGMENT

We thank Ioline Henter (NIMH) for invaluable editorial assistance.

KEY POINTS

QUESTION: What is the ^{18}F-FDG fetal dosimetry in pregnant women with cancer imaged with PET/MRI?

PERTINENT FINDINGS: Dosimetric values estimated with PET/MRI confirm that the ^{18}F-FDG fetal dose is very low.

IMPLICATIONS FOR PATIENT CARE: Clinically appropriate ^{18}F-FDG scans in women with cancer should not be withheld because of pregnancy.

REFERENCES

1. Russell JR, Stabin MG, Sparks RB. Placental transfer of radiopharmaceuticals and dosimetry in pregnancy. *Health Phys.* 1997;73:747–755.
2. Stabin MG. Proposed addendum to previously published fetal dose estimate tables for ^{18}F-FDG. *J Nucl Med.* 2004;45:634–635.
3. Zanotti-Fregonara P, Champion C, Trebossen R, Maroy R, Devaux JY, Hindie E. Estimation of the beta+ dose to the embryo resulting from ^{18}F-FDG administration during early pregnancy. *J Nucl Med.* 2008;49:679–682.
4. Zanotti-Fregonara P, Chastan M, Edet-Sanson A, et al. New Fetal dose estimates from ^{18}F-FDG administered during pregnancy: standardization of dose calculations and estimations with voxel-based anthropomorphic phantoms. *J Nucl Med.* 2016; 57:1760–1763.
5. Stabin MG. New-generation fetal dose estimates for radiopharmaceuticals. *J Nucl Med.* 2018;59:1005–1006.
6. Ishiguro T, Nishikawa N, Ishii S, et al. PET/MR imaging for the evaluation of cervical cancer during pregnancy. *BMC Pregnancy Childbirth.* 2021;21:288.
7. Stabin M, Watson E, Cristy M, et al. *Mathematical Models and Specific Absorbed Fractions of Photon Energy in the Nonpregnant Adult Female and at the End of Each Trimester of Pregnancy.* ORNL Report ORNL/TM-12907. Oak Ridge National Laboratory (ORNL): 1995.
8. International Commission on Radiological Protection (ICRP). ICRP publication 106: radiation dose to patients from radiopharmaceuticals—addendum 3 to ICRP publication 53. *Ann ICRP.* 2008;38:1–197.
9. Stabin MG, Sparks RB, Crowe E. OLINDA/EXM: the second-generation personal computer software for internal dose assessment in nuclear medicine. *J Nucl Med.* 2005;46:1023–1027.
10. Zanotti-Fregonara P, Stabin MG. New fetal radiation doses for ^{18}F-FDG based on human data. *J Nucl Med.* 2017;58:1865–1866.
11. Stabin M, Farmer A. OLINDA/EXM 2.0: The new generation dosimetry modeling code. *J Nucl Med.* 2012;53(suppl 1):585.
12. Zanotti-Fregonara P. Radiation absorbed dose to the embryo and fetus from radiopharmaceuticals. *Semin Nucl Med.* 2022;52:140–148.
13. Brent RL. Saving lives and changing family histories: appropriate counseling of pregnant women and men and women of reproductive age, concerning the risk of

diagnostic radiation exposures during and before pregnancy. *Am J Obstet Gynecol.* 2009;200:4–24.
14. Zanotti-Fregonara P, Hindie E. Performing nuclear medicine examinations in pregnant women. *Phys Med.* 2017;43:159–164.
15. Zanotti-Fregonara P. Pregnancy should not rule out ^{18}FDG PET/CT for women with cancer. *Lancet.* 2012;379:1948.
16. Stabin MG. Uncertainties in internal dose calculations for radiopharmaceuticals. *J Nucl Med.* 2008;49:853–860.
17. Gear JI, Cox MG, Gustafsson J, et al. EANM practical guidance on uncertainty analysis for molecular radiotherapy absorbed dose calculations. *Eur J Nucl Med Mol Imaging.* 2018;45:2456–2474.
18. Zanotti-Fregonara P, Jan S, Champion C, et al. In vivo quantification of 18f-fdg uptake in human placenta during early pregnancy. *Health Phys.* 2009;97:82–85.
19. Vandenberghe S, Moskal P, Karp JS. State of the art in total body PET. *EJNMMI Phys.* 2020;7:35.
20. Zanotti-Fregonara P, Chen K, Liow JS, Fujita M, Innis RB. Image-derived input function for brain PET studies: many challenges and few opportunities. *J Cereb Blood Flow Metab.* 2011;31:1986–1998.
21. Zanotti-Fregonara P, Laforest R, Wallis JW. Fetal radiation dose from ^{18}F-FDG in pregnant patients imaged with PET, PET/CT, and PET/MR. *J Nucl Med.* 2015;56:1218–1222.
22. Takalkar AM, Khandelwal A, Lokitz S, Lilien DL, Stabin MG. ^{18}F-FDG PET in pregnancy and fetal radiation dose estimates. *J Nucl Med.* 2011;52:1035–1040.
23. Zanotti-Fregonara P, Jan S, Taieb D, et al. Absorbed ^{18}F-FDG dose to the fetus during early pregnancy. *J Nucl Med.* 2010;51:803–805.
24. Zanotti-Fregonara P, Koroscil TM, Mantil J, Satter M. Radiation dose to the fetus from [^{18}F]-FDG administration during the second trimester of pregnancy. *Health Phys.* 2012;102:217.
25. Calais J, Hapdey S, Tilly H, Vera P, Chastan M. Hodgkin's disease staging by FDG PET/CT in a pregnant woman. *Nucl Med Mol Imaging.* 2014;48:244–246.
26. Erdogan EB, Ekmekcioglu O, Vatankulu B, Ergul N, Demir M, Sonmezoglu K. An unknown pregnancy at term detected by a FDG-PET/CT study in a patient with Hodgkin's lymphoma: a case report. *Rev Esp Med Nucl Imagen Mol.* 2015;34:201–202.

Erratum

In the article "Choice Is Good at Times: The Emergence of [^{64}Cu]Cu-DOTATATE–Based Somatostatin Receptor Imaging in the Era of [^{68}Ga]Ga-DOTATATE," by Jha et al. (*J Nucl Med*. 2022;63:1300–1301), gallium-68 was incorrectly cited at editing as having a lower positron energy and lower positron range than copper-64. The corrected sentence should read: "*Copper-64 has a lower positron energy than Gallium-68 (0.65 vs. 1.90 MeV), resulting in a lower positron range (0.56 vs. 3.5 mm) that provides superior spatial resolution, improved imaging quality, and enhanced detection of small lesions (7).*" We regret the error.

^{68}Ga-Citrate PET of Healthy Men: Whole-Body Biodistribution Kinetics and Radiation Dose Estimates

Sami Suilamo[1,2], Xiang-Guo Li[3–5], Petteri Lankinen[6,7], Vesa Oikonen[3], Tuula Tolvanen[1,7], Pauliina Luoto[3,7], Riikka Viitanen[3], Antti Saraste[3,7,8], Marko Seppänen[7,9], Laura Pirilä[10,11], Ulla Hohenthal[12], and Anne Roivainen[3,5,7]

[1]Department of Medical Physics, Turku University Hospital, Turku, Finland; [2]Department of Oncology and Radiotherapy, Turku University Hospital, Turku, Finland; [3]Turku PET Centre, University of Turku, Turku, Finland; [4]Department of Chemistry, University of Turku, Turku, Finland; [5]InFLAMES Research Flagship Center, University of Turku, Turku, Finland; [6]Department of Orthopaedics and Traumatology, Turku University Hospital and University of Turku, Turku, Finland; [7]Turku PET Centre, Turku University Hospital, Turku, Finland; [8]Heart Center, Turku University Hospital, Turku, Finland; [9]Department of Clinical Physiology and Nuclear Medicine, Turku University Hospital, Turku, Finland; [10]Department of Rheumatology and Clinical Immunology, Division of Medicine, Turku University Hospital; Turku, Finland; [11]Department of Medicine, University of Turku, Turku, Finland; and [12]Department of Infectious Diseases, Division of Medicine, Turku University Hospital, Turku, Finland

^{68}Ga-citrate has one of the simplest chemical structures of all ^{68}Ga-radiopharmaceuticals, and its clinical use is justified by the proven medical applications using its isotope-labeled compound ^{67}Ga-citrate. To support broader application of ^{68}Ga-citrate in medical diagnosis, further research is needed to gain clinical data from healthy volunteers. In this work, we studied the biodistribution of ^{68}Ga-citrate and subsequent radiation exposure from it in healthy men. **Methods:** ^{68}Ga-citrate was prepared with an acetone-based radiolabeling procedure compliant with good manufacturing practices. Six healthy men (age 41 ± 12 y, mean ± SD) underwent sequential whole-body PET/CT scans after an injection of 204 ± 8 MBq of ^{68}Ga-citrate. Serial arterialized venous blood samples were collected during PET imaging, and the radioactivity concentration was measured with a γ-counter. Urinary voids were collected and measured. The MIRD bladder-voiding model with a 3.5-h voiding interval was used. A model using a 70-kg adult man and the MIRD schema was used to estimate absorbed doses in target organs and effective doses. Calculations were performed using OLINDA/EXM software, version 2.0. **Results:** Radioactivity clearance from the blood was slow, and relatively high radioactivity concentrations were observed over the whole of the 3-h measuring period. Although radioactivity excretion via urine was rather slow (biologic half-time, 69 ± 24 h), the highest decay-corrected concentrations in urinary bladder contents were measured at the 90- and 180-min time points. Moderate concentrations were also seen in kidneys, liver, and spleen. The source organs showing the largest residence times were muscle, liver, lung, and heart contents. The heart wall received the highest absorbed dose, 0.077 ± 0.008 mSv/MBq. The mean effective dose (International Commission on Radiological Protection publication 103) was 0.021 ± 0.001 mSv/MBq. **Conclusion:** PET imaging with ^{68}Ga-citrate is associated with modest radiation exposure. A 200-MBq injection of ^{68}Ga-citrate results in an effective radiation dose of 4.2 mSv, which is in the same range as other ^{68}Ga-labeled tracers. This suggests the feasibility of clinical studies using ^{68}Ga-citrate imaging in humans and the possibility of performing multiple scans in the same subjects across the course of a year.

Key Words: biodistribution; ^{68}Ga-citrate; PET; pharmacokinetics; radiation dose

J Nucl Med 2022; 63:1598–1603
DOI: 10.2967/jnumed.122.263884

For PET imaging, ^{68}Ga is a transition metal that can be used as ^{68}Ga-citrate or ^{68}Ga-chloride and also in its chelated forms with biomolecules (e.g., chelator-conjugated peptides). ^{68}Ga-labeled pharmaceuticals are frequently used in nuclear medicine and can conveniently be manufactured with kits and fully automated commercially available devices (*1*). ^{68}Ga-citrate is one such ^{68}Ga-radiopharmaceutical that has entered the clinical trial stage, and its use in PET is based on Ga^{3+} uptake and transportation mechanisms. Ga^{3+} is considered an analog of Fe^{3+} and binds to transferrin and other biomolecules in vivo. Although only a few human studies using ^{68}Ga-citrate PET have been performed (*2–13*), ^{68}Ga-citrate has already been shown to be a sensitive and specific PET tracer for the imaging of infection and inflammation, including inflammatory bowel disease (*3*), bone infection (*4*), intraabdominal infection (*5*), and prosthetic joint infection (*12*). In addition, we recently observed unexpectedly high ^{68}Ga-citrate accumulation in atherosclerotic lesions in patients with *Staphylococcus aureus* bacteremia (*8*). Furthermore, patients with high-grade glioma, hepatocellular carcinoma, and prostate cancer have been imaged with ^{68}Ga-citrate according to the hypothesis that Ga^{3+} uptake should increase in these tumors because of upregulated activity of transferrin receptor (*7,9–11*). Evidence from clinical and preclinical investigations (*7,14,15*) suggests that ^{68}Ga-citrate has potential in several clinical applications and that further research is warranted.

The purpose of this clinical study was to determine the biodistribution of intravenously administered ^{68}Ga-citrate in healthy male volunteers. This information will help to determine the optimal PET protocol for ^{68}Ga-citrate imaging of inflammatory and infectious diseases and cancer. The whole-body imaging should allow identification of those organs that are most exposed to ionizing radiation and allow calculation of the dose absorbed by each organ.

Received Jan. 28, 2022; revision accepted Mar. 7, 2022.
For correspondence or reprints, contact Anne Roivainen (anne.roivainen@utu.fi).
Published online Mar. 10, 2022.

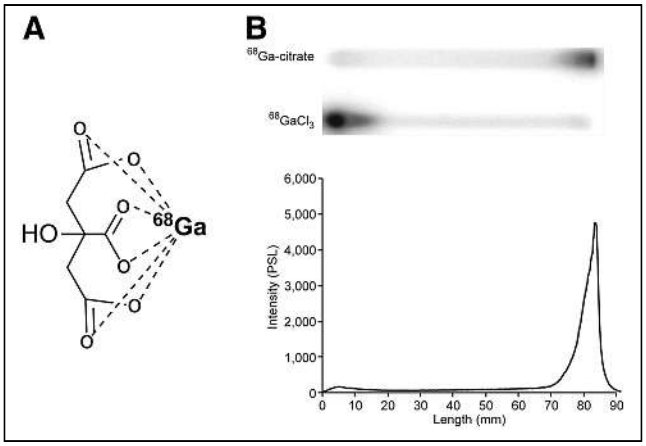

FIGURE 1. (A) Chemical structure of ^{68}Ga-citrate. (B) Quality control of ^{68}Ga-citrate with instant thin-layer chromatography developed using methanol/acetic acid (9:1, *v/v*) as mobile phase and visualized and quantified by autoradiography.

MATERIALS AND METHODS

Chemicals and Reagents

All chemicals were purchased from commercial sources and were of reagent, analytic, ultrapure, or European Pharmacopeia grade.

Preparation of ^{68}Ga-Citrate

^{68}Ga-citrate (Fig. 1A) was produced according to an established protocol (*3*). Aqueous hydrochloric acid (0.1 M, 6 mL) was used to elute ^{68}Ga radioactivity from a ^{68}Ge/^{68}Ga generator (IGG-100, 1,850 MBq; Eckert and Ziegler Isotope Products), and the ^{68}Ga-eluate was passed through a cation-exchange cartridge (Strata X-C; Phenomenex Inc.). The retained ^{68}Ga was eluted into a reaction vial with acidified acetone (800 μL, containing 0.02 M HCl and 3.25% water). The acetone was removed by evaporation for 4 min at 110°C, and sodium citrate buffer (4 mL) was added. After 4 min, the reaction mixture was sterile-filtrated into an end-product vial and diluted with saline (9 mg/mL, 6 mL). Radiochemical purity was measured by instant thin-layer chromatography with methanol/acetic acid (9:1, *v/v*) as a mobile phase.

Subjects

Six healthy male volunteers (age, 41 ± 13 y; weight, 75 ± 4 kg; height, 177 ± 4 cm) participated in this trial. ^{68}Ga-citrate was injected via a catheter inserted into an antecubital vein, and blood samples were drawn through another catheter inserted into the contralateral arm.

Before the start of this clinical trial, approvals were obtained from the joint Ethics Committee of the University of Turku and Turku University Hospital, as well as from the Finnish Medicines Agency. Full informed consent was obtained in writing from all subjects beforehand. This study is registered at ClinicalTrials.gov (NCT01951300).

Questionnaires were used to assess the absence of significant medical, neurologic, and psychiatric history and of any history of alcohol or drug abuse. In addition, routine blood tests, electrocardiography, a physical examination, and a review of medical history were performed for each subject.

PET/CT Imaging

The biodistribution of ^{68}Ga-citrate was imaged using a Discovery 690 PET/CT scanner (GE Healthcare). This scanner combines 64-slice CT with PET acquired using 24 rings of lutetium-yttrium-orthosilicate detectors, which provide 47 imaging planes with an axial field of view of 15.7 cm. A low-dose CT scan for attenuation correction and anatomic reference was acquired before the PET scan, using a voltage of 120 kV and current of 10 mA. Whole-body PET acquisitions were made 1, 5, 10, 20, 30, 90, and 180 min after an intravenous injection of 204 ± 8 MBq of ^{68}Ga-citrate. The acquisition times per bed position were 20, 30, 65, 65, 120, 240, and 240 s, respectively. The scanning at 90 min after injection included 14 bed positions covering the range from the head to the toes, whereas all other scans used only 8 bed positions covering the range from the head to mid thighs.

PET images were reconstructed using a time-of-flight 3D VUE Point algorithm (GE Healthcare) with 2 iterations, 24 subsets, and a postprocessing filter of 6.4 mm in full width at half maximum. Scatter correction, random counts, and dead-time corrections were all incorporated into the reconstruction algorithm. The final matrix size was 192 × 192 × 47 voxels. The plane thickness of the PET scanner was 3.27 mm, and the axial spatial resolution for 3-dimensional mode was 4.74 mm in full width at half maximum at a 1-cm offset from the center of the field of view (*16*).

Blood and Urine Measurements

Serial arterialized (the arm was heated with a wrapped heating pad) venous blood samples were collected into heparinized tubes at 1, 5, 10, 20, 30, 60, 90, 180, and 240 min after the injection of ^{68}Ga-citrate. The radioactivity of the whole blood was measured with an automatic γ-counter (1480 Wizard 3″; EG&G Wallac). Plasma was separated by centrifugation (2,100*g* for 5 min at 4°C), and the plasma radioactivity was measured. The plasma concentration at baseline (C_0) was estimated by fitting a monoexponential function to the plasma concentrations collected between 5 and 30 min.

The subjects were asked to urinate during 2 breaks in the PET imaging session and again after the session. The mean times for urination were 61 min after injection, 163 min after injection, and 218 min after injection. Urinary voids were collected, the total volume was measured, and a 2.5-mL sample was taken for radioactivity measurement with a VDC 405 dose calibrator (Veenstra Instruments).

Distribution Kinetics and Radiation Dose Estimates

Eclipse software (version 13.6; Varian Medical Systems) was used to define the radioactivity concentrations of the source organs at different time points. The source organ volumes either were defined on CT images or were the volumes of the organs of the reference man (*17*).

Residence times in source organs were calculated from area under the time–activity curves. The curves were defined by fitting a sum of 2 exponential functions. The MIRD bladder-voiding model (*18*) with a 3.5-h voiding interval was used. A model with a 70-kg adult man and MIRD schema (*19*) was used to estimate the absorbed doses in the target organs and the effective doses. Calculations were performed using OLINDA/EXM software, version 2.0. In addition, OLINDA 1.0 results were calculated.

RESULTS

Radiochemistry

The manufactured ^{68}Ga-citrate fulfilled all the product quality specifications (Supplemental Table 1; supplemental materials are available at http://jnm.snmjournals.org) for clinical use. The radiochemical purity was at least 95%, pH was in the range of 3.0 − 7.0, and the acetone content was no more than 0.5%. An example instant thin-layer chromatography plot used to determine radiochemical purity is shown in Figure 1B.

Biodistribution and Biokinetics

Whole-body dynamic PET/CT imaging data were obtained from 6 subjects over a period of 180 min after ^{68}Ga-citrate administration. Figure 2 shows representative images from a subject. The radioactivity concentrations in 20 organs or tissues of interest

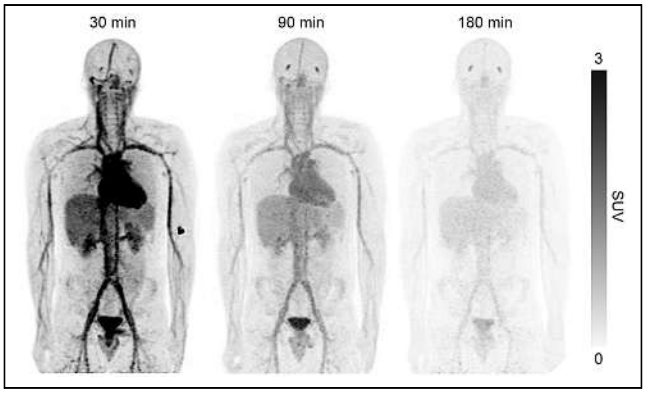

FIGURE 2. Whole-body distribution of 195 MBq of ^{68}Ga-citrate in healthy 22-y-old man (73 kg).

were quantified at time points of 1, 5, 10, 20, 30, 90, and 180 min, and the results are presented in Supplemental Table 2. At 30 min after injection, SUVs in the brain, heart contents, kidneys, liver, trabecular bone, and red marrow were 0.26 ± 0.04 (mean ± SD), 5.16 ± 0.48, 3.15 ± 0.46, 2.78 ± 0.25, 0.70 ± 0.15, and 1.80 ± 0.12, respectively. Figure 3 shows time–activity curves for the 20 organs or tissues, revealing the whole-body distribution kinetics of radioactivity over the 180 min after ^{68}Ga-citrate administration.

The mean voided radioactivity at a mean void time of 61 min after injection (during a break between PET imaging session) was 1.76 ± 0.47 percentage injected dose (Fig. 4). All 6 subjects were able to urinate during the first PET imaging session break, 3 were able to urinate between imaging session 2 and 3, and 2 after the complete imaging session.

Radioactivity clearance from the blood was slow (Fig. 5). The C_0 in SUV units was 17.3 ± 1.8 g/mL (Supplemental Table 3). The inverse of C_0, which is related to the total plasma volume, was 0.059 ± 0.006 L/kg. The plasma concentration at 4 h ($n = 5$) was 5.8 ± 0.6 g/mL, and its inverse, which may be related to the extracellular volume of the body, was 0.17 ± 0.02 L/kg.

Residence Times and Radiation Dose Estimates

The residence times (normalized numbers of disintegrations) were determined for the source organs and the remainder of the body of each subject, and their mean ± SD, range, and coefficient of variation are listed in Table 1. The coefficients of variation were in the range of 4%−49%. The largest residence times were in muscle (0.365 ± 0.043 h), liver (0.091 ± 0.017 h), lungs (0.079 ± 0.008 h), and heart contents (0.048 ± 0.006 h).

The organ dose estimates (Table 2) were calculated for a 70-kg adult man. The organs with the highest doses were the heart wall (0.077 ± 0.008 mSv/MBq), urinary bladder wall (0.039 ± 0.010 mSv/MBq), kidneys (0.036 ± 0.004 mSv/MBq), and lungs (0.036 ± 0.003 mSv/MBq). The lowest dose was in the brain (0.004 ± 0.001 mSv/MBq). The mean effective dose (International Commission on Radiological Protection publication 103) (*20*) was 0.021 ± 0.001 mSv/MBq. Thus, the effective dose from 200 MBq of injected radioactivity of ^{68}Ga-citrate was 4.2 mSv.

Organ dose estimates according to OLINDA 1.0 are presented in Supplemental Table 4.

DISCUSSION

We previously studied ^{68}Ga-citrate in experimental disease models, as well as in patients with infections (*8,15,21*). The

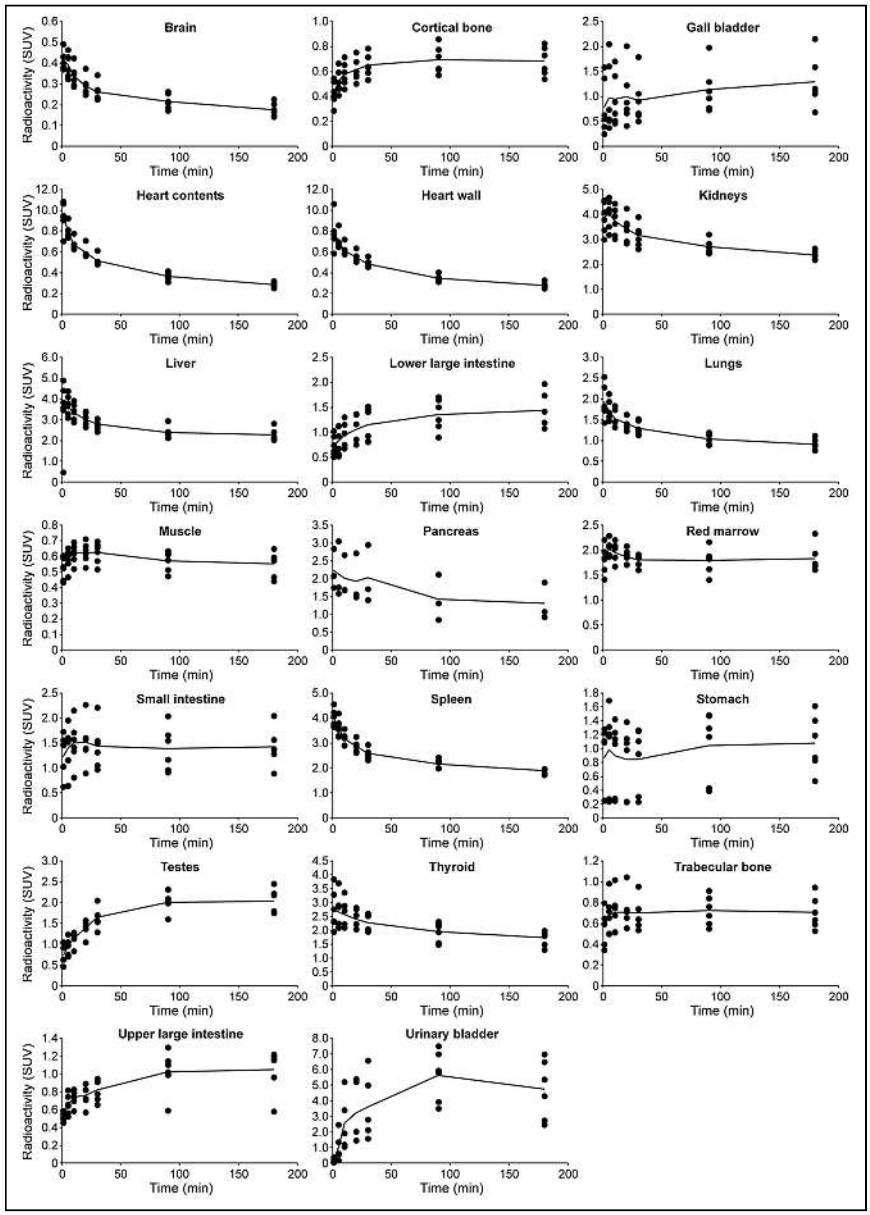

FIGURE 3. Time–activity curves of main organs. Circles represent each individual, and line is average.

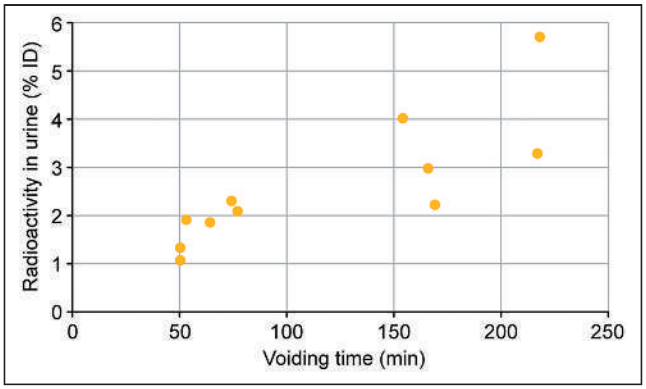

FIGURE 4. Percentage of injected ^{68}Ga-citrate radioactivity dose (%ID) in urine as function of time.

current study was a basic investigation in healthy humans to collect data on whole-body distribution kinetics and radiation dose estimates, which will be useful in planning future clinical trials with ^{68}Ga-citrate.

Preparation of ^{68}Ga-Citrate

The radiopharmaceutical ^{68}Ga-citrate was produced using a straightforward protocol (*3*). The acetone-based cation-exchange cartridge elution method is an effective option for concentrating ^{68}Ga radioactivity eluted from a generator (*1*). In our hospital, this method is used to manufacture 3 radiopharmaceuticals, including ^{68}Ga-citrate, in a fully automated manner. Citrate is a natural ligand that can coordinate some metal ions, including gallium. Because of the nature of the nuclear physics of ^{68}Ga, the molarity of ^{68}Ga in a batch of eluate from a ^{68}Ge/^{68}Ga generator is tiny. By contrast, the molarity of citrate (0.14 mmol) is in great excess to ensure efficient coordination, which is neither feasible nor typical in the production of many other ^{68}Ga-radiopharmaceuticals. In this sense, citrate acts also as a vehicle, in addition to its role as a chelator. On instant thin-layer chromatography, the chromatography behaviors of ^{68}Ga-citrate and free ^{68}Ga show a clear difference (Fig. 1B); free ^{68}Ga remains at the baseline whereas ^{68}Ga-citrate migrates up on the instant thin-layer chromatography, with a retention factor of 0.93. As there is not a citrate dose limit set in the European Pharmacopeia; quantification of the citrate in the end-product formulation is not relevant in the quality control procedure.

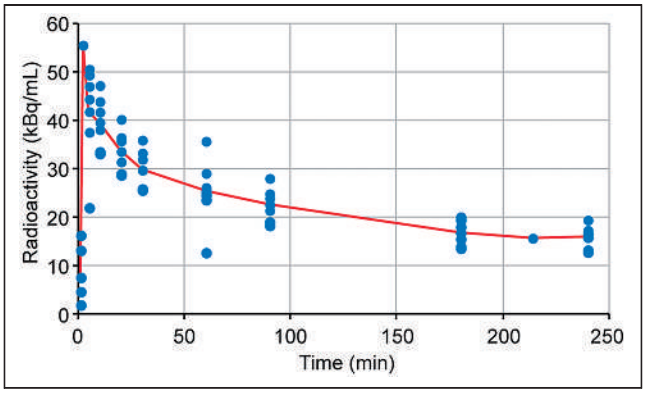

FIGURE 5. Concentration of radioactivity in arterialized venous plasma as function of time after ^{68}Ga-citrate injection. Dots represent each individual, and line is average.

TABLE 1
Residence Times (Hours) in Source Organs After Injection of ^{68}Ga-Citrate

Organ	Mean ± SD	COV (%)	Range
Brain	0.008 ± 0.001	19	0.006–0.009
Gallbladder contents	0.000 ± 0.000	48	0.000–0.001
Left colon	0.002 ± 0.001	23	0.001–0.003
Small intestine	0.012 ± 0.003	27	0.007–0.016
Stomach contents	0.009 ± 0.004	38	0.004–0.013
Right colon	0.002 ± 0.001	23	0.001–0.003
Rectum	0.002 ± 0.001	25	0.001–0.003
Heart contents	0.048 ± 0.006	12	0.041–0.055
Heart wall	0.027 ± 0.004	13	0.024–0.033
Kidneys	0.020 ± 0.003	14	0.017–0.023
Liver	0.091 ± 0.017	19	0.077–0.121
Lungs	0.079 ± 0.008	10	0.066–0.088
Muscle	0.365 ± 0.043	12	0.299–0.420
Pancreas	0.005 ± 0.002	49	0.003–0.008
Red marrow	0.046 ± 0.004	10	0.038–0.052
Cortical bone	0.032 ± 0.005	15	0.026–0.040
Trabecular bone	0.009 ± 0.002	22	0.007–0.012
Spleen	0.009 ± 0.002	28	0.006–0.012
Testes	0.002 ± 0.000	15	0.001–0.002
Thyroid	0.001 ± 0.000	19	0.000–0.001
Urinary bladder contents	0.021 ± 0.008	37	0.013–0.035
Remainder of body	0.810 ± 0.033	4	0.767–0.858

COV = coefficient of variation (SD/mean × 100).

PET Imaging and Biodistribution

In a typical ^{68}Ga-radiopharmaceutical, the ^{68}Ga-radionuclide is attached to a targeting molecule, such as a peptide, and the targeting molecule takes the radioactivity to the specific organs and tissues to be imaged. In the case of ^{68}Ga-citrate, the imaging and biodistribution are most probably based on the biologic mechanisms of $^{68}Ga^{3+}$, which can be chelated in vivo with biomolecules, including ferritins (*13*). This implies that in vivo transmetalation takes place, even though citrate has sufficient strength to coordinate $^{68}Ga^{3+}$ in the manufacturing procedures. However, comparison studies have indicated that the imaging performance of ^{68}Ga-citrate is better than that of intravenously injected ^{68}Ga-chloride, at least as far as the limited available evidence shows (*15*), which might be an indication that citrate plays a role as a vehicle in the in vivo biodistribution. In this study, particular care was taken to ensure that the ^{68}Ga-citrate injection did not involve any gallium colloids, which usually accompany the ^{68}Ge/^{68}Ga generator eluate or are formed if injected as ^{68}Ga-chloride.

For the PET imaging, each subject was intravenously administered 204 ± 8 MBq of ^{68}Ga-citrate. In a routine PET procedure performed in our hospital, such as one using the standard tracer ^{18}F-FDG, the typical radioactivity dose is 4 MBq/kg of body weight. In this study, we used 204 ± 8 MBq (2.7 ± 0.2 MBq/kg)

TABLE 2
Organ Doses and Effective Doses (mSv/MBq) After Injection of ^{68}Ga-Citrate

Organ	Mean ± SD	COV (%)	Range
Adrenals	0.019 ± 0.001	4	0.018–0.020
Brain	0.004 ± 0.001	12	0.004–0.005
Breasts	0.013 ± 0.000	2	0.012–0.013
Colon, left	0.021 ± 0.002	7	0.019–0.023
Colon, right	0.017 ± 0.001	4	0.016–0.018
Esophagus	0.015 ± 0.000	2	0.015–0.016
Eyes	0.011 ± 0.000	3	0.010–0.011
Gallbladder wall	0.017 ± 0.001	6	0.016–0.019
Heart wall	0.077 ± 0.008	11	0.067–0.087
Kidneys	0.036 ± 0.004	12	0.031–0.041
Liver	0.033 ± 0.005	16	0.029–0.043
Lungs	0.036 ± 0.003	8	0.031–0.040
Osteogenic cells	0.017 ± 0.001	6	0.015–0.018
Pancreas	0.020 ± 0.007	36	0.015–0.034
Prostate	0.013 ± 0.000	2	0.012–0.013
Rectum	0.020 ± 0.001	7	0.018–0.022
Red marrow	0.020 ± 0.001	5	0.019–0.022
Salivary glands	0.012 ± 0.000	3	0.011–0.012
Small intestine	0.022 ± 0.002	11	0.019–0.025
Spleen	0.032 ± 0.007	23	0.025–0.044
Stomach wall	0.024 ± 0.004	15	0.018–0.027
Testes	0.022 ± 0.003	13	0.019–0.026
Thymus	0.016 ± 0.000	2	0.016–0.017
Thyroid	0.017 ± 0.002	14	0.014–0.021
Urinary bladder wall	0.039 ± 0.010	26	0.029–0.057
Total body	0.015 ± 0.000	1	0.014–0.015
Effective dose, ICRP 60 (*27*)	0.023 ± 0.001	3	0.021–0.023
Effective dose, ICRP 103 (*20*)	0.021 ± 0.001	3	0.020–0.022

COV = coefficient of variation (SD/mean × 100); ICRP = International Commission on Radiological Protection.

of ^{68}Ga-citrate per subject, which is in the typical dose range of our ^{68}Ga-radiopharmaceutical PET studies. The mass of gallium injected was negligible. It is noteworthy that when gallium is administered as a drug in high doses, the biodistribution is known to change (*22,23*).

The sequential whole-body imaging was performed for 180 min to monitor the tracer kinetics in vivo. For visualization purposes, we prepared representative PET/CT images from a 22-y-old man and scaled the SUVs from 1 to 3 (Fig. 2). These images clearly show that the radioactivity concentration was much higher in heart, liver, lungs, and kidneys than in other organs. At 180 min after injection, the whole-body radioactivity concentration became very low, an indication of a sufficient data collection time range. To further quantify the radioactivity concentration in the 20 organs of interest, time–activity curves were drawn from 0 to 180 min after administration (Fig. 3). Among the organs and tissues, the time–activity curves from gallbladder, lower large intestine (left colon and rectum), testes, and upper large intestine (right colon) were still increasing slightly at 180 min. It was not clear what factors might have caused the slight accumulations in these organs. In cortical bone, red marrow, small intestine, and trabecular bone, the time–activity curves showed a steady radioactivity residence along with time. In the urinary bladder, the general trend of radioactivity development was an initial increase and then a decrease. In the rest of the organs, the time–activity curves decreased to varying extents over the period.

The radioactivity concentration in plasma stayed at a high level (Fig. 5), similar to that reported previously for the ^{68}Ge/^{68}Ga generator eluate ^{68}Ga-chloride in a study on rats (*24*); the slow decrease at 3–4 h prevents reliable estimation of the total area under the curve (from time zero to infinity) and total clearance. In previous animal studies, we found that the in vivo kinetics of ^{68}Ga-citrate and ^{68}Ga-chloride differed, possibly because the chelating properties of citrate prevent the precipitation of $^{68}Ga(OH)_3$ (*15*).

Radiation Dose Estimates

To determine the radiation burden, we analyzed the kinetics of radioactivity concentration in the main organs of healthy men up to 3 h after an intravenous bolus injection of ^{68}Ga-citrate. In addition to the SD and range, the coefficient of variation was used to indicate the precision and repeatability of the measurements among the 6 subjects. Our results revealed that the heart wall received the highest radiation dose, followed by the urinary bladder wall. This may be partially due to the relatively slow blood clearance and urinary excretion as the main clearance route. However, the relatively slow blood clearance was not a problem for target visualization in previous studies. The organ with the lowest radiation exposure was the brain (0.004 ± 0.001 mSv/MBq). Overall, the effective dose of ^{68}Ga-citrate (0.021 ± 0.001 mSv/MBq) was comparable to that of widely used PET tracers, including ^{68}Ga-DOTANOC (0.025 mSv/MBq) (*25*) and ^{18}F-FDG (0.019 mSv/MBq) (*26*). For example, a 200-MBq dose of ^{68}Ga-citrate may result in an effective dose of 4.2 ± 0.2 mSv.

CONCLUSION

The radiation burden from administration of ^{68}Ga-citrate for PET imaging is comparable to that of other commonly used ^{68}Ga-radiopharmaceuticals. The low radiation exposure of ^{68}Ga-citrate would allow for studies with multiple scans in the same individuals over the course of a year.

DISCLOSURE

The study was conducted within the Finnish Centre of Excellence in Cardiovascular and Metabolic Diseases, supported by the Academy of Finland, University of Turku, Turku University Hospital, and Åbo Akademi University. The study was financially supported by grants from the State Research Funding of Turku University Hospital and the Sigrid Jusélius Foundation. No other potential conflict of interest relevant to this article was reported.

ACKNOWLEDGMENTS

We thank the technical and nursing staff at Turku PET Centre for their assistance in this work, and we thank Timo Kattelus for preparing figures.

KEY POINTS

QUESTION: What are the distribution kinetics of ^{68}Ga-citrate in healthy humans, and what is the radiation burden resulting from its administration?

PERTINENT FINDINGS: Six healthy men underwent dynamic whole-body PET/CT imaging with blood and urine measurements. ^{68}Ga-citrate showed slow clearance from the blood circulation through renal excretion. The highest radiation exposure was to the heart wall. The effective dose of 0.021 mSv/MBq is similar to that of other commonly used ^{68}Ga tracers.

IMPLICATIONS FOR PATIENT CARE: The characteristics of ^{68}Ga-citrate are favorable for human studies involving multiple scans in the same subject over the course of a year.

REFERENCES

1. Käkelä M, Luoto P, Viljanen T, et al. Adventures in radiosynthesis of clinical grade [^{68}Ga]Ga-DOTA-Siglec-9. *RSC Advances.* 2018;8:8051–8056.
2. Mintun MA, Dennis DR, Welch MJ, Mathias CJ, Schuster DP. Measurements of pulmonary vascular permeability with PET and gallium-68 transferrin. *J Nucl Med.* 1987;28:1704–1716.
3. Rizzello A, Pierro DD, Lodi F, et al. Synthesis and quality control of ^{68}Ga citrate for routine clinical PET. *Nucl Med Commun.* 2009;30:542–545.
4. Nanni C, Errani C, Boriani L, et al. ^{68}Ga-citrate PET/CT for evaluating patients with infections of the bone: preliminary results. *J Nucl Med.* 2010;51:1932–1936.
5. Kumar V, Boddeti DK, Evans SG, Angelides S. ^{68}Ga-citrate-PET for diagnostic imaging of infection in rats and for intra-abdominal infection in a patient. *Curr Radiopharm.* 2012;5:71–75.
6. Vorster M, Maes A, Jacobs A, et al. Evaluating the possible role of ^{68}Ga-citrate PET/CT in the characterization of indeterminate lung lesions. *Ann Nucl Med.* 2014;28:523–530.
7. Behr SC, Aggarwal R, Seo Y, et al. A feasibility study showing [^{68}Ga]citrate PET detects prostate cancer. *Mol Imaging Biol.* 2016;18:946–951.
8. Salomäki SP, Kemppainen J, Hohenthal U, et al. Head-to-head comparison of ^{68}Ga-citrate and ^{18}F-FDG PET/CT for detection of infectious foci in patients with *Staphylococcus aureus* bacteraemia. *Contrast Media Mol Imaging.* 2017;2017:3179607.
9. Aggarwal R, Behr SC, Paris PL, et al. Real-time transferrin-based PET detects MYC-positive prostate cancer. *Mol Cancer Res.* 2017;15:1221–1229.
10. Aparici CM, Behr SC, Seo Y, et al. Imaging hepatocellular carcinoma with ^{68}Ga-citrate PET: first clinical experience. *Mol Imaging.* 2017;16:1536012117723256.
11. Behr SC, Villanueva-Meyer JE, Li Y, et al. Targeting iron metabolism in high-grade glioma with ^{68}Ga-citrate PET/MR. *JCI Insight.* 2018;3:e93999.
12. Tseng JR, Chang YH, Yang LY, et al. Potential usefulness of ^{68}Ga-citrate PET/CT in detecting infected lower limb prostheses. *EJNMMI Res.* 2019;9:2.
13. Xu T, Chen Y. Research progress of [^{68}Ga]citrate PET's utility in infection and inflammation imaging: a review. *Mol Imaging Biol.* 2020;22:22–32.
14. Nielsen OL, Afzelius P, Bender D, et al. Comparison of autologous ^{111}In-leukocytes, ^{18}F-FDG, ^{11}C-methionine, ^{11}C-PK11195 and ^{68}Ga-citrate for diagnostic nuclear imaging in a juvenile porcine haematogenous *Staphylococcus aureus* model. *Am J Nucl Med Mol Imaging.* 2015;5:169–182.
15. Lankinen P, Noponen T, Autio A, et al. A comparative ^{68}Ga-citrate and ^{68}Ga-chloride PET/CT imaging of *Staphylococcus aureus* osteomyelitis in the rat tibia. *Contrast Media Mol Imaging.* 2018;2018:9892604.
16. Bettinardi V, Presotto L, Rapisarda E, Picchio L, Gianolli L, Gilardi MC. Physical performance of the new hybrid PET/CT Discovery-690. *Med Phys.* 2011;38:5394–5411.
17. International Commission on Radiological Protection. Basic anatomical and physiological data for use in radiological protection: reference values. *ICRP Publication 89*. Pergamon Press; 2002.
18. Thomas SR, Stabin MG, Chin-Tu C, Samaratunga RC. MIRD pamphlet no. 14 revised: a dynamic urinary bladder model for radiation dose calculations. *J Nucl Med.* 1999;40(suppl):102S–123S.
19. Siegel JA, Thomas SR, Stubbs JB, et al. MIRD pamphlet no. 16: techniques for quantitative radiopharmaceutical biodistribution data acquisition and analysis for use in human radiation dose estimates. *J Nucl Med.* 1999;40(suppl):37S–61S.
20. ICRP publication 103: the 2007 recommendations of the International Commission on Radiological Protection. *Ann ICRP.* 2007;37:1–332.
21. Aro E, Seppänen M, Mäkelä KT, Luoto P, Roivainen A, Aro HT. PET/CT to detect adverse reactions to metal debris in patients with metal-on-metal hip arthroplasty: an exploratory prospective study. *Clin Physiol Funct Imaging.* 2018;38:847–855.
22. Bernstein LR. Mechanisms of therapeutic activity for gallium. *Pharmacol Rev.* 1998;50:665–682.
23. AR-501 (gallium citrate): novel anti-infective for the growing problem of antibiotic resistance. Aridis Pharmaceuticals website. https://www.aridispharma.com/ar-501/. Accessed July 20, 2022.
24. Autio A, Virtanen H, Tolvanen T, et al. Absorption, distribution and excretion of intravenously injected ^{68}Ge/^{68}Ga generator eluate in healthy rats, and estimation of human radiation dosimetry. *EJNMMI Res.* 2015;5:117.
25. Pettinato C, Sarnelli A, Di Donna M, et al. ^{68}Ga-DOTANOC: biodistribution and dosimetry in patients affected by neuroendocrine tumors. *Eur J Nucl Med Mol Imaging.* 2008;35:72–79.
26. ICRP publication 80: recalculated dose data for 19 frequently used radiopharmaceuticals from ICRP publication 53. *Ann ICRP.* 1998;28:47–83.
27. ICRP publication 60: recommendation of the International Commission on Radiological Protection. *Ann ICRP.* 1991;21:493–502.

Evaluation of Data-Driven Rigid Motion Correction in Clinical Brain PET Imaging

Matthew G. Spangler-Bickell[1,2], Samuel A. Hurley[2], Ali Pirasteh[2,3], Scott B. Perlman[2], Timothy Deller[1], and Alan B.McMillan[2,3]

[1]*PET/MR Engineering, GE Healthcare, Waukesha, Wisconsin;* [2]*Radiology, University of Wisconsin–Madison, Madison, Wisconsin; and* [3]*Medical Physics, University of Wisconsin–Madison, Madison, Wisconsin*

Head motion during brain PET imaging can significantly degrade the quality of the reconstructed image, leading to reduced diagnostic value and inaccurate quantitation. A fully data-driven motion correction approach was recently demonstrated to produce highly accurate motion estimates (<1 mm) with high temporal resolution (≥1 Hz), which can then be used for a motion-corrected reconstruction. This can be applied retrospectively with no impact on the clinical image acquisition protocol. We present a reader-based evaluation and an atlas-based quantitative analysis of this motion correction approach within a clinical cohort. **Methods:** Clinical patient data were collected over 2019–2020 and processed retrospectively. Motion was estimated using image-based registration on reconstructions of ultrashort frames (0.6–1.8 s), after which list-mode reconstructions that were fully motion-corrected were performed. Two readers graded the motion-corrected and uncorrected reconstructions. An atlas-based quantitative analysis was performed. Paired Wilcoxon tests were used to test for significant differences in reader scores and SUVs between reconstructions. The Levene test was used to determine whether motion correction had a greater impact on quantitation in the presence of motion than when motion was low. **Results:** Fifty standard clinical ^{18}F-FDG brain PET datasets (age range, 13–83 y; mean ± SD, 59 ± 20 y; 27 women) from 3 scanners were collected. The reader study showed a significantly different, diagnostically relevant improvement by motion correction when motion was present ($P = 0.02$) and no impact in low-motion cases. Eight percent of all datasets improved from diagnostically unacceptable to acceptable. The atlas-based analysis demonstrated a significant difference between the motion-corrected and uncorrected reconstructions in cases of high motion for 7 of 8 regions of interest ($P < 0.05$). **Conclusion:** The proposed approach to data-driven motion estimation and correction demonstrated a clinically significant impact on brain PET image reconstruction.

Key Words: PET; image reconstruction; data-driven motion correction; brain imaging

J Nucl Med 2022; 63:1604–1610
DOI: 10.2967/jnumed.121.263309

As the spatial resolution of modern whole-body PET scanners reaches 2–4 mm in full width at half maximum, together with improved sensitivity and time-of-flight resolution, it is becoming increasingly likely that even slight head motion may substantially degrade the reconstructed image. Although patient motion with translations of up to 15 mm and rotations of up to 4 degrees have been reported (*1,2*), less motion is quite common. Various motion-tracking and correction techniques have been presented for head motion (*2–7*). These usually use an external tracking device (such as a camera) to track a marker attached to the head (*5*), or they directly track the head (*6*). The motion estimates can then be used to perform frame-based reconstructions (*8*) or a full event-by-event motion-corrected (MoCo) reconstruction (*9,10*). However, none of these motion correction approaches have been implemented into widespread standard clinical routine, for several reasons. Some patient motion can be partially managed through head restraints and by discarding motion-corrupted portions of the data. To date, most motion-tracking methods rely on external hardware around the scanner (such as cameras) or attached to the patient (such as head markers), which complicate routine clinical protocols. Until recently, there has not been a substantial effort from vendors to incorporate motion correction into their products; efforts have thus remained predominantly within the research setting.

Fully data-driven approaches to motion correction that do not require external hardware have been presented. These usually estimate when motion occurred so that the data can be suitably framed (*11*), or they may estimate the motion itself to be used in a MoCo reconstruction (*12–15*). Because of the typically low count rates in PET imaging and long reconstruction times, the temporal resolution used for such motion estimation is usually on the order of tens of seconds or longer. Such low temporal resolutions may lead to residual intraframe motion blurring and inaccurate motion estimates. Alternatively, when higher temporal resolutions are used (on the order of ~1 s), as described previously (*12,13*), the motion is estimated using centroid-of-distribution or inertial tensor calculations.

In this work, we evaluated a recently proposed approach to data-driven motion estimation and correction (*16,17*). The motion was estimated using rigid image registration on reconstructed images of very short frames. The estimated motion was then used in a full event-by-event MoCo list-mode reconstruction of the data, including all PET corrections. The approach is completely data-driven and can be applied retrospectively. An evaluation on 50 standard clinical ^{18}F-FDG brain PET datasets is presented, showing the results of a reader study and an atlas-based quantitation analysis.

Received Oct. 1, 2021; revision accepted Jan. 25, 2022.
For correspondence or reprints, contact Matthew G. Spangler-Bickell (matthew.spangler-bickell@ge.com).
Published online Jan. 27, 2022.

MATERIALS AND METHODS

Data

Patient data were acquired at the Wisconsin Institutes for Medical Research at the University of Wisconsin over 2019 and 2020, from a 4-ring Discovery MI PET/CT device ($n = 11$; 20-cm axial field of view), a Discovery 710 PET/CT device ($n = 18$), and a SIGNA PET/MRI device ($n = 21$) (all from GE Healthcare). Fifty consecutive ^{18}F-FDG brain PET datasets were collected retrospectively, and none were rejected. All datasets were routine clinical imaging studies, and the need to obtain consent was waived by the institutional review board. Preliminary results using these datasets were presented at the 2021 annual meeting of the Society of Nuclear Medicine and Molecular Imaging (*18*); the current work presents a more thorough analytic and statistical evaluation.

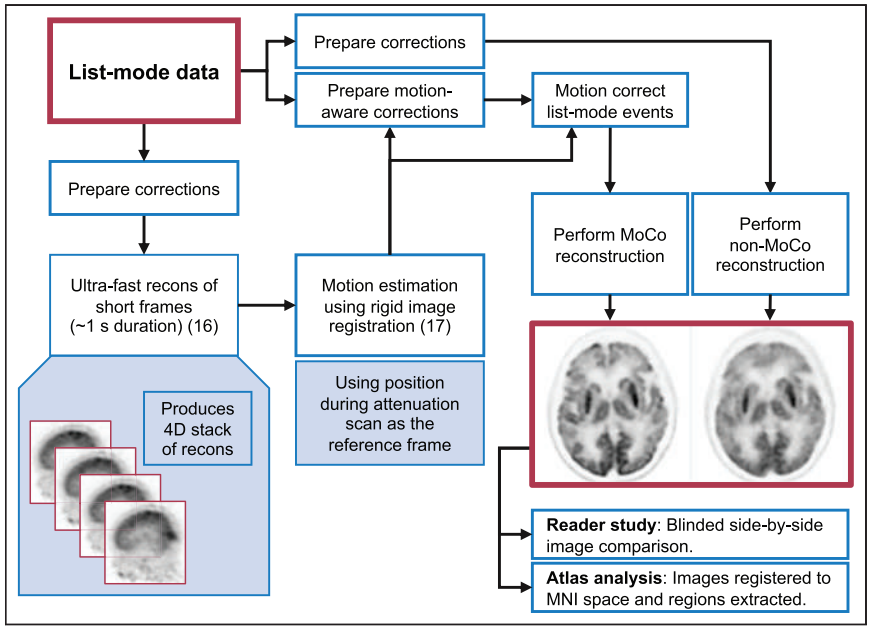

FIGURE 1. Flowchart of reconstruction process and analysis. 4D = 4-dimensional; MNI = Montreal Neurological Institute; recons = reconstructions.

Motion Estimation and Image Reconstruction

The data were processed in 2 steps before being analyzed. Figure 1 shows a flowchart of the study. First, ultrafast reconstructions of very short frames (*16*) (0.6–1.8 s, set automatically and adjusted at each frame to ensure a constant 500×10^3 true and scattered events per frame (*17*)) were performed for the entire scan duration, and image-based registration was then performed on these frames to estimate the motion. Rigid registration was performed using a least-squares metric and a gradient descent optimizer; further details were given in a previous publication (*17*). The 6 degrees of freedom of the motion were thus estimated directly at about 1 Hz, with an accuracy of less than 1 mm (measured as the mean error in absolute displacement of a mesh of points moved by the estimated motion) (*17*). The reference frame for the image registrations was chosen to ensure that the PET reconstruction aligned with the attenuation map. For PET/MRI, the MRI acquisitions for the attenuation map occur concurrently with the PET acquisitions; thus, the PET frames corresponding to data acquired during the MRI attenuation correction pulse sequence were averaged to create the reference frame. For PET/CT, however, the CT acquisitions occur before the PET acquisitions; thus, after estimating motion using the first PET frame as the reference, a single automatic cross-modality registration is performed using a mutual-information metric to set this reference frame to align with the CT image. The mean of all the short PET frames, after being aligned according to the estimated motion, was used for this registration. For 12 of the 29 PET/CT datasets, the automated cross-modality registration between the PET and the CT scans was suboptimal and manual intervention was required to ensure good registration. We will make this registration step more robust in the future to ensure fully automated processing.

The data were categorized into 4 motion groups using a metric based on the magnitude of the motion for each dataset. Similarly to previous investigators (*19,20*), we categorized the motion by moving points in image space and measuring their displacement. Although others have used an average displacement, we were interested in the maximum extent of the motion, and thus 2 points at the extreme extent of the brain were sufficient. Two points located in image space at 70 mm anterior and 70 mm posterior to the brain center were chosen and moved according to the estimated motion parameters. The brain center relative to the scanner center was set at a typically observed value for each scanner: for the PET/MRI device at 0, 40, and 20 mm for left–right, anterior–posterior, and superior–inferior, respectively (the anterior–posterior offset was due to the head coil used), and for both PET/CT devices at 0, 0, and 20 mm, respectively. The median absolute displacement from the reference was calculated for each point. The larger of these 2 medians was used as a metric to classify the datasets into 4 motion groups: low (median displacement < 1 mm), offset (median displacement < 1 mm but initial displacement > 2 mm), medium (median displacement = 1–2 mm), and high (median displacement > 2 mm).

The offset-motion group captures those datasets with little motion during the PET acquisition but with a large offset between the attenuation map acquisition and the PET acquisition (this usually applies only to PET/CT scans). This group classification was chosen empirically on the basis of our experience with many clinical datasets.

After estimation of head motion, a full reconstruction was performed, with each event being corrected according to the estimated motion, as shown in Figure 1. List-mode time-of-flight–based block sequential regularization expectation maximization (*21,22*) was performed with a β-parameter of 50. Spatially variant point-spread function modeling was performed using a hybrid image-space/projection-space approach (*23*). For clarity, the list-mode maximum likelihood expectation maximization with motion correction (*9,10*) is given here; subsets and a regularization term are added for the block sequential regularization expectation maximization:

$$\lambda_j^{n+1} = \frac{\lambda_j^n}{\bar{s}_j} \sum_m^M c_{i'_m j} \frac{1}{\sum_k c_{i'_m k} \lambda_k^n + \frac{S'_{i_m} + R_{i_m}}{a_{i'_m} e_{i_m} \sigma_{i_m}}},$$

$$\bar{s}_j = \sum_p^P w_p \sum_l^L c_{l'_p j} a_{l'_p} e_l \sigma_l,$$

where λ_j^n is the image value at pixel j and iteration n, i_m is the line of response (LOR, the line joining a detecting crystal pair) i associated with list-mode event m, M is the total number of list-mode events, i'_m is the MoCo LOR i for event m, c_{ij} is the system matrix, S'_i is the motion-aware scatter contribution along LOR i, R_i is the randoms contribution, a_i is the attenuation correction factor through the patient attenuation map along LOR i, e_i is the attenuation correction factor through the attenuating material exterior to

TABLE 1
Likert-Scale Scoring for Image Evaluation

Score	Criteria	Diagnostic acceptability
1	Very poor	Nondiagnostic
2	Poor	Nondiagnostic
3	Acceptable	Diagnostic
4	Good	Diagnostic
5	Excellent	Diagnostic

TABLE 2
Distribution of Datasets Among Defined Motion Groups

Group	All scanners	Discovery 710	Discovery	Signa
Low	15 (30%)	4	1	10
Offset	9 (18%)	4	5	0
Medium	14 (28%)	6	4	4
High	12 (24%)	4	1	7

the patient along LOR i, and σ_i is the scanner sensitivity factor (crystal efficiency and dead time) for LOR i. The time-averaged sensitivity image $\bar{s}$ is calculated by moving the endpoints of each LOR (l, of which there are L in the scanner) by a particular set of motion parameters p, backprojecting the appropriate attenuation and sensitivity factors, and calculating the time-weighted (w_p) average across all the motion data, P. The attenuation factors a_i and e_i are handled separately since the patient is moving whereas the rest of the attenuating material is not; therefore, the MoCo LORs (i'_m) are used for the patient attenuation correction factors.

Additionally, a non-MoCo list-mode reconstruction was performed for comparison.

Reader Study

The MoCo and non-MoCo reconstructions were randomized and read by a masked nuclear medicine physician with 36 y of experience and a dual–board-certified nuclear medicine physician and radiologist with fellowship training in nuclear medicine and body MRI with 2 y of experience. Images were evaluated on a 5-point Likert scale for sharpness and diagnostic quality, as specified in Table 1. The readers were not aware of the motion groups of the datasets; these were used only during the analysis.

Quantitative Analysis

An atlas-based analysis of the quantitative accuracy of the reconstructions was performed. The reconstructions were individually and nonrigidly registered to an aggregated ^{18}F-FDG atlas in Montreal Neurosciences Institute–152 image space (*24,25*) using the Advanced Normalization Tools toolbox (*26*). Eight regions of interest (ROIs) were extracted and analyzed: frontal lobe, occipital lobe, temporal lobe, parietal lobe, cerebellum, left/right cerebral cortex, and whole cerebral cortex.

Statistical Analysis

For the reader study, interreader variability was tested using 2 metrics: the modified interrater agreement index (r^*_{wg}) was used to evaluate the 5-point Likert scores (*27*), and the Cohen κ (*28*) was used to evaluate agreement on whether an image was diagnostically acceptable (i.e., having a Likert score of ≥3). These tests were conducted for both reader questions and for the non-MoCo and MoCo reconstructions.

Using the average Likert scores for the 2 readers, paired Wilcoxon tests were conducted to test for significant differences between the median scores of the MoCo and non-MoCo reconstructions at a 2-sided significance level of $P < 0.05$, using the statistical toolbox in MATLAB (MathWorks). Correction was made for the false-discovery rate using the Benjamini–Hochberg procedure with a rate (Q-value) of 10%.

For the atlas-based quantitative analysis, paired Wilcoxon tests for significant differences between the medians of ROI SUV_{max} in the MoCo and non-MoCo reconstructions within each motion group were conducted at a 2-sided significance level of $P < 0.05$, with false-discovery-rate correction. Additionally, the relative differences between the SUV_{max} of the MoCo and non-MoCo reconstructions were calculated, and Levene tests (*29*) were conducted to determine whether the variance in these differences for each motion group was significantly different from the low-motion group, indicating that motion correction had made a quantitative difference in reconstructions when motion was present. A 2-sided significance level of $P < 0.05$ was used, and false-discovery-rate correction was applied.

RESULTS

Patient Characteristics and Injected Activity

Patient age ranged from 13–83 y (mean ± SD, 59 ± 20 y). There were 27 women. The injected activity was 390 ± 24 MBq for the Discovery 710 (55 ± 4 min uptake time, 15-min duration, 4.6 ± 1.1×10^8 counts), 400 ± 26 MBq for the Discovery MI (56 ± 5 min uptake time, 15-min duration, $8.9 \pm 2.3 \times 10^8$ counts), and 450 ± 85 MBq for the SIGNA (63 ± 13 min uptake time, 25-min duration [except for 3 datasets with a 11- to 15-min duration], $17.2 \pm 5.3 \times 10^8$ counts).

Motion Estimation

The number of datasets in each motion group is shown in Table 2, and the distribution of the displacement metric is shown in Figure 2.

Motion Correction Case Studies

Figure 3 shows examples of reconstructions from the low-, offset-, and high-motion groups. The relative-difference images were calculated as (MoCo − non-MoCo)/MoCo × 100%.

Reader Study

The results of the interreader variability analysis are shown in Table 3. Agreement between the readers was high according to all tests. Notably, agreement on whether an image was diagnostically acceptable (κ) was higher (no disagreement) for the MoCo reconstructions than for the non-MoCo reconstructions (for which there was 1 disagreement). The Likert scores for the 2 readers are shown in Figure 4 for the 2 questions. In 5 (10%) of the 50 datasets, the diagnostic quality of the reconstruction with motion correction improved by at least 1 on the Likert scale. The non-MoCo reconstructions for 4 (8%) datasets were rated as not diagnostically acceptable, and for all of these the MoCo reconstructions were rated as diagnostically acceptable. The

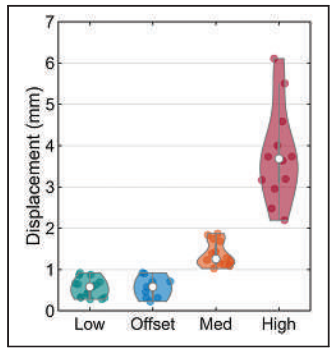

FIGURE 2. Violin plots (*30*) showing distribution of estimated motion for all datasets within 4 motion groups. Width of violins indicates density of data points, and length indicates range of data. Actual data points are scattered within violins, with white dot being median.

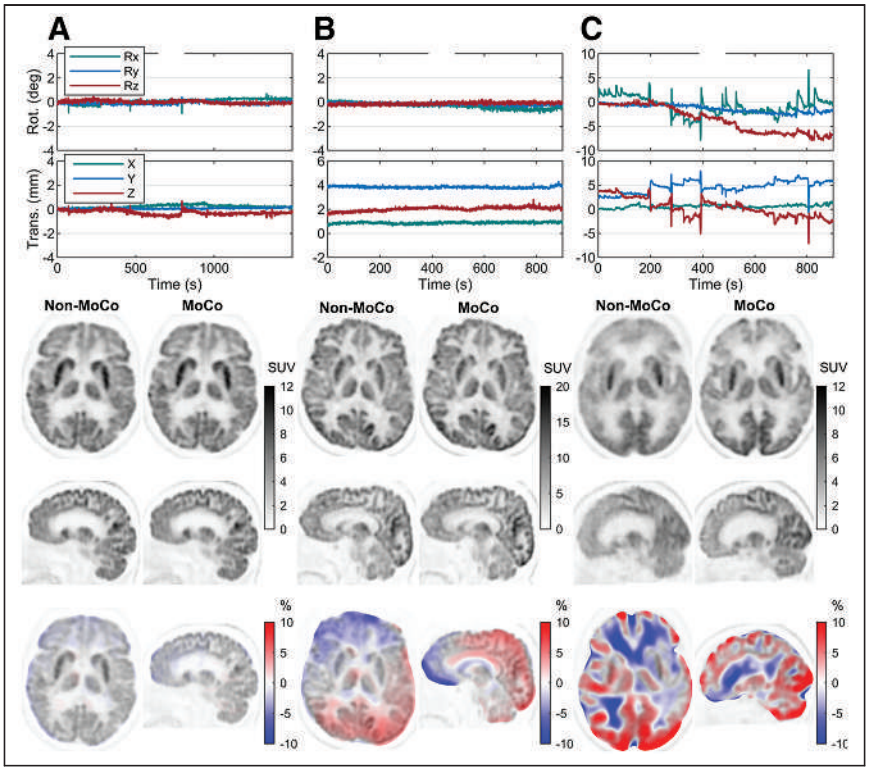

FIGURE 3. Example reconstructions for 3 case studies from low-motion (A), offset-motion (B), and high-motion (C) groups. All 3 are PET/CT data. Six degrees of freedom of motion data are plotted at top. Smoothed relative differences between images are shown at bottom overlayed on MoCo image. Low-motion case demonstrates that when there is little motion, motion correction has very small effect on reconstruction. Offset case shows that although no obvious differences are visible between images, relative-difference image shows gradient due to misalignment of Non-MoCo image with attenuation map. In high-motion case, much of blurring due to motion visible in Non-MoCo image has been removed in MoCo image. Rot. = rotation; Trans. = translation.

results of the paired Wilcoxon tests on the reader scores are shown in Table 4.

Quantitative Analysis

The relative differences in ROI SUV_{max} between the MoCo and non-MoCo reconstructions are shown in Figure 5, calculated as (MoCo SUV_{max} − non-MoCo SUV_{max})/MoCo $SUV_{max} \times 100\%$. Table 5 presents the results of the statistical analysis.

Figure 5 shows that the relative differences in SUV_{max} between the MoCo and non-MoCo reconstructions were larger in the higher-motion groups than in the low-motion group. In the high-motion group, the SUV_{max} of the parietal lobe in the MoCo reconstructions differed from that in the non-MoCo reconstructions by 1.5% ± 2.7%, with a maximum of 6.6%, and in the temporal lobe the SUV_{max} differed by 1.8% ± 2.6%, with a maximum of 8.2%. In all cases, the SUV_{max} in the MoCo reconstruction is assumed to be more accurate, whether it was higher or lower than the non-MoCo reconstruction, since the former ensures better alignment with the attenuation map and has reduced motion blurring. Table 5 demonstrates that in the high-motion group the SUV_{max} significantly differed between the MoCo and non-MoCo reconstructions in 7 of 8 ROIs. Even in the offset-motion group, in which there was minimal motion during the PET acquisition, motion correction made a significant difference in 5 of 8 ROI SUV_{max} results because of the improved alignment with the attenuation map. The Levene tests indicated that the variance in relative differences between the MoCo and non-MoCo reconstructions was higher for 7 of the 8 ROIs in the medium- and high-motion groups than in the low-motion group (Table 5). These variances can be seen in the extent of the plots in Figure 5, comparing the higher-motion groups with the low-motion group. Table 5 indicates that when there was high motion, the motion correction significantly changed the reconstruction. The results of the reader study then confirm that the MoCo reconstructions were preferred.

TABLE 3
Results of Interreader Variability Analysis (High Agreement in All Cases)

	Non-MoCo		MoCo	
Parameter	r^*_{wg}	κ	r^*_{wg}	κ
Image sharpness	0.98	0.85	0.98	1
Diagnostic quality	0.98	0.85	0.98	1

DISCUSSION

An evaluation of a fully data-driven motion estimation and correction technique for reconstruction of brain PET datasets has been presented. Fifty standard clinical ^{18}F-FDG brain PET datasets were processed retrospectively, acquired on 1 PET/MRI and 2 PET/CT scanners. No additional motion-tracking hardware was used during the scan, and there was no impact on the standard clinical routine. The motion estimation used a temporal resolution of about 1 s and detected motion of more than 1 mm in 70% (35/50) of cases and more than 2 mm in 24% (12/50) of cases, the latter of which usually resulted in visually obvious differences between the MoCo and non-MoCo reconstructions. The masked reader study showed that the MoCo

TABLE 4
P Values of Paired Wilcoxon Tests Between MoCo and Non-MoCo Reconstructions, According to Reader Likert Scores

Motion group	Low	Offset	Medium	High	All*
Image sharpness	>0.99	>0.99	0.06	0.02†	0.003†
Diagnostic quality	>0.99	>0.99	0.13	0.02†	0.003†

*All motion groups considered together.
†Significant difference ($P < 0.05$, false-discovery-rate–corrected).

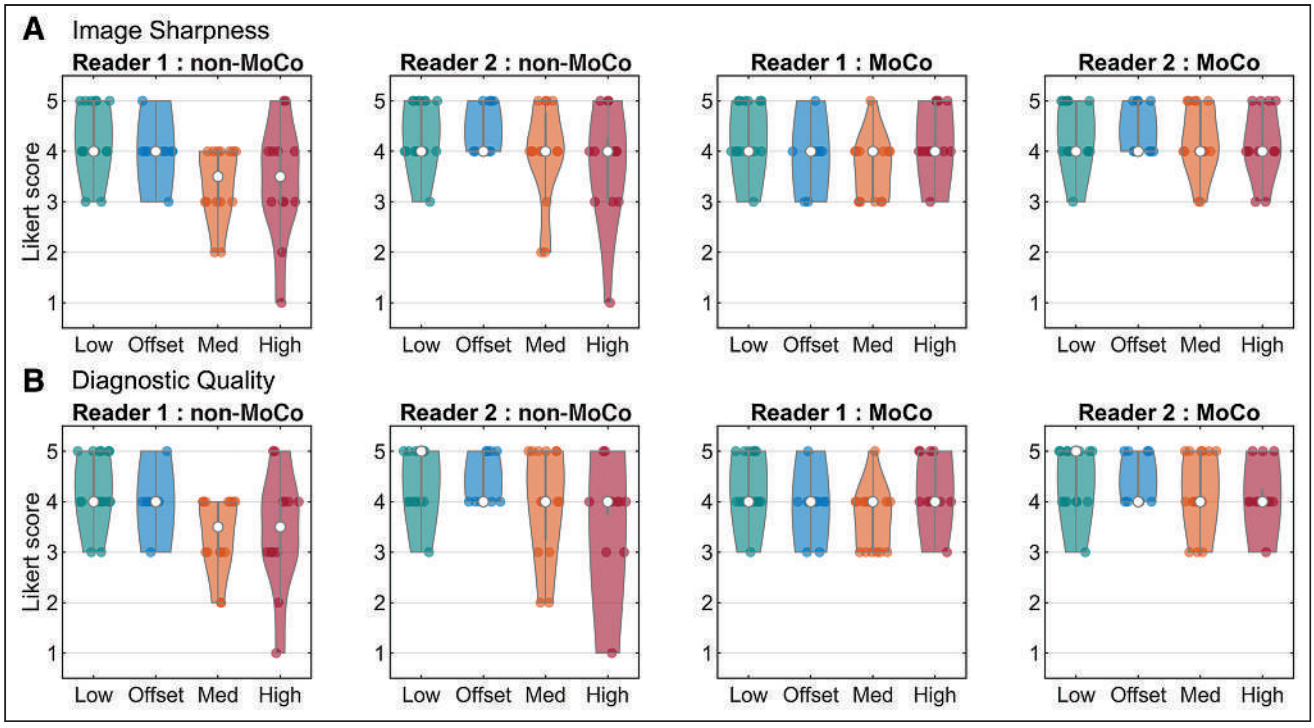

FIGURE 4. Likert scores for MoCo and non-MoCo reconstructions for 2 questions: image sharpness (A) and diagnostic quality (B). In non-MoCo cases, reader scores had more variation among datasets in higher-motion groups, with some images not being diagnostically acceptable. In MoCo cases, scores were consistent across all motion groups.

reconstructions improved the diagnostic quality in 10% (5/50) of the datasets, and the improvement was significant in the high-motion group ($P = 0.02$) and when considering all the data ($P = 0.003$). In 8% (4/50) of the datasets, which is a substantial portion of the cohort, the image was improved from diagnostically unacceptable to acceptable. The atlas-based quantitative analysis found significant differences ($P < 0.05$) in the SUV_{max} in 7 of the 8 ROIs in the medium- and high-motion groups and no significant differences in 5

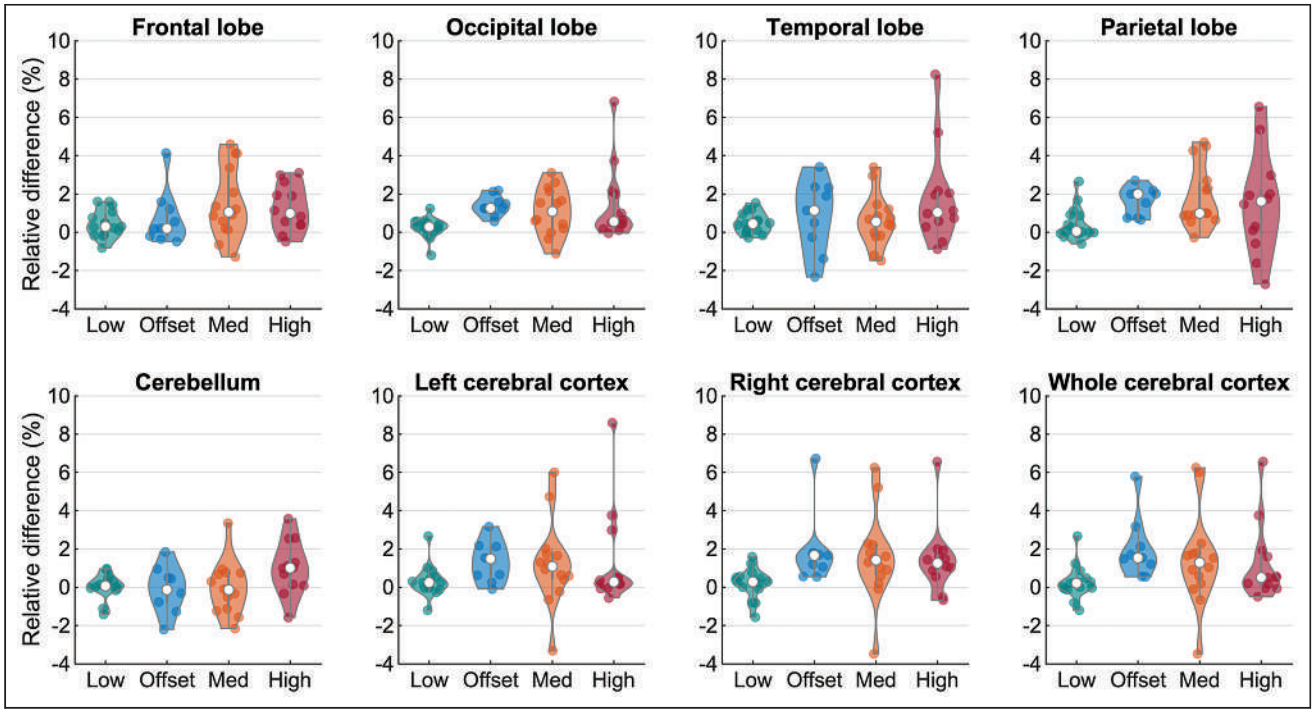

FIGURE 5. Relative differences between SUV_{max} of ROIs extracted from MoCo and non-MoCo reconstructions. Differences are larger in higher-motion groups, as expected. Since MoCo reconstruction ensures better alignment with attenuation map, SUV_{max} is expected to be more accurate in MoCo reconstructions than in non-MoCo reconstructions, regardless of which is greater or lesser.

TABLE 5
Results from Paired Wilcoxon Tests on ROI SUV_{max} of MoCo and Non-MoCo Images and from Levene Tests on Variance of ROI SUV_{max} Relative-Difference Values

	Wilcoxon test on SUV_{max}				Levene test on relative difference in SUV_{max}		
Site	Low	Offset	Medium	High	Offset	Medium	High
Frontal lobe	0.03*	0.25	0.009*	0.007*	0.10	0.002*	0.02*
Occipital lobe	0.03*	0.004*	0.009*	0.001*	0.73	0.001*	0.005*
Temporal lobe	0.007*	0.16	0.10	0.007*	0.001*	0.04*	0.01*
Parietal lobe	0.11	0.004*	<0.001*	0.08	0.89	0.01*	0.009*
Cerebellum	0.39	>0.99	0.71	0.03*	0.05	0.04*	0.04*
Left cerebral cortex	0.09	0.008*	0.02*	0.03*	0.20	0.0499*	0.01*
Right cerebral cortex	0.21	0.004*	0.01*	0.009*	0.24	0.07	0.24
Whole cerebral cortex	0.21	0.004*	0.03*	0.02*	0.13	0.04*	0.03*

*Significant difference ($P < 0.05$, false-discovery-rate–corrected).

of 8 ROIs in the low-motion group. The reader study confirmed that the image quality of the MoCo reconstructions was preferred over the non-MoCo reconstructions when motion was present and did not affect the scores when no motion was present, while the atlas-based analysis confirmed that motion correction does affect the quantitation of the reconstructions in the presence of motion.

Our study incorporated data from 3 scanners with very different geometries, with the axial field of view ranging from 157 to 250 mm, and all scanners benefitted from motion correction. The higher sensitivity and time-of-flight resolution of modern scanners allows for use of shorter frame durations for motion estimation and, hence, improved temporal sampling. To optimize temporal sampling, scanner-specific optimization may be necessary (*17*). Motion estimation and reconstruction were performed in a research setting and took approximately 2 h, which was about 30% longer than the non-MoCo reconstruction of the same dataset. Significantly faster reconstruction is expected with software optimization and dedicated hardware (e.g., graphics processing units) to ensure that the approach can be clinically feasible in future work.

This study had some limitations. We focused on ^{18}F-FDG because it is the most common clinically used radiotracer. However, assuming that accurate motion estimates can be obtained with other radiotracers, we expect that motion correction would have a similar effect on reconstructions of such datasets. Accurate motion estimation has been demonstrated previously with ^{18}F-florbetaben using this approach (*17*). Optical motion tracking was not available for comparison, as the data were processed retrospectively, and such a comparison was not the intention of this work. This work did not include examinations for which the activity distribution of the radiotracer inside the brain may change substantially during the scan, such as an ^{15}O-H_2O brain perfusion study, since the reference frame used for registration would not be representative of the entire dataset. Although an approach for motion estimation in such cases would be more challenging and was outside of the scope of the current work, we believe that a data-driven solution is possible; such a solution is the topic of ongoing research. Lastly, whereas image quality before and after motion correction was evaluated, the diagnostic implications of the MoCo images were not fully investigated. Considering the promising nature of our current results, we plan to further investigate the clinical impact of the application.

CONCLUSION

We have presented an evaluation of a data-driven technique for correction of head motion in brain PET imaging. We demonstrated that motion is prevalent among standard clinical datasets and that motion correction has a significant impact on reconstructions, both qualitatively and quantitatively. The application of motion correction was not detrimental to image quality or quantification when no motion was present. Because motion is a known confounder of clinical brain PET, using data-driven motion correction will likely have important implications for diagnostic and research studies in which motion may occur. Given that the proposed solution relies entirely on retrospective reconstruction, it can readily be adopted into routine PET imaging procedures.

DISCLOSURE

Matthew Spangler-Bickell and Timothy Deller are employees of GE Healthcare. Research reported in this publication was supported by the National Institute of Biomedical Imaging and Bioengineering of the National Institutes of Health under award R01EB026708. No other potential conflict of interest relevant to this article was reported.

KEY POINTS

QUESTION: How effective is the proposed data-driven head motion correction technique?

PERTINENT FINDINGS: Motion was observed in 70% of the study cohort, consisting of 50 consecutively acquired datasets. A reader study showed that all datasets that were deemed diagnostically unacceptable without motion correction (8%, 4/50) were then diagnostically acceptable with motion correction, with a significant improvement in cases of high motion. An 8-ROI atlas-based quantitative analysis concluded that motion correction had a significant impact on SUV_{max} (≤9%) in 65% of the ROIs.

IMPLICATIONS FOR PATIENT CARE: Patient motion would no longer be a concern for ^{18}F-FDG PET brain imaging when using this technology; patients could be scanned regardless of motion risk, and any motion would be corrected.

REFERENCES

1. Bloomfield PM, Spinks TJ, Reed J, et al. The design and implementation of a motion correction scheme for neurological PET. *Phys Med Biol.* 2003;48:959–978.
2. Lopresti BJ, Russo A, Jones WF, et al. Implementation and performance of an optical motion tracking system for high resolution brain PET imaging. *IEEE Trans Nucl Sci.* 1999;46:2059–2067.
3. Daube-Witherspoon M, Yan Y, Green M, Carson R, Kempner K, Herscovitch P. Correction for motion distortion in PET by dynamic monitoring of patient position [abstract]. *J Nucl Med.* 1990;31(suppl):816.
4. Fulton RR, Meikle SR, Eberl S, Pfeiffer J, Constable CJ, Fulham MJ. Correction for head movements in positron emission tomography using an optical motion-tracking system. *IEEE Trans Nucl Sci.* 2002;49:116–123.
5. Spangler-Bickell MG, Khalighi MM, Hoo C, et al. Rigid motion correction for brain PET/MR imaging using optical tracking. *IEEE Trans Radiat Plasma Med Sci.* 2019;3:498–503.
6. Kyme AZ, Aksoy M, Henry DL, Bammer R, Maclaren J. Marker-free optical stereo motion tracking for in-bore MRI and PET-MRI application. *Med Phys.* 2020; 47:3321–3331.
7. Kyme AZ, Fulton RR. Motion estimation and correction in SPECT, PET and CT. *Phys Med Biol.* 2021;66(18).
8. Picard Y, Thompson CJ. Motion correction of PET images using multiple acquisition frames. *IEEE Trans Med Imaging.* 1997;16:137–144.
9. Carson RE, Barker WC, Liow JS, Johnson CA. Design of a motion-compensation OSEM list-mode algorithm for resolution-recovery reconstruction for the HRRT. *IEEE Nucl Sci Symp Conf Rec.* 2003;5:3281–3285.
10. Rahmim A, Bloomfield P, Houle S, et al. Motion compensation in histogram-mode and list-mode EM reconstructions: beyond the event-driven approach. *IEEE Trans Nucl Sci.* 2004;51:2588–2596.
11. Schleyer PJ, Dunn JT, Reeves S, Brownings S, Marsden PK, Thielemans K. Detecting and estimating head motion in brain PET acquisitions using raw time-of-flight PET data. *Phys Med Biol.* 2015;60:6441–6458.
12. Feng T, Yang D, Zhu W, Dong Y, Li H. Real-time data-driven rigid motion detection and correction for brain scan with listmode PET. In: *2016 IEEE Nuclear Science Symposium, Medical Imaging Conference and Room-Temperature Semiconductor Detector Workshop (NSS/MIC/RTSD)*. IEEE;2016:1–4.
13. Rezaei A, Spangler-Bickell M, Schramm G, Van Laere K, Nuyts J, Defrise M. Rigid motion tracking using moments of inertia in TOF-PET brain studies. *Phys Med Biol.* 2021;66(18).
14. Jin X, Mulnix T, Gallezot JD, Carson RE. Evaluation of motion correction methods in human brain PET imaging: a simulation study based on human motion data. *Med Phys.* 2013;40:102503.
15. Mukherjee JM, Lindsay C, Mukherjee A, et al. Improved frame-based estimation of head motion in PET brain imaging. *Med Phys.* 2016;43:2443–2454.
16. Spangler-Bickell MG, Deller TW, Bettinardi V, Jansen F. Ultra-fast list-mode reconstruction of short PET frames and example applications. *J Nucl Med.* 2021; 62:287–292.
17. Spangler-Bickell MG, Hurley SA, Deller TW, et al. Optimizing the frame duration for data-driven rigid motion estimation in brain PET imaging. *Med Phys.* 2021;48: 3031–3041.
18. Spangler-Bickell M, Hurley S, Pirasteh A, Perlman S, Deller T, McMillan A. Clinical evaluation of data-driven motion corrected reconstruction for PET brain imaging [abstract]. *J Nucl Med.* 2021;62(suppl 1):59.
19. Tisdall MD, Hess AT, Reuter M, Meintjes EM, Fischl B, Van Der Kouwe AJW. Volumetric navigators for prospective motion correction and selective reacquisition in neuroanatomical MRI. *Magn Reson Med.* 2012;68: 389–399.
20. Measuring transformation error by RMS deviation. Wellcome Centre Integrative Neuroimaging website. http://www.fmrib.ox.ac.uk/analysis/techrep/tr99mj1/tr99mj1/index.html. Published February 11, 2003. Accessed June 23, 2022.
21. Ahn S, Fessler JA. Globally convergent image reconstruction for emission tomography using relaxed ordered subsets algorithms. *IEEE Trans Med Imaging.* 2003; 22:613–626.
22. Spangler-Bickell MG, Deller T, Jansen F. Accelerated regularised list-mode PET reconstruction using subset relaxation. In: *2019 IEEE Nuclear Science Symposium and Medical Imaging Conference (NSS/MIC)*. IEEE; 2019:1–3.
23. Deller TW, Ahn S, Jansen FP, et al. Implementation and image quality benefit of a hybrid-space PET point spread function. Presented at: IEEE Nuclear Science Symposium and Medical Imaging Conference; October 20, 2021; Yokohama, Japan [virtual].
24. Darkner S. FDG-PET template MNI152 1mm. UCPH Research website. https://research.ku.dk/search/result/?pure=en%2Fpublications%2Ffdgpet-template-mni152-1mm(5cf2edbb-e75b-4f90-ac4c-89e6ef1bc3f6).html. Published 2013. Accessed June 23, 2022.
25. Harvard-Oxford cortical and subcortical structural atlases. NeuroVault website. https://identifiers.org/neurovault.collection:262. Accessed June 23, 2022.
26. Advanced normalization tools. stnava website. http://stnava.github.io/ANTs/. Accessed June 23, 2022.
27. O'Neill TA. An overview of interrater agreement on Likert scales for researchers and practitioners. *Front Psychol.* 2017;8:777.
28. Cohen J. A coefficient of agreement for nominal scales. *Educ Psychol Meas.* 1960; 20:37–46.
29. Leven H. Robust tests for equality of variances. In: Olkin I., ed. *Contributions to Probability and Statistics: Essays in Honor of Harold Hotelling.* Stanford University Press; 1960:279–292.
30. Violin plots for Matlab. GitHub website. https://github.com/bastibe/Violinplot-Matlab. Accessed June 23, 2022.

Impact of ComBat Harmonization on PET Radiomics-Based Tissue Classification: A Dual-Center PET/MRI and PET/CT Study

Doris Leithner[1], Heiko Schöder[1], Alexander Haug[2], H. Alberto Vargas[1], Peter Gibbs[1], Ida Häggström[1], Ivo Rausch[3], Michael Weber[2], Anton S. Becker[1], Jazmin Schwartz[4], and Marius E. Mayerhoefer[1,5]

[1]Department of Radiology, Memorial Sloan Kettering Cancer Center, New York, New York; [2]Department of Biomedical Imaging and Image-Guided Therapy, Division of Nuclear Medicine, Medical University of Vienna, Vienna, Austria; [3]Center for Medical Physics and Biomedical Engineering, Medical University of Vienna, Vienna, Austria; [4]Department of Medical Physics, Memorial Sloan Kettering Cancer Center, New York, New York; and [5]Department of Biomedical Imaging and Image-Guided Therapy, Division of General and Pediatric Radiology, Medical University of Vienna, Vienna, Austria

Our purpose was to determine whether ComBat harmonization improves ^{18}F-FDG PET radiomics-based tissue classification in pooled PET/MRI and PET/CT datasets. **Methods:** Two hundred patients who had undergone ^{18}F-FDG PET/MRI (2 scanners and vendors; 50 patients each) or PET/CT (2 scanners and vendors; 50 patients each) were retrospectively included. Gray-level histogram, gray-level cooccurrence matrix, gray-level run-length matrix, gray-level size-zone matrix, and neighborhood gray-tone difference matrix radiomic features were calculated for volumes of interest in the disease-free liver, spleen, and bone marrow. For individual feature classes and a multiclass radiomic signature, tissue was classified on ComBat-harmonized and unharmonized pooled data, using a multilayer perceptron neural network. **Results:** Median accuracies in training and validation datasets were 69.5% and 68.3% (harmonized), respectively, versus 59.5% and 58.9% (unharmonized), respectively, for gray-level histogram; 92.1% and 86.1% (harmonized), respectively, versus 53.6% and 50.0% (unharmonized), respectively, for gray-level cooccurrence matrix; 84.8% and 82.8% (harmonized), respectively, versus 62.4% and 58.3% (unharmonized), respectively, for gray-level run-length matrix; 87.6% and 85.6% (harmonized), respectively, versus 56.2% and 52.8% (unharmonized), respectively, for gray-level size-zone matrix; 79.5% and 77.2% (harmonized), respectively, versus 54.8% and 53.9% (unharmonized), respectively, for neighborhood gray-tone difference matrix; and 86.9% and 84.4% (harmonized), respectively, versus 62.9% and 58.3% (unharmonized), respectively, for radiomic signature. **Conclusion:** ComBat harmonization may be useful for multicenter ^{18}F-FDG PET radiomics studies using pooled PET/MRI and PET/CT data.

Key Words: PET/MRI; radiomics; harmonization

J Nucl Med 2022; 63:1611–1616
DOI: 10.2967/jnumed.121.263102

Radiomics, a computer-assisted technique for extraction of quantitative features from diagnostic images (*1,2*), is increasingly being applied to PET (*3*). However, PET radiomic features are known to be sensitive to image acquisition and reconstruction parameter variations, instrumentation bias (*4*), and probably injected dose and are therefore of limited use in multicenter studies without further preprocessing.

ComBat harmonization was proposed and has been successfully used by Orlhac et al. to correct PET radiomic data for differences in imaging device and acquisition protocols while preserving biologic and pathophysiologic associations (*5*). Notably, previous studies applying ComBat to PET radiomics used data almost exclusively from different PET/CT scanners (*5–11*) but did not include PET/MRI data. Since PET/MRI relies on a fundamentally different, MRI-based method for PET attenuation correction (AC) (*12*), differences in PET radiomics may be more pronounced between PET/MRI and PET/CT. To our knowledge, only 2 studies compared ^{18}F-FDG PET radiomic feature values obtained with PET/CT and PET/MRI. Vuong et al. compared ^{18}F-FDG PET radiomic feature values of 9 patients with lung lesions who underwent PET/MRI and subsequent PET/CT after a single ^{18}F-FDG injection, that is, with PET performed at different time points, which, because of the differences in counts, is likely to affect radiomic feature values (*13*). Correlation coefficients suggested that 50% of texture features were not robust or stable between the 2 scans, but the effects of this feature instability on radiomics-based classification were not investigated, and no harmonization was applied. Tsujikawa et al. compared the ^{18}F-FDG PET radiomics of 15 patients with gynecologic or oral cavity/oropharyngeal cancers who underwent PET/CT and subsequent PET/MRI after a single ^{18}F-FDG injection, that is, also at different time points (*14*). Contrary to Vuong et al., these authors reported a generally high correlation between PET/CT- and PET/MRI-based radiomic features; in particular, textural features were less affected by differences in scanners and scan protocols than were conventional and histogram features, possibly because of the use of resampling with 64 bins (i.e., a bin width of 0.4). The impact of ComBat harmonization was not evaluated in either study.

Therefore, our dual-center study aimed to determine the impact of ComBat harmonization in a larger, pooled ^{18}F-FDG PET/MRI and PET/CT radiomic dataset with real-world—in part, marked—intrinsic heterogeneity between institutions and vendors in terms of acquisition parameters according to standard clinical practice. We focused on discrimination between visually similar but biologically different tissues, as a surrogate for lesions with similar tracer uptake. Rather than investigating statistical differences between

Received Aug. 25, 2021; revision accepted Jan. 26, 2022.
For correspondence or reprints, contact Doris Leithner (leithned@mskcc.org).
Published online Feb. 24, 2022.

numeric radiomic feature values, we used tissue classification accuracy as the main outcome measure, to simulate conditions comparable to those of current clinical radiomics trials.

MATERIALS AND METHODS

Patients and Design

Two hundred consecutive patients (92 women, 108 men; mean age, 46.2 ± 17.3 y) who had undergone whole-body ^{18}F-FDG PET/MRI or PET/CT for clinical purposes from January 2010 to December 2020 were retrospectively included. This Health Insurance Portability and Accountability Act–compliant study was approved by the Institutional Review Boards of Memorial Sloan Kettering Cancer Center and the Medical University of Vienna; the need to obtain informed consent was waived. Inclusion criteria were no evidence of disease in the liver, spleen, or bone marrow according to imaging, pathology, and clinical reports, as well as imaging performed on 1 of 4 specified scanners (50 patients per scanner). Exclusion criteria were glucose levels above 180 mg/dL before PET, substantial ^{18}F-FDG extravasation, or imaging artifacts obscuring analyzed tissues.

Imaging Protocols. At the first center (Memorial Sloan Kettering Cancer Center), PET/MRI was performed on a Signa PET/MRI scanner and PET/CT on a Discovery 690 scanner (both GE Healthcare) (Supplemental Table 1; supplemental materials are available at http://jnm.snmjournals.org). PET was performed 1 h after intravenous injection of 444 MBq ± 10% of ^{18}F-FDG. For AC, a 2-point Dixon LAVA (liver acquisition with volume acceleration) T1-weighted sequence was used for PET/MRI and an unenhanced, low-dose spiral CT series for PET/CT. Signa PET/MRI used a standard *z*-axis filter with a cutoff of 5 mm, and Discovery 690 PET/CT used a heavy *z*-axis filter and gaussian transaxial filter with a 6.4-mm cutoff.

At the second center (Medical University of Vienna), PET/MRI was performed on a Biograph mMR scanner and PET/CT on a Biograph TruePoint 64 scanner (both Siemens). PET was performed 1 h after intravenous injection of a 3 MBq/kg dose of ^{18}F-FDG. For AC, an axial 2-point Dixon VIBE (volumetric interpolated breath-hold examination) T1-weighted sequence was used for PET/MRI and a contrast-enhanced, full-dose spiral CT venous-phase series for PET/CT. For the Biograph TruePoint64 PET/CT, no postreconstruction filter was used, and for the Biograph mMR PET/MRI, a gaussian filter of 2 mm in full width at half maximum was used.

Image Analysis and Harmonization

Using the Beth-Israel PET/CT viewer and the International Biomarker Standardization Initiative–compliant PyRadiomics plugins for FIJI (*15–17*), 3-dimensional radiomic features were extracted from the liver, spleen, and bone marrow (vertebral body L4) using manually defined 2.5-cm^3 spheric volumes of interest (Fig. 1). The 3 tissues were chosen because they are relatively homogeneous, meaning that variations in volume-of-interest placement should not have a relevant impact on feature values; they are large enough to allow placement of a sufficiently large volume of interest of identical size and shape; and they have a visually similar ^{18}F-FDG PET pattern in terms of degree of tracer uptake and image texture. In addition, a fourth volume of interest of the same size was placed in the aorta to measure blood pool radiomic features. Before feature extraction, intensity discretization using a fixed bin width of 0.5 and spatial resampling to 1.5 × 1.5 × 1.5 mm voxels using B-spline interpolation were applied; discretization and resampling values were chosen because they are in the range of optimal settings for histogram and texture features reported by Yip et al. (*18*). Nineteen features were calculated for gray-level histogram, 24 for gray-level cooccurrence matrix, 16 for gray-level run-length matrix, 16 for gray-level size-zone matrix, and 5 for neighborhood gray-tone difference matrix (a feature list is provided in Supplemental Table 2; equations can be found at https://pyradiomics.readthedocs.io/en/latest/features.html). ComBat harmonization (without empiric Bayes assumption, with parametric adjustments and 4 batches) was applied to all features, separately for the individual analyzed tissues, as previously described (*5*).

FIGURE 1. Representative ^{18}F-FDG PET image showing volume-of-interest placement in 3-tissue model: liver (blue), spleen (green), and bone marrow (red).

Statistical Analysis

Cases were randomly assigned to a training dataset (70%; 140 patients) and a validation dataset (30%; 60 patients); assignment to training and validation datasets was repeated 5 times (i.e., 5-fold cross-validation) and was identical for unharmonized and harmonized datasets to ensure comparability. Separately for unharmonized and harmonized datasets, and independently for the different feature classes (gray-level histogram, gray-level cooccurrence matrix, gray-level run-length matrix, gray-level size-zone matrix, and neighborhood gray-tone difference matrix), a multilayer perceptron neural network (MLP-NN (*19*); 1 hidden layer with at least 3 neurons) was used to discriminate between liver, spleen, and bone marrow to generate a 3-tissue model and then by also adding blood pool data to generate a 4-tissue model, using all features of a class as input. Median accuracies were calculated for training and validation datasets in the 3-tissue and the 4-tissue models, and Wilcoxon signed-rank tests were used to compare differences in accuracies between paired unharmonized and harmonized datasets. In addition, for the 3-tissue model, areas under the receiver-operating characteristic curves (AUCs) were calculated for validation data using a pairwise (i.e., 1 vs. 2 tissues) approach. Three-dimensional scatterplots were used to visualize scanner-specific and organ-specific clustering in both unharmonized and harmonized datasets.

To generate radiomic signatures for tissue discrimination, principal-component analysis (based on Eigenvalues > 1, maximum of 25 iterations for convergence) based on all features of all classes was performed separately for 3-tissue and 4-tissue models. Principal radiomic components were used as input for the MLP-NN, and accuracies and areas under the curve were calculated.

To investigate the impact of the number of hidden layers for MLP-NN classification—that is, to test whether the MLP-NN would, by itself, be able to correct for technical differences between PET/CT and PET/MRI scanners with an additional hidden layer—MLP-NN classification was again performed on the unharmonized dataset of the 3-tissue model, this time using the scanner type as an additional nominal input variable (factor) and using a network architecture with 1 hidden layer first and then an architecture with 2 hidden layers.

Generalized estimating equation–based casewise classifications from all 5 MLP-NN iterations performed using radiomic signatures were applied to model the impact of scanner type, organ, method (unharmonized and harmonized), and all 2- and 3-way interactions on the percentage of correctly classified volumes of interest, taking into account multiple measurements per patient. All tests, including MLP-NN, were performed using SPSS, version 24.0 (IBM). The specified level of significance was a *P* value of less than 0.05.

RESULTS

3-Tissue Model

Using unharmonized datasets consisting of pooled data from the 4 scanners, ^{18}F-FDG PET radiomics-based tissue discrimination yielded median accuracies ranging from 50.0% to 62.4% for individual feature classes (Table 1). The multiclass radiomic signature (10 principal components) provided 62.9% median accuracy in the training dataset and 58.3% in the validation dataset. Depending on the feature class, areas under the curve for 1-tissue versus 2-tissue discrimination suggested poorer separability of the spleen from the other tissues; separation of liver and bone marrow from the other 2 tissues was similar for most feature classes (Fig. 2).

ComBat harmonization significantly improved ^{18}F-FDG PET radiomics-based tissue discrimination for all feature classes, but most prominently for gray-level cooccurrence matrix features (median accuracy, +38.5 percentage points [p.p.] in the training cohort and +36.1 p.p. in the validation cohort) and gray-level size-zone matrix features (median accuracy, +31.4 p.p. in the training cohort and +32.8 p.p. in the validation cohort) (Table 1; Fig. 3). Tissue classification was also improved for the radiomic signature (10 principal components), with a median accuracy of 86.9% in the training dataset (+24.0 p.p. compared with unharmonized data) and 84.4% in the validation dataset (+26.1 p.p. compared with unharmonized data). Similarly, areas under the curve for 1-tissue versus 2-tissue discrimination were markedly improved in all cases (Fig. 2). Notably, generalized estimating equation analyses revealed lower classification accuracies (i.e., higher misclassification rates) in the PET/MRI cohort than in the PET/CT cohort (Supplemental Table 3).

4-Tissue Model

Using unharmonized datasets, ^{18}F-FDG PET radiomics-based tissue discrimination yielded median accuracies ranging from 39.6% to 46.3% for individual feature classes (Table 2). The multiclass radiomic signature (11 principal components) provided slightly better results, with 51.6% median accuracy in the training dataset and 48.8% in the validation dataset. Again, ComBat harmonization significantly improved ^{18}F-FDG PET radiomics-based tissue discrimination for all feature classes except gray-level histogram, but most prominently for gray-level size-zone matrix (median accuracy, +41.6 p.p. in the training cohort and +42.9 p.p. in the validation cohort) and neighborhood gray-tone difference matrix (median accuracy, +20.6 p.p. in the training cohort and +18.8 p.p. in the validation cohort) (Table 2). Tissue classification was also improved for the radiomic signature (10 principal components), with a median accuracy of 82.1% in the training dataset (+30.5 p.p. compared with unharmonized data) and 81.3% in the validation dataset (+32.5 p.p. compared with unharmonized data).

Similar to the 3-tissue model, accuracies were lower (i.e., the percentage of misclassified cases was higher) in the PET/MRI cohort than in the PET/CT cohort (Supplemental Table 3).

Impact of Number of Hidden Layers for MLP-NN

Using radiomic signatures (principal components) extracted from unharmonized data in the 3-tissue model, MLP-NN classification with 1 hidden layer yielded median accuracies of 71.0% (range, 66.0%–71.1%) in the training set and 62.8% (range, 59.4%–71.1%) in the validation set. With 2 hidden layers, median accuracies were 71.0% (range, 64.5%–74.0%) in the training set

TABLE 1
Tissue Classification Based on Radiomic Feature Classes and Signatures in 3-Tissue Model

	Unharmonized		Harmonized		
Classification accuracy	Median	Range	Median	Range	*P*
Gray-level histogram					
Training	59.5	57.4–62.1	69.5	66.0–77.1	0.043
Validation	58.9	53.3–61.1	68.3	58.3–73.9	0.043
Gray-level cooccurrence matrix					
Training	53.6	47.9–56.7	92.1	88.1–95.2	0.043
Validation	50.0	48.9–55	86.1	80.6–90.6	0.043
Gray-level run-length matrix					
Training	62.4	58.8–64.5	84.8	82.4–89.5	0.043
Validation	58.3	57.2–62.8	82.8	73.9–87.8	0.043
Gray-level size-zone matrix					
Training	56.2	52.9–57.9	87.6	84.0–89.0	0.042
Validation	52.8	51.7–58.3	85.6	74.4–90.6	0.043
Neighborhood gray-tone difference matrix					
Training	54.8	53.3–55.7	79.5	75.5–82.9	0.043
Validation	53.9	50–59.4	77.2	73.9–85.0	0.042
Radiomic signature					
Training	62.9	61–63.6	86.9	86.0–90.0	0.043
Validation	58.3	55.6–63.9	84.4	76.7–86.7	0.043

Data are percentages.

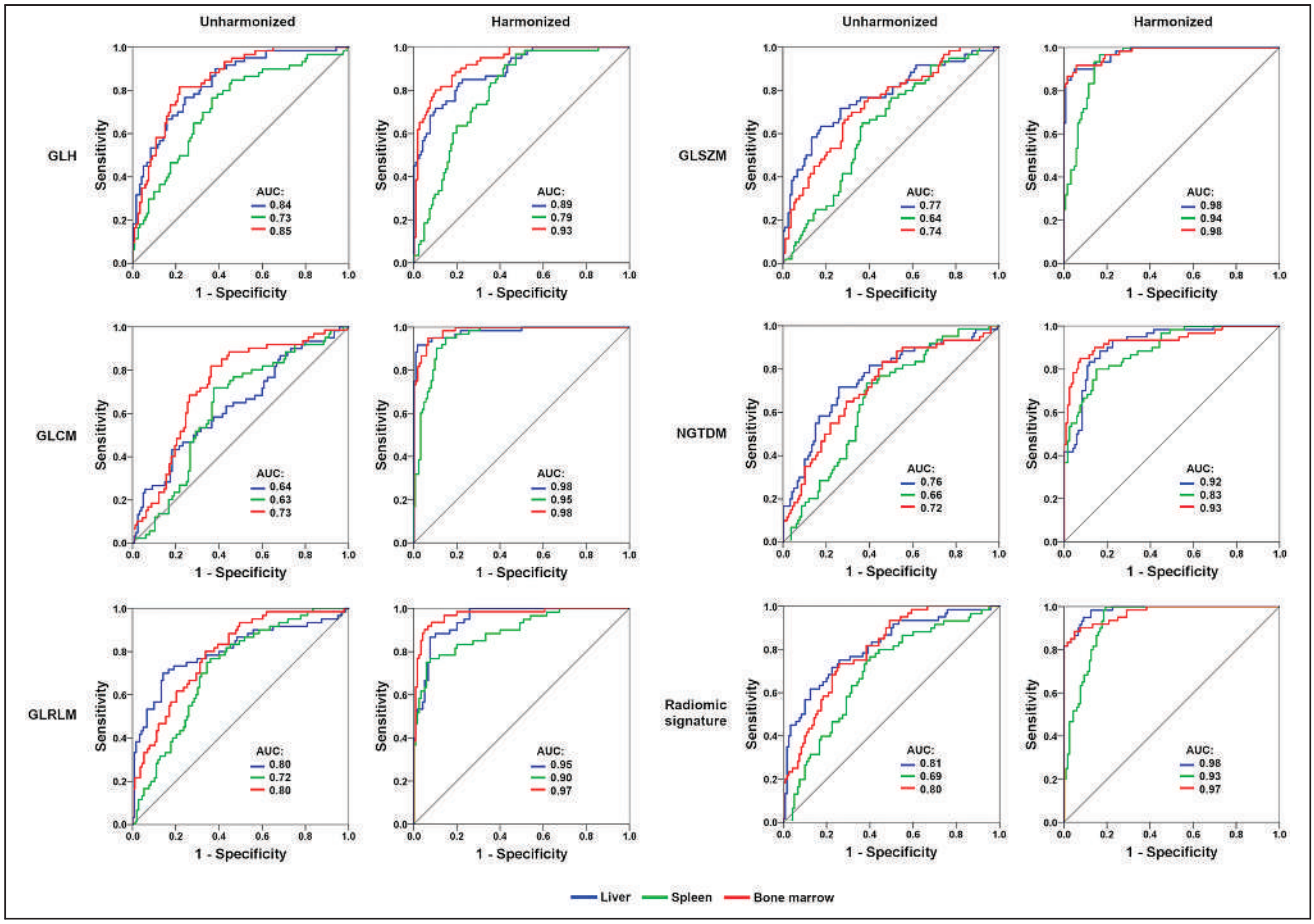

FIGURE 2. Receiver-operating-characteristic curves (validation set) for pairwise (1 vs. 2) MLP-NN–based tissue discrimination (median of 5 iterations shown). After ComBat harmonization, areas under curve are clearly improved for individual radiomic feature classes and radiomic signatures. GLCM = gray-level cooccurrence matrix; GLH = gray-level histogram; GLRLM = gray-level run-length matrix; GLSZM = gray-level size-zone matrix; NGTDM = neighboring gray-tone difference matrix.

and 67.2% (range, 61.1%–70.0%) in the validation set. Differences between MLP-NN with 1 hidden layer and MLP-NN with 2 hidden layers were significant neither in the training set ($P = 0.89$) nor in the validation set ($P = 0.27$).

DISCUSSION

Our results suggest that ComBat harmonization enables successful ^{18}F-FDG PET radiomics-based tissue classification in pooled PET/MRI and PET/CT datasets. ComBat led to substantial and statistically significant gains in classification accuracies for both individual radiomic feature classes and multiclass radiomic signatures (Table 1; Fig. 2), as typically applied in radiomics research, and in both the 3-tissue and the 4-tissue models, though at different accuracies probably because of introduction of a tissue (i.e., blood pool) without actual intrinsic structure.

ComBat harmonization is a postreconstruction algorithm based on empiric Bayes estimation (*20*). Originally developed to reduce the batch effect in genomic data, ComBat has recently been applied to multicenter PET, CT, and MRI data (*5,21,22*). Several PET radiomics studies with heterogeneous datasets used ComBat to improve classification (*6–11*), but very few investigated the actual effects of ComBat on PET radiomics-based classification. In patients with cervical cancer, and using data from 3 centers, Lucia et al. reported a combined ^{18}F-FDG PET/CT and MRI radiomics-based locoregional control prediction accuracy of 98% for harmonized data and 86% for unharmonized data (*6*). Da-Ano et al. observed similar trends when testing different ComBat modifications in a slightly extended cervical cancer cohort and for several classifiers (*23*). However, ComBat did not improve cervical cancer survival prediction when ^{18}F-FDG PET features were combined with clinical parameters (*8*).

Although for PET/CT, the CT component provides attenuation coefficients and correction factors for PET AC, the standard approach in PET/MRI is a T1-weighted gradient-echo Dixon sequence to generate an AC map for separation of soft tissue, fat, lung, and air (*12*). This approach, although robust (*24*), leads to systematic underestimation of attenuation coefficients in the presence of cortical bone (*25*). Further, uniform attenuation coefficients are assigned to the separated tissue types in MRI-based AC, meaning that, contrary to CT AC maps (*26*), no noise is present in the MRI AC maps. Noise, therefore, does not translate into PET images using MRI-based AC. These differences may affect not only SUVs but also PET radiomic features and, thus, comparability between PET/MRI- and PET/CT-based metrics. Figure 3 clearly illustrates the clustering of radiomic features (represented by the top 3 principal components) to the different scanners in the unharmonized datasets. ComBat decreased or resolved this scanner-specific clustering and improved organ-specific

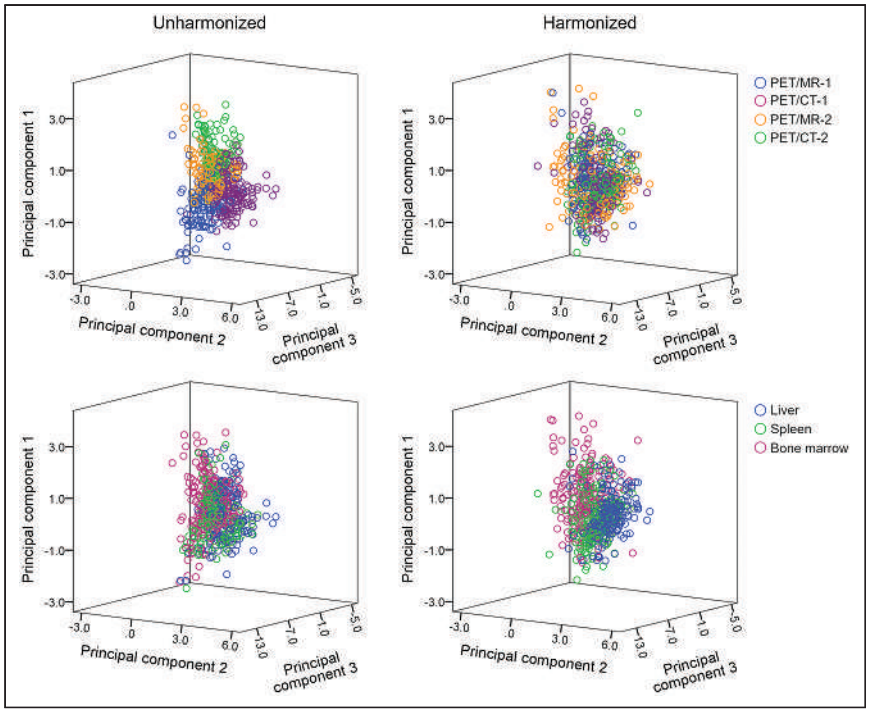

FIGURE 3. Three-dimensional scatterplots showing obvious scanner-specific clustering within unharmonized dataset, which is decreased or resolved in harmonized dataset. Conversely, clustering according to tissue type (liver, spleen, and bone marrow) is improved in harmonized dataset; in particular, liver cluster (blue) is now clearly visible.

clustering, leading to higher classification accuracies in both the 3-tissue and the 4-tissue models (Tables 1 and 2). Notably, there was an imbalance between PET/MRI and PET/CT in terms of accuracies, with PET/MRI data showing slightly lower accuracies than PET/CT in the unharmonized datasets and clearly lower accuracies after harmonization (Supplemental Table 3)—that is, the benefit of ComBat application was greater for PET/CT than for PET/MRI.

We used an MLP-NN for tissue classification, which—though a long-established machine learning algorithm—is not as commonly used in radiomics research as are other algorithms. However, MLP-NN has often yielded better results than other, more popular techniques, such as random forests (*27–31*). The use of MLP-NN also enabled us to explore the impact of an additional hidden layer on classification results, which led to slight but statistically nonsignificant improvement of results. Although we cannot rule out that other algorithms might have achieved even better classification accuracy, it seems unlikely that the choice of a different algorithm would have affected our main result, that is, that ComBat

TABLE 2
Tissue Classification Based on Radiomic Feature Classes and Signatures in 4-Tissue Model

	Unharmonized		Harmonized		
Classification accuracy	Median	Range	Median	Range	*P*
Gray-level histogram					
Training	46.3	44.8–48.9	56.1	53.6–60.4	0.043
Validation	45.8	42.5–49.2	53.8	46.3–56.3	0.043
Gray-level cooccurrence matrix					
Training	43.4	37.5–46.1	62.7	60.5–64.3	0.043
Validation	39.2	36.7–41.7	57.5	50.8–65.0	0.042
Gray-level run-length matrix					
Training	46.3	43.4–47.1	63.0	57.3–64.5	0.042
Validation	41.7	40.4–47.9	59.2	52.5–61.7	0.043
Gray-level size-zone matrix					
Training	43.4	41.4–43.8	86.0	83.0–87.5	0.043
Validation	39.6	36.3–42.9	82.5	68.8–85.0	0.043
Neighborhood gray-tone difference matrix					
Training	42.1	39.6–45.0	62.7	60.0–64.3	0.043
Validation	42.5	36.7–46.7	61.3	57.1–65.8	0.043
Radiomic signature					
Training	51.6	48.2–56.6	82.1	80.0–86.3	0.042
Validation	48.8	42.9–50.8	81.3	67.5–82.9	0.043

Data are percentages.

improves tissue classification in technically heterogeneous datasets. The retrospective design of our study together with our use of clinical PET scans (for which raw data were not stored in our institutions) precluded us from using more uniform image acquisition and reconstruction settings. Although this technical heterogeneity within pooled PET data from different institutions reflects clinical reality, use of predefined, more uniform imaging protocols, such as in prospective multicenter studies, is likely to decrease the impact of ComBat harmonization or even make its use unnecessary.

CONCLUSION

Our data suggest that radiomics studies using pooled ^{18}F-FDG PET data from PET/MRI and PET/CT devices are feasible and should apply ComBat harmonization as a preprocessing step, at least in retrospective technically heterogeneous datasets, as well as prospectively if no uniform imaging protocol is implemented. We expect this strategy to improve the generalizability of results and facilitate the development of radiomics-based applications for use in clinical practice.

DISCLOSURE

This research was funded in part through NIH/NCI Cancer Center support grant P30 CA008748. Marius Mayerhoefer received speaker honoraria from Siemens, GE, and Bristol-Myers Squibb. Heiko Schöder received honoraria from Aileron Therapeutics for a consultancy. No other potential conflict of interest relevant to this article was reported.

KEY POINTS

QUESTION: Is ComBat harmonization useful in pooled PET/MRI and PET/CT radiomic data?

PERTINENT FINDINGS: ComBat improves PET radiomics-based tissue classification for both individual radiomic feature classes and multiclass radiomic signatures.

IMPLICATIONS FOR PATIENT CARE: ComBat harmonization should be applied in multicenter radiomics studies using pooled PET/MRI and PET/CT data.

REFERENCES

1. Aerts HJ, Velazquez ER, Leijenaar RT, et al. Decoding tumour phenotype by noninvasive imaging using a quantitative radiomics approach. *Nat Commun.* 2014;5:4006.
2. Gillies RJ, Kinahan PE, Hricak H. Radiomics: images are more than pictures, they are data. *Radiology.* 2016;278:563–577.
3. Mayerhoefer ME, Materka A, Langs G, et al. Introduction to radiomics. *J Nucl Med.* 2020;61:488–495.
4. Zwanenburg A. Radiomics in nuclear medicine: robustness, reproducibility, standardization, and how to avoid data analysis traps and replication crisis. *Eur J Nucl Med Mol Imaging.* 2019;46:2638–2655.
5. Orlhac F, Boughdad S, Philippe C, et al. A postreconstruction harmonization method for multicenter radiomic studies in PET. *J Nucl Med.* 2018;59:1321–1328.
6. Lucia F, Visvikis D, Vallières M, et al. External validation of a combined PET and MRI radiomics model for prediction of recurrence in cervical cancer patients treated with chemoradiotherapy. *Eur J Nucl Med Mol Imaging.* 2019;46:864–877.
7. Mayerhoefer ME, Riedl CC, Kumar A, et al. Radiomic features of glucose metabolism enable prediction of outcome in mantle cell lymphoma. *Eur J Nucl Med Mol Imaging.* 2019;46:2760–2769.
8. Ferreira M, Lovinfosse P, Hermesse J, et al. [^{18}F]FDG PET radiomics to predict disease-free survival in cervical cancer: a multi-scanner/center study with external validation. *Eur J Nucl Med Mol Imaging.* 2021;48:3432–3443.
9. Dissaux G, Visvikis D, Da-Ano R, et al. Pretreatment ^{18}F-FDG PET/CT radiomics predict local recurrence in patients treated with stereotactic body radiotherapy for early-stage non-small cell lung cancer: a multicentric study. *J Nucl Med.* 2020;61:814–820.
10. Hotta M, Minamimoto R, Gohda Y, et al. Prognostic value of ^{18}F-FDG PET/CT with texture analysis in patients with rectal cancer treated by surgery. *Ann Nucl Med.* 2021;35:843–852.
11. Mayerhoefer ME, Riedl CC, Kumar A, et al. [^{18}F]FDG-PET/CT radiomics for prediction of bone marrow involvement in mantle cell lymphoma: a retrospective study in 97 patients. *Cancers (Basel).* 2020;12:1138.
12. Martinez-Möller A, Souvatzoglou M, Delso G, et al. Tissue classification as a potential approach for attenuation correction in whole-body PET/MRI: evaluation with PET/CT data. *J Nucl Med.* 2009;50:520–526.
13. Vuong D, Tanadini-Lang S, Huellner MW, et al. Interchangeability of radiomic features between [^{18}F]-FDG PET/CT and [^{18}F]-FDG PET/MR. *Med Phys.* 2019;46:1677–1685.
14. Tsujikawa T, Tsuyoshi H, Kanno M, et al. Selected PET radiomic features remain the same. *Oncotarget.* 2018;9:20734–20746.
15. Kanoun S, Tal I, Berriolo-Riedinger A, et al. Influence of software tool and methodological aspects of total metabolic tumor volume calculation on baseline [^{18}F]FDG PET to predict survival in Hodgkin lymphoma. *PLoS One.* 2015;10:e0140830.
16. Zwanenburg A, Vallières M, Abdalah MA, et al. The image biomarker standardization initiative: standardized quantitative radiomics for high-throughput image-based phenotyping. *Radiology.* 2020;295:328–338.
17. van Griethuysen JJM, Fedorov A, Parmar C, et al. Computational radiomics system to decode the radiographic phenotype. *Cancer Res.* 2017;77:e104–e107.
18. Yip SSF, Parmar C, Kim J, Huynh E, Mak RH, Aerts HJWL. Impact of experimental design on PET radiomics in predicting somatic mutation status. *Eur J Radiol.* 2017;97:8–15.
19. LeCun Y, Bengio Y, Hinton G. Deep learning. *Nature.* 2015;521:436–444.
20. Johnson WE, Li C, Rabinovic A. Adjusting batch effects in microarray expression data using empirical Bayes methods. *Biostatistics.* 2007;8:118–127.
21. Orlhac F, Frouin F, Nioche C, Ayache N, Buvat I. Validation of a method to compensate multicenter effects affecting CT radiomics. *Radiology.* 2019;291:53–59.
22. Orlhac F, Lecler A, Savatovski J, et al. How can we combat multicenter variability in MR radiomics? Validation of a correction procedure. *Eur Radiol.* 2021;31:2272–2280.
23. Da-Ano R, Masson I, Lucia F, et al. Performance comparison of modified ComBat for harmonization of radiomic features for multicenter studies. *Sci Rep.* 2020;10:10248.
24. Rausch I, Rust P, Difranco MD, et al. Reproducibility of MRI Dixon-based attenuation correction in combined PET/MR with applications for lean body mass estimation. *J Nucl Med.* 2016;57:1096–1101.
25. Aznar MC, Sersar R, Saabye J, et al. Whole-body PET/MRI: the effect of bone attenuation during MR-based attenuation correction in oncology imaging. *Eur J Radiol.* 2014;83:1177–1183.
26. Hsiao IT, Gindi G. Noise propagation from attenuation correction into PET reconstructions. *IEEE Trans Nucl Sci.* 2002;49:90–97.
27. Yun J, Park JE, Lee H, Ham S, Kim N, Kim HS. Radiomic features and multilayer perceptron network classifier: a robust MRI classification strategy for distinguishing glioblastoma from primary central nervous system lymphoma. *Sci Rep.* 2019;9:5746.
28. Hyun SH, Ahn MS, Koh YW, Lee SJ. A machine-learning approach using PET-based radiomics to predict the histological subtypes of lung cancer. *Clin Nucl Med.* 2019;44:956–960.
29. Sun T, Wang J, Li X, et al. Comparative evaluation of support vector machines for computer aided diagnosis of lung cancer in CT based on a multi-dimensional data set. *Comput Methods Programs Biomed.* 2013;111:519–524.
30. Mao B, Ma J, Duan S, Xia Y, Tao Y, Zhang L. Preoperative classification of primary and metastatic liver cancer via machine learning-based ultrasound radiomics. *Eur Radiol.* 2021;31:4576–4586.
31. Vukicevic AM, Milic V, Zabotti A, et al. Radiomics-based assessment of primary Sjögren's syndrome from salivary gland ultrasonography images. *IEEE J Biomed Health Inform.* 2020;24:835–843.

CALL FOR ABSTRACTS

If you are a young professional in the field, we invite you to a submit clinical or scientific abstract for the **2023 SNMMI Mid-Winter and ACNM Annual Meeting** on one of the following topics:

- Aspects of Clinical and Basic Science in Nuclear Medicine
- Correlative Imaging in Nuclear Medicine and Radiology
- Nuclear Pharmacy and Physics
- Nuclear Cardiology
- Theranostics
- Quality and Safety in Nuclear Medicine

2023 ACNM Annual Meeting Abstract AWARDS

Learn more about award opportunities available when you submit your abstract for the 2023 ACNM Annual Meeting.

ABSTRACT SUBMISSION DEADLINE:

OCTOBER 12, 2022

www.snmmi.org/MWM2023

JANUARY 26-28

2023

SNMMI 2023 Mid-Winter Meeting

ACNM ANNUAL MEETING

SNMMI MID-WINTER AND ACNM ANNUAL MEETING

San Francisco

SNMMI Designated Radiopharmaceutical Therapy Centers of Excellence

SNMMI designated centers meet strict regulatory, training, qualification, experience, and performance criteria to help assure patients, their families, referring physicians, and payors that rigorous procedures are in place and followed, leading to appropriate patient selection and outcomes from radiopharmaceutical therapy.

THE FOLLOWING SITES HAVE BEEN DESIGNATED AS SNMMI RADIOPHARMACEUTICAL THERAPY CENTERS OF EXCELLENCE:

CLINICAL CENTERS OF EXCELLENCE

- ARA Theranostics Center
- ChristianaCare
- Excel Diagnostics and Nuclear Oncology Center
- Hoag Memorial Hospital Presbyterian
- Kettering Health Main Campus
- Northwestern Memorial Hospital

COMPREHENSIVE CENTERS OF EXCELLENCE

- Ahmanson Translational Theranostics Division, David Geffen School of Medicine at UCLA, UCLA Heath Medical Center
- Dana-Farber /Brigham and Women's Cancer Center
- Duke University Health
- Emory University Hospital
- M Health Fairview University of Minnesota Medical Center - East Bank Hospital
- Mayo Clinic
- Medstar Georgetown University Hospital
- MD Anderson Cancer Center
- Memorial Sloan Kettering Cancer Center
- Mount Sinai Health System
- SSM Saint Louis University Hospital
- Stanford University - Stanford HealthCare
- The Ohio State University Wexner Medical Center - The James Hospital and Solove Research Institute
- University of California, San Francisco
- University of Colorado Anschutz Medical Center
- University of Iowa
- University of Pittsburgh Medical Center (UPMC)
- University of Wisconsin - Madison

SNMMI is currently accepting applications from centers based in the United States (its territories) and Canada.

Visit **www.snmmi.org/RPTCoE** to get started.

SNMMI Value Initiative
SOCIETY OF NUCLEAR MEDICINE & MOLECULAR IMAGING

NOW AVAILABLE

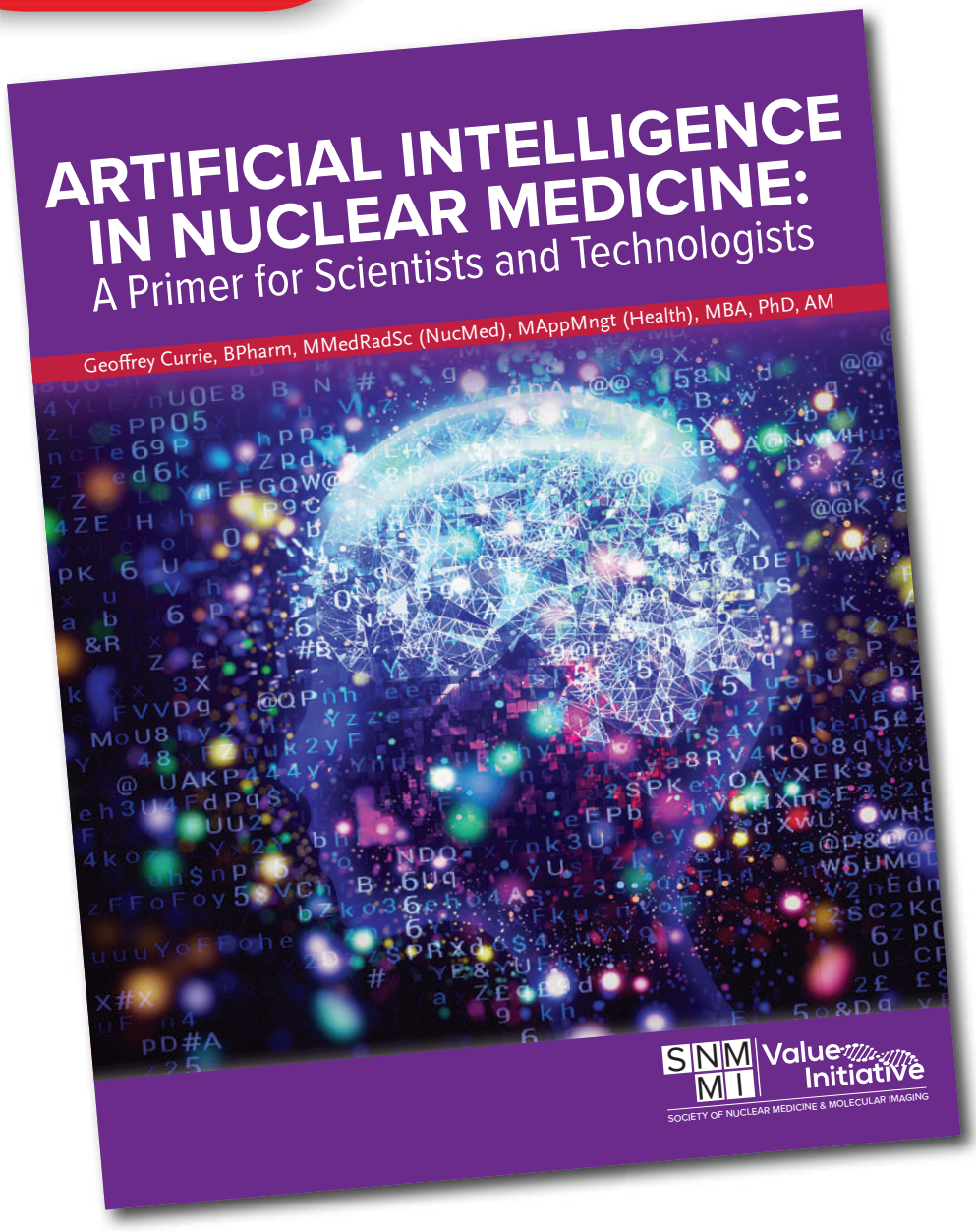

Artificial Intelligence in Nuclear Medicine: A Primer for Scientists and Technologists provides a grounding in how artificial intelligence, artificial neural networks, machine learning, and deep learning work; how their capabilities improve outcomes; how and where they should be integrated into your clinical and research practice; and the challenges and considerations involved in their implementation.

Grab your copy today!

www.snmmi.org/AIbook

Streamlined. Simple. Accurate.

CRC® Dose Calibrator Family

Combine the speed and accuracy you need to measure and prepare doses with the performance and reliability that you've come to expect in one of the industry's finest packages.

CRC® - PC Smart Chamber
Network Ready with Remote Connectivity
The Most Advanced in Dose Calibration.

CRC®-55tPET Dose Calibrator (Touch Screen)
Speed and accuracy to measure
and prepare doses.

Driving Innovation... Together

Two leading brands of nuclear medicine products and technology, the **Capintec™** and **Biodex™** teams have joined forces under Mirion Medical.

CAPINTEC
A MIRION MEDICAL COMPANY

OPS-4306 - 07/22

Visit capintec.com to learn how we can support your unique requirements.

10/22

The Journal of Nuclear Medicine

October 2022 ▪ Vol. 63 ▪ Pages 1455–1616